

ISTANBUL TECHNICAL UNIVERSITY ★ GRADUATE SCHOOL OF SCIENCE
ENGINEERING AND TECHNOLOGY

**SEISMIC BEHAVIOR OF RC COLUMNS WITH CORRODED
PLAIN AND DEFORMED REINFORCING BARS**

Ph.D. THESIS
Çağlar GÖKSU

Department of Civil Engineering
Structure Engineering Programme

JANUARY 2012

ISTANBUL TECHNICAL UNIVERSITY ★ GRADUATE SCHOOL OF SCIENCE
ENGINEERING AND TECHNOLOGY

**SEISMIC BEHAVIOR OF RC COLUMNS WITH CORRODED
PLAIN AND DEFORMED REINFORCING BARS**

Ph.D.Thesis

**Çağlar GÖKSU
(501042002)**

Department of Civil Engineering

Structure Engineering Programme

Thesis Advisor: Prof. Dr. Alper İLKİ

JANUARY 2012

İSTANBUL TEKNİK ÜNİVERSİTESİ ★ FEN BİLİMLERİ ENSTİTÜSÜ

**KOROZYONA UĞRAMIŞ DÜZ VE NERVÜRLÜ DONATILI BETONARME
KOLONLARIN DEPREM YÜKLERİ ALTINDA DAVRANIŞI**

**DOKTORA TEZİ
Çağlar GÖKSU
(501042002)**

İnşaat Mühendisliği Anabilim Dalı

Yapı Mühendisliği Programı

Tez Danışmanı : Prof.Dr. Alper İLKİ

OCAK 2012

Çağlar GÖKSU, a Ph.D. student of ITU Graduate School of 501042002, successfully defended the dissertation entitled “SEISMIC BEHAVIOR OF RC COLUMNS WITH CORRODED PLAIN AND DEFORMED REINFORCING BARS”, which she prepared after fulfilling the requirements specified in the associated legislations, before the jury whose signatures are below.

Thesis Advisor : **Prof. Dr. Alper İLKİ**
İstanbul Technical University

Jury Members : **Prof. Dr. Hulusi ÖZKUL**
İstanbul Technical University

Assoc.Prof. Dr. Şevket ÖZDEN
Kocaeli University

Prof. Dr. Zekai CELEP
İstanbul Technical University

Prof. Dr. Abdurrahman GÜNER
Istanbul University

Date of Submission : 10 September 2011

Date of Defense : 25 January 2012

FOREWORD

I would like to thank to Prof.Dr. Alper İLKİ for his guidance with his whole knowledge and experiences in every aspect of this thesis. It was great chance and honour for me to complete the thesis under his supervision.

I would like to thank to Prof. Dr. Hulusi ÖZKUL and Assoc.Prof.Dr. Şevket ÖZDEN for their interest during the thesis and being member of the PhD examining committee.

I would like to thank to Prof.Dr. Zekai CELEP, Prof.Dr. Abdurrahman GÜNER and Prof.Dr. Nahit KUMBASAR for their advices.

I am grateful to Res.Assist. Cem DEMİR, Bahadır DEMİRTAŞ (M.Sc.), Ergün BİNBİR (M.Sc.), Res.Assist. Mustafa CÖMERT, Deniz Korhan DALGIÇ (M.Sc.), Pınar İNCİ (M.Sc.) and Aygül AYDOĞMUŞ (B.Sc.) for their significant contributions during the experimental phase of this thesis.

I would like to thank to Assoc.Prof.Dr. Kutlu DARILMAZ and Assist.Prof.Dr. Kutay ORAKÇAL for their significant contributions during the theoretical phase of this thesis.

I would like to thank to the staff of Structural and Earthquake Engineering and Building Materials Laboratories for their hard work and technical assistances. I would like to thank to Assoc.Prof.Dr. Yılmaz AKKAYA and the staff at ITU Marmaray Laboratory for optical microscope, Prof.Dr. Rüstem ASLAN and the staff at ITU ROTAM for 3D scanner and Prof.Dr. Mustafa ÜRGEN, Behiye YÜKSEL (PhD.) and the staff at ITU Corrosion Laboratory for corrosion cleaning process.

I am grateful to ITU Scientific Research Department (Scientific Research Project No:32794), Telateks Textile Company, Nuh Concrete Co., and Oyak Concrete Co. for financial support.

Special thanks to my dear parents (Mehmet GÖKSU and Raziye GÖKSU) for emotional and financial support throughout my whole life.

January 2012

Çağlar GÖKSU

TABLE OF CONTENTS

	<u>Page</u>
TABLE OF CONTENTS	ix
LIST OF FIGURES	xxi
SUMMARY	xxxvii
ÖZ	xxxix
1. INTRODUCTION	1
2. CORROSION	3
2.1 Reinforced Concrete and Corrosion.....	3
2.2 Mechanism of Reinforcement Corrosion	4
2.3 Chloride Induced Corrosion.....	4
2.4 Carbonation Induced Corrosion	5
2.5 Effects of Corrosion on Structural Capacity of Reinforced Concrete.....	6
2.6 Corrosion Products.....	6
2.7 Corrosion Measurements	7
2.7.1 Half-cell potential method.....	7
2.7.2 Linear polarization method	8
2.8 Accelerated Corrosion Process	9
3. OVERVIEW of LITERATURE	11
3.1 Studies on the Effect of Corrosion on Mechanical Properties of Reinforcing Bars	11
3.2 Studies on the Flexural Behavior of RC Members with Corroded Reinforcement	14
3.3 Studies on the Effect of Corrosion on Bond	14
3.4 Studies on Corrosion Monitoring of RC Members	18
3.5 A Review of Relevant Codes and Standards on Corrosion of Reinforcing Bars	18
3.6 A Review of Shear Strength Degradation with Displacement Ductility.....	19
4. EXPERIMENTAL DESIGN	21
4.1 Design of Specimens.....	21
4.1.1 First type specimens.....	21
4.1.2 Second type specimens	23
4.1.3 Third type specimen.....	25
4.2 Shear Strength	25
4.2.1 First and third type specimens	25
4.2.2 Second type specimens	27
4.2.3 Shear strength degradation with displacement ductility	28
4.2.4 Calculation of lap splice length for the first and the third type specimens (TS500, 2000)	29
4.2.5 Calculation of lap splice length for the second type specimens (TS500, 2000)	31
4.3 Test setup	32
4.3.1 Testing Procedure.....	32

4.3.2 Instrumentation.....	33
4.3.2.1 LVDTs.....	34
4.3.2.2 Straingauges	34
4.4 Loading History.....	39
5. SPECIMEN PREPARATION	41
5.1 Footings	41
5.2 Columns	42
6. TEST RESULTS	45
6.1 Test Results of Materials.....	45
6.1.1 Concrete	45
6.1.2 Reinforcing bars	47
6.2 Test Result of the First Type Specimens	48
6.2.1 LS-X0	48
6.2.2 LS-X6.....	55
6.2.3 LS-X8	61
6.2.4 LS-X12.....	68
6.2.5 LS-X21	75
6.2.6 LS-X28	82
6.3 Test Result of the Second Type Specimens.....	89
6.3.1 NS-X0.....	89
6.3.2 NS-X9.....	95
6.3.3 NS-X13.....	102
6.3.4 NS-X16.....	109
6.3.5 NS-X22.....	116
6.3.6 NS-X54.....	123
6.4 Test Result of the Third Type Specimen.....	129
6.4.1 LS-X19-H.....	129
6.5 Test Results of Uniaxial Tension Tests.....	136
6.5.1 Mechanical characteristics of corroded deformed reinforcing bars	139
6.6 Summary of the Section	146
7. OVERALL EVALUATION OF TEST RESULTS	147
7.1 Test Results of the First and the Third Type Specimens.....	147
7.2 Test Results of the Second Type Specimens.....	156
7.3 Contribution of Displacement Components to the Lateral Displacement of Columns	164
8. ANALYTICAL STUDY	171
8.1 The Effect of Bond Mechanism on the Seismic Performance of Low Strength RC Columns with Corroded Plain Reinforcing Bars.....	171
8.2 Analytical Study on the Seismic Performance of Normal Strength RC Columns with Corroded Deformed Reinforcing Bars	178
8.2.1 Analyzed member	178
8.2.2 Analytical procedure	181
8.2.3 Comparison with experimental data.....	183
8.3 An Analytical study on RC Frame Building with Corroded Deformed Reinforcing Bars	189
8.3.1 Analyzed building	189
8.3.2 Analytical procedure	190
8.3.2.1 Moment-rotation relationships	190
8.3.2.2 Pushover analysis	194
8.3.2.3 Determination of the Seismic Performance Level of the Building ..	196

8.3.2.4 Nonlinear Time History Analysis	224
9. CONCLUSIONS	227
REFERENCES.....	231
APPENDICES.....	237
CURRICULUM VITAE.....	495

ABBREVIATIONS

a_1	: Modal acceleration
a	: Constant
A_0	: Effective ground acceleration coefficient
A	: Area of polarized reinforcing steel
$A(T)$: Spectral acceleration coefficient
A_w	: Atomic weight
b	: Tafel slope
C_{R1}	: Spectral displacement amplification factor for the first mode
d	: Lateral displacement of the tip of the column
e	: Eccentricity due to horizontal displacement of the column
E_c	: Elasticity modulus of concrete
E_{corr}	: Corrosion potential
F	: Faraday's constant
F_y	: Yield strength of corroded bars
F_{max}	: Maximum strength of corroded bars
F_u	: Ultimate strength of corroded bars
F_{y0}	: Yield strength of uncorroded reinforcing bars
F_{max0}	: Maximum strength of uncorroded reinforcing bars
F_{u0}	: Ultimate strength of uncorroded reinforcing bars
f'_c	: Average compressive strength of concrete
f_{ck}	: Characteristic compressive strength of concrete
f_r	: Relative rib area
f_{yd}	: Design yield strength of the reinforcing bars
f_{ctd}	: Design tensile strength of the concrete
G	: Shear modulus
G	: Dead load
GV	: Safety limit
GC	: Collapsing limit
h	: Polarization
h	: Effective depth
H	: Column height
I	: Moment of inertia
I	: Building importance factor
i_{corr}	: Corrosion current density
I_{corr}	: Corrosion current
L	: Column height
l_{PL}	: Plastic hinge length of the column
l_o	: Lap splice length
l_b	: Anchorage length
m	: Mass of metal dissolved
m_N	: Lumped story mass
M	: Moment
M_0	: Theoretical flexural capacity

MN	: Minimum Damage Limit
M_{y1}	: Effective modal mass in y direction
n	: Valency
n	: Live load participation factor
N_k	: Axial load capacity
P	: Applied lateral load
P_0	: Theoretical lateral load capacity of the specimen ignoring corrosion
P_{max}	: Maximum lateral load
Q	: Live load
Q_{corr1}	: Ratio of the maximum cross-section loss to the original cross-section is an indicator for the maximum local loss of cross-section (maximum pit)
Q_{corr2}	: Ratio of average cross-section loss to the original cross-section, is an indicator for the average loss of cross-section throughout the length of reinforcing bars
R_p	: Polarization resistance
R_y	: Seismic load reduction factor in y direction
$S(T)$: Spectrum coefficient
S_{ae}	: Elastic spectral acceleration in y direction
S_{de}	: Linear elastic spectral displacement in y direction
S_{di}	: Nonlinear spectral displacement demand in y direction
s	: Stirrup spacing
t	: Time
T_1	: Period of a building at the first mode
T_A, T_B	: Soil characteristic spectral periods
U_{yN}	: Top displacement
V_y	: Base shear force
V_n	: Nominal shear strength
V_c	: Contribution to nominal shear strength from concrete
V_s	: Contribution to nominal shear strength from transverse reinforcement
x	: Attack penetration (bar radius reduction)
x_{PL}	: Average plastic curvature
χ_p	: Plastic curvature
χ_T	: Total curvature
χ_y	: Equivalent yield curvature
ω_1	: Circular frequency for the first mode
δ_d	: Lateral deviation
$\delta_{elastic}$: Elastic displacement
$\delta_{plastic}$: Ultimate plastic displacement
$\delta@P_{max}$: Lateral displacement corresponding to maximum lateral load
δ_{res}	: Residual displacement
δ_{shear}	: Displacement due to shear
δ_{un}	: Displacement at which unloading began
δ_u	: Ultimate displacement
ΔE	: Change in potential
ΔI	: Change in current
α	: Rib inclination
β	: Rib face angle
μ_δ	: Displacement ductility factor
ν	: Poisson's ratio
ρ_s	: Existing volumetric ratio of transverse reinforcement of column

- ρ_{sm} : Required volumetric ratio of transverse reinforcement of column
 θ_{pl} : Plastic rotation of the assumed plastic hinge
 ϵ_c : Strain demand of unconfined concrete
 ϵ_{cc} : Strain demand of confined concrete
 ϵ_s : Strain demand of reinforcing bar
 Φ_{N1} : Mode shape vector for the first mode at $(N)^{th}$ story in y direction
 $\Theta_{plastic}$: Plastic rotation demands
 Γ_{y1} : Participation factor for the first mode at $(N)^{th}$ story in y direction

LIST OF TABLES

	<u>Page</u>
Table 4.1 : Properties of the first type specimens.	23
Table 4.2 : Properties of the second type specimens.	24
Table 4.3 : Properties of the third type specimens.	25
Table 4.4 : Required lap splice lengths for smooth reinforcing bars according to design strengths of materials and experimentally determined material strengths (TS500, 2000).	31
Table 4.5 : Properties of surface strain gauges.	37
Table 4.6 : Properties of strain gauges on the starter bars.	37
Table 4.7 : Properties of strain gauges on the longitudinal bars.	37
Table 4.8 : Properties of strain gauges on the transverse bars.	37
Table 4.9 : Properties of specimens.	40
Table 4.10 : Properties of specimens.	40
Table 6.1 : Concrete mix constituents for the footings of the first and the third type specimens.	45
Table 6.2 : Concrete mix constituents for the columns of the first and the third type specimens.	45
Table 6.3 : Concrete mix constituents for the columns of the second type specimens.	46
Table 6.4 : The mechanical characteristics of reinforcing bars.	47
Table 6.5 : Summary of the seismic behavior of LS-X0.	50
Table 6.6 : Summary of the seismic behavior of LS-X6.	58
Table 6.7 : Summary of the seismic behavior of LS-X8.	64
Table 6.8 : Width, location and orientation of the cracks.	68
Table 6.9 : Summary of the seismic behavior of LS-X12.	71
Table 6.10 : Width, location and orientation of the cracks.	75
Table 6.11 : Summary of the seismic behavior of LS-X21.	78
Table 6.12 : Width, location and orientation of the cracks.	82
Table 6.13 : Summary of the seismic behavior of LS-X28.	85
Table 6.14 : Summary of the seismic behavior of NS-X0.	92
Table 6.15 : Summary of the seismic behavior of NS-X9.	99
Table 6.16 : Summary of the seismic behavior of NS-X13.	105
Table 6.17 : Width, location and orientation of the cracks.	109
Table 6.18 : Summary of the seismic behavior of NS-X16.	113
Table 6.19 : Width, location and orientation of the cracks.	116
Table 6.20 : Summary of the seismic behavior of NS-X22.	120
Table 6.21 : Width, location and orientation of the cracks.	123
Table 6.22 : Summary of the seismic behavior of NS-X54.	126
Table 6.23 : Width, location and orientation of the cracks.	129
Table 6.24 : Summary of the seismic behavior of LS-X19-H.	133

Table 6.25	: The average values of standard deviations and variation coefficients of ratios of predicted/measured mechanical characteristics.	145
Table 7.1	: Failure mechanisms of the first and the third type specimens (The numbers given in Table are the drift ratios).	154
Table 7.2	: Test results of the first and the third type specimens.	155
Table 7.3	: Failure mechanisms of specimens (The numbers given in Table are the drift ratios).	164
Table 7.4	: Test results of the second type specimens.	164
Table 8.1	: Moment-curvature and stress-strain relationships of Point A and B of ... Specimen LS-X21.	176
Table 8.2	: Moment-curvature and stress-strain relationships of Point A and B of ... Specimen LS-X28.	177
Table 8.3	: Elastic and plastic deformations of the hypothetical columns.	181
Table 8.4	: Properties of the tested pieces.	184
Table 8.5	: Analytical moment-curvature and stress-strain relationships of Point A, B and C.	187
Table 8.6	: Properties of the columns.	191
Table 8.7	: Definition of damage limits (TSDC, 2007).	199
Table 8.8	: The parameters used in determining of performance levels of buildings.	199
Table 8.9	: Total curvature demand of base columns of S0 building.	201
Table 8.10	: Damage regions for base columns of S0 building.	202
Table 8.11	: Total curvature demand of base columns of S10-3 building.	204
Table 8.12	: Damage regions for base columns of S10-3 building.	205
Table 8.13	: Total curvature demand of base columns of S10-6 building.	206
Table 8.14	: Damage regions for base columns of S10-6 building.	207
Table 8.15	: Total curvature demand of base columns of S10-12 building.	208
Table 8.16	: Damage regions for base columns of S10-12 building.	209
Table 8.17	: Total curvature demand of base columns of S20-3 building.	210
Table 8.18	: Damage regions for base columns of S20-3 building.	211
Table 8.19	: Total curvature demand of base columns of S20-6 building.	212
Table 8.20	: Damage regions for base columns of S20-6 building.	213
Table 8.21	: Total curvature demand of base columns of S20-12 building.	214
Table 8.22	: Damage regions for base columns of S20-12 building.	215
Table 8.23	: Total curvature demand of base columns of S30-3 building.	216
Table 8.24	: Damage regions for base columns of S30-3 building.	217
Table 8.25	: Total curvature demand of base columns of S30-6 building.	218
Table 8.26	: Damage regions for base columns of S30-6 building.	219
Table 8.27	: Total curvature demand of base columns of S30-12 building.	220
Table 8.28	: Damage regions for base columns of S30-12 building.	221
Table 8.29	: Strain values of K1 and K2 columns of S30-3 and S30-6 buildings.	224
Table 8.30	: Earthquake records.	225
Table B.1	: Distance between the concrete surface of the columns and the LVDTs.	247
Table C.1	: Crack propagation of LS-X0 while pushing.	248
Table C.2	: Crack propagation of LS-X0 while pulling.	249
Table C.3	: Crack propagation of LS-X6 while pushing.	250
Table C.4	: Crack propagation of LS-X6 while pulling.	251
Table C.5	: Crack propagation of LS-X8 while pushing.	252
Table C.6	: Crack propagation of LS-X8 while pulling.	254

Table C.7	: Crack propagation of LS-X12 while pushing.....	256
Table C.8	: Crack propagation of LS-X12 while pulling.	258
Table C.9	: Crack propagation of LS-X21 while pushing.....	260
Table C.10	: Crack propagation of LS-X21 while pulling.	261
Table C.11	: Crack propagation of LS-X28 while pushing.....	262
Table C.12	: Crack propagation of LS-X28 while pulling.	263
Table C.13	: Crack propagation of NS-X0 while pushing.....	264
Table C.14	: Crack propagation of NS-X0 while pulling.	265
Table C.15	: Crack propagation of NS-X9 while pushing.....	266
Table C.16	: Crack propagation of NS- X9 while pulling.....	268
Table C.17	: Crack propagation of NS-X13 while pushing.....	270
Table C.18	: Crack propagation of NS-X13 while pulling.	271
Table C.19	: Crack propagation of NS-X16 while pushing.....	272
Table C.20	: Crack propagation of NS-X16 while pulling.....	273
Table C.21	: Crack propagation of NS-X22 while pushing.....	274
Table C.22	: Crack propagation of NS-X22 while pulling.	275
Table C.23	: Crack propagation of NS-X54 while pushing.....	276
Table C.24	: Crack propagation of NS-X54 while pulling.....	277
Table C.25	: Crack propagation of LS-X19-H while pushing.....	278
Table C.26	: Crack propagation of LS-X19-H while pulling.	279
Table İ.1	: Damage regions for base columns of S0 building for SYLMAR,1994.....	477
Table İ.2	: Damage regions for base columns of S10-12 building for SYLMAR, 1994.....	478
Table İ.3	: Damage regions for base columns of S0 building for DUZCE, 1999	479
Table İ.4	: Damage regions for base columns of S10-12 building for DUZCE, ... 1999.....	480
Table İ.5	: Damage regions for base columns of S0 building for BİNGÖL,..... 2003.....	481
Table İ.6	: Damage regions for base columns of S10-12 building for BİNGÖL, . 2003.....	482
Table İ.7	: Damage regions for base columns of S0 building for MEXICO, 1980.....	483
Table İ.8	: Damage regions for base columns of S10-12 building for MEXICO, 1980.....	484
Table İ.9	: Damage regions for base columns of S0 building for KOBE, 1995.... 485	
Table İ.10	: Damage regions for base columns of S10-12 building for KOBE, 1995.....	486
Table İ.11	: Damage regions for base columns of S0 building for KOCAELİ, 1999.....	487
Table İ.12	: Damage regions for base columns of S10-12 building for KOCAELİ, 1999.. ..	488

LIST OF FIGURES

	<u>Page</u>
Figure 2.1	: Variations in the cross-sectional shape of pits: a) Narrow, deep, b) .. Elliptical, c) Wide, shallow, d) Subsurface, e) Undercutting, f1) Microstructural orientation, horizontal, f2) Microstructural orientation, vertical (ASTM-G46-94, 1994)..... 5
Figure 2.2	: Relative volumes of iron and its reaction product (Mansfeld, 1981). 7
Figure 2.3	: Copper-copper sulfate half cell circuitry (ASTM C876-99). 8
Figure 2.4	: General appearance of columns, the accelerated corrosion setup and measurement of corrosion potential. 10
Figure 4.1	: Theoretical moment-curvature relationships of the first type..... specimens. 22
Figure 4.2	: Theoretical moment-curvature relationships of the second type specimens. 24
Figure 4.3	: Theoretical moment-curvature relationships of third type specimen. 25
Figure 4.4	: The relationship of the shear strength degradation with displacement ductility and lateral load-displacement interaction of the first and third type specimens. 29
Figure 4.5	: Test setup (Demirtaş, 2008). 33
Figure 4.6	: Preparation of specimen for the test: (a) Maintaining the specimen to the adaptor footing, (b) Axial load setup, (c) Placement of post tensioning tendons. 33
Figure 4.7	: The location of the LVDTs. 34
Figure 4.8	: (a) Cleaning the surfaces of the reinforcing bars from rust with grindstone, (b) Gluing the straingauges on the reinforcing bars, (c) ... Application of the isolation material (N-1), (d) Wrapping with VM- . tape isolation strap. 35
Figure 4.9	: Location of the straingauges (a) at the starter bars, and (b) at longitudinal and transverse bars. 35
Figure 4.10	: The locations of the surface straingauges. 36
Figure 4.11	: The location of the straingauges: (a) the first and the third type specimens, and (b) the second type specimens. 38
Figure 4.12	: Loading history of (a) the first and the third type specimens, (b) the . second type specimens. 39
Figure 5.1	: Views from preparation of footing: (a) Steel molds, (b) Wood molds, (c) Hooks and PVC pipes, (d) Placement of concrete to footing, (e) Curing application. 41
Figure 5.2	: Preparation of columns (a) Chipping at the interface, (b) Bonding straingauges to the starter bars, (c) Placement of plastic spacers for .. concrete cover, (d) Placement of molds. 42

Figure 5.3	: Preparation of columns: (a) Application of curing to the columns, (b) Preparation of standard cylinder specimens, (c) Addition of CaCl_2 to the concrete.	43
Figure 5.4	: The first, the second and the third type specimens.	44
Figure 6.1	: The 28, 90, 180, 360 day compressive strength and elasticity modulus values of the first and the third type specimens.	46
Figure 6.2	: The 28, 180, 360 day compressive strength and elasticity modulus values of the second type specimens.	46
Figure 6.3	: Stress-strain relationships of a) longitudinal bars ($\phi 14$) and b) transverse bars ($\phi 8$) of S220.	47
Figure 6.4	: Stress-strain relationships of a) longitudinal bars ($\phi 14$) and b) transverse bars ($\phi 8$) of S420.	47
Figure 6.5	: a) North, and b) South view of the LS-X0 specimen after -0.50% drift ratio.	48
Figure 6.6	: a) North, and b) South view of the LS-X0 specimen after -1.50% drift ratio.	48
Figure 6.7	: a) North, and b) South view of the LS-X0 specimen after -2.50% drift ratio.	49
Figure 6.8	: a) North, and b) South view of the LS-X0 specimen after -3.50% drift ratio.	49
Figure 6.9	: a) North, and b) South view of the LS-X0 specimen after -5.00% drift ratio.	50
Figure 6.10	: Lateral load/Theoretical load capacity versus displacement for LS-X0.	51
Figure 6.11	: Test setup with measurement system used in obtaining moment-curvature relationship.	52
Figure 6.12	: Moment-curvature relationships obtained for a) 0-20 mm, b) 20-150 mm, c) 150-300 mm gauge lengths.	53
Figure 6.13	: Strain distribution of the starter bars of LS-X0 a) while pushing, b) while pulling.	54
Figure 6.14	: Strain distribution of the longitudinal bars of LS-X0 a) while pushing b) while pulling.	54
Figure 6.15	: a) North, and b) South view of the LS-X6 specimen after -0.50% drift ratio.	55
Figure 6.16	: a) North, and b) South view of the LS-X6 specimen after -1.50% drift ratio.	56
Figure 6.17	: a) North, and b) South view of the LS-X6 specimen after -2.50% drift ratio.	56
Figure 6.18	: a) North, and b) South view of the specimen LS-X6 after -3.50% drift ratio.	57
Figure 6.19	: a) North, and b) South view of the specimen LS-X6 after -6.00% drift ratio.	57
Figure 6.20	: Lateral load/Theoretical load capacity versus displacement for LS-X6.	58
Figure 6.21	: Moment-curvature relationships obtained for a) 20 mm, b) 150 mm, c) 300 mm gauge lengths.	59
Figure 6.22	: Strain distribution of the starter bars of LS-X6 a) while pushing, b) while pulling.	60
Figure 6.23	: Strain distribution of the longitudinal bars of LS-X6 a) while pushing b) while pulling.	61

Figure 6.24	: Pattern of cracks formed due to corrosion: (a) North, (b) South.	61
Figure 6.25	: a) North, and b) South view of the specimen LS-X8 after -0.50% drift ratio.....	62
Figure 6.26	: a) North, and b) South view of the specimen LS-X8 after -1.50% drift ratio.....	62
Figure 6.27	: a) North, and b) South view of the LS-X8 specimen after -2.50% drift ratio.....	63
Figure 6.28	: a) North, and b) South view of the LS-X8 specimen after -3.50% drift ratio.....	63
Figure 6.29	: a) North, and b) South view of the LS-X8 specimen after -4.00% drift ratio.....	64
Figure 6.30	: Lateral load/Theoretical load capacity versus displacement for LS-X8.....	65
Figure 6.31	: Moment-curvature relationships obtained for a) 0-20 mm, b) 20-150 mm, c) 150-300 mm gauge lengths.....	66
Figure 6.32	: Strain distribution of the starter bars of LS-X8 a) while pushing, b) while pulling.	67
Figure 6.33	: Strain distribution of the longitudinal bars of LS-X8 a) while pushing b) while pulling.	67
Figure 6.34	: Pattern of cracks formed due to corrosion: (a) North, (b) South.	68
Figure 6.35	: a) North, and b) South view of the specimen LS-X12 after -0.10% drift ratio.....	69
Figure 6.36	: a) North, and b) South view of the specimen LS-X12 after -1.50% drift ratio.....	70
Figure 6.37	: a) North, and b) South view of the LS-X12 specimen after -2.50% drift ratio.....	70
Figure 6.38	: a) North, and b) South view of the specimen LS-X12 after -3.00% drift ratio.....	71
Figure 6.39	: Lateral load/Theoretical load capacity versus displacement for LS-X12.....	72
Figure 6.40	: Moment-curvature relationships obtained for a) 0-20 mm, b) 20-150 mm, c) 150-300 mm gauge lengths.....	73
Figure 6.41	: Strain distribution of the starter bars of LS-X12 a) while pushing, b) while pulling.	74
Figure 6.42	: Strain distribution of the longitudinal bars of LS-X12 a) while pushing b) while pulling.	74
Figure 6.43	: Pattern of cracks formed due to corrosion: (a) North, (b) South.	75
Figure 6.44	: a) North, and b) South view of the specimen LS-X21 after -0.10% drift ratio.....	76
Figure 6.45	: a) North, and b) South view of the specimen LS-X21 after -1.50% drift ratio.....	77
Figure 6.46	: a) North, and b) South view of the LS-X21 specimen after -2.50% drift ratio.....	77
Figure 6.47	: a) North, and b) South view of the LS-X21 specimen after -3.00% drift ratio.....	78
Figure 6.48	: Lateral load/Theoretical load capacity versus displacement for LS-X21.....	79
Figure 6.49	: Moment-curvature relationships obtained for a) 0-20 mm, b) 20-150 mm, c) 150-300 mm gauge lengths.....	80

Figure 6.50	: Strain distribution of the starter bars of LS-X21 a) while pushing, b) while pulling.....	81
Figure 6.51	: Strain distribution of the longitudinal bars of LS-X21 a) while pushing b) while pulling.....	81
Figure 6.52	: Pattern of cracks formed due to corrosion: (a) North, (b) South.	82
Figure 6.53	: The appearances of existing sub-standard RC frame structures.	83
Figure 6.54	: a) North, and b) South view of the LS-X28 specimen after -0.10% drift ratio.....	83
Figure 6.55	: a) North, and b) South view of the LS-X28 specimen after -1.50% drift ratio.....	84
Figure 6.56	: a) North, and b) South view of the LS-X28 specimen after -2.50% drift ratio.....	84
Figure 6.57	: a) North, and b) South view of the LS-X28 specimen after -3.50% drift ratio.....	85
Figure 6.58	: Lateral load/Theoretical load capacity versus displacement for LS-X28.....	86
Figure 6.59	: Moment-curvature relationships obtained for a) 0-20 mm, b) 20-150 mm, c) 150-300 mm gauge lengths.....	87
Figure 6.60	: Strain distribution of the starter bars of LS-X28 a) while pushing, b) while pulling.....	88
Figure 6.61	: Strain distribution of the longitudinal bars of LS-X28 a) while pushing b) while pulling.....	88
Figure 6.62	: a) North, and b) South view of the NS-X0 specimen after -0.50% drift ratio.....	89
Figure 6.63	: a) North, and b) South view of the NS-X0 specimen after -1.50% drift ratio.....	90
Figure 6.64	: a) North, and b) South view of the NS-X0 specimen after -2.50% drift ratio.....	90
Figure 6.65	: a) North, and b) South view of the NS-X0 specimen after 6.00% drift ratio.....	91
Figure 6.66	: Lateral load/Theoretical load capacity versus displacement for the specimen NS-X0.	92
Figure 6.67	: Moment-curvature relationships obtained for a) 0-20 mm, b) 20-150 mm, c) 150-300 mm gauge lengths.....	93
Figure 6.68	: Strain distribution of the starter bars of NS-X0 a) while pushing, b) while pulling.....	94
Figure 6.69	: Strain distribution of the longitudinal bars of NS-X0 a) while pushing b) while pulling.....	95
Figure 6.70	: a) North, and b) South view of the NS-X9 specimen after -0.50% drift ratio.....	95
Figure 6.71	: a) North, and b) South view of the NS-X9 specimen after -1.50% drift ratio.....	96
Figure 6.72	: a) North, and b) South view of the specimen NS-X9 after -2.50% drift ratio.....	97
Figure 6.73	: a) North, and b) South view of the specimen NS-X9 after -3.50% drift ratio.....	97
Figure 6.74	: a) North, and b) South view of the specimen NS-X9 after 8.00% drift ratio.....	98
Figure 6.75	: Lateral load/Theoretical load capacity versus displacement for NS-X9.....	99

Figure 6.76	: Moment-curvature relationships obtained for a) 0-20 mm, b) 20-150 mm, c) 150-300 mm gauge lengths.....	100
Figure 6.77	: Strain distribution of the starter bars of NS-X9 a) while pushing, b) while pulling.	101
Figure 6.78	: Strain distribution of the longitudinal bars of NS-X9 a) while pushing b) while pulling.	102
Figure 6.79	: a) North, and b) South view of the specimen NS-X13 after -0.50% drift ratio.....	102
Figure 6.80	: a) North, and b) South view of the specimen NS-X13 after -1.50% drift ratio.....	103
Figure 6.81	: a) North, and b) South view of the specimen NS-X13 after 2.50% drift ratio.....	104
Figure 6.82	: a) North, and b) South view of the specimen NS-X13 after -3.50% drift ratio.....	104
Figure 6.83	: a) North, and b) South view of the specimen NS-X13 after -6.00% drift ratio.....	105
Figure 6.84	: Lateral load/Theoretical load capacity versus displacement for NS-X13.....	106
Figure 6.85	: Moment-curvature relationships obtained for a) 0-20 mm, b) 20-150 mm, c) 150-300 mm gauge lengths.....	107
Figure 6.86	: Strain distribution of the starter bars of NS-X13 a) while pushing, b) while pulling.	108
Figure 6.87	: Strain distribution of the longitudinal bars of NS-X13 a) while pushing b) while pulling.	108
Figure 6.88	: Pattern of cracks formed due to corrosion: (a) North, (b) South. ..	109
Figure 6.89	: a) North, and b) South view of the specimen NS-X16 after -0.25% drift ratio.....	110
Figure 6.90	: a) North, and b) South view of the NS-X16 specimen after -1.50% drift ratio.....	111
Figure 6.91	: a) North, and b) South view of the specimen NS-X16 after -2.50% drift ratio.....	111
Figure 6.92	: a) North, and b) South view of the specimen NS-X16 after -3.50% drift ratio.....	112
Figure 6.93	: a) North, and b) South view of the NS-X16 specimen after -5.00% drift ratio.....	112
Figure 6.94	: Lateral load/Theoretical load capacity versus displacement for NS-X16.....	114
Figure 6.95	: Moment-curvature relationships obtained for a) 20 mm, b) 150 mm, c) 300 mm gauge lengths.	115
Figure 6.96	: Strain distribution of the starter bars of NS-X16 a) while pushing, b) while pulling.	116
Figure 6.97	: Strain distribution of the longitudinal bars of NS-X16 a) while pushing b) while pulling.	116
Figure 6.98	: Pattern of cracks formed due to corrosion: (a) North, (b) South. ..	117
Figure 6.99	: a) North, and b) South view of the NS-X22 specimen after -0.75% drift ratio.....	117
Figure 6.100	: a) North, and b) South view of the NS-X22 specimen after -1.50% drift ratio.....	118
Figure 6.101	: a) North, and b) South view of the NS-X22 specimen after -2.50% drift ratio.....	118

Figure 6.102	: a) North, and b) South view of the NS-X22 specimen after -3.50% ... drift ratio.....	119
Figure 6.103	: a) North, and b) South view of the specimen NS-X22 after -6.00% ... drift ratio.....	119
Figure 6.104	: Lateral load/Theoretical load capacity versus displacement for NS-... X22.	121
Figure 6.105	: Moment-curvature relationships obtained for a) 0-20 mm, b) 20-150 mm, c) 150-300 mm gauge lengths.	122
Figure 6.106	: Strain distribution of the starter bars of NS-X22 a) while pushing, b) while pulling.....	123
Figure 6.107	: Strain distribution of the longitudinal bars of NS-X22 a) while pushing b) while pulling.....	123
Figure 6.108	: Pattern of cracks formed due to corrosion: (a) North, (b) South....	124
Figure 6.109	: a) North, and b) South view of the specimen NS-X54 after -1.00% ... drift ratio.....	124
Figure 6.110	: a) North, and b) South view of the NS-X54 specimen after -2.50% ... drift ratio.....	125
Figure 6.111	: a) North, and b) South view of the NS-X54 specimen after -5.00% ... drift ratio.....	125
Figure 6.112	: Lateral load/Theoretical load capacity versus displacement for NS-... X54.	127
Figure 6.113	: Moment-curvature relationships obtained for a) 20 mm, b) 150 mm, c) 300 mm gauge lengths.	128
Figure 6.114	: Strain distribution of the starter bars of NS-X54 a) while pushing, b) while pulling.....	129
Figure 6.115	: Strain distribution of the longitudinal bars of NS-X54 a) while pushing b) while pulling.....	129
Figure 6.116	: Pattern of cracks formed due to corrosion: (a) North, (b) South....	130
Figure 6.117	: a) North, and b) South view of the specimen LS-X19-H after -0.10% drift ratio.....	130
Figure 6.118	: a) North, and b) South view of the specimen LS-X19-H after -2.00% drift ratio.....	131
Figure 6.119	: a) North, and b) South view of the specimen LS-X19-H after -3.00% drift ratio.....	131
Figure 6.120	: a) North, and b) South view of the specimen LS-X19-H after -4.00% drift ratio.....	132
Figure 6.121	: a) North, and b) South view of the LS-X19-H specimen after -5.00% drift ratio.....	133
Figure 6.122	: Lateral load/Theoretical load capacity versus displacement for LS-... X19-H.	134
Figure 6.123	: Moment-curvature relationships obtained for a) 20 mm, b) 150 mm, c) 300 mm gauge lengths.	135
Figure 6.124	: Strain distribution of the starter bars of LS-X19-H a) while pushing, b) while pulling.	136
Figure 6.125	: Strain distribution of the longitudinal bars of LS-X19-H a) while pushing b) while pulling.....	136
Figure 6.126	: Cleaning process of corroded reinforcement removed from reinforced concrete test specimens.....	137
Figure 6.127	: The test setup and a fractured bar after the test.....	138
Figure 6.128	: ATOS 3D optical scanner.	138

Figure 6.129	: Variation of a,b) Yield strength, c,d) Maximum strength, e,f) Ultimate strength g,h) Apparent yield stress, i,j) Apparent maximum stress, k,l) Apparent ultimate stress, m,n) Effective yield stress, o,p) Effective maximum stress, r,s) Effective ultimate stress t,u) Ultimate strain with respect to maximum and average cross-section losses.....	142
Figure 7.18	: Displacement components against total displacements of the second type specimens a) NS-X0, b) NS-X9, c) NS-X13, d) NS-X16, e) NS-X22, f) NS-X54.....	168
Figure 8.1	: Bond stress variation with corrosion level.....	171
Figure 8.2	: SAP 2000 models used in analytical predictions a) Single bar model with link elements for slip dominated specimens, b) Column model for flexure dominated specimens.	173
Figure 8.3	: Analytical bond stress-slip relationship a) CEB-FIB, 1990 model, b) Proposed model.....	173
Figure 8.4	: Experimental and analytical considerations of slip dominated specimens.	174
Figure 8.5	: Experimental and analytical considerations of the first type specimens.	175
Figure 8.6	: Comparison of proposed model with the experimental results.....	178
Figure 8.7	: Column model taken into account for parametric analysis.....	179
Figure 8.8	: Idealized corrosion patterns of the columns.	180
Figure 8.9	: Moment-curvature relationships of the hypothetical columns by BAKE (2000).	181
Figure 8.10	: Theoretical load-displacement relationships of the hypothetical columns.	183
Figure 8.11	: Locations of the plastic hinge and lumped elastic rotations.	185
Figure 8.12	: Analytical and experimental lateral load-displacement relationships of a) Uncorroded and b) Corroded specimens.	186
Figure 8.13	: Experimental moment-curvature and stress-strain relationships corresponding to Point A, B and C.	188_Toc321953449
Figure 8.14	: a) A typical floor plan of the building, b) Properties and reinforcing cage of columns (Note: Dimensions are in mm units).	189
Figure 8.15	: Moment-curvature relationships of cross sections of (a) 30×80 cm for 10% axial load level, (b) 30×80 cm for 5% axial load level, (c) 65×65 cm for 10% axial load level, (d) 65×65 cm for 5% axial load level with different cross-section losses.....	192
Figure 8.16	: The assumed dimensions of the pits on a typical reinforcing bar of column (Dimension units in mm).	193
Figure 8.17	: Moment-rotation relationships for the plastic hinges of the columns.	194
Figure 8.18	: Base shear-drift ratio relationships for the structures as a function of section loss of reinforcing bars and number of corrosion pits.	195
Figure 8.19	: The damage regions of sections (TSDC, 2007).	199
Figure 8.20	: Modal capacity diagram and elastic demand spectrum relationship.	200
Figure 8.21	: Capacity curve of S0 building.	201
Figure 8.22	: Modal capacity diagram and elastic demand spectrum relationship.	203
Figure 8.23	: Capacity curve of S10-3.	203

Figure 8.24	: a) Modal capacity diagram and elastic demand spectrum relationship, b) Capacity curve of S10-6.....	206
Figure 8.25	: a) Modal capacity diagram and elastic demand spectrum relationship, b) Capacity curve of S10-12.....	208
Figure 8.26	: a) Modal capacity diagram and elastic demand spectrum relationship, b) Capacity curve of S20-3.....	210
Figure 8.27	: a) Modal capacity diagram and elastic demand spectrum relationship, b) Capacity curve of S20-6.....	212
Figure 8.28	: a) Modal capacity diagram and elastic demand spectrum relationship, b) Capacity curve of S20-12.....	214
Figure 8.29	: a) Modal capacity diagram and elastic demand spectrum relationship, b) Capacity curve of S30-3.....	216
Figure 8.30	: a) Modal capacity diagram and elastic demand spectrum relationship, b) Capacity curve of S30-6.....	218
Figure 8.31	: a) Modal capacity diagram and elastic demand spectrum relationship, b) Capacity curve of S30-12.....	220
Figure 8.32	: Damage levels of base columns of S0, S10-3, S10-6 and S10-12..... buildings.....	222
Figure 8.33	: Damage levels of base columns of S0, S20-3, S20-6 and S20-12 buildings.....	223
Figure 8.34	: Damage levels of base columns of S0, S30-3, S30-6 and S30-12 buildings.....	223
Figure 8.35	: a) Main aspects of inelastic behavior, b) Pattern of cyclic moment-..... rotation relationships assigned to potential plastic hinges (PERFORM- 3D, 2007).	225
Figure A.1	: Reinforcing cage of the first type specimens (south side).....	238
Figure A.2	: Reinforcing cage of the first type specimens (east side).	239
Figure A.3	: Details of reinforcing cage of the first type specimens.	240
Figure A.4	: Reinforcing cage of the second type specimens (south side).	241
Figure A.5	: Reinforcing cage of the second type specimens (east side).....	242
Figure A.6	: Details of reinforcing cage of the second type specimens.....	243
Figure A.7	: Reinforcing cage of the third type specimens (south side).....	244
Figure A.8	: Reinforcing cage of the third type specimens (east side).	245
Figure A.9	: Details of reinforcing cage of the third type specimens.	246
Figure D.1	: LS-X0.	282
Figure D.2	: LS-X6.	284
Figure D.3	: LS-X8.	287
Figure D.4	: LS-X12.	289
Figure D.5	: LS-X21.	291
Figure D.6	: LS-X28.	293
Figure D.7	: LS-X19-H.	296
Figure D.8	: NS-X0.	299
Figure D.9	: NS-X9.....	301
Figure D.10	: NS-X13.....	303
Figure D.11	: NS-X22.....	306
Figure D.12	: NS-X16.....	309
Figure D.13	: NS-X54.....	311
Figure E.1	: a) North, and b) South view of LS-X0 after -0.5% drift ratio.	314
Figure E.2	: Crack pattern of LS-X0 after -0.5% drift ratio.	314
Figure E.3	: a) North, and (b) south view of LS-X0 after -0.75% drift ratio.	315

Figure E.4	: Crack pattern of LS-X0 after -0.75% drift ratio.	315
Figure E.5	: a) North, and b) South view of LS-X0 after -1% drift ratio.	316
Figure E.6	: Crack pattern of LS-X0 after -1% drift ratio.	316
Figure E.7	: a) North, and b) South view of LS-X0 after -1.5% drift ratio.	317
Figure E.8	: Crack pattern of LS-X0 after -1.5% drift ratio.	317
Figure E.9	: a) North, and b) South view of specimen LS-X0 after -2% drift ratio.	318
Figure E.10	: Crack pattern of LS-X0 after -2% drift ratio.	318
Figure E.11	: a) North, and b) South view of LS-X0 after -2.5% drift ratio.	319
Figure E.12	: Crack pattern of LS-X0 after -2.5% drift ratio.	319
Figure E.13	: a) North, and b) South view of LS-X0 after -3% drift ratio.	320
Figure E.14	: Crack pattern of LS-X0 after -3% drift ratio.	320
Figure E.15	: a) North, and b) South view of LS-X0 after -3.5% drift ratio.	321
Figure E.16	: Crack pattern of LS-X0 after 3.5% drift ratio.	321
Figure E.17	: a) North, and b) South view of LS-X0 after -4% drift ratio.	322
Figure E.18	: Crack pattern of LS-X0 after -4% drift ratio.	322
Figure E.19	: a) North, and b) South view of LS-X0 after -4.5% drift ratio.	323
Figure E.20	: Crack pattern of LS-X0 after -4.5% drift ratio.	323
Figure E.21	: a) North, and b) South view of LS-X0 after -5% drift ratio.	324
Figure E.22	: Crack pattern of LS-X0 after -5% drift ratio.	324
Figure E.23	: a) North, and b) South view of LS-X6 after -0.5% drift ratio.	325
Figure E.24	: Crack pattern of LS-X6 after -0.5% drift ratio.	325
Figure E.25	: a) North, and b) South view of LS-X6 after -1% drift ratio.	326
Figure E.26	: Crack pattern of LS-X6 after -1% drift ratio.	326
Figure E.27	: a) North, and b) South view of LS-X6 after -1.5% drift ratio.	327
Figure E.28	: Crack pattern of LS-X6 after -1.5% drift ratio.	327
Figure E.29	: a) North, and b) South view of LS-X6 after -2% drift ratio.	328
Figure E.30	: Crack pattern of LS-X6 after -2% drift ratio.	328
Figure E.31	: a) North, and (b) South view of LS-X6 after -2.5% drift ratio.	329
Figure E.32	: Crack pattern of LS-X6 after -2.5% drift ratio.	329
Figure E.33	: a) North, and b) South view of LS-X6 after -3% drift ratio.	330
Figure E.34	: Crack pattern of LS-X6 after -3% drift ratio.	330
Figure E.35	: a) North, and b) South view of LS-X6 after -3.5% drift ratio.	331
Figure E.36	: Crack pattern of LS-X6 after -3.5% drift ratio.	331
Figure E.37	: a) North, and b) South view of LS-X6 after -4% drift ratio.	332
Figure E.38	: Crack pattern of LS-X6 after -4% drift ratio.	332
Figure E.39	: a) North, and b) South view of LS-X6 after -4.5% drift ratio.	333
Figure E.40	: Crack pattern of LS-X6 after -4.5% drift ratio.	333
Figure E.41	: a) North, and b) South view of LS-X6 after -5% drift ratio.	334
Figure E.42	: Crack pattern of LS-X6 after -5% drift ratio.	334
Figure E.43	: a) North, and (b) South view of LS-X8 after -0.25% drift ratio.	335
Figure E.44	: Crack pattern of LS-X8 after -0.25% drift ratio.	335
Figure E.45	: (a) North, and (b) South view of LS-X8 after -0.5% drift ratio.	336
Figure E.46	: Crack pattern of LS-X8 after -0.5% drift ratio.	336
Figure E.47	: a) North, and b) South view of LS-X8 after -0.75% drift ratio.	337
Figure E.48	: Crack pattern of LS-X8 after -0.75% drift ratio.	337
Figure E.49	: a) North, and b) South view of LS-X8 after -1% drift ratio.	338
Figure E.50	: Crack pattern of LS-X8 after -1% drift ratio.	338
Figure E.51	: (a) North, and (b) South view of LS-X8 after -1.5% drift ratio.	339
Figure E.52	: Crack pattern of LS-X8 after -1.5% drift ratio.	339

Figure E.53 : (a) North, and (b) South view of LS-X8 after -2% drift ratio.	340
Figure E.54 : Crack pattern of LS-X8 after -2% drift ratio.	340
Figure E.55 : a) North, and b) South view of LS-X8 after -2.5% drift ratio.	341
Figure E.56 : Crack pattern of LS-X8 after -2.5% drift ratio.	341
Figure E.57 : a) North, and b) South view of LS-X8 after -3% drift ratio.	342
Figure E.58 : Crack pattern of LS-X8 after -3% drift ratio.	342
Figure E.59 : a) North, and b) South view of LS-X8 after -3.5% drift ratio.	343
Figure E.60 : Crack pattern of LS-X8 after -3.5% drift ratio.	343
Figure E.61 : a) North, and b) South view of LS-X8 after -4% drift ratio.	344
Figure E.62 : Crack pattern of LS-X8 after -4% drift ratio.	344
Figure E.63 : a) North, and b) South view of LS-X12 after -0.1% drift ratio.	345
Figure E.64 : Crack pattern of LS-X12 after -0.1% drift ratio.	345
Figure E.65 : a) North, and b) South view of LS-X12 after -0.25% drift ratio.	346
Figure E.66 : Crack pattern of LS-X12 after -0.25% drift ratio.	346
Figure E.67 : a) North, and b) South view of LS-X12 after -0.5% drift ratio.	347
Figure E.68 : Crack pattern of LS-X12 after -0.5% drift ratio.	347
Figure E.69 : a) North, and b) South view of LS-X12 after -0.75% drift ratio.	348
Figure E.70 : Crack pattern of LS-X12 after -0.75% drift ratio.	348
Figure E.71 : a) North, and b) South view of LS-X12 after -1% drift ratio.	349
Figure E.72 : Crack pattern of LS-X12 after -1% drift ratio.	349
Figure E.73 : a) North, and b) South view of LS-X12 after -1.5% drift ratio.	350
Figure E.74 : Crack pattern of LS-X12 after -1.5% drift ratio.	350
Figure E.75 : a) North, and b) South view of LS-X12 after -2% drift ratio.	351
Figure E.76 : Crack pattern of LS-X12 after -2% drift ratio.	351
Figure E.77 : a) North, and b) South view of LS-X12 after -2.5% drift ratio.	352
Figure E.78 : Crack pattern of LS-X12 after -2.5% drift ratio.	352
Figure E.79 : a) North, and b) South view of LS-X12 after -3% drift ratio.	353
Figure E.80 : Crack pattern of LS-X12 after -3% drift ratio.	353
Figure E.81 : a) North, and b) South view of LS-X21 after -0.1% drift ratio.	354
Figure E.82 : Crack pattern of LS-X21 after -0.1% drift ratio.	354
Figure E.83 : a) North, and b) South view of LS-X21 after -0.25% drift ratio.	355
Figure E.84 : Crack pattern of LS-X21 after -0.25% drift ratio.	355
Figure E.85 : a) North, and b) South view of LS-X21 after -0.5% drift ratio.	356
Figure E.86 : Crack pattern of LS-X21 after -0.5% drift ratio.	356
Figure E.87 : a) North, and b) South view of LS-X21 after -0.75% drift ratio.	357
Figure E.88 : Crack pattern of LS-X21 after -0.75% drift ratio.	357
Figure E.89 : a) North, and b) South view of LS-X21 after -1% drift ratio.	358
Figure E.90 : Crack pattern of LS-X21 after -1% drift ratio.	358
Figure E.91 : (a) North, and (b) South view of LS-X21 after -1.5% drift ratio.	359
Figure E.92 : Crack pattern of LS-X21 after -1.5% drift ratio.	359
Figure E.93 : a) North, and b) South view of LS-X21 after -2% drift ratio.	360
Figure E.94 : Crack pattern of LS-X21 after -2% drift ratio.	360
Figure E.95 : a) North, and b) South view of LS-X21 after -2.5% drift ratio.	361
Figure E.96 : Crack pattern of LS-X21 after -2.5% drift ratio.	361
Figure E.97 : a) North, and b) South view of LS-X21 after -3% drift ratio.	362
Figure E.98 : Crack pattern of LS-X21 after -3% drift ratio.	362
Figure E.99 : a) North, and b) South view of LS-X28 after -0.1% drift ratio.	363
Figure E.100 : Crack pattern of LS-X28 after -0.1% drift ratio.	363
Figure E.101 : a) North, and b) South view of LS-X28 after -0.25% drift ratio.	364
Figure E.102 : Crack pattern of LS-X28 after -0.25% drift ratio.	364

Figure E.103 :	a) North, and b) South view of LS-X28 after -0.5% drift ratio....	365
Figure E.104 :	Crack pattern of LS-X28 after -0.5% drift ratio.....	365
Figure E.105 :	a) North, and b) South view of LS-X28 after -0.75% drift ratio..	366
Figure E.106 :	Crack pattern of LS-X28 after -0.75% drift ratio.....	366
Figure E.107 :	a) North, and b) South view of LS-X28 after -1% drift ratio.....	367
Figure E.108 :	Crack pattern of LS-X28 after -1% drift ratio.....	367
Figure E.109 :	a) North, and b) South view of LS-X28 after -1.5% drift ratio....	368
Figure E.110 :	Crack pattern of LS-X28 after -1.5% drift ratio.....	368
Figure E.111 :	a) North, and b) South view of LS-X28 after -2% drift ratio.....	369
Figure E.112 :	Crack pattern of LS-X28 after -2% drift ratio.....	369
Figure E.113 :	a) North, and b) South view of LS-X28 after -2.5% drift ratio....	370
Figure E.114 :	Crack pattern of LS-X28 after -2.5% drift ratio.....	370
Figure E.115 :	a) North, and b) South view of LS-X28 after -3% drift ratio.....	371
Figure E.116 :	Crack pattern of LS-X28 after -3% drift ratio.....	371
Figure E.117 :	a) North, and b) South view of LS-X19-H after -0.1% drift ratio.	372
Figure E.118 :	Crack pattern of LS-X19-H after -0.1% drift ratio.	372
Figure E.119 :	a) North, and b) South view of LS-X19-H after -0.25% drift ratio. ...	373
Figure E.120 :	Crack pattern of LS-X19-H after -0.25% drift ratio.	373
Figure E.121 :	a) North, and b) South view of LS-X19-H after -0.5% drift ratio.	374
Figure E.122 :	Crack pattern of LS-X19-H after -0.5% drift ratio.	374
Figure E.123 :	a) North, and b) South view of LS-X19-H after -0.75% drift ratio. ...	375
Figure E.124 :	Crack pattern of LS-X19-H after -0.75% drift ratio.	375
Figure E.125 :	a) North, and b) South view of LS-X19-H after -1% drift ratio. .	376
Figure E.126 :	Crack pattern of LS-X19-H after -1% drift ratio.	376
Figure E.127 :	a) North, and b) South view of LS-X19-H after -1.5% drift ratio.	377
Figure E.128 :	Crack pattern of LS-X19-H after -1.5% drift ratio.	377
Figure E.129 :	a) North, and b) South view of LS-X19-H after -2% drift ratio. .	378
Figure E.130 :	Crack pattern of LS-X19-H after -2% drift ratio.	378
Figure E.131 :	a) North, and b) South view of LS-X19-H after -2.5% drift ratio.	379
Figure E.132 :	Crack pattern of LS-X19-H after -2.5% drift ratio.	379
Figure E.133 :	a) North, and b) South view of LS-X19-H after -3% drift ratio. .	380
Figure E.134 :	Crack pattern of LS-X19-H after -3% drift ratio.	380
Figure E.135 :	a) North, and b) South view of LS-X19-H after -3.5% drift ratio.	381
Figure E.136 :	Crack pattern of LS-X19-H after -3.5% drift ratio.	381
Figure E.137 :	a) North, and b) South view of LS-X19-H after -4% drift ratio. .	382
Figure E.138 :	Crack pattern of LS-X19-H after -4% drift ratio.	382
Figure E.139 :	a) North, and b) South view of LS-X19-H after -4.5% drift ratio.	383
Figure E.140 :	Crack pattern of LS-X19-H after -4.5% drift ratio.	383
Figure E.141 :	a) North, and b) South view of LS-X19-H after -5% drift ratio. .	384
Figure E.142 :	Crack pattern of LS-X19-H after -5% drift ratio.	384
Figure E.143 :	(a) North, and (b) South view of NS-X0 after -0.1% drift ratio. .	385
Figure E.144 :	Crack pattern of NS-X0 after -0.1% drift ratio.	385

Figure E.145: a) North, and b) South view of NS-X0 after -0.25% drift ratio.....	386
Figure E.146: Crack pattern of NS-X0 after -0.25% drift ratio.....	386
Figure E.147: a) North, and b) South view of NS-X0 after -0.5% drift ratio.....	387
Figure E.148: Crack pattern of NS-X0 after -0.5% drift ratio.....	387
Figure E.149: a) North, and b) South view of NS-X0 after -0.75% drift ratio.....	388
Figure E.150: Crack pattern of NS-X0 after -0.75% drift ratio.....	388
Figure E.151: a) North, and b) South view of NS-X0 after -1% drift ratio.....	389
Figure E.152: Crack pattern of NS-X0 after -1% drift ratio.....	389
Figure E.153: a) North, and b) South view of NS-X0 after 1.5% drift ratio.....	390
Figure E.154: Crack pattern of NS-X0 after -1.5% drift ratio.....	390
Figure E.155: a) North, and b) South view of NS-X0 after -2% drift ratio.....	391
Figure E.156: Crack pattern of NS-X0 after -2% drift ratio.....	391
Figure E.157: a) North, and b) South view of NS-X0 after -2.5% drift ratio.....	392
Figure E.158: Crack pattern of NS-X0 after -2.5% drift ratio.....	392
Figure E.159: a) North, and b) South view of NS-X0 after -3% drift ratio.....	393
Figure E.160: Crack pattern of NS-X0 after -3% drift ratio.....	393
Figure E.161: a) North, and b) South view of NS-X0 after -3.5% drift ratio.....	394
Figure E.162: Crack pattern of NS-X0 after -3.5% drift ratio.....	394
Figure E.163: a) North, and b) South view of NS-X0 after -4% drift ratio.....	395
Figure E.164: Crack pattern of NS-X0 after -4% drift ratio.....	395
Figure E.165: a) North, and b) South view of NS-X0 after -5% drift ratio.....	396
Figure E.166: Crack pattern of NS-X0 after -5% drift ratio.....	396
Figure E.167: a) North, and b) South view of NS-X9 after -0.5% drift ratio.....	397
Figure E.168: Crack pattern of NS-X9 after -0.5% drift ratio.....	397
Figure E.169: a) North, and b) South view of NS-X9 after -0.75% drift ratio.....	398
Figure E.170: Crack pattern of NS-X9 after -0.75% drift ratio.....	398
Figure E.171: a) North, and b) South view of NS-X9 after -1% drift ratio.....	399
Figure E.172: Crack pattern of NS-X9 after -1% drift ratio.....	399
Figure E.173: a) North, and b) South view of NS-X9 after -1.5% drift ratio.....	400
Figure E.174: Crack pattern of NS-X9 after -1.5% drift ratio.....	400
Figure E.175: a) North, and b) South view of NS-X9 after -2% drift ratio.....	401
Figure E.176: Crack pattern of NS-X9 after -2% drift ratio.....	401
Figure E.177: a) North, and b) South view of NS-X9 after -2.5% drift ratio.....	402
Figure E.178: Crack pattern of NS-X9 after -2.5% drift ratio.....	402
Figure E.179: a) North, and b) South view of NS-X9 after -3% drift ratio.....	403
Figure E.180: Crack pattern of NS-X9 after -3% drift ratio.....	403
Figure E.181: a) North, and b) South view of NS-X9 after -3.5% drift ratio.....	404
Figure E.182: Crack pattern of NS-X9 after -3.5% drift ratio.....	404
Figure E.183: a) North, and b) South view of NS-X9 after -4% drift ratio.....	405
Figure E.184: Crack pattern of NS-X9 after -4% drift ratio.....	405
Figure E.185: a) North, and b) South view of NS-X9 after -4.5% drift ratio.....	406
Figure E.186: Crack pattern of NS-X9 after -4.5% drift ratio.....	406
Figure E.187: a) North, and b) South view of NS-X9 after -5% drift ratio.....	407
Figure E.188: Crack pattern of NS-X9 after -5% drift ratio.....	407
Figure E.189: a) North, and b) South view of NS-X9 after -6% drift ratio.....	408
Figure E.190: Crack pattern of NS-X9 after -6% drift ratio.....	408
Figure E.191: a) North, and b) South view of NS-X9 after -7% drift ratio.....	409
Figure E.192: Crack pattern of NS-X9 after -7% drift ratio.....	409
Figure E.193: a) North, and b) South view of NS-X9 after -8% drift ratio.....	410
Figure E.194: Crack pattern of NS-X9 after -8% drift ratio.....	410

Figure E.195: a) North, and b) South view of NS-X13 after -0.1% drift ratio.....	411
Figure E.196: Crack pattern of NS-X13 after -0.1% drift ratio.....	411
Figure E.197: a) North, and b) South view of NS-X13 after -0.25% drift ratio.....	412
Figure E.198: Crack pattern of NS-X13 after -0.25% drift ratio.....	412
Figure E.199: a) North, and b) South view of NS-X13 after -0.5% drift ratio.....	413
Figure E.200: Crack pattern of NS-X13 after -0.5% drift ratio.....	413
Figure E.201: a) North, and b) South view of NS-X13 after -0.75% drift ratio.....	414
Figure E.202: Crack pattern of NS-X13 after -0.75% drift ratio.....	414
Figure E.203: a) North, and b) South view of NS-X13 after -1% drift ratio.....	415
Figure E.204: Crack pattern of NS-X13 after -1% drift ratio.....	415
Figure E.205: a) North, and b) South view of NS-X13 after -1.5% drift ratio.....	416
Figure E.206: Crack pattern of NS-X13 after -1.5% drift ratio.....	416
Figure E.207: a) North, and b) South view of NS-X13 after -2% drift ratio.....	417
Figure E.208: Crack pattern of NS-X13 after -2% drift ratio.....	417
Figure E.209: a) North, and b) South view of NS-X13 after -2.5% drift ratio.....	418
Figure E.210: Crack pattern of NS-X13 after -2.5% drift ratio.....	418
Figure E.211: a) North, and b) South view of NS-X13 after -3% drift ratio.....	419
Figure E.212: Crack pattern of NS-X13 after -3% drift ratio.....	419
Figure E.213: a) North, and b) South view of NS-X13 after -3.5% drift ratio.....	420
Figure E.214: Crack pattern of NS-X13 after -3.5% drift ratio.....	420
Figure E.215: (a) North, and (b) South view of NS-X13 after -4% drift ratio.....	421
Figure E.216: Crack pattern of NS-X13 after -4% drift ratio.....	421
Figure E.217: (a) North, and (b) South view of NS-X13 after -4.5% drift ratio.....	422
Figure E.218: Crack pattern of NS-X13 after -4.5% drift ratio.....	422
Figure E.219: a) North, and b) South view of NS-X13 after -5% drift ratio.....	423
Figure E.220: Crack pattern of NS-X13 after -5% drift ratio.....	423
Figure E.221: a) North, and b) South view of NS-X13 after -6% drift ratio.....	424
Figure E.222: Crack pattern of NS-X13 after -6% drift ratio.....	424
Figure E.223: a) North, and b) South view of NS-X16 after -0.1% drift ratio.....	425
Figure E.224: Crack pattern of NS-X16 after -0.1% drift ratio.....	425
Figure E.225: a) North, and b) South view of NS-X16 after -0.25% drift ratio.....	426
Figure E.226: Crack pattern of NS-X16 after -0.25% drift ratio.....	426
Figure E.227: a) North, and b) South view of NS-X16 after -0.5% drift ratio.....	427
Figure E.228: Crack pattern of NS-X16 after -0.5% drift ratio.....	427
Figure E.229: a) North, and b) South view of NS-X16 after -0.75% drift ratio.....	428
Figure E.230: Crack pattern of NS-X16 after -0.75% drift ratio.....	428
Figure E.231: (a) North, and (b) South view of NS-X16 after -1% drift ratio.....	429
Figure E.232: Crack pattern of NS-X16 after -1% drift ratio.....	429
Figure E.233: a) North, and b) South view of NS-X16 after -1.5% drift ratio.....	430
Figure E.234: Crack pattern of NS-X16 after -1.5% drift ratio.....	430
Figure E.235: a) North, and b) South view of NS-X16 after -2% drift ratio.....	431
Figure E.236: Crack pattern of NS-X16 after -2% drift ratio.....	431
Figure E.237: a) North, and b) South view of NS-X16 after -2.5% drift ratio.....	432
Figure E.238: Crack pattern of NS-X16 after -2.5% drift ratio.....	432
Figure E.239: a) North, and b) South view of NS-X16 after -3% drift ratio.....	433
Figure E.240: Crack pattern of NS-X16 after -3% drift ratio.....	433
Figure E.241: a) North, and b) South view of NS-X16 after -3.5% drift ratio.....	434
Figure E.242: Crack pattern of NS-X16 after -3.5% drift ratio.....	434
Figure E.243: a) North, and b) South view of NS-X16 after -4% drift ratio.....	435
Figure E.244: Crack pattern of NS-X16 after -4% drift ratio.....	435

Figure E.245: a) North, and b) South view of NS-X16 after -4.5% drift ratio.....	436
Figure E.246: Crack pattern of NS-X16 after -4.5% drift ratio.....	436
Figure E.247: a) North, and b) South view of NS-X16 after -5% drift ratio.....	437
Figure E.248: Crack pattern of NS-X16 after -5% drift ratio.....	437
Figure E.249: a) North, and b) South view of NS-X22 after -0.1% drift ratio.....	438
Figure E.250: Crack pattern of NS-X22 after -0.1% drift ratio.....	438
Figure E.251: a) North, and b) South view of NS-X22 after -0.25% drift ratio.....	439
Figure E.252: Crack pattern of NS-X22 after -0.25% drift ratio.....	439
Figure E.253: (a) North, and (b) South view of NS-X22 after -0.5% drift ratio.	440
Figure E.254: Crack pattern of NS-X22 after -0.5% drift ratio.....	440
Figure E.255: a) North, and b) South view of NS-X22 after -0.75% drift ratio.....	441
Figure E.256: Crack pattern of NS-X22 after -0.75% drift ratio.....	441
Figure E.257: a) North, and b) South view of NS-X22 after -1% drift ratio.....	442
Figure E.258: Crack pattern of NS-X22 after -1% drift ratio.....	442
Figure E.259: a) North, and b) South view of NS-X22 after -1.5% drift ratio.....	443
Figure E.260: Crack pattern of NS-X22 after -1.5% drift ratio.....	443
Figure E.261: a) North, and b) South view of NS-X22 after -2% drift ratio.....	444
Figure E.262: Crack pattern of NS-X22 after -2% drift ratio.....	444
Figure E.263: a) North, and b) South view of NS-X22 after -2.5% drift ratio.....	445
Figure E.264: Crack pattern of NS-X22 after -2.5% drift ratio.....	445
Figure E.265: a) North, and b) South view of NS-X22 after -3% drift ratio.....	446
Figure E.266: Crack pattern of NS-X22 after -3% drift ratio.....	446
Figure E.267: a) North, and b) South view of NS-X22 after 3.5% drift ratio.	447
Figure E.268: Crack pattern of NS-X22 after -3.5% drift ratio.....	447
Figure E.269: a) North, and b) South view of NS-X22 after -4% drift ratio.....	448
Figure E.270: Crack pattern of NS-X22 after -4% drift ratio.....	448
Figure E.271: a) North, and b) South view of NS-X22 after -4.5% drift ratio.....	449
Figure E.272: Crack pattern of NS-X22 after -4.5% drift ratio.....	449
Figure E.273: a) North, and b) South view of NS-X22 after -6% drift ratio.....	450
Figure E.274: Crack pattern of NS-X22 after -6% drift ratio.....	450
Figure E.275: (a) North, and (b) South view of NS-X54 after -0.1% drift ratio.	451
Figure E.276: Crack pattern of NS-X54 after -0.1% drift ratio.....	451
Figure E.277: a) North, and b) South view of NS-X54 after -0.25% drift ratio.....	452
Figure E.278: Crack pattern of NS-X54 after -0.25% drift ratio.....	452
Figure E.279: a) North, and b) South view of NS-X54 after -0.5% drift ratio.....	453
Figure E.280: Crack pattern of NS-X54 after -0.5% drift ratio.....	453
Figure E.281: a) North, and b) South view of NS-X54 after -0.75% drift ratio.....	454
Figure E.282: Crack pattern of NS-X54 after -0.75% drift ratio.....	454
Figure E.283: a) North, and b) South view of NS-X54 after -1% drift ratio.....	455
Figure E.284: Crack pattern of NS-X54 after -1% drift ratio.....	455
Figure E.285: a) North, and b) South view of NS-X54 after -1.5% drift ratio.....	456
Figure E.286: Crack pattern of NS-X54 after -1.5% drift ratio.....	456
Figure E.287: a) North, and b) South view of NS-X54 after 2% drift ratio.	457
Figure E.288: Crack pattern of NS-X54 after -2% drift ratio.....	457
Figure E.289: a) North, and b) South view of NS-X54 after -2.5% drift ratio.....	458
Figure E.290: Crack pattern of NS-X54 after -2.5% drift ratio.....	458
Figure E.291: a) North, and b) South view of NS-X54 after -3% drift ratio.	459
Figure E.292: Crack pattern of NS-X54 after -3% drift ratio.....	459
Figure E.293: a) North, and b) South view of NS-X54 after -3.5% drift ratio.....	460
Figure E.294: Crack pattern of NS-X54 after -3.5% drift ratio.....	460

Figure E.295	: a) North, and b) South view of NS-X54 after -4% drift ratio.	461
Figure E.296	: Crack pattern of NS-X54 after -4% drift ratio.	461
Figure E.297	: a) North, and b) South view of NS-X54 after -4.5% drift ratio.	462
Figure E.298	: Crack pattern of NS-X54 after -4.5% drift ratio.	462
Figure E.299	: a) North, and b) South view of NS-X54 after -5% drift ratio.	463
Figure E.300	: Crack pattern of NS-X54 after -5% drift ratio.	463
Figure F.1	: a) Appearance of reinforcing bar taken out from the specimen LS-.... X0, b) Surface condition of the reinforcement bar observed through . an optical stereo microscope, c) Scan view of the reinforcement bar . with 3D optical scanner.	464
Figure F.2	: a) Appearance of reinforcing bar taken out from the specimen LS-.... X6, b) Surface condition of the reinforcement bar observed through . an optical stereo microscope, c) Scan view of the reinforcement bar . with 3D optical scanner.	465
Figure F.3	: a) Appearance of reinforcing bar taken out from the specimen LS-.... X8, b) Surface condition of the reinforcement bar observed through . an optical stereo microscope, c) Scan view of the reinforcement bar . with 3D optical scanner.	466
Figure F.4	: a) Appearance of reinforcing bar taken out from the specimen LS-.... X12, b) Surface condition of the reinforcement bar observed through an optical stereo microscope, c) Scan view of the reinforcement bar with 3D optical scanner.	467
Figure F.5	: a) Appearance of reinforcing bar taken out from the specimen LS-.... X21, b) Surface condition of the reinforcement bar observed through an optical stereo microscope, c) Scan view of the reinforcement bar with 3D optical scanner.	468
Figure F.6	: a) Appearance of reinforcing bar taken out from the specimen LS-.... X28, b) Surface condition of the reinforcement bar observed through an optical stereo microscope.	469
Figure F.7	: a) Appearance of reinforcing bar taken out from the specimen NS- ... X0, b) Surface condition of the reinforcement bar observed through . an optical stereo microscope, c) Scan view of the reinforcement bar . with 3D optical scanner.	470
Figure F.8	: a) Appearance of reinforcing bar taken out from the specimen NS- ... X13, b) Surface condition of the reinforcement bar observed through an optical stereo microscope, c) Scan view of the reinforcement bar with 3D optical scanner.	471
Figure F.9	: a) Appearance of reinforcing bar taken out from the specimen NS- ... X16, b) Surface condition of the reinforcement bar observed through an optical stereo microscope, c) Scan view of the reinforcement bar with 3D optical scanner.	472
Figure F.10	: a) Appearance of reinforcing bar taken out from the specimen NS- ... X22, b) Surface condition of the reinforcement bar observed through an optical stereo microscope, c) Scan view of the reinforcement bar with 3D optical scanner.	473
Figure F.11	: a) Appearance of reinforcing bar taken out from the specimen NS- ... X54, b) Surface condition of the reinforcement bar observed through an optical stereo microscope.	474

Figure F.12	: a) Appearance of reinforcing bar taken out from the specimen LS- X19-H, b) Surface condition of the reinforcement bar observed	474
Figure G.1	: Earthquake records scaled to 0.95g.....	475
Figure H.1	: Drift ratio-time relationships for first stories of S0, S10-12 buildings.	476
Figure J.1	: The view of damage levels of base columns of S0 ve S10-12	
	buildings on plan for SYLMAR, 1994.....	489
Figure J.2	: The view of damage levels of base columns of S0 ve S10-12	
	buildings on plan for KOBE, 1995.....	490
Figure J.3	: The view of damage levels of base columns of S0 ve S10-12	
	buildings on plan for BİNGÖL, 2003.	491
Figure J.4	: The view of damage levels of base columns of S0 ve S10-12	
	buildings on plan for MEXICO, 1980.....	492
Figure J.5	: The damage levels of base columns of S0 ve S10-12 buildings on	
	plan for DUZCE, 1999.	493
Figure J.6	: The damage levels of base columns of S0 ve S10-12 buildings on	
	plan for KOCAELİ, 1999.....	494

SEISMIC BEHAVIOR OF RC COLUMNS WITH CORRODED PLAIN AND DEFORMED REINFORCING BARS

SUMMARY

One of the major problems of the construction sector is the rehabilitation of the old and damaged structure stock. Corrosion of reinforcing bars and the resultant cracks in concrete structural members are among the most common reasons of damage that require repair, particularly in humid environments, where porosity of concrete is relatively higher or when the ingredients of concrete include chloride. Depending on the corrosion level, loss of bond between concrete and steel reinforcement, loss of cross-sectional area of reinforcing bar and cracking of concrete cover can be observed.

In this thesis, an experimental and an analytical study is carried out for investigating the seismic performance of the corrosion damaged RC columns with plain and deformed bars. Three types of specimens were produced and subjected to accelerated corrosion process. For accelerated corrosion, calcium chloride (CaCl_2) was added into the mixing water during concrete casting to develop rapid corrosion. After casting, to increase the corrosion rate even more, calcium chloride solution was sprayed over sides of the columns and a fixed potential of 6 Volts was applied. The corrosion potential and rate values were periodically measured by linear polarization and half-cell potential methods by using corrosionmeter. Then, the specimens were tested under constant axial load and reversed cyclic loads. The first type specimens represent the existing structures, which were built without complying the design codes (low strength and low quality concrete, plain bars, insufficient transverse reinforcement and detailing) which are usually encountered in Turkey. The second type of specimens was constructed in accordance with new design code (normal strength and good quality concrete, deformed bars, sufficient transverse reinforcement and detailing). The third type specimen was similar to the first type specimens with an additional hook detailing of longitudinal bars.

For summarizing the test results, a number of behaviour characteristics; such as strength, displacement capacity, ductility, strain distribution, moment-curvature relationship and displacement components, which are among main indicators of seismic performance, are evaluated. According to the test results, slip of column main bars at the column-footing interface dominated the behavior of the first type specimens. The reference specimen did not reach its theoretical load capacity due to slip, while the specimen with corroded reinforcing bars, which were heavily corroded, reached its theoretical load capacity considering the cross-sectional area of corroded reinforcing bars due to an increase in bond between plain bars and concrete. Although, the strength of the specimen with heavily corroded reinforcing bars was higher than the reference specimen due to better bond characteristics resulting from corrosion products, displacement capacity was reduced remarkably when compared with reference specimen. According to the test results, flexural effects dominated the behavior of the second group specimens. The reinforcing bars of reference specimen

and the specimen with heavily corroded reinforcing bars ruptured at 8% and 2% drift ratios, respectively, which indicated a remarkable loss in displacement capacity due to corrosion. The loss in displacement capacity is at least as important as degradation of strength in terms of seismic performance.

In the analytical phase of the study, the effect of corrosion on bond mechanism and the effect of localized plastic deformations of steel bars due to corrosion were investigated.

Nonlinear pushover analysis and nonlinear time history analysis of a hypothetical RC structure which has columns with corroded deformed reinforcing bars (with the assumption of pitting corrosion) was investigated.

The aim of the study is to obtain a substantial database by evaluating the test results and improving the analytical methods for the seismic performance assessment of buildings with corrosion damaged structural members.

KOROZYONA UĞRAMIŞ DÜZ VE NERVÜRLÜ DONATILI BETONARME KOLONLARIN DEPREM YÜKLERİ ALTINDA DAVRANIŞI

ÖZ

Yaşlı ve hasarlı yapı stokunun rehabilite edilmesi inşaat sektörünün önündeki en büyük problemlerin başında gelmektedir. Özellikle rutubetli çevre koşullarında, beton kalitesinin düşük olduğu durumlarda veya beton bileşiminde kullanılan malzemelerin klor ihtiva etmesi durumunda meydana gelen donatı çeliği korozyonu ve bunun sonucunda betonda oluşan çatlaklar, onarım gerektiren hasarların arasında en yaygınlarından biridir. Korozyon miktarına bağlı olarak, donatı ve beton arasındaki aderansın olumsuz yönde etkilenmesi, donatı kesitinin azalması ve paspayının çatlayarak ayrılması görülebilir.

Tez kapsamında, korozyona uğramış düz yüzeyli ve nervürlü donatıya sahip betonarme kolonların yatay yükler altındaki davranışı deneysel ve analitik olarak incelenmiştir. Deneysel çalışma için üç tip numune üretilmiş ve numuneler hızlandırılmış korozyon işlemine maruz bırakılmıştır. Hızlandırılmış korozyon işlemi için, beton karışımına kalsiyumklorür (CaCl_2) çözeltisi ilave edilmiş, numunelere belirli aralıklarla CaCl_2 çözeltisi püskürtülmüş ve anot ve katod bölgeleri arasında 6 Volt sabit potansiyel farkı uygulanmıştır. Korozyon potansiyeli ve akım değerleri belirli aralıklarla lineer polarizasyon ve yarı-hücre potansiyeli ölçüm teknikleri kullanılarak korozyonmetre ile ölçülmüştür. Numuneler, sabit eksenel yük ve tersinir çevrimsel yük altında denenmiştir. Birinci tip numuneler, Türkiye'deki yapılarda sıklıkla karşılaşılan, ilgili yönetmeliklere uygun olmayan şekilde inşa edilmiş (düşük dayanımlı beton, düz yüzeyli donatı, kancasız bindirmeli ekli, yetersiz enine donatı ve detayları) yapı elemanlarını temsil etmektedir. İkinci tip numuneler, Türkiye'de geçerli deprem yönetmeliğine uygun (normal dayanımlı beton, nervürlü donatı, yeterli enine donatı ve detayları) şekilde üretilmiştir. Üçüncü tip numune, birinci tip numuneler ile aynı özelliğe sahip olup ek olarak boyuna donatıda kanca bulunmaktadır.

Deney sonunda elde edilen dayanım, yerdeğiştirme kapasitesi, süneklik, donatıda oluşan şekildeğiştirme dağılımı, moment-eğrilik ilişkileri ve yerdeğiştirme bileşenleri değerlendirilerek korozyona uğramış betonarme kolonların deprem yükleri altında davranışı açıklanmaya çalışılmıştır. Deney sonuçlarına göre, birinci tip numunelerde, kolon-temel arayüzünde donatıların sıyrılması etkili olmuştur. Referans numune, sıyrılma davranışı sebebiyle teorik kapasitesine ulaşamamıştır. İleri seviyede korozyona uğramış donatıya sahip numunenin, korozyon ürünlerinin düz donatı üzerinde birikmesi ile beton ve donatı arasındaki aderansın bir miktar artması sonucu korozyonlu duruma göre yapılan kesit hesabına göre teorik kapasitesine ulaştığı gözlenmiştir. Bu tip numunelerde, korozyon sebebiyle düz donatı ve beton arasındaki aderansın bir miktar artması sonucu dayanım bir miktar artmış, ancak yerdeğiştirme kapasitesi azalmıştır. Deney sonuçlarına göre, ikinci tip numunelerin göçme modunda eğilme davranışı hakim olmuştur. Donatı kesitinin azalması sonucu, referans numunenin filiz donatısı %8 öteleme oranında koparken, ileri seviyede

korozyona uğramış donatıya sahip numunenin filiz donatısının %2 öteleme oranında kopması yerdeğiştirme kapasitesinde önemli oranda azalma olduğunu göstermektedir. Yapıların deprem performansı açısından, yerdeğiştirme kapasitesindeki azalma en az dayanımdaki azalma kadar önemlidir.

Analitik çalışmada, korozyonun aderans dayanımına etkisi ve korozyon sebebiyle donatıdaki plastik deformasyonların oyuklar etrafında toplanmasının etkisi araştırılmıştır.

Ayrıca, kolon donatıları korozyona uğrayan (oyuklanma korozyonu sonucu varsayımı ile) kuramsal bir betonarme binanın, doğrusal olmayan itme analizi ve doğrusal olmayan zaman tanım alanında analizi yapılmıştır.

Elde edilen deneysel sonuçların değerlendirilmesi ve korozyona uğramış elemanların deprem davranışlarının belirlenmesini sağlayan analitik yöntemlerin geliştirilmesi ile önemli bir deneysel veri tabanı oluşturulması amaçlanmıştır.

1. INTRODUCTION

The corrosion of steel reinforcing bars in concrete has received increasing attention in recent years because of its widespread occurrence in certain types of structures and the high cost of corrosion repairs. Since Turkey is on a high seismic risk zone with a large existing structure stock which has substandard detailing (low strength concrete, insufficient amount of transverse bars in the potential plastic hinge regions), durability issues such as corrosion of reinforcing steel requires special attention.

The solid products of corrosion occupy a greater volume than the original steel and exert substantial expansive stresses on the surrounding concrete, resulting in cracks along the direction of the corroded reinforcing bar. Concurrently, the cross-sectional area of the reinforcement is reduced and the bond between steel and concrete is lost (ACI-222R-01, 2001).

The most common corrosion types are uniform and pitting corrosion where the initiation of corrosion is mostly by carbonation and by chlorides, respectively. Pitting corrosion is more dangerous in RC structures due to small shapes or ribs on the surface and in different variations under the surface. Concentration of plastic deformations of reinforcing bars only at the most heavily corroded sections rather than occurring all through the potential plastic hinge length has a very remarkable adverse effect on the displacement capacity of the existing buildings. It is known that the displacement capacity is as important as strength, particularly for the buildings, which are designed to exhibit a ductile behavior during earthquakes.

Nine chapters, a list of references, and eleven appendices are included in the thesis.

In chapter one, the scope of the thesis is described with a general introduction.

In chapter two, corrosion in reinforced concrete, mechanism and types of corrosion, corrosion measurement techniques and accelerated corrosion process used in this study are described.

In chapter three, review of the effect of corrosion on mechanical properties of reinforcing bars, flexural behavior of RC members with corroded reinforcement,

previous experimental and analytical studies on various constitutive bond stress-slip models available in literature, studies on corrosion monitoring of RC members, the emphasize of corrosion of reinforcing bars in relevant codes and standards are introduced.

In chapter four, the characteristics of specimens, and the test setup with its instrumentation are introduced.

In chapter five, the preparation of specimens are introduced.

In chapter six, test results of materials, column specimens with the evaluation of lateral load-displacement relationships, moment-curvature relationships and strain distributions and uniaxial tension tests and test results of uniaxial tension tests are reported.

In chapter seven, the comparison of all column specimens with each other are reported.

In chapter eight, firstly, the description and numerical formulation of the proposed analytical model on the effect of bond mechanism of the plain bars is presented. Chapter eight also provides information on correlation of the analytical model with results of the column specimen tests as well as the comparison of the analytical model with the additional experimental study in the literature with corroded plain bars. Secondly, an analytical study was performed for determining the effect of different pit distributions due to corrosion on the columns with deformed reinforcing bars and correlation of the analytical model with results of the column specimen tests. Thirdly, the effect of corrosion is demonstrated quantitatively through nonlinear pushover and nonlinear time history analyses of a hypothetical RC frame building. For obtaining more general conclusions, different corrosion intensities and distributions of reinforcing bars, and different earthquake records are considered in the analyses.

2. CORROSION

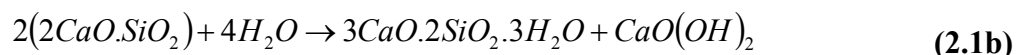
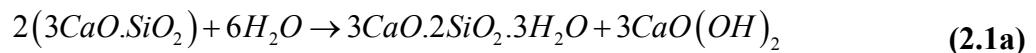
Corrosion can be explained as an electrochemical reaction between a metal and its environment that produces a deterioration of the material and its properties (ASTM G15-04).

2.1 Reinforced Concrete and Corrosion

The high-alkaline environment in concrete protect reinforcing steel from corrosion by creating a tightly adhering film that passivates the steel which reduces the corrosion rate to an insignificant level. Corrosion of steel can occur if the concrete does not resist the ingress of corrosion causing substances or the structure is not designed suitable for the environment.

The composition and availability of the pore solution in concrete are the controlling factors of corrosion of the reinforcing steel rather than the concrete itself. The components of the concrete determine the pH of the pore solution, the total porosity, and the pore-size distribution.

When portland cement hydrates, the calcium silicates react with water to form calcium silicate hydrates and calcium hydroxide [Ca(OH)₂]. The Ca(OH)₂ provides alkali surrounding (pH level at 12.5~13.0) in pore solution which has better protection against corrosion for the pore solution. The main hydration reactions of cement can be shown as follows:



The other factors beside pH that affect the corrosion in concrete are the water-cementitious materials ratio, aggregate, curing conditions and corrosion inhibitors (ACI-222R-01, 2001).

2.2 Mechanism of Reinforcement Corrosion

The corrosion of steel in concrete is an electrochemical process. Electrochemical process consists of two half-cell reactions (anodic and cathodic reactions), electrolyte and metallic (conductor) connection. The anodic and cathodic half-cell reactions are as follows:

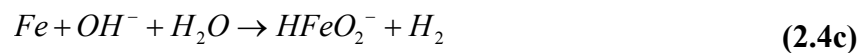
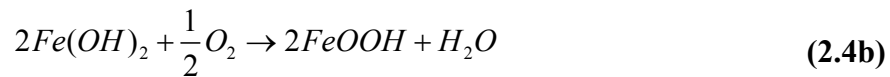
Anodic half-cell reaction is capable of producing electrons (the ionization of iron to form ferrous ions) as shown by Eq. (2.2).



Cathodic half-cell reaction is capable of consuming electrons (the reduction of oxygen to form hydroxyl ion) as shown by Eq. (2.3).



Finally, the iron and hydroxyl ions react with each other to form rust (Eq. (2.4)).

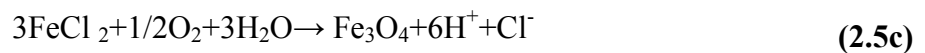


There are two types of corrosion; carbonation induced and chloride induced.

2.3 Chloride Induced Corrosion

For RC structures, exposure to chloride ions is the major cause of corrosion of reinforcing bars. The source of chlorides may be accelerating admixtures, sea-dredged aggregates, contaminants, marine environments, industrial brine or deicing salts. The chloride ions become incorporated in the film at localized weak spots by creating ionic defects and allowing easy ionic transport. Once the active corrosion occurs at these locations, it proceeds autocatalytically (self-feeding manner). The chloride and ferrous ions react to form a soluble complex that diffuses away from the anodic site. When the complex reaches a region of high pH it breaks down,

precipitating an insoluble iron hydroxide and liberating the chloride ion to remove more iron from the reinforcing steel bar (Eq. (2.5)). As the region of local breakdown of the passive film becomes anodic, more chloride ions are attracted to that area of the steel than to the surrounding cathodic areas and the local concentration of chloride ions is increased.



The rate of diffusion of chlorides depends on water/cement ratio, the type of cement, the specific cation associated with the chloride, the temperature and the maturity of the concrete (ACI-222R-01, 2001). The variations in the cross-sectional shape of pits in pitting corrosion are shown in Figure 2.1.

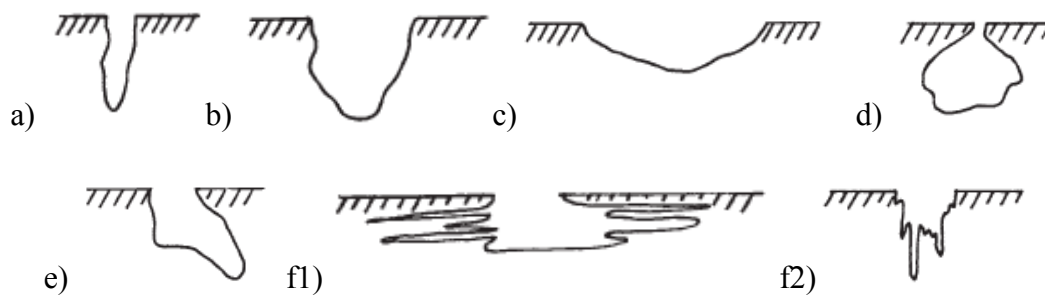
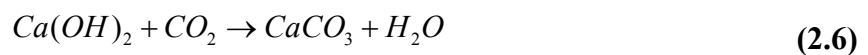


Figure 2.1 : Variations in the cross-sectional shape of pits: a) Narrow, deep, b) Elliptical, c) Wide, shallow, d) Subsurface, e) Undercutting, f1) Microstructural orientation, horizontal, f2) Microstructural orientation, vertical (ASTM-G46-94, 1994).

2.4 Carbonation Induced Corrosion

Carbonation is the neutralization of concrete by reaction between the alkaline components of the cement paste and carbondioxide (CO_2) in the atmosphere as shown by Eq. (2.6).



As the reaction proceeds in solution, the first indication of carbonation is a decrease in pH of the pore solution to 8.5 at which level the passive film on steel is damaged. The major factors that influence uniform corrosion are the effect of wet/dry cycles, high temperatures, thin concrete cover, presence of cracks, high porosity associated with a low cement content and high water/cement ratio (ACI-222R-01, 2001).

2.5 Effects of Corrosion on Structural Capacity of Reinforced Concrete

The effects of corrosion on structural capacity of reinforced concrete depend on the type of the reinforcing bar. The contribution of friction to bond is the major component of strength when slip occurs in plain round bars, while bond comes to depend principally on the bearing and mechanical interlock between ribs rolled on the surface of the bar and the surrounding concrete under increasing slip in ribbed bars (CEB-FIB, 2000).

Corrosion affect bond strength by increasing the diameter of a corroding bar, radial stresses between the bar/and the surrounding concrete and the frictional component of bond. At subsequent stages, corrosion leads to development of longitudinal cracking and a reduction in the resistance to the bursting forces generated by bond action. Corrosion products at the bar/concrete interface affect friction at the interface. Corrosion reduces the height of the ribs of a deformed bar above the bar core. The layer of corrosion products formed by oxidation of the steel force the concrete away from the bar and reduce the effective bearing area of the ribs which causes disengagement of the ribs and concrete (CEB-FIB, 2000).

2.6 Corrosion Products

The iron hydroxides have a much larger specific volume than the steel (Figure 2.2) and exert substantial expansive stresses on the surrounding concrete (ACI 222R-01, 2001). Following the exhaustion of the tensile strain capacity of concrete, longitudinal cracks develop (CEB-FIB, 2000). Consequently, the cross-sectional area of the reinforcing steel is reduced. With time, structural distress may occur either because of loss of bond between the reinforcing steel and concrete due to deterioration (ACI 222R-01, 2001).

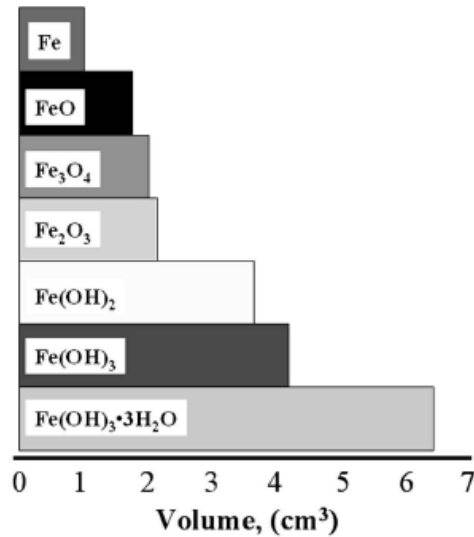


Figure 2.2 : Relative volumes of iron and its reaction product (Mansfeld, 1981).

2.7 Corrosion Measurements

The existing state and the future performance of the structure can be determined by the corrosion measurement of the reinforcing steel embedded in the concrete. The corrosion rate and mechanism could be obtained by corrosion measurement either by visual inspections and/or electrochemical methods. Main corrosion measurement methods used in this study are half-cell potential and linear polarization methods.

The factors that affect the rate and level of corrosion of steel reinforcement embedded in concrete are environmental factors like oxygen and moisture, chloride-ion content of concrete, exposure to wetting and drying conditions, heterogeneity in the concrete and the reinforcing steel, pH of the concrete pore water, carbonation of the portland cement paste, cracks in the concrete, stray currents and galvanic effects due to contact between dissimilar metals or dissimilar zones on the same bar. Design features and construction practices of the structure also play an important role in the corrosion of embedded steel (ACI-222R-01, 2001).

2.7.1 Half-cell potential method

Half-cell potential method is used to estimate the electrical half-cell potential of reinforcing steel for determining the corrosion activity of the reinforcing steel. The copper-copper sulfate half cell circuitry is shown in Figure 2.3. The circuitry consists of half-cell, electrical junction device, electrical contact solution, voltmeter, electrical lead wire. Half-cell potential of the reinforcing bar gives idea of the chemistry of the

electrode environment rather than being an indicator of corrosion current. If potentials of the measured area are positive than -0.20 V CSE, in the range of -0.20 to -0.35 V CSE or negative than -0.35 V CSE, it indicates that no corrosion activity (90% probability), uncertain corrosion activity or corrosion activity (90% probability), respectively (ASTM C876-99).

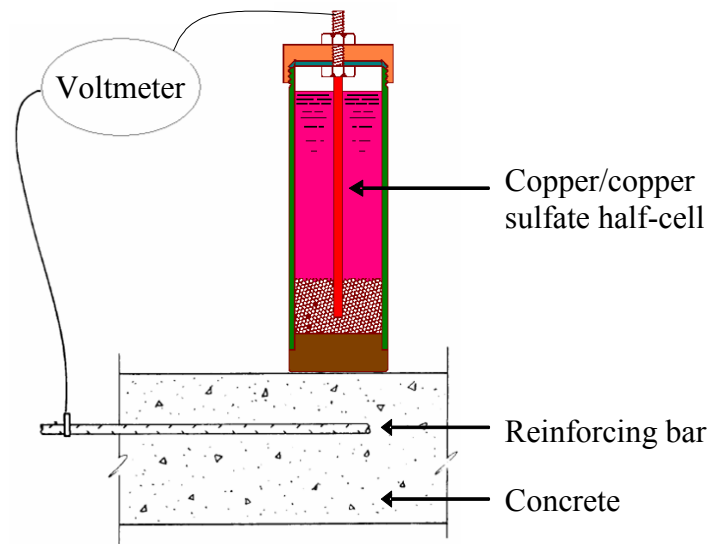


Figure 2.3 : Copper-copper sulfate half cell circuitry (ASTM C876-99).

2.7.2 Linear polarization method

As the requirement of a charge balance of the anodic and cathodic half-cell reactions are always equal, no net current occurs, so the current density can be measured. The balance must be displaced from equilibrium by applying an external potential and measuring the resultant net current. Linear polarization (LPR) method is based on the acceptance of the linear relationship between the small changes in the corrosion potential of the metal and the applied current. There are three electrodes in this method which are working electrode (reinforcing steel), a counter electrode (usually a nonreactive metal) and a reference electrode (copper-copper sulfate halfcell). The LPR device applies small voltage or current perturbations to the working electrode via the counter electrode and measures the corresponding current or voltage responses. The reference electrode measures the initial corrosion potential and the shifts in potential of the working electrode. The voltage and current data are then converted to the corrosion rate. The corrosion current can be converted to a rate of loss of metal from the surface of the steel by Faraday's law (Eq. (2.5)).

$$m = \frac{ItA_w}{nF} \quad (2.7)$$

where, m is the mass of metal dissolved or converted to oxide, g, I is current, A, t is time, s, A_w is atomic weight, n is valency and F is Faraday's constant (96500 coulombs/equivalent mass). Bae and Belarbi (2009), Wang et al. (2004), Pantazopoulou et al. (2001) used Faraday's Law in determining the steel weight loss while Rodriguez et al. (1994a-b), Coronelli (2002), Stanish et al. (1999) determined the percentage or the loss in the diameter of the reinforcing bar by dividing the section loss to the original section.

2.8 Accelerated Corrosion Process

All the test specimens except reference ones were subjected to accelerated corrosion process to reach a certain significant level of corrosion within the experimental scheduled timing of the thesis.

For accelerated corrosion, calcium chloride (CaCl_2) was added into the mixing water during concrete to develop rapid corrosion in the early stages when the concrete mixture is still plastic. The weight of calcium chloride was 4% of the cement weight. After casting, to increase the corrosion rate even more, calcium chloride solution was sprayed to the outer sides of the columns and a fixed potential of 6 Volts was applied. During accelerated corrosion, the longitudinal reinforcement was connected to a power supply so as to behave as the anode of the electrochemical corrosion cell. The cathode was the steel mesh wrapped around the column. The corrosion potential and rate values were periodically measured by linear polarization and half-cell potential methods. The general appearance of columns, accelerated corrosion setup and measurement of corrosion potential with Gecor8 corrosionmeter are shown in Figure 2.4.

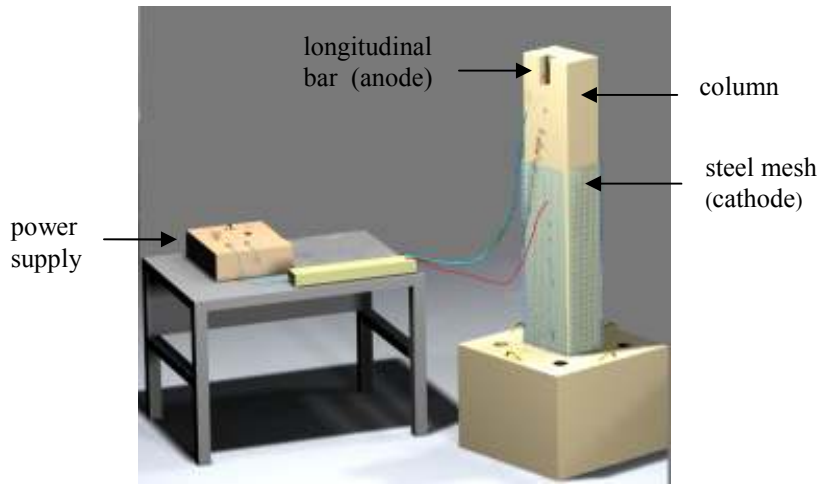


Figure 2.4 : General appearance of columns, the accelerated corrosion setup and measurement of corrosion potential.

3. OVERVIEW OF LITERATURE

Corrosion of reinforcement have been studied by several researchers. This section is arranged to collect experimental and analytical studies from the literature. Since these studies were performed outside Turkey, typical Turkish structure with substandard detailing were not taken into consideration. These studies are on the effect of corrosion on mechanical properties of reinforcing bars, the flexural behavior of RC members with corroded reinforcement, the effect of corrosion on bond, corrosion monitoring of RC members, consideration of corrosion in recent codes and standards, and shear strength degradation with displacement ductility.

3.1 Studies on the Effect of Corrosion on Mechanical Properties of Reinforcing Bars

Castel et al. (2000) studied the influence of the loss of bond between steel and concrete. The simulation of bond loss was performed by creating local notch in steel cross-section that simulates pitting corrosion attack. Local reductions of cross-sections performed increase by 10% in the ultimate strength but showed 50-70% ductility loss. Ductility loss seems to be more dependent on the presence of the notch than its depth. The phenomenon can be due to a partial yielding of the steel cross-section at the notch tip (stress-concentration) until the total cross-section reaches its elastic limit. When all the cross-section reaches the elastic limit, a large part of yielding reserve is already consumed at the notch tip, leading to a premature rupture of the bar.

Youlin et al. (2003) studied the effect of corrosion on the yield strength, tensile strength and elongation rate of some kinds of steel bars (hot rolled bright steel bar, hot rolled ribbed steel bar, cold finishing steel bar, high strength steel wire and tyre cord) which are artificially corroded and taken out from actual structures. The hot rolled steel bar is found to be the most corrosion-resistant due to inner stress arised from secondary processing. As the steel bar has small diameter it corrodes faster due to the fact that the smaller diametered steel bar has relatively larger reduction in

section under same corrosion depth. The experiments have shown that corrosion has not apparent impact on the stress-strain constitutive relation of all tested grades except hot rolled bright specimens, but a tendency of reduced ductility. The strength of steel bar is calculated based on the real area of the bar without corrosion in order to make an objective comparison for impact on the strength of loaded steel bar by corrosion. The yield and tensile strength of bars reduced by the corrosion. Corrosion has more apparent impact on ductility than on strength. Corroded hot rolled steel bar has relatively smaller reduction in ductility with respect to other specimens. The experiments with corroded steel bars taken from actual structures showed a reduction in strength, shorter yield step, smaller deformation limit, smaller yield-tensile ratio and yield close to tensile rupture. The authors mentioned that the results show a discrete distribution of reduction in strength and different amplitude of yield strength and tensile strength. It is also mentioned that experiment has errors, the test pieces are dispersed and it is hard to find out an quantitatively apparent rule for evaluation of strength after corrosion.

In the study of the Cairns et al. (2005), the effect of corrosion on mechanical properties of reinforcing bars is investigated through physical tests on bars with simulated and real corrosion damage and through a numerical model. Plain and deformed bars were subjected to accelerated corrosion process and tested under uniaxial tension. From the tests, it is mentioned that the loss of ductility is significantly more than the loss in yield strength with increasing corrosion.

Apostolopoulos and Michalopoulos (2006) studied the impact of corrosion on mass loss, high and low cycle fatigue properties of Bst500s steel which is used extensively in Greece between 1990 and 2005. 12 mm diameter steel bars were subjected to accelerated corrosion process and tests were carried out low and high cycle fatigue levels. The results of the experiments have shown that as the corrosion level increases the strength properties (yield and fracture points) and the ductility properties (energy density and elongation to fracture) decrease.

An experimental investigation was carried out by Apostolopoulos (2008) on B500c deformed steel reinforcing bars of 8, 12, 16 and 18 mm diameter which were artificially corroded. The mechanical properties were evaluated in terms of nominal and effective yield and ultimate stress. The nominal yield stress is calculated as the ratio of the load capacity divided by the initial non-corroded cross-sectional area of

the steel bars while the effective yield stress is calculated as the ratio of the load capacity divided by the true cross-sectional area of the corroded specimens. Nominal yield stress, effective yield stress, nominal ultimate stress, effective ultimate stress, uniform elongation and energy density decreases as the corrosion increases. For the specimens with smaller diameters, the degradation rate of the uniform elongation and the energy density due to corrosion was higher because the same amount of pits and notches that are present in the smaller diameters create greater damage, since they occupy greater percentage of surface area for equal corrosion durations.

Apostolopoulos and Papadakis (2008) investigated the tensile behavior of artificially corroded Class Bst420 reinforcing bars, which were used in Greece between 1960 and 1990. Apparent stress is calculated as the quotient of the load capacity divided by the initial, uncorroded section of the steel bars, while effective stress is calculated as the quotient of the load capacity divided by the true cross-section of the corroded specimens, which is calculated as a function of mass and length of specimens. Apostolopoulos and Papadakis (2008) mentioned that stress which is applied to bars increases due to corrosion and this increase in stress reduces the safety factors taken for the properties of the reinforcing steel. The reduction of the cross-section of a reinforcing bar reduces the moment of inertia and hence the maximum buckling load of the steel bar. According to the test results, effective yield stress remain constant while apparent yield stress decreases with the increasing corrosion. Effective and apparent ultimate stress decreases as the corrosion increases. According to the test results of reinforcing bars ($\phi 10$) embedded for years in real structures and exposed in natural corrosion, a small amount of corrosion has proportional effect on yield and ultimate stress, an exponential effect on elongation to failure and energy density.

In the study of the Graeff et al. (2008), section loss of reinforcing bars at different corrosion levels is investigated. 3D scanner is used in determining the section losses of reinforcing bars. According to the results of the investigation, consideration of the loss of section of the reinforcing bars in the assessment of reinforced concrete structures is emphasized.

3.2 Studies on the Flexural Behavior of RC Members with Corroded Reinforcement

Bousias et al. (2002) carried out flexural tests on cantilever columns of 250 mm×500 mm with 18 mm diameter longitudinal bars and 8 mm smooth transverse bars at 200 mm. The specimens, which were subjected to accelerated corrosion process, were tested under constant axial load and reversed cyclic loading after retrofitting with fiber reinforced polymers (FRP). It has been observed from the tests that FRP retrofitting does not increase the strength of the columns, however improves the deformation capacity of the columns significantly.

Mangat and Elgarf (1999) carried out flexural tests on beams of 150 mm×100 mm cross-section and 910 mm long with 10 mm diameter deformed bars and 6 mm transverse bars at a spacing of 70 mm. The specimens, which were subjected to accelerated corrosion process, were tested under four-point bending. From the tests, the flexural load capacity and deflection of beams decreased significantly due to the reduction in cross-section of reinforcing bars and loss of bond.

3.3 Studies on the Effect of Corrosion on Bond

Analytical bond stress-slip relationship for monotonic loading is shown in Figure 3.1 (CEB-FIP, 1990). The parameters were defined for the mean bond-stress-slip relationship for deformed and plain bars.

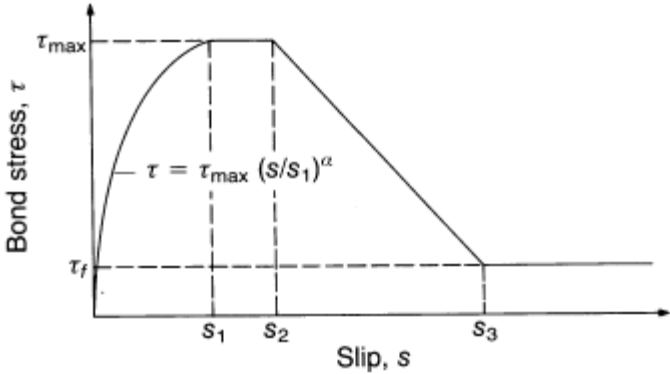


Figure 3.1: Analytical bond stress-slip relationship for monotonic loading.

According to CEB-FIB, 2000 residual bond strength for plain bars is calculated by Eq (3.1).

$$\rho_{tr} = \frac{\text{transverse reinforcement area}}{\text{area of the main bars}} \quad (3.1)$$

If $\rho_{tr} > 0.25$;

$$f_b = 4.75 - 4.64x \quad (3.1a)$$

x is the attack penetration (bar radius reduction, mm).

If $\rho_{tr} < 0.25$;

$$f_b = 10.04 + \left(-6.62 + 1.98 \left(\frac{\rho_{tr}}{0.25} \right) \right) (1.14 + x) \quad (3.1b)$$

It is highlighted that equations are applicable once longitudinal cover cracks develop, and are not applicable to small amounts of corrosion. The experimental values show that x ranged from 0.04 to 0.5 mm, but $x = 1.0$ mm is reasonable according to the authors. Eq. (3.1b) becomes negative at corrosion penetrations greater than 0.4 mm if there are no stirrups. This proposal gives bond strength values for each attack penetration, taking account of the actual residual stirrup section at the anchorage length. If the equations applied to the evaluation of composite interaction at intermediate parts of the bar, ρ_{tr} should be calculated from Eq. (3.2) where s is the stirrup spacing (mm).

$$\rho_{tr} = \text{number of stirrups} \cdot \frac{200}{s} \text{ (at anchorage length)} \quad (3.2)$$

According to CEB-FIB (2000), only the relative rib area is assumed to be effected by corrosion, all the other parameters including the confining force developed by concrete cover and characteristics of the bar-concrete interface remain constant. The original ribs have been assumed annular with a height of 0.0625 times bar diameter at a spacing of 0.8 times diameter, giving a relative rib area of 0.078. Residual bond strength for deformed bars is calculated from Eq. (3.3) where f_r is the relative rib area, β is the rib face angle (45°), α is the rib inclination (60°).

$$f_b = 15.5f_r + 0.039\beta + 0.007\alpha \quad (3.3)$$

Coronelli (2002), Wang and Liu (2004) and Bhargava et al. (2007) used the model proposed by Cairns and Abdullah (1996). In the model, the cover concrete is

idealized as thick-walled cylinder which composed of elastic outer part and cracked inner part. Tastani and Pantazopoulou (2007) and Xu et al. (2007) also used the idealization of concrete cover as thick-walled cylinder in determining the behavior of corroded bar anchorages and in modelling the bond strength of corroded plain bars, respectively. Xu et al. (2007) mentioned that the corrosion will increase the friction coefficient due to the change of roughness of the bar surface; on the other hand, the corrosion pressure will provide an additional radial force on the concrete wall.

In the study of Lundgren (2001) and Fang et al. (2006b), the model of the bond mechanism is presented as a frictional model describing the relations between the stresses and the deformations by using elasto-plastic theory. The volume increase of the corrosive products compared with the virgin steel was modelled in a corrosion layer. The volume of the rust relative to the uncorroded steel was given as input into the model.

Fang et al. (2004), Fang et al. (2006a), Fang et al. (2006b) carried out pullout tests on concrete prisms of 140 mm×140 mm×180 mm with 20 mm diameter longitudinal bars and 6 mm transverse bars. The embedment length to bar diameter ratio was chosen as 4.0. The tensile strength of smooth bars and deformed bars are 440 MPa and 521 MPa, respectively. The water/cement ratio was chosen as 0.44. The 28-day concrete strength was 52 MPa. Sodiumchloride was added to the concrete mixture to accelerate the corrosion process. The specimens were immersed in a 5% sodiumchloride solution for 3 days before subjecting to accelerated corrosion. During corrosion process specimens were fully immersed in the solution and accelerated corrosion was achieved by applying adjustable voltage and current. Amount of rebar corrosion was reported as the loss of metal weight relative to the original rebar weight. The corrosion percent was varied from 0% for control specimens to 9% for other specimens. The specimens were tested in an MTS testing machine. From the tests, the bond strength of deformed reinforcing bar specimens decreased, whereas that of smooth bar specimens increased with the increasing corrosion.

Fang et al. (2006b) carried out pullout test specimens which are similar to the Fang et al. (2004) and Fang et al. (2006a) under cyclic loading.

In the study of Lundgren et al. (2009), the parameters given by CEB-FIP (1990) is modified and the bond-slip response of corroded reinforcement is obtained by

shifting the bond-slip curve of uncorroded reinforcement along the slip axis.

Coronelli and Gambarova (2004) investigated the structural behavior of RC beams with corrosion damage. The authors used finite element approach for modelling the effect of corrosion by reducing the geometry of the finite elements representing the steel and concrete with the modification of material properties of steel and concrete and their bond characteristics.

Auyeung et al. (2000) proposed Eq. (3.4) and Eq. (3.5) for expressing the bond strength and the reduction in failure slip with respect to corrosion for deformed reinforcing bars.

Maaddawy et al. (2005) proposed a bond stress-slip relationship for deformed reinforcing bars, based on CEB-FIB (1990) except the neglecting of the ascending branch of the curve. The maximum bond stress, μ_{max} , is modified to account for the effect of corrosion.

Pregartner et al. (2004) mentioned that unlike the generic bond model which is based on observations from ribbed bars, the stress slip relationship for plain bars may be considered to maintain the peak value for a considerable distance after the maximum bond stress is attained.

The significant result in literature review is up to about 1% percent corrosion, the bond strength increases with increasing corrosion and with further corrosion, the bond stress declines (CEB-FIB 2000, Coronelli 2002, Stanish 1999, Fang et al. 2004, Fang et al. 2006, Al Sulaimani et al. 1990, Wang and Liu 2008, Auyeung 2000).

There are different and valuable findings about the difference between the bond strength of plain and ribbed bars. Some of the researchers found the maximum bond strength of specimens with deformed bars is 3.5~6.9 times as high as for the bond strength of the specimen with smooth bars (Fang et al., 2004) while the others found the maximum bond strength of specimens with smooth bars is 28.6% of deformed bars (Mo and Chan, 1996). In the study of Balazs (2007), the residual bond strength for plain bars is found about two-third of that of deformed bars owing to the differences in frictional coefficients for concrete to steel (in case of plain bars) or concrete to concrete (in case of deformed bars).

3.4 Studies on Corrosion Monitoring of RC Members

Song and Saraswathy (2007) studied on the inspection and monitoring techniques for the assessment of the corroded reinforcement and application of these techniques for RC structures. Some of these techniques that are reviewed by Song and Saraswathy (2007) are; surface potential measurements, concrete resistivity measurement, LPR resistance measurement, Tafel extrapolation, galvanostatic pulse transient method, electrochemical impedance spectroscopy, harmonic analysis, noise analysis, embeddable corrosion monitoring sensor, cover thickness measurements, Ultrasonic pulse velocity technique, x-ray, gamma radiography measurement, infrared thermograph, electrochemical and visual inspection. Measurement of surface potential and LPR resistance techniques were used in the assessment of corroded reinforcement in this thesis.

Feliu et al. (1990) studied on determining the polarization resistance of RC members with corroded reinforcement on-site. Galvanostatic method is proposed by Feliu et al. (1990) which uses two counter electrodes to apply the precise bounding of the action of the electrical signal to the reinforcement instead of potentiostatic method.

3.5 A Review of Relevant Codes and Standards on Corrosion of Reinforcing Bars

Existing codes do not contain specific guidance on the effect of corroded reinforcing bars except emphasizing that corroded reinforcement should be taken into consideration during the examining of the physical condition of existing reinforced concrete elements (Eurocode 8, 2005, FEMA 356, 2000). Turkish Seismic Design Code (2007) implies that reinforcement corrosion should be considered in calculating the capacity of the structure. ASCE/SEI-41 (2007) is one step forward by implying that if reinforcing bar corrosion is observed in the condition assessment causing reduced capacity, sectional properties shall be reduced accordingly, using principles of structural mechanics. Therefore, consideration of effects of corrosion on the structural behavior is left to the judgement of designers.

3.6 A Review of Shear Strength Degradation with Displacement Ductility

Sezen and Moehle (2004) defined a ductility-related factor which depends on the crack openings in the concrete, leading to loss of anchorage of the transverse reinforcement and some degradation in its contribution to shear resistance, reduction in bond capacity for the longitudinal and transverse reinforcement. The shear strength degradation with increasing displacement ductility demand is shown in Figure 3.2.

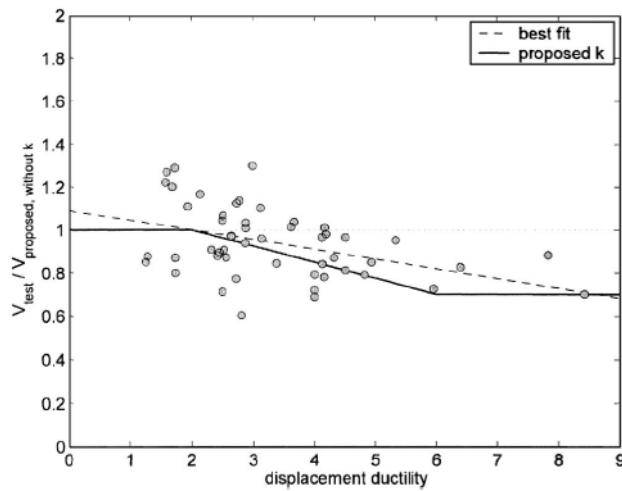


Figure 3.2: Shear strength degradation with displacement ductility (Sezen and Moehle, 2004).

The displacement ductility is defined as the ratio of the ultimate displacement to yield displacement according to Sezen and Moehle (2004). The yield displacement is found by drawing a secant to intersect the lateral load-displacement relation at 70% of the maximum applied shear, then the line was extended to intersect the horizontal line corresponding to the maximum applied shear, and the yield displacement was obtained as the projection of this point on the horizontal axis. The ultimate displacement is defined as the displacement corresponding to termination of the test.

According to Figure 3.2, the shear strength is constant up to displacement ductility 2, then decreases with a slope until displacement ductility 6, and then remains constant. The decreasing shear strength versus displacement ductility relation is found from Figure 3.2 by Eq. (3.4).

$$y = -0.0065x + 1.1 \quad (3.4)$$

4. EXPERIMENTAL DESIGN

4.1 Design of Specimens

Three types of specimens were produced for investigating the effect of corrosion to the seismic behavior of the columns in the thesis.

4.1.1 First type specimens

The specimens represent typical low strength RC columns with substandard detailing in Turkey and many other developing countries. In the notations of the specimens, the first and second terms represent low strength concrete (L: Low, S: Strength) and third term denotes the cross-section loss percentage (X) of the reinforcing bar due to corrosion. The cross-section loss percentage was determined by dividing the difference between the original cross-section and existing cross-section area to the original cross-section area. The existing cross-section area is the area of the existing diameter of the reinforcing bar which is determined by dividing all the bars into 10 mm long pieces and measuring each 10 mm long piece of four longitudinal bars both in 0° and 90° directions with caliper after the tests and cleaning process. Then the average diameter of these measured diameters was accepted as the existing diameter of the reinforcing bar. Six rectangular columns were cast with cross-section dimensions of 200×300 mm. The height of all columns was 1400 mm and the columns were supported by a footing of size $700 \times 700 \times 500$ mm. The mean compressive strength of the concrete of the first type specimens was 3.7 MPa (after 180 days). Clear cover was 20 mm from the transverse bars. The geometric longitudinal steel reinforcement ratio and volumetric ratio of transverse bars were 1% and 0.45%, respectively. Two different types of reinforcing bars were used. S220 plain bars with a diameter of 14 mm (measured diameter 14.55 mm) which had an average yield strength of 338 MPa were used as longitudinal bars and S220 plain steel bars with a diameter of 8 mm (measured diameter 8.37 mm) which had an average yield strength of 378 MPa were used as transverse bars. The specimens have insufficient spacing of transverse bars at the measuring zone (200 mm). Axial load

capacity of the columns is calculated by Eq. (4.1) and Eq. (4.2) which is $\approx 57\%$ (≈ 124000 kN) of column axial load capacity. The weight of test setup is 3841 N. The cyclic behavior of the columns was dominated by flexure. The average moment capacities of the columns which were calculated by XTRACT (2007) computer program were 34.2 kNm (Figure 4.1). In the moment-curvature analysis, for unconfined and confined concrete stress-strain behavior, the models proposed by Mander et al. (1988) are used. Steel reinforcing bars are assumed to behave in an elastic-plastic manner with strain hardening.

$$N_k = f'_c \cdot b \cdot h$$

$$= 0.57 \cdot 3.7 \cdot 200 \cdot 300 = 126540 \text{ N} \quad (4.1)$$

$$N_k = 126540 - 3841 = 122699 \text{ N} \quad (4.2)$$

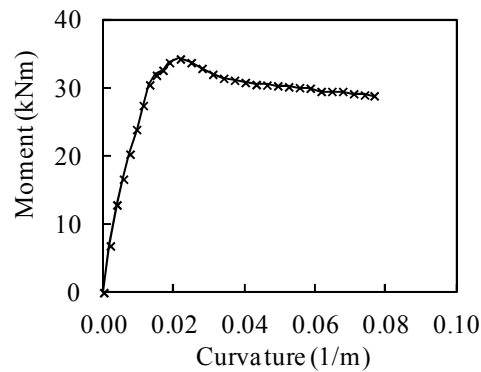


Figure 4.1 : Theoretical moment-curvature relationships of the first type specimens.

According to the theoretical calculation of the first type specimens, the mode of column failure was with the crushing of concrete cover, followed by crushing of core concrete and then yielding of longitudinal tension bar.

After production, all specimens except the reference one (LS-X0) were subjected to accelerated corrosion. Properties of the first and third type specimens are shown in Table 4.1. The reinforcing cage of the first type specimens are given in Appendix A.

Table 4.1 : Properties of the first type specimens.

Specimen	Specimen Type	Concrete compressive strength of columns (MPa)	Concrete compressive strength of footing (MPa)	Reinforcement of footing	Reinforcement of column
LS-X0	1	3.7	23.3	S420	S220
LS-X6	1	3.7	23.3	S420	S220
LS-X8	1	3.7	23.3	S420	S220
LS-X12	1	3.7	23.3	S420	S220
LS-X21	1	3.7	23.3	S420	S220
LS-X28	1	3.7	23.3	S420	S220

4.1.2 Second type specimens

The specimens, represent the construction in compliance with recent seismic design codes. In the notations of the specimens, the first and second terms represent normal strength concrete (N: Normal, S: Strength) and third term denotes the cross-section loss (X) on the reinforcing bar. The cross-section loss percentage was determined by dividing the difference between the original cross-section and existing cross-section area to the original cross-section area. The existing cross-section area is the area of the existing diameter of the reinforcing bar which is determined by dividing all the bars into 10 mm long pieces and measuring each 10 mm long piece of four longitudinal bars both in 0° and 90° directions with caliper after the tests and cleaning process. Then the minimum diameter (maximum loss) of these measured diameters was accepted as the existing diameter of the reinforcing bar. Six rectangular columns were cast with cross-section dimensions of 200×300 mm. The height of all columns was 1400 mm and the columns were supported by a footing of size 700×700×500 mm. The mean compressive strengths of second type was 25.5 MPa (at 28 days of age). Clear cover was 20 mm from the transverse bar. The geometric longitudinal steel reinforcement ratio and volumetric ratio of transverse bars were 1% and 0.88%, respectively. Two different types of reinforcing bars were used. S420 deformed bars with a diameter of 14 mm (measured diameter 13.80 mm) which had an average yield strength of 460 MPa were used as longitudinal bars and S420 deformed bars with a diameter of 8 mm (measured diameter 8.22 mm) which had an average yield strength of 486 MPa were used as transverse bars. The spacing of transverse bars at the measuring zone is 100 mm which is sufficient. Axial load capacity of the columns is calculated by Eq. (4.3) and Eq. (4.4) which is ≈18% (≈282000 kN) of column axial load capacity. The weight of test setup is 3841 N.

$$N_k = f'_c \cdot b \cdot h$$

$$= 0.18 \cdot 25.5 \cdot 200 \cdot 300 = 275400 \text{ N} \quad (4.3)$$

$$N_k = 275400 - 3841 = 271559 \text{ N} \quad (4.4)$$

The cyclic behavior of the columns was dominated by flexure. The average moment capacities of the columns calculated by XTRACT (2007) computer program were 67.4 kNm (Figure 4.2).

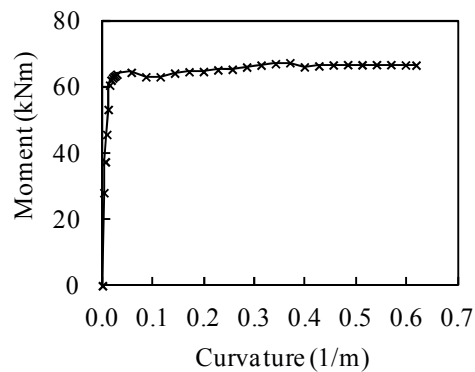


Figure 4.2 : Theoretical moment-curvature relationships of the second type specimens.

According to the theoretical calculation of the second type specimens, the mode of column failure was with the crushing of concrete cover and yielding of longitudinal tension bar simultaneously and followed by crushing of core concrete. After production, all specimens except the reference ones were subjected to accelerated corrosion. Properties of the second type specimens are shown in Table 4.2. The reinforcing cage of the first type specimens are given in Appendix A.

Table 4.2 : Properties of the second type specimens.

Specimen	Specimen Type	Concrete compressive strength of columns (MPa)	Concrete compressive strength of footing (MPa)	Reinforcement of footing	Reinforcement of column
NS-X0	2	25.5	23.3	S420	S420
NS-X9	2	25.5	23.3	S420	S420
NS-X13	2	25.5	23.3	S420	S420
NS-X22	2	25.5	23.3	S420	S420
NS-X16	2	25.5	23.3	S420	S420
NS-X54	2	25.5	23.3	S420	S420

4.1.3 Third type specimen

Third type specimen has the same characteristics with the first type specimens with an additional hook detailing at the longitudinal bar. The average moment capacity of the column calculated by XTRACT (2007) computer program by using Mander Model was 34.2 kNm (Figure 4.3). The reinforcing cage of the third type specimen is given in Appendix A.

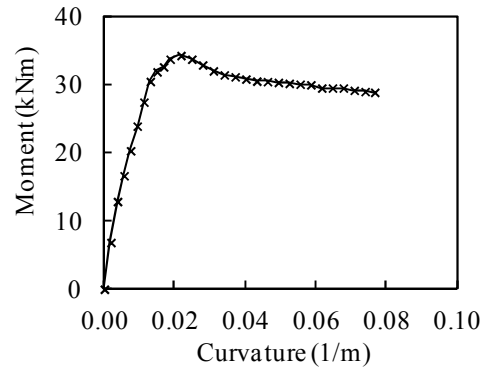


Figure 4.3 : Theoretical moment-curvature relationships of third type specimen.

According to the theoretical moment-curvature relationships of third type specimen, the mode of column failure was with the crushing of concrete cover, crushing of core concrete and yielding of longitudinal tension bar, subsequently.

Table 4.3 : Properties of the third type specimens.

Specimen	Specimen Type	Concrete compressive strength of columns (MPa)	Concrete compressive strength of footing (MPa)	Reinforcement of footing	Reinforcement of column
LS-X19-H	3	3.7	23	S420	S220

4.2 Shear Strength

4.2.1 First and third type specimens

Two proposed models from TS500 (2000) and Sezen and Moehle (2004) are selected for determination of shear strength of the first and the third type specimens.

According to TS500 (2000), the nominal shear strength capacity, V_r , is calculated as the sum of contributions from concrete, V_c and the transverse reinforcement, V_w .

The concrete contribution to shear strength is given by Eq. (4.5).

$$V_c = 0.8 \cdot V_{cr} \quad (4.5)$$

$$V_{cr} = 0.65 \cdot f_{ct} \cdot b \cdot (h - d') \cdot \left(1 + \gamma \cdot \frac{N}{b \cdot h}\right) \quad (4.5a)$$

$$= 0.65 \cdot 0.82 \cdot 200 \cdot (300 - 35.64) \cdot \left(1 + 0.07 \cdot \frac{111000}{200 \cdot 300}\right) = 32006 \text{ N}$$

$$f_{ck} = \frac{f_c}{1.5} \quad (4.5b)$$

$$f_{ck} = 1.5 \cdot 3.7 = 5.55 \text{ MPa}$$

$$f_{ct} = 0.35 \cdot \sqrt{f_{ck}} \quad (4.5c)$$

$$f_{ct} = 0.35 \cdot \sqrt{5.55} = 0.82 \text{ MPa}$$

In case of axial compression, γ is taken as 0.07 (TS500, 2000).

$$V_c = 0.8 \cdot 32006 = 25604 \text{ N}$$

Total shear strength is calculated by Eq. (4.6).

$$V_r = V_w + V_c \quad (4.6)$$

The contribution of transverse reinforcement is calculated as follows:

$$V_w = \frac{A_{sw}}{s} \cdot f_{yw} \cdot d \quad (4.6a)$$

$$V_w = \frac{2\pi \cdot 8.37^2 / 4}{200} \cdot 378 \cdot \left(300 - 20 - \left(\frac{8.37}{2}\right)\right) = 57365 \text{ N}$$

$$V_r = 57365 + 25604 = 82970 \text{ N}$$

According to Sezen and Moehle (2004), the nominal shear strength, V_n , is calculated as the sum of contributions from concrete, V_c and the transverse reinforcement, V_s (Eq. (4.7)).

$$V_n = V_c + V_s \quad (4.7)$$

The concrete contribution to shear strength is given by:

$$V_c = k \left(\frac{0.5\sqrt{f'_c}}{a/d} \sqrt{1 + \frac{P}{0.5\sqrt{f'_c} A_g}} \right) 0.8 A_g \quad (4.7a)$$

$$V_c = 1 \left(\frac{0.5\sqrt{3.7}}{1200/264.3} \sqrt{1 + \frac{111000}{0.5 \cdot \sqrt{3.7} \cdot 200 \cdot 300}} \right) 0.8 \cdot 200 \cdot 300 = 17388 \text{ N}$$

The contribution of transverse reinforcement is calculated as follows:

$$V_s = k \frac{A_v f_y d}{s} \quad (4.7b)$$

$$V_s = 1 \frac{110 \cdot 378 \cdot 264.35}{200} = 54981.9 \text{ N}$$

$$V_n = 17388 + 54981.9 = 72371 \text{ N}$$

4.2.2 Second type specimens

Shear strength model from TS500 (2000) is selected for shear strength determination of the second type specimens.

The concrete contribution to shear strength is given by Eq. (4.8).

$$V_c = 0.8 \cdot V_{cr} \quad (4.8)$$

$$V_{cr} = 0.65 \cdot f_{ct} \cdot b \cdot (h - d') \cdot \left(1 + \gamma \cdot \frac{N}{b \cdot h}\right) \quad (4.8a)$$

$$V_{cr} = 0.65 \cdot 2.16 \cdot 200 \cdot (300 - 35.1) \cdot \left(1 + 0.07 \cdot \frac{285600}{200 \cdot 300}\right) = 99381 \text{ N}$$

$$f_{ck} = \frac{f_c}{1.5} \quad (4.8b)$$

$$f_c = 1.5 \cdot 25.5 = 38.25 \text{ MPa}$$

$$f_{ct} = 0.35 \cdot \sqrt{f_c} \quad (4.8c)$$

$$f_{ct} = 0.35 \cdot \sqrt{38.25} = 2.16 \text{ MPa}$$

In case of axial compression γ is taken as 0.07 (TS 500, 2000).

$$V_c = 0.8 \cdot 99168 = 79505 \text{ N}$$

Total shear strength is calculated by Eq. (4.9).

$$V_r = V_w + V_c \quad (4.9)$$

The contribution of transverse reinforcement is calculated as follows:

$$V_w = \frac{A_{sw}}{s} f_{yw} \cdot d \quad (4.9a)$$

$$V_w = \frac{2\pi \cdot 8.22^2 / 4}{200} \cdot 486 \cdot \left(300 - 20 - \left(\frac{8.22}{2} \right) \right) = 141624 \text{ N}$$

$$V_r = 141624 + 79505 = 221128 \text{ N}$$

4.2.3 Shear strength degradation with displacement ductility

The shear strength degradation versus displacement ductility and lateral load versus displacement interaction relationships were determined according to Sezen and Moehle (2004) for the first and the third type specimens as described in Chapter 3.6.

Based on the moment-curvature relationships obtained by XTRACT (2007), the lateral load versus displacement relationships were determined according to Eq. (4.10). In Eq. (4.10), P is the lateral load, M is the moment, and L is the column height. The relationship of the shear strength degradation with displacement ductility and lateral load-displacement interaction of the first and the third type specimens are shown in Figure 4.4. As seen from the figure, the first and third type specimens are expected to fail before they reach shear strength.

$$P = \frac{M}{L} \quad (4.10)$$

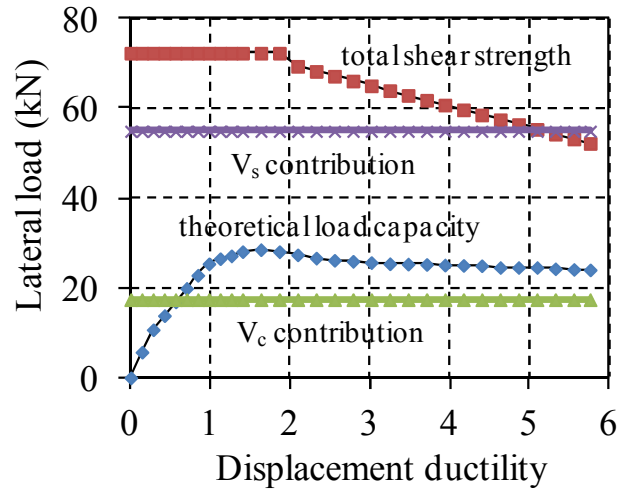


Figure 4.4 : The relationship of the shear strength degradation with displacement ductility and lateral load-displacement interaction of the first and third type specimens.

In determining the shear-displacement ductility relationship, the obtained shear strength values from Sezen and Moehle (2004) model were taken constant up to displacement ductility 2, then assumed to decrease with slope (Eq. 3.4) up to displacement ductility 6.

4.2.4 Calculation of lap splice length for the first and the third type specimens (TS500, 2000)

The specimens have inadequate lap splice length at the story levels. According to TS500 (2000), lap splice length can be determined by using the design yield strength of the reinforcing bar (f_{yd}) and the design tensile strength of the concrete (f_{ctd}). Lap splice length, l_o , is directly related with the anchorage length, l_b , and can be calculated by Eq. (4.11). The anchorage length (l_b) for plain reinforcing bars can be calculated by Eq. (4.11).

$$l_o = c \cdot l_b \quad (4.11)$$

$c = 1.5$ if all lap splices are formed at the same section.

$$l_b = 0.24 \cdot \phi \cdot \frac{f_{yd}}{f_{ctd}} \quad (4.11a)$$

$$f_y = 338 \text{ MPa}$$

$$f_{yd} = \frac{f_y}{1.15} = \frac{338}{1.15} = 292 \text{ MPa} \quad (4.11b)$$

$$f_c = 3.7 \text{ MPa}$$

$$f_{ct} = 0.35 \cdot \sqrt{f_{ck}} = 0.35 \cdot \sqrt{5.55} = 0.82 \text{ MPa} \quad (4.11c)$$

$$l_b = 0.24 \cdot \phi \cdot \frac{f_{yd}}{f_{ctd}} = 0.24 \cdot \phi \cdot \frac{292}{0.82} = 86\phi$$

For the first type specimens;

$$l_o = 1.5 \cdot 86\phi = 129\phi$$

In the case of existing hook as in third type specimen l_b can be reduced by $\frac{3}{4}$.

$$l_b = 86 \cdot 0.75 = 64.5\phi$$

$$l_o = 1.5 \cdot 64.5\phi = 97\phi$$

Lap splice lengths for first and third type specimens were constructed as 40ϕ which is approximately $\frac{1}{3}$ of calculated lap splice length according to TS500 (2000).

The required lap splice lengths for first and third type specimens calculated according to TS500 (2000), for design ($f'_c=10$ MPa, $f_y=220$ MPa) and actual material strength values ($f'_c=3.7$ MPa; $f_y=338$ MPa) are presented in Table 4.4. It should be noted that as the actual yield strength of longitudinal bars was higher and concrete strength was lower in the experimental work than the values considered during design, like the case of majority of existing structures, the required lap splice lengths are remarkably higher in case of actual material strengths used in the experimental study.

Table 4.4 : Required lap splice lengths for smooth reinforcing bars according to design strengths of materials and experimentally determined material strengths (TS500, 2000).

Specimens	Considering design strength of materials	Considering the experimental determined material strengths
First type specimens	51 ϕ	129
Third type specimens	39 ϕ	97

4.2.5 Calculation of lap splice length for the second type specimens (TS500, 2000)

Lap splice length, l_o , is directly related with the anchorage length, l_b , and can be calculated by Eq. (4.12) according to TS500 (2000).

$$l_o = c \cdot l_b \quad (4.12)$$

$c = 1.5$ if all lap splices are formed at the same section.

The anchorage length (l_b) for deformed reinforcing bars can be calculated by Eq. (4.19).

$$l_b = 0.12 \cdot \phi \cdot \frac{f_{yd}}{f_{ctd}} \quad (4.12a)$$

$$f_{yk} = 460 \text{ MPa}$$

$$f_{yd} = \frac{f_y}{1.15} = \frac{460}{1.15} = 400 \text{ MPa} \quad (4.12b)$$

$$f_c = 25.5 \text{ MPa}$$

$$f_{ct} = 0.35 \cdot \sqrt{f_c} = 0.35 \cdot \sqrt{25.5} = 1.76 \text{ MPa} \quad (4.12c)$$

$$l_b = 0.12 \phi \cdot \frac{400}{1.76} = 27 \phi$$

$$l_o = 1.5 \cdot 27 \phi = 40 \phi$$

Lap splice lengths for the second type specimens were constructed as 40ϕ .

4.3 Test setup

4.3.1 Testing Procedure

All specimens were tested at Istanbul Technical University Structural and Earthquake Engineering Laboratory.

The transverse load was applied at the tip of the specimen, approximately at 1200 mm height from the base of the column with a MTS hydraulic actuator of 250 kN capacity. An axial load of 124 kN ($\approx 57\%$ of column axial load capacity) and 282 kN ($\approx 18\%$ of column axial load capacity) was applied through a jack at the top of the columns for the first and the third type specimens and the second type specimens, respectively. The axial load was applied via two 6-wire-strand post tensioning tendons. The tendons passed through steel beam between the two sides of the column. At the top of the column, the tendons were attached to an another steel beam which allowed the tendons to be loaded by a centrally located post tensioning jack. The load was measured by load cell which was located on the jack. The specimens were tested under constant axial load and reversed cyclic flexure. The experimental test setup of the specimens is shown in Figure 4.5.

Following the anchorage of the specimen on the adaptor footing, vertical lines were drawn every 50 mm on the surface of the specimens to observe the crack pattern. The cracks formed due to corrosion and/or shrinkage was marked on the surface of the specimens. Ten mm diameter holes were drilled at 20 mm, 150 mm and 300 mm above the footing for mounting the LVDTs which were used to measure the displacement and calculate the moment-curvature relationships. The steps for the preparation of the specimen for the test can be seen in Figure 4.6

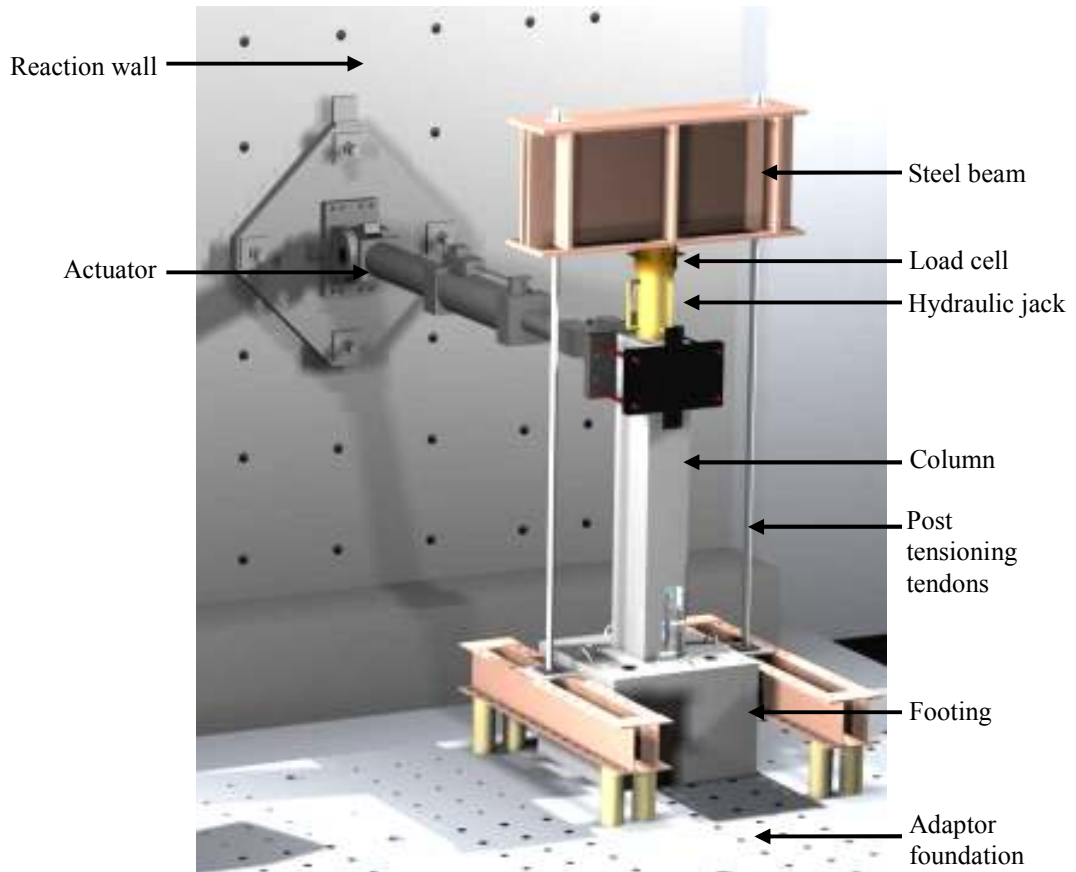


Figure 4.5 : Test setup (Demirtaş, 2008).

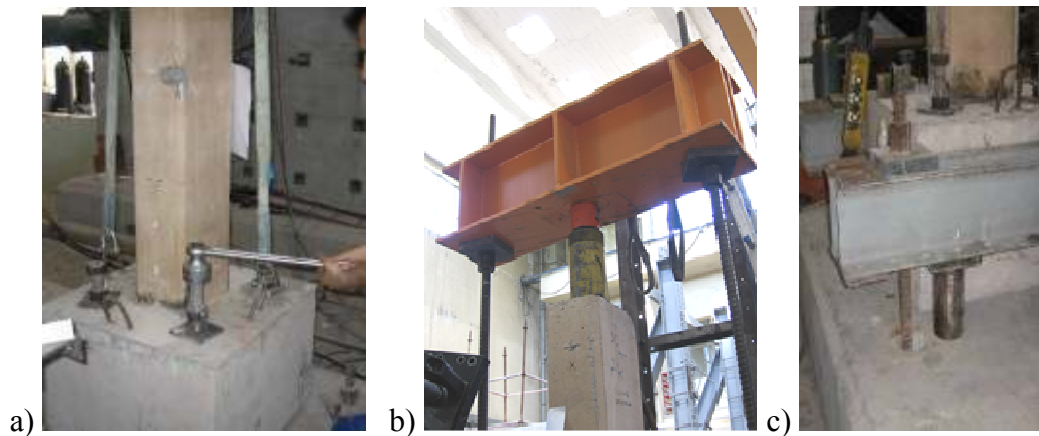


Figure 4.6 : Preparation of specimen for the test: (a) Maintaining the specimen to the adaptor footing, (b) Axial load setup, (c) Placement of post tensioning tendons.

4.3.2 Instrumentation

Instrumentation of the specimens was a combination of TML transducers, FLA-3-11-3LT, PL-60-11-1L, HBM-K-LY41-6/120-3-3M group strain gauges, TML load cell and the interior load cell and interior transducer of MTS actuator. The data of these instruments reached TML TDS 303 data logger through TML ASW-50C switch box.

4.3.2.1 LVDTs

For evaluating the average curvature values of the specimens, six LVDTs were placed vertically parallel to the column measuring in 20 mm, 150 mm and 300 mm gauge lengths. Two of six LVDTs were CDP50 while four of six LVDTs were CDP25 type. For measuring the lateral displacement of the column, two LVDTs were placed horizontally at the mid (CDP100) and tip (SDP200) of the column length. Two of three LVDTs were placed on the footing for measuring the possible rotations, and one of three LVDTs was placed horizontally at the mid of the footing. The locations of the LVDTs are shown in Figure 4.7.

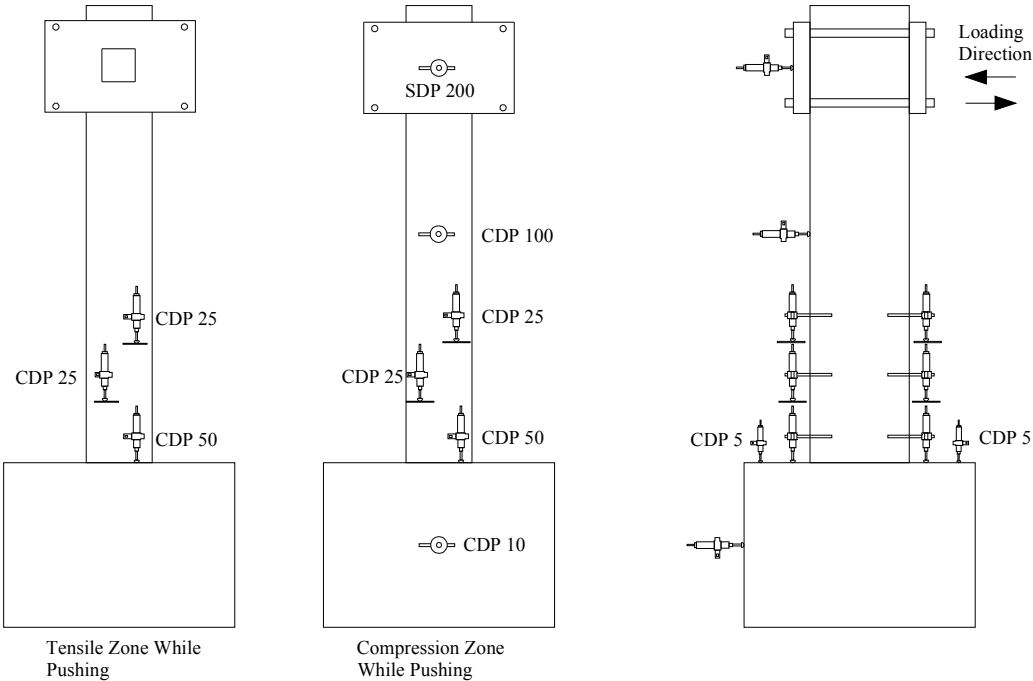


Figure 4.7 : The location of the LVDTs.

4.3.2.2 Straingauges

Straingauges were used to monitor strain development and strain profiles in the longitudinal and transverse reinforcement. The preparation of the surfaces of the reinforcing bars for adhering the straingauges are shown in Figure 4.8. The location of the straingauges at the starter, longitudinal and transverse bars are shown in Figure 4.9. The straingauges were also placed on starter bars to footing interface to allow the strain profile across the column to be monitored and check if the longitudinal reinforcement reached yield limits or not. The straingauges were adhered on the reinforcing cage of the specimens before casting. The surfaces of the reinforcing bars

were cleaned from rust with grindstone, and then with acetone. Strain gauges were adhered to these surfaces with cyanoacrylate based adhesive. Before the strain gauges were wrapped with an VM-tape isolation strap and one ply of insulated band, N-1 (water resistant material) was applied on the strain gauges. The notes which specified the locations and the types of the strain gauges were attached at the tip of the cables of the strain gauges.

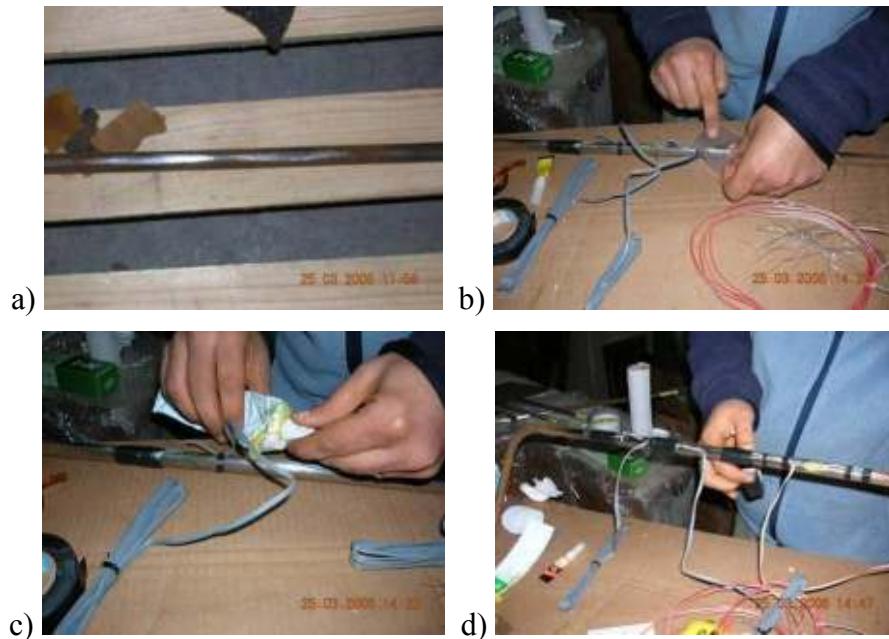


Figure 4.8 : (a) Cleaning the surfaces of the reinforcing bars from rust with grindstone, (b) Gluing the strain gauges on the reinforcing bars, (c) Application of the isolation material (N-1), (d) Wrapping with VM-tape isolation strap.

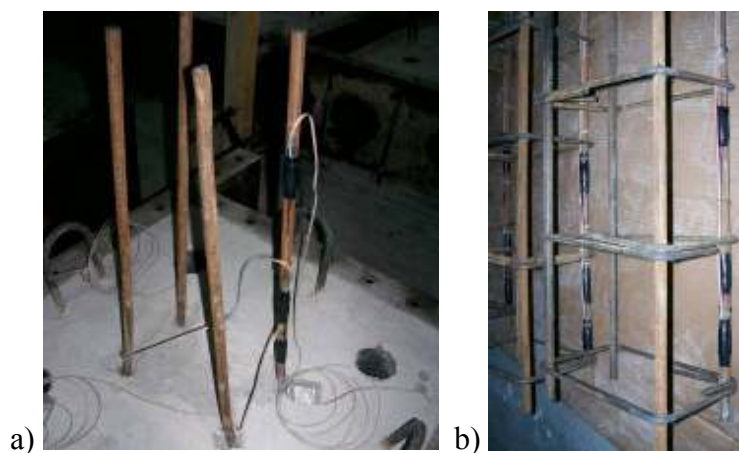


Figure 4.9 : Location of the strain gauges (a) at the starter bars, and (b) at longitudinal and transverse bars.

Four strain gauges were glued on the reinforcement in footing, four strain gauges were glued on the transverse bars, three strain gauges were glued on the longitudinal bars

and three strain gauges were glued on the starter bars. For measuring the strains on the transverse direction, strain gauges were glued to the surface of the columns on the same level with the transverse reinforcement. Before strain gauges were glued to the surface of the specimens with a strong glue, patex and sandpaper were applied to the surface and then cleaned with acetone. The locations of the surface strain gauges were shown in Figure 4.10.

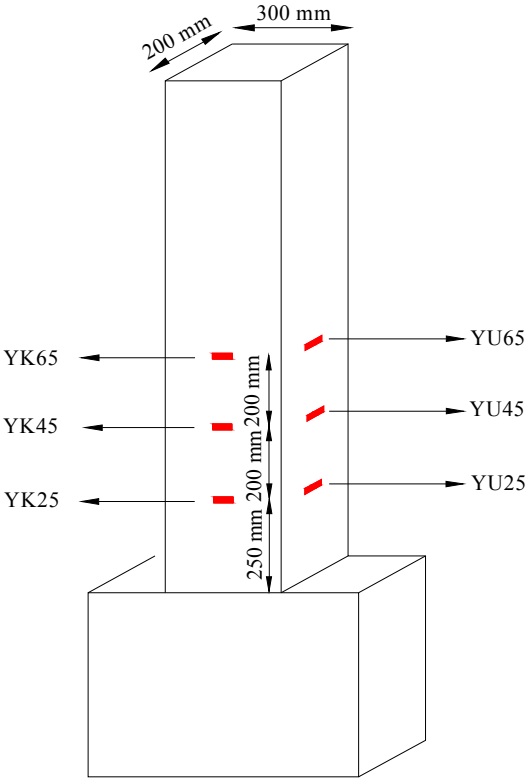


Figure 4.10 : The locations of the surface strain gauges.

Properties of surface strain gauges are presented in Table 4.5. The locations of the strain gauges of the specimens are shown in Figure 4.11. The properties of strain gauges on starter bars, longitudinal bars and transverse bars are shown in Table 4.6, Table 4.7 and Table 4.8, respectively.

Table 4.5 : Properties of surface straingauges.

Straingauges	Type of straingauge	Location	Gauge factor
YU65	PL60-11-1-L	650 mm above the footing on the long direction of the transverse reinforcement	2.09±1%
YU45	PL60-11-1-L	450 mm above the footing on the long direction of the transverse reinforcement	2.09±1%
YU25	PL60-11-1-L	250 mm above the footing on the long direction of the transverse reinforcement	2.09±1%
YK65	PL60-11-1-L	650 mm above the footing on the short direction of the transverse reinforcement	2.09±1%
YK45	PL60-11-1-L	650 mm above the footing on the short direction of the transverse reinforcement	2.09±1%
YK25	PL60-11-1-L	650 mm above the footing on the short direction of the transverse reinforcement	2.09±1%

Table 4.6 : Properties of straingauges on the starter bars.

Straingauges	Type of straingauge	Location above the footing	Gauge factor
TF1	K-LY41-6/120-3-3M	-10 mm	2.06±1%
TF10	K-LY41-6/120-3-3M	-100 mm	2.06±1%
TF20	FLA-3-11-3LT	-200 mm	2.13±1%
TF30	FLA-3-11-3LT	-300 mm	2.13±1%
FD10	K-LY41-6/120-3-3M	100 mm	2.06±1%
FD20	K-LY41-6/120-3-3M	200 mm	2.06±1%
FD40	K-LY41-6/120-3-3M	400 mm	2.06±1%

Table 4.7 : Properties of straingauges on the longitudinal bars.

Straingauges	Type of straingauge	Location above the footing	Gauge factor
KD10	K-LY41-6/120-3-3M	100 mm	2.06±1%
KD20	K-LY41-6/120-3-3M	200 mm	2.06±1%
KD40	K-LY41-6/120-3-3M	400 mm	2.06±1%

Table 4.8 : Properties of straingauges on the transverse bars.

Straingauges	Type of straingauge	Location	Gauge factor
EDU1	FLA-3-11-3LT	On the long direction of the 1 st transverse reinforcement	2.13±1%
EDU2/EDU3	FLA-3-11-3LT	On the long direction of the 2 nd /3 rd transverse reinforcement	2.13±1%
EDK1	FLA-3-11-3LT	On the short direction of the 1 st transverse reinforcement	2.13±1%
EDK2/ EDK3	FLA-3-11-3LT	On the short direction of the 2 nd /3 rd transverse reinforcement	2.13±1%

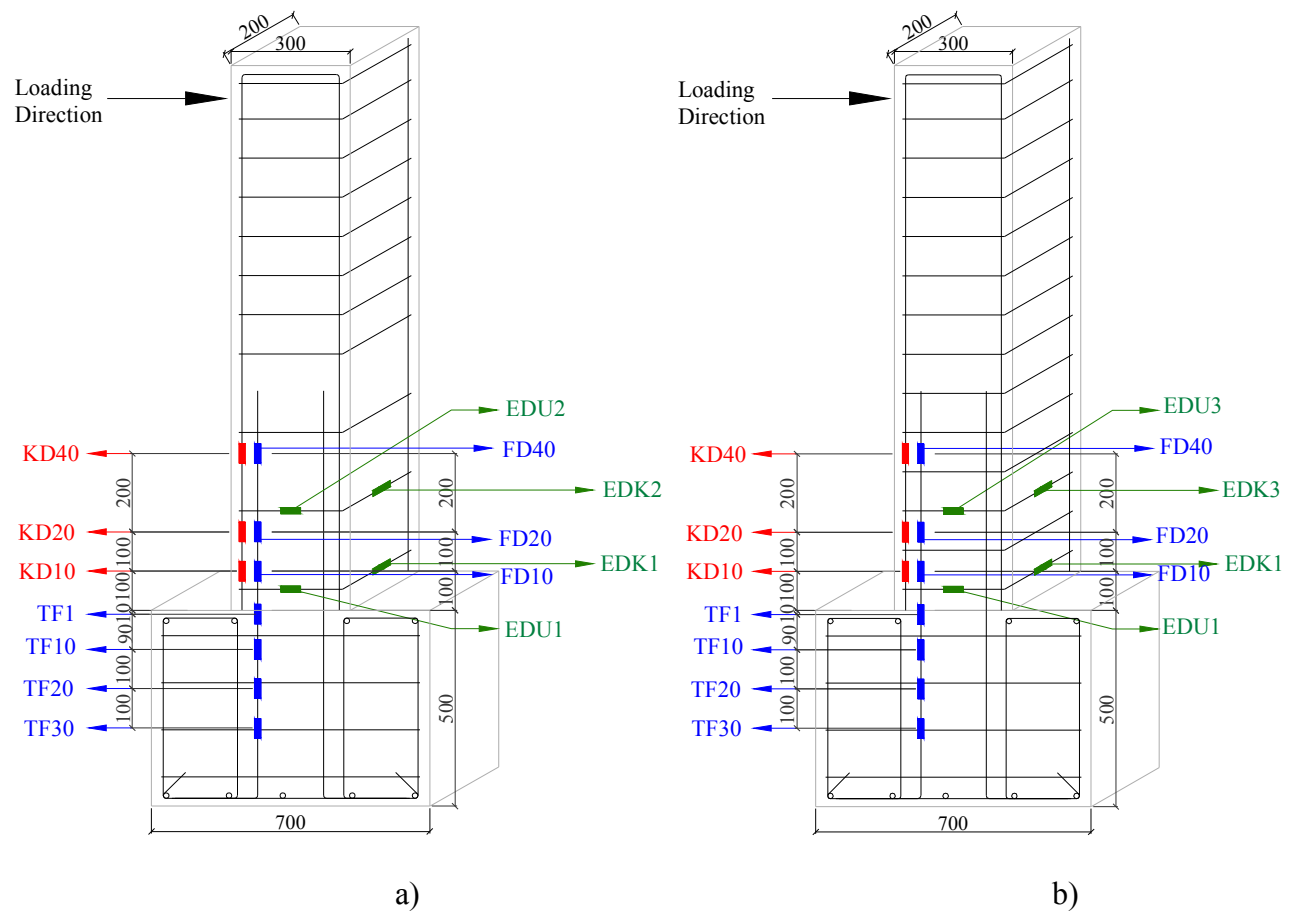


Figure 4.11 : The location of the strain gauges: (a) the first and the third type specimens, and (b) the second type specimens.

4.4 Loading History

A displacement based loading history was used for all specimens. To simulate the seismic actions, reversed lateral displacements were applied for pulling and pushing cycles to the specimens. Drift ratios (d/L) were calculated as the ratio of the lateral displacement of the tip of the column (d), to the column length (L). Loading history of the specimens are shown in Figure 4.12. The loading history was composed of excursions at certain drift ratios (± 0.0010 (± 1.2 mm), ± 0.0025 (± 3.00 mm), ± 0.0050 (± 6.00 mm), ± 0.0075 (± 9.00 mm), ± 0.0100 (± 12 mm), ± 0.0150 (± 18 mm), ± 0.0200 (± 24 mm), ± 0.0250 (± 30 mm), ± 0.0300 (± 36 mm), ± 0.0350 (± 42 mm), ± 0.0400 (± 48 mm), ± 0.0450 (± 54 mm), ± 0.0500 (± 60 mm), ± 0.0600 (± 72 mm), ± 0.0700 (± 84 mm), ± 0.0800 (± 96 mm)) for pulling and pushing cycles.

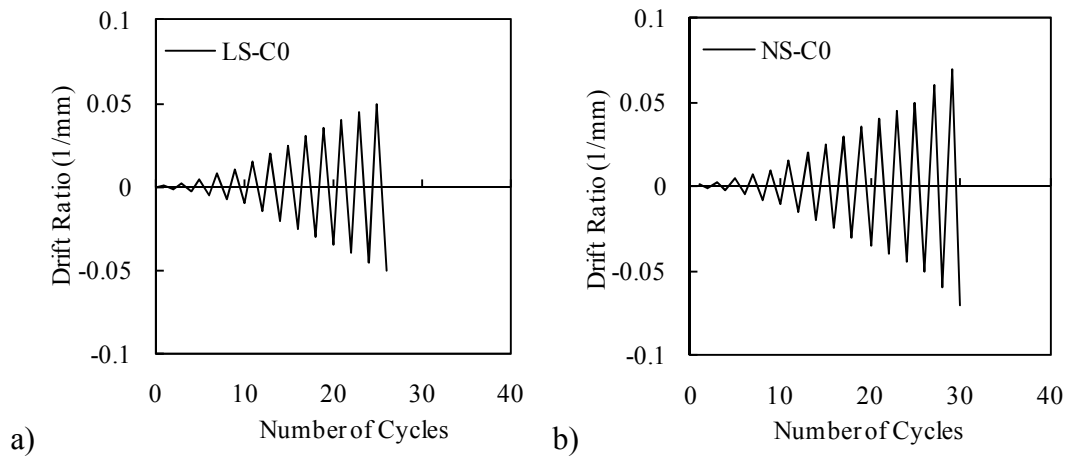


Figure 4.12 : Loading history of (a) the first and the third type specimens, (b) the second type specimens.

The properties of all specimens in case of exposed time to accelerated corrosion and corrosion potential measurements are presented in Table 4.9 and Table 4.10, respectively. E_{corr} is the corrosion potential measured by corrosionmeter. According to ASTM C876 (1999) corrosion potential less than -500 mV, between -500 ~ -350 mV and higher than -200 mV indicated corrosion activity of severe, high (90% probability) and low (10% probability) corrosion risk.

Table 4.9 : Properties of specimens.

Types of Specimens	Specimens	Accelerated corrosion time (day)	Exposed time to atmospheric conditions (day)	Maximum crack width (mm)
First type	LS-X0	-	-	-
	LS-X6	24	-	-
	LS-X8	30	-	0.1
	LS-X12	51	-	1.2
	LS-X21	96	43	1.6
	LS-X28	96	43	3.1
Second type	NS-X0	-	-	-
	NS-X9	-	-	-
	NS-X13	31	-	-
	NS-X16	95	43	1.4
	NS-X22	64	-	0.6
	NS-X54	95	487	2.7
Third type	LS-X19-H	96	43	2.4

Table 4.10 : Properties of specimens.

Types of Specimens	Specimens	E_{corr} (mV)	Date of test	Column age at the time of testing (days)	Axial load (kN)
First type	LS-X0	-75	01.06.2007	350	124.0
	LS-X6	-460	24.05.2007	342	124.0
	LS-X8	-475	10.09.2007	451	124.0
	LS-X12	-524	14.05.2008	698	124.0
	LS-X21	-539	04.12.2008	902	124.0
	LS-X28	-495	17.02.2010	1342	124.0
Second type	NS-X0	-113	13.06.2007	335	282.0
	NS-X9		18.09.2008	798	282.0
	NS-X13	-464	17.09.2007	431	282.0
	NS-X16	-464	24.12.2008	895	282.0
	NS-X22	-501	06.08.2008	755	282.0
	NS-X54	-514	11.02.2010	1309	282.0
Third type	LS-X19-H	-506	19.02.2010	1344	124.0

5. SPECIMEN PREPARATION

Preparation of specimens was started on 25.03.2006 at Telateks. After the production of the specimens, they were taken to the ITU Structural and Earthquake Engineering Laboratory on 01.09.2006.

5.1 Footings

Steel and wood formworks were prepared for the footings of specimens (Fig. 5.1a-b).

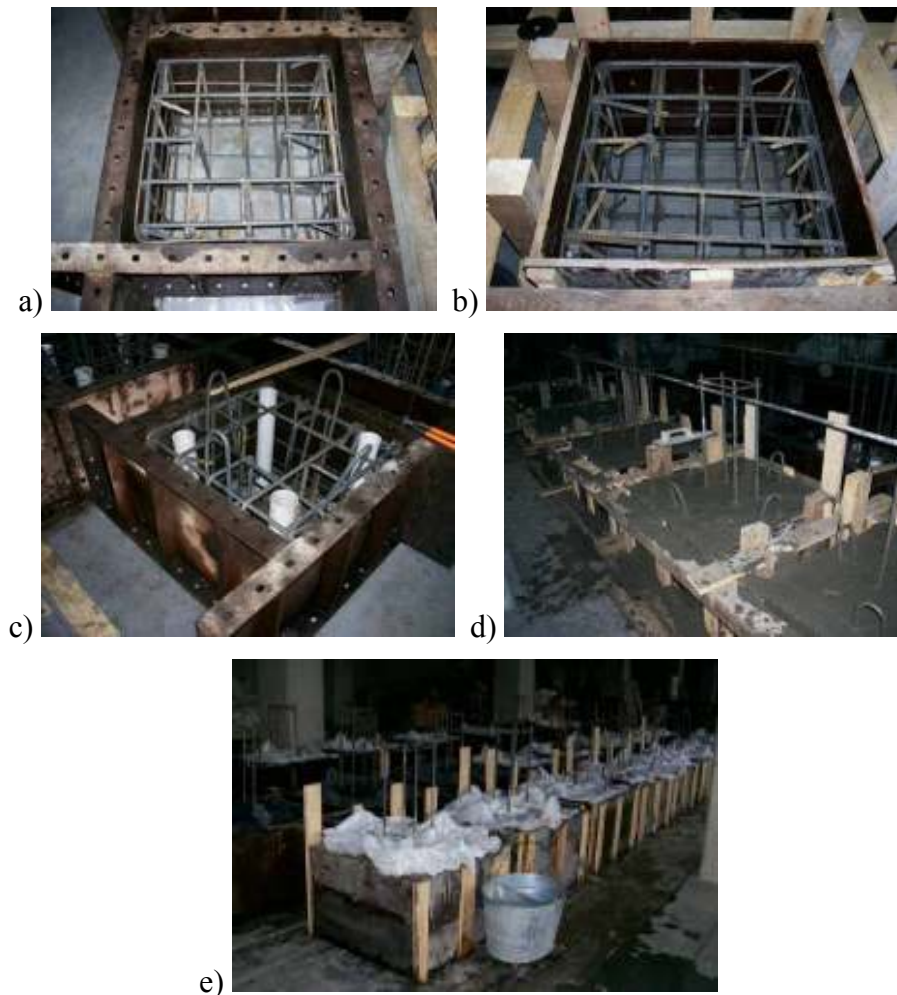


Figure 5.1 : Views from preparation of footing: (a) Steel molds, (b) Wood molds, (c) Hooks and PVC pipes, (d) Placement of concrete to footing, (e) Curing application.

The footing cage was placed in the formworks after the strain gauges were glued to the starter bars. The bottom extension of the four hooks, used for specimen transport, was placed under the reinforcement cage. Four plastic pipes, 70 mm in diameter, were placed in footing reinforcement cage in order to anchor the specimen to adaptor footing (Fig. 5.1c). The concrete for the footing was cast on 05.04.2006 by Nuh Beton A.Ş (Figure 5.1 5.1d).

Concrete was vibrated during the placement of concrete. Six standard cylinder specimens (150×300 mm) were taken for 28th day compressive strength tests, during the casting of concrete of footings. Curing was applied for six days after casting of concrete (Fig. 5.1e). Specimens were cured with water twice a day and specimens were covered with a fabric which has low permeability.

5.2 Columns

For the bond between the column and the footing, chipping was performed at the interface (Fig. 5.2a).



Figure 5.2 : Preparation of columns (a) Chipping at the interface, (b) Bonding strain gauges to the starter bars, (c) Placement of plastic spacers for concrete cover, (d) Placement of molds.

Before the placement of reinforcing cages, plastics for concrete cover were placed to the transverse reinforcement (Fig. 5.2b). Reinforcing cages were prepared by adhering strain gauges on to the reinforcement (Fig. 5.2c). 20 mm thick plywood molds were prepared to use during concrete casting (Fig. 5.2d). All the molds were oiled before concrete casting.

The columns of the first and the third type specimens were cast on 16.06.2006 while the columns of second type specimens were cast on 13.07.2006, which were provided by Oyak Beton A.Ş. Curing was applied for five days after casting of concrete of columns (Figure 5.3a). During the concreting of columns, two standard cylinder specimens (150×300 mm) without CaCl₂ and fifteen standard cylinder specimens (150×300 mm) with CaCl₂ were taken for 28, 90, 180 and 360th days compressive strength tests (Figure 5.3b). Seven slump tests were performed. Concrete was vibrated during the placement of concrete. After the casting of reference specimens, CaCl₂ was added to the concrete batch (Figure 5.3c).

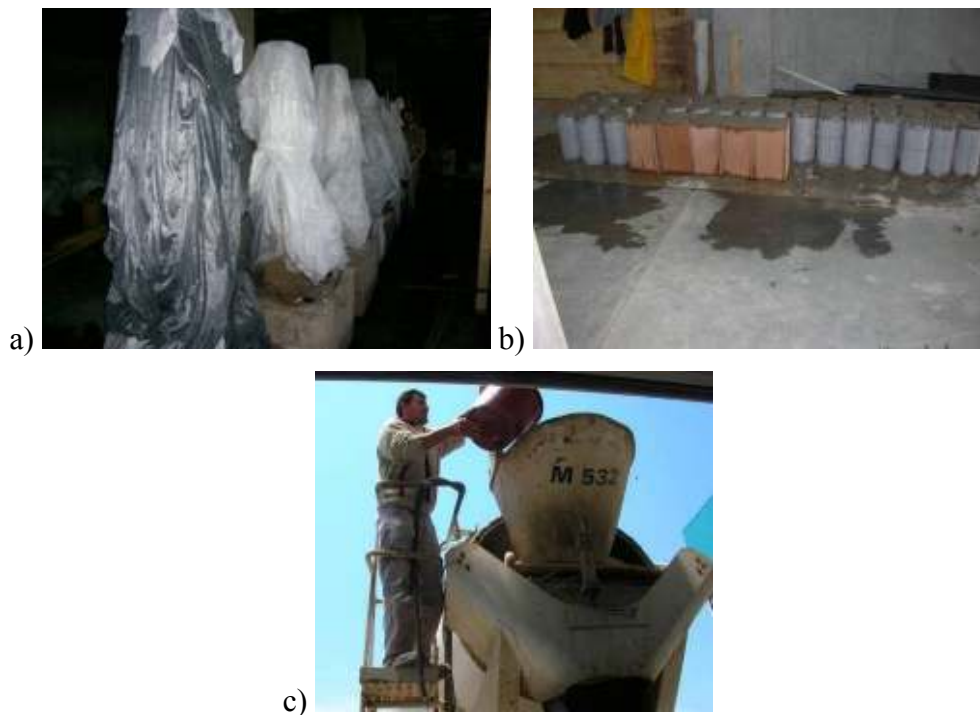


Figure 5.3 : Preparation of columns: (a) Application of curing to the columns, (b) Preparation of standard cylinder specimens, (c) Addition of CaCl₂ to the concrete.

The process which was applied for the first and the third type, was performed for the the second type specimens similarly (Figure 5.4).



Figure 5.4 : The first, the second and the third type specimens.

6. TEST RESULTS

6.1 Test Results of Materials

6.1.1 Concrete

Concrete mix constituents for footing and the first and the third type specimens are shown in Table 6.1 and Table 6.2, respectively. The stress-strain relationship of concrete was obtained by performing compressive strength tests on standard 150×300 mm cylinder specimens. The elasticity modulus of concrete is 6186 MPa.

Table 6.1 : Concrete mix constituents for the footings of the first and the third type specimens.

Constituents	(kg/m ³)	Properties
Cement	252	
Ash	148	
Water	240	
Crushed sand	398	
Sand	307	
Crushed Aggregate No.1	399	≤ 12 mm
Crushed Aggregate No.2	481	≤ 22 mm
Total	2225	

Table 6.2 : Concrete mix constituents for the columns of the first and the third type specimens.

Constituents	(kg/m ³)	Properties
Crushed sand No.1	672	0 - 3 mm
Crushed sand No.2	574	0 - 5 mm
Coarse Aggregate No.1	666	5 - 12 mm
Cement	197	CEM2 42.5R
Water	189	
Total	2298	

Concrete mix constituents for the columns of the second type specimens are shown in Table 6.3. The elasticity modulus of concrete is 23048 MPa. The 28, 180, 360 day compressive strength and elasticity modulus values of the concrete are shown in Figure 6.1 and Figure 6.2 for different type of specimens, respectively.

Table 6.3 : Concrete mix constituents for the columns of the second type specimens.

Constituents	(kg/m ³)	Properties
Crushed sand	487	0-4 mm
Coarse Aggregate No.1	510	4-16 mm
Coarse Aggregate No.2	511	8-22 mm
Natural sand	369	0-1 mm
Cement	315	CEM2 42.5R
Water	159	
Ash	40	
Air entrainment	%1.8	
TOTAL	2391	

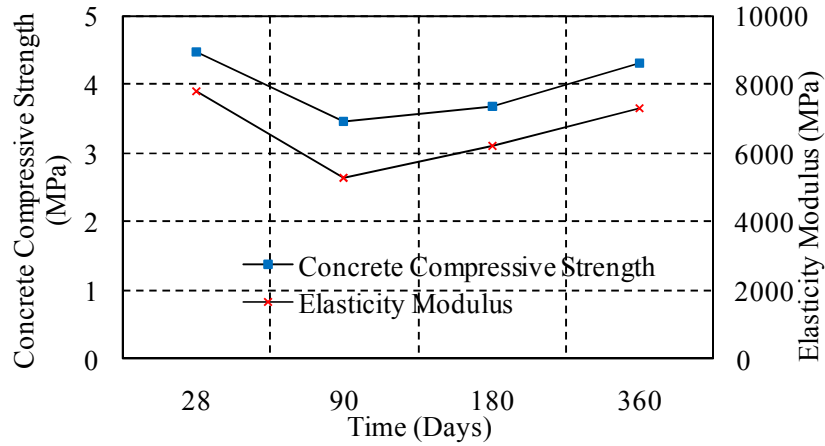


Figure 6.1 : The 28, 90, 180, 360 day compressive strength and elasticity modulus values of the first and the third type specimens.

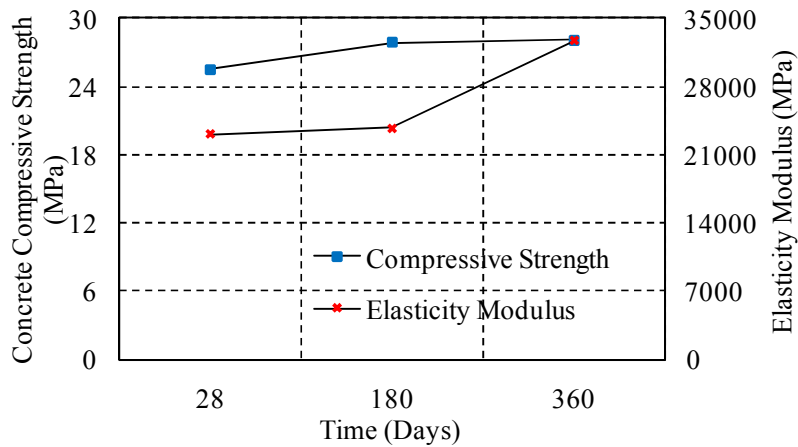


Figure 6.2 : The 28, 180, 360 day compressive strength and elasticity modulus values of the second type specimens.

6.1.2 Reinforcing bars

Stress-strain relationships of reinforcing bars of S220 longitudinal bars and transverse bars are shown in Figure 6.3. The average mechanical characteristics of 14 mm diameter longitudinal and 10 mm diameter transverse bars are given in Table 6.4. In this table; f_y , f_{max} , f_u are yield, maximum and ultimate tensile stresses, and ϵ_y , ϵ_{max} and ϵ_u are the tensile strains corresponding to f_y , f_{max} and f_u , respectively.

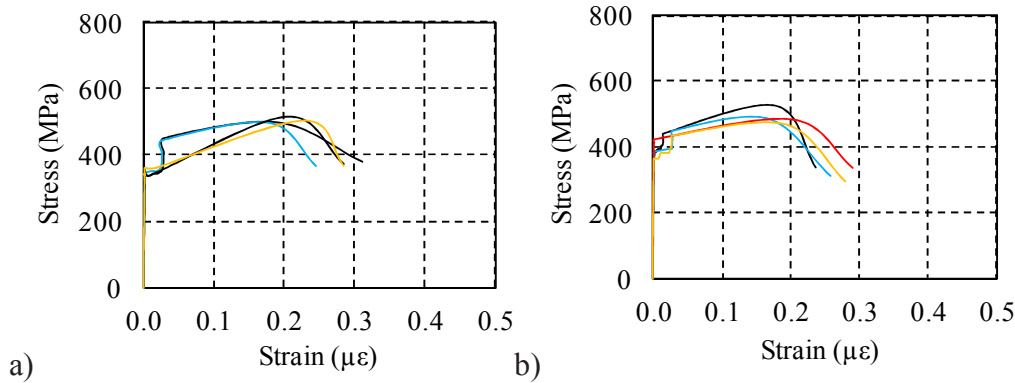


Figure 6.3 : Stress-strain relationships of a) longitudinal bars ($\phi 14$) and b) transverse bars ($\phi 8$) of S220.

Stress-strain relationships of reinforcing bars of S420 longitudinal bars and transverse bars are shown in Figure 6.4.

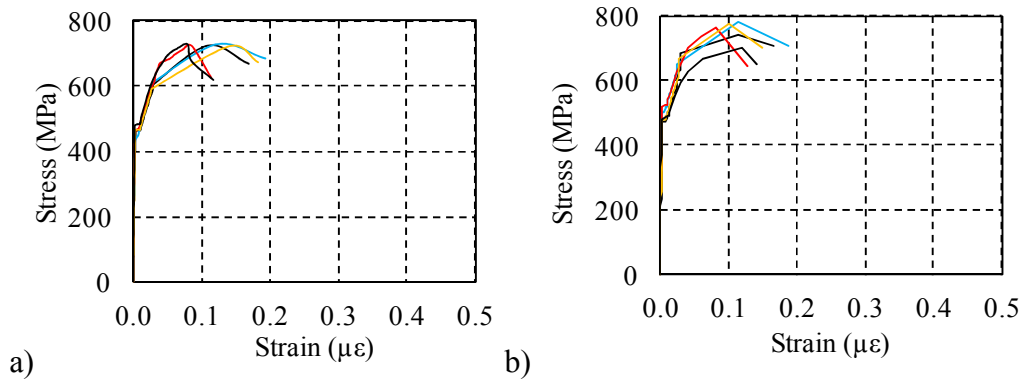


Figure 6.4 : Stress-strain relationships of a) longitudinal bars ($\Phi 14$) and b) transverse bars ($\Phi 8$) of S420.

Table 6.4 : The mechanical characteristics of reinforcing bars.

Reinforcing bars		f_y (MPa)	ϵ_y	f_{max} (MPa)	ϵ_{max}	f_u (MPa)	ϵ_u
S220	$\phi 14$	337	0.0016	499	0.2148	366	0.2838
	$\phi 8$	377	0.0018	494	0.1895	324	0.3202
S420	$\Phi 14$	460	0.0022	724	0.0926	652	0.1156
	$\Phi 8$	486	0.0023	755	0.0785	681	0.1343

6.2 Test Result of the First Type Specimens

6.2.1 LS-X0

No cracks were observed while loading to target displacements of ± 1.2 mm (drift ratio 0.10%) and ± 3 mm (drift ratio 0.25%).

First flexural crack was observed at the interface of the column and footing during loading to target displacement of 6 mm (drift ratio 0.50%). The view of the specimen LS-X0 after -0.50% drift ratio is shown in Figure 6.5.

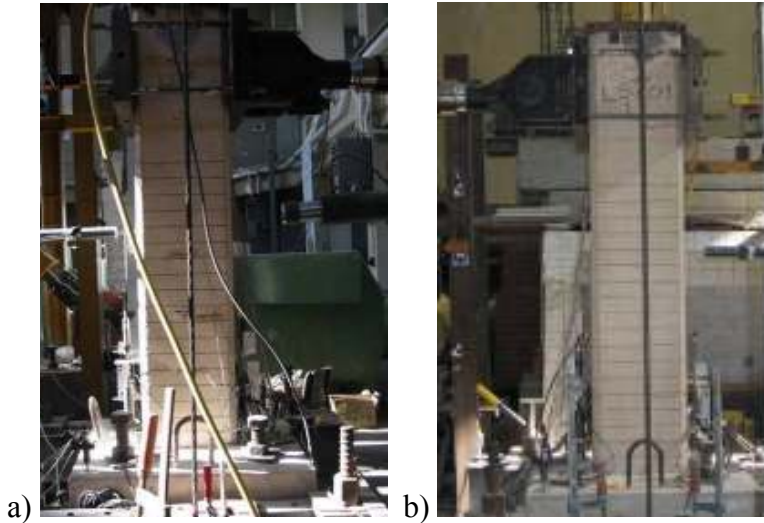


Figure 6.5 : a) North, and b) South view of the LS-X0 specimen after -0.50% drift ratio.

Second flexural crack was observed 250 mm above the footing during loading to target displacement of 12 mm (drift ratio 1.00%). The view of the specimen LS-X0 after -1.50% drift ratio is shown in Figure 6.6.

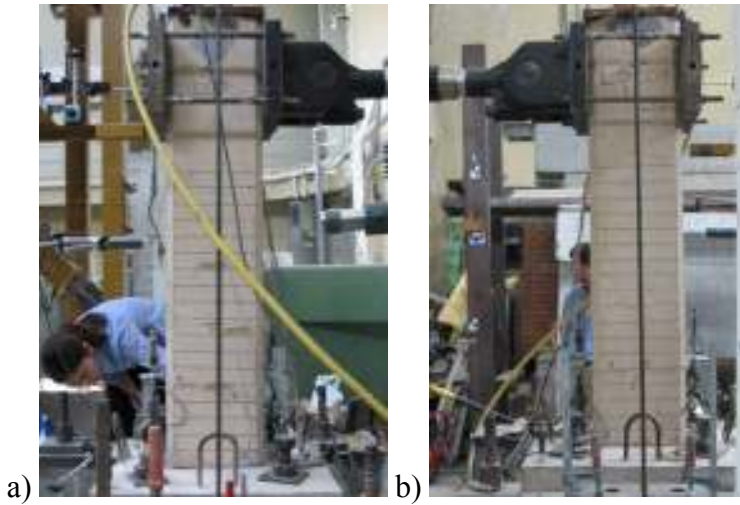


Figure 6.6 : a) North, and b) South view of the LS-X0 specimen after -1.50% drift ratio.

During loading to target displacement of 24 mm (drift ratio 2.00%), vertical cracks formed at the lap splice zone. Similar type of damages occurred at the opposite side while the column was subjected to pulling. The view of the specimen LS-X0 after -2.50% drift ratio is shown in Figure 6.7.

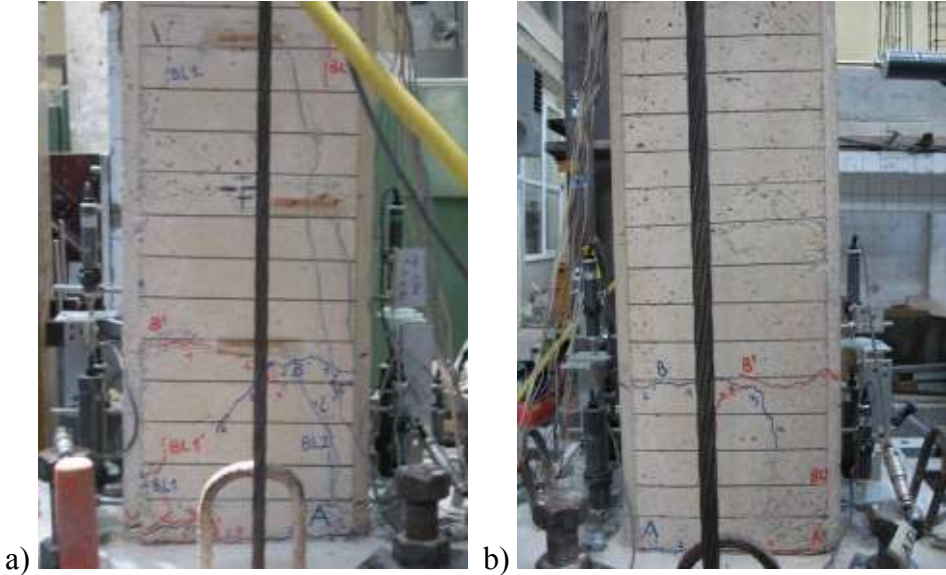


Figure 6.7 : a) North, and b) South view of the LS-X0 specimen after -2.50% drift ratio.

During loading to target displacement of 42 mm (drift ratio 3.50%) concrete cover spalled. The view of the specimen LS-X0 after -3.50% drift ratio is shown in Figure 6.8.

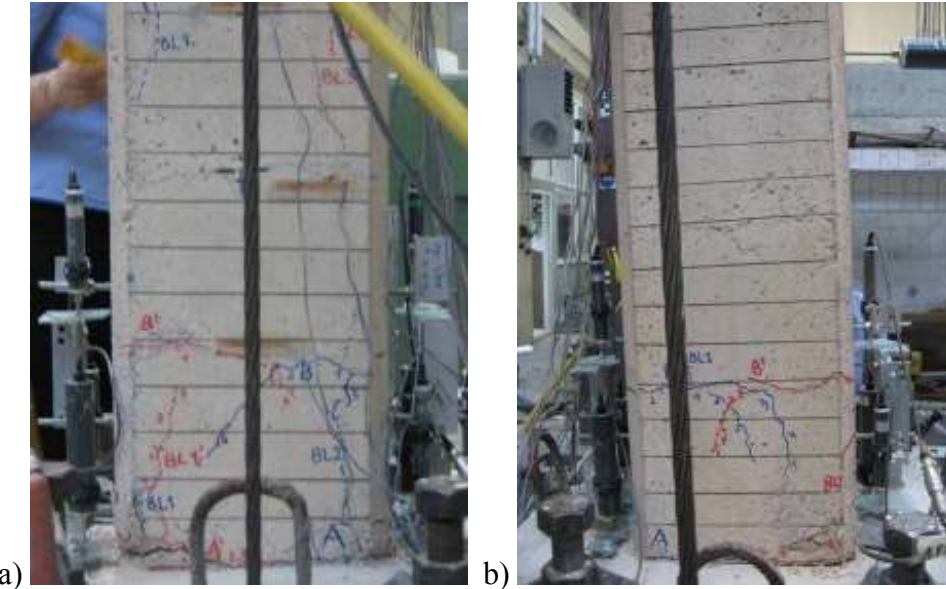


Figure 6.8 : a) North, and b) South view of the LS-X0 specimen after -3.50% drift ratio.

As the testing progressed, cracks generally accumulated 300 mm above the footing. The view of the specimen LS-X0 specimen after -5.00% drift ratio is shown in Figure 6.9.

Summary of the seismic behavior of specimen LS-X0 is shown in Table 6.5. Crack propagation of the specimen LS-X0 while pushing and pulling cycles are given in Appendix C.

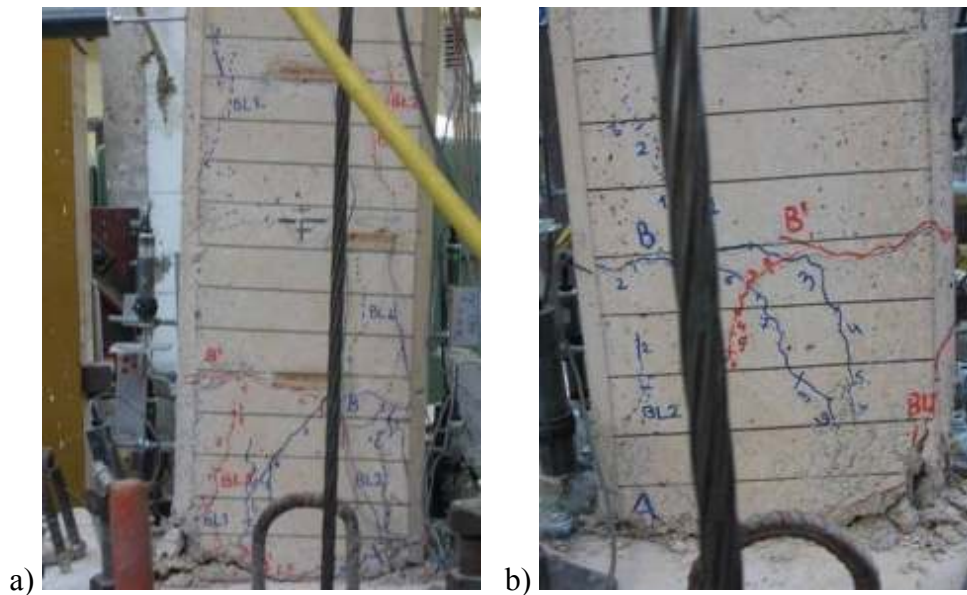


Figure 6.9 : a) North, and b) South view of the LS-X0 specimen after -5.00% drift ratio.

Table 6.5 : Summary of the seismic behavior of LS-X0.

Drift ratio (%)	δ (mm/mm)	P (kN)	Observations
0.1	± 1.2	4.67/-6.74	No crack was observed.
2.5	± 3.0	10.27/-11.91	No crack was observed.
0.5	± 6.0	14.72 /-15.23	First flexural crack at column-footing interface was observed.
0.75	± 9.0	16.19 /-16.17	
1.0	± 12.0	15.91/-16.48	Flexural shear cracks was observed.
1.5	± 18.0	15.88 /-15.86	
2.00	± 24.0	15.28 /-15.46	Vertical cracks, indicating slip, formed at the interface of the column and footing and lap splice zone during pulling and pushing cycles.
2.50	± 30.0	14.80 /-14.36	Crushing started at the interface of the column and footing at the compression zone.
3.0	± 36.0	14.10 /-13.31	
3.50	± 42.0	13.63 /-11.03	Concrete cover spalled at the north side of the column at the compression zone. Concrete crushed at the south side of the column.
4.0	± 48.0	12.67/-10.00	
4.50	± 54.0	11.58 /-8.32	
5.0	± 60.0	9.95 /-6.82	Specimen underwent excessive deformation out of its axis and test was ended by decreasing the axial load.

Force-displacement relationship of the specimen LS-X0 is presented in Figure 6.10. In this figure, P is applied lateral load and P_0 is the theoretical lateral load capacity of the specimen determined without considering the effect of corrosion. First flexural crack, first shear crack, first vertical crack, crushing of concrete cover, spalling of concrete cover, maximum strain on the starter bar and maximum strain on the longitudinal bar are marked on the figure. As seen from Figure 6.10, no strength loss was observed. The decline is due to the horizontal component of the axial load. As the line of action of the axial load does not pass through the column base during the tests of all column specimens, to account P- Δ effects, the effect of axial load resolved to its horizontal and vertical components. Then, the horizontal components of the axial load subtracted from the force applied by the actuator and the net horizontal force obtained. This correction was done due to PEER (2004) Case 4.

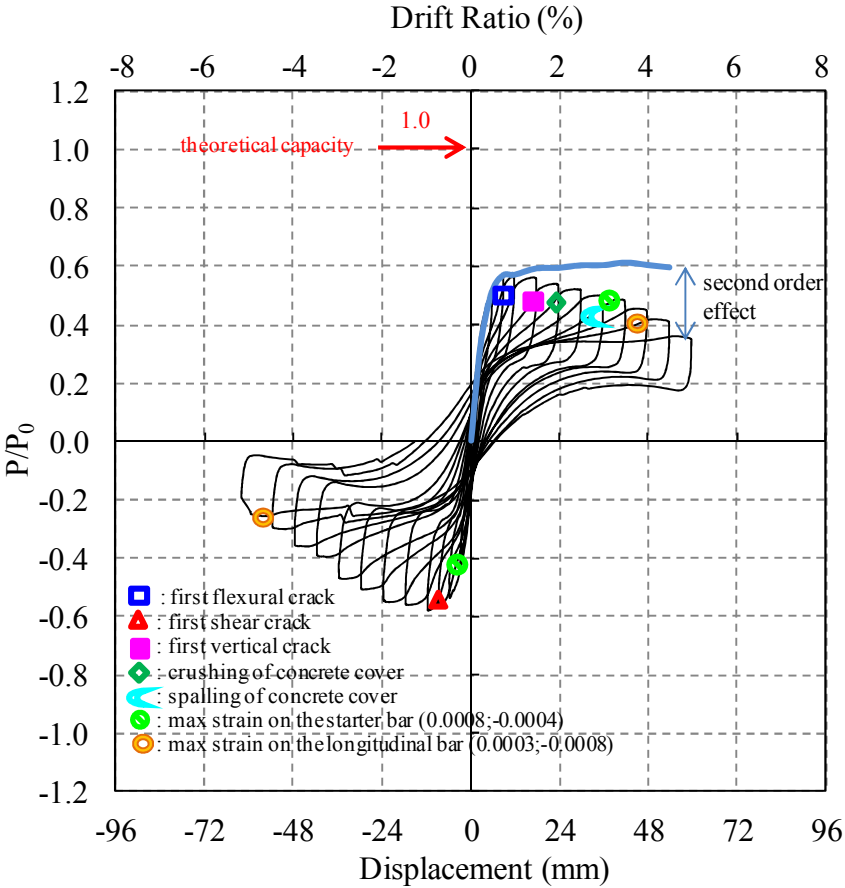


Figure 6.10 : Lateral load/Theoretical load capacity capacity versus displacement for LS-X0.

For the observation of distribution of damages, moment-curvature relationships were obtained at different gauge lengths at the potential plastic hinge zones (Figure 6.11).

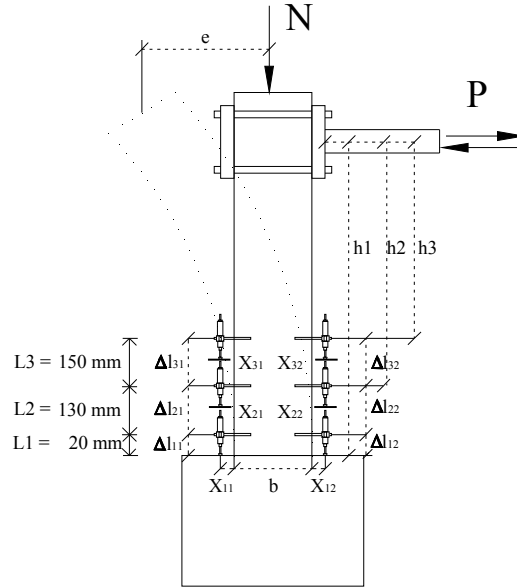


Figure 6.11 : Test setup with measurement system used in obtaining moment-curvature relationship.

The calculation of the moment-curvature relationships are performed assuming that plane sections remain plain. Moment is calculated by using Eq. (6.1) taking into account the second-order effects. In the equation, P is the lateral load, H is the column height, N is the axial load, and e is the eccentricity due to horizontal displacement of the column, subjected to lateral load, P .

$$M = P \cdot H + N \cdot e \quad (6.1)$$

For the calculation of moment-curvature relationships, the average curvature values were obtained in 20 mm, 150 mm and 300 mm above the footing. Curvatures were calculated by dividing the obtained strains from the LVDTs to the distance between the LVDTs (Eq. (6.2)).

$$x = \frac{\varepsilon_1 + \varepsilon_2}{b + X_{11} + X_{12}} \quad (6.2)$$

Distances between the concrete surfaces of the specimens and the LVDTs of the specimens are presented in Appendix B.

Average experimental moment-curvature relationships obtained for critical sections of the specimen LS-X0 are presented in Figure 6.12.

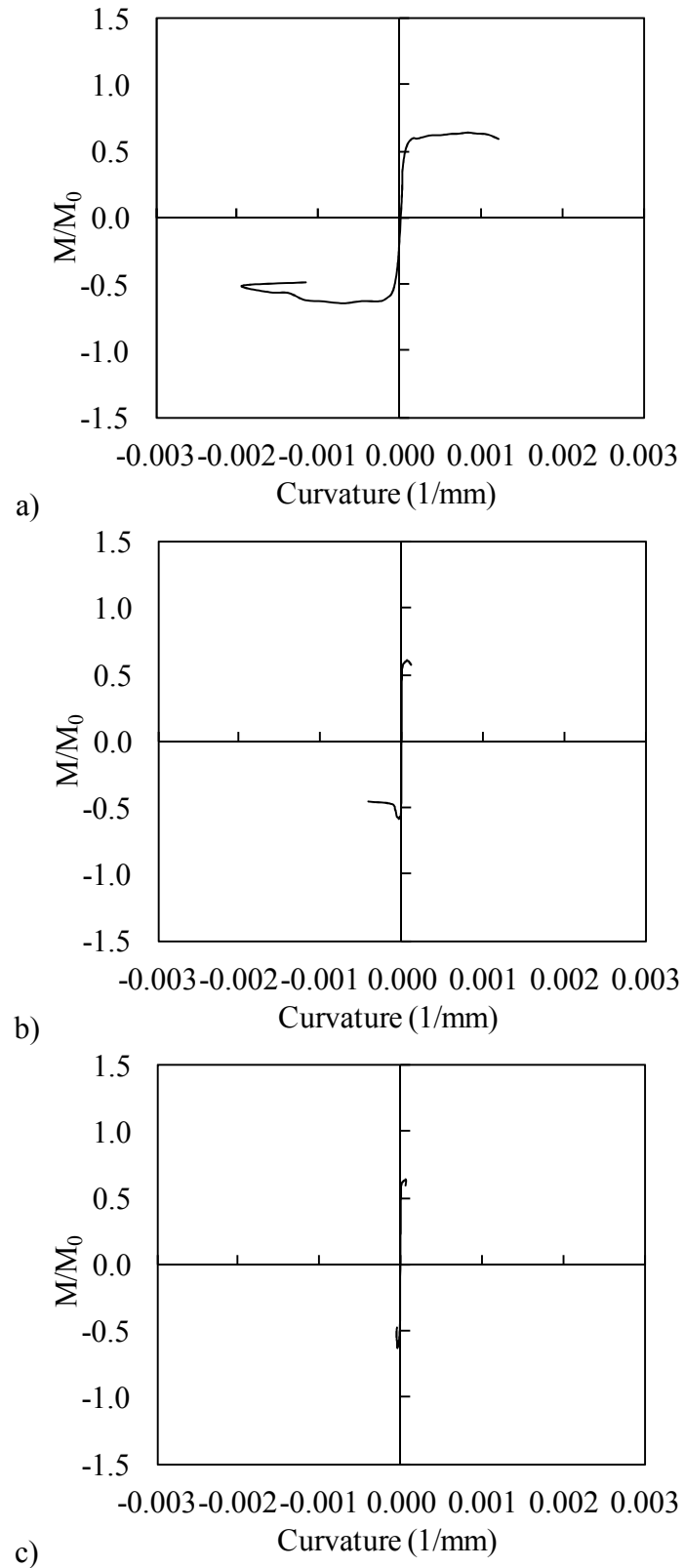


Figure 6.12 : Moment-curvature relationships obtained for a) 0-20 mm, b) 20-150 mm, c) 150-300 mm gauge lengths.

For the calculation of moment-curvature relationships, the average curvature values obtained for the ranges of 0-20 mm, 20-150 mm and 150-300 mm heights above the footing were taken

into account. As seen from Figure 6.12, the curvature values of the member measured in 20-150 mm and 150-300 mm height above the support are in the order of 5.10^{-5} (1/mm), while the curvatures measured in 0-20 mm height are in the order of 3.10^{-3} (1/mm). According to Figure 6.12, it is of interest to note that the damage is accumulated especially in 20 mm height of the member from top of the base.

According to the data from the straingauges on the starter bars of the LS-X0, the maximum strain while pushing was 0.0008, measured from the strain gauge at +200 mm above the footing for P=13.63 kN at 0.035 drift ratio; the maximum strain while pulling was -0.0004, measured from the strain gauge at +100 mm above the footing when P=-11.91 kN at -0.0025 drift ratio. According to the data from the straingauges on the longitudinal bars of the LS-X0, the maximum strain while pushing was 0.0003, measured from the strain gauge at +400 mm above the footing when P=12.67 kN at 0.04 drift ratio; the maximum strain while pulling was -0.0008, measured from the strain gauge at +200 mm above the footing when P=-6.82 kN at -0.05 drift ratio. Strain distribution of the starter bars and longitudinal bars of LS-X0 while pushing and pulling are shown in Figure 6.13 and Figure 6.14, respectively. As seen from Figure 6.13 and Figure 6.14, the strain values did not reach yield strain.

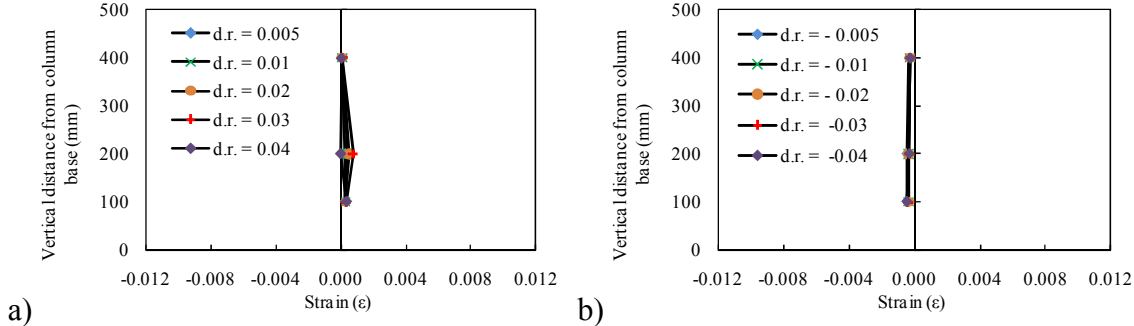


Figure 6.13 : Strain distribution of the starter bars of LS-X0 a) while pushing, b) while pulling.

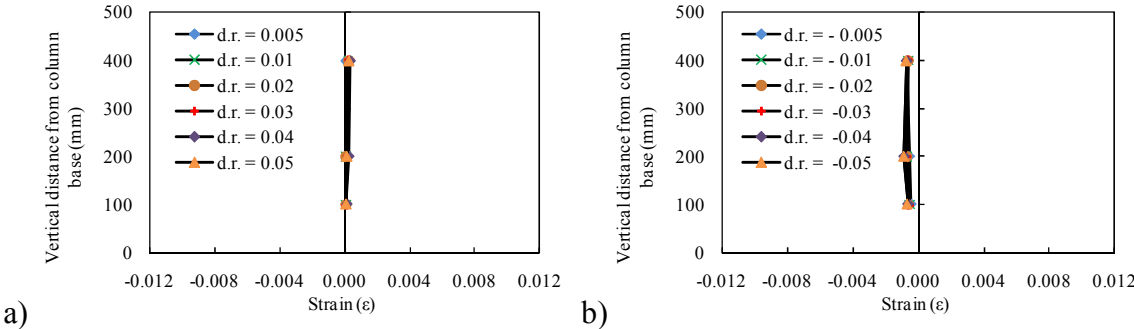


Figure 6.14 : Strain distribution of the longitudinal bars of LS-X0 a) while pushing b) while pulling.

6.2.2 LS-X6

This specimen was tested the first. The first three loading cycles were force-controlled, and later the test was performed displacement-controlled. No cracks were observed while loading to target force of 5.49 kN (drift ratio 0.0875%) and 10.94 kN (drift ratio 0.23%) which were 20% and 40% of the force theoretically calculated by BAKE (2000), respectively.

First flexural crack was observed at the interface of the column and footing (A-north, A-south) and (B-north) and shear crack (B-south) during loading to target force of 15.08 kN (drift ratio 0.6%). As the 60% of the force theoretically calculated from BAKE could not be reached in the pulling cycle, later the test was performed displacement-controlled. During loading to target displacement of -9.6 mm (drift ratio 0.80%) flexural cracks were observed at the interface of the column and footing (A'-north). Other flexural cracks (B'-north, A'-south, B'-south) and vertical cracks were observed at north and south sides. The view of the specimen LS-X6 after -0.50% drift ratio is shown in Figure 6.15.

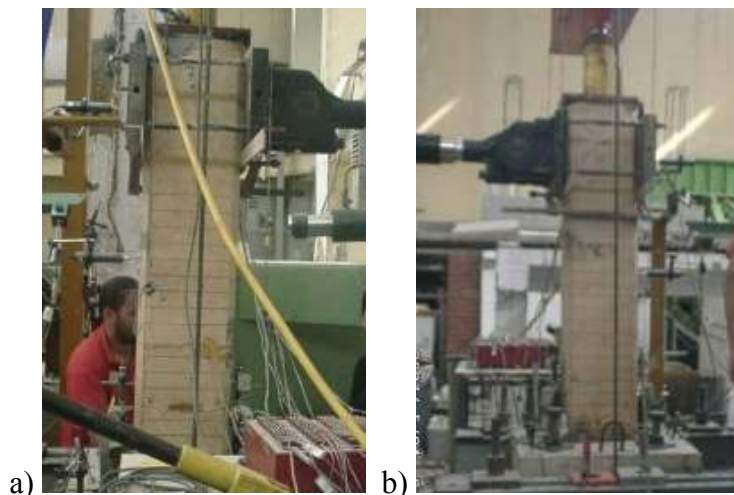


Figure 6.15 : a) North, and b) South view of the LS-X6 specimen after -0.50% drift ratio.

During loading to target displacement of 12 mm (drift ratio 1.00%), propagation of the existing crack (B-north) and vertical crack at the south side were observed. During loading to target displacement of -12 mm (drift ratio -1.00%) flexural crack was observed at the interface of the column and footing (C'-south).

During loading to target displacement of -18 mm (drift ratio -1.50%), shear cracks (C'-north, D'-north, D'-south), propagation of existing cracks (A'-south, B'-south) and vertical cracks were observed. The view of the specimen LS-X6 after -1.50% drift ratio is shown in Figure 6.16.

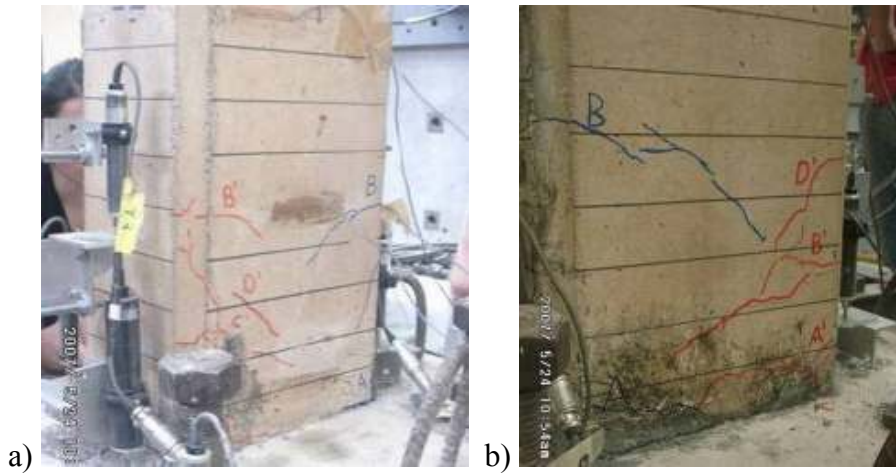


Figure 6.16 : a) North, and b) South view of the LS-X6 specimen after -1.50% drift ratio.

During loading to target displacement of 24 mm (drift ratio 2.00%) flexural crack (C-south) and vertical crack at south side were observed. During loading to target displacement of -24 mm (drift ratio -2.00%) flexural crack (E'-north) and propagation of existing crack (D'-north) were observed.

During loading to target displacement of -30 mm (drift ratio -2.50%), propagation of existing cracks (D'-north, E'-north, D'-south, B'-south) and vertical cracks at north and south sides were observed. The view of the specimen LS-X6 specimen after -2.50% drift ratio is shown in Figure 6.17.

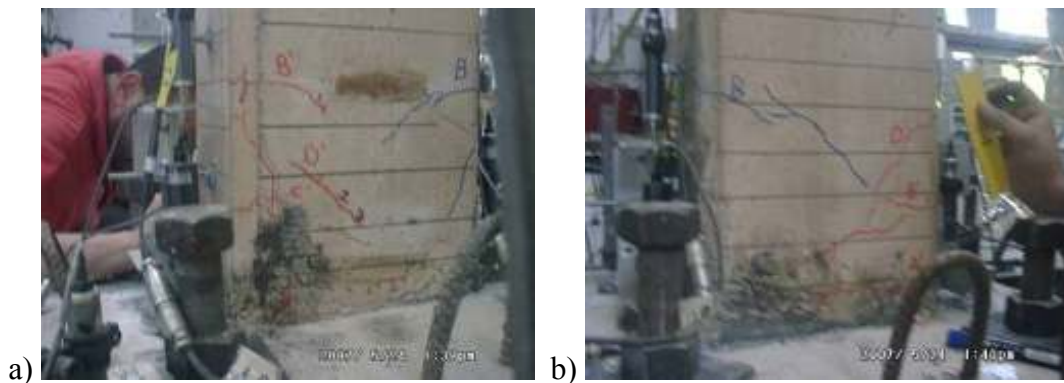


Figure 6.17 : a) North, and b) South view of the LS-X6 specimen after -2.50% drift ratio.

During loading to target displacement of 42 mm (drift ratio 3.50%), vertical crack at north side and propagation of existing crack (A-south) were observed. The view of the specimen LS-X6 after -3.50% drift ratio is shown in Figure 6.18.

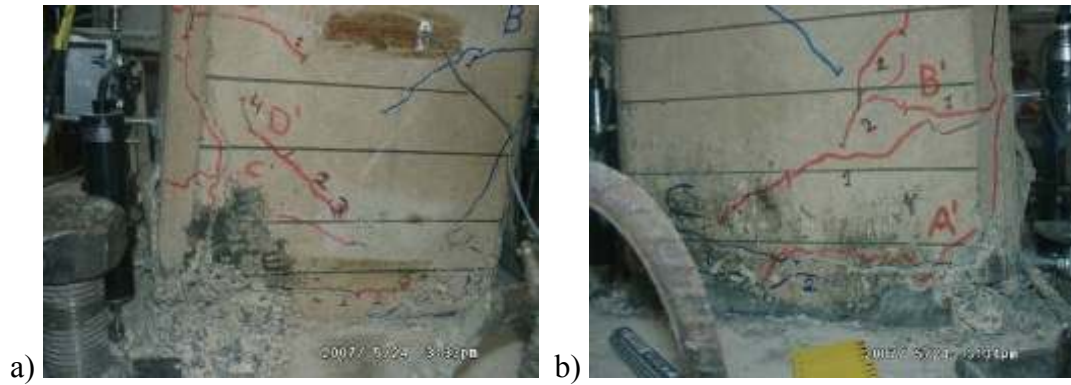


Figure 6.18 : a) North, and b) South view of the specimen LS-X6 after -3.50% drift ratio.

During loading to target displacement of 48 mm (drift ratio 4.00%) vertical crack at south side and propagation of existing crack (A-south) were observed. During loading to target displacement of -48 mm (drift ratio -4.00%) propagation of existing cracks (D'-north, E'-north) were observed. During loading to target displacement of -60 mm (drift ratio -5.00%) propagation of existing crack (D'-north) was observed.

The view of the specimen LS-X6 after -6.00% drift ratio is shown in Figure 6.19. Summary of the seismic behavior of the specimen LS-X6 is shown in Table 6.6. Crack propagation of the specimen LS-X6 while pushing and pulling cycles are given in Appendix C.

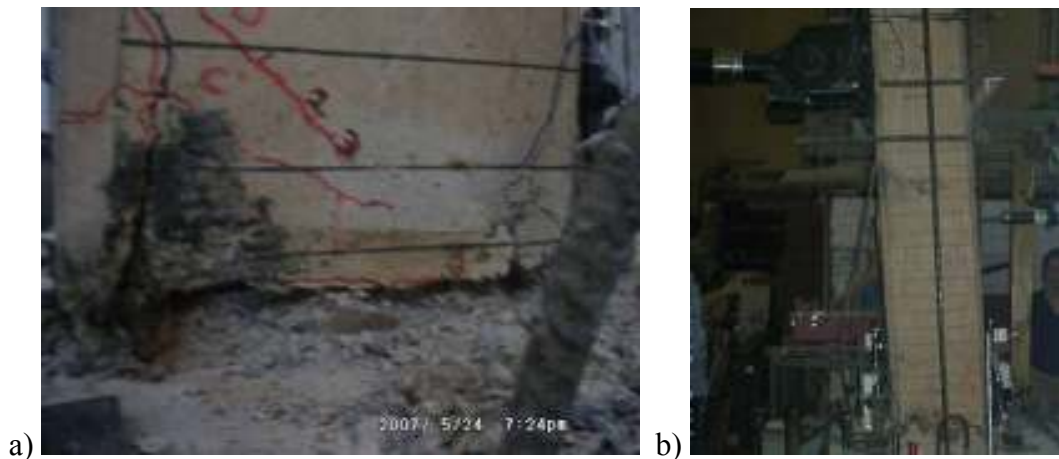


Figure 6.19 : a) North, and b) South view of the specimen LS-X6 after -6.00% drift ratio.

Force-displacement relationship of LS-X6 is presented in Figure 6.20. In this figure, P is applied lateral load and P_0 is the theoretical lateral load capacity of the specimen determined without considering the effect of corrosion. First flexural crack, first shear crack, first vertical crack, crushing of concrete cover, spalling of concrete cover, maximum strain on the starter bar and maximum strain on the longitudinal bar are marked on the figure. As seen from Figure 6.20, strength loss was observed.

Average experimental moment-curvature relationships obtained for critical sections of LS-X6 are presented in Figure 6.21.

Table 6.6 : Summary of the seismic behavior of LS-X6.

Drift ratio (%)	δ (mm/mm)	P (kN)	Observations
0.875/-0.917	1.05 / -1.1	± 5.49	No crack was observed.
0.23/-0.29	2.8 / -3.5	± 10.94	No crack was observed.
0.6/-0.8	7.2 / -9.6	15.08 / -12.68	First flexural crack was observed at column-footing interface while pushing. Shear crack was observed. Vertical cracks, indicating slip, were observed.
1.0	± 12.0	14.93 / -11.42	
1.5	± 18.0	14.38 / -10.66	Vertical cracks, indicating slip, were observed at the lapsplice zone.
2.00	± 24.0	12.59 / -9.75	
2.50	± 30.0	11.94 / -8.43	
3.0	± 36.0	11.24 / -7.81	Concrete cover spalled at the compression zone.
3.50	± 42.0	10.68 / -6.86	
4.0	± 48.0	9.65 / -5.60	
4.50	± 54.0	8.95 / -4.99	Concrete cover spalled completely.
5.0	± 60.0	7.81 / -4.23	
6.0	± 72.0	6.07 / -1.91	Specimen underwent excessive deformation out of its axis and test was ended by decreasing the axial load.

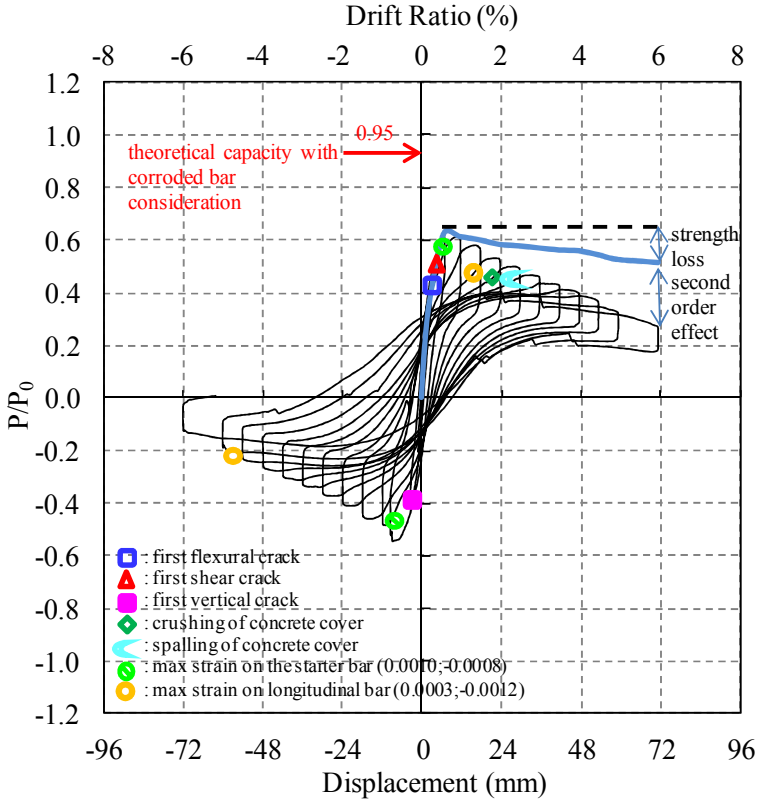


Figure 6.20 : Lateral load/Theoretical load capacity versus displacement for LS-X6.

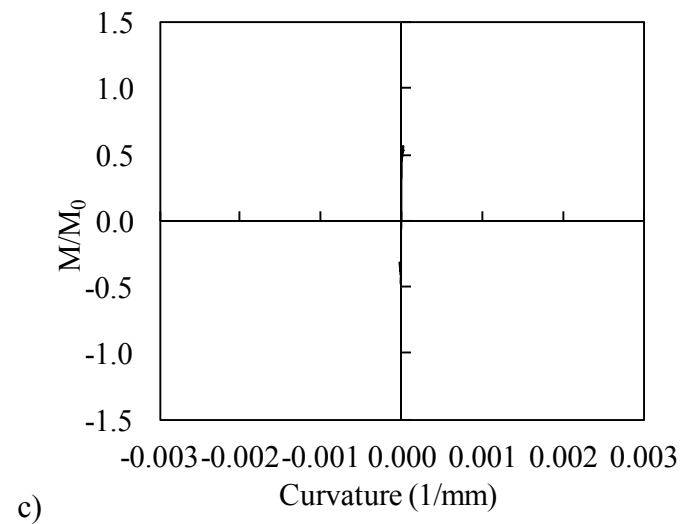
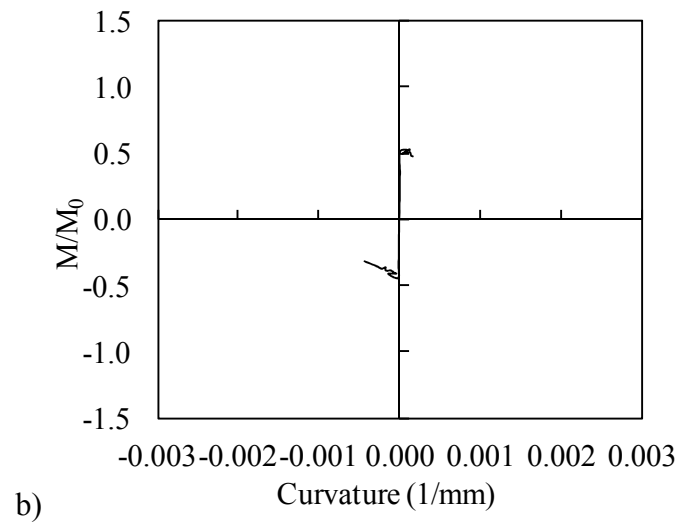
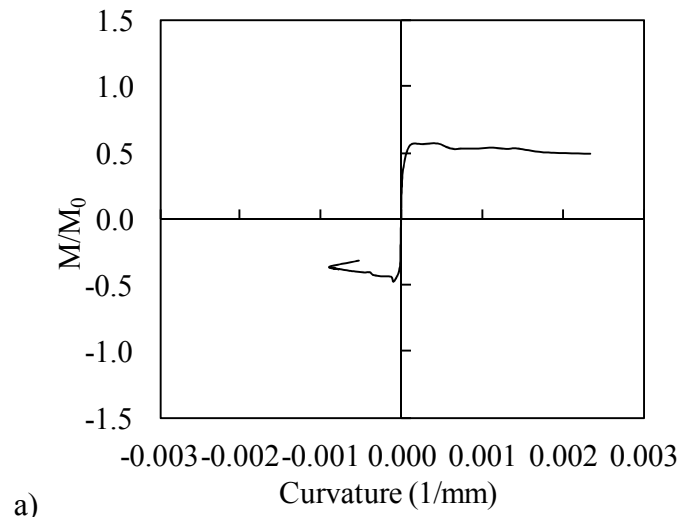


Figure 6.21 : Moment-curvature relationships obtained for a) 20 mm, b) 150 mm, c) 300 mm gauge lengths.

For the calculation of moment-curvature relationships, the average curvature values which were obtained for the ranges of 0-20 mm, 20-150 mm and 150-300 mm heights above the footing were taken into account. As seen from Figure 6.21, the curvature values of the member measured in 20-150 mm and 150-300 mm height above the support are in the order of $5 \cdot 10^{-5}$ (1/mm), while the curvatures measured in 0-20 mm height are in the order of $3 \cdot 10^{-3}$ (1/mm). According to Figure 6.21, it is of interest to note that the damage is accumulated especially in 20 mm height of the member from top of the base according to the moment-curvature relationships.

According to the data from the straingauges on the starter bars of the LS-X6, the maximum strain while pushing was 0.0010, measured from the strain gauge at +100 mm above the footing when $P=15.08$ kN at 0.006 drift ratio; the maximum strain while pulling was -0.0008, measured from the strain gauge at +100 mm above the footing when $P=-11.42$ kN at -0.01 drift ratio. According to the data from the straingauges on the longitudinal bars of the LS-X6, the maximum strain while pushing was 0.0003, measured from the strain gauge at +400 mm above the footing when $P=14.38$ kN at 0.015 drift ratio; the maximum strain while pulling was -0.0012, measured from the strain gauge at +100 mm above the footing when $P=-4.23$ kN at -0.05 drift ratio. Strain distribution of the starter bars and longitudinal bars of LS-X6 while pushing and pulling are shown in Figure 6.22 and Figure 6.23, respectively. As seen from Figure 6.22 and Figure 6.23, the strain values are higher than specimen LS-X0, but did not reach yield strain.

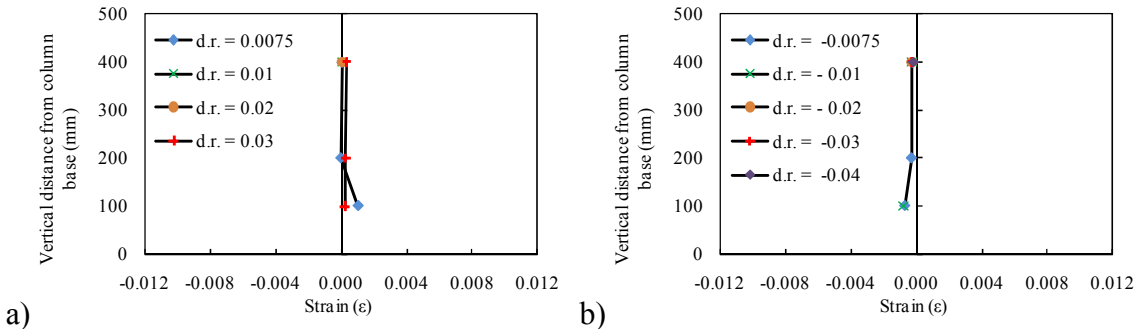


Figure 6.22 : Strain distribution of the starter bars of LS-X6 a) while pushing, b) while pulling.

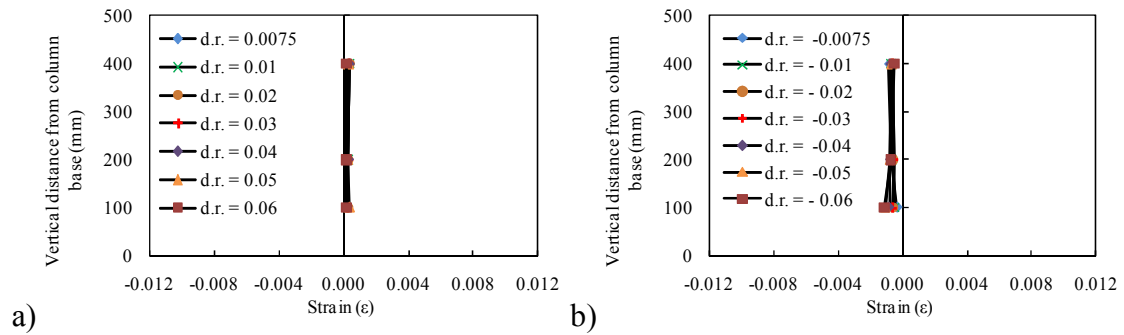


Figure 6.23 : Strain distribution of the longitudinal bars of LS-X6 a) while pushing b) while pulling.

6.2.3 LS-X8

Unlike the specimen LS-X6, specimen LS-X8 has horizontal cracks along the transverse reinforcement above the footing 250 mm, 450 mm, 700 mm, 850 mm and 950 mm on north side and 250 mm, 450 mm, 650 mm, 850 mm and 950 mm on south side of the column. Pattern of existing cracks are shown in Figure 6.24.

No cracks were observed while loading to target displacements of ± 1.2 mm (drift ratio 0.10%) and ± 3 mm (drift ratio 0.25%).

First shear cracks of 0.2 mm width were observed at both sides of the column (A-north, A-south, B-south) during loading to target displacement of 6 mm (drift ratio 0.50%). During loading to target displacement of -6 mm (drift ratio -0.50%) shear cracks of 0.2 mm width were observed at both sides of the column (A'-north, A'-south). The view of the specimen LS-X8 after -0.50% drift ratio is shown in Figure 6.25.

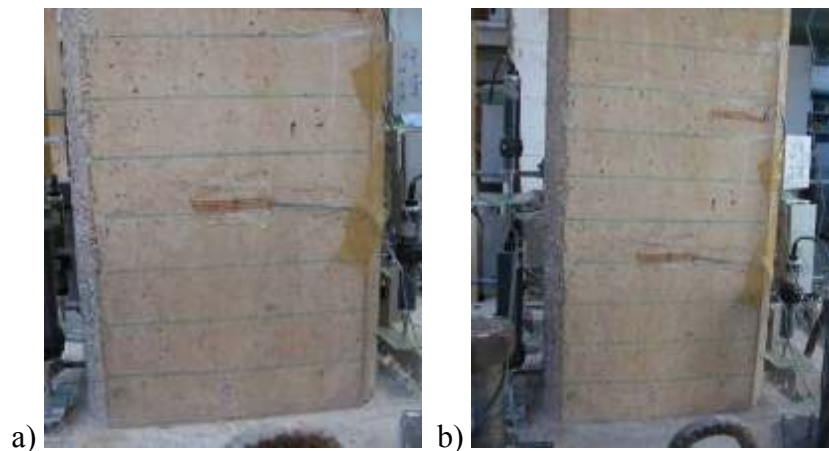


Figure 6.24 : Pattern of cracks formed due to corrosion: (a) North, (b) South.

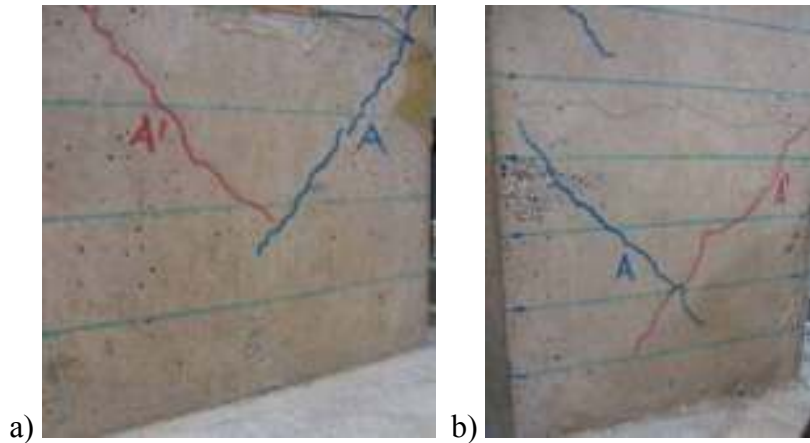


Figure 6.25 : a) North, and b) South view of the specimen LS-X8 after -0.50% drift ratio.

First flexural crack at the interface of the column and footing (C-south), vertical crack (D-south) and propagation of existing shear cracks were observed during loading to target displacement of 9.0 mm (drift ratio 0.75%). During loading to target displacement of -9.0 mm (drift ratio -0.75%) flexural crack (B'-north) at the interface of the column and footing was observed.

During loading to target displacement of 12.0 mm (drift ratio 1.00%) vertical cracks (B-north, E-south, H-south) and shear cracks (F-south, G-south) were observed. During loading to target displacement of -12.0 mm (drift ratio -1.00%) flexural crack (C'-north), shear crack (B'-south, C'-south, E'-south) and vertical crack (D'-south, F'-south) were observed.

During loading to target displacement of 18.0 mm (drift ratio 1.50%) flexural crack at the interface of the column and footing (C-north), flexural cracks (D-north, I-south) and shear cracks (J-south) were observed. During loading to target displacement of -18.0 mm (drift ratio -1.50%) propagation of existing cracks and vertical cracks (D'-north, E'-north, F'-north, G'-north) were observed. The view of the specimen LS-X8 after -1.50% drift ratio is shown in Figure 6.26.

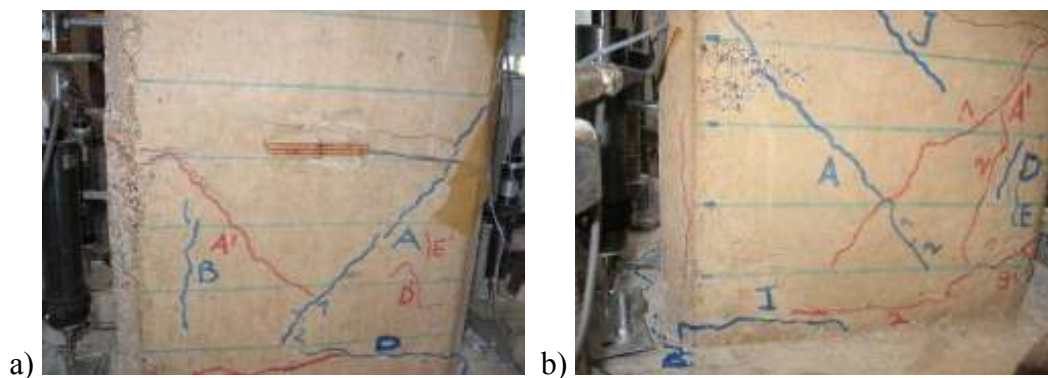


Figure 6.26 : a) North, and b) South view of the specimen LS-X8 after -1.50% drift ratio.

During loading to target displacement of -24.0 mm (drift ratio 2.0%) flexural crack (H'-north) and shear crack (I'-north) were observed.

During loading to target displacement of 30.0 mm (drift ratio 2.5%) vertical crack (E-north) and spalling of concrete cover were observed. The view of the specimen LS-X8 after -2.50% drift ratio is shown in Figure 6.27.

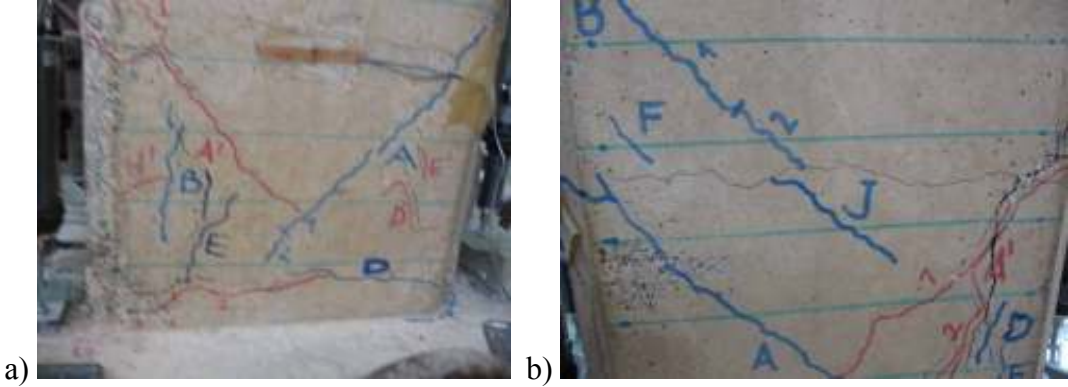


Figure 6.27 : a) North, and b) South view of the LS-X8 specimen after -2.50% drift ratio.

During loading to target displacement of -30.0 mm (drift ratio -2.5%) flexural crack (G'-south) was observed.

During loading to target displacement of -36.0 mm (drift ratio -3.0%) vertical crack (K'-north) and shear crack (J'-north) were observed. The view of the specimen LS-X8 after -3.50% drift ratio is shown in Figure 6.28.

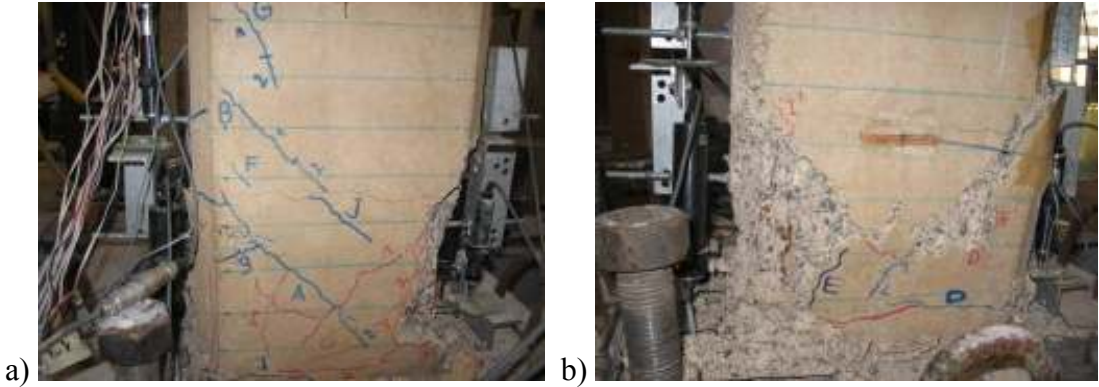


Figure 6.28 a) North, and b) South view of the LS-X8 specimen after -3.50% drift ratio.

During loading to target displacement of 54.0 mm (drift ratio 4.50%) specimen underwent excessive lateral deformation out of its axis and test was ended by decreasing the axial load. The view of the specimen LS-X8 after -4.00% drift ratio is shown in Figure 6.29. Summary of the seismic behavior of specimen LS-X8 is shown in Table 6.7.



Figure 6.29 : a) North, and b) South view of the LS-X8 specimen after -4.00% drift ratio.

Table 6.7 : Summary of the seismic behavior of LS-X8.

Drift ratio (%)	δ (mm/mm)	P (kN)	Observations
0.10	± 1.2	5.22 / -5.09	No crack was observed.
0.25	± 3.0	10.43 / -9.57	No crack was observed.
0.50	± 6.0	14.12 / -12.76	First shear cracks and vertical crack were observed.
0.75	± 9.0	15.70 / -13.74	First flexural crack at column-footing interface was observed.
1.0	± 12.0	15.68 / -13.19	Flexural, shear and vertical cracks were observed.
1.5	± 18.0	15.13 / -11.79	Propagation of existing crack at column-footing interface was observed.
2.00	± 24.0	13.29 / -10.70	Flexural and shear cracks were observed.
2.50	± 30.0	11.90 / -9.78	Flexural and vertical cracks were observed. Spalling and crushing started at the concrete cover.
3.0	± 36.0	10.87 / -9.33	Shear and vertical cracks were observed.
3.50	± 42.0	10.23 / -6.08	
4.0	± 48.0	7.94 / -4.70	
4.50	± 54.0	Target displacement was not reached.	Specimen underwent excessive lateral deformation out of its axis and test was ended by decreasing the axial load.

Crack propagation of LS-X8 while pushing and pulling cycles are given in Appendix C (Table C.5). Force-displacement relationship of LS-X8 is presented in Figure 6.30. In this figure, P is applied lateral load and P_0 is the theoretical lateral load capacity of the specimen determined without considering the effect of corrosion. First flexural crack, first shear crack, first vertical crack, yielding of starter bar, yielding of transverse bar, crushing of concrete cover, spalling of concrete cover, maximum strain on the starter bar and maximum strain on the longitudinal bar are marked on the figure. As seen from Figure 6.30, strength loss was observed.

Average experimental moment-curvature relationships obtained for critical sections of LS-X8 are presented in Figure 6.31. For the calculation of moment-curvature relationships, the average curvature values which were obtained for the ranges of 0-20 mm, 20-150 mm and 150-300 mm heights above the footing were taken into account. As seen from the figure, the curvature values of the member measured in 20-150 mm and 150-300 mm height above the support are in the order of $5 \cdot 10^{-5}$ (1/mm), while the curvatures measured in 0-20 mm height are in the order of $3 \cdot 10^{-3}$ (1/mm). According to Figure 6.31, it is of interest to note that the damage is accumulated especially in 20 mm height of the member from top of the base according to the moment-curvature relationships.

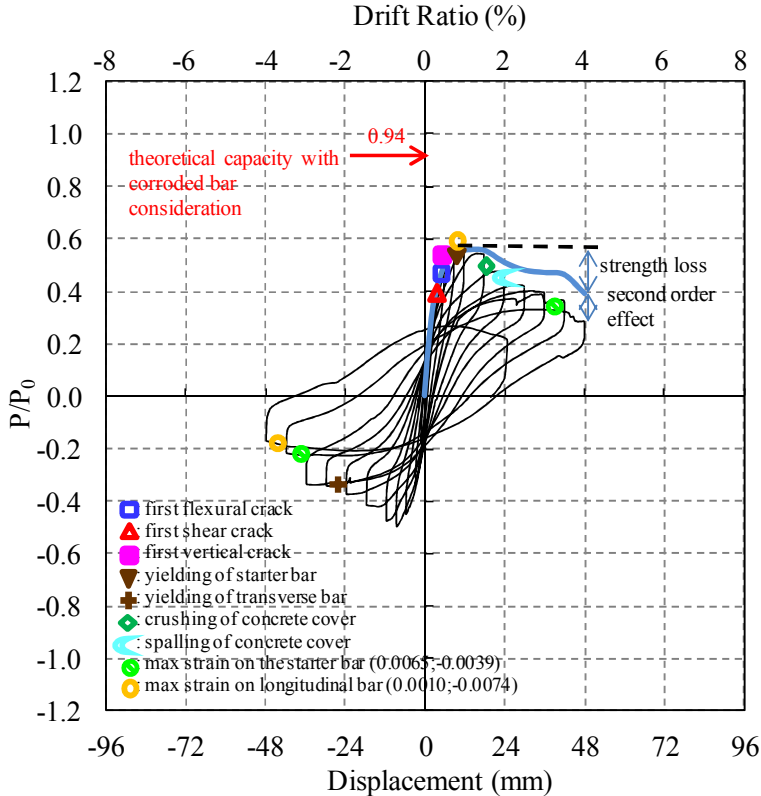


Figure 6.30 : Lateral load/Theoretical load capacity versus displacement for LS-X8.

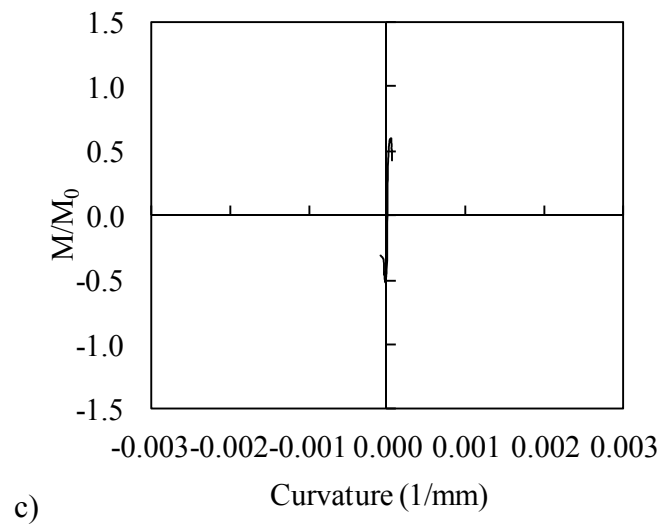
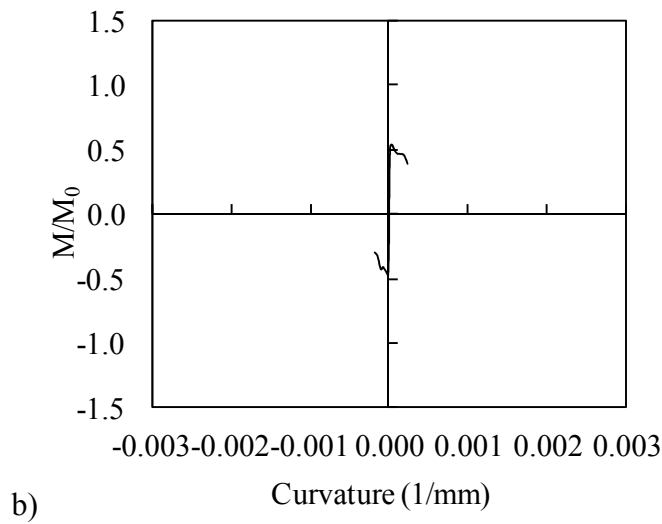
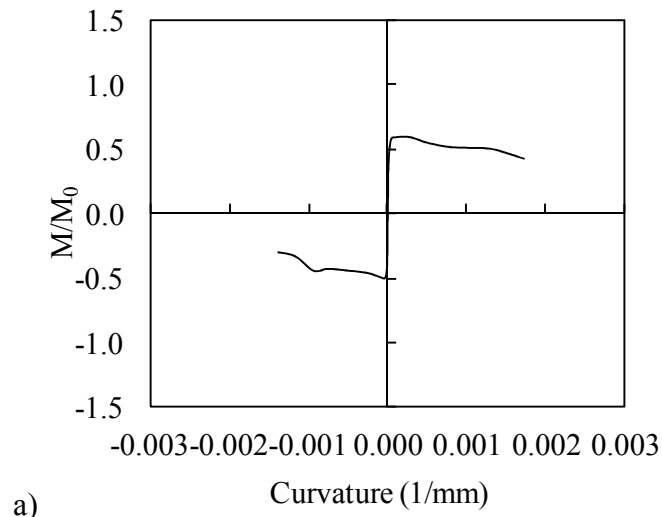


Figure 6.31 : Moment-curvature relationships obtained for a) 0-20 mm, b) 20-150 mm, c) 150-300 mm gauge lengths.

According to the data from the strain gauges on the starter bars of the LS-X8, the maximum strain while pushing was 0.0065, measured from the strain gauge at +200 mm above the footing when $P=7.94$ kN at 0.04 drift ratio; the maximum strain while pulling was -0.0039, measured from the strain gauge at +100 mm above the footing when $P=-6.08$ kN at -0.035 drift ratio. According to the data from the strain gauges on the longitudinal bars of the LS-X8, the maximum strain while pushing was 0.0010, measured from the strain gauge at +200 mm above the footing when $P=15.68$ kN at 0.01 drift ratio; the maximum strain while pulling was -0.0074, measured from the strain gauge at +100 mm above the footing when $P=-4.70$ kN at -0.04 drift ratio. Strain distribution of the starter bars and longitudinal bars of LS-X8 while pushing and pulling are shown in Figure 6.32 and Figure 6.33, respectively. As seen from the figures, the strain values are higher than specimen LS-X0, but did not reach yield strain.

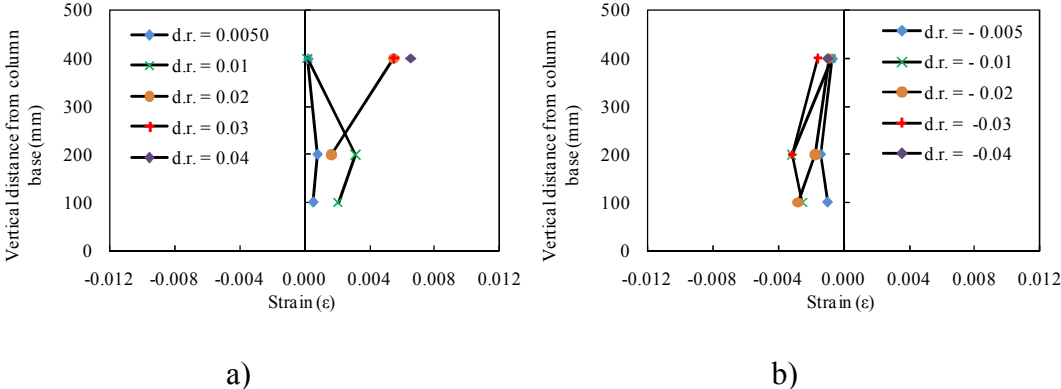


Figure 6.32 : Strain distribution of the starter bars of LS-X8 a) while pushing, b) while pulling.

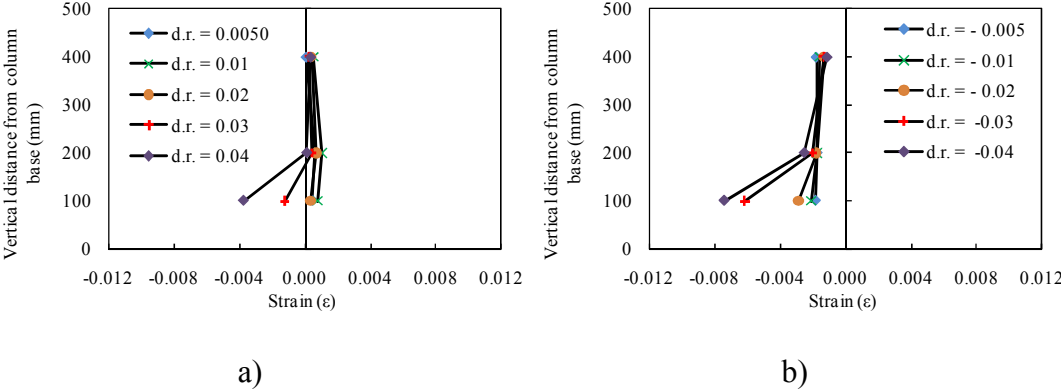


Figure 6.33 : Strain distribution of the longitudinal bars of LS-X8 a) while pushing b) while pulling.

6.2.4 LS-X12

Unlike the specimens LS-X6 and LS-X8, specimen LS-X12 has vertical cracks along the longitudinal reinforcement and horizontal cracks along the transverse reinforcement. Width, location and orientation of the cracks are presented in Table 6.8. Pattern of cracks formed due to corrosion are shown in Figure 6.34.

Table 6.8 : Width, location and orientation of the cracks

Crack width	Crack location	Crack orientation
0.3 mm	20-25 cm above the footing	along the No.1 longitudinal reinforcement
1.2 mm	5-45 cm above the footing	along the No.2 longitudinal reinforcement
0.1 mm	15-25 cm above the footing	along the No.3 longitudinal reinforcement
0.9 mm	0-65 cm above the footing	along the No.4 longitudinal reinforcement

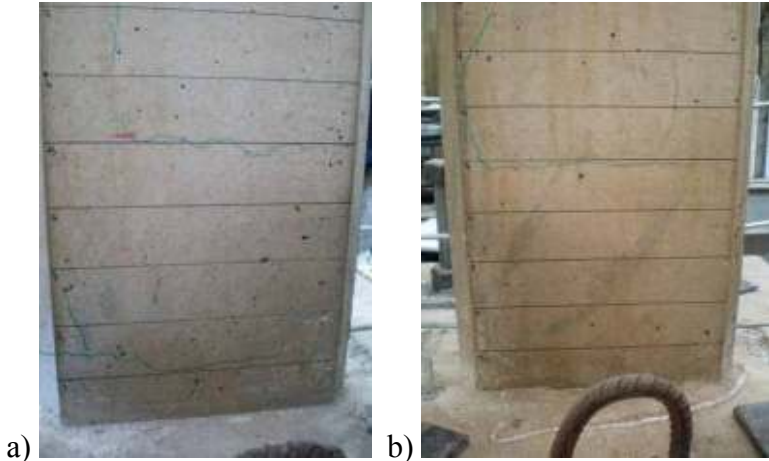


Figure 6.34 : Pattern of cracks formed due to corrosion: (a) North, (b) South.

A vertical crack of 0.1 mm width opening was observed at the column (A-south) during loading to target displacement of 1.24 mm (drift ratio 0.10%). During loading to target displacement of -1.24 mm (drift ratio 0.10%) flexural crack (A'-north, B'-north) was observed. Theth view of the specimen LS-X12 after -0.10% drift ratio is shown in Figure 6.35.

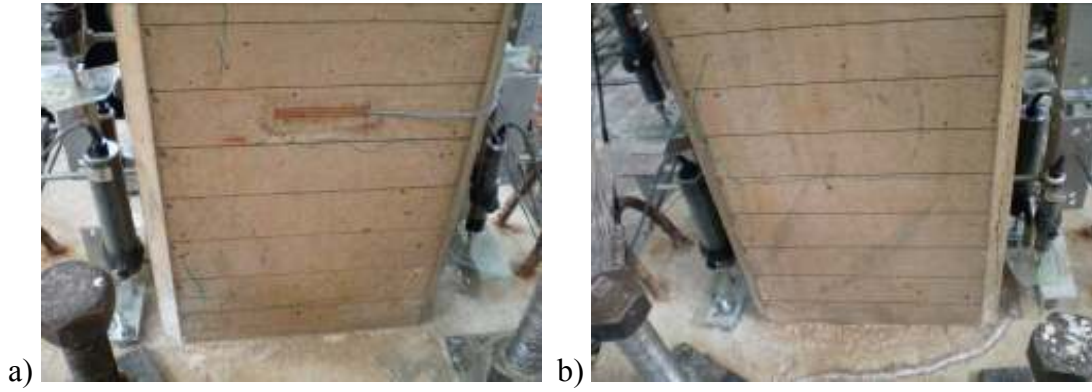


Figure 6.35 : a) North, and b) South view of the specimen LS-X12 after -0.10% drift ratio.

No cracks were observed while loading to target displacement of ± 3 mm (drift ratio 0.25%).

During loading to target displacement of 6.2 mm (drift ratio 0.50%) shear cracks (A-north, B-south) were observed. During loading to target displacement of -6.2 mm (drift ratio -0.50%) flexural cracks (C'-north, D'-north, A'-south) and vertical cracks (E'-north, F'-north) were observed.

During loading to target displacement of 9.3 mm (drift ratio 0.75%) flexural crack at the interface of the column and footing (D-north, C-south) and (E-north), shear cracks (B-north, C-north, D-south, F-south, G-south) and vertical cracks (H-south, I-south) were observed. Crushing of concrete cover (E-south) started at the compression zone. During loading to target displacement of -9.3 mm (drift ratio -0.75%) vertical cracks (G'-north, D'-south, F'-south), flexural cracks at the interface of the column and footing (H'-north, E'-south), flexural crack (B'-south) and shear cracks (C'-south) were observed.

During loading to target displacement of +12.4 mm (drift ratio 1.00%) propagation of flexural crack at the interface of the column and footing, vertical crack (F-north) and flexure crack (G-yanyüz) were observed. During loading to target displacement of -12.4 mm (drift ratio -1.00%) shear cracks (I'-north, G'-side, K'-south), vertical cracks (H'-south, J'-south, I'-south, L'-south, M'-south) and propagation of existing cracks were observed.

During loading to target displacement of +18.6 mm (drift ratio 1.50%) shear crack (H-north), vertical crack (I-north) and propagation of existing cracks were observed. During loading to target displacement of -18.6 mm (drift ratio -1.50%) shear cracks (K-north, L-north) and flexural cracks (M-north, N-south) were observed. The view of the specimen LS-X12 after -1.50% drift ratio is shown in Figure 6.36.

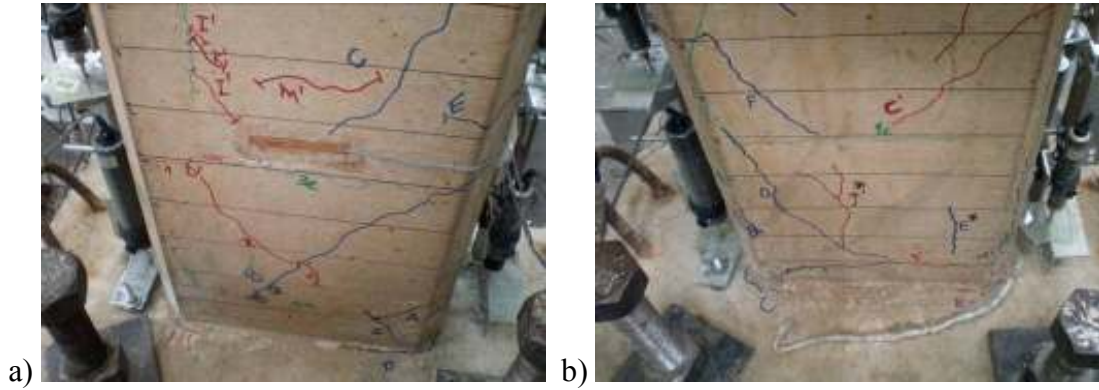


Figure 6.36 : a) North, and b) South view of the specimen LS-X12 after -1.50% drift ratio.

During loading to target displacement of +24.8 mm (drift ratio 2.00%) vertical crack (J-north, M-north, K- south), shear cracks (K-north, J-south) and flexural crack (L-north) were observed. Propagation of existing cracks were observed. During loading to target displacement of -24.8 mm (drift ratio -2.00%) shear cracks (O'-yanyüz, P'-south) were observed.

During loading to target displacement of -31.0 mm (drift ratio -2.50%) vertical cracks (R'-south, S'-south) were observed. The view of the specimen LS-X12 after -2.50% drift ratio is shown in Figure 6.37.

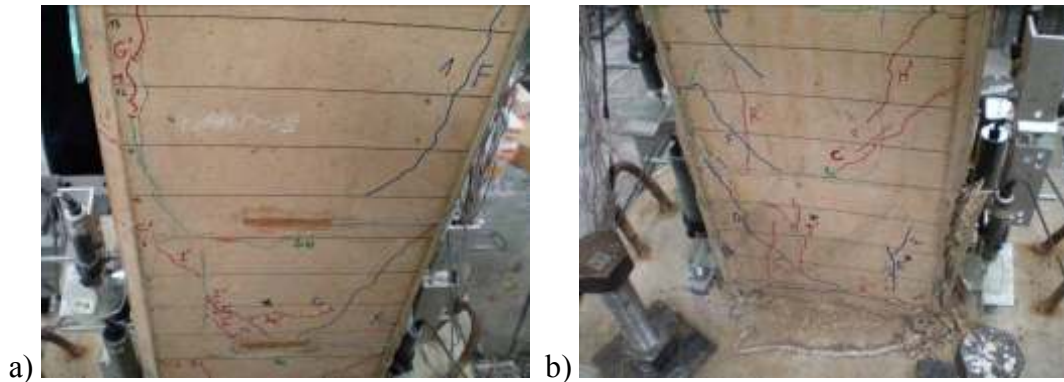


Figure 6.37 : a) North, and b) South view of the LS-X12 specimen after -2.50% drift ratio.

During loading to target displacement of +37.2 mm (drift ratio %3.500) vertical cracks (M-south) was observed. Buckling of longitudinal reinforcement was observed. Specimen underwent excessive deformation out of its axis and test was ended by decreasing the axial load. The view of the specimen LS-X12 after -3.00% drift ratio is shown in Figure 6.38.

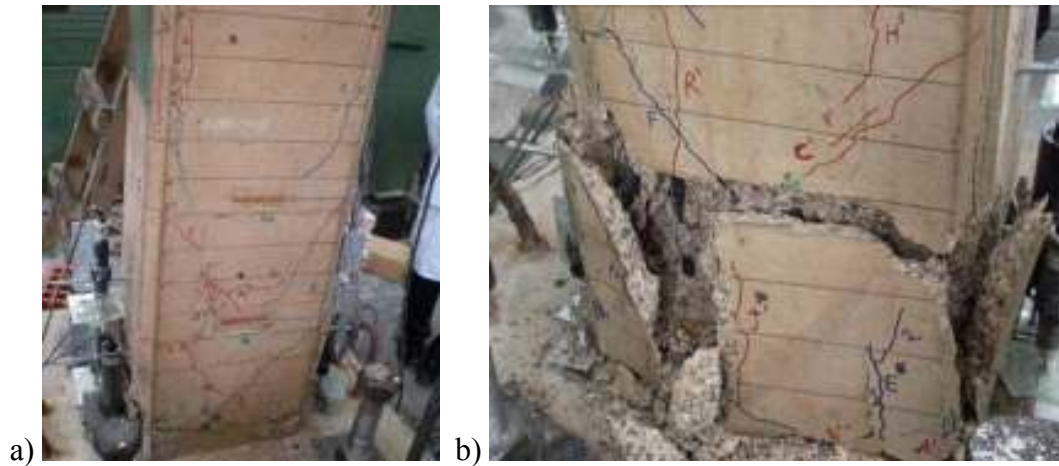


Figure 6.38 : a) North, and b) South view of the specimen LS-X12 after -3.00% drift ratio.

Summary of the seismic behavior of the specimen LS-X12 is shown in Table 6.9. Crack propagation of the specimen LS-X12 while pushing and pulling cycles are given in Appendix C. Force-displacement relationship of the specimen LS-X12 is presented in Figure 6.39. In this figure, P is applied lateral load and P_0 is the theoretical lateral load capacity of the specimen determined without considering the effect of corrosion. As seen from Figure 6.39, strength loss was observed.

Table 6.9 : Summary of the seismic behavior of LS-X12.

Drift ratio (%)	δ (mm/mm)	P (kN)	Observations
0.10	± 1.2	4.0 / -4.9	First vertical cracks were observed.
0.25	± 3.0	9.1 / -9.7	
0.50	± 6.0	12.8 / -13.1	First shear and flexural cracks were observed.
0.75	± 9.0	15.9 / -14.2	First flexural crack at column-footing interface was observed. Crushing started at compression zone at concrete cover.
1.0	± 12.0	15.3 / -14.1	Propagation of shear cracks at tension zone were observed.
1.5	± 18.0	14.6 / -12.9	Propagation of flexural crack at the interface of column and footing were observed.
2.00	± 24.0	12.7 / -11.0	Propagation of shear damage was observed. Spalling of the concrete cover started.
2.50	± 30.0	10.6 / -8.7	Concrete cover spalled completely.
3.0	± 36.0	8.5 / -3.1	Buckling of longitudinal bar was observed. Specimen underwent excessive lateral displacement out of its axis and test was ended by decreasing the axial load.

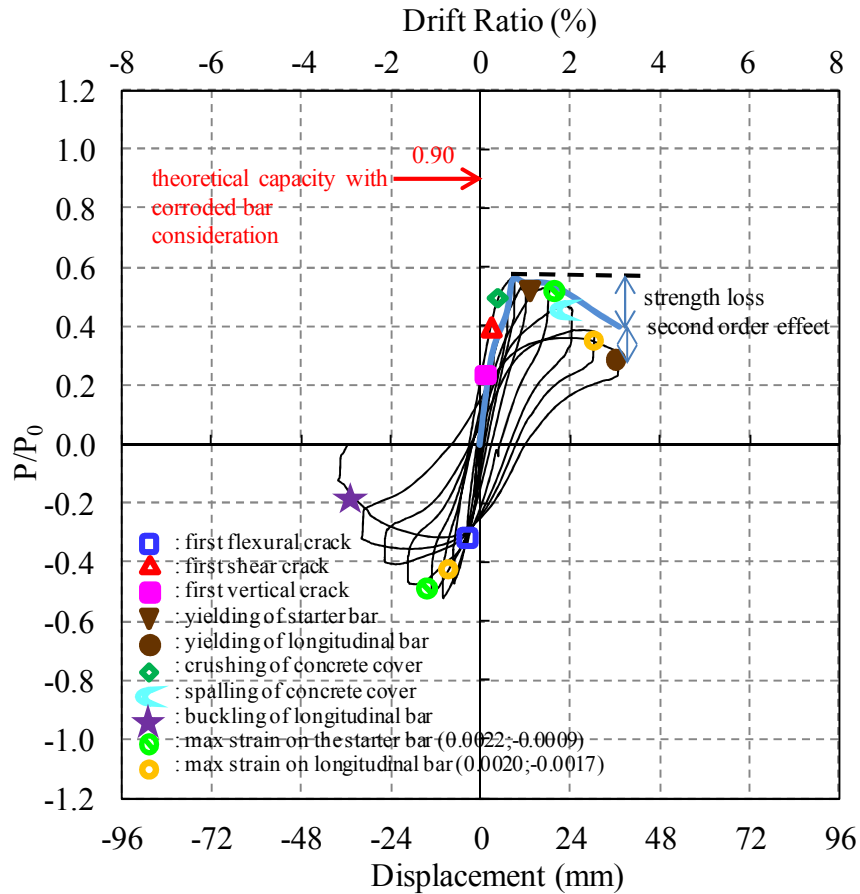


Figure 6.39 : Lateral load/Theoretical load capacity versus displacement for LS-X12.

Average experimental moment-curvature relationships obtained for critical sections of LS-X12 are presented in Figure 6.40. For the calculation of moment-curvature relationships, the average curvature values which were obtained for the ranges of 0-20 mm, 20-150 mm and 150-300 mm heights above the footing were taken into account. As seen from Figure 6.12, the curvature values of the member measured in 20-150 mm and 150-300 mm height above the support are in the order of $5 \cdot 10^{-5}$ (1/mm), while the curvatures measured in 0-20 mm height are in the order of $3 \cdot 10^{-3}$ (1/mm). According to Figure 6.40, it is of interest to note that the damage is accumulated especially in 20 mm height of the member from top of the base according to the moment-curvature relationships.

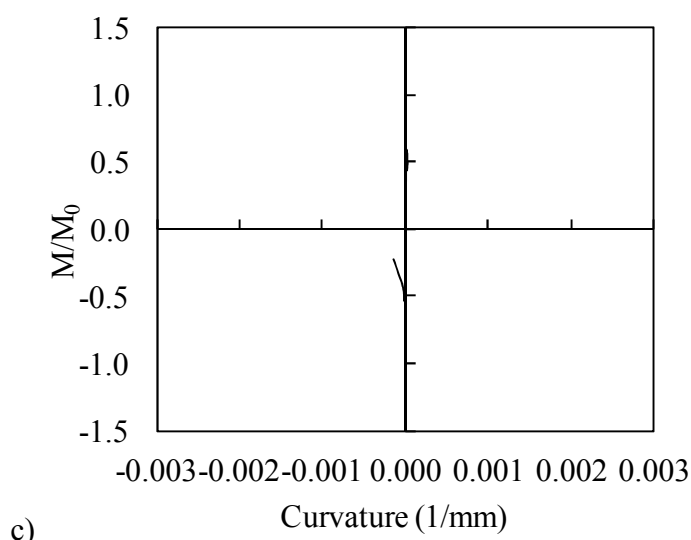
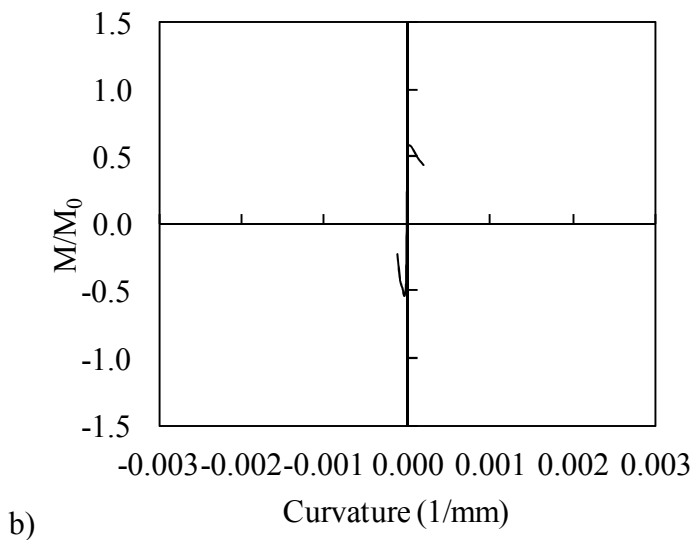
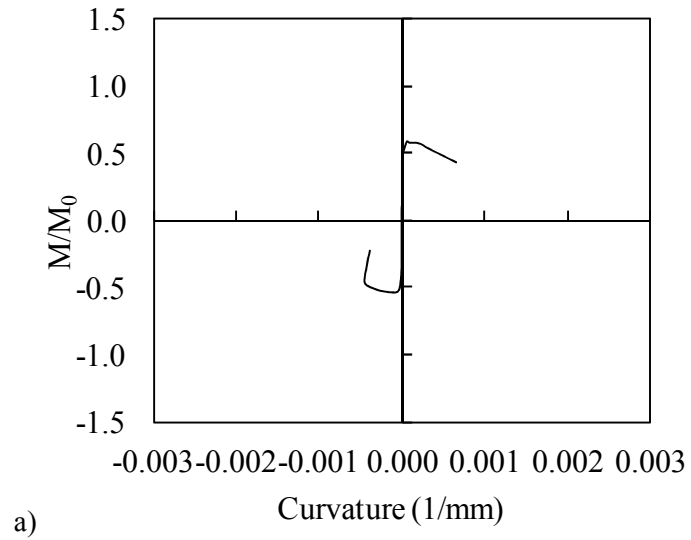


Figure 6.40 : Moment-curvature relationships obtained for a) 0-20 mm, b) 20-150 mm, c) 150-300 mm gauge lengths.

According to the data from the straingauges on the starter bars of the LS-X12, the maximum strain while pushing was 0.0022, measured from the strain gauge at +200 mm above the footing when P=12.7 kN at 0.02 drift ratio; the maximum strain while pulling was -0.0009, measured from the strain gauge at +200 mm above the footing when P=-12.9 kN at -0.015 drift ratio. According to the data from the straingauges on the longitudinal bars of the LS-X12, the maximum strain while pushing was 0.0020, measured from the strain gauge at +200 mm above the footing when P=8.5 kN at 0.03 drift ratio; the maximum strain while pulling was -0.0017, measured from the strain gauge at +200 mm above the footing when P=-14.2 kN at -0.0075 drift ratio. Strain distribution of the starter bars and longitudinal bars of LS-X12 while pushing and pulling are shown in Figure 6.41 and Figure 6.42, respectively. As seen from the figures, the strain values are higher than specimen LS-X0, but did not reach yield strain.

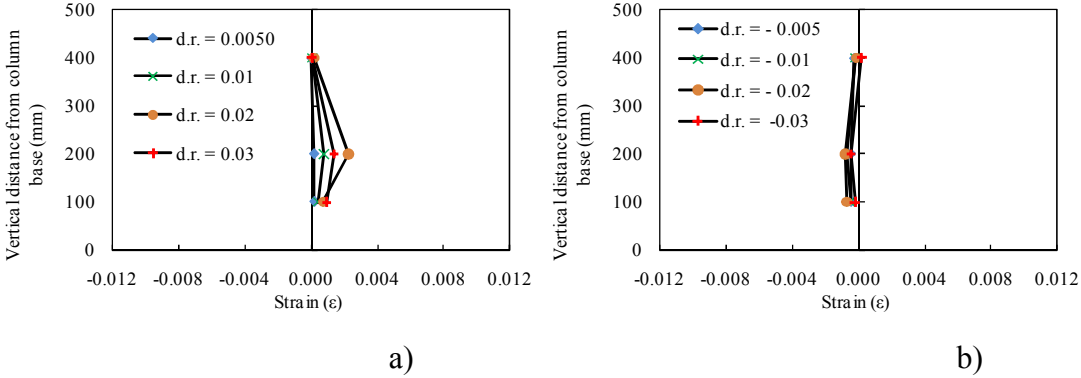


Figure 6.41 : Strain distribution of the starter bars of LS-X12 a) while pushing, b) while pulling.

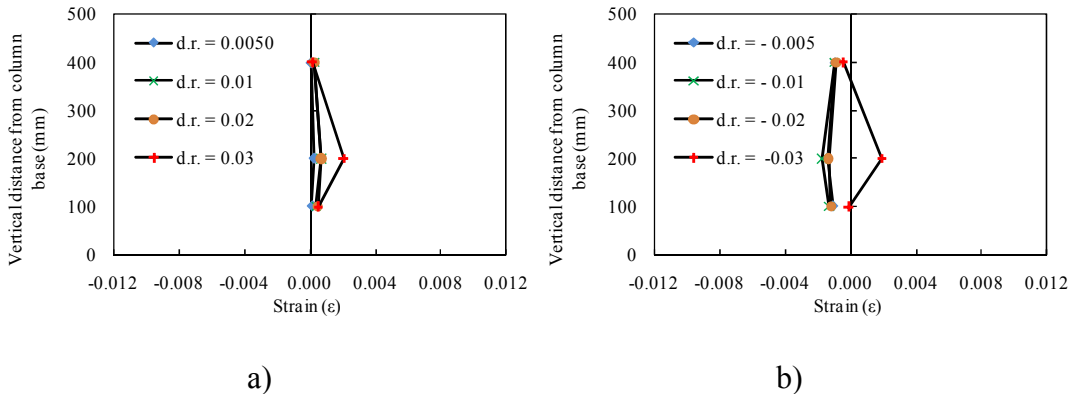


Figure 6.42 : Strain distribution of the longitudinal bars of LS-X12 a) while pushing b) while pulling.

6.2.5 LS-X21

Similar to the specimen LS-X12, specimen LS-X21 has vertical cracks along the longitudinal reinforcement and horizontal cracks along the transverse reinforcement. Width, location and orientation of the cracks are presented in Table 6.10.

Table 6.10 : Width, location and orientation of the cracks.

Crack width	Crack location	Crack orientation
1.0 mm	above the footing	along the No.1 longitudinal reinforcement
1.6 mm	above the footing	along the No.2 longitudinal reinforcement
1.2 mm	above the footing	along the No.3 longitudinal reinforcement
0.6 mm	above the footing	along the No.4 longitudinal reinforcement

Pattern of cracks formed due to corrosion are shown in Figure 6.43.

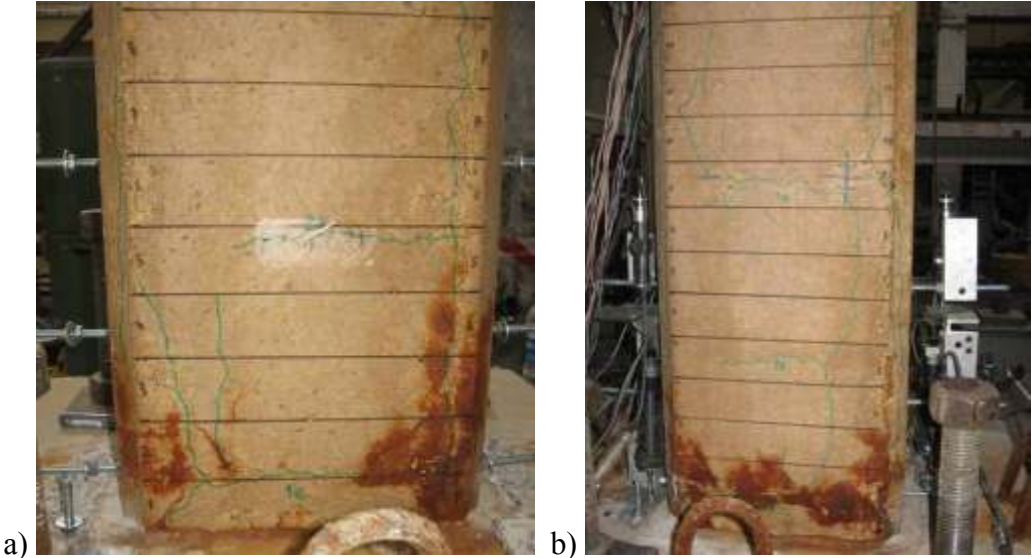


Figure 6.43 : Pattern of cracks formed due to corrosion: (a) North, (b) South.

No cracks were observed while loading to target displacements of ± 1.2 mm (drift ratio 0.10%), ± 3 mm (drift ratio 0.25%) and ± 6 mm (drift ratio 0.50%).

During loading to target displacement of +9.00 mm (drift ratio 0.75%) shear cracks (A-north, B-north, A-south, B-south) and vertical cracks (C-north, C-south) were observed. During loading to target displacement of -9.00 mm (drift ratio -0.75%) flexural cracks (A'-north, A'-south) and vertical crack (B'-south). The view of the specimen LS-X21 after -0.10% drift ratio is shown in Figure 6.44.

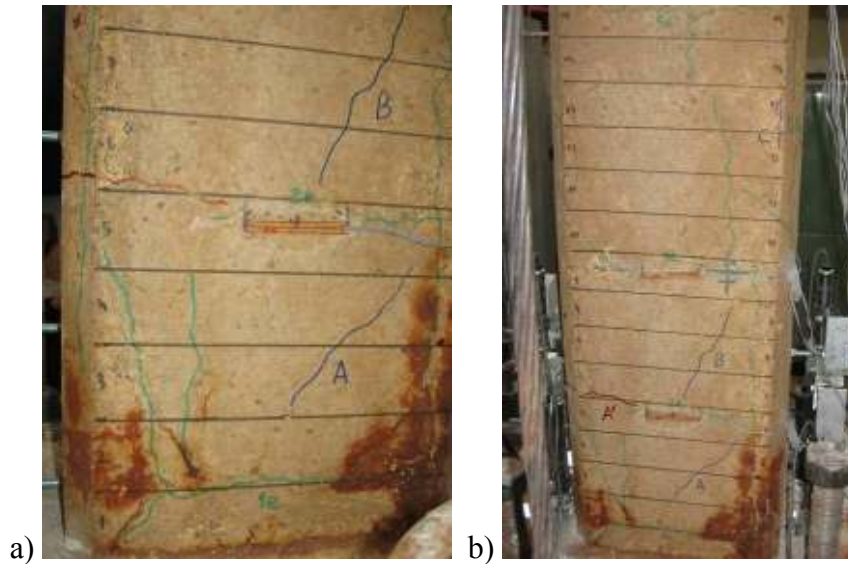


Figure 6.44 : a) North, and b) South view of the specimen LS-X21 after -0.10% drift ratio.

During loading to target displacement of +12.00 mm (drift ratio 1.00%) shear cracks (D-north, E-south), vertical cracks (F-south), flexural cracks (D-south) and propagation of (A-north) were observed. During loading to target displacement of -12.00 mm (drift ratio -1.00%) vertical cracks (B'-north, C'-north, C'-south, D'-south) were observed. Crushing of concrete cover started.

During loading to target displacement of +18.0 mm (drift ratio 1.50%) vertical cracks (E-north, F-north), propagation of existing cracks (C-north, D-north, B-north, A-south) were observed. Spalling of concrete cover started. During loading to target displacement of -18.0 mm (drift ratio -1.50%) vertical cracks (E'-south, F'-south, G'-south) were observed. Crushing of concrete cover started. The view of the specimen LS-X21 after -1.50% drift ratio is shown in Figure 6.45.

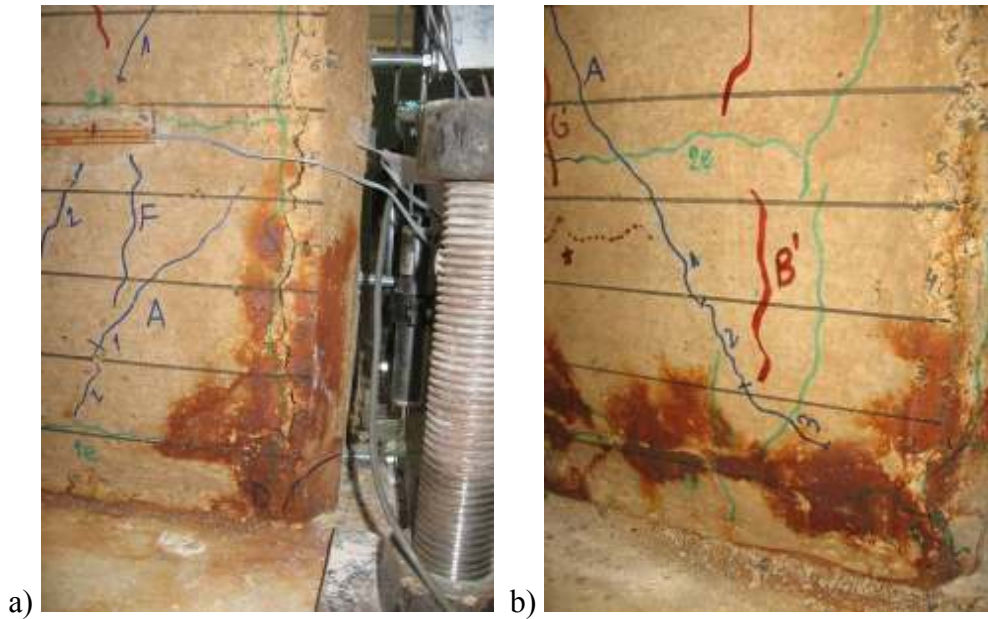


Figure 6.45 : a) North, and b) South view of the specimen LS-X21 after -1.50% drift ratio.

During loading to target displacement of +24.0 mm (drift ratio 2.00%) flexural crack (G-north) and shear crack (G-south) were observed. During loading to target displacement of -24.0 mm (drift ratio -2.00%) shear crack (D'-north) were observed. During loading to target displacement of ± 30.0 mm (drift ratio 2.50%) propagation of existing cracks were observed. The view of the specimen LS-X21 after -2.50% drift ratio is shown in Figure 6.46.

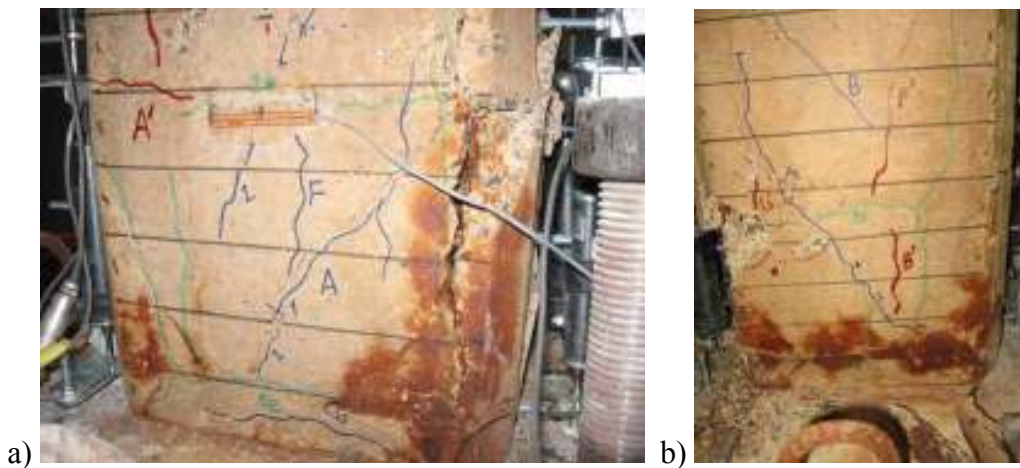


Figure 6.46 : a) North, and b) South view of the LS-X21 specimen after -2.50% drift ratio.

During loading to target displacement of ± 36.0 mm (drift ratio 3.00%) buckling of longitudinal reinforcement was observed. Concrete cover spalled completely. Specimen underwent excessive lateral displacement out of its axis and test was ended by decreasing the axial load. The view of the specimen LS-X21 after -3.00% drift ratio is shown in Figure 6.47.

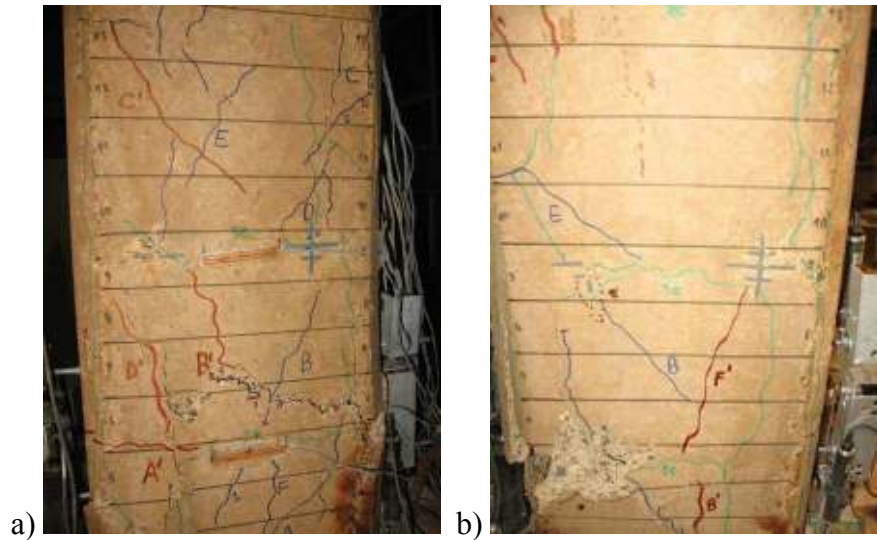


Figure 6.47 : a) North, and b) South view of the LS-X21 specimen after -3.00% drift ratio.

Summary of the seismic behavior of specimen LS-X21 is shown in Table 6.11. Crack propagation of LS-X21 while pushing and pulling cycles are given in Appendix C.

Force-displacement relationship of LS-X21 is presented in Figure 6.48.

Table 6.11 : Summary of the seismic behavior of LS-X21.

Drift ratio (%)	δ (mm/mm)	P (kN)	Observations
0.10	± 1.2	6.18 / -6.88	No crack was observed.
0.25	± 3.0	12.71 / -12.88	No crack was observed.
0.50	± 6.0	19.29 / -17.25	No crack was observed.
0.75	± 9.0	22.22 / -17.64	Shear, flexural and vertical cracks were observed.
1.0	± 12.0	23.11 / -15.49	Shear, flexural and vertical cracks were observed. Crushing of concrete cover started.
1.5	± 18.0	20.10 / -12.48	Propagation of existing cracks and vertical crack were observed. Spalling of concrete cover started.
2.00	± 24.0	15.99 / -10.44	Shear and flexural cracks were observed. Buckling of longitudinal reinforcement was observed.
2.50	± 30.0	13.93 / -7.87	
3.0	± 36.0	11.10 / -6.04	Concrete cover spalled completely. Specimen underwent excessive lateral displacement out of its axis and test was ended by decreasing the axial load.

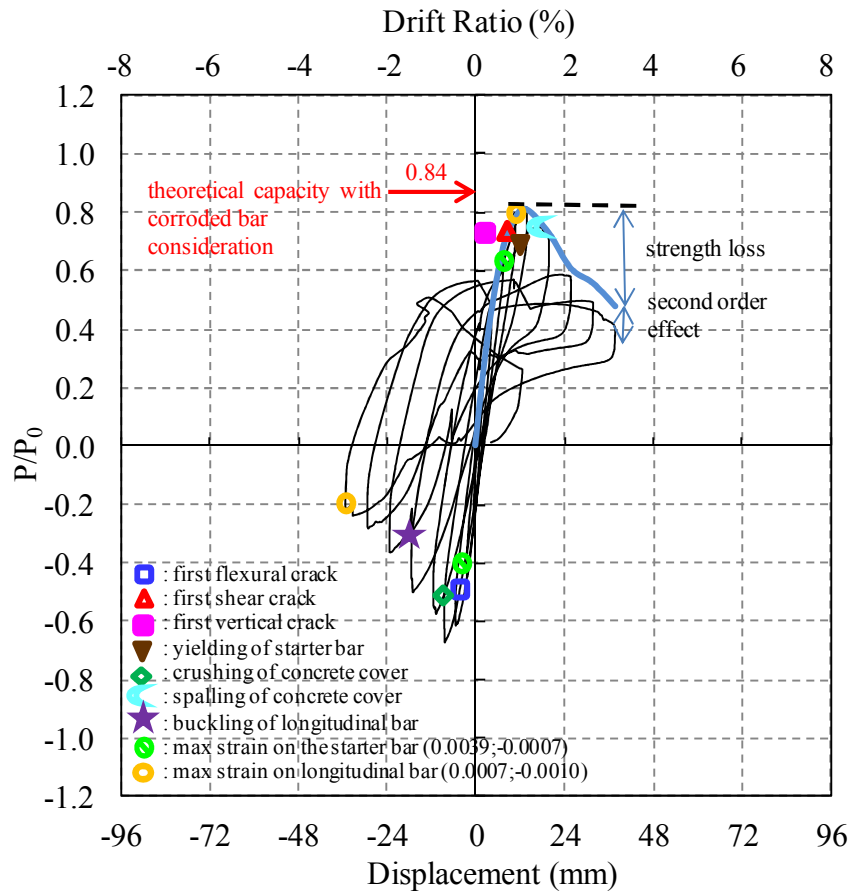


Figure 6.48 : Lateral load/Theoretical load capacity versus displacement for LS-X21.

In this figure, P is applied lateral load and P_0 is the theoretical lateral load capacity of the specimen determined without considering the effect of corrosion. First flexural crack, first shear crack, first vertical crack, yielding of starter bar, crushing of concrete cover, spalling of concrete cover, buckling of longitudinal bar, maximum strain on the starter bar and maximum strain on the longitudinal bar are marked on the figure. As seen from Figure 6.48, strength loss was observed.

Average experimental moment-curvature relationships obtained for critical sections of LS-X21 are presented in Figure 6.49. For the calculation of moment-curvature relationships, the average curvature values obtained for the ranges of 0-20 mm, 20-150 mm and 150-300 mm heights above the footing are taken into account. As seen from Figure 6.12, the curvature values of the member measured in 20-150 mm and 150-300 mm height above the support are in the order of $5 \cdot 10^{-5}$ (1/mm), while the curvatures measured in 0-20 mm height are in the order of $3 \cdot 10^{-3}$ (1/mm). According to the figure, it is of interest to note that the damage is accumulated especially in 20 mm height of the member from top of the base according to the moment-curvature relationships.

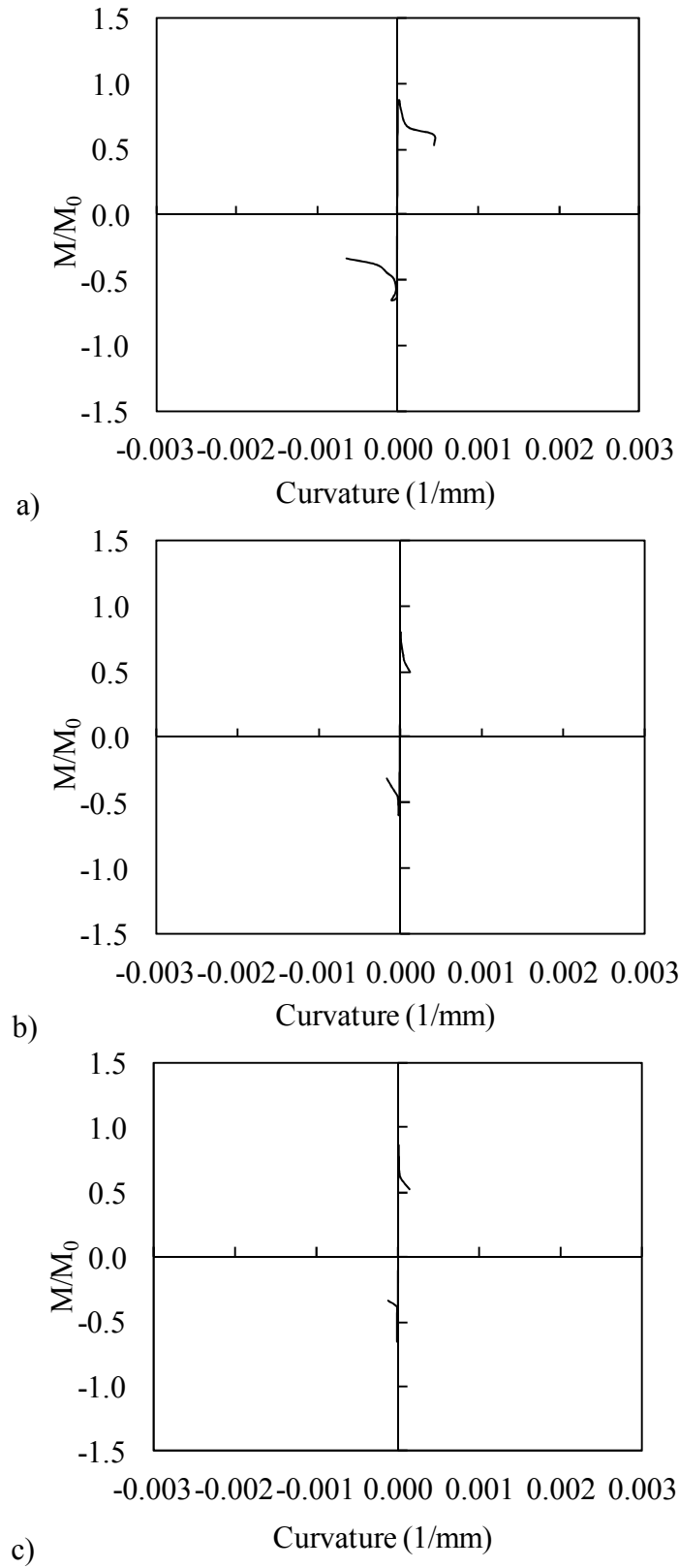


Figure 6.49 : Moment-curvature relationships obtained for a) 0-20 mm, b) 20-150 mm, c) 150-300 mm gauge lengths.

According to the data from the strain gauges on the starter bars of the LS-X21, the maximum strain while pushing was 0.0039, measured from the strain gauge at +400 mm above the footing when $P=20.10$ kN at 0.015 drift ratio; the maximum strain while pulling was -0.0007, measured from the strain gauge at +400 mm above the footing when $P=-17.25$ kN at -0.005 drift ratio. According to the data from the strain gauges on the longitudinal bars of the LS-X21, the maximum strain while pushing was 0.0007, measured from the strain gauge at +400 mm above the footing when $P=23.11$ kN at 0.01 drift ratio; the maximum strain while pulling was -0.0010, measured from the strain gauge at +200 mm above the footing when $P=-6.04$ kN at -0.03 drift ratio. Strain distribution of the starter bars and longitudinal bars of LS-X21 while pushing and pulling are shown in Figure 6.50 and Figure 6.51, respectively. As seen from Figure 6.50 and Figure 6.51, the strain values are higher than specimen LS-X0, and reach yield strain.

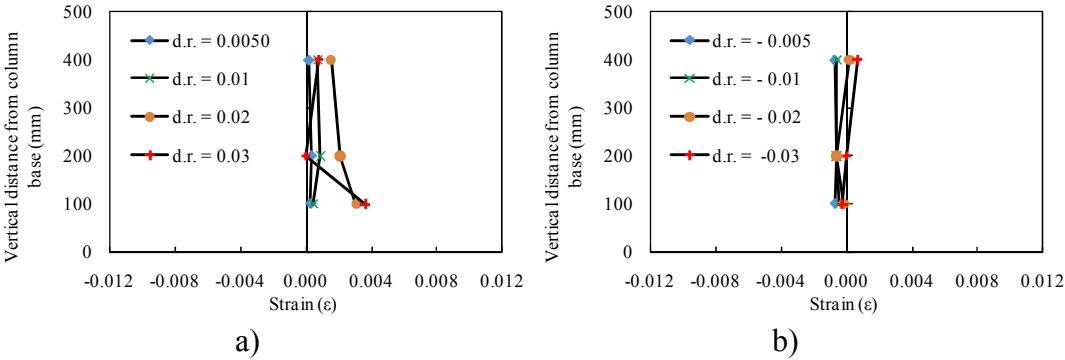


Figure 6.50 : Strain distribution of the starter bars of LS-X21 a) while pushing, b) while pulling.

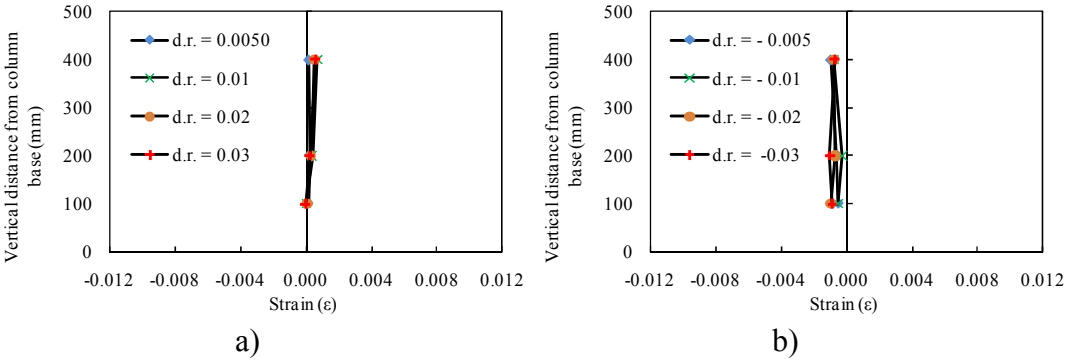


Figure 6.51 : Strain distribution of the longitudinal bars of LS-X21 a) while pushing b) while pulling.

6.2.6 LS-X28

Similar to the specimen LS-X12 and LS-X21, specimen LS-X28 has vertical cracks along the longitudinal reinforcement and horizontal cracks along the transverse reinforcement. Width, location and orientation of the cracks are presented in Table 6.12. Pattern of cracks formed due to corrosion are shown in Figure 6.52.

Table 6.12 : Width, location and orientation of the cracks.

Crack width	Crack location	Crack orientation
1.3 mm	above the footing	along the No.1 longitudinal reinforcement
2.3 mm	above the footing	along the No.2 longitudinal reinforcement
3.1 mm	above the footing	along the No.3 longitudinal reinforcement
1.4 mm	above the footing	along the No.4 longitudinal reinforcement

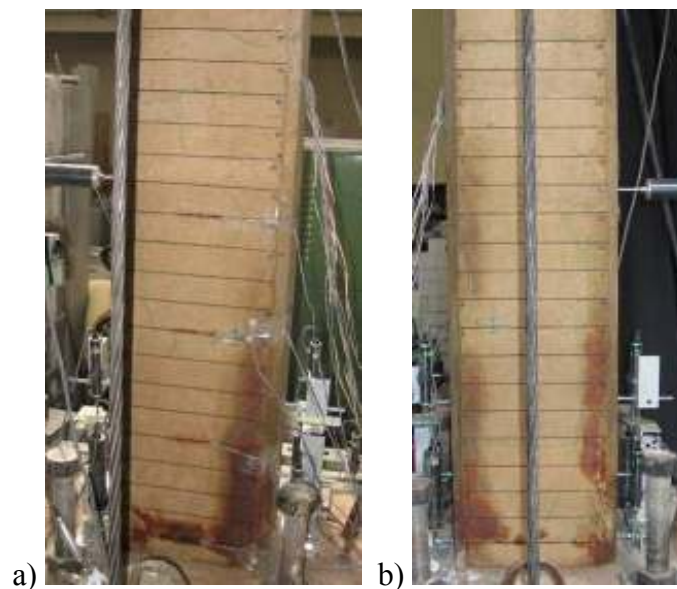


Figure 6.52 : Pattern of cracks formed due to corrosion: (a) North, (b) South.

It should be noted that generally due to corrosion of reinforcing bars of structural members of relatively old sub-standard buildings constructed with low quality concrete have horizontal and vertical cracks along the reinforcing bars. The typical appearances of columns of existing sub-standard RC frame buildings with corroded reinforcement are shown in Figure 6.53.



Figure 6.53 : The appearances of existing sub-standard RC frame structures.

No cracks were observed while loading to target displacements of ± 1.2 mm (drift ratio 0.10%), ± 3 mm (drift ratio 0.25%) and ± 6 mm (drift ratio 0.50%).

First flexural cracks at the interface of the column and footing (A-north, A-south) were observed during loading to target displacement of 9.0 mm (drift ratio 0.75%). During loading to target displacement of -9.0 mm (drift ratio -0.75%) flexural crack (A'-north, A'-south) at the interface of the column and footing was observed. The view of the specimen LS-X28 after -0.10% drift ratio is shown in Figure 6.54.

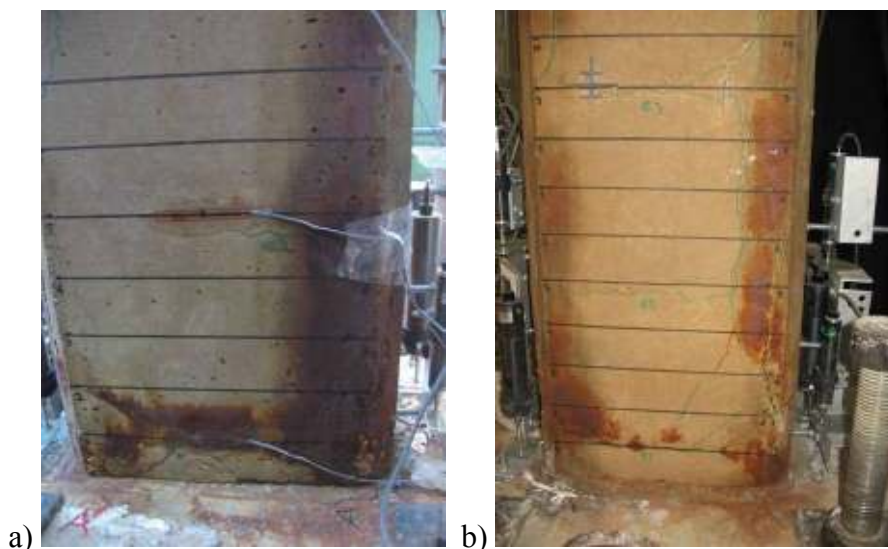


Figure 6.54 : a) North, and b) South view of the LS-X28 specimen after -0.10% drift ratio.

During loading to target displacement of 18.0 mm (drift ratio 1.50%) propagation of existing cracks (A-north, A-south) were observed. During loading to target displacement of -18.0 mm

(drift ratio -1.50%) vertical crack and propagation of existing crack (A'-south) were observed. The view of the specimen LS-X28 after -1.50% drift ratio is shown in Figure 6.55.

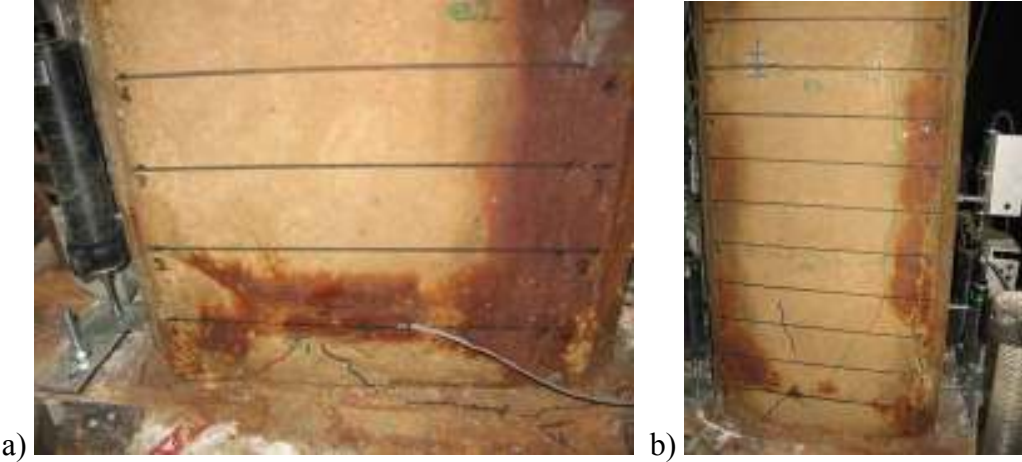


Figure 6.55 : a) North, and b) South view of the LS-X28 specimen after -1.50% drift ratio.

During loading to target displacement of 24.0 mm (drift ratio 2.00%) vertical cracks (B-north, C-south) and shear cracks (C-north, D-north, B-south) were observed. Crushing of concrete cover started. During loading to target displacement of -24.0 mm (drift ratio -2.00%) flexural cracks (B'-north, C'-north) and vertical cracks (B'-south, C'-south) were observed.

During loading to target displacement of 30.0 mm (drift ratio 2.50%) buckling of longitudinal reinforcement was observed. Concrete cover spalled completely. The view of the specimen LS-X28 after -2.50% drift ratio is shown in Figure 6.56.

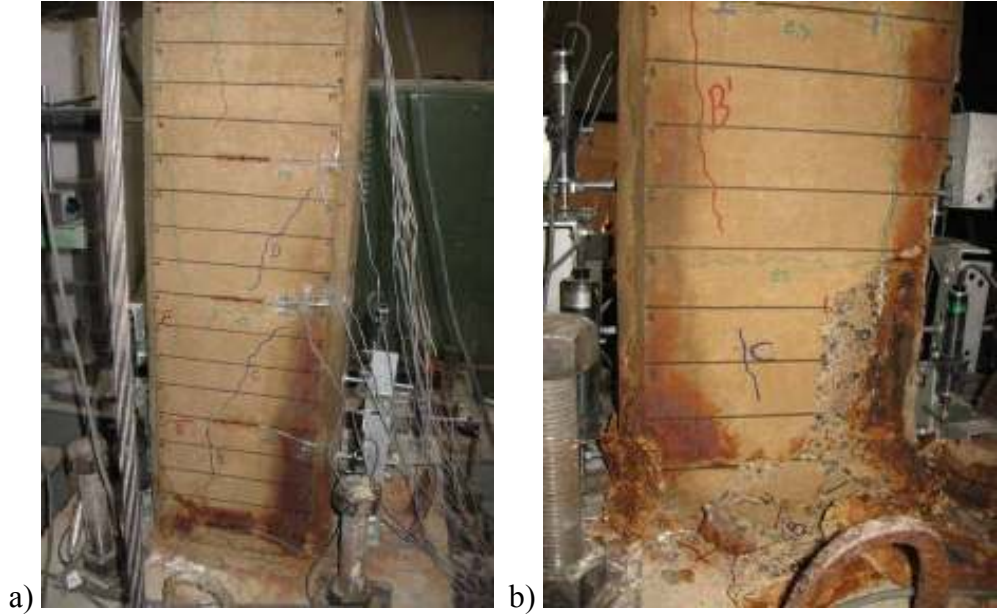


Figure 6.56 : a) North, and b) South view of the LS-X28 specimen after -2.50% drift ratio.

During loading to target displacement of 42.0 mm (drift ratio %3.50) specimen underwent excessive lateral displacement out of its axis and test was ended by decreasing the axial load. The view of the specimen LS-X28 after -3.50% drift ratio is shown in Figure 6.57. Summary of the seismic behavior of specimen LS-X28 is shown in Table 6.13. Crack propagation of LS-X28 while pushing and pulling cycles are given in Appendix C.

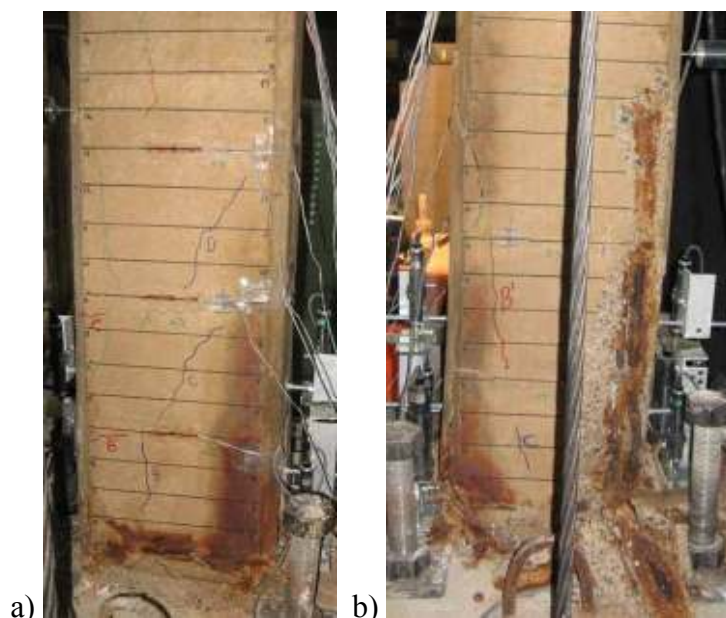


Figure 6.57 : a) North, and b) South view of the LS-X28 specimen after -3.50% drift ratio.

Table 6.13 : Summary of the seismic behavior of LS-X28.

Drift ratio (%)	δ (mm/mm)	P (kN)	Observations
0.10	± 1.2	4.20/-4.14	No crack was observed.
0.25	± 3.0	8.71/-8.10	No crack was observed.
0.50	± 6.0	12.64/-14.53	No crack was observed.
0.75	± 9.0	17.41/-15.74	First flexural crack at column-footing interface was observed.
1.00	± 12.0	19.46/-18.23	Propagation of existing cracks and vertical crack were observed.
1.50	± 18.0	20.53/-18.68	Propagation of existing cracks and vertical crack were observed.
2.00	± 24.0	19.43/-17.26	Shear, flexural and vertical cracks were observed. Crushing started at the concrete cover.
2.50	± 30.0	16.12/-10.29	Spalling of concrete cover was observed. Buckling of longitudinal reinforcement was observed.
3.00	± 36.0	11.03/-5.73	
3.50	+42.0	9.16	Concrete cover spalled completely. Specimen underwent excessive lateral displacement out of its axis and test was ended by decreasing the axial load.

Force-displacement relationship of LS-X28 is presented in Figure 6.58. In this figure, P is applied lateral load and P_0 is the theoretical lateral load capacity of the specimen determined without considering the effect of corrosion. First flexural crack, first shear crack, first vertical crack, yielding of starter bar, yielding of longitudinal bar, crushing of concrete cover, spalling of concrete cover, buckling of longitudinal bar, maximum strain on the starter bar and maximum strain on the longitudinal bar are marked on the figure. As seen from the figure, strength loss was observed.

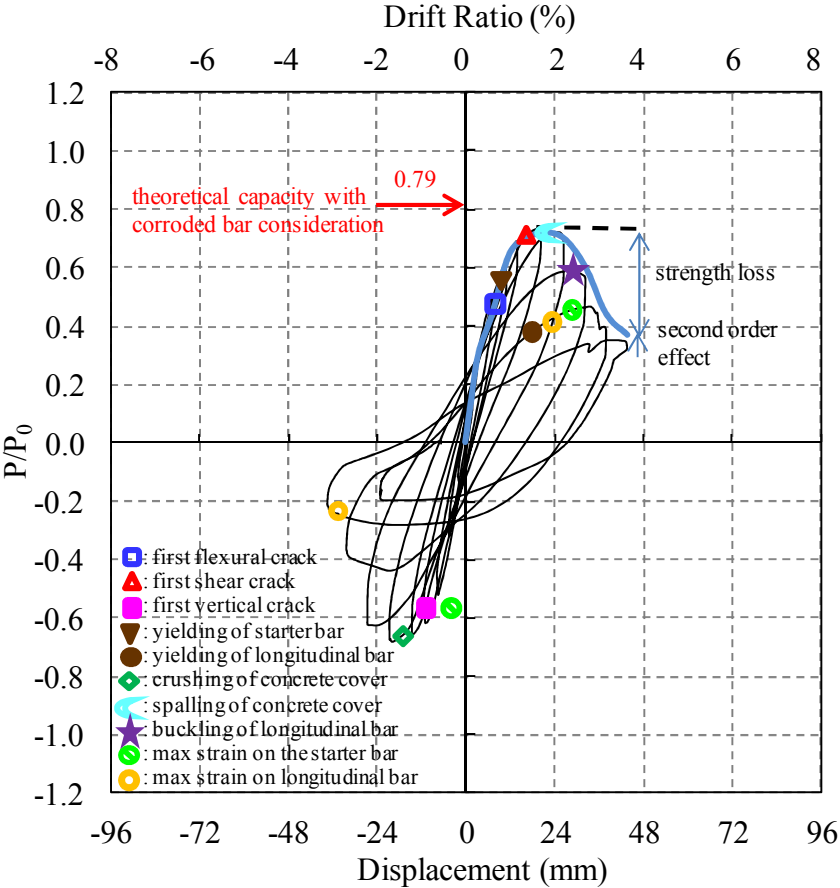


Figure 6.58 : Lateral load/Theoretical load capacity versus displacement for LS-X28.

Average experimental moment-curvature relationships obtained for critical sections of LS-X28 are presented in Figure 6.59. For the calculation of moment-curvature relationships, the average curvature values which were obtained for the ranges of 0-20 mm, 20-150 mm and 150-300 mm heights above the footing were taken into account. As seen from the figure, the curvature values of the member measured in 20-150 mm and 150-300 mm height above the support are in the order of $5 \cdot 10^{-5}$ (1/mm), while the curvatures measured in 0-20 mm height are in the order of $3 \cdot 10^{-3}$ (1/mm). According to the figure, it is of interest to note that the damage is accumulated especially in 20 mm height of the member from top of the base according to the moment-curvature relationships.

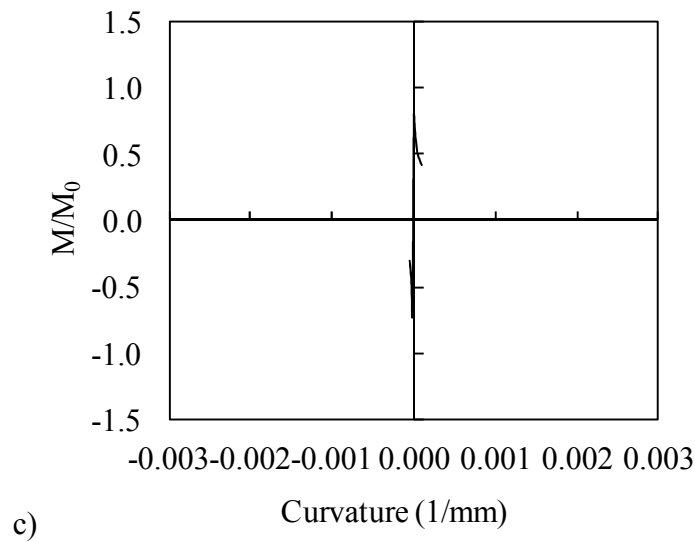
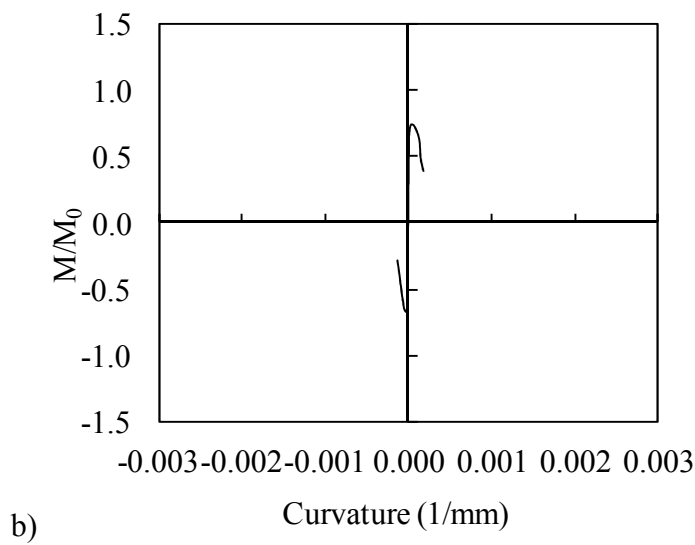
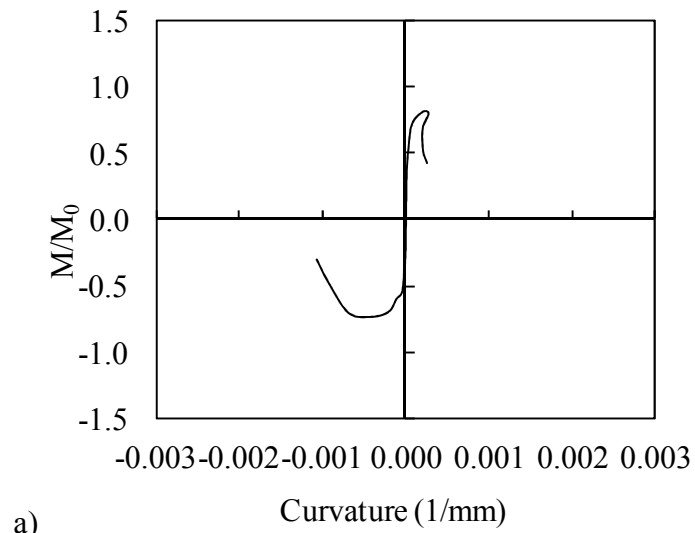


Figure 6.59 : Moment-curvature relationships obtained for a) 0-20 mm, b) 20-150 mm, c) 150-300 mm gauge lengths.

According to the data from the strain gauges on the starter bars of the LS-X28, the maximum strain while pushing was 0.0046, measured from the strain gauge at +400 mm above the footing when P=11.03 kN at 0.03 drift ratio; the maximum strain while pulling was -0.0008, measured from the strain gauge at +100 mm above the footing when P=-18.23 kN at -0.01 drift ratio. According to the data from the strain gauges on the longitudinal bars of the LS-X28, the maximum strain while pushing was 0.0017, measured from the strain gauge at +200 mm above the footing when P=11.03 kN at 0.03 drift ratio; the maximum strain while pulling was -0.0071, measured from the strain gauge at +100 mm above the footing when P=-5.73 kN at -0.03 drift ratio. Strain distribution of the starter bars and longitudinal bars of LS-X28 while pushing and pulling are shown in Figure 6.60 and Figure 6.61, respectively. As seen from Figure 6.60 and Figure 6.61, the strain values are higher than specimen LS-X0, and reach yield strain.

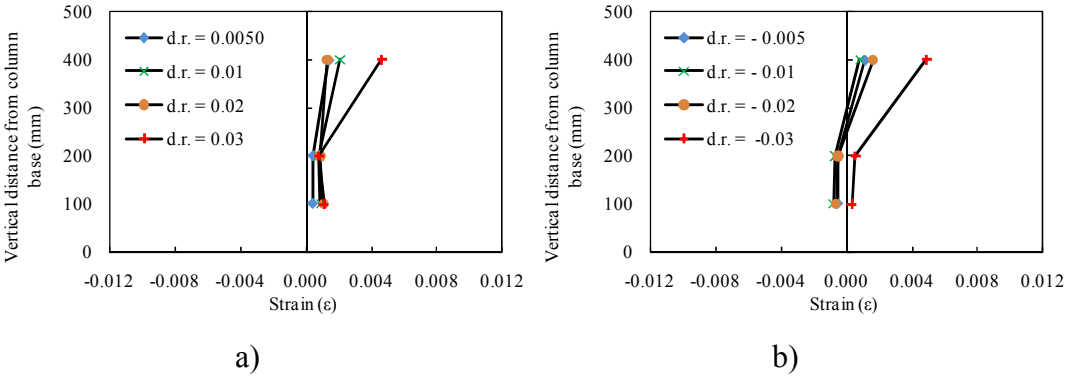


Figure 6.60 : Strain distribution of the starter bars of LS-X28 a) while pushing, b) while pulling.

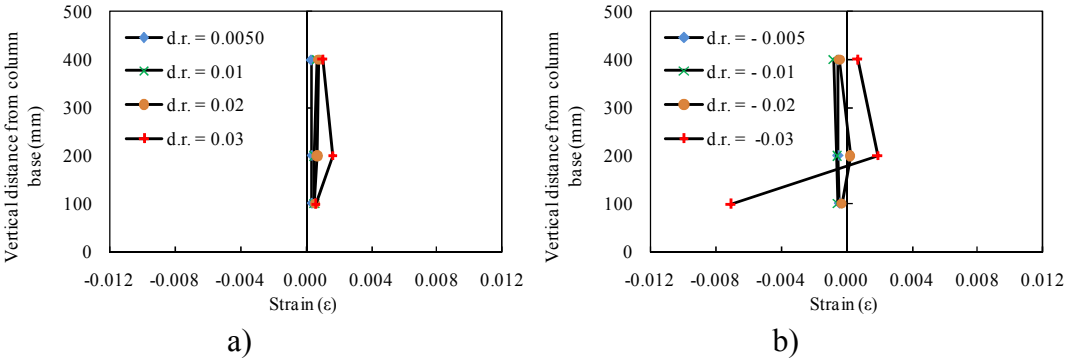


Figure 6.61 : Strain distribution of the longitudinal bars of LS-X28 a) while pushing b) while pulling.

6.3 Test Result of the Second Type Specimens

6.3.1 NS-X0

No cracks were observed while loading to target displacements of ± 1.2 mm (drift ratio 0.10%) and ± 3 mm (drift ratio 0.25%).

First flexural cracks at the interface of the column and footing (A-north, A-south) were observed during loading to target displacement of 6.0 mm (drift ratio 0.50%). During loading to target displacement of -6.0 mm (drift ratio -0.50%) flexural cracks (A'-north, A'-south) at the interface of the column and footing was observed. The view of the specimen NS-X0 after -0.50% drift ratio is shown in Figure 6.62.

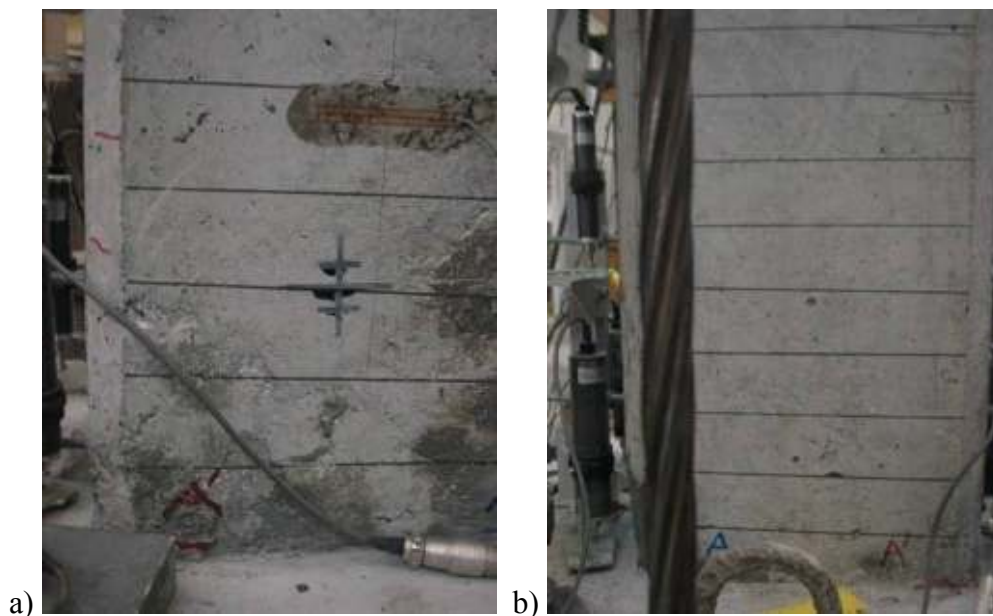


Figure 6.62 : a) North, and b) South view of the NS-X0 specimen after -0.50% drift ratio.

During loading to target displacement of 9.0 mm (drift ratio 0.75%) flexural cracks (B-north, C-north, D-north, B-south, C-south, D-south) were observed. During loading to target displacement of -9.0 mm (drift ratio -0.75%) flexural cracks (B'-north, C'-north, D'-north, E'-north, F'-north, B'-south, C'-south, D'-south, E'-south, F'-south) were observed.

During loading to target displacements of 12.0 mm (drift ratio 1.00%) and -12.0 mm (drift ratio -1.00%) propagation of existing cracks (A-north, B-north, C-north, D-north, A-south, B-south, C-south, D-south) and (A'-south, B'-south, C'-south) were observed, respectively.

During loading to target displacements of 18.0 mm (drift ratio 1.50%) and -18.0 mm (drift ratio -1.50%) propagation of existing cracks (B-north, C-south, D-south) and (E'-north) were observed, respectively. Shear crack (G'-south) was observed during loading to -18.0 mm (drift

ratio -%1.50) was observed. The view of the specimen NS-X0 specimen after -1.50% drift ratio is shown in Figure 6.63.

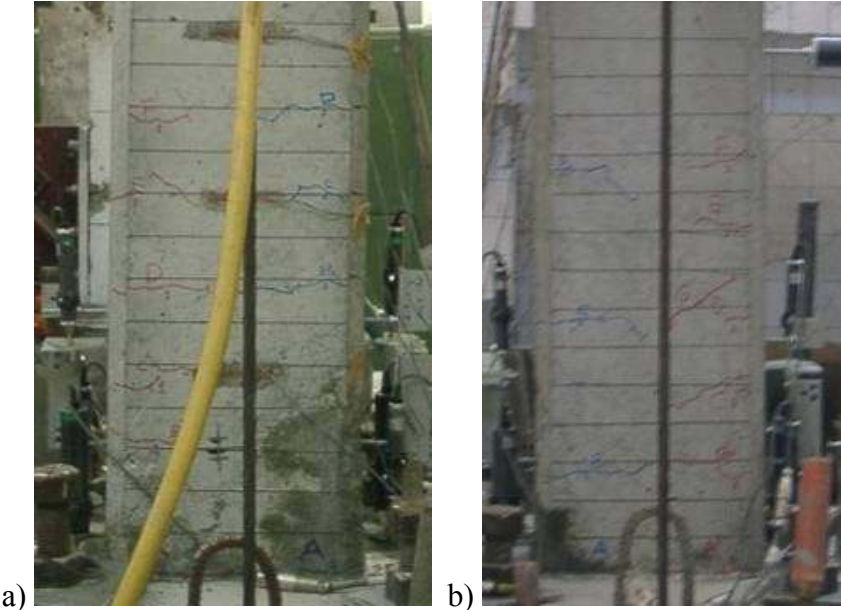


Figure 6.63 : a) North, and b) South view of the NS-X0 specimen after -1.50% drift ratio.

During loading to target displacements of 24.0 mm (drift ratio 2.00%) and -24.0 mm (drift ratio -%2.00) propagation of existing cracks (D-north) and (E'-south) were observed, respectively.

During loading to target displacements of 30.0 mm (drift ratio 2.50%) and -30.0 mm (drift ratio -%2.50) propagation of existing cracks (B-north, D-north, C-south, D-south) and (F'-north) were observed, respectively. The view of the specimen NS-X0 after -2.50% drift ratio is shown in Figure 6.64.

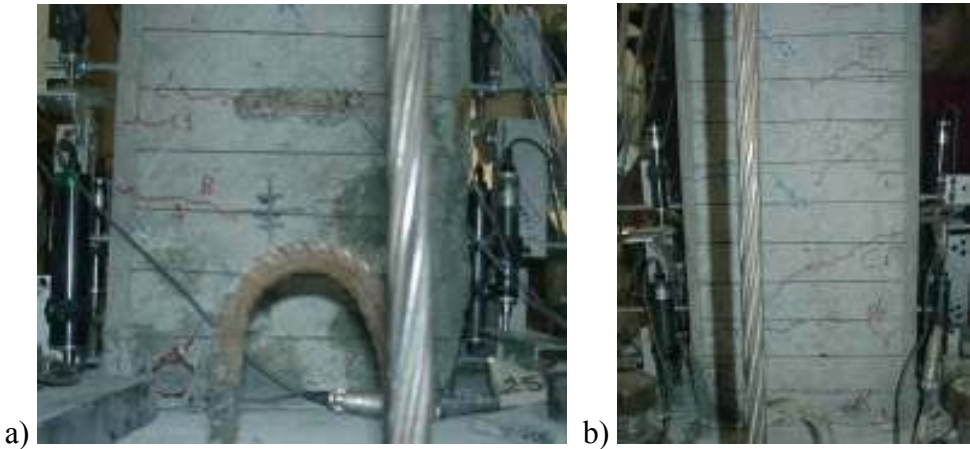


Figure 6.64 : a) North, and b) South view of the NS-X0 specimen after -2.50% drift ratio.

During loading to target displacements of 36.0 mm (drift ratio 3.00%) and -36.0 mm (drift ratio -%3.00) propagation of existing cracks (C-south) and (F'-north, E'-south) were observed, respectively. During loading to target displacements of 36.0 mm (drift ratio 3.00%) vertical crack was observed at north side of the column.

During loading to target displacements of 42.0 mm (drift ratio 3.50%) and -42.0 mm (drift ratio -%3.50) propagation of existing cracks (B-north, D-north, D-south) and (E'-north, F'-north, G'-south) were observed, respectively. During loading to target displacements of 36.0 mm (drift ratio 3.00%) vertical crack was observed at south side of the column. The view of the specimen NS-X0 after -6.00% drift ratio is shown in Figure 6.65.

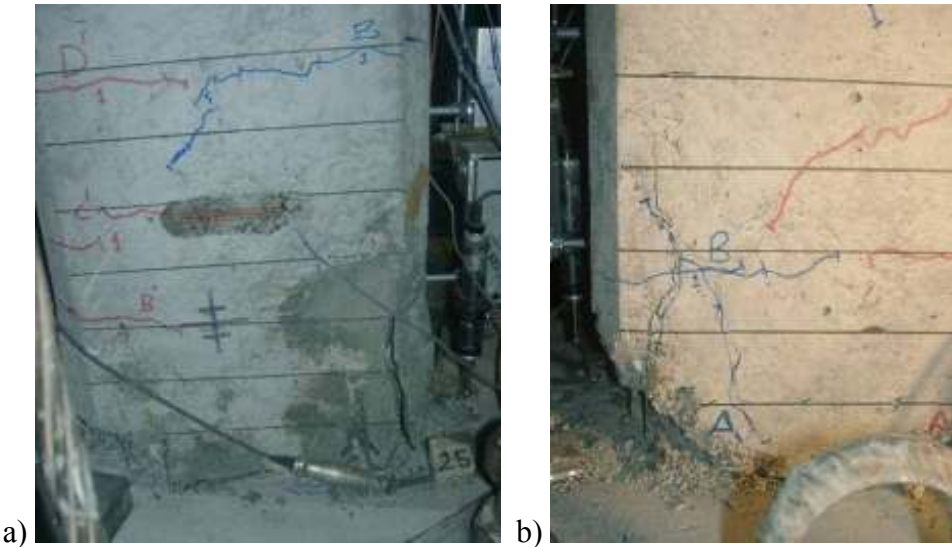


Figure 6.65 : a) North, and b) South view of the NS-X0 specimen after 6.00% drift ratio.

During loading to target displacement of 96.0 mm (drift ratio 8.00%) specimen underwent excessive lateral displacement out of its axis and test was ended by decreasing the axial load. Summary of the seismic behavior of specimen NS-X0 is shown in Table 6.14. Crack propagation of NS-X0 while pushing and pulling cycles are given in Appendix C.

Force-displacement relationship of NS-X0 is presented in Figure 6.66. In this figure, P is applied lateral load and P_0 is the theoretical lateral load capacity of the specimen determined without considering the effect of corrosion. First flexural crack, first vertical crack, yielding of starter bar, crushing of concrete cover, spalling of concrete cover, fracture of starter bar, maximum strain on the starter bar and maximum strain on the longitudinal bar are marked on the figure. As seen from Figure 6.66, strength loss was observed.

Table 6.14 : Summary of the seismic behavior of NS-X0.

Drift ratio (%)	δ (mm/mm)	P (kN)	Observations
0.10	±1.2	13.37 / -16.35	No crack was observed.
0.25	±3.0	26.23 / -26.80	No crack was observed.
0.50	±6.0	39.53 / -38.49	First flexural crack at column-footing interface was observed.
0.75	±9.0	49.15 / -44.21	Flexural cracks were observed.
1.0	±12.0	54.21 / -46.98	Propagation of existing cracks was observed.
1.5	±18.0	56.25 / -47.59	Spalling of concrete cover was observed. Propagation of existing cracks were observed.
2.00	±24.0	55.46 / -45.88	Propagation of existing cracks were observed.
2.50	±30.0	53.95 / -42.17	Propagation of existing cracks were observed.
3.0	±36.0	51.58 / -40.27	Vertical crack was observed. Spalling of concrete cover was observed.
3.50	±42.0	49.27 / -37.80	Vertical crack was observed.
4.0	±48.0	46.15 / -34.99	
4.5	±54.0	43.85 / -32.98	
5.0	±60.0	41.65 / -31.04	
6.0	±72.0	38.65 / -26.29	
7.0	±84.0	32.07 / -22.59	Specimen underwent excessive lateral displacement out of its axis and test was ended by decreasing the axial load.

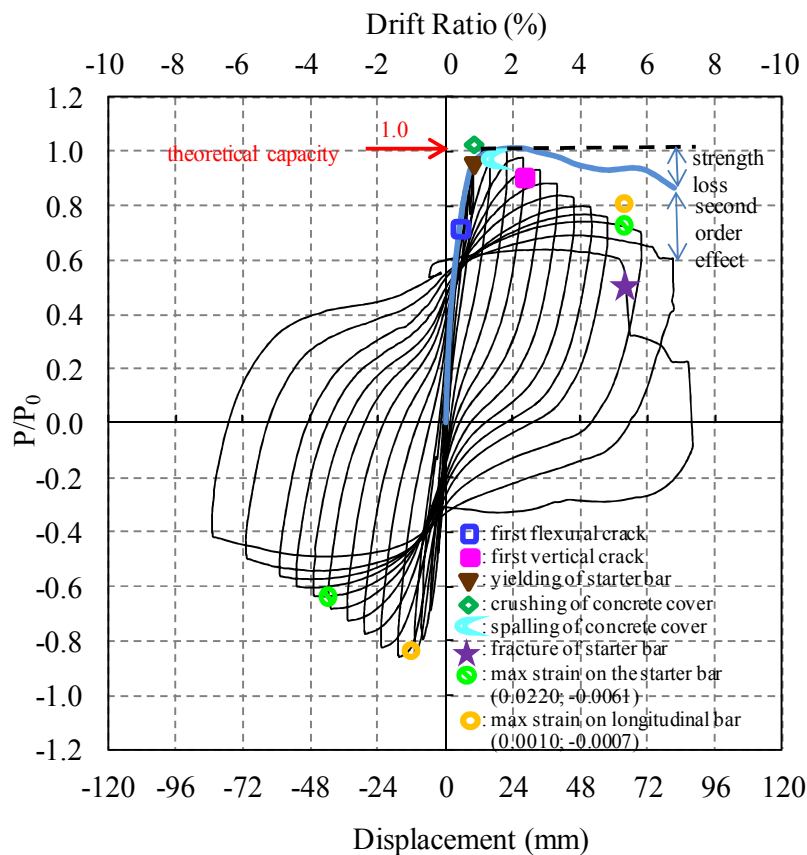


Figure 6.66 : Lateral load/Theoretical load capacity versus displacement for the specimen NS-X0.

Average experimental moment-curvature relationships obtained for critical sections of NS-X0 are presented in Figure 6.67.

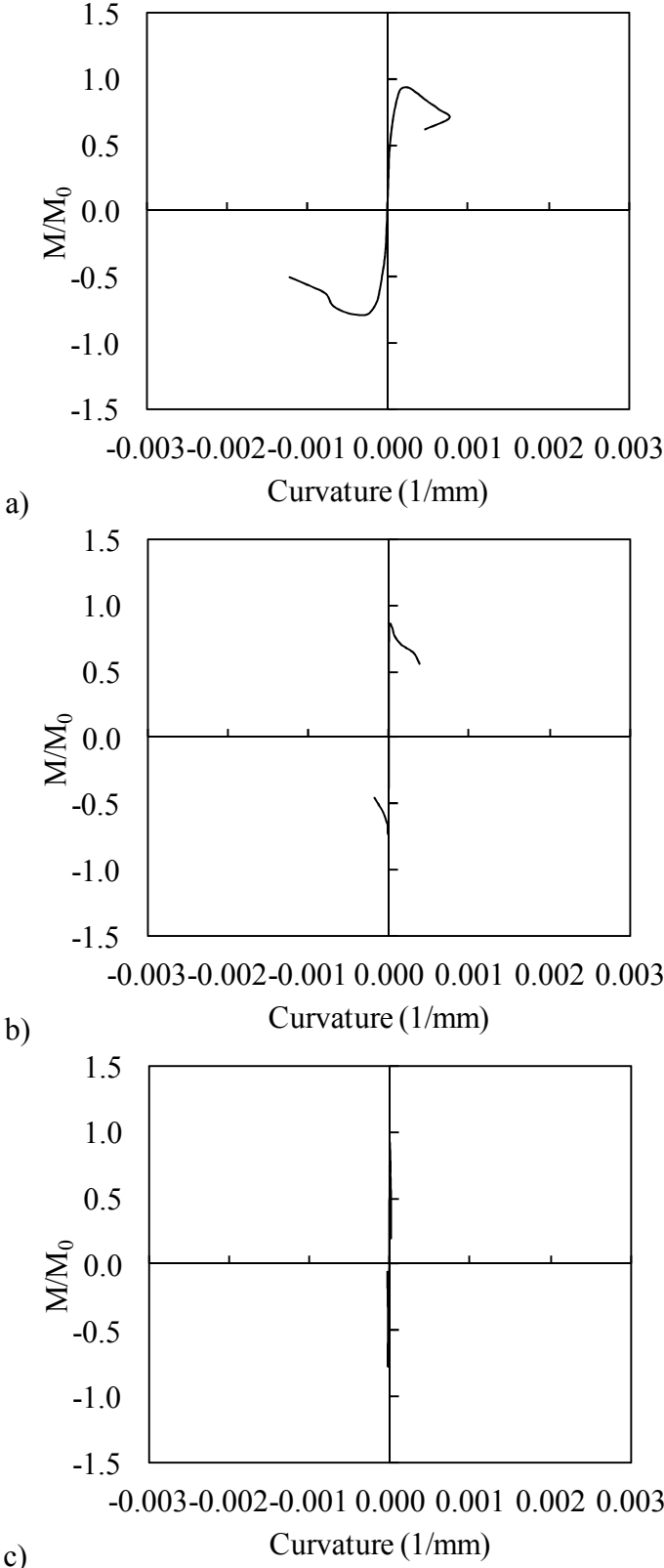


Figure 6.67 : Moment-curvature relationships obtained for a) 0-20 mm, b) 20-150 mm, c) 150-300 mm gauge lengths.

For the calculation of moment-curvature relationships, the average curvature values which were obtained for the ranges of 0-20 mm, 20-150 mm and 150-300 mm heights above the footing are taken into account. As seen from the figure, the curvature values of the member measured in 20-150 mm and 150-300 mm height above the support are in the order of $5 \cdot 10^{-5}$ (1/mm), while the curvatures measured in 0-20 mm height are in the order of $3 \cdot 10^{-3}$ (1/mm). According to figure, it is of interest to note that the damage is accumulated especially in 20 mm height of the member from top of the base according to the moment-curvature relationships.

According to the data from the straingauges on the starter bars of the specimen NS-X0, the maximum strain while pushing was 0.0222, measured from the strain gauge at +100 mm above the footing when $P=41.65$ kN at 0.05 drift ratio; the maximum strain while pulling was -0.0061, measured from the strain gauge at +100 mm above the footing when $P=-34.99$ kN at -0.04 drift ratio. According to the data from the straingauges on the longitudinal bars of the NS-X0, the maximum strain while pushing was 0.0010, measured from the strain gauge at +400 mm above the footing when $P=38.65$ kN at 0.06 drift ratio; the maximum strain while pulling was -0.0007, measured from the strain gauge at +400 mm above the footing when $P=-47.59$ kN at -0.015 drift ratio. Strain distribution of the starter bars and longitudinal bars of NS-X0 while pushing and pulling are shown in Figure 6.68 and Figure 6.69, respectively. As seen from Figure 6.68 and Figure 6.69, the strain values of starter bars reach yield strain.

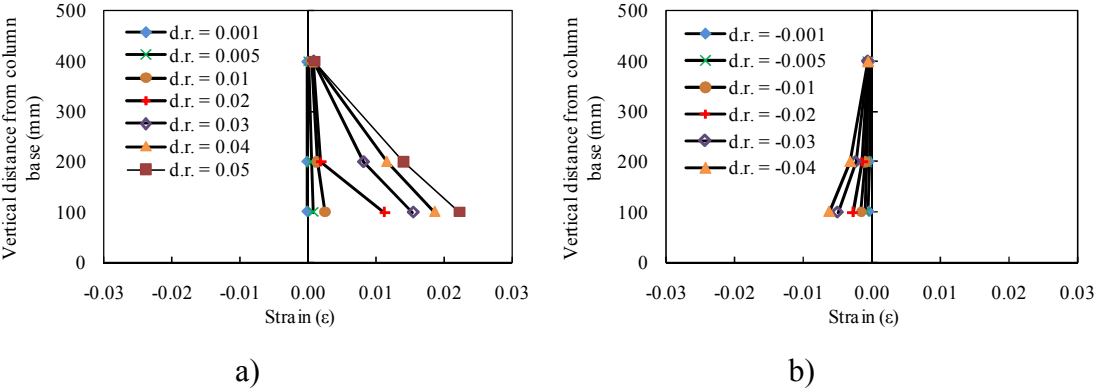


Figure 6.68 : Strain distribution of the starter bars of NS-X0 a) while pushing, b) while pulling.

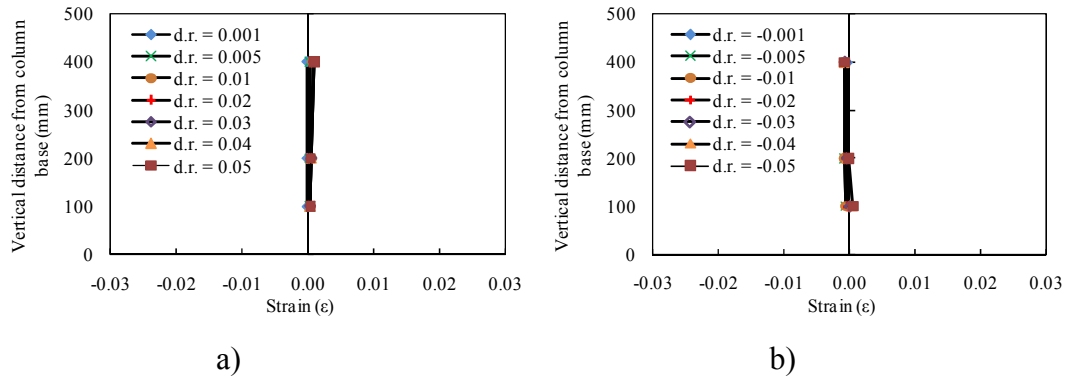


Figure 6.69 : Strain distribution of the longitudinal bars of NS-X0 a) while pushing b) while pulling.

6.3.2 NS-X9

No cracks were observed while loading to target displacements of ± 1.2 mm (drift ratio 0.10%) and ± 3 mm (drift ratio 0.25%).

First flexural cracks (A-north, A-south) at the interface of the column and footing and (B-north) were observed during loading to target displacement of 6 mm (drift ratio 0.50%). During loading to target displacement of -6 mm (drift ratio -0.50%) flexural cracks (A'-north, A'-south) at the interface of the column and footing and (B'-north, B'-south) were observed. The view of the specimen NS-X9 after -0.50% drift ratio is shown in Figure 6.70.

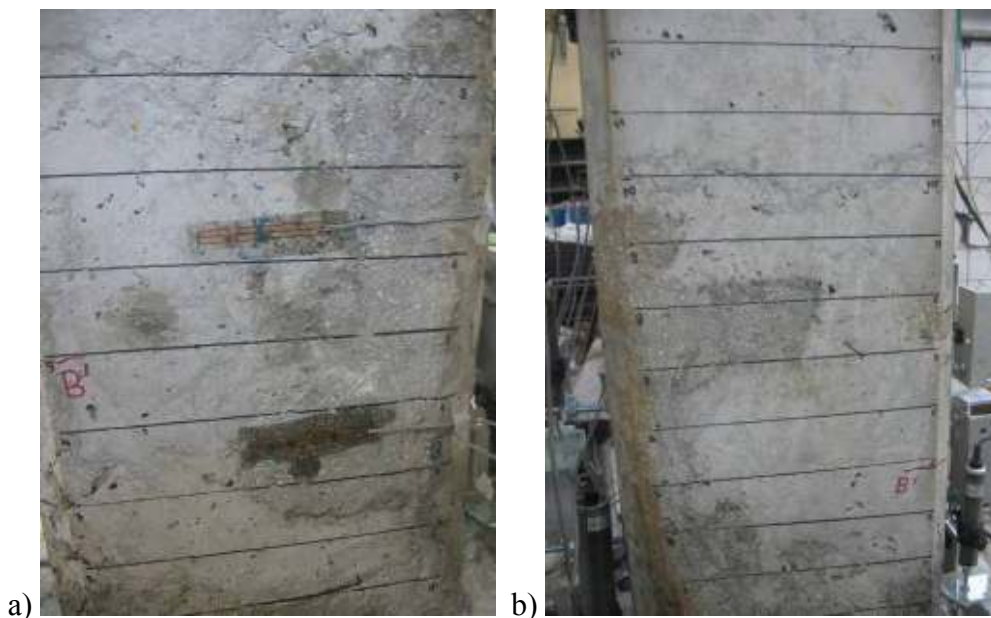


Figure 6.70 : a) North, and b) South view of the NS-X9 specimen after -0.50% drift ratio.

During loading to target displacement of 9.0 mm (drift ratio 0.75%) flexural crack (B-south) was observed. During loading to target displacement of -9.0 mm (drift ratio -0.75%) flexural

cracks (D'-north, E'-north, F'-north, C'-south, D'-south, E'-south), vertical crack (C'-north) and propagation of existing crack (D'-south, F'-south) were observed.

During loading to target displacement of 12.0 mm (drift ratio 1.00%) flexural cracks (C-north, D-north, E-north, D-north, C-south, D-south, E-south, F-south) were observed. During loading to target displacement of -12.0 mm (drift ratio -1.00%) flexural crack (G'-north), vertical crack (F'-north) and propagation of existing cracks (A'-south, B'-north) were observed.

During loading to target displacement of 18.0 mm (drift ratio 1.50%) propagation of existing crack (E-north) was observed. During loading to target displacement of -18.0 mm (drift ratio -1.50%) vertical crack (G'-south) and propagation of existing cracks (F'-south) were observed. The view of the specimen NS-X9 after -1.50% drift ratio is shown in Figure 6.71.

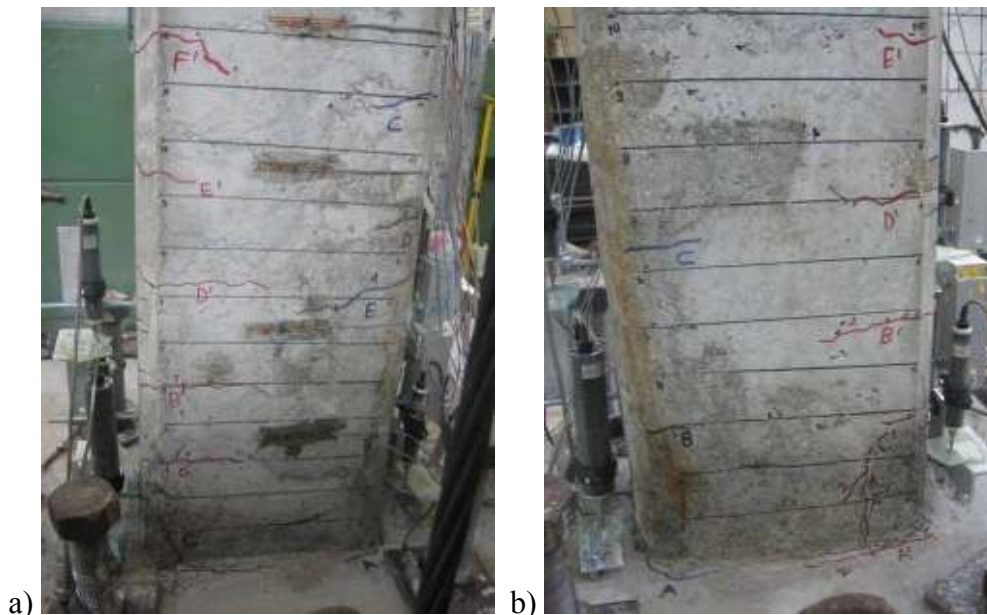


Figure 6.71 : a) North, and b) South view of the NS-X9 specimen after -1.50% drift ratio.

During loading to target displacements of 24.0 mm (drift ratio 2.00%) and -24.0 mm (drift ratio -2.00) propagation of existing cracks (A-north, B-north, C-north, A-south) and (B'-north, E'-north, F'-north, B'-south, F'-south) were observed, respectively. During loading to target displacements of 24.0 mm (drift ratio 2.00%) vertical crack (G-south) was observed. During loading to target displacements of -24.0 mm (drift ratio -2.00%) vertical crack (H'-south) and flexural cracks (H'-north, E'-south, I'-south) were observed.

During loading to target displacements of 30.0 mm (drift ratio 2.50%) and -30.0 mm (drift ratio -2.50) propagation of existing cracks (D-south) and (I'-north) were observed,

respectively. During loading to target displacements of 30.0 mm (drift ratio 2.50%) vertical crack (F-north) was observed. The view of the specimen NS-X9 after -2.50% drift ratio is shown in Figure 6.72.

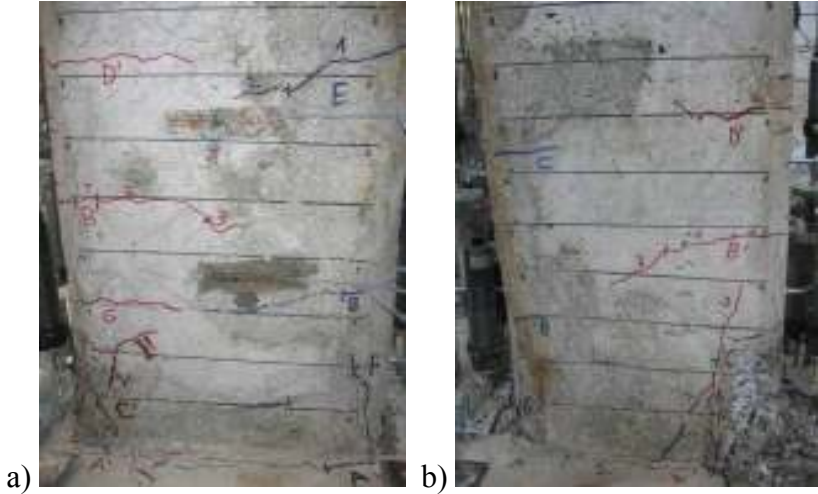


Figure 6.72 : a) North, and b) South view of the specimen NS-X9 after -2.50% drift ratio.

During loading to target displacements of 36.0 mm (drift ratio 3.00%) and -36.0 mm (drift ratio -3.00%) propagation of existing cracks (F-north, G-south) and (F'-south) were observed, respectively. During loading to target displacements of 36.0 mm (drift ratio 3.00%) vertical crack was observed.

During loading to target displacements of 42.0 mm (drift ratio 3.50%) vertical crack (H-south) was observed. During loading to target displacements of -42.0 mm (drift ratio -3.50%) propagation of existing crack (B'-north) was observed. The view of the specimen NS-X9 after -3.50% drift ratio is shown in Figure 6.73.

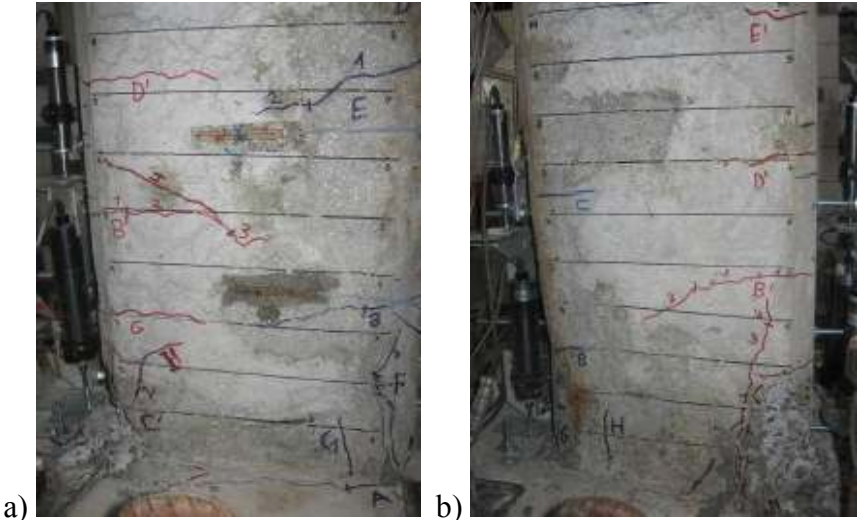


Figure 6.73 : a) North, and b) South view of the specimen NS-X9 after -3.50% drift ratio.

During loading to target displacements of 48.0 mm (drift ratio 4.00%) and -48.0 mm (drift ratio -4.00%) propagation of existing cracks (G-north, G-south, H-south) and (F'-south) were observed.

During loading to target displacements of -60.0 mm (drift ratio -5.00%) propagation of existing cracks (C'-north, F'-south) were observed.

During loading to target displacements of -96.0 mm (drift ratio -8.00%) specimen underwent excessive lateral displacement out of its axis and test was ended by decreasing the axial load. The view of the specimen NS-X9 after -8.00% drift ratio is shown in Figure 6.74. Summary of the seismic behavior of the specimen NS-X9 is shown in Table 6.15.

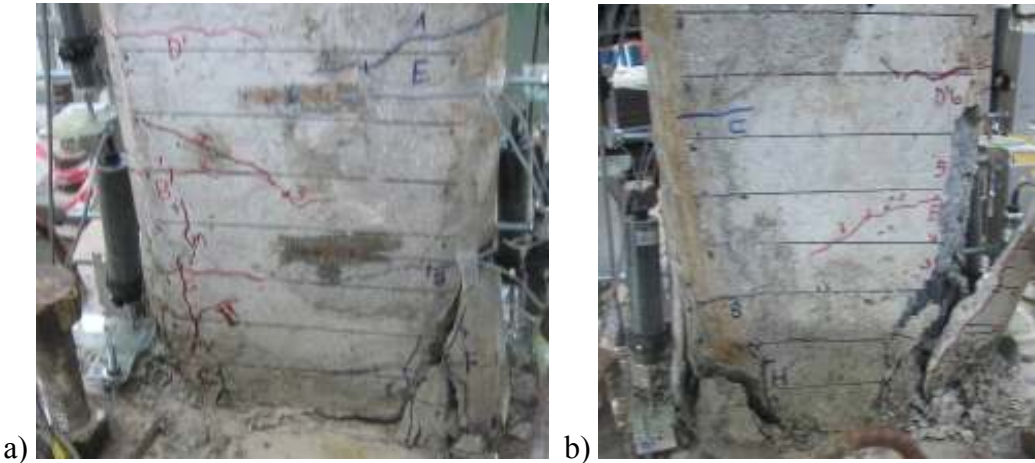


Figure 6.74 : a) North, and b) South view of the specimen NS-X9 after 8.00% drift ratio.

Crack propagation of the specimen NS-X9 while pushing and pulling cycles are given in Appendix C.

Force-displacement relationship of the specimen NS-X9 is presented in Figure 6.75. In this figure, P is applied lateral load and P_0 is the theoretical lateral load capacity of the specimen determined without considering the effect of corrosion. First flexural crack, first vertical crack, yielding of transverse bar, crushing of concrete cover, spalling of concrete cover, fracture of starter bar, maximum strain on the starter bar and maximum strain on the longitudinal bar are marked on the figure. As seen from Figure 6.75, strength loss was observed.

Table 6.15 : Summary of the seismic behavior of NS-X9.

Drift ratio (%)	δ (mm/mm)	P (kN)	Observations
0.10	± 1.2	10.94 / -13.66	No crack was observed.
0.25	± 3.0	21.04 / -25.58	No crack was observed.
0.50	± 6.0	30.10 / -38.53	First flexural crack at column-footing interface was observed.
0.75	± 9.0	35.90 / -48.01	Propagation of existing cracks, flexural cracks and vertical crack were observed.
1.0	± 12.0	43.07 / -51.13	Propagation of existing crack and vertical crack and flexural cracks were observed.
1.5	± 18.0	45.04 / -53.23	Propagation of existing crack and vertical crack were observed.
2.00	± 24.0	44.39 / -53.56	Propagation of existing cracks, flexural cracks and vertical cracks were observed.
2.50	± 30.0	42.78 / -51.16	Propagation of existing cracks and vertical crack were observed.
3.0	± 36.0	41.16 / -49.06	Propagation of existing cracks and vertical crack were observed.
3.50	± 42.0	39.24 / -46.04	Propagation of existing crack and vertical crack were observed.
4.0	± 48.0	36.61 / -44.62	Propagation of existing cracks were observed.
4.5	± 54.0	34.32 / -42.33	
5.0	± 60.0	32.35 / -39.87	Propagation of existing cracks were observed.
6.0	± 72.0	29.22 / -36.61	
7.0	± 84.0	24.00 / -30.89	
8.0	+96.0	20.65	Specimen underwent excessive lateral displacement out of its axis and test was ended by decreasing the axial load.

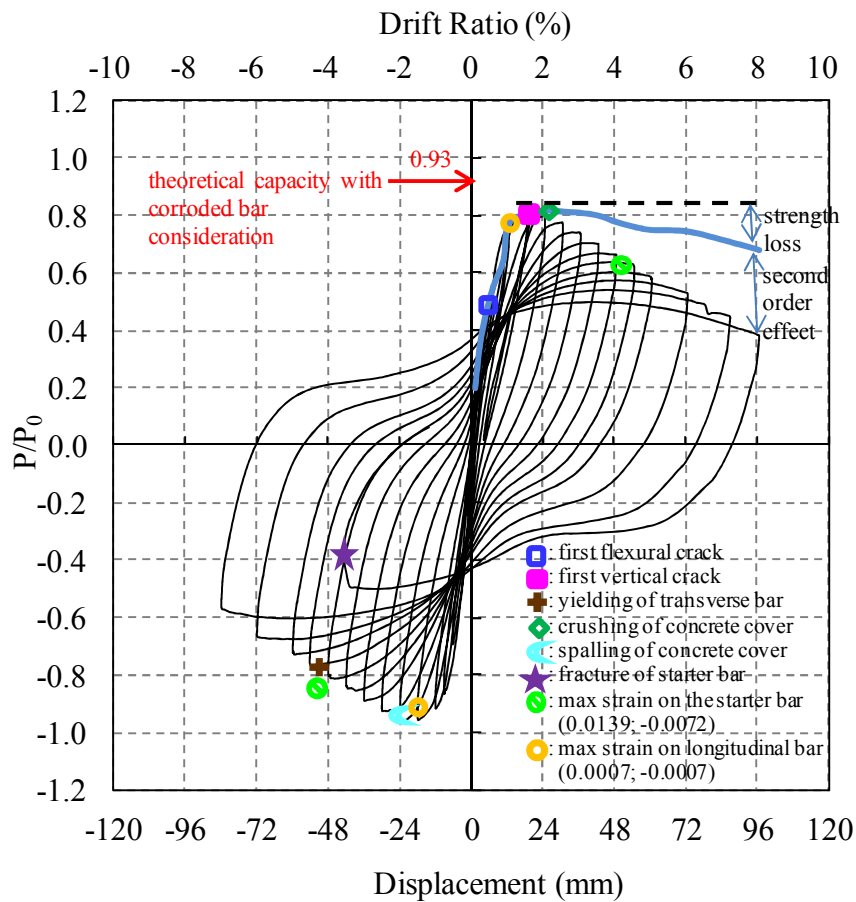


Figure 6.75 : Lateral load/Theoretical load capacity versus displacement for NS-X9.

Average experimental moment-curvature relationships obtained for critical sections of NS-X9 are presented in Figure 6.76.

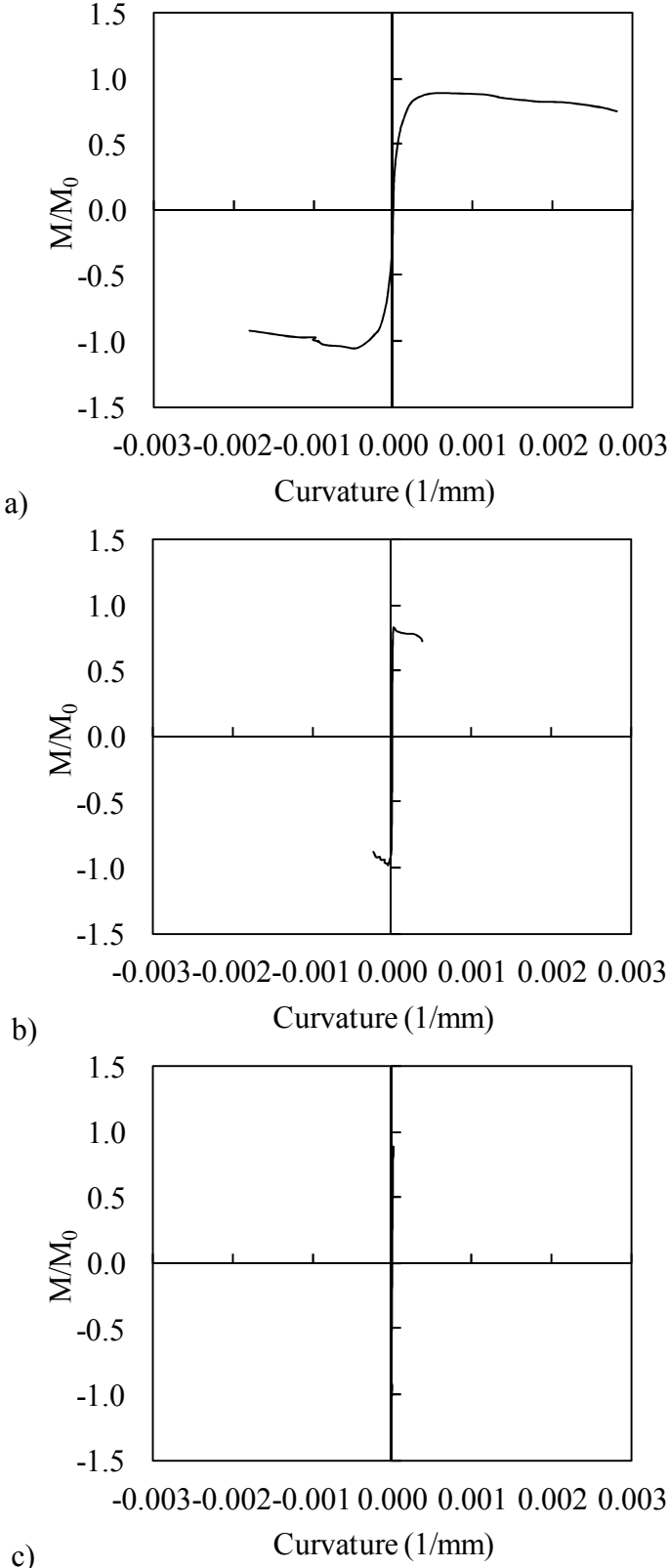


Figure 6.76 : Moment-curvature relationships obtained for a) 0-20 mm, b) 20-150 mm, c) 150-300 mm gauge lengths.

For the calculation of moment-curvature relationships, the average curvature values which were obtained for the ranges of 0-20 mm, 20-150 mm and 150-300 mm heights above the footing were taken into account. As seen from the figure, the curvature values of the member measured in 20-150 mm and 150-300 mm height above the support are in the order of 5.10^{-5} (1/mm), while the curvatures measured in 0-20 mm height are in the order of 3.10^{-3} (1/mm). According to the figure, it is of interest to note that the damage is accumulated especially in 20 mm height of the member from top of the base according to the moment-curvature relationships.

According to the data from the straingauges on the starter bars of the NS-X9, the maximum strain while pushing was 0.0139, measured from the strain gauge at +200 mm above the footing when $P=32.35$ at 0.05 drift ratio; the maximum strain while pulling was -0.0072, measured from the strain gauge at +200 mm above the footing when $P=-39.87$ kN at -0.05 drift ratio. According to the data from the straingauges on the longitudinal bars of the NS-X9, the maximum strain while pushing was 0.0007, measured from the strain gauge at +400 mm above the footing when $P=45.04$ kN at 0.015 drift ratio; the maximum strain while pulling was -0.0007, measured from the strain gauge at +400 mm above the footing when $P=-53.56$ kN at -0.02 drift ratio. Strain distribution of the starter bars and longitudinal bars of NS-X9 while pushing and pulling are shown in Figure 6.77 and Figure 6.78, respectively. As seen from Figure 6.77 and Figure 6.78, the strain values of starter bars reach yield strain and are lower than NS-X0.

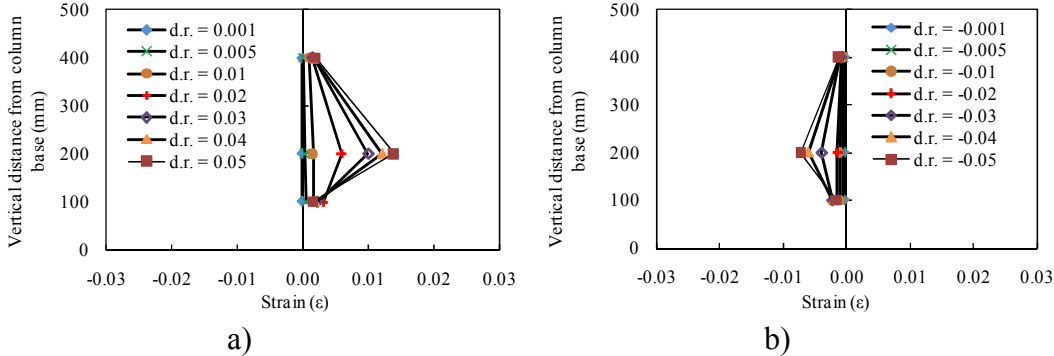


Figure 6.77 : Strain distribution of the starter bars of NS-X9 a) while pushing, b) while pulling.

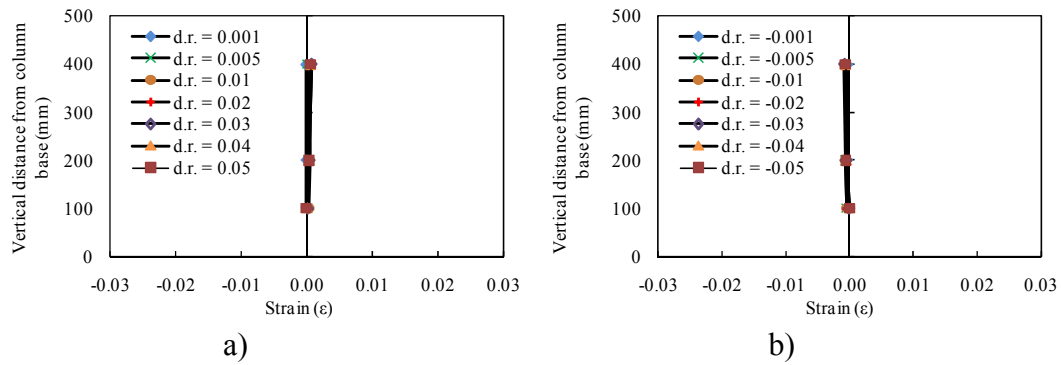


Figure 6.78 : Strain distribution of the longitudinal bars of NS-X9 a) while pushing b) while pulling.

6.3.3 NS-X13

No cracks were observed while loading to target displacements of ± 1.2 mm (drift ratio 0.10%) and ± 3 mm (drift ratio 0.25%).

First flexural cracks (A-north, A-south) were observed at the interface of the column and footing during loading to target displacement of 6 mm (drift ratio 0.50%). During loading to target displacement of -6 mm (drift ratio -0.50%) flexural cracks were observed at both sides of the column (A'-north, A'-south). The view of the specimen NS-X13 after -0.50% drift ratio is shown in Figure 6.79.

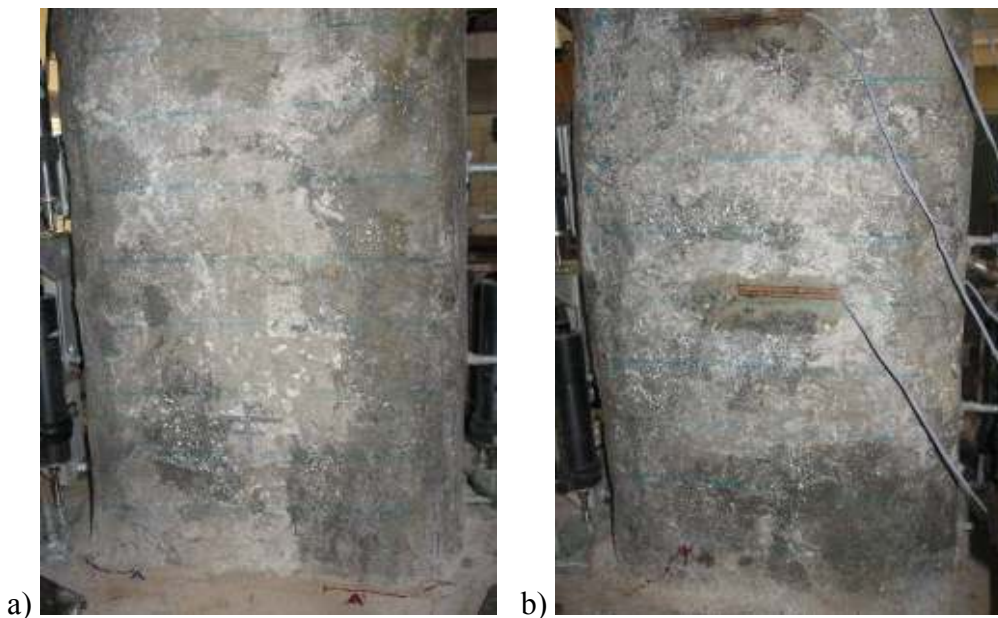


Figure 6.79 : a) North, and b) South view of the specimen NS-X13 after -0.50% drift ratio.

During loading to target displacement of 9.0 mm (drift ratio 0.75%) propagation of existing crack (A-south) was observed. During loading to target displacement of -9.0 mm (drift ratio -0.75%) vertical cracks (BL₁'-north, BL₁'-south) were observed.

During loading to target displacement of 12.0 mm (drift ratio 1.00%) flexural crack (B-south) and vertical crack (BL₁-south) were observed. During loading to target displacement of -12.0 mm (drift ratio -1.00%) propagation of existing cracks (A'-north, BL₁'-south, A'-south) were observed.

During loading to target displacement of 18.0 mm (drift ratio 1.50%) vertical crack (B-north) and propagation of existing cracks (A-north, BL₁-south) were observed. During loading to target displacement of -18.0 mm (drift ratio -1.50%) vertical crack at north side and propagation of existing cracks (A'-north, BL₁'-south, A'-south) were observed. The view of the specimen NS-X13 after -1.50% drift ratio is shown in Figure 6.80.

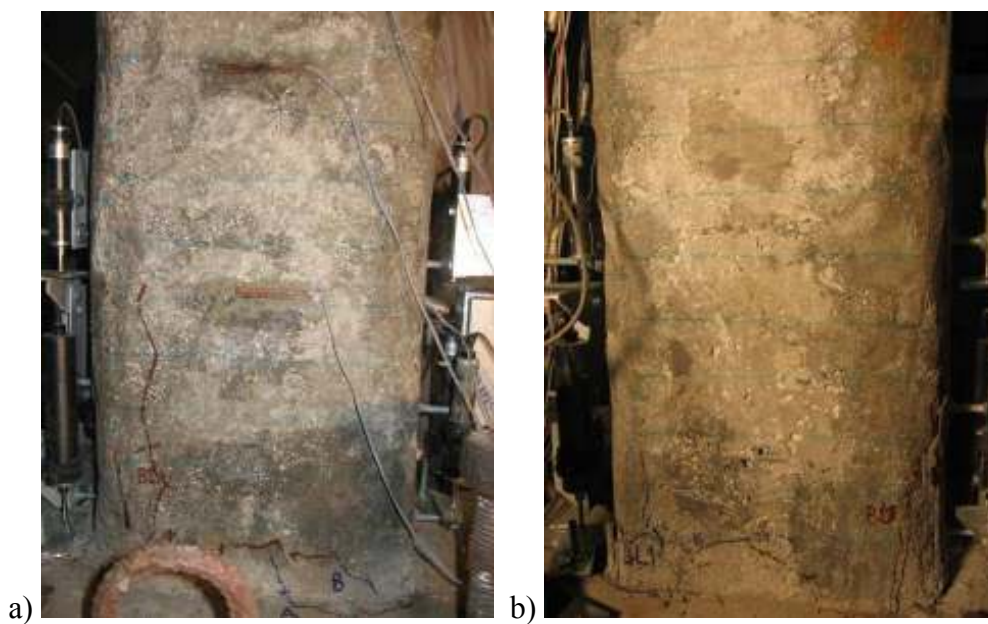


Figure 6.80 : a) North, and b) South view of the specimen NS-X13 after -1.50% drift ratio.

During loading to target displacement of 24.0 mm (drift ratio 2.00%) propagation of existing cracks (B-north, BL₁-south) were observed. During loading to target displacement of -24.0 mm (drift ratio -2.00%) propagation of existing cracks (A'-north) and vertical crack and flexural crack (B'-south) were observed.

During loading to target displacement of 30.0 mm (drift ratio 2.50%) flexural crack (C-north), vertical crack (BL₁-north) and propagation of existing cracks (A-north, B-north, BL₁-south) were observed. During loading to target displacement of -30.0 mm (drift ratio -2.50%) propagation of existing cracks (A'-north) and vertical crack and flexural crack (B'-south) were observed. During loading to target displacement of -30.0 mm'ye gidilirken (drift ratio -%2.50) propagation of existing crack (B-south) was observed. The view of the specimen NS-X13 after -2.50% drift ratio is shown in Figure 6.81.

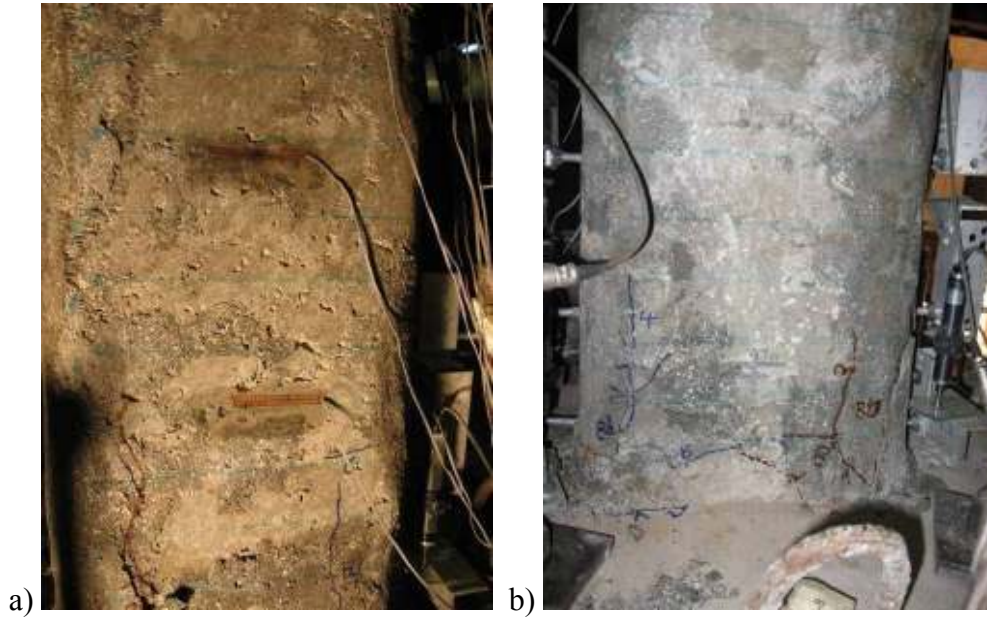


Figure 6.81 : a) North, and b) South view of the specimen NS-X13 after 2.50% drift ratio.

During loading to target displacement of -36.0 mm (drift ratio -%3.00) propagation of existing cracks (BL₁'-north, BL₁'-south) were observed. The view of the specimen NS-X13 after -3.50% drift ratio is shown in Figure 6.82.

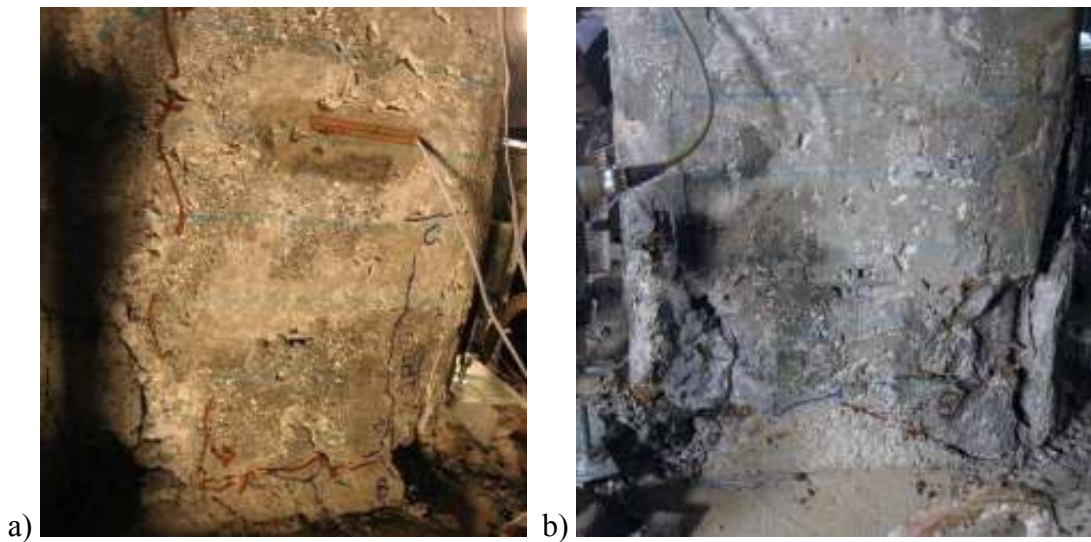


Figure 6.82 : a) North, and b) South view of the specimen NS-X13 after -3.50% drift ratio.

During loading to target displacement of -48.0 mm (drift ratio -%4.00) propagation of existing crack (A'-north) was observed. The view of the specimen NS-X13 after -6.00% drift ratio is shown in Figure 6.83.

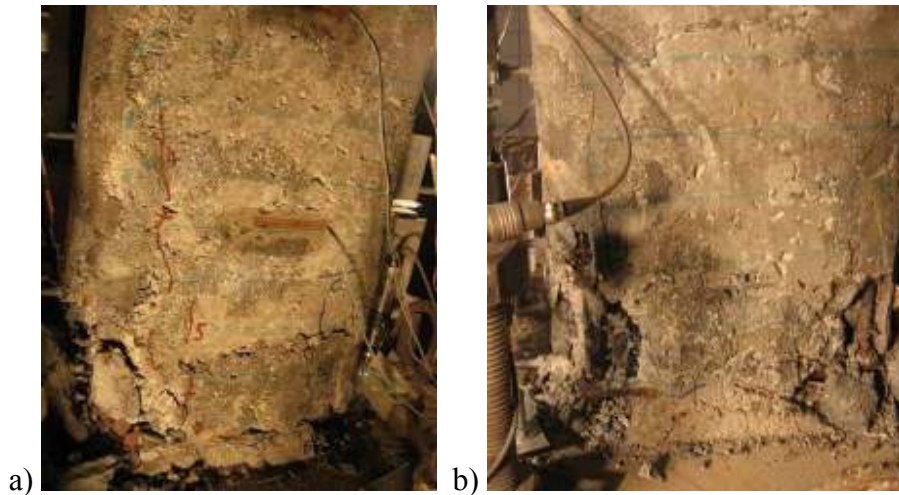


Figure 6.83 : a) North, and b) South view of the specimen NS-X13 after -6.00% drift ratio.

During loading to target displacement of 84.0 mm (drift ratio %7.00) specimen underwent excessive lateral displacement out of its axis and test was ended by decreasing the axial load. Summary of the seismic behavior of the specimen NS-X13 is shown in Table 6.16. Crack propagation of NS-X13 while pushing and pulling cycles is given in Appendix C.

Table 6.16 : Summary of the seismic behavior of NS-X13.

Drift ratio (%)	δ (mm/mm)	P (kN)	Observations
0.10	± 1.2	11.21 / -17.71	No crack was observed.
%0.25	± 3.0	25.09 / -30.63	No crack was observed.
0.50	± 6.0	36.42/ -39.32	First flexural crack at column-footing interface was observed.
0.75	± 9.0	41.85/ -41.95	Propagation of existing cracks and vertical cracks were observed.
1.0	± 12.0	42.39 / -41.53	Propagation of existing cracks, flexural crack and vertical cracks were observed.
1.5	± 18.0	40.32 / -39.69	Propagation of existing cracks and vertical cracks were observed. Crushing of concrete was observed.
2.00	± 24.0	37.10 / -37.36	Propagation of existing cracks, flexural crack and vertical cracks were observed. Spalling of concrete was observed.
2.50	± 30.0	33.03 / -35.60	Propagation of existing cracks, flexural crack and vertical crack were observed.
3.0	± 36.0	30.64 / -34.37	Propagation of existing cracks were observed.
3.50	± 42.0	28.38/ -32.46	
4.0	± 48.0	26.48 / -31.60	Propagation of existing cracks were observed.
4.5	± 54.0	24.67/-30.04	
5.0	± 60.0	23.18 / -28.90	
6.0	± 72.0	20.40/ -26.98	Specimen underwent excessive lateral displacement out of its axis and test was ended by decreasing the axial load.

Force-displacement relationship of NS-X13 is presented in Figure 6.84. In this figure, P is applied lateral load and P_0 is the theoretical lateral load capacity of the specimen determined without considering the effect of corrosion. First flexural crack, first vertical crack, yielding of starter bar, crushing of concrete cover, spalling of concrete cover, fracture of starter bar, maximum strain on the starter bar and maximum strain on the longitudinal bar are marked on the figure. As seen from Figure 6.84, strength loss was observed. Average experimental moment-curvature relationships obtained for critical sections of NS-X13 are presented in Figure 6.85. For the calculation of moment-curvature relationships, the average curvature values which were obtained for the ranges of 0-20 mm, 20-150 mm and 150-300 mm heights above the footing were taken into account. As seen from the figure, the curvature values of the member measured in 20-150 mm and 150-300 mm height above the support are in the order of 5.10^{-5} (1/mm), while the curvatures measured in 0-20 mm height are in the order of 3.10^{-3} (1/mm). According to the figure, it is of interest to note that the damage is accumulated especially in 20 mm height of the member from top of the base according to the moment-curvature relationships.

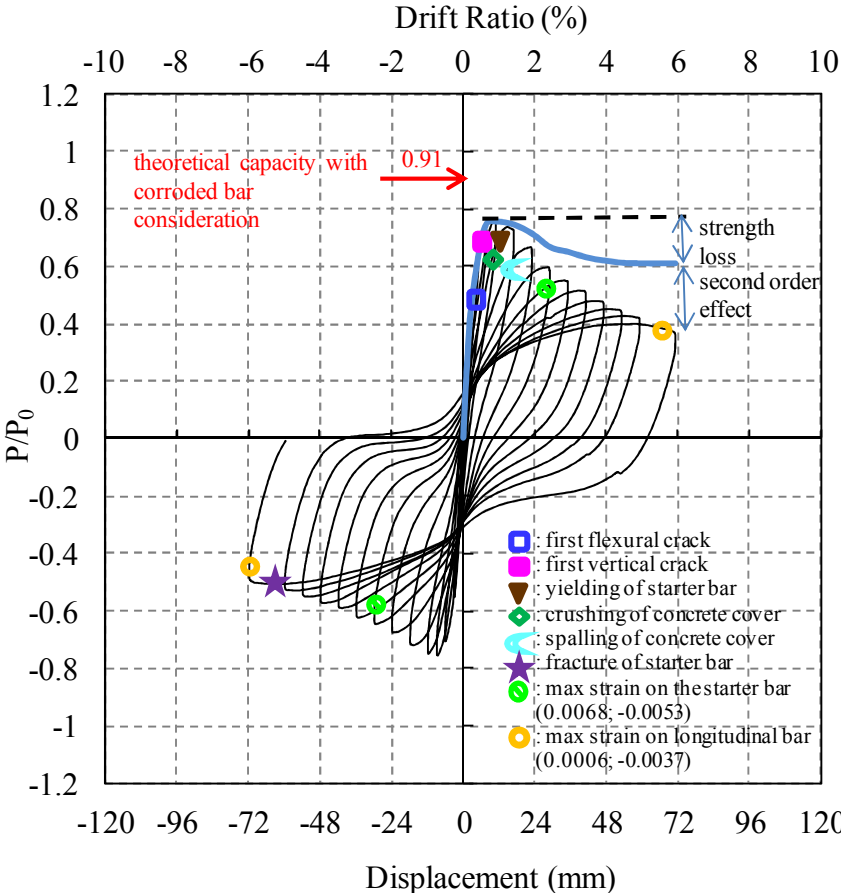


Figure 6.84 : Lateral load/Theoretical load capacity versus displacement for NS-X13.

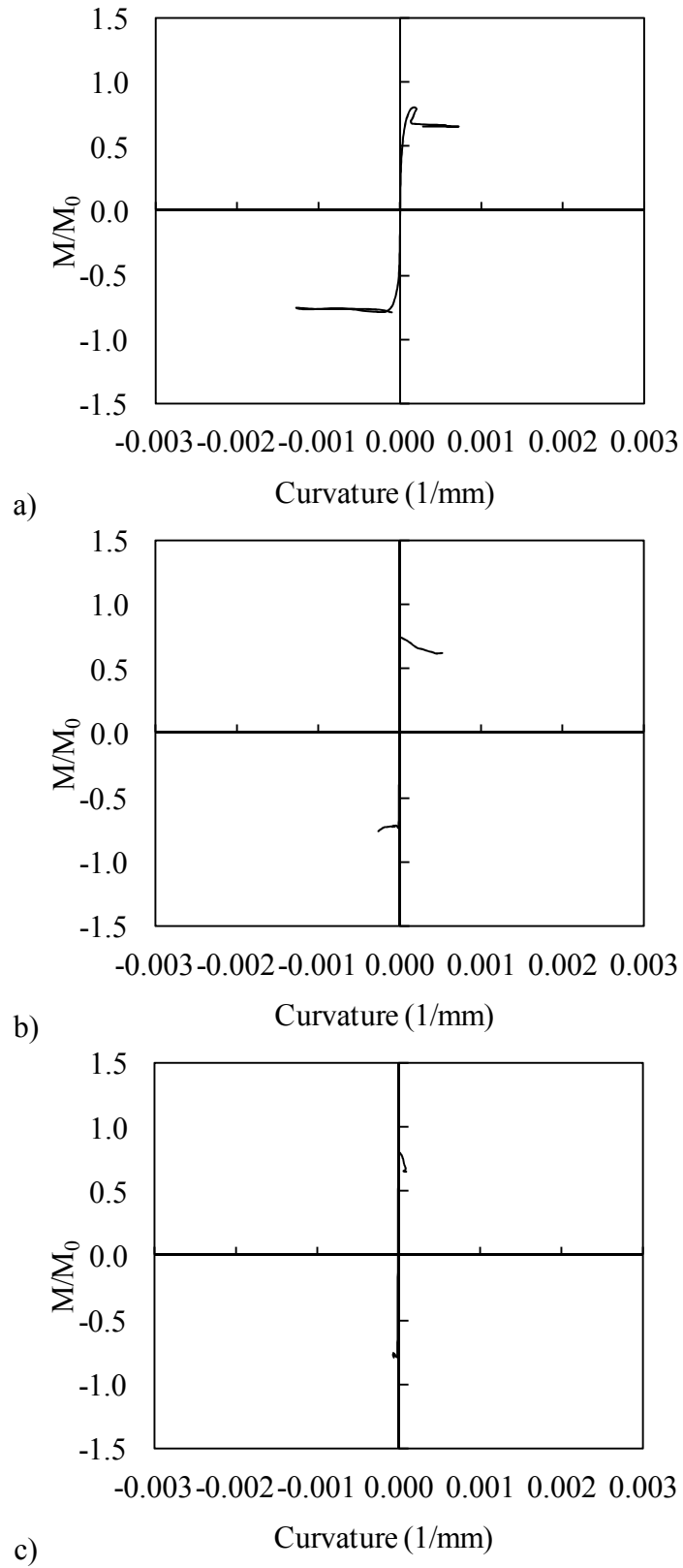


Figure 6.85 : Moment-curvature relationships obtained for a) 0-20 mm, b) 20-150 mm, c) 150-300 mm gauge lengths.

According to the data from the strain gauges on the starter bars of the NS-X13, the maximum strain while pushing was 0.0067, measured from the strain gauge at +100 mm above the footing when P=30.64 kN at 0.03 drift ratio; the maximum strain while pulling was -0.0053, measured from the strain gauge at +100 mm above the footing when P=-32.46 kN at -0.035 drift ratio. According to the data from the strain gauges on the longitudinal bars of the NS-X13, the maximum strain while pushing was 0.0006, measured from the strain gauge at +400 mm above the footing when P=20.40 kN at 0.06 drift ratio; the maximum strain while pulling was -0.0037, measured from the strain gauge at +100 mm above the footing when P=-26.98 kN at -0.06 drift ratio. Strain distribution of the starter bars and longitudinal bars of NS-X13 while pushing and pulling are shown in Figure 6.86 and Figure 6.87, respectively. As seen from the figures, the strain values of starter bars reach yield strain and lower than NS-X0.

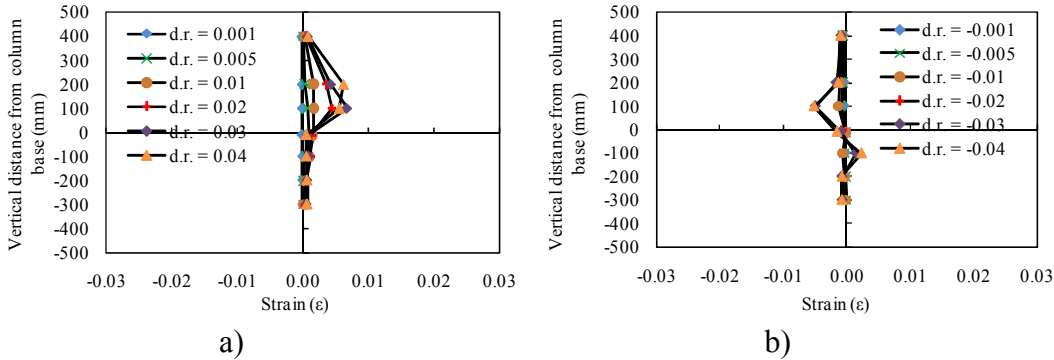


Figure 6.86 : Strain distribution of the starter bars of NS-X13 a) while pushing, b) while pulling.

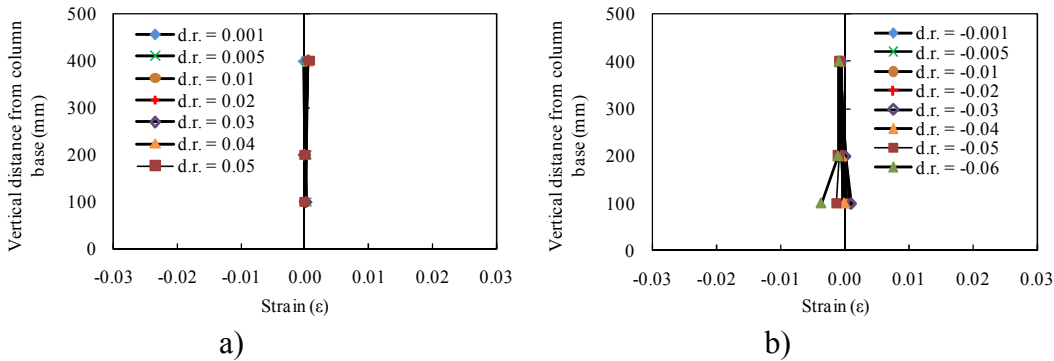


Figure 6.87 : Strain distribution of the longitudinal bars of NS-X13 a) while pushing b) while pulling.

6.3.4 NS-X16

Unlike the specimen NS-X13, specimen NS-X16 has vertical cracks along the longitudinal reinforcement and horizontal cracks along the transverse reinforcement. Width, location and orientation of the cracks are presented in Table 6.17. Pattern of cracks formed due to corrosion are shown in Figure 6.88.

Table 6.17 : Width, location and orientation of the cracks.

Crack width	Crack location	Crack orientation
0.9 mm	above the footing	along the No.1 longitudinal reinforcement
1.0 mm	above the footing	along the No.2 longitudinal reinforcement
1.2 mm	above the footing	along the No.3 longitudinal reinforcement
1.4 mm	above the footing	along the No.4 longitudinal reinforcement

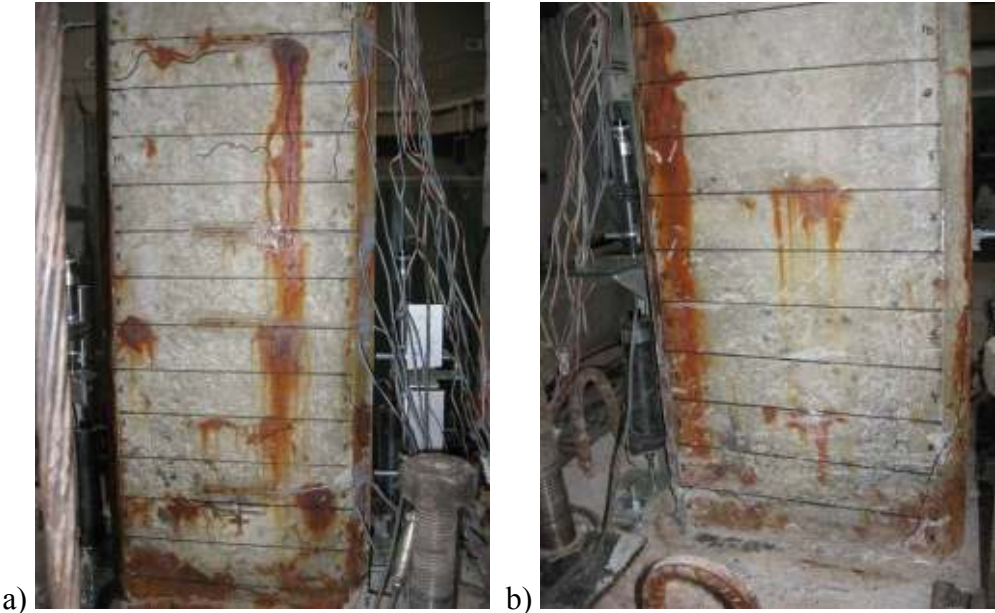


Figure 6.88 : Pattern of cracks formed due to corrosion: (a) North, (b) South.

No cracks were observed while loading to target displacement of ± 1.2 mm.

First flexural crack (A-south) was observed during loading to target displacement of 3.0 mm (drift ratio 0.25%). The view of the specimen NS-X16 after -0.25% drift ratio is shown in Figure 6.89.

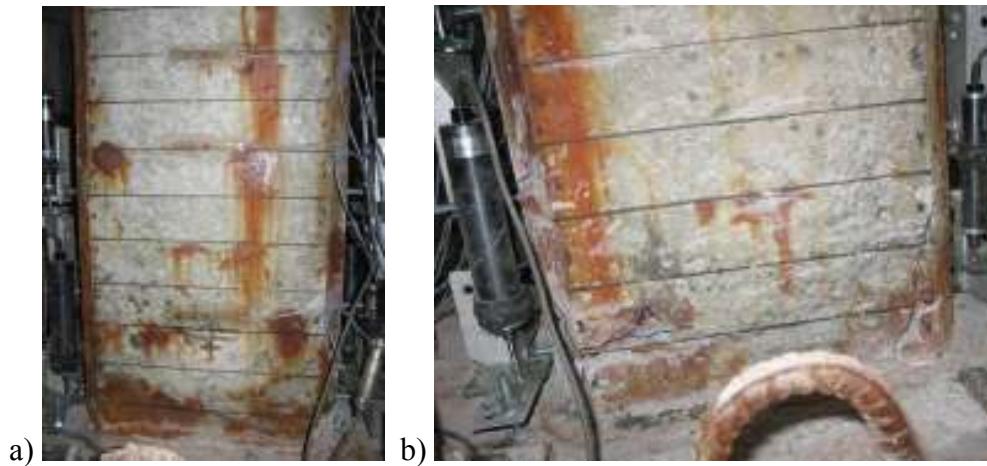


Figure 6.89 : a) North, and b) South view of the specimen NS-X16 after -0.25% drift ratio.

During loading to target displacement of 6.0 mm (drift ratio 0.50%) flexural crack (A-north) was observed. During loading to target displacement of -6.0 mm (drift ratio -0.50%) flexural cracks (A'-north, B'-north, A'-south, B'-south) were observed.

During loading to target displacement of 9.0 mm (drift ratio 0.75%) flexural crack (B-north, B-south) at the interface of the column and footing was observed. During loading to target displacement of -9.0 mm (drift ratio -0.75%) flexural cracks (C'-north, C'-south) at the interface of the column and footing and (D'-north) and vertical crack (D'-south) were observed.

During loading to target displacement of 12.0 mm (drift ratio 1.00%) vertical crack (C-south) and propagation of existing crack (B-north) were observed. During loading to target displacement of -12.0 mm (drift ratio -1.00%) propagation of existing crack (A'-north) was observed.

During loading to target displacement of 18.0 mm (drift ratio 1.50%) vertical cracks (C-north, D-south) and propagation of existing cracks (B-south) were observed. During loading to target displacement of -18.0 mm (drift ratio -1.50%) vertical crack (F'-south), flexural crack (E'-south) and propagation of existing cracks (A'-north) were observed. The view of the specimen NS-X16 after -1.50 % drift ratio is shown in Figure 6.90.

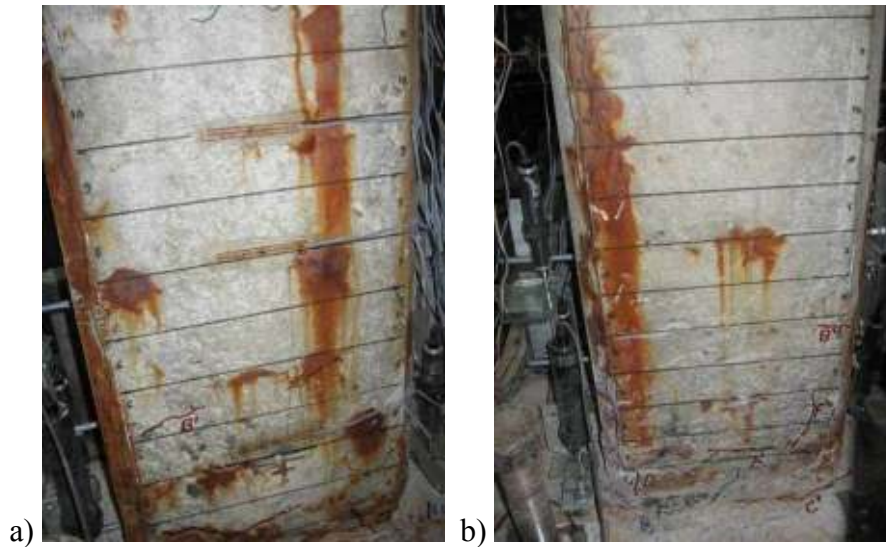


Figure 6.90 : a) North, and b) South view of the NS-X16 specimen after -1.50% drift ratio.

During loading to target displacement of -24.0 mm (drift ratio -2.00%) propagation of existing cracks (A'-south, F'-south) were observed.

During loading to target displacements of 30.0 mm (drift ratio 2.50%) and -30.0 mm (drift ratio -2.50%) propagation of existing cracks (D-south) and (A'-north) were observed, respectively. The view of the specimen NS-X16 after -2.50% drift ratio is shown in Figure 6.91. The view of the specimen NS-X16 after -5.00% drift ratio is shown in Figure 6.93.

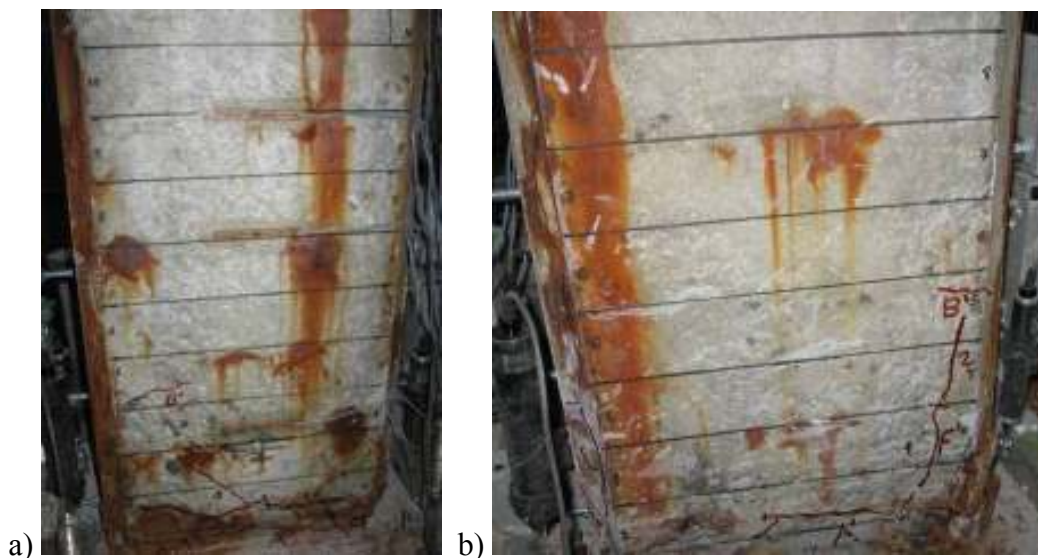


Figure 6.91 : a) North, and b) South view of the specimen NS-X16 after -2.50% drift ratio.

During loading to target displacement of 36.0 mm (drift ratio 3.00%) propagation of existing crack (D-south) was observed. The view of the specimen NS-X16 after -3.50% drift ratio is shown in Figure 6.92.

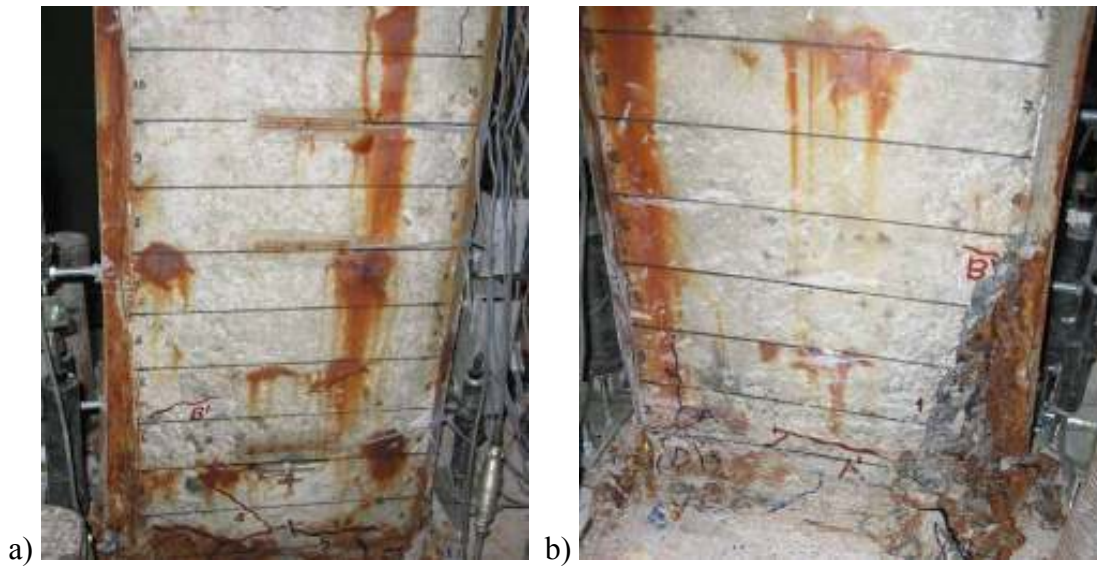


Figure 6.92 : a) North, and b) South view of the specimen NS-X16 after -3.50% drift ratio.

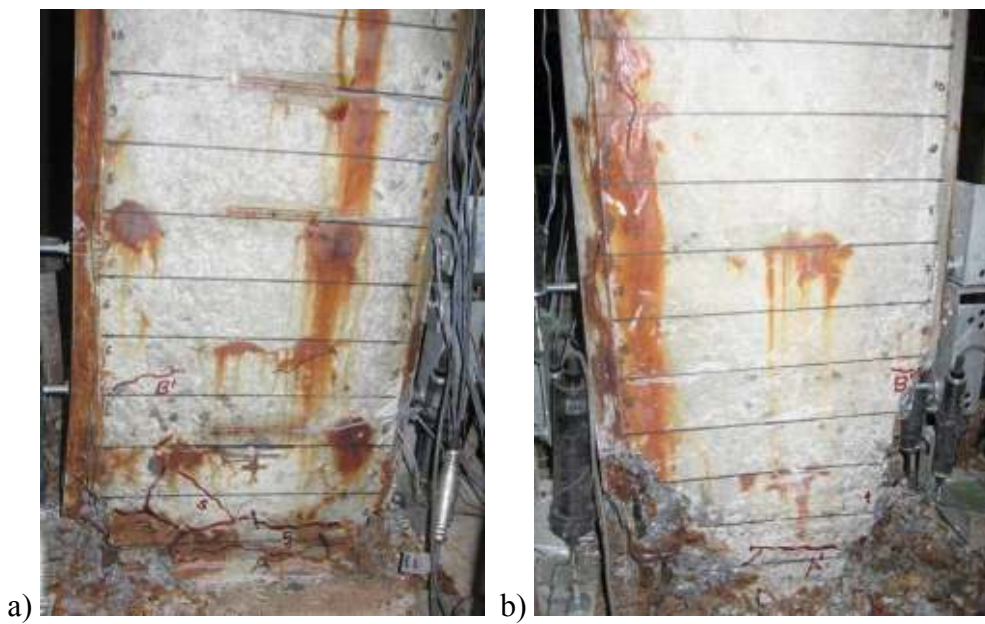


Figure 6.93 : a) North, and b) South view of the NS-X16 specimen after -5.00% drift ratio.

During loading to target displacement of 72.0 mm (drift ratio 6.00%) specimen underwent excessive lateral displacement out of its axis and test was ended by decreasing the axial load. Summary of the seismic behavior of specimen NS-X16 is shown in Table 6.18. Crack propagation of NS-X16 while pushing and pulling cycles is given in Appendix C.

Table 6.18 : Summary of the seismic behavior of NS-X16.

Drift ratio (%)	δ (mm/mm)	P (kN)	Observations
0.10	± 1.2	9.91 / -14.45	No crack was observed.
0.25	± 3.0	23.47 / -30.10	First flexural crack was observed.
0.50	± 6.0	37.68 / -37.95	Flexural cracks were observed.
0.75	± 9.0	42.95 / -41.27	Flexural crack at the interface of the column and footing, and vertical cracks were observed.
1.0	± 12.0	44.91 / -42.16	Propagation of existing cracks and vertical crack were observed.
1.5	± 18.0	46.08 / -43.56	Flexural crack, vertical cracks and propagation of existing cracks were observed. Spalling of concrete cover was observed.
2.00	± 24.0	45.04 / -42.42	Propagation of existing cracks were observed.
2.50	± 30.0	39.87 / -41.48	Propagation of existing cracks were observed.
3.0	± 36.0	40.05 / -40.03	Propagation of existing cracks were observed.
3.50	± 42.0	34.52 / -37.94	
4.0	± 48.0	35.84 / -35.53	
4.5	± 54.0	33.42 / -33.44	
5.0	± 60.0	5.28 / -16.54	Specimen underwent excessive lateral displacement out of its axis and test was ended by decreasing the axial load.

Force-displacement relationship of NS-X16 is presented in Figure 6.94. In this figure, P is applied lateral load and P_0 is the theoretical lateral load capacity of the specimen determined without considering the effect of corrosion. First flexural crack, first vertical crack, yielding of starter bar, crushing of concrete cover, spalling of concrete cover, fracture of starter bar, maximum strain on the starter bar and maximum strain on the longitudinal bar are marked on the figure. As seen from the figure, strength loss was observed.

Average experimental moment-curvature relationships obtained for critical sections of NS-X16 are presented in Figure 6.95. For the calculation of moment-curvature relationships, the average curvature values, which were obtained for the ranges of 0-20 mm, 20-150 mm and 150-300 mm heights above the footing, were taken into account. As seen from the figure, the curvature values of the member measured in 20-150 mm and 150-300 mm height above the support are in the order of $5 \cdot 10^{-5}$ (1/mm), while the curvatures measured in 0-20 mm height are in the order of $3 \cdot 10^{-3}$ (1/mm). According to the figure, it is of interest to note that the damage is accumulated especially in 20 mm height of the member from top of the base according to the moment-curvature relationships.

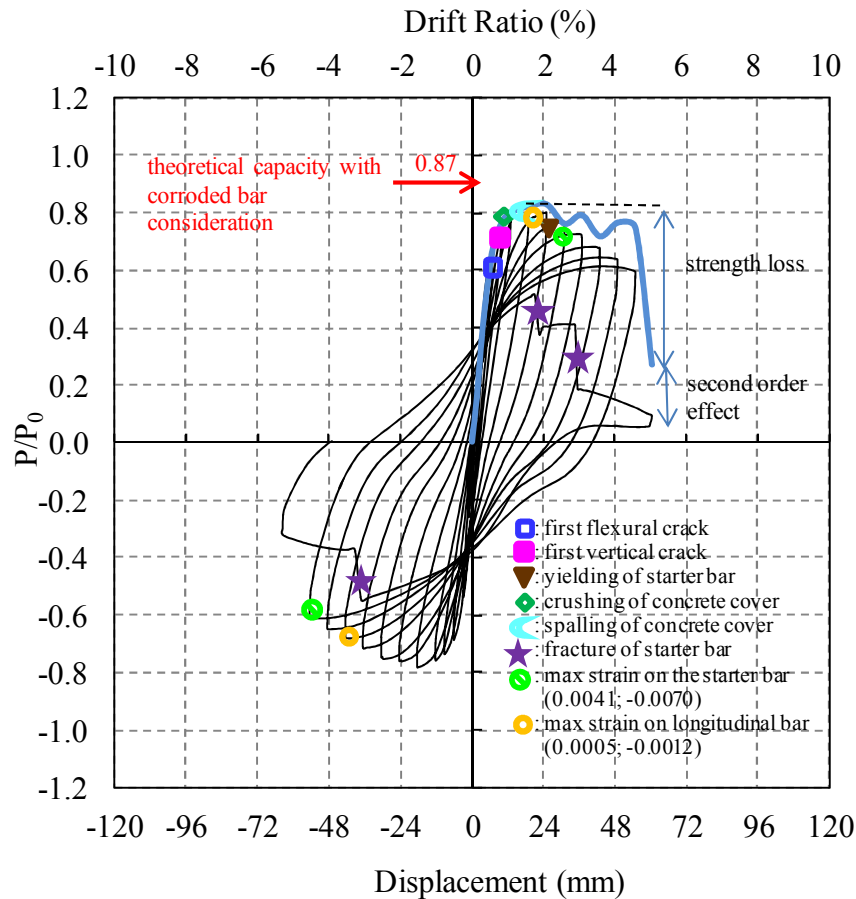


Figure 6.94 : Lateral load/Theoretical load capacity versus displacement for NS-X16.

According to the data from the strain gauges on the starter bars of the, the maximum strain while pushing was 0.0041, measured from the strain gauge at +100 mm above the footing when $P=40.05$ kN at 0.03 drift ratio; the maximum strain while pulling was -0.0070, measured from the strain gauge at +100 mm above the footing when $P=-33.44$ kN at -0.045 drift ratio. According to the data from the strain gauges on the longitudinal bars of the NS-X16, the maximum strain while pushing was 0.0005, measured from the strain gauge at +200 mm above the footing when $P=45.04$ kN at 0.02 drift ratio; the maximum strain while pulling was -0.0012, measured from the strain gauge at +200 mm above the footing when $P=-40.03$ kN at -0.03 drift ratio. Strain distribution of the starter bars and longitudinal bars of NS-X16 while pushing and pulling are shown in Figure 6.96 and Figure 6.97, respectively. As seen from Figure 6.96 and Figure 6.97, the strain values of starter bars reach yield strain and are lower than NS-X0.

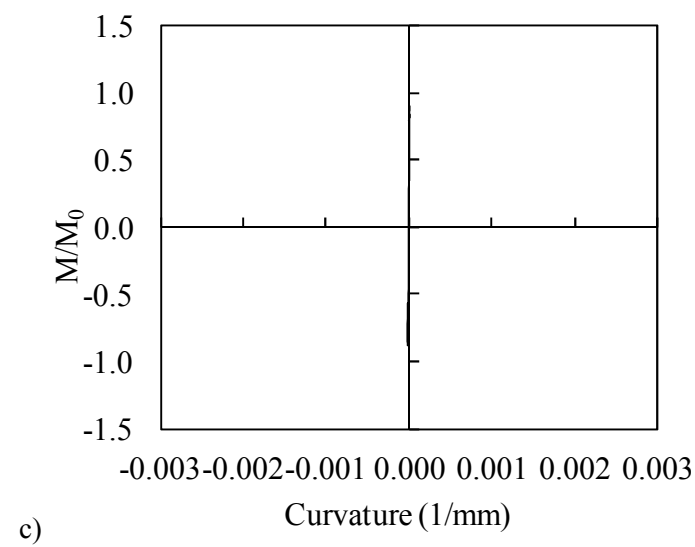
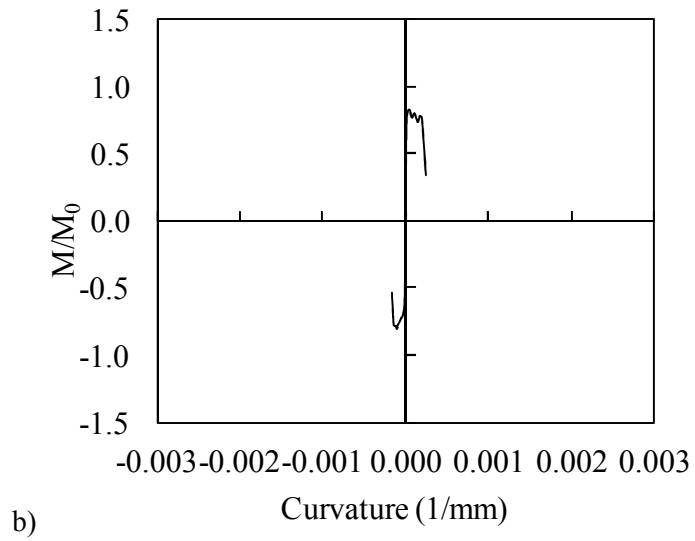
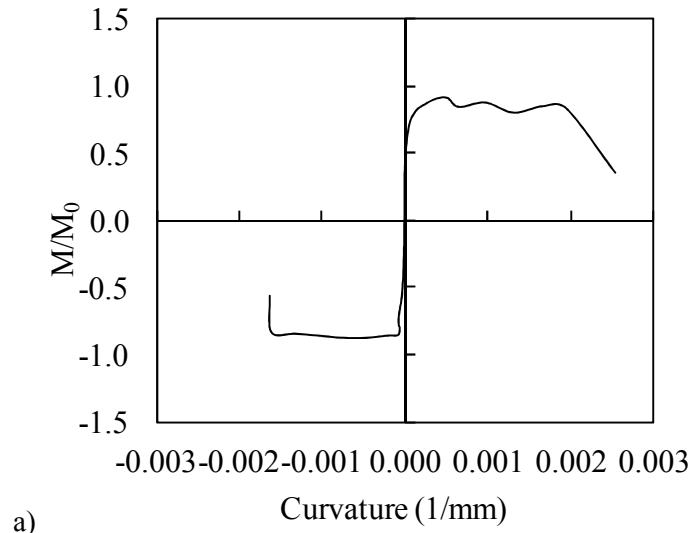


Figure 6.95 : Moment-curvature relationships obtained for a) 20 mm, b) 150 mm, c) 300 mm gauge lengths.

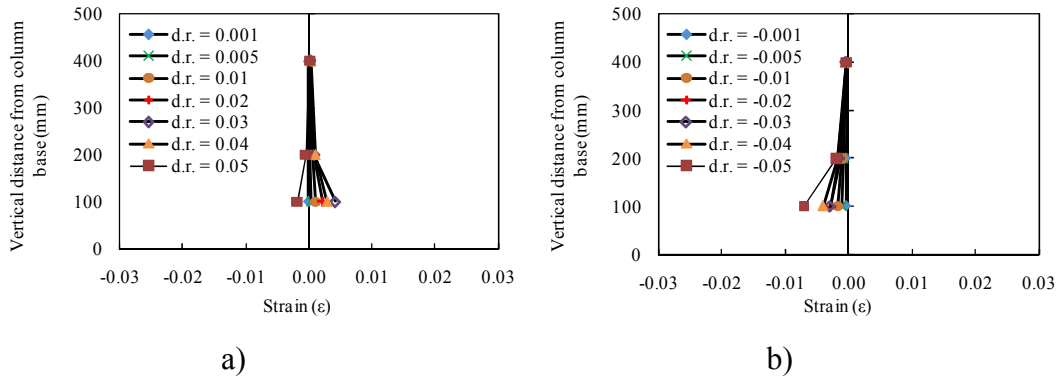


Figure 6.96 : Strain distribution of the starter bars of NS-X16 a) while pushing, b) while pulling.

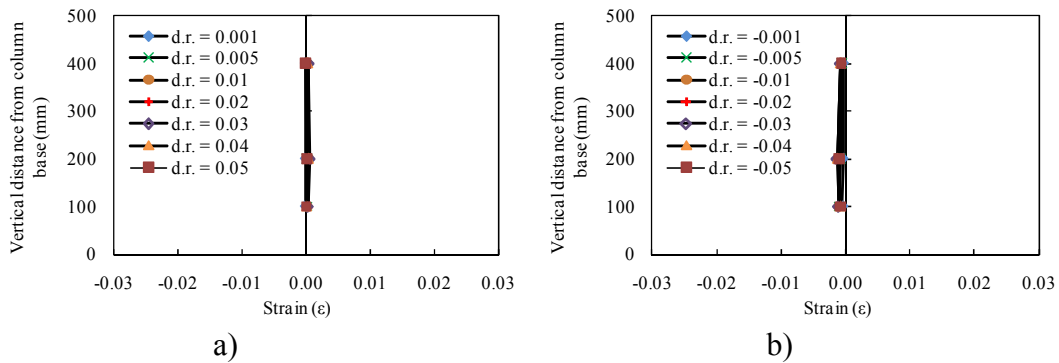


Figure 6.97 : Strain distribution of the longitudinal bars of NS-X16 a) while pushing b) while pulling.

6.3.5 NS-X22

Similar to the specimen NS-X16, specimen NS-X22 has vertical cracks along the longitudinal reinforcement and horizontal cracks along the transverse reinforcement. Width, location and orientation of the cracks are presented in Table 6.19.

Table 6.19 : Width, location and orientation of the cracks.

Crack width	Crack location	Crack orientation
0.1 mm	above the footing	along the No.1 longitudinal reinforcement
0.6 mm	above the footing	along the No.2 longitudinal reinforcement
0.4 mm	above the footing	along the No.3 longitudinal reinforcement
0.3 mm	above the footing	along the No.4 longitudinal reinforcement

Pattern of cracks formed due to corrosion are shown in Figure 6.98.

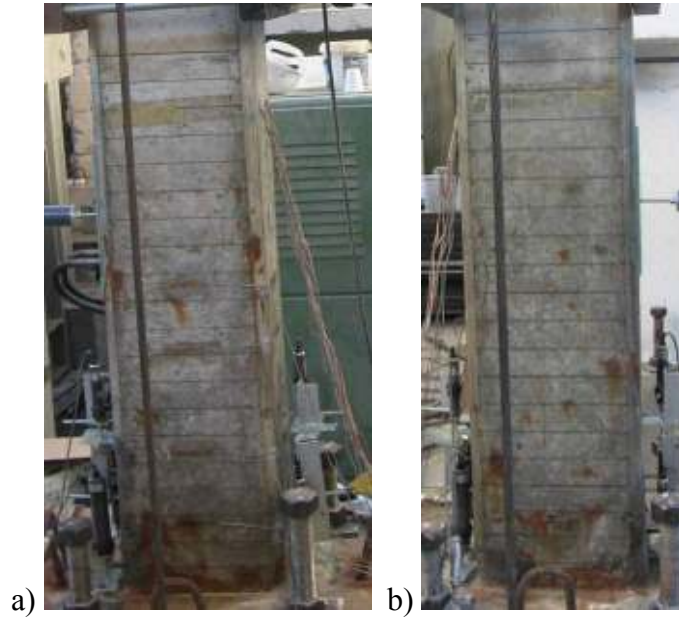


Figure 6.98 : Pattern of cracks formed due to corrosion: (a) North, (b) South.

No cracks were observed while loading to target displacements of ± 1.2 mm (drift ratio 0.10%), ± 3 mm (drift ratio 0.25%), ± 6 mm (drift ratio 0.50%) and $+9$ mm (drift ratio 0.75%).

First flexural cracks (A'-north, A'-south) at the interface of the column and footing and (B'-south) and vertical crack (B'-north) were observed during loading to target displacement of 9.0 mm (drift ratio 0.75%). The view of the specimen NS-X22 after -0.75% drift ratio is shown in Figure 6.99.

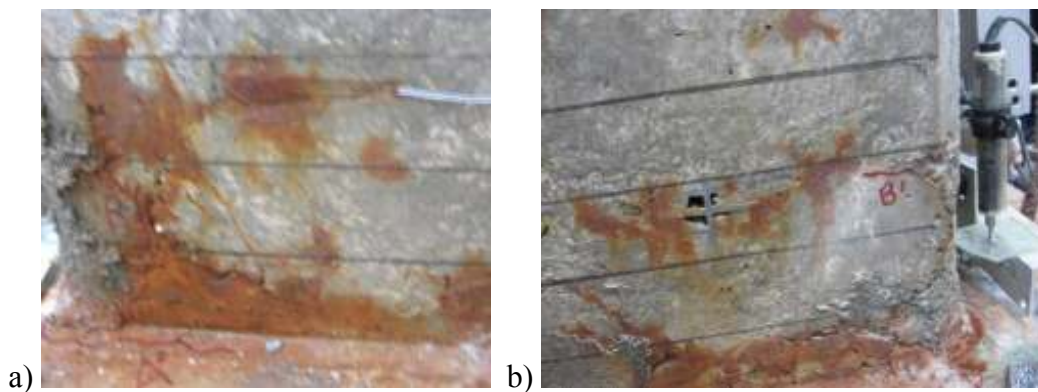


Figure 6.99 : a) North, and b) South view of the NS-X22 specimen after -0.75% drift ratio.

During loading to target displacement of 12.0 mm (drift ratio 1.00%) flexural cracks (A-north, A-south) at the interface of the column and foundation and flexural cracks (B-north, C-north, B-south, C-south, D-south, E-south) were observed. During loading to target displacement of -12.0 mm (drift ratio -1.00%) vertical cracks (C'-north, C'-south) were observed.

During loading to target displacement of 18.0 mm (drift ratio 1.50%) propagation of existing

cracks (A-north, B-north, A-south) were observed. During loading to target displacement of -18.0 mm (drift ratio -1.50%) flexural cracks (D'-south, E'-south) and propagation of existing crack (A'-north) were observed. The view of the specimen NS-X22 after -1.50% drift ratio is shown in Figure 6.100.

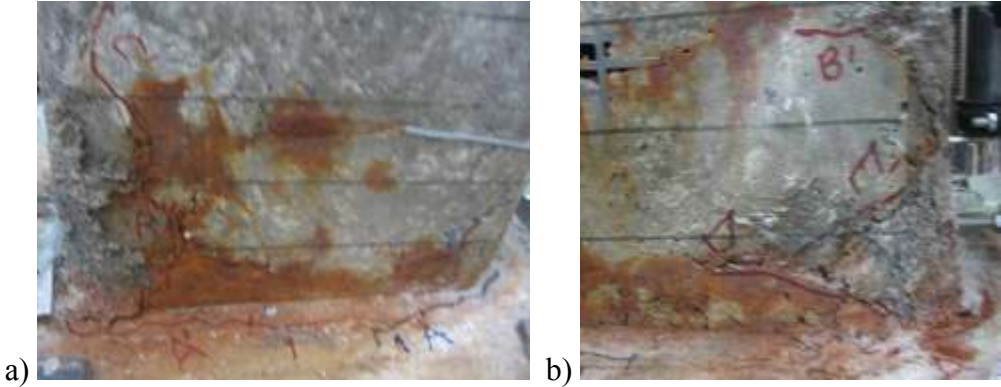


Figure 6.100 : a) North, and b) South view of the NS-X22 specimen after -1.50% drift ratio.

During loading to target displacement of 24.0 mm (drift ratio 2.00%) flexural crack (D-north) was observed. During loading to target displacement of -24.0 mm (drift ratio -2.00%) flexural crack (F'-south) and vertical crack (F'-north) were observed.

During loading to target displacement of 30.0 mm (drift ratio 2.50%) flexural cracks (E-north, F-south) were observed. The views of the NS-X22 specimen after -2.50% and -3.50% drift ratio are shown in Figure 6.101 and Figure 6.102, respectively.

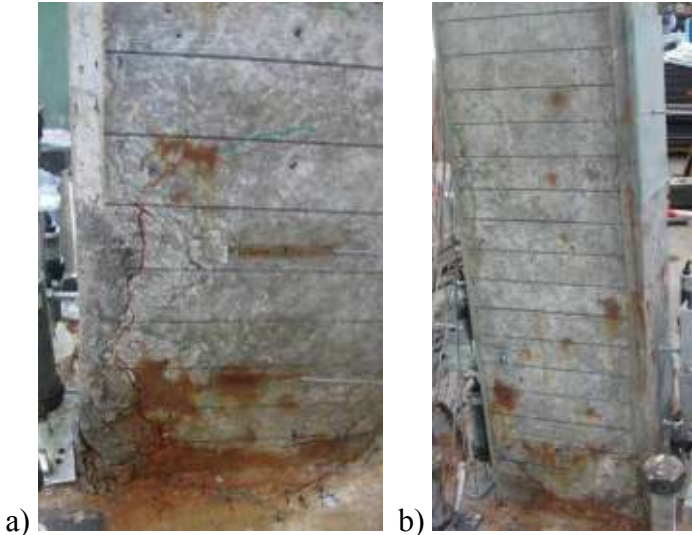


Figure 6.101 : a) North, and b) South view of the NS-X22 specimen after -2.50% drift ratio.

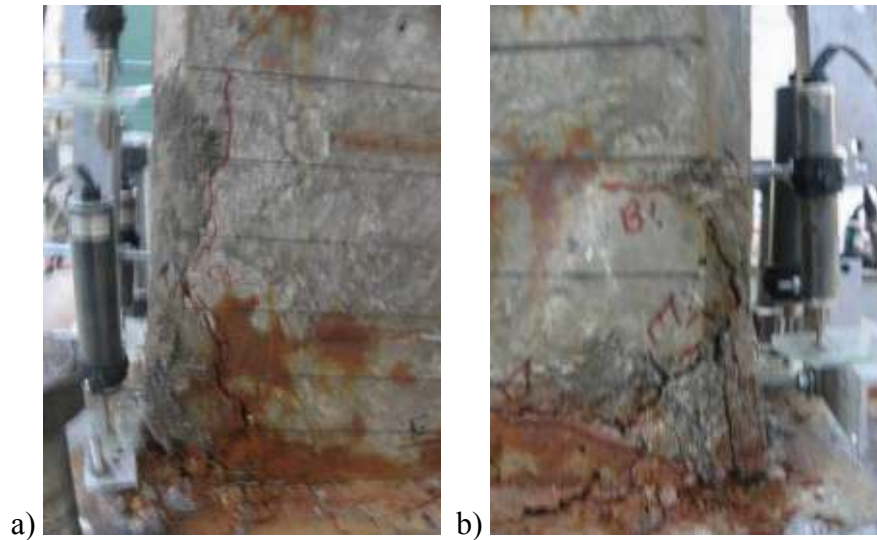


Figure 6.102 : a) North, and b) South view of the NS-X22 specimen after -3.50% drift ratio.

During loading to target displacement of 48.0 mm (drift ratio 4.00%) flexural cracks (G-south, H-south) were observed. The view of the specimen NS-X22 after -6.00% drift ratio is shown in Figure 6.103.

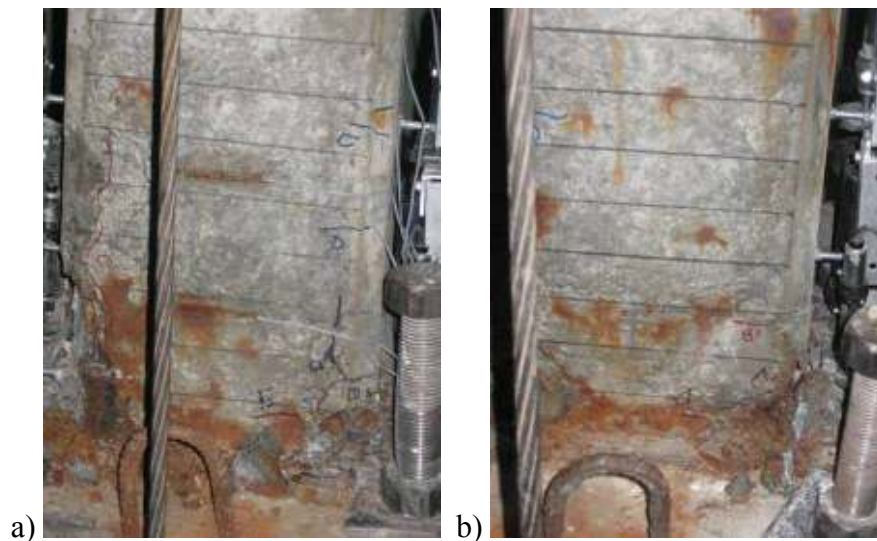


Figure 6.103 : a) North, and b) South view of the specimen NS-X22 after -6.00% drift ratio.

During loading to target displacement of 84.0 mm (drift ratio 7.00%) specimen underwent excessive lateral displacement out of its axis and test was ended by decreasing the axial load. Summary of the seismic behavior of specimen NS-X22 is shown in Table 6.20.

Table 6.20 : Summary of the seismic behavior of NS-X22

Drift ratio (%)	δ (mm/mm)	P (kN)	Observations
0.10	± 1.2	11.57 / -15.33	No crack was observed.
0.25	± 3.0	24.61 / -28.05	No crack was observed.
0.50	± 6.0	37.43 / -39.43	First flexural crack at column-footing interface was observed.
0.75	± 9.0	43.41 / -42.90	Flexural and vertical cracks were observed.
1.0	± 12.0	44.93 / -44.19	Propagation of cracks were observed at the interface of the column and footing. Flexural and vertical cracks were observed.
1.5	± 18.0	46.01 / -46.21	Propagation of existing cracks and flexural cracks were observed.
2.00	± 24.0	45.69 / -46.87	Flexural and vertical cracks were observed.
2.50	± 30.0	44.48 / -45.84	Flexural cracks were observed. Crushing of concrete cover was observed.
3.0	± 36.0	42.94 / -43.70	
3.50	± 42.0	41.23 / -42.42	
4.0	± 48.0	39.64 / -40.77	Vertical cracks were observed.
4.5	± 54.0	24.59 / -38.73	Spalling of concrete cover was observed.
5.0	± 60.0	22.85 / -33.91	
6.0	± 72.0	4.45 / -17.07	Specimen underwent excessive lateral displacement out of its axis and test was ended by decreasing the axial load.

Crack propagation of NS-X22 while pushing and pulling cycles are given in Appendix C.

Force-displacement relationship of NS-X22 is presented in Figure 6.104. In this figure, P is applied lateral load and P_0 is the theoretical lateral load capacity of the specimen determined without considering the effect of corrosion. First flexural crack, first vertical crack, yielding of starter bar, yielding of transverse bar, crushing of concrete cover, spalling of concrete cover, fracture of starter bar, maximum strain on the starter bar and maximum strain on the longitudinal bar are marked on the figure. As seen from Figure 6.104, strength loss was observed.

Average experimental moment-curvature relationships which were obtained for critical sections of NS-X22 are presented in Figure 6.105. For the calculation of moment-curvature relationships, the average curvature values which were obtained for the ranges of 0-20 mm, 20-150 mm and 150-300 mm heights above the footing were taken into account. As seen from Figure 6.105, the curvature values of the member measured in 20-150 mm and 150-300 mm height above the support are in the order of 5.10^{-5} (1/mm), while the curvatures measured in 0-20 mm height are in the order of 3.10^{-3} (1/mm). According to Figure 6.105, it is of interest to note that the damage is accumulated especially in 20 mm height of the member from top of the base according to the moment-curvature relationships.

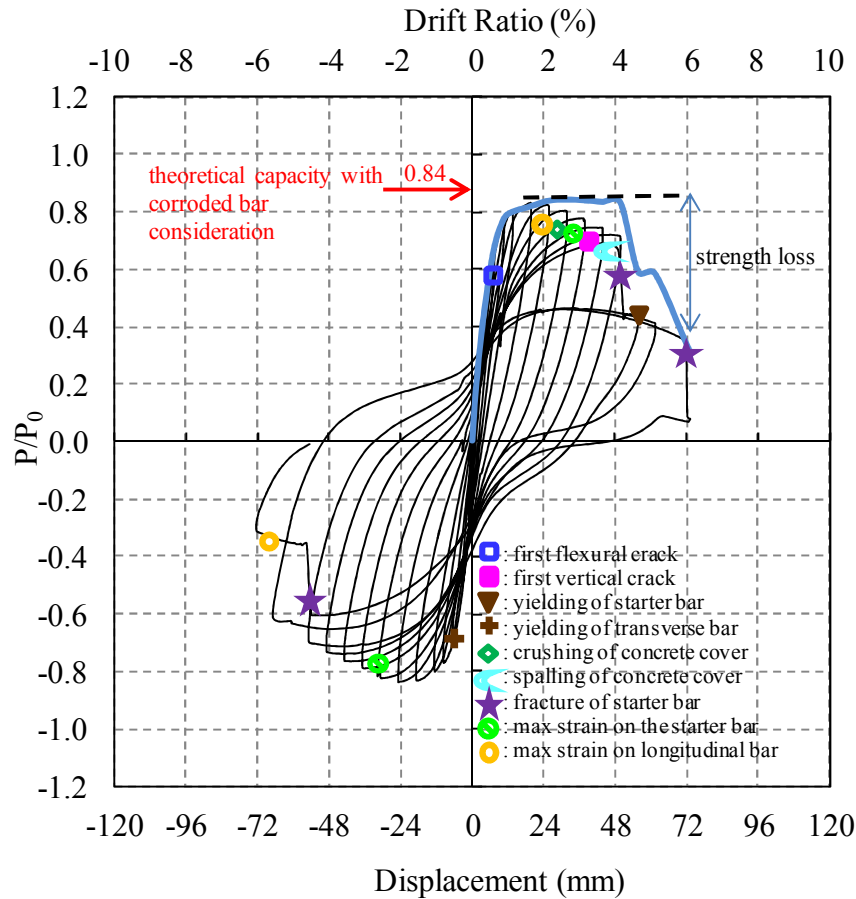


Figure 6.104 : Lateral load/Theoretical load capacity versus displacement for NS-X22.

According to the data from the strain gauges on the starter bars of the, the maximum strain while pushing was 0.00406, measured from the strain gauge at +100 mm above the footing when $P=41.23$ kN at 0.035 drift ratio; the maximum strain while pulling was -0.0018, measured from the strain gauge at +100 mm above the footing when $P=-43.70$ kN at -0.03 drift ratio. According to the data from the strain gauges on the longitudinal bars of the NS-X22, the maximum strain while pushing was 0.00054, measured from the strain gauge at +400 mm above the footing when $P=44.48$ kN at 0.025 drift ratio; the maximum strain while pulling was -0.0004, measured from the strain gauge at +200 mm above the footing when $P=-17.07$ kN at -0.06 drift ratio. Strain distribution of the starter bars and longitudinal bars of NS-X22 while pushing and pulling are shown in Figure 6.106 and Figure 6.107, respectively. As seen from Figure 6.106 and Figure 6.107, the strain values of starter bars reach yield strain and are lower than NS-X0.

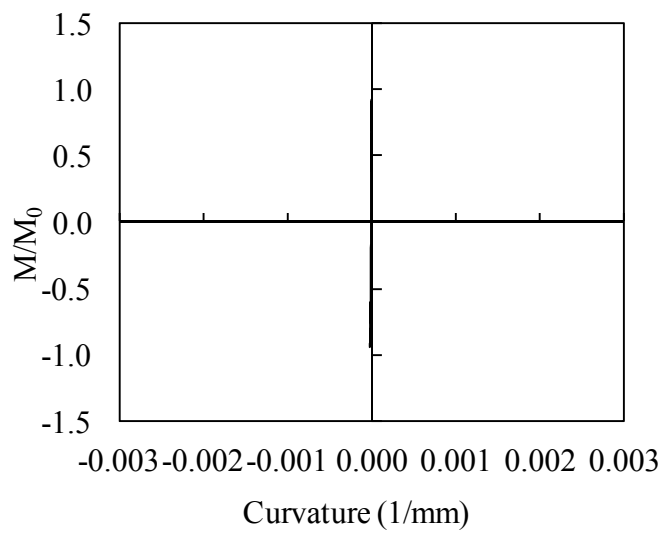
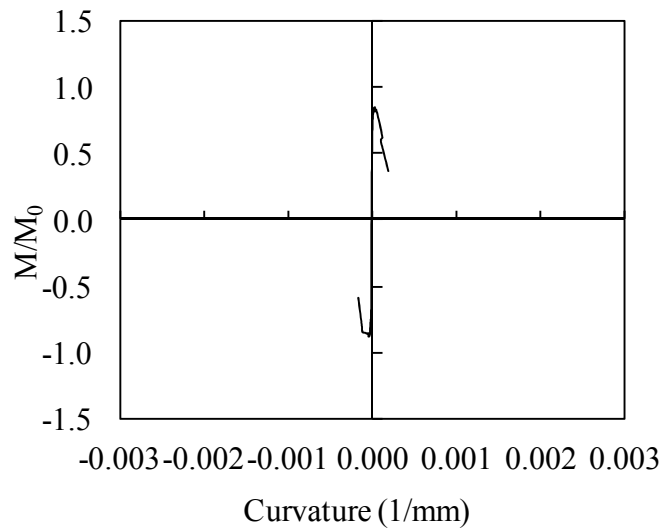
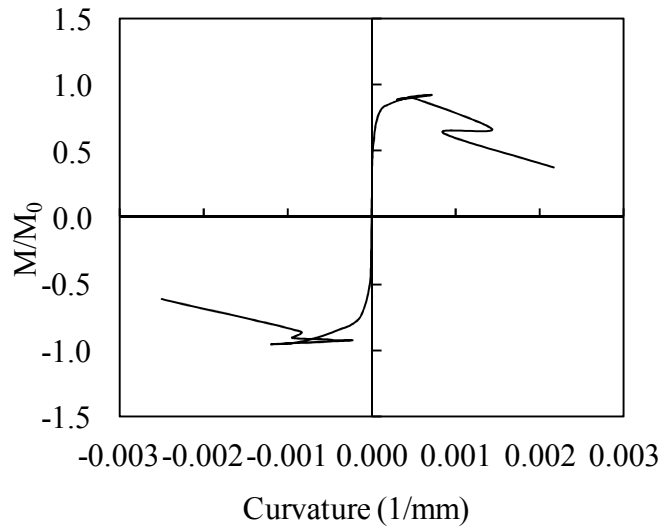


Figure 6.105 : Moment-curvature relationships obtained for a) 0-20 mm, b) 20-150 mm, c) 150-300 mm gauge lengths.

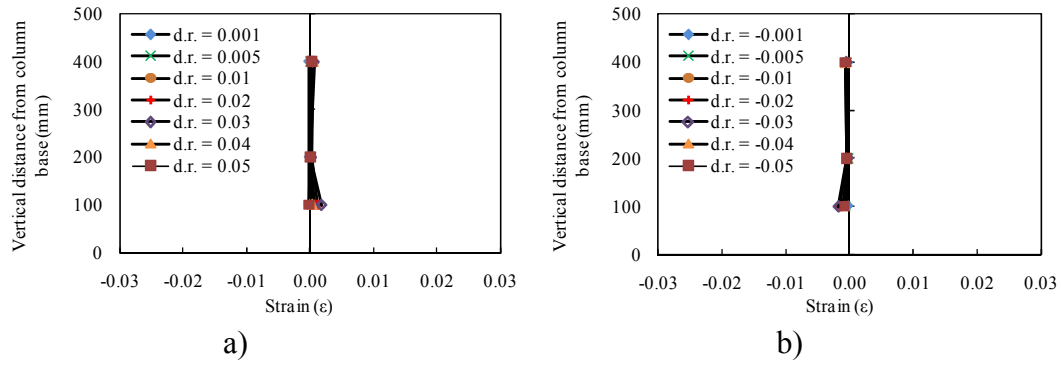


Figure 6.106 : Strain distribution of the starter bars of NS-X22 a) while pushing, b) while pulling.

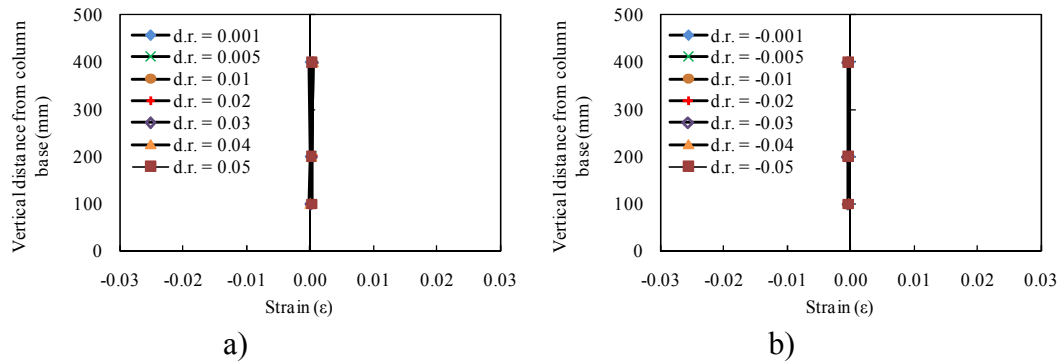


Figure 6.107 : Strain distribution of the longitudinal bars of NS-X22 a) while pushing b) while pulling.

6.3.6 NS-X54

Similar to the specimen NS-X22 and NS-X16, specimen NS-X54 has vertical cracks along the longitudinal reinforcement and horizontal cracks along the transverse reinforcement. Width, location and orientation of the cracks are presented in Table 6.21. Pattern of cracks formed due to corrosion are shown in Figure 6.108.

Table 6.21 : Width, location and orientation of the cracks.

Crack width	Crack location	Crack orientation
2.7 mm	above the footing	along the No.1 longitudinal reinforcement
2.1 mm	above the footing	along the No.2 longitudinal reinforcement
1.4 mm	above the footing	along the No.3 longitudinal reinforcement
2.4 mm	above the footing	along the No.4 longitudinal reinforcement

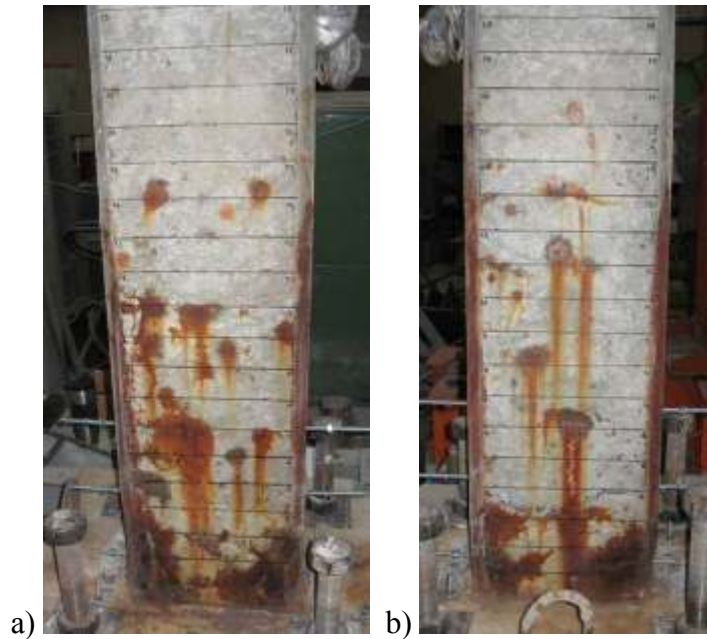


Figure 6.108 : Pattern of cracks formed due to corrosion: (a) North, (b) South.

No cracks were observed while loading to target displacements of ± 1.2 mm (drift ratio 0.10%), ± 3 mm (drift ratio 0.25%) and ± 6 mm (drift ratio 0.50%).

First flexural cracks (A-north, A-south) at the interface of the column and footing were observed during loading to target displacement of 9.0 mm (drift ratio 0.75%).

During loading to target displacement of 12.0 mm (drift ratio 1.00%) flexural cracks (B-north, B-south) were observed. During loading to target displacement of -12.0 mm (drift ratio -1.00%) flexural cracks (A'-north, A'-south) at the interface of the column and footing were observed. Crushing of concrete cover started. The view of the specimen NS-X54 after -1.00% drift ratio is shown in Figure 6.109.

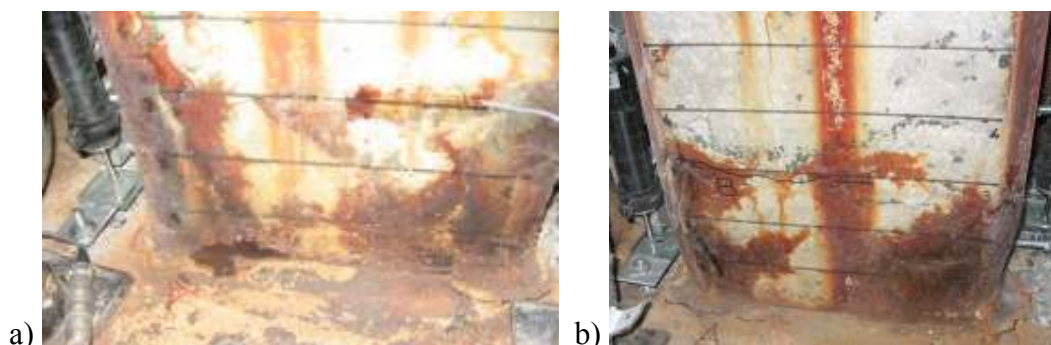


Figure 6.109 : a) North, and b) South view of the specimen NS-X54 after -1.00% drift ratio.

During loading to target displacement of -18.0 mm (drift ratio -1.50%) flexural crack (B'-south) and propagation of existing cracks (A'-north, A'-south) were observed. The view of the

specimen NS-X54 after -1.50 drift ratio is shown in Figure 6.109.

During loading to target displacement of 30.0 mm (drift ratio 2.50%) propagation of existing cracks (A-north, A-south) were observed. During loading to target displacement of -30.0 mm (drift ratio -2.50%) spalling of concrete cover started. The view of the specimen NS-X54 after -2.50 drift ratio is shown in Figure 6.110.

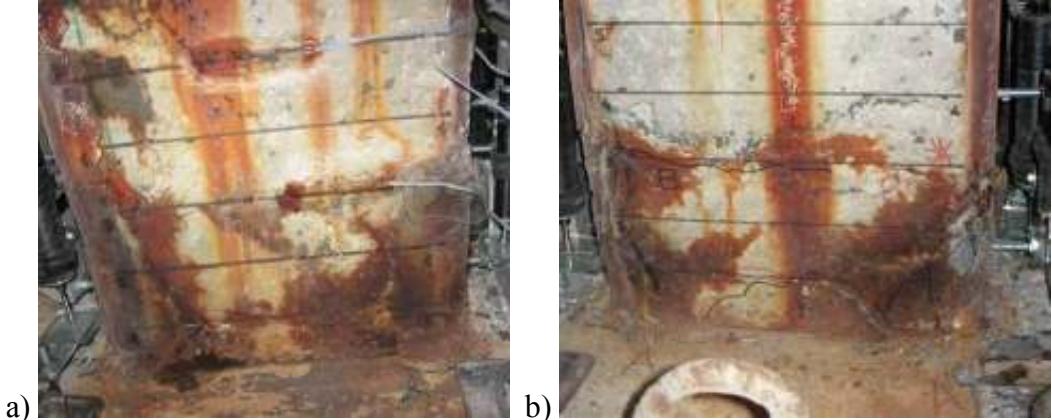


Figure 6.110 : a) North, and b) South view of the NS-X54 specimen after -2.50% drift ratio.

The view of the specimen NS-X54 after -5.00% drift ratio is shown in Figure 6.111.

During loading to target displacement of 72.0 mm (drift ratio 6.00%) specimen underwent excessive lateral displacement out of its axis and test was ended by decreasing the axial load. Summary of the seismic behavior of specimen NS-X54 is shown in Table 6.22. Crack propagation of NS-X54 while pushing and pulling cycles is given in Appendix C.

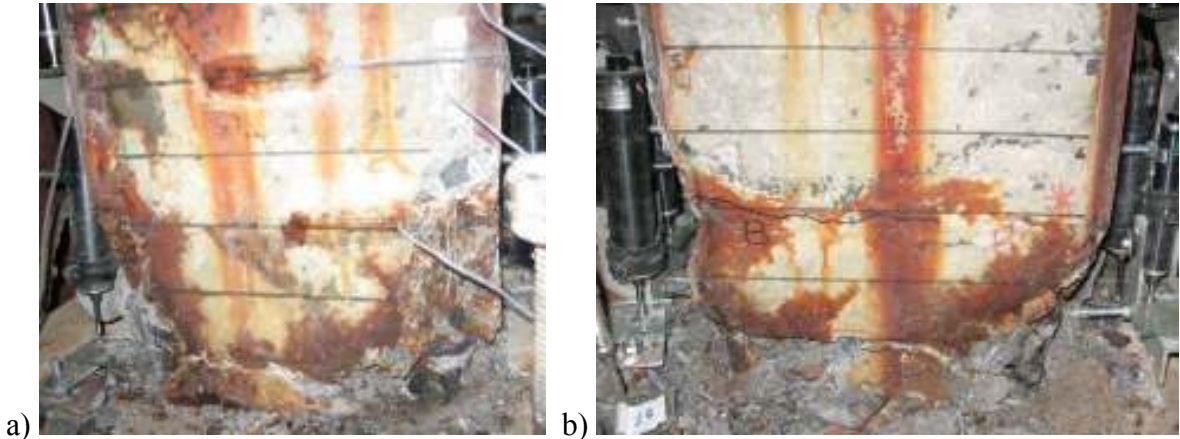


Figure 6.111 : a) North, and b) South view of the NS-X54 specimen after -5.00% drift ratio.

Table 6.22 : Summary of the seismic behavior of NS-X54.

Drift ratio (%)	δ (mm/mm)	P (kN)	Observations
%0.10	± 1.2	8.36/-7.32	No crack was observed.
%0.25	± 3.0	15.93/-16.77	No crack was observed.
%0.50	± 6.0	31.30/-24.68	No crack was observed.
%0.75	± 9.0	35.36/-32.10	First flexural crack at column-footing interface was observed.
%1.0	± 12.0	40.32/-38.02	Flexural cracks and crushing of concrete cover were observed.
%1.5	± 18.0	39.56/-40.19	Propagation of existing cracks and flexural crack were observed.
%2.00	± 24.0	32.22/-39.44	
2.50	± 30.0	30.08/-38.10	Propagation of existing cracks and spalling of concrete cover were observed.
3.0	± 36.0	24.86/-30.27	
3.50	± 42.0	24.54/-26.38	
4.0	± 48.0	22.10/-23.46	
4.5	± 54.0	20.06/-11.71	
5.0	± 60.0	17.19/-9.41	Specimen underwent excessive lateral displacement out of its axis and test was ended by decreasing the axial load.

Force-displacement relationship of NS-X54 is presented in Figure 6.112. In this figure, P is applied lateral load and P_0 is the theoretical lateral load capacity of the specimen determined without considering the effect of corrosion. First flexural crack, yielding of starter bar, crushing of concrete cover, spalling of concrete cover, fracture of starter bar, maximum strain on the starter bar and maximum strain on the longitudinal bar are marked on the figure. As seen from Figure 6.112, strength loss was observed.

Average experimental moment-curvature relationships obtained for critical sections of NS-X54 are presented in Figure 6.113. For the calculation of moment-curvature relationships, the average curvature values which were obtained for the ranges of 0-20 mm, 20-150 mm and 150-300 mm heights above the footing were taken into account. As seen from Figure 6.113, the curvature values of the member measured in 20-150 mm and 150-300 mm height above the support are in the order of 5.10^{-5} (1/mm), while the curvatures measured in 0-20 mm height are in the order of 3.10^{-3} (1/mm). According to Figure 6.113, it is of interest to note that the damage is accumulated especially in 20 mm height of the member from top of the base according to the moment-curvature relationships.

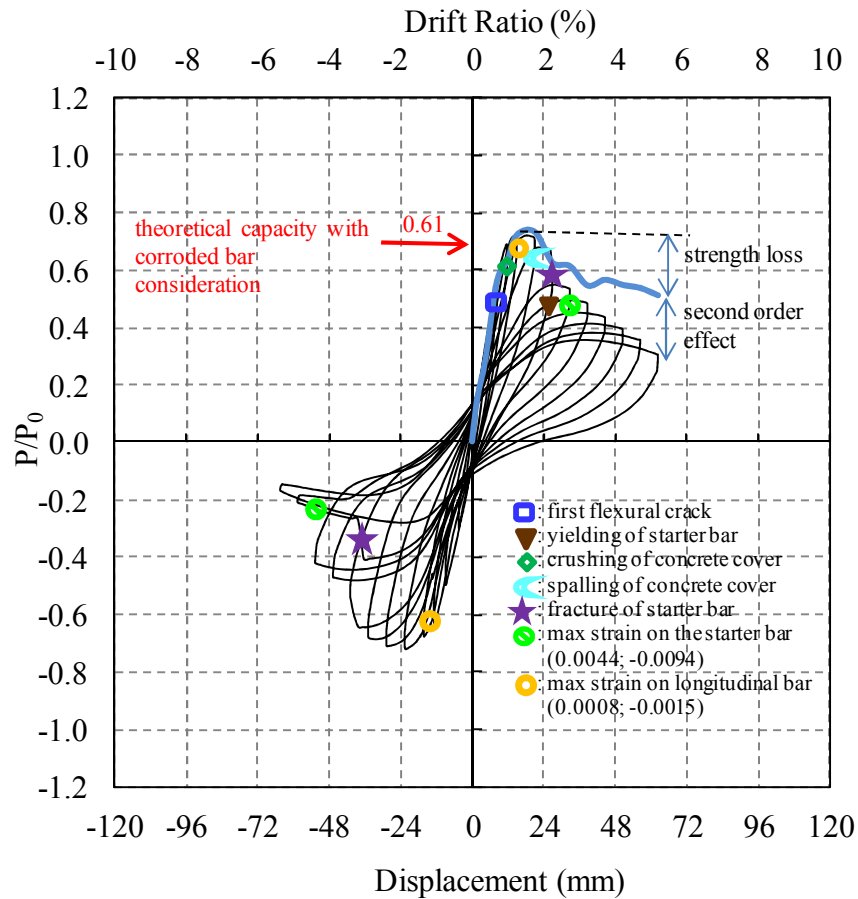


Figure 6.112 : Lateral load/Theoretical load capacity versus displacement for NS-X54.

According to the data from the strain gauges on the starter bars, the maximum strain while pushing was 0.0044, measured from the strain gauge at +100 mm above the footing when $P=30.08$ kN at 0.025 drift ratio; the maximum strain while pulling was -0.0094, measured from the strain gauge at +100 mm above the footing when $P=-9.41$ kN at -0.05 drift ratio. According to the data from the strain gauges on the longitudinal bars of the NS-X54, the maximum strain while pushing was 0.0008, measured from the strain gauge at +400 mm above the footing when $P=39.56$ kN at 0.015 drift ratio; the maximum strain while pulling was -0.0015, measured from the strain gauge at +100 mm above the footing when $P=-39.44$ kN at -0.02 drift ratio. Strain distribution of the starter bars and longitudinal bars of NS-X54 while pushing and pulling are shown in Figure 6.114 and Figure 6.115, respectively. As seen from Figure 6.114 and Figure 6.115, the strain values of starter bars reach yield strain and are lower than NS-X0.

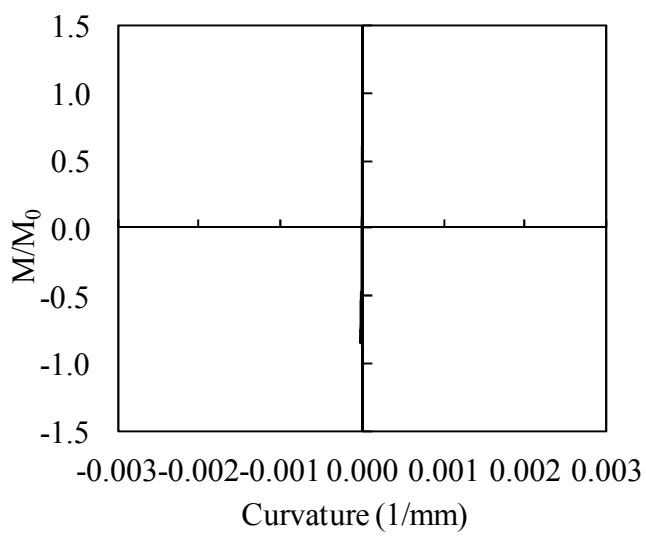
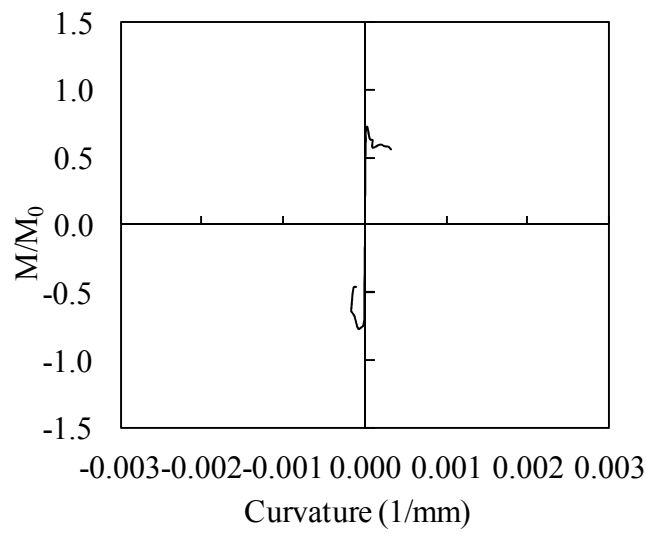
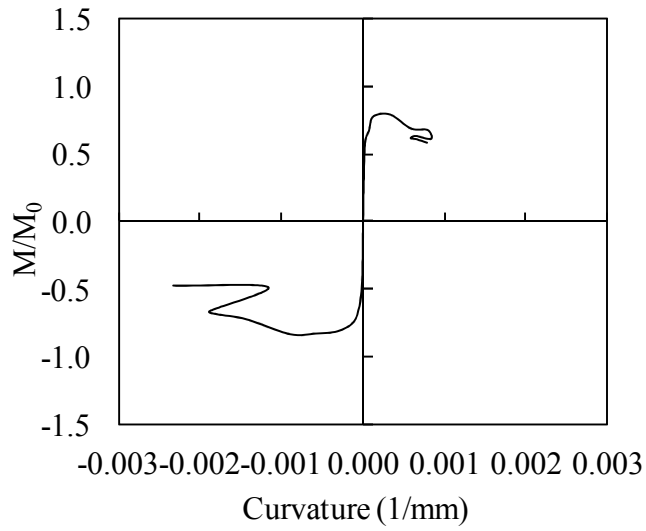


Figure 6.113 : Moment-curvature relationships obtained for a) 20 mm, b) 150 mm, c) 300 mm gauge lengths.

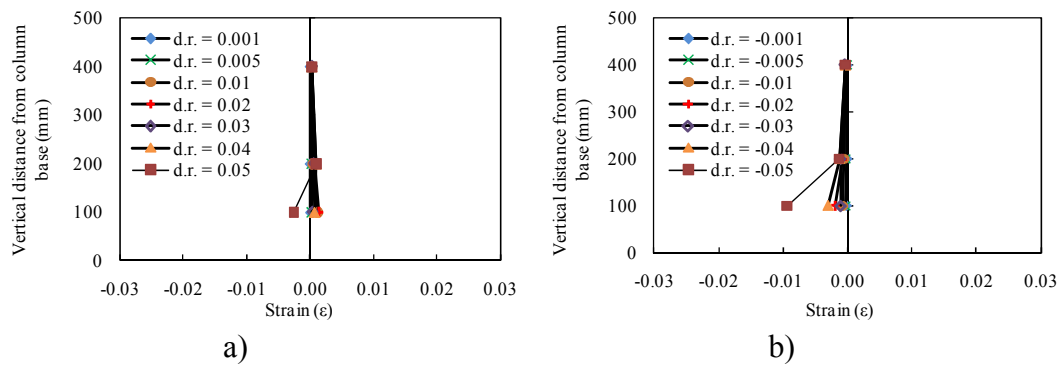


Figure 6.114 : Strain distribution of the starter bars of NS-X54 a) while pushing, b) while pulling.

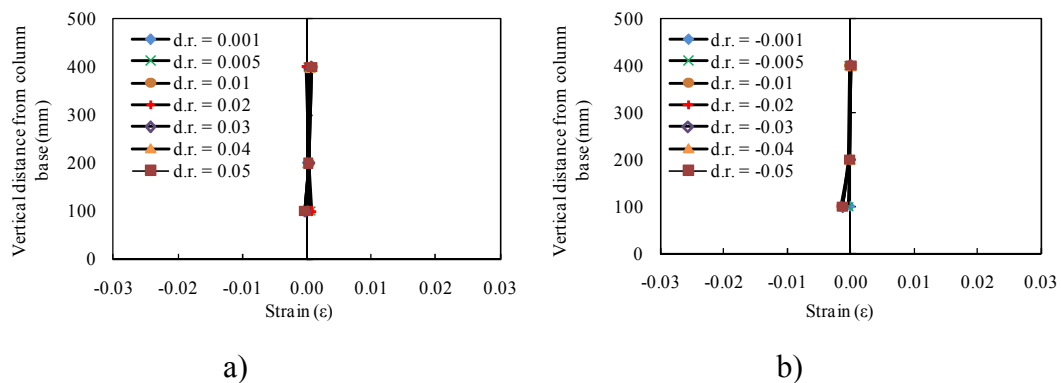


Figure 6.115 : Strain distribution of the longitudinal bars of NS-X54 a) while pushing b) while pulling.

6.4 Test Result of the Third Type Specimen

6.4.1 LS-X19-H

Similar to the specimen LS-X12, LS-X21 and LS-X28, specimen LS-X19-H has vertical cracks along the longitudinal reinforcement and horizontal cracks along the transverse reinforcement. Width, location and orientation of the cracks are presented in Table 6.23. Pattern of cracks formed due to corrosion are shown in Figure 6.116.

Table 6.23 : Width, location and orientation of the cracks.

Crack width	Crack location	Crack orientation
0.6 mm	above the footing	along the No.1 longitudinal reinforcement
1.3 mm	above the footing	along the No.2 longitudinal reinforcement
2.4 mm	above the footing	along the No.3 longitudinal reinforcement
1.5 mm	above the footing	along the No.4 longitudinal reinforcement

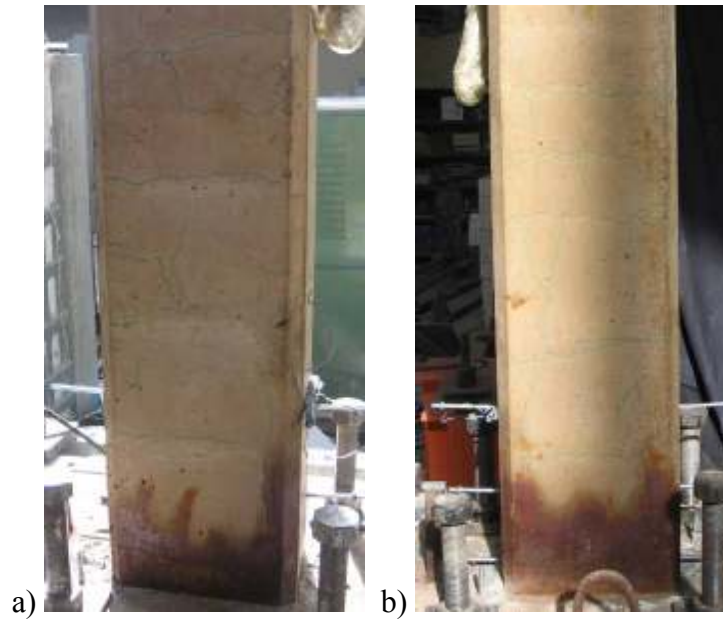


Figure 6.116 : Pattern of cracks formed due to corrosion: (a) North, (b) South.

No cracks were observed while loading to target displacements of ± 1.2 mm (drift ratio 0.10%), ± 3 mm (drift ratio 0.25%).

First flexural cracks (A-north, A-south) and (A'-north) were observed during loading to target displacements of 6.0 mm (drift ratio 0.50%) and -6.00 mm (drift ratio -%0.50) at the interface of the column and footing, respectively.

During loading to target displacement of -9.00 mm (drift ratio -%0.75) flexural crack (A'-south) at the interface of the column and footing was observed. The view of the specimen LS-X19-H after -0.10% drift ratio is shown in Figure 6.117.

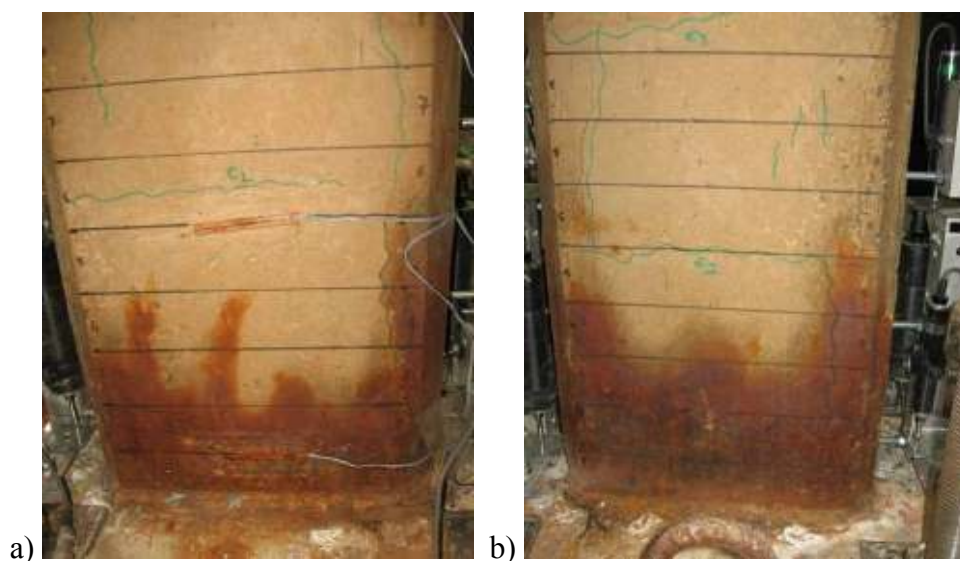


Figure 6.117 : a) North, and b) South view of the specimen LS-X19-H after -0.10% drift ratio.

During loading to target displacements of 24.0 mm (drift ratio 2.00%) and -24.0 mm (drift ratio 2.00%) vertical cracks (B-north) and (B'-north) were observed, respectively. The view of the specimen LS-X19-H after -2.00% drift ratio is shown in Figure 6.118.



Figure 6.118 : a) North, and b) South view of the specimen LS-X19-H after -2.00% drift ratio.

During loading to target displacement of 30.0 mm (drift ratio 2.50%) flexural crack (C-south) and shear cracks (B-south) was observed. During loading to target displacement of -30.0 mm (drift ratio -2.50%) shear cracks (B'-north, C'-south, D'-south, F'-south) and vertical cracks (E'-south, G'-south, H'-south) were observed.

During loading to target displacement of 36.0 mm (drift ratio 3.00%) vertical crack (C-north) was observed. The view of the specimen LS-X19-H after -3.00% drift ratio is shown in Figure 6.119.

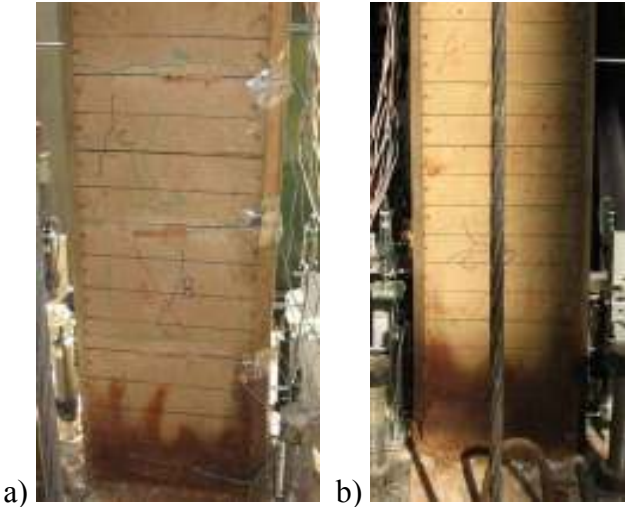


Figure 6.119 : a) North, and b) South view of the specimen LS-X19-H after -3.00% drift ratio.

During loading to target displacement of 42.0 mm (drift ratio 3.50%) shear crack (D-south) and vertical crack (E-south) were observed. Spalling of concrete cover started.

During loading to target displacement of 48.0 mm (drift ratio 4.00%) shear crack (F-south) was observed. During loading to target displacement of -48.0 mm (drift ratio -4.00%) shear cracks (F'-north, I'-south, J'-south, K1'-south, M'-south) and vertical cracks (D'-north, E'-north, G'-north, H'-north, I'-north, K2'-south, N'-south) were observed. The view of the specimen LS-X19-H after -4.00% drift ratio is shown in Figure 6.120.

During loading to target displacement of 54.0 mm (drift ratio %4.50) propagation of existing crack (B-south) was observed.

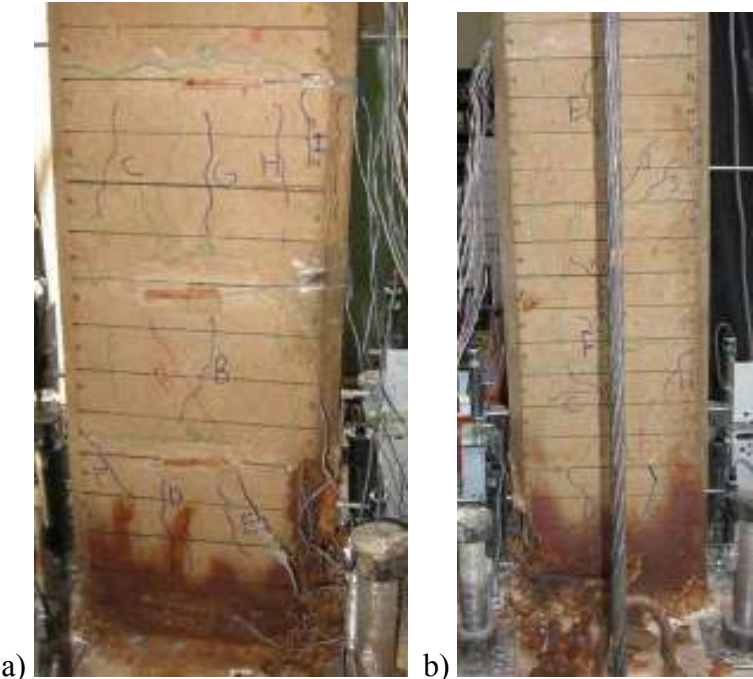


Figure 6.120 : a) North, and b) South view of the specimen LS-X19-H after -4.00% drift ratio.

During loading to target displacement of -60.0 mm (drift ratio -5.00%) specimen underwent excessive lateral displacement out of its axis and test was ended by decreasing the axial load. Concrete cover spalled completely. The view of the specimen LS-X19-H after -5.00% drift ratio is shown in Figure 6.120. Summary of the seismic behavior of the specimen LS-X19-H is shown in Table 6.24. Crack propagation of LS-X19-H while pushing and pulling cycles is shown in Appendix C.

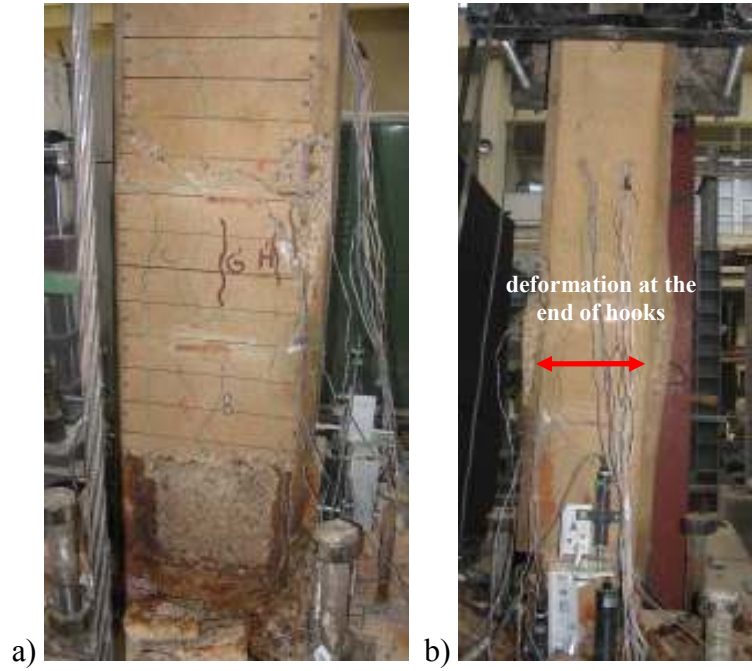


Figure 6.121 : a) North, and b) South view of the LS-X19-H specimen after -5.00% drift ratio.

Table 6.24 : Summary of the seismic behavior of LS-X19-H.

Drift ratio (%)	δ (mm/mm)	P (kN)	Observations
0.10	± 1.2	3.32/-5.12	No crack was observed.
0.25	± 3.0	7.62/-9.64	No crack was observed.
0.50	± 6.0	12.46/-15.93	First flexural crack at column-footing interface was observed.
0.75	± 9.0	15.35/-20.26	Flexural crack at column-footing interface was observed.
1.0	± 12.0	17.54/-21.68	
1.5	± 18.0	18.80/-23.17	Crushing started at the concrete cover.
2.00	± 24.0	19.00/-23.67	Vertical cracks formed. Concrete cover spalled.
2.50	± 30.0	19.08/-23.52	Shear, flexure and vertical cracks formed.
3.0	± 36.0	18.68/-21.87	Vertical cracks formed.
3.50	± 42.0	16.58/-19.41	
4.00	± 48.0	12.60/-14.54	Shear and vertical cracks formed.
4.50	± 54.0	8.76/-11.28	Propagation of existing cracks were observed.
5.00	± 60.0	6.48/-0.49	Concrete cover spalled completely. Specimen underwent excessive lateral displacement out of its axis and test was ended by decreasing the axial load.

Force-displacement relationship of LS-X19-H is presented in Figure 6.122. In this figure, P is applied lateral load and P_0 is the theoretical lateral load capacity of the specimen determined without considering the effect of corrosion. First flexural crack, first shear crack, first vertical crack, yielding of starter bar, crushing of concrete cover, spalling of concrete cover, fracture of starter bar, maximum strain on the starter bar and maximum strain on the longitudinal bar are marked on the figure. As seen from Figure 6.122, strength loss was observed.

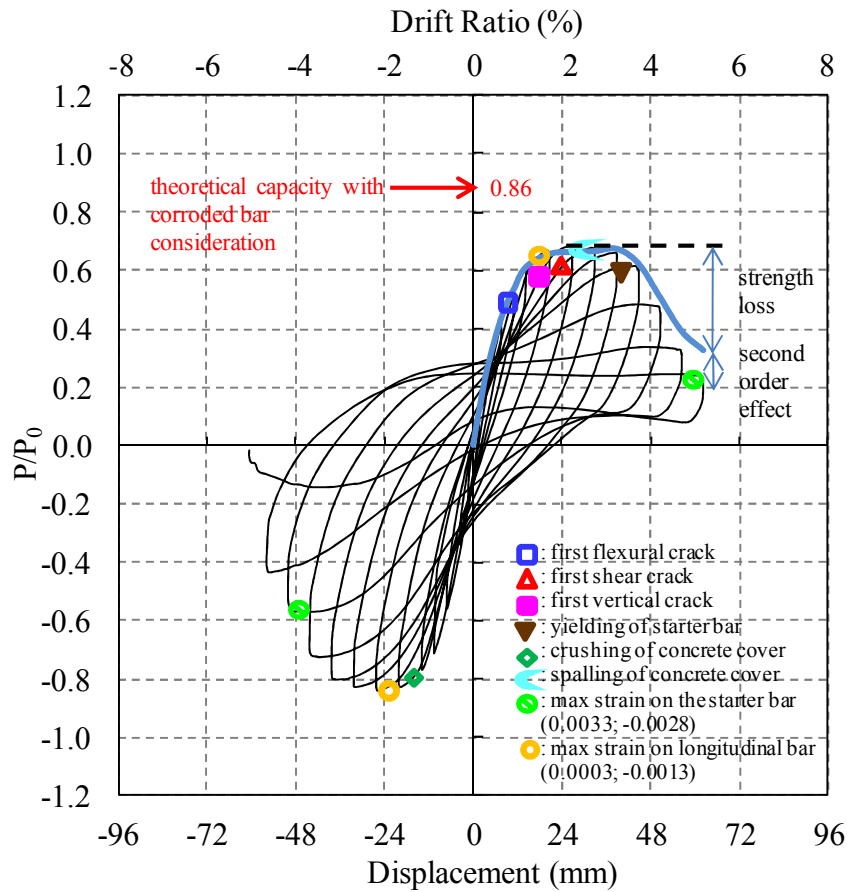


Figure 6.122 : Lateral load/Theoretical load capacity versus displacement for LS-X19-H.

Average experimental moment-curvature relationships obtained for critical sections of LS-X19-H are presented in Figure 6.123. For the calculation of moment-curvature relationships, the average curvature values which were obtained for the ranges of 0-20 mm, 20-150 mm and 150-300 mm heights above the footing were taken into account. As seen from Figure 6.123, the curvature values of the member measured in 20-150 mm and 150-300 mm height above the support are in the order of $5 \cdot 10^{-5}$ (1/mm), while the curvatures measured in 0-20 mm height are in the order of $3 \cdot 10^{-3}$ (1/mm). According to Figure 6.123, it is of interest to note that the damage is accumulated especially in 20 mm height of the member from top of the base according to the moment-curvature relationships.

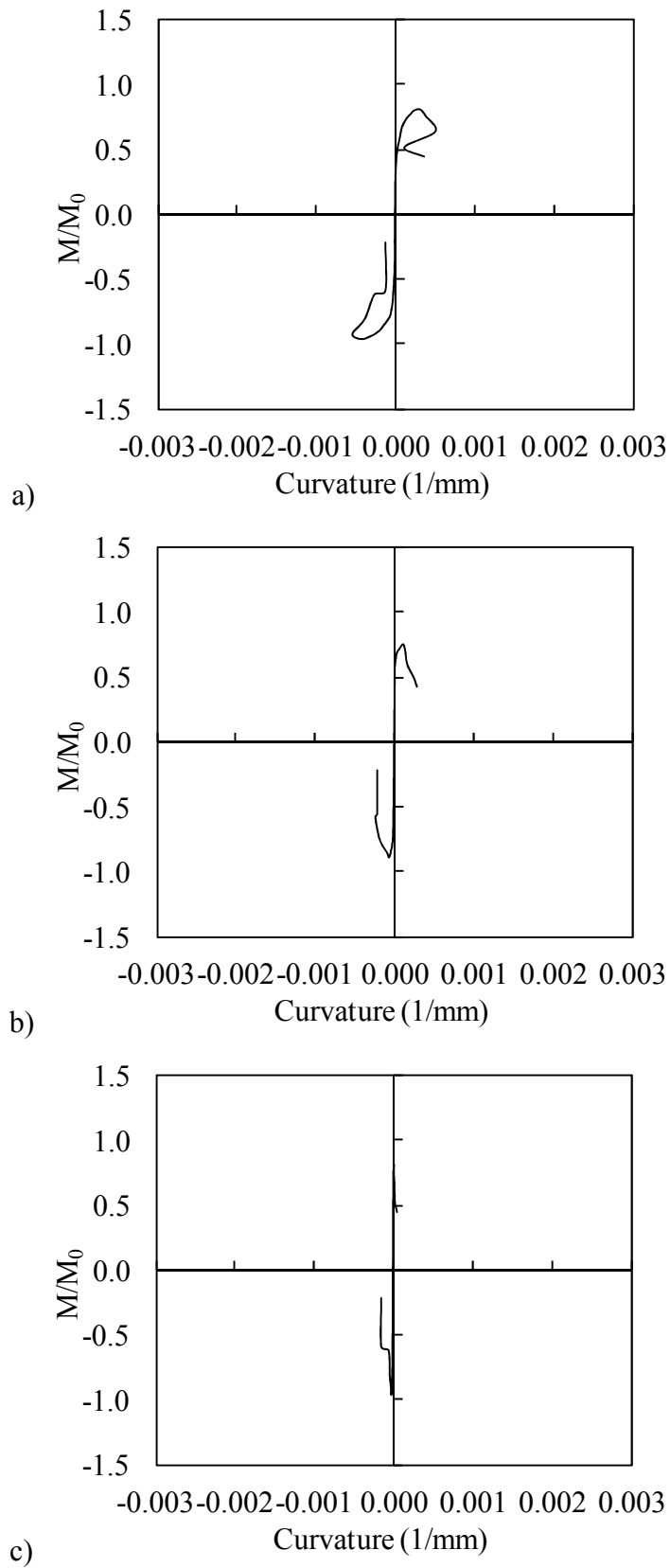


Figure 6.123 : Moment-curvature relationships obtained for a) 20 mm, b) 150 mm, c) 300 mm gauge lengths.

According to the data from the strain gauges on the starter bars, the maximum strain while pushing was 0.0033, measured from the strain gauge at +100 mm above the footing when P=6.48 kN at 0.05 drift ratio; the maximum strain while pulling was -0.0028, measured from the strain gauge at +100 mm above the footing when P=-14.54 kN at -0.04 drift ratio. According to the data from the strain gauges on the longitudinal bars of the LS-X19-H, the maximum strain while pushing was 0.0003, measured from the strain gauge at +100 mm above the footing when P=18.80 kN at 0.015 drift ratio; the maximum strain while pulling was -0.0013, measured from the strain gauge at +400 mm above the footing when P=-23.67 kN at -0.02 drift ratio. Strain distribution of the starter bars and longitudinal bars of LS-X19-H while pushing and pulling are shown in Figure 6.124 and Figure 6.125. As seen from Figure 6.124 and Figure 6.125, the strain values of starter bars reach yield strain.

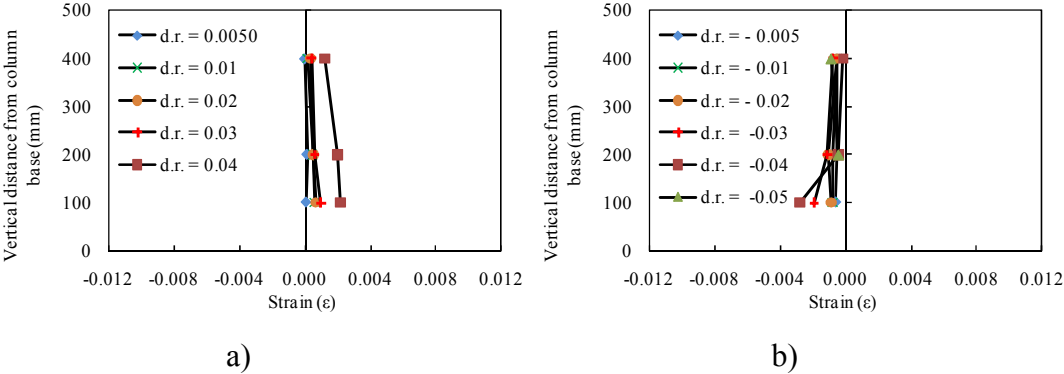


Figure 6.124 : Strain distribution of the starter bars of LS-X19-H a) while pushing, b) while pulling.

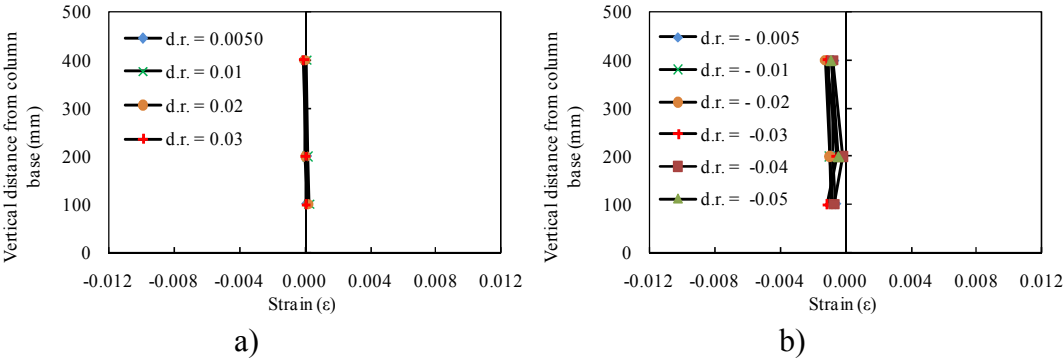


Figure 6.125 : Strain distribution of the longitudinal bars of LS-X19-H a) while pushing b) while pulling.

6.5 Test Results of Uniaxial Tension Tests

After the tests, the reinforcing bars were removed out of concrete, cleaned in accordance with ASTM G1-03 (2003) and tested under uniaxial tension.

The solution, prepared for removing the rust and concrete dust from reinforcing bars, contains 1000 mL hydrochloric acid (HCl), 20 g antimony trioxide (Sb_2O_3) and 50 g stannous chloride (SnCl_2). The reinforcing bars were put into solution for 25 minutes at 25°C in an ultrasonic pool (Figure 6.126). After cleaning with the hydrochloric acid solution, the reinforcing bars were cleaned by water, neutralized by acetone and dried for few hours.



Figure 6.126 : Cleaning process of corroded reinforcement removed from reinforced concrete test specimens.

Thereafter, the reinforcing bars were photographed and the surface condition of the reinforcing bars were observed through an optical stereo microscope. The general appearance of a typical corroded reinforcing bar taken out from the column, the surface condition of the reinforcement bars observed through an optical stereo microscope and scan view of the reinforcement bar with 3D optical scanner are given in Appendix F.

Tensile tests were carried out in accordance with ASTM A370 (2010). The tension test setup and a fractured bar after the test are shown in Figure 6.127. During the tensile tests, the strains were measured by two strain gauges which were bonded on the diagonally opposite surfaces of the bar.



Figure 6.127 : The test setup and a fractured bar after the test.

After the tensile test, for the unaffected parts of the bars, the local uniform losses in the cross-sections of reinforcing bars were determined by dividing the bars into 10 mm long pieces and measuring the diameter of each piece with micrometer depth gauge in two mutually perpendicular directions (0° , 90°). The uniform cross-section losses of the corroded bars are calculated as the average of diameters obtained from volumetric measurement of 10 mm long pieces. Then the 10 mm long pieces were also scanned under 3D optical scanner (Figure 6.128). ATOS 3D to obtain the images with grid projection method. White light was projected through CCD cameras with resolution of 1.3 megapixel onto the pieces and 12 images were obtained per second. To get the geometry of the pieces, shots from different angles were underwent. As a result, 3-D point cloud data was created by processing the images from the camera. In order to prevent the independent surfaces, black and white dots were used as reference on the pieces and the plane where the pieces were placed.



Figure 6.128 : ATOS 3D optical scanner.

The general appearance of a typical corroded reinforcing bar taken out from the column, the surface condition of the reinforcement bars observed through an optical stereo microscope and scan view of the reinforcement bar with 3D optical scanner are shown in Appendix F. As seen in figures in Appendix F, there are almost no pits in reference specimens (no corrosion), while the depth of the pits increase due to the increased corrosion on the other specimens.

6.5.1 Mechanical characteristics of corroded deformed reinforcing bars

For evaluating the mechanical characteristics of corroded reinforcing bars properly, two definitions (Q_{corr1} and Q_{corr2}) are made for representing the corrosion levels of reinforcing bars.

Q_{corr1} : the ratio of the maximum cross-section loss to the original cross-section is an indicator for the maximum local loss of cross-section (maximum pit).

Q_{corr2} : the ratio of difference of the original cross-section and cross-section found from measuring the weight and length to the original cross-section, is an indicator for the average loss of cross-section throughout the length of reinforcing bars.

It should be noted that maximum cross-section loss is determined by comparing the section losses of each 10 mm long piece of the reinforcing bars. It is clear that while maximum cross-section loss may play a more important role on the behavior in certain cases (such as fracture of the bar), average cross-section loss may be more governing in some other cases (such as bond or buckling).

The variation of strength and deformability characteristics of corroded reinforcing bars with respect to variation of Q_{corr1} and Q_{corr2} are presented in Figure 6.129. In these figures, F_y , F_{max} and F_u are the yield, maximum and ultimate strengths of corroded bars, respectively. In these figures, F_{y0} , F_{max0} and F_{u0} are used for the yield, maximum and ultimate strengths of uncorroded reinforcing bars, respectively. It should be noted that the strengths in these figures are tensile forces resisted by the corroded bars, not the tensile stresses, which can not be calculated reliably. The apparent and effective stresses are calculated as given in Apostolopoulos and Papadakis (2008). The apparent stress is calculated as the quotient of the load capacity, divided by the uncorroded cross-section of reinforcing bars while the effective stress is calculated as the quotient of the load capacity divided by the corroded cross-sections (considering both maximum local loss and average losses of cross-sections).

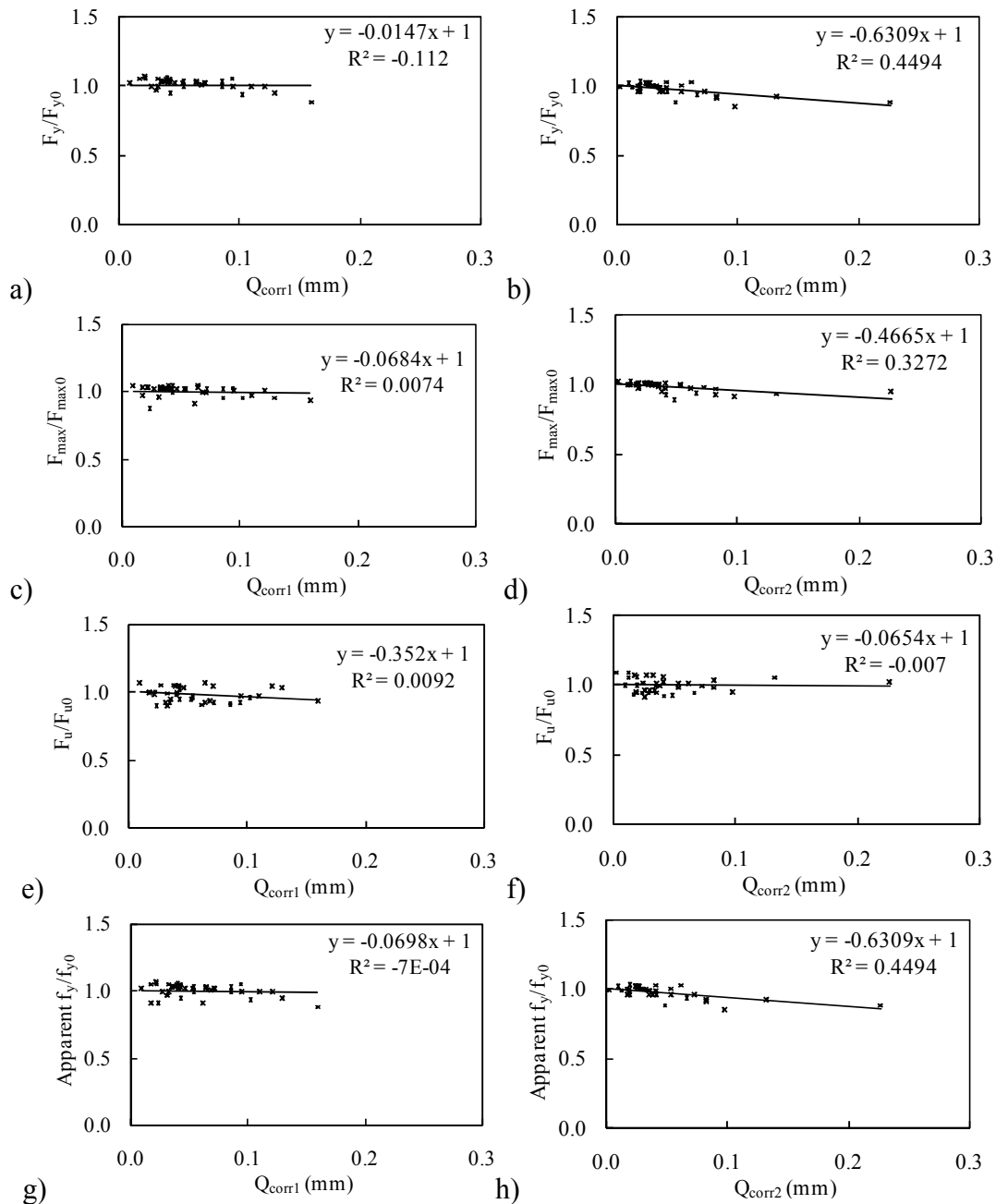


Figure 6.129 : Variation of a,b) Yield strength, c,d) Maximum strength, e,f) Ultimate strength g,h) Apparent yield stress, i,j) Apparent maximum stress, k,l) Apparent ultimate stress, m,n) Effective yield stress, o,p) Effective maximum stress, r,s) Effective ultimate stress t,u) Ultimate strain with respect to maximum and average cross-section losses

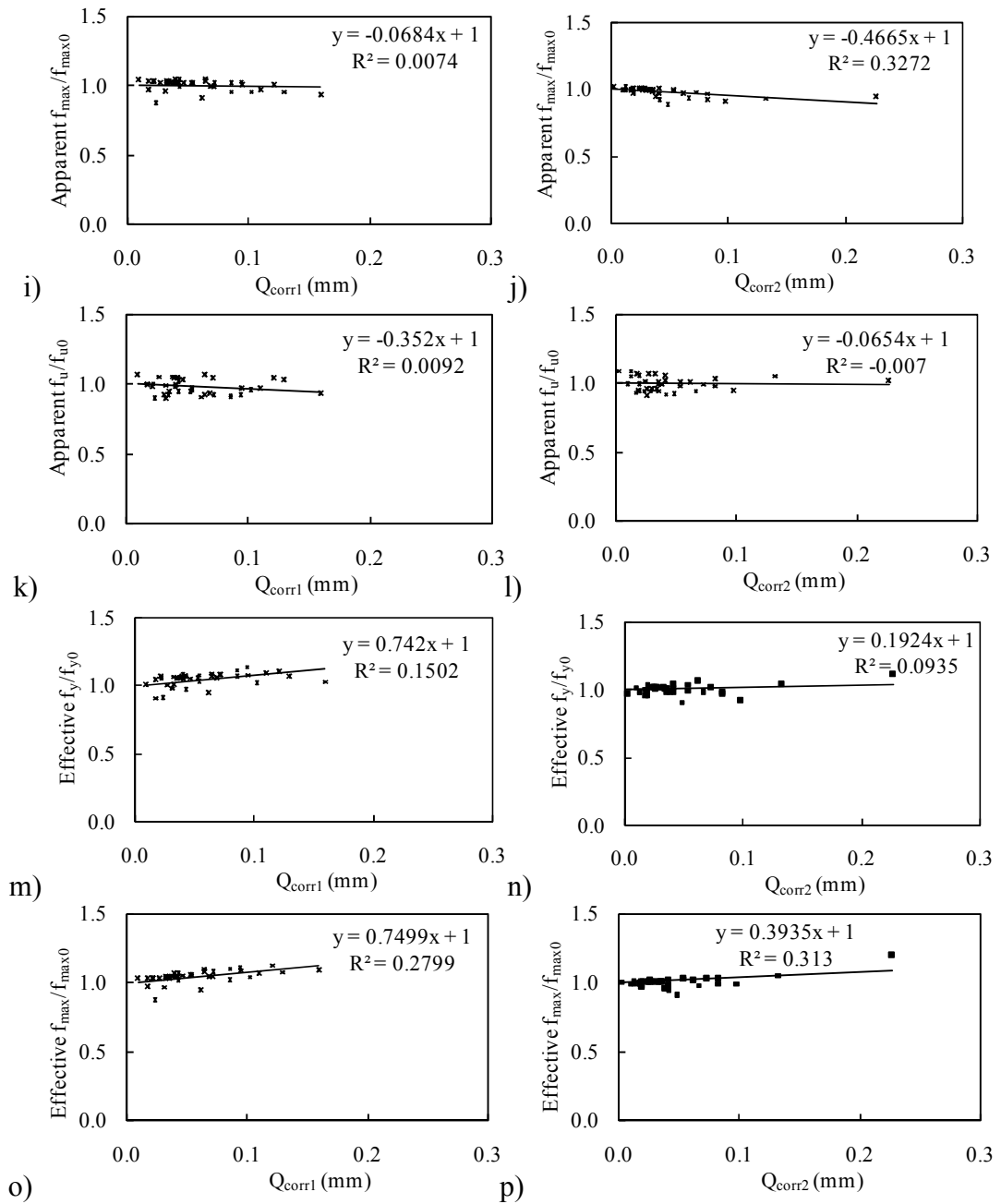


Figure 6.129 (contd.) : Variation of a,b) Yield strength, c,d) Maximum strength, e,f) Ultimate strength g,h) Apparent yield stress, i,j) Apparent maximum stress, k,l) Apparent ultimate stress, m,n) Effective yield stress, o,p) Effective maximum stress, r,s) Effective ultimate stress t,u) Ultimate strain with respect to maximum and average cross-section losses.

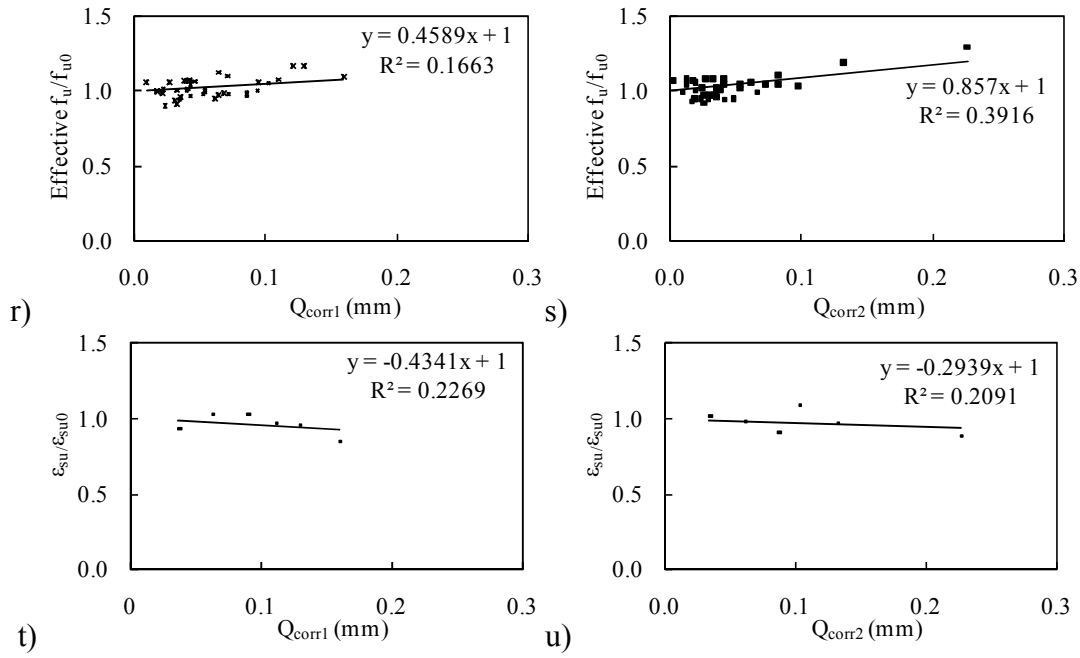


Figure 6.129 (contd.) : Variation of a,b) Yield strength, c,d) Maximum strength, e,f) Ultimate strength g,h) Apparent yield stress, i,j) Apparent maximum stress, k,l) Apparent ultimate stress, m,n) Effective yield stress, o,p) Effective maximum stress, r,s) Effective ultimate stress t,u) Ultimate strain with respect to maximum and average cross-section losses.

As seen in these figures clearly, the yield, maximum and ultimate strengths are remarkably affected from corrosion, with higher loss of strength in case of higher values of Q_{corr1} and Q_{corr2} . While there is a large scatter, in general, the effect of corrosion is more severe on yield strength. Although the large scatter of test results do not allow a very reliable evaluation, the regression analysis of these results lead to the following equations:

$$\frac{F_y}{F_{y0}} = 1 - 0.0147 \cdot Q_{corr1} \quad (7.1)$$

$$\frac{F_y}{F_{y0}} = 1 - 0.6309 \cdot Q_{corr2} \quad (7.2)$$

$$\frac{F_{max}}{F_{max0}} = 1 - 0.0684 \cdot Q_{corr1} \quad (7.3)$$

$$\frac{F_{max}}{F_{max0}} = 1 - 0.4665 \cdot Q_{corr2} \quad (7.4)$$

$$\frac{F_u}{F_{u0}} = 1 - 0.3520 \cdot Q_{\text{corr1}} \quad (7.5)$$

$$\frac{F_u}{F_{u0}} = 1 - 0.0654 \cdot Q_{\text{corr2}} \quad (7.6)$$

$$\text{Apparent } \frac{f_y}{f_{y0}} = 1 - 0.0698 \cdot Q_{\text{corr1}} \quad (7.7)$$

$$\text{Apparent } \frac{f_y}{f_{y0}} = 1 - 0.6309 \cdot Q_{\text{corr2}} \quad (7.8)$$

$$\text{Apparent } \frac{f_{\text{max}}}{f_{\text{max}0}} = 1 - 0.0684 \cdot Q_{\text{corr1}} \quad (7.9)$$

$$\text{Apparent } \frac{f_{\text{max}}}{f_{\text{max}0}} = 1 - 0.4665 \cdot Q_{\text{corr2}} \quad (7.10)$$

$$\text{Apparent } \frac{f_u}{f_{u0}} = 1 - 0.3520 \cdot Q_{\text{corr1}} \quad (7.11)$$

$$\text{Apparent } \frac{f_u}{f_{u0}} = 1 - 0.0654 \cdot Q_{\text{corr2}} \quad (7.12)$$

$$\text{Effective } \frac{f_y}{f_{y0}} = 1 + 0.7420 \cdot Q_{\text{corr1}} \quad (7.13)$$

$$\text{Effective } \frac{f_y}{f_{y0}} = 1 + 0.1924 \cdot Q_{\text{corr2}} \quad (7.14)$$

$$\text{Effective } \frac{f_{\text{max}}}{f_{\text{max}0}} = 1 + 0.7499 \cdot Q_{\text{corr1}} \quad (7.15)$$

$$\text{Effective } \frac{f_{\text{max}}}{f_{\text{max}0}} = 1 + 0.3935 \cdot Q_{\text{corr2}} \quad (7.16)$$

$$\text{Effective } \frac{f_u}{f_{u0}} = 1 + 0.4589 \cdot Q_{\text{corr1}} \quad (7.17)$$

$$\text{Effective } \frac{f_u}{f_{u0}} = 1 + 0.8570 \cdot Q_{\text{corr2}} \quad (7.18)$$

$$\frac{\varepsilon_{su}}{\varepsilon_{su0}} = 1 - 0.4341 \cdot Q_{\text{corr1}} \quad (7.19)$$

$$\frac{\varepsilon_{su}}{\varepsilon_{su0}} = 1 - 0.2939 \cdot Q_{corr2} \quad (7.20)$$

There is no meaningful correlation between the variation of strain hardening, maximum and ultimate strain in corroded reinforcing bars with respect to variation of corrosion level (Q_{corr1} and Q_{corr2}). It should further be noted that the determination of the ultimate steel strain considering the length of ten times bar diameter around the fracture zone (as suggested by various standards such as DIN488 (1986) and TS708 (1996)) may be misleading due to concentration of plastic deformations at and around the maximum pit.

The averages, standard deviations and variation coefficients of ratios of predicted/measured mechanical characteristics of corroded reinforcing bars are presented in Table 6.25 A-U are calculated according to the ratios given in the footnote of Table 6.25. It is apparent that these equations should be used carefully considering the large scatter of the test results. It should also be mentioned that the validity of these equations is limited to the range of corrosion level considered in this study.

Table 6.25 : The average values of standard deviations and variation coefficients of ratios of predicted/measured mechanical characteristics.

	Average Ratio	Standard deviation	Variation coefficients
A ^{*1}	0.987	0.040	0.001
B ^{*2}	0.997	0.035	0.001
C ^{*3}	0.994	0.042	0.001
D ^{*4}	1.001	0.029	0.000
E ^{*5}	1.005	0.053	0.002
F ^{*6}	1.005	0.051	0.002
G ^{*7}	0.993	0.049	0.002
H ^{*8}	0.997	0.035	0.001
I ^{*9}	0.994	0.042	0.001
J ^{*10}	1.001	0.029	0.000
K ^{*11}	1.005	0.053	0.002
L ^{*12}	1.001	0.052	0.002
M ^{*13}	0.998	0.046	0.002
N ^{*14}	1.007	0.035	0.001
O ^{*15}	1.000	0.040	0.001
P ^{*16}	1.012	0.031	0.001
R ^{*17}	1.012	0.056	0.003
S ^{*18}	1.018	0.055	0.003
T ^{*19}	0.985	0.063	0.004
U ^{*20}	0.991	0.091	0.008

$$*1: A = \frac{\left(\frac{F_y}{F_{y0}}\right)_{\text{predicted}}}{\left(\frac{F_y}{F_{y0}}\right)_{\text{measured}}}; \quad *2: B = \frac{\left(\frac{F_y}{F_{y0}}\right)_{\text{predicted}}}{\left(\frac{F_y}{F_{y0}}\right)_{\text{measured}}}; \quad *3: C = \frac{\left(\frac{F_{\max}}{F_{\max 0}}\right)_{\text{predicted}}}{\left(\frac{F_{\max}}{F_{\max 0}}\right)_{\text{measured}}}; \quad *4: D = \frac{\left(\frac{F_{\max}}{F_{\max 0}}\right)_{\text{predicted}}}{\left(\frac{F_{\max}}{F_{\max 0}}\right)_{\text{measured}}}; \quad *5: E = \frac{\left(\frac{F_u}{F_{u0}}\right)_{\text{predicted}}}{\left(\frac{F_u}{F_{u0}}\right)_{\text{measured}}};$$

$$*6: F = \frac{\left(\frac{F_u}{F_{u0}}\right)_{\text{predicted}}}{\left(\frac{F_u}{F_{u0}}\right)_{\text{measured}}}; \quad *7: G = \frac{\text{Apparent}\left(\frac{f_y}{f_{y0}}\right)_{\text{predicted}}}{\text{Apparent}\left(\frac{f_y}{f_{y0}}\right)_{\text{measured}}}; \quad *8: H = \frac{\text{Apparent}\left(\frac{f_y}{f_{y0}}\right)_{\text{predicted}}}{\text{Apparent}\left(\frac{f_y}{f_{y0}}\right)_{\text{measured}}}; \quad *9: I = \frac{\text{Apparent}\left(\frac{f_{\max}}{f_{\max 0}}\right)_{\text{predicted}}}{\text{Apparent}\left(\frac{f_{\max}}{f_{\max 0}}\right)_{\text{measured}}};$$

$$*10: J = \frac{\text{Apparent}\left(\frac{f_{\max}}{f_{\max 0}}\right)_{\text{predicted}}}{\text{Apparent}\left(\frac{f_{\max}}{f_{\max 0}}\right)_{\text{measured}}}; \quad *11: K = \frac{\text{Apparent}\left(\frac{f_u}{f_{u0}}\right)_{\text{predicted}}}{\text{Apparent}\left(\frac{f_u}{f_{u0}}\right)_{\text{measured}}}; \quad *12: L = \frac{\text{Apparent}\left(\frac{f_u}{f_{u0}}\right)_{\text{predicted}}}{\text{Apparent}\left(\frac{f_u}{f_{u0}}\right)_{\text{measured}}}; \quad *13: \dots$$

$$M = \frac{\text{Effective}\left(\frac{f_y}{f_{y0}}\right)_{\text{predicted}}}{\text{Effective}\left(\frac{f_y}{f_{y0}}\right)_{\text{measured}}}; \quad *14: N = \frac{\text{Effective}\left(\frac{f_y}{f_{y0}}\right)_{\text{predicted}}}{\text{Effective}\left(\frac{f_y}{f_{y0}}\right)_{\text{measured}}}; \quad *15: O = \frac{\text{Effective}\left(\frac{f_{\max}}{f_{\max 0}}\right)_{\text{predicted}}}{\text{Effective}\left(\frac{f_{\max}}{f_{\max 0}}\right)_{\text{measured}}}; \quad *16: P = \frac{\text{Effective}\left(\frac{f_{\max}}{f_{\max 0}}\right)_{\text{predicted}}}{\text{Effective}\left(\frac{f_{\max}}{f_{\max 0}}\right)_{\text{measured}}};$$

$$*17: R = \frac{\text{Effective}\left(\frac{f_u}{f_{u0}}\right)_{\text{predicted}}}{\text{Effective}\left(\frac{f_u}{f_{u0}}\right)_{\text{measured}}}; \quad *18: S = \frac{\text{Effective}\left(\frac{f_u}{f_{u0}}\right)_{\text{predicted}}}{\text{Effective}\left(\frac{f_u}{f_{u0}}\right)_{\text{measured}}}; \quad *19: T = \frac{\left(\frac{\varepsilon_{su}}{\varepsilon_{su0}}\right)_{\text{predicted}}}{\left(\frac{\varepsilon_{su}}{\varepsilon_{su0}}\right)_{\text{measured}}}; \quad *20: U = \frac{\left(\frac{\varepsilon_{su}}{\varepsilon_{su0}}\right)_{\text{predicted}}}{\left(\frac{\varepsilon_{su}}{\varepsilon_{su0}}\right)_{\text{measured}}};$$

6.6 Summary of the Section

The first, the second and the third type specimens are tested under certain axial load and reversed cyclic loads. The test results are evaluated in terms of lateral load-displacement relationships, strain distributions and moment-curvature relationships. As seen in the figures, slip dominated the behavior of the first type specimens. None of the specimens of the first type reach their theoretical load capacity considering uncorroded reinforcing bar. The first type specimens did not reach their theoretical load capacity considering corroded reinforcing bar except LS-X21 and LS-X28 which were heavily corroded. LS-X21 and LS-X28 are assumed to reach their theoretical load capacity considering corroded reinforcing bar due to increase in bond between plain bars and concrete. Only the starter bars of LS-X21 and LS-X28 yielded. As seen in the figures, flexure dominated the behavior of the second type specimens. NS-X0 and NS-X9 reached their theoretical capacity considering uncorroded reinforcing bar. All the specimens except NS-X0 and NS-X9 reach their theoretical load capacity considering corroded reinforcing bar. All the starter bars of the second type specimens yielded. The strains gradually decrease due to corrosion of the reinforcing bars.

7. OVERALL EVALUATION OF TEST RESULTS

7.1 Test Results of the First and the Third Type Specimens

The envelopes of load-displacement curves for the first and the third type specimens are shown in Figure 7.1.

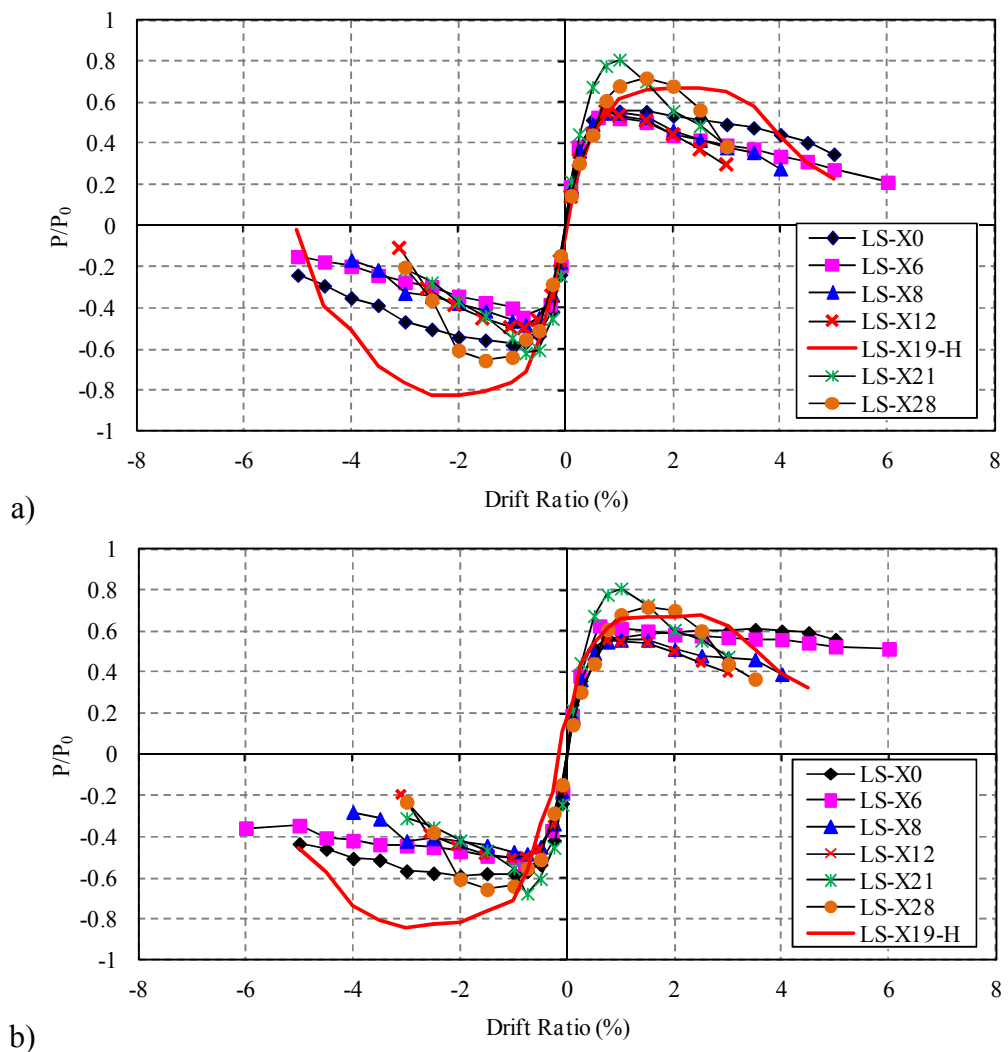


Figure 7.1 : Envelopes of the load-displacement curves for the first and the third type specimens a) without considering $P-\Delta$ effects, b) considering $P-\Delta$ effects.

In this figure, P is the applied lateral load and P_0 is the theoretical lateral load capacity of the specimen determined without considering the effect of corrosion. It should be noted that none of the specimens could reach their theoretical flexural

strengths (≈ 26 kN). As seen from Figure 7.1, all the specimens with corroded reinforcing bars experienced substantial degradation in ductility. Strength degradation accompanying with ductility loss was observed until 12% loss in cross-sectional area of longitudinal bars, after 12%, increase of strength with increasing loss in cross-sectional area of longitudinal bars maybe attributed to the effect of corrosion products at the concrete-bar interface, which increase the bond strength of plain bars.

The behavior of LS-X21 in the pushing direction and the behavior of LS-X19-H in the pulling direction is selected in evaluating these specimens.

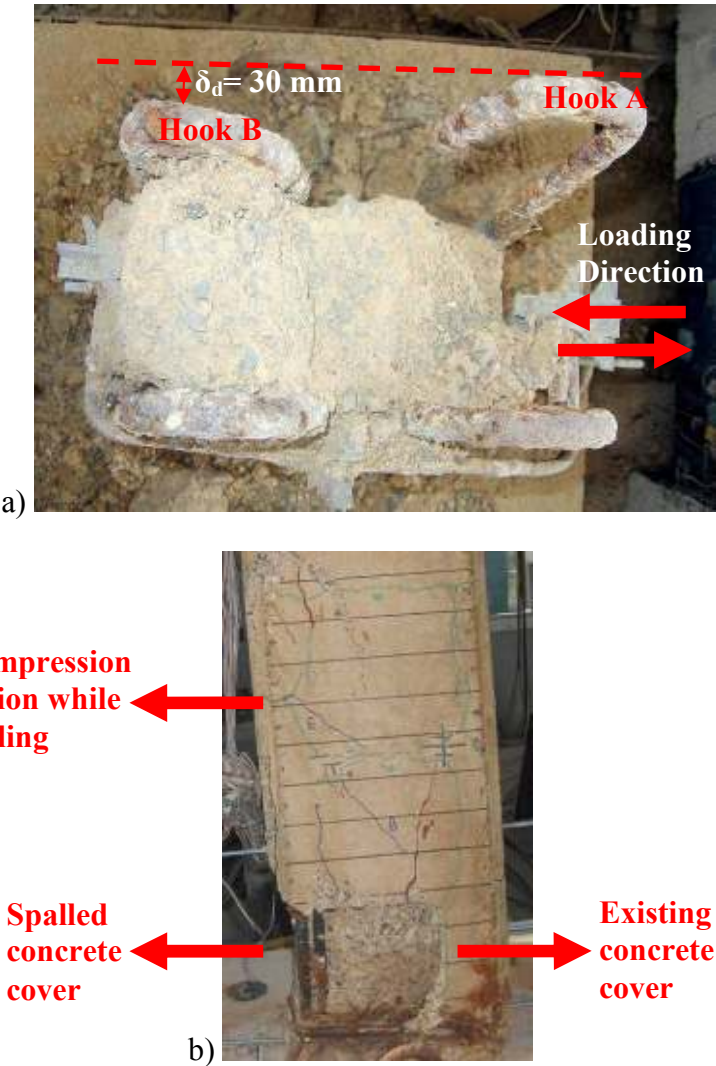


Figure 7.2 : Views from a) Reinforcing cage of LS-X19-H, b) Damages of concrete of LS-X21 (after the test).

As seen from Figure 7.2, there is a lateral deviation (δ_d in the figure) between the reinforcing bars of LS-X19-H, for this reason one of the hooks (shown with B in the figure) has a thicker concrete cover resulting with more flexural capacity of LS-X19-

H in the pulling direction. As also seen from Figure 7.2, there is more damage in concrete in compression region while pulling resulting in higher flexural capacity of LS-X21 in the pushing direction. LS-X19-H with hooked lap splice performed relatively less pinched hysteresis curve, the same lateral strength and higher plastic deformation capacity with respect to LS-X21, which of two specimens had approximately the same level of corrosion (Figure 7.1). The merge of the lap spliced with hooked plain bars, up to a certain drift ratio, hook controlled the behavior of RC member under lateral loads. It is interesting to note that, the existence of hook can be said to be very effective even with low strength concrete and the main factor that affected the behavior of lap spliced specimens with plain bars.

The variation of ratios of residual plastic displacements (δ_{res}) to the displacement at which unloading began (δ_{un}) with respect to drift ratios are presented in Figure 7.3.

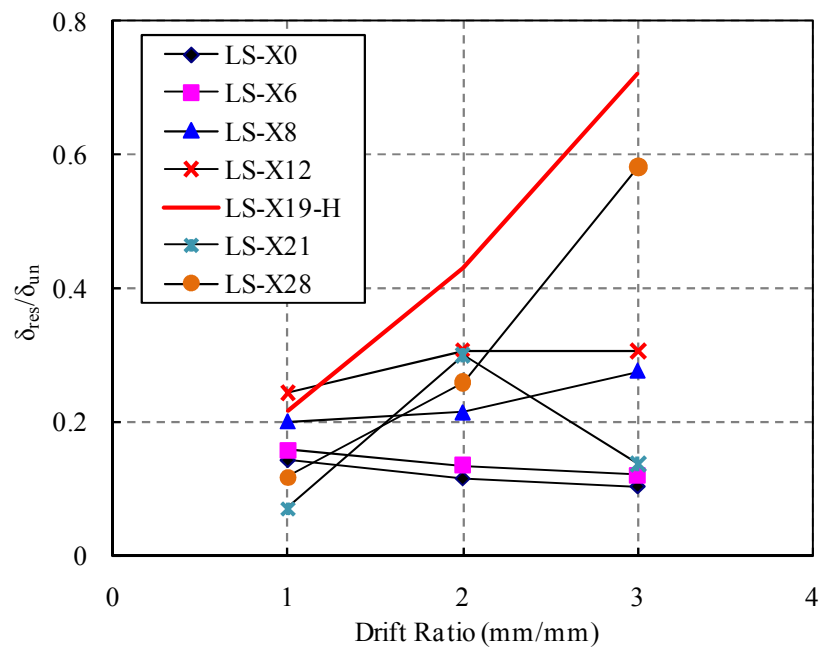


Figure 7.3 : The variation of residual displacement for the first and the third type specimens.

As seen in Figure 7.3, δ_{res}/δ_{un} ratios for specimens LS-X0, LS-X6, LS-X12 and LS-X21 decreased with increasing drift ratios, while δ_{res}/δ_{un} ratios for specimens LS-X8, LS-X28 and LS-X19-H increased. As the specimens without corrosion and with low level corrosion were dominated by slip behavior, δ_{res} is less than the specimens with higher corrosion level which were dominated by flexural behavior due to the bond resulting from corrosion products.

The variation of axial strains of longitudinal bars and starter bars at different locations are presented in Figure 7.4 and Figure 7.5.

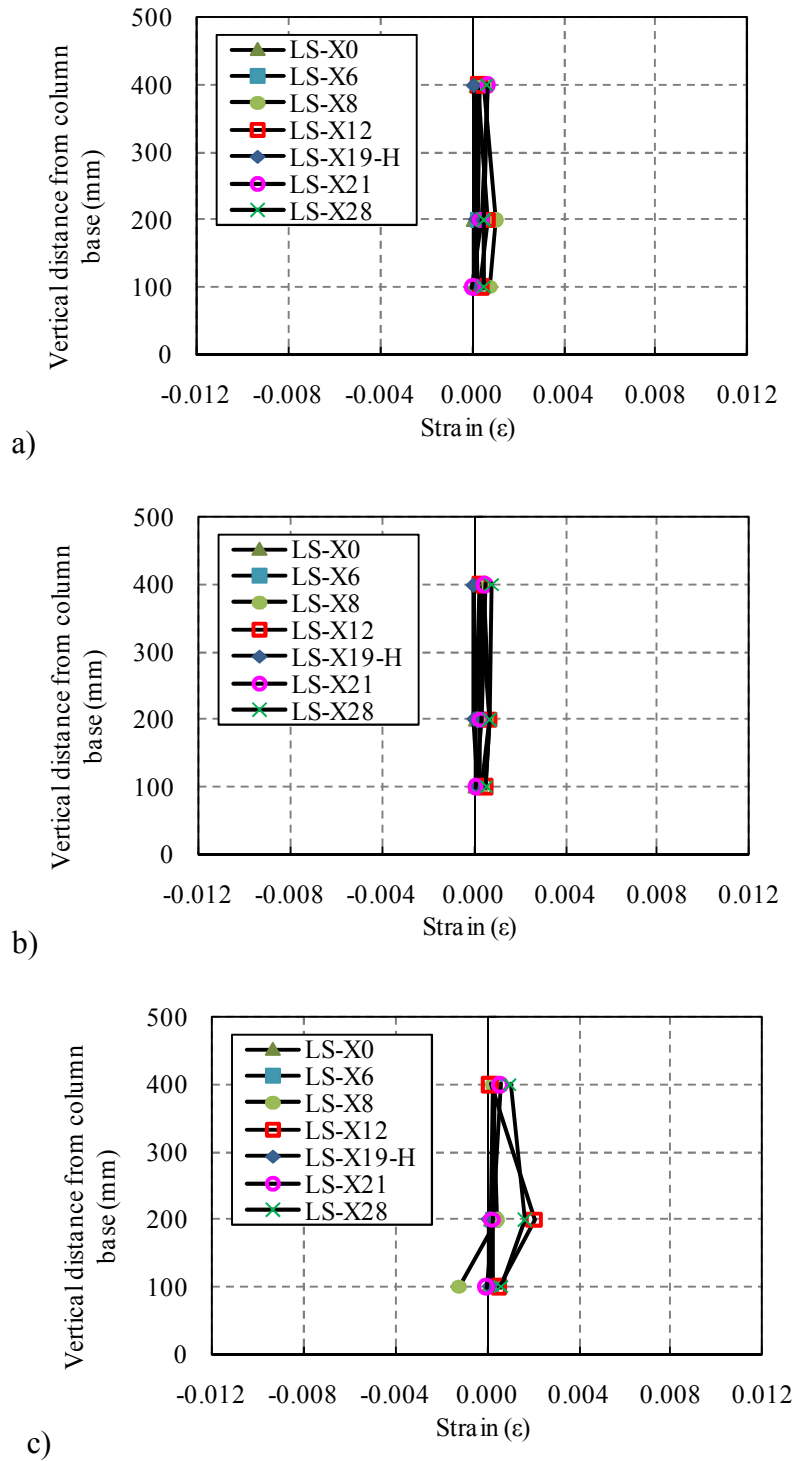


Figure 7.4 : Strain distribution of longitudinal reinforcement at a) 1%, b) 2%, c) 3% drift ratios.

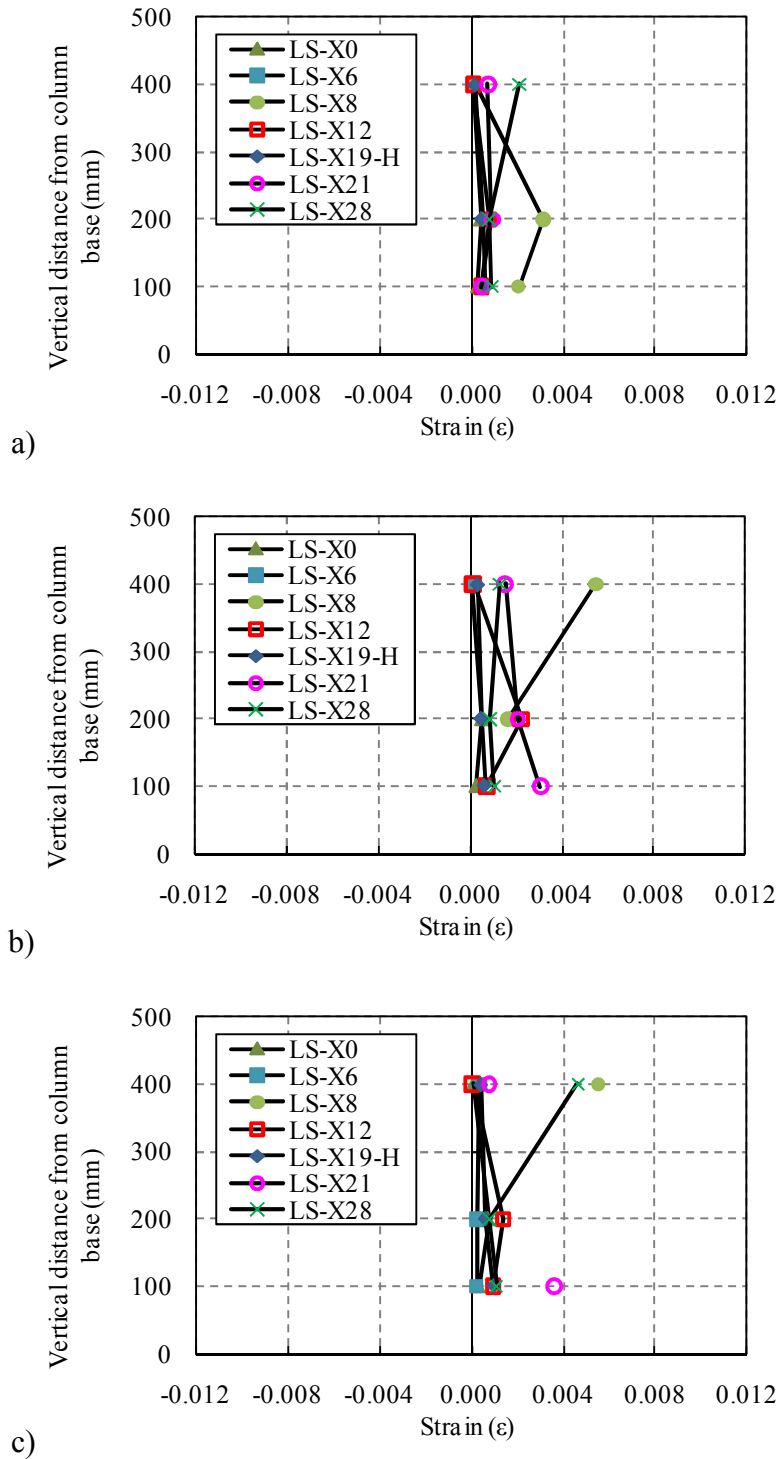


Figure 7.5 : Strain distribution of the starter bars at a) 1%, b) 2%, c) 3% drift ratios.

These strain values are measured at drift ratios of 1%, 2% and 3%. According to the strain measurements obtained by strain gauges, due to effect of slip, the reinforcing bars are not stressed remarkably in the case of specimens with low level corrosion. As seen in Figure 7.5, the strains were higher in case of specimens with more corroded reinforcing bars. On the other hand, the tensile strains of the starter bars of

LS-X21 and LS-X28 reached the yield strain due to bond resulting from corrosion products. None of the longitudinal bars yielded. The longitudinal bars of LS-X12 and LS-X28 reach the yield strain due to bending caused by buckling (Figure 7.6). Moreover, only the transverse steel bars of LS-X8 yielded.

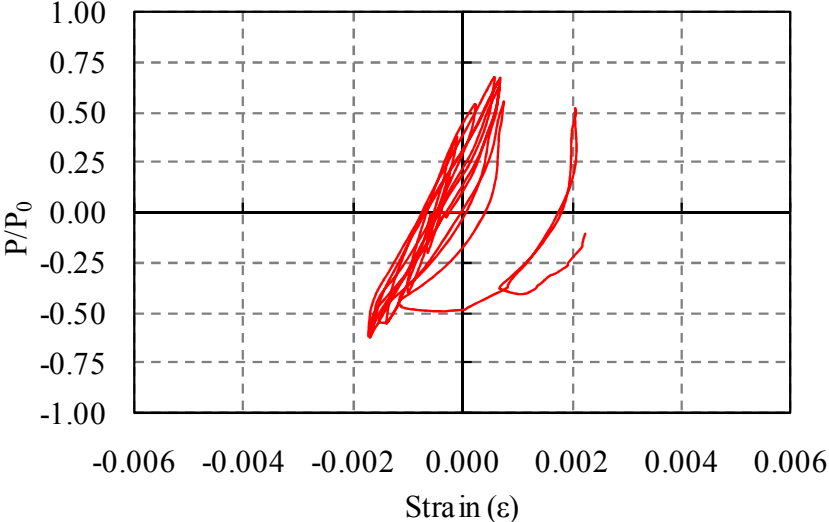
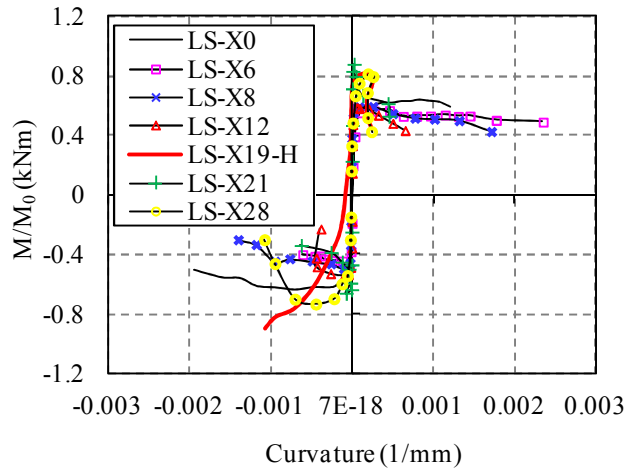


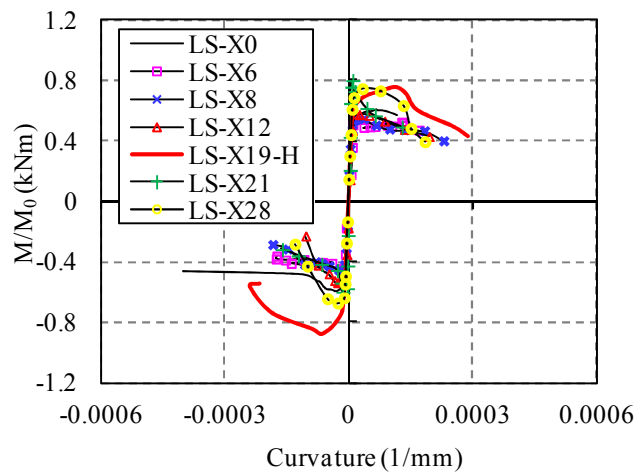
Figure 7.6 : Tensile strains due to bending caused by buckling.

Moment-curvature relationships obtained for different gauge lengths are shown in Figure 7.7. In this figure, M is the moment which is calculated by using Eq. (5.1) under the consideration of second-order effects and M_0 is the theoretical flexural capacity of the specimen determined without considering the effect of corrosion. The curvature values of the column measured in 150 mm and 300 mm gauge length above the footing are in the order of 10^{-5} (1/mm), while the curvatures measured in 20 mm gauge length are in the order of 10^{-3} (1/mm).

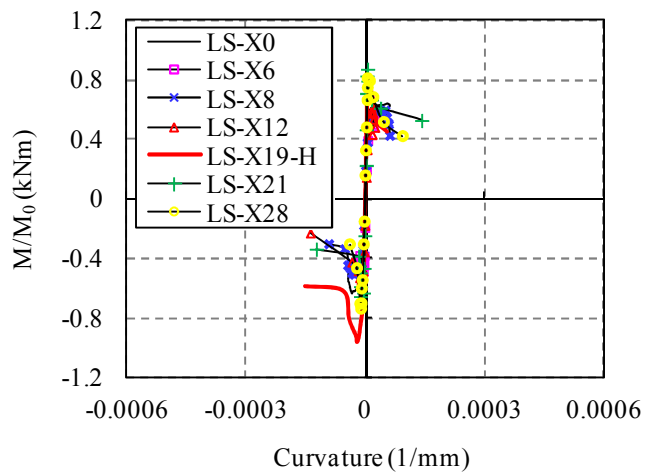
The drawing which shows the calculation of energy dissipation capacity and energy dissipation capacities of the first and the third type specimens are presented in Figure 7.8. As seen in this figure, the energy dissipation capacities of the specimens LS-X0 without corrosion and specimens with minimal corrosion (LS-X6 and LS-X8) are similar, the energy dissipated by the LS-X21 is the lowest while LS-X19-H and LS-X28 are remarkably higher due to their significantly higher flexural strength.



a)



b)



c)

Figure 7.7 : Moment-curvature relationships obtained for different gauge lengths a) Gauge length between 0-20 mm, b) Gauge length between 20-150 mm, c) Gauge length between 150-300 mm.

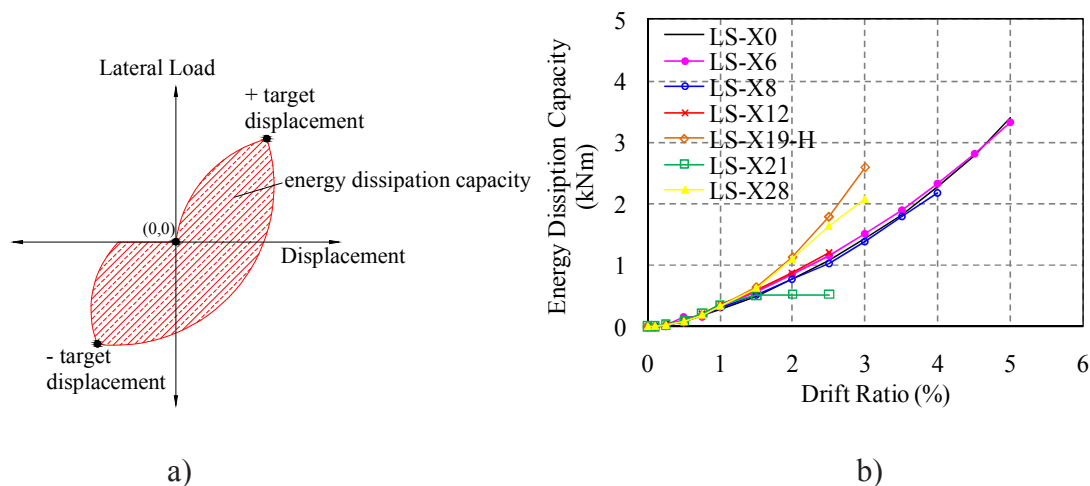


Figure 7.8 : a) Calculation of energy dissipation capacity, b) Energy dissipation capacity of the first and the third type specimens.

The failure mechanisms of the first and the third type specimens are presented in Table 7.1.

Table 7.1 : Failure mechanisms of the first and the third type specimens (The numbers given in Table are the drift ratios).

Failure mechanisms	Specimens						
	LS-X0	LS-X6	LS-X8	LS-X12	LS-X19-H	LS-X21	LS-X28
First flexural crack	0.50%	0.75%	0.75%	-0.50%	0.50%	0.75%	0.75%
Yielding of longitudinal bar	-	-	-	-	-	-	-
Yielding of starter bar	-	-	1.00%	1.50%	4.00%	1.50%	0.75%
Yielding of transverse bar	-	-	-2.50%	-	-	-	-
Crushing of concrete cover	2.50%	2.50%	2.00%	0.75%	1.50%	-1.00%	-1.50%
Spalling of concrete cover	3.50%	3.00%	2.50%	2.00%	2.00%	1.50%	2.00%
Buckling of longitudinal bar	-	-	-	-3.00%	-	-2.00%	2.50%
Fracture of longitudinal bar	-	-	-	-	-	-	-
Maximum strength while pushing	3.5 %	0.5 %	1.5%	0.75%	3.0%	1.00%	1.50%
Strength loss with respect to maximum load at 3% drift ratio	0%	7.14%	15.43%	28.39%	0%	41.06%	38.74%

The test results, including the the maximum load, displacement corresponding to maximum load (P_{max} and δ_{max}) and the displacement ductility factor μ_{δ} are given in Table 7.2. The displacement ductility factor μ_{δ} is defined as the ratio between the

ultimate displacement, δ_u and δ_{max} . The ultimate displacement is defined as the displacement corresponding to the displacement at which the applied load dropped to 85% of the maximum load.

Table 7.2 : Test results of the first and the third type specimens.

Specimens	$\delta@P_{max}$ (kN)	δ_{max} (mm)	δ_u (mm)	μ_δ
LS-X0	17.41	42		
LS-X6	17.90	6	57	9.5
LS-X8	15.96	18	36	2
LS-X12	15.90	9	28	3.1
LS-X19-H	19.30	18	45	2.5
LS-X21	23.11	12	23	1.9
LS-X28	20.53	18	30	1.6

As it can be seen from the figures of the crack patterns (Appendice E), supporting the measurements, the damage was accumulated especially in 25-35 mm high zone of the column from top of the base (footing) in specimens LS-X0, LS-X6, LS-X8 indicating slip. The damage started to distribute with increasing corrosion in specimen LS-X12 and fully distributed in specimens with remarkably high corrosion (LS-X19-H, LS-X21, LS-X28). In all first type specimens, it is possible to observe vertical cracks initiated at the tips of the lap spliced bars, which were formed due to compression. The concrete cover, subjected to compression, crushed and eventually spalled. The cracks, which started as a flexural crack and continued as a shear crack, do not propagate deep inside the width of the specimens. Another evidence that these cracks do not result from shear is that the first and the third type specimens did not even reach their theoretical flexural capacity (Figure 4.4).

The longitudinal bars of specimens LS-X12, LS-X21, LS-X28 “buckled during the test. This maybe due to the fact that 1) Longitudinal bars elongate upwards during pushing but the axial load on the opposite direction constrains this deformation. These opposite forces result in buckling of longitudinal bars, 2) Since the bars had undergone high level of corrosion, initial vertical cracks formed due to corrosion before testing resulting in earlier spalling of concrete cover and insufficient transverse bars during the testing. Since the concrete cover spalled completely at the lap splice region, the starter bar slipped in the damaged zone and did not buckle.

7.2 Test Results of the Second Type Specimens

The envelopes of load-displacement curves for the second type specimens are shown in Figure 7.9.

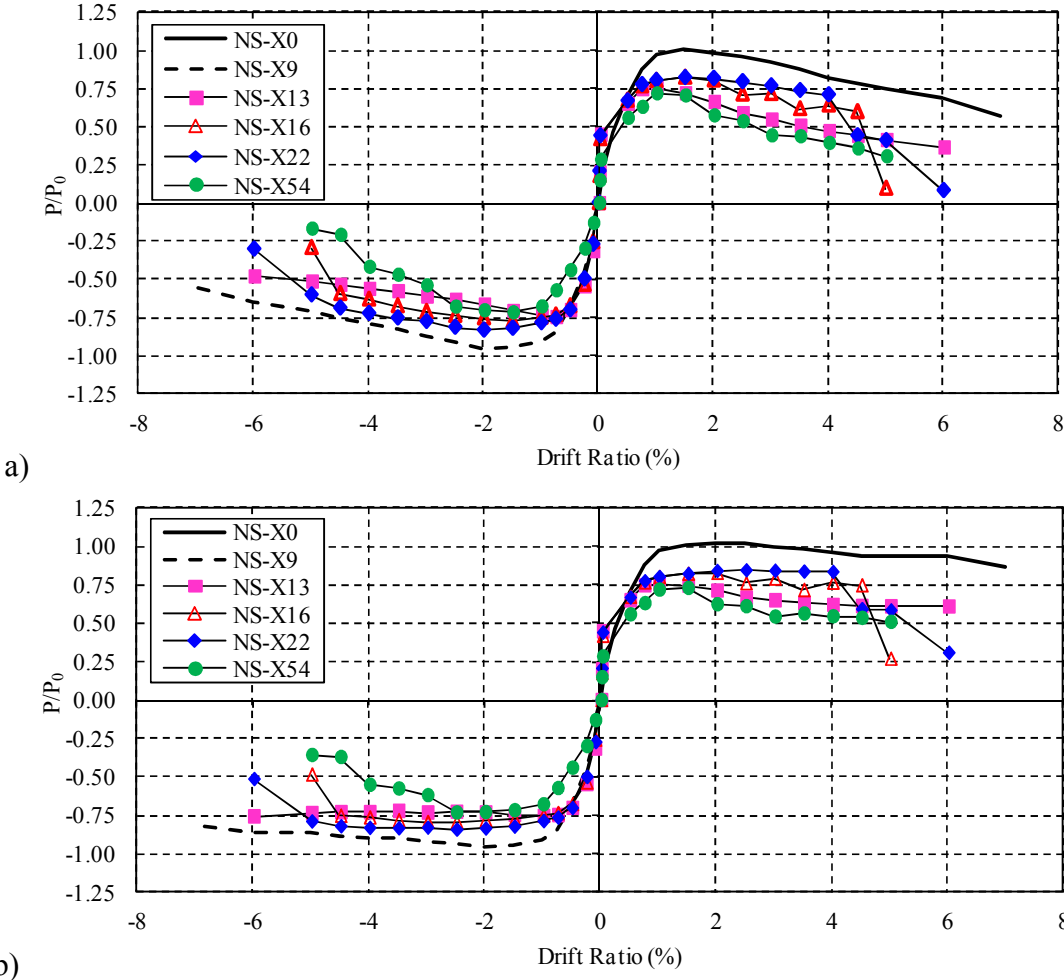


Figure 7.9 : Envelopes of the load-displacement curves for the second type specimens a) without considering $P-\Delta$ effects, b) considering $P-\Delta$ effects.

In this figure, P is the applied lateral load and P_0 is the theoretical lateral load capacity of the specimen determined without considering the effect of corrosion. As seen in this figure, reference specimen without corrosion and specimen with minimal corrosion reached their flexural capacity (≈ 52 KN). All the specimens with corroded reinforcing bars experienced strength degradation and gradually loss in deformation capacity when compared to the reference specimen. As seen from the load-displacement curves of specimens NS-X0 and NS-X9, there is difference between the loads while pulling and pushing. This is because, the repair mortar did not bond with the existing concrete and performed early spalling in specimen NS-X0, while

the repair mortar was compacted better and performed well in specimen NS-X9. For this reason, the side with the better performance was taken into consideration in Figure 7.9.

The relationship of $\delta_{rupture}$, $\varepsilon_s/\varepsilon_{su}$, and p_L/p_{L0} with section loss is presented in Figure 7.10. In this figure $\delta_{rupture}$ is the displacement where the bar ruptures, ε_s is the strain of the reinforcing bar, ε_{su} is the ultimate strain of the reinforcing bar without corrosion, and p_L is the plastic hinge length, p_{L0} is the plastic hinge length of the column without corroded reinforcing bars.

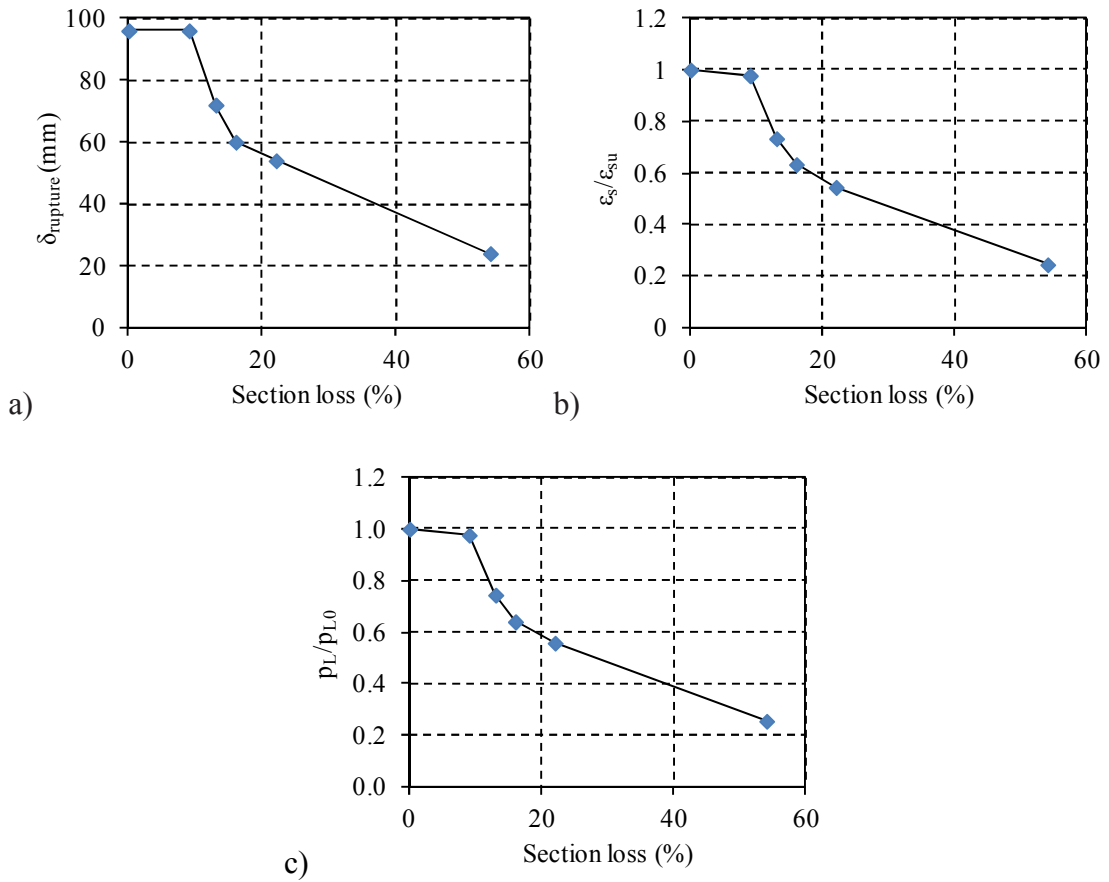


Figure 7.10 : Relationship of a) $\delta_{rupture}$, b) $\varepsilon_s/\varepsilon_{su}$, and c) p_L/p_{L0} with section loss.

As seen in Figure 7.10 a), based on test results, due to the cross-section losses resulting from corrosion, as the section loss increases, the reinforcing bar experienced early rupture. The same relationship can be obtained in case of $\varepsilon_s/\varepsilon_{su}$ (Figure 7.10 b). This relationship is obtained by dividing the displacements to the column height (rotations obtained), and by dividing the rotations to the plastic hinge length (curvatures obtained). The corresponding ε_s values are determined from the theoretical moment-curvature relationship with consideration of section loss. In order to explain in case of plastic hinge length, ultimate curvatures are obtained due to

moment-curvature relationship with the consideration of corrosion (Figure 7.10c). Then, the rotations were obtained from dividing displacement to column height, relationship is obtained by dividing the displacements to the column height (rotations were obtained), and by dividing the rotations to the ultimate curvatures (plastic hinge lengths were obtained).

The variation of ratios of residual plastic displacements (δ_{res}) to the displacement at which unloading began (δ_{un}) with respect to drift ratios are presented in Figure 7.11. As seen from the figure, δ_{res} of highly corroded specimen is less than δ_{res} of the other specimens. This is due to the fact that although all the specimens experienced flexural behavior, the behavior of the specimens with certain corrosion level did not perform well when considered with the specimens without corrosion and with minimal corrosion. Energy dissipation capacities of the second type specimens calculated as the area enclosed by the hysteresis loops, are presented in Figure 7.12.

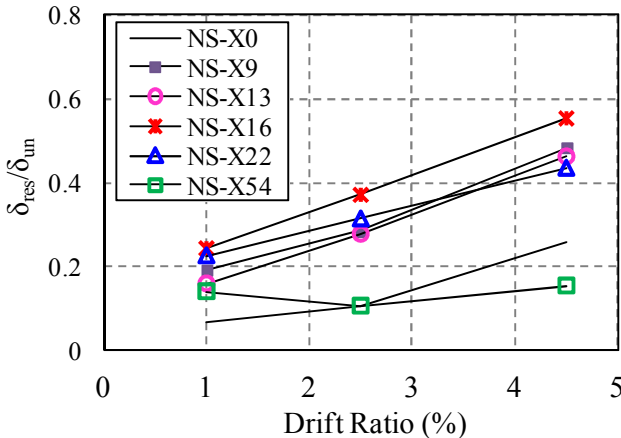


Figure 7.11 : The variation of residual displacement for the second type specimens.

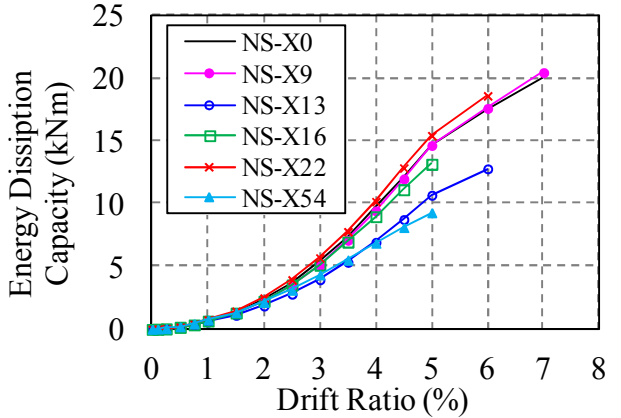


Figure 7.12 : Energy dissipation capacity of the second type specimens.

As seen in this figure, while the energy dissipation capacities of the specimens NS-X0 without corrosion and specimen with minimal corrosion (NS-X9) are similar, the energy dissipated by the most corroded specimen (NS-X54) is the lowest due to its remarkably lower flexural strength and drift capacity.

The variations of axial strains of longitudinal bars and starter bars at different locations are presented in Figure 7.13 and Figure 7.14. These strain values were measured at drift ratios of 1%, 3% and 4%. While the starter bars yielded in all specimens, column longitudinal bars did not yield in any of the specimens indicating that stresses in the column reinforcement were transferred to starter bars around a zone of smaller moments rather than maximum moment zone. While the tensile strains in the base of the specimen NS-X0 were distributed and strains higher than yield strain, and the strains at the same location were much smaller in specimens with corroded reinforcement. The strain values were less in case of specimens with corrosion and gradual degradation was experienced. On the other hand, only the transverse steel bars of NS-X9 yielded.

Moment-curvature relationships obtained for different gauge lengths are shown in Figure 7.15. In Figure 7.15, M is the moment which is calculated by using Eq. (5.1) under the consideration of second-order effects and M_0 is the theoretical flexural capacity of the specimen determined without considering the effect of corrosion. Furthermore, distribution of curvatures, as seen in Figure 7.15, shows that the damage is localized in cases of corroded specimens. This may be attributed to the gradual loss of bond in case of corroded specimens with increasing drifts, causing more pinched hysteresis curves resulting in smaller energy dissipation capability compared to specimen NS-X0.

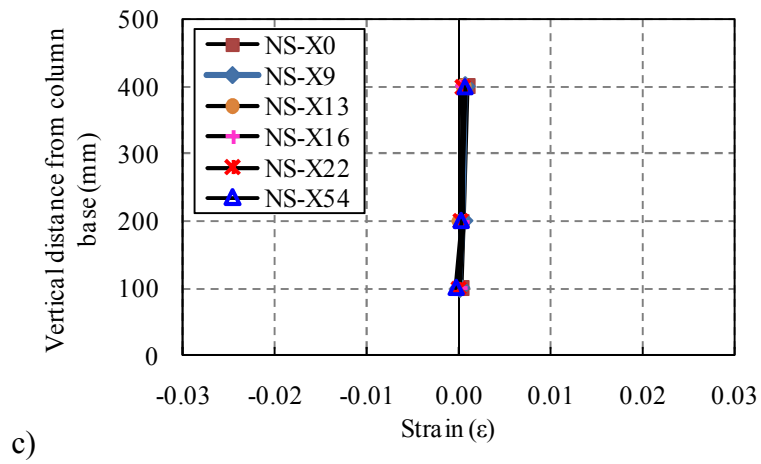
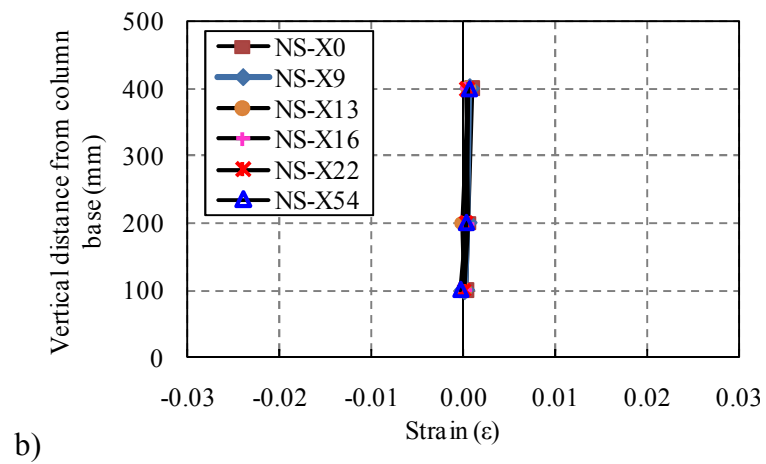
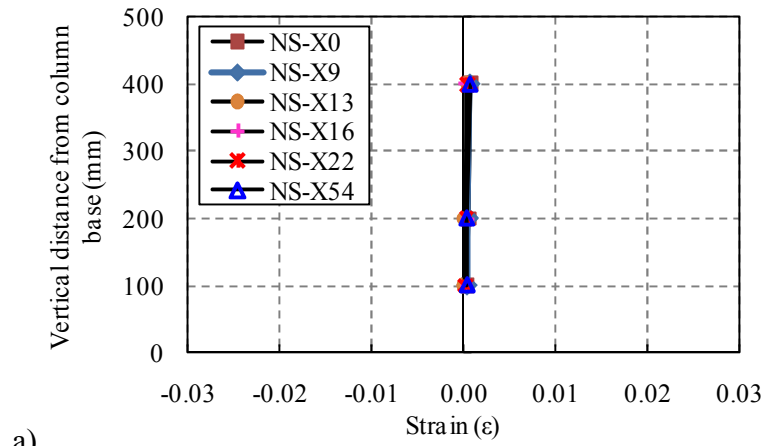
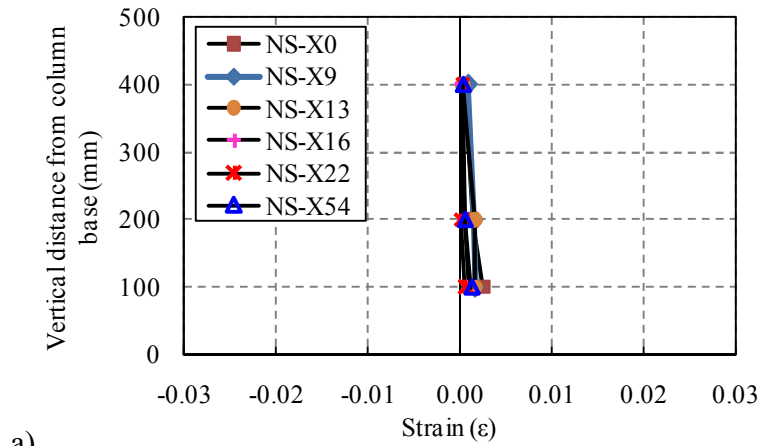
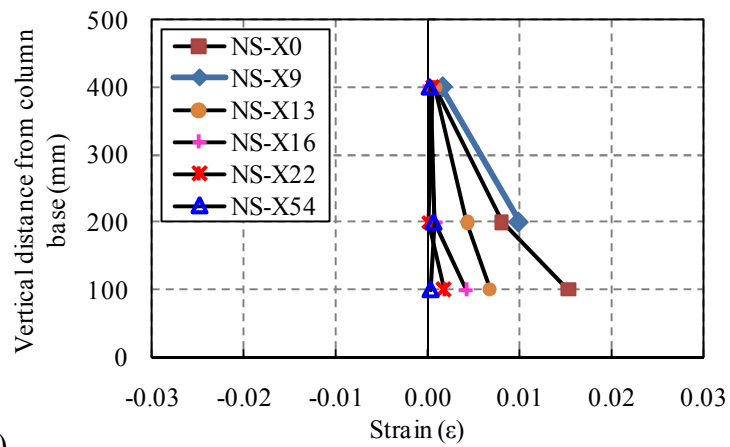


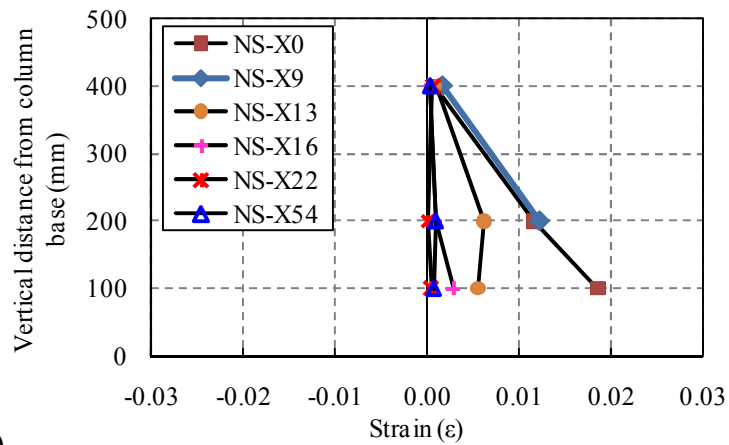
Figure 7.13 : Strain distribution of longitudinal reinforcing bars at a) 1%, b) 3%, c) 4% drift ratios.



a)



b)



c)

Figure 7.14 : Strain distribution of the starter bars at a) 1%, b) 3%, c) 4% drift ratios.

The failure mechanisms of the second type specimens are presented in Table 7.3. As seen from Table 7.3, the tensile bars were fractured gradually due to corrosion. The early fracture of reinforcing bars of specimens may be related with two main

observations; 1) The damage was more localized in these specimens causing larger reinforcement strains in smaller lengths of column starter bars, which may result with higher strains in smaller drifts, 2) Damage of column starter bars at the base of the column, where was the most susceptible zone to the corrosion damage. Smaller diameter of starter bars due to corrosion may result accumulation of excessive lateral displacements around the corroded zone while the strains are not as high in other parts. It should be noted that no premature failure due to buckling of compression bars was observed due to closely spaced transverse bars. It is interesting to note that corrosion of longitudinal bars did not prevent the transfer of tensile stresses from column bars to starter bars even though initial vertical cracks had occurred before testing. Even after application of lateral loads and reaching significant drifts (around 4%) the increase of these damages was not accompanied with a bond failure at the lap splices of longitudinal bars.

The test results, including the the maximum load, displacement corresponding to maximum load (P_{max} and δ_{max}) and the displacement ductility factor μ_{δ} are given in Table 7.4. The displacement ductility factor μ_{δ} is defined as the ratio of the ultimate displacement, δ_u to δ_{max} . The ultimate displacement is defined as the displacement corresponding to the displacement at which the applied load dropped to 85% of the maximum load. As seen from table, μ_{δ} decreases gradually with the increasing section loss.

While the damage was distributed in reference specimen NS-X0 and specimen with minimal corrosion (NS-X9), the damage was localized to the interface of column and footing in the case of other highly corroded specimens. No shear crack and vertical cracks initiated at the tips of the lap spliced bars were observed.

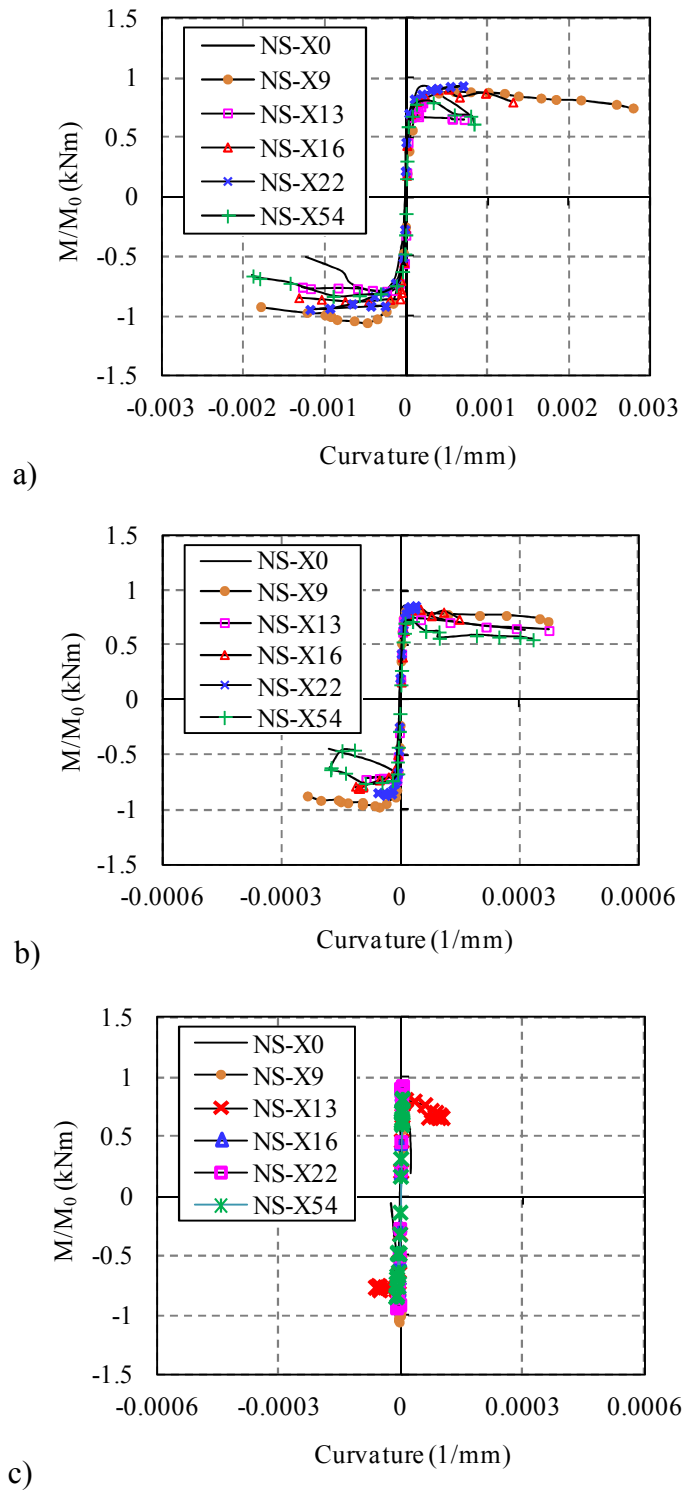


Figure 7.15 : Moment-curvature relationships obtained for different gauge lengths
 (a) Gauge length between 0-20 mm, (b) Gauge length between 20-150 mm, (c) Gauge length between 150-300 mm.

Table 7.3 : Failure mechanisms of specimens (The numbers given in Table are the drift ratios).

Failure mechanisms	Specimens					
	NS-X0	NS-X9	NS-X13	NS-X16	NS-X22	NS-X54
First flexural crack	0.5%	0.5%	0.5%	0.5%	0.5%	0.75%
Yielding of longitudinal bar	-	-	-	-	-	-
Yielding of starter bar	1%	1.5%	1.5%	2.5%	3.5%	2.5%
Yielding of transverse bar	-	-4.5%	-	-0.75%	-	-
Crushing of concrete cover	1%	2.5%	1.5%	1%	2.5%	1%
Spalling of concrete cover	1.5%	-2.5%	2%	1.5%	4.5%	2%
Buckling of longitudinal bar	-	-	-	-	-	-
Fracture of longitudinal bar	8%	-8%	-6	5%	4.5%	2%
Maximum strength while pushing	2.0%	2.0%	1.5%	2.0%	2.5%	1.5%
Strength loss with respect to maximum load at 4.5% drift ratio	7.2%	7.0%	17.8%	9.8%	30.0%	26.7%

Table 7.4 : Test results of the second type specimens.

Specimens	P_{max} (kN)	$\delta@P_{max}$ (mm)	δ_u (mm)	μ_δ
NS-X0	56.92	24	84	3.5
NS-X9	45.73	24	96	4.0
NS-X13	42.39	18	42	2.3
NS-X16	46.43	24	42	1.7
NS-X22	47.35	30	51	1.7
NS-X54	40.95	18	24	1.3

7.3 Contribution of Displacement Components to the Lateral Displacement of Columns

The lateral displacement of the columns are assumed to be resulting from flexure (when a lateral load is applied to the column and a lateral displacement occurs at the end of the column since there are no end restraints against horizontal displacement), shear (when applied lateral load produces shear stresses at the end of the column) and the slip of the longitudinal reinforcement in the support (when the bars are fully anchored in the footing, strain penetration occurs along the part of the bar due to the force transfer between the bars and the concrete in the support) (Lehman and Moehle, 2000) (Figure 7.16).

The displacement components corresponding total displacements of the first and the second type specimens are shown in Figure 7.17 and Figure 7.18, respectively. According to Figure 7.17, the cyclic behaviors of the reference specimen and the specimens with minimal corrosion (LS-X0, LS-X6, LS-X8 and LS-X12) were dominated by slip while the cyclic behaviors of LS-X21 and LS-X28 were

dominated by flexure. In specimens with plain bars, the behavior is expected to be dominated by slip due to poor bond mechanism of plain bars. The flexure dominated behavior of specimens LS-X21 and LS-X28 maybe attributed to the effect of corrosion products at the concrete-bar interface, which increase the bond strength of plain bars. According to Figure 7.18, the cyclic behaviors of all second type specimens were dominated by flexure.

The displacement due to flexure is obtained from LVDT's both at 20-150 and 150-300 mm. Firstly, strains are found from the differences between the data of LVDT's placed on the opposite sides of the column, then strains are converted to curvatures by dividing the strains to the distance between LVDT's. The curvatures are converted to rotations by multiplying with plastic hinge length. The rotations are converted to displacements by multiplying with column height. The displacement due to shear is obtained by Eq. (7.1) and Eq. (7.2). The displacement due to slip is obtained from LVDT's at 0-20 mm similar to that due to flexure. The elastic displacement resulting from elastic bending, $\delta_{elastic}$, is obtained by Eq. (7.3). In the equations, A is cross-section area of the column, E is elastic modulus, G is shear modulus, L is column height, P is the lateral load, I is the moment of inertia and ν is the poisson's ratio.

$$\delta_{shear} = \frac{P}{A \cdot G} \cdot L \quad (7.1)$$

$$G = \frac{E}{2(1+\nu)} \quad (7.2)$$

$$\delta_{elastic} = \frac{PL^3}{3EI} \quad (7.3)$$

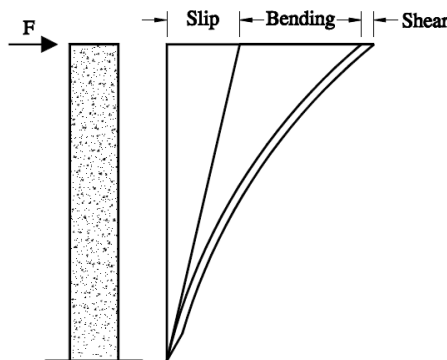


Figure 7.16 : Displacement components for a cantilever column (Lehman and Moehle 2000).

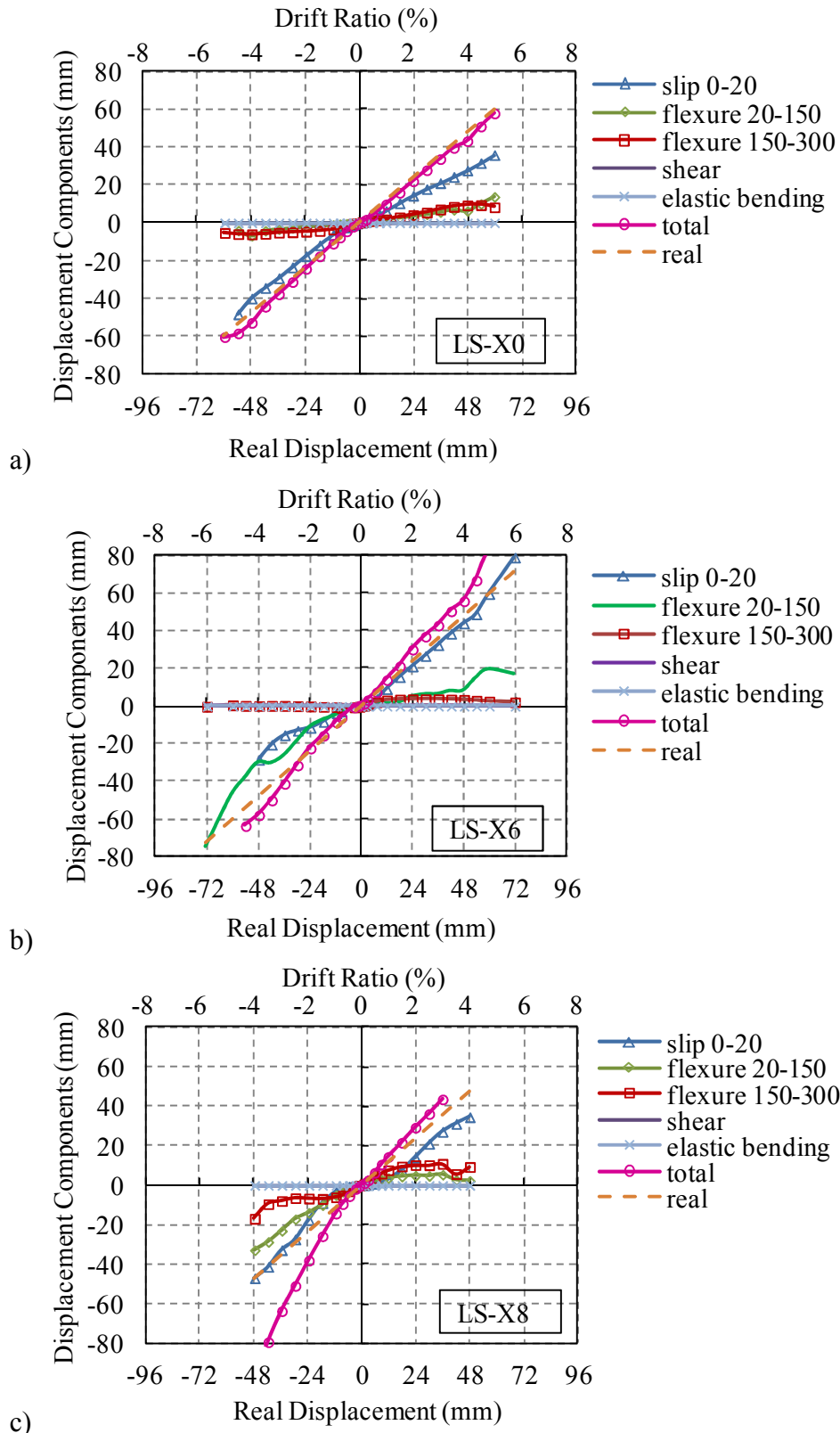
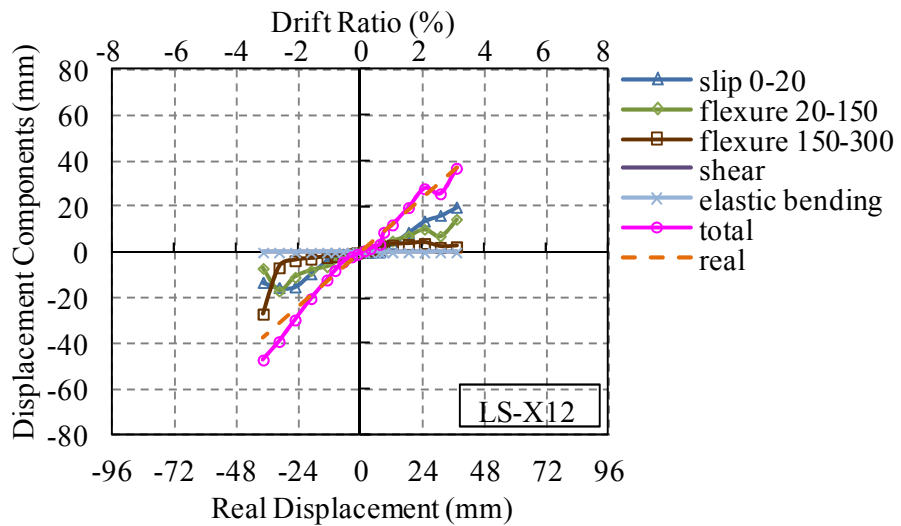
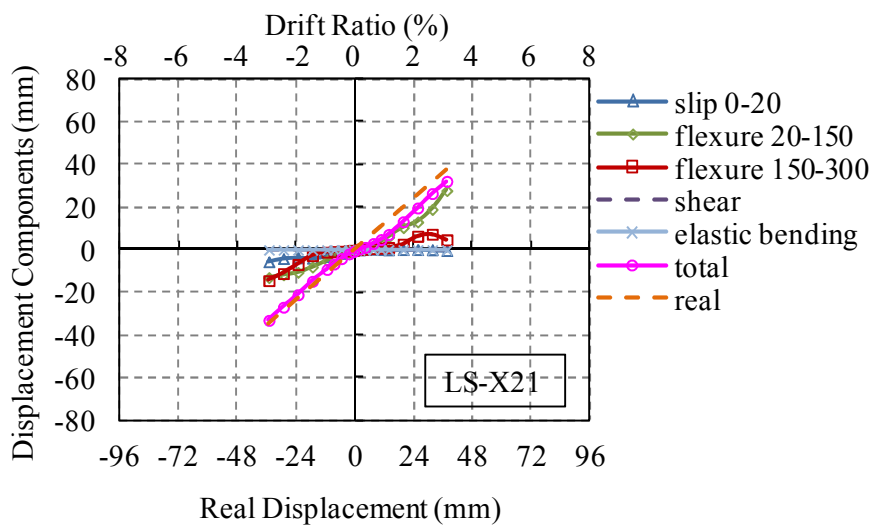


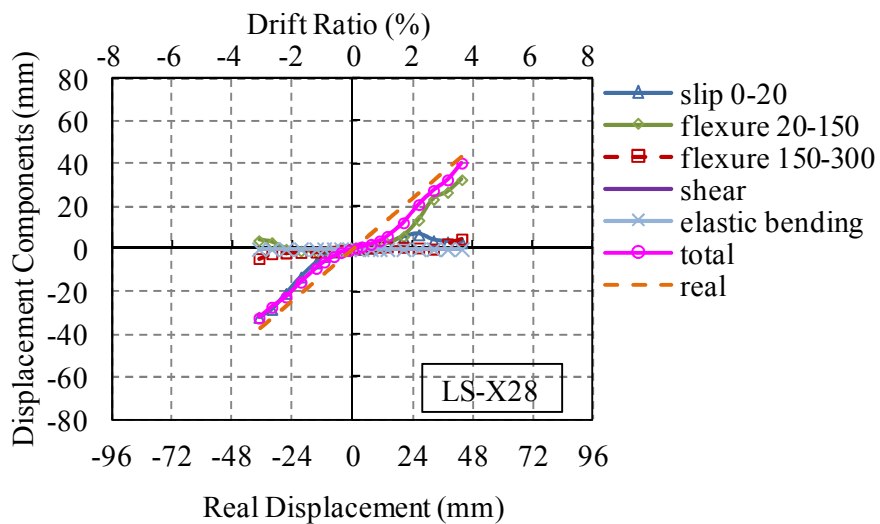
Figure 7.17 : Displacement components against total displacements of the specimens a) LS-X0, b) LS-X6, c) LS-X8, d) LS-X12, e) LS-X21, f) LS-X28.



d)



e)



f)

Figure 7.17 (contd.) : Displacement components against total displacements of the specimens a) LS-X0, b) LS-X8, c) LS-X6, d) LS-X12, e) LS-X21, f) LS-X28.

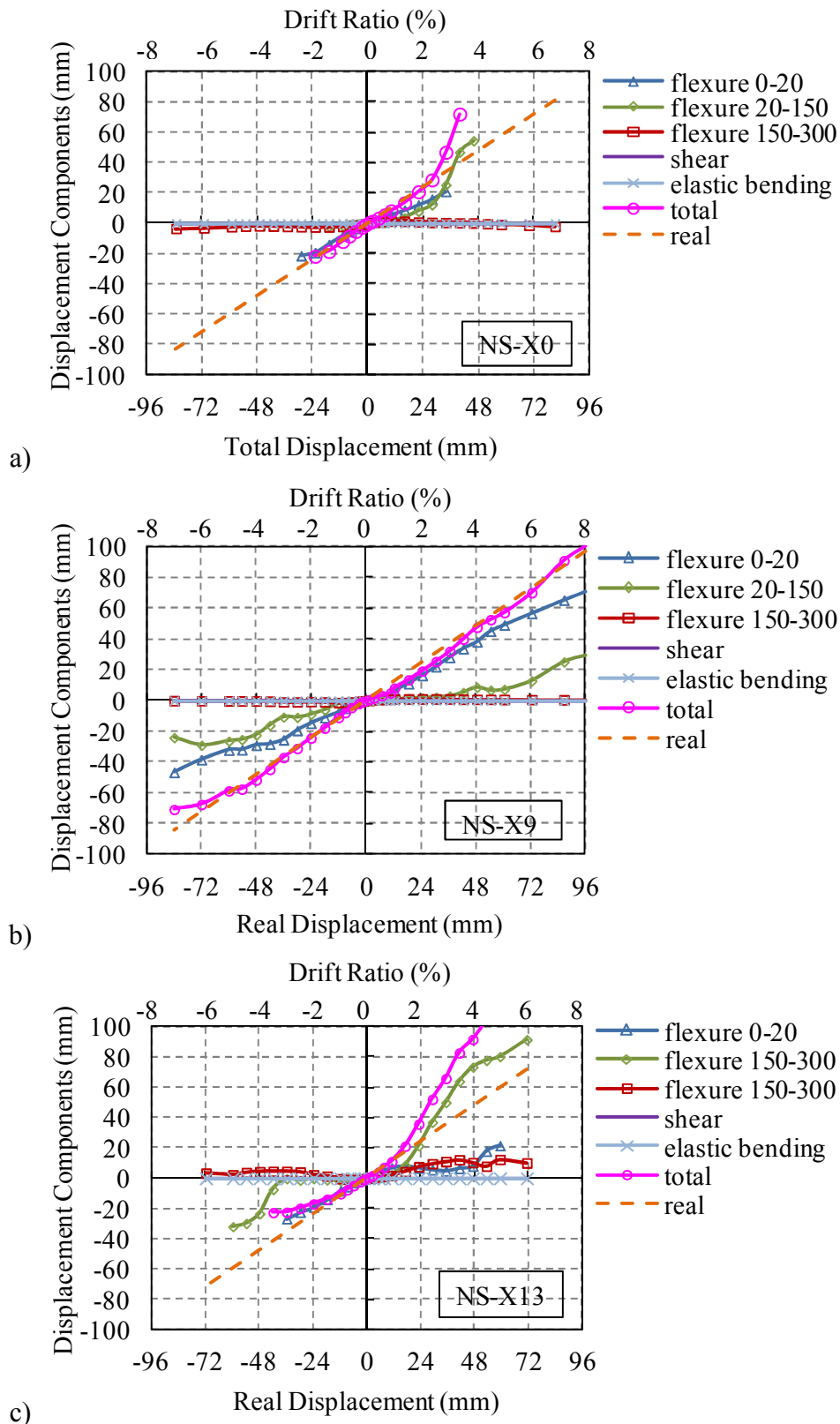


Figure 7.18 : Displacement components against total displacements of the second type specimens a) NS-X0, b) NS-X9, c) NS-X13, d) NS-X16, e) NS-X22, f) NS-X54.

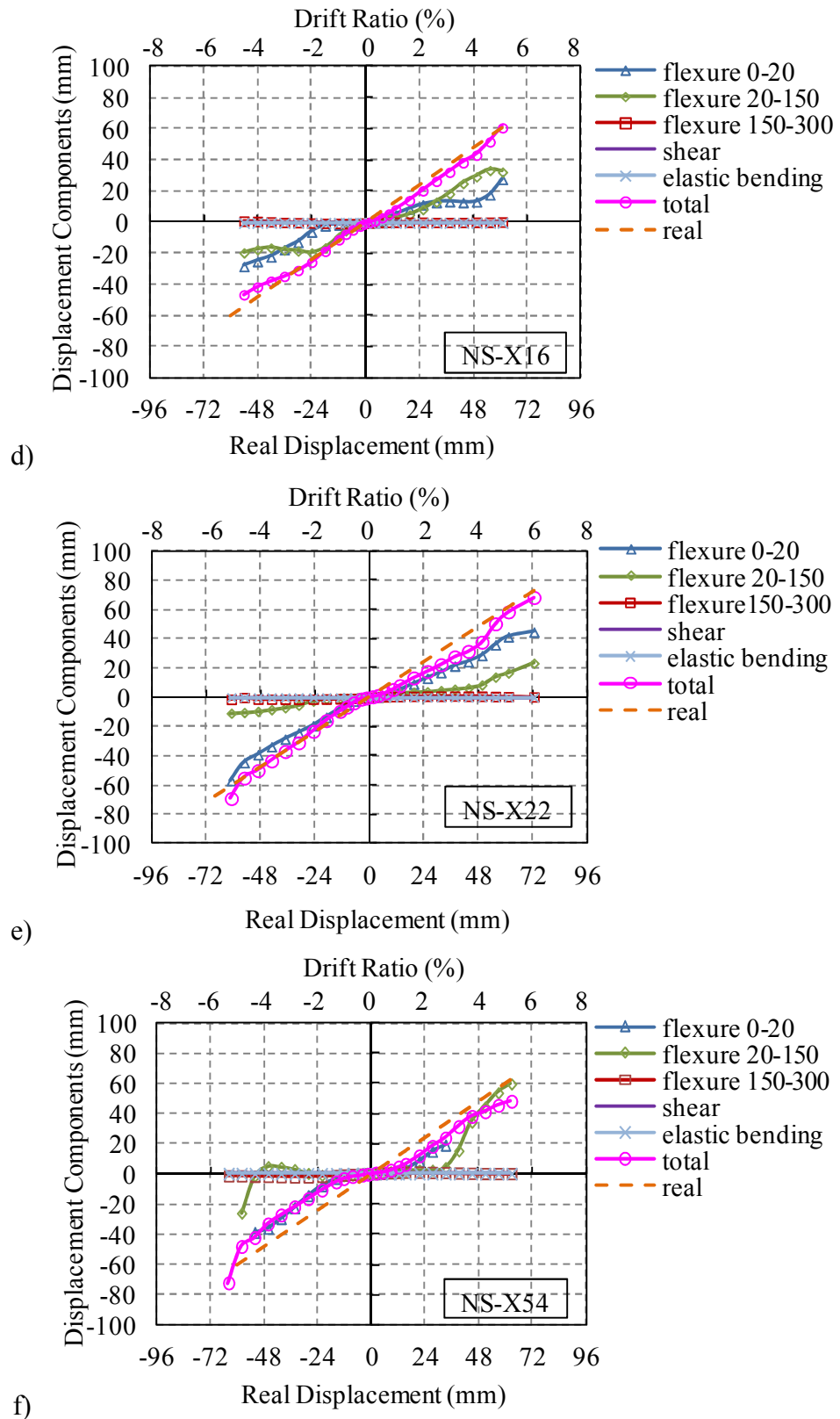


Figure 7.18 (contd.) : Displacement components against total displacements of the second type specimens a) NS-X0, b) NS-X9, c) NS-X13, d) NS-X16, e) NS-X22, f) NS-X54.

The displacement components against total displacements of the third type specimen are shown in Figure 7.1, which is dominated by flexure.

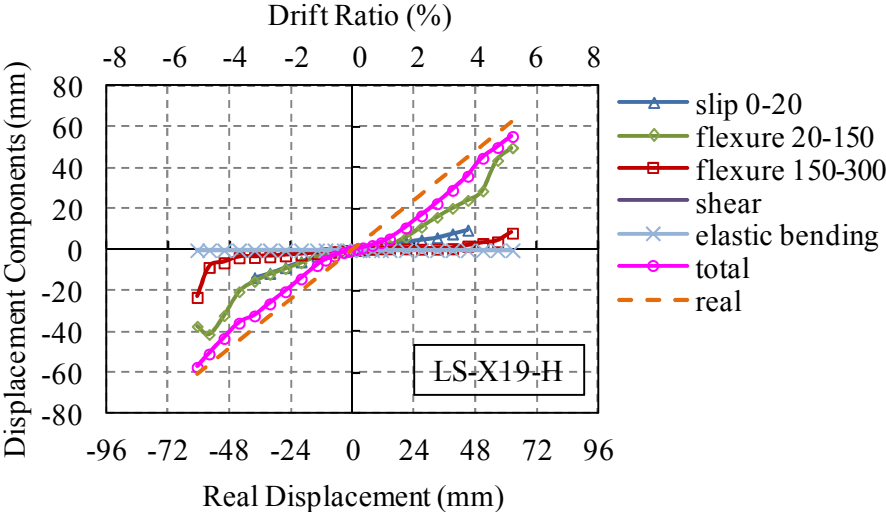


Figure 7.19 : Displacement components against total displacements of the third type specimen.

The strain-drift ratio relationship of specimens and the views and crack patterns of specimens are given in Appendix D and E, respectively.

8. ANALYTICAL STUDY

8.1 The Effect of Bond Mechanism on the Seismic Performance of Low Strength RC Columns with Corroded Plain Reinforcing Bars

As described in Chapter 3, it has been shown that up to a certain limit, the bond strength increases as the corrosion increases (CEB-FIB, 2000; Coronelli, 2002; Stanish, 1999; Fang et al., 2004; Fang et al., 2006; Al-Sulaimani et al., 1990; Wang and Liu, 2008; Auyeung, 2000). Fang et al. 2004 reported that, bond strength of smooth reinforcing bars increased with increasing corrosion level. The bond stress variation with corrosion level, which is defined as loss in cross-section, is presented in Figure 8.1. As seen from the figure, at section losses higher than 12%, bond stress increases due to the yielding of reinforcing bars of specimens LS-X21 and LS-X28 which results from corrosion products at the surface of the bars. The bond stresses obtained from Eq. (8.1) and Eq. (8.2) for section losses of 0-12% and 13-25%, respectively.

$$\tau = 0.15\sqrt{f_{ck}} \quad (8.1)$$

$$\tau = \frac{\sigma_s \cdot d_b}{4 \cdot l_b} \quad (8.2)$$

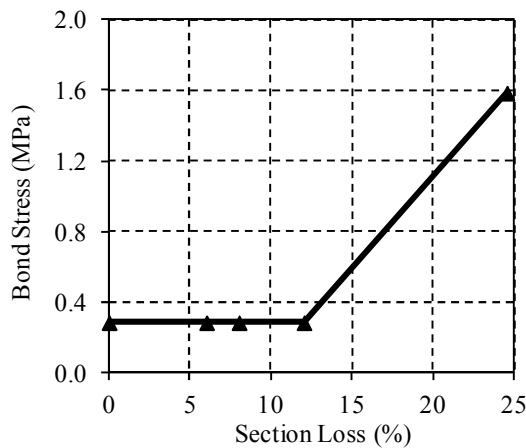


Figure 8.1 : Bond stress variation with corrosion level.

Slip behavior was clearly observed on specimens LS-X0 and LS-X6. Furthermore, slip behavior was observed on specimens LS-X8 and LS-X12. The strain gauges on starter bars at 100 mm (LS-X8) and 200 mm (LS-X12) shows that the starter bars yielded. It should be noted that the strain gauges were just on one starter bar. As the specimens LS-X8 and LS-X12 did not reach their theoretical strength, the strains obtained from strain gauges of these specimens did not increase as expected. Furthermore, among the displacement components of the total displacement, slip displacement dominates the overall behavior of specimens LS-X8 and LS-X12 (Figure 7.17).

The bond-slip behavior is simulated using single bar model. Single bar was used to model the influence of slip along the splice length of the column by Reyes (1999) and Cho and Pincheira (2005). In their model, the single bar consists of truss element to represent the reinforcing bar and uniaxial zero length spring elements represent the bond between the concrete and reinforcing bar along a discrete length dx . In the study of Harajli et al. (2004) and Reyes (1999), where one, four, ten, one-hundred elements were used, the results show that the number of local bond stress-slip elements affect the overall response of models. Using only one zero-length bond-stress slip element yielded substantially different response compared to four, ten or one hundred elements in which similar responses were obtained.

In the proposed single bar model, the bar of 560 mm length (lap splice length of starter bars), is divided into 10 segments. A nonlinear link is defined between the segments to represent the local bond resistance on the surface of the bar (Fig. 8.2a). Then the force-slip relation was assigned to the links and pullout analysis was performed on a single bar. The force due to slip is defined by Eq. (8.3). In Eq. (8.3), τ is the bond stress for plain bars obtained from CEB-FIB (1990), ϕ is the diameter of the reinforcing bar, l_b is the lap splice length of starter bar. The first branch of the force-slip relationship is used as described in CEB-FIB (1990). The second branch of the force-slip relationship is obtained from the test results of specimens in which slip dominated the behavior. The analytical bond stress-slip relationship in CEB-FIB (1990) and the proposed model are presented in Figure 8.3. The α values are 0.01, 0.02, 0.03 for specimens LS-X6, LS-X8 and LS-X12, respectively. The force-slip deformation relationship was obtained (Figs. 8.4a-d). As seen from the figure, the theoretical and experimental force-slip relationships are compared and a good

agreement between the experimentally measured and predicted overall force-displacements were obtained. The elastic deformations are removed from the displacement due to slip.

$$F_{slip} = \tau \cdot \pi \cdot \phi \cdot l_b \quad (8.3)$$

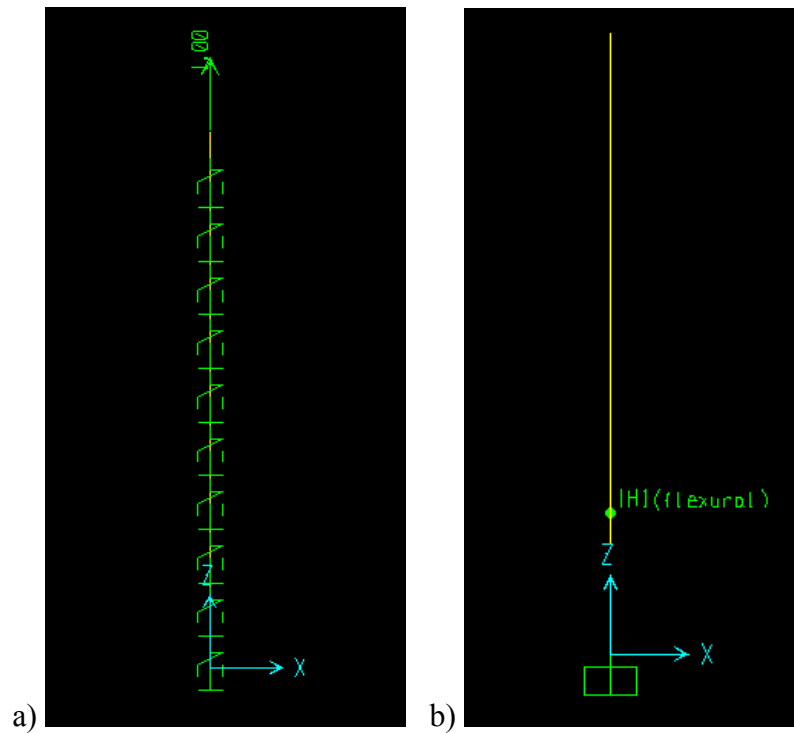


Figure 8.2 : SAP 2000 models used in analytical predictions a) Single bar model with link elements for slip dominated specimens, b) Column model for flexure dominated specimens.

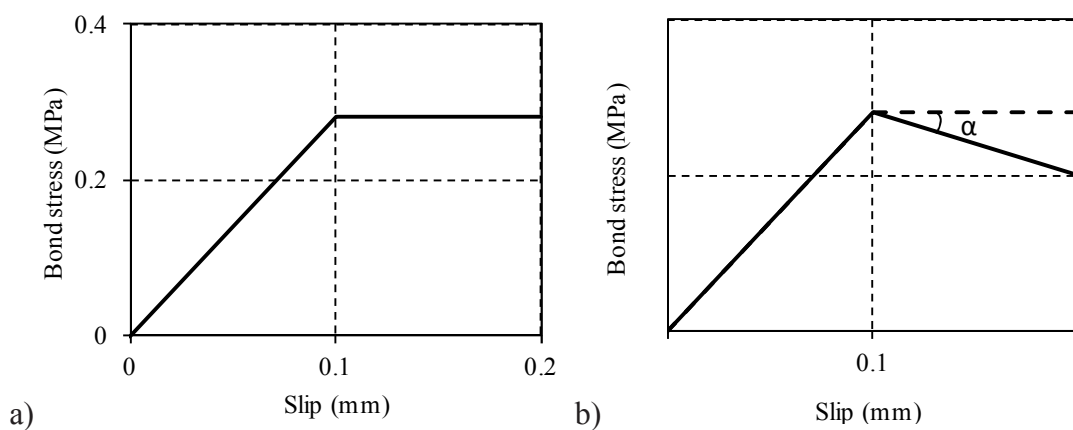


Figure 8.3 : Analytical bond stress-slip relationship a) CEB-FIB, 1990 model, b) Proposed model.

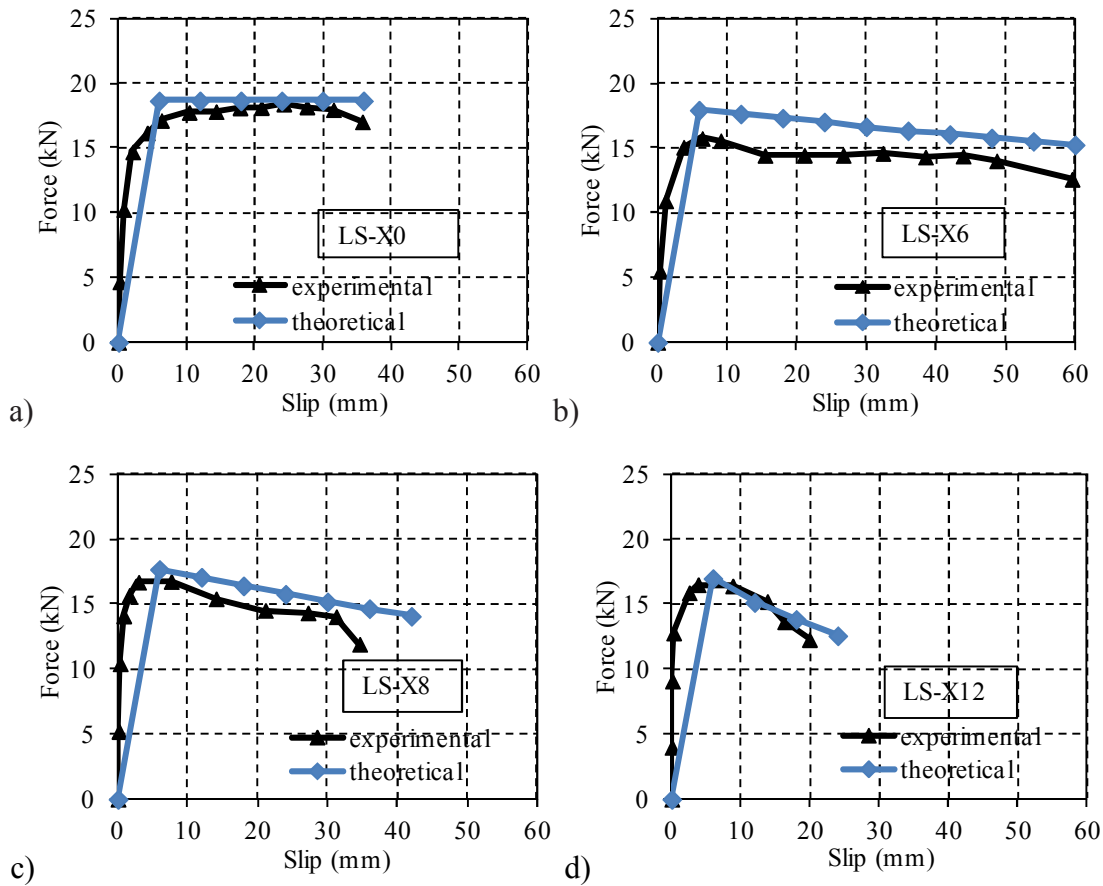


Figure 8.4 : Experimental and analytical considerations of slip dominated specimens.

The flexural responses of the columns are modeled using a cantilever column model consisting of nonlinear moment-rotation hinge assuming plasticity is concentrated at the column base and curvature is distributed linearly over the remainder of the column height as shown in the study by Melek (2006) (See Fig. 8.2b). The column with flexural hinges at the column base were defined with SAP2000 for the specimens LS-X21 and LS-X28 in which flexure dominated the behavior due to the strong bond resulting from the corrosion. The moment-curvature relationship was obtained by XTRACT (2007) cross-section analysis software. The curvatures were converted to rotation by multiplying with the plastic hinge length. Plastic hinge length is assumed to be $h/2$ (150 mm) as proposed by TSDC (2007), where h represents the effective depth of cross-section of column in bending. Then the moment-rotation relationship was assigned to flexural hinges and pushover analysis was performed (Figs. 8.5a-b). In Figs. 8.5a-b, the theoretical and experimental force-displacement relationships are compared. As seen from figures, the theoretical and experimental force-displacement relationships are compared and a good agreement between the experimentally measured and predicted overall force-displacements

were obtained.

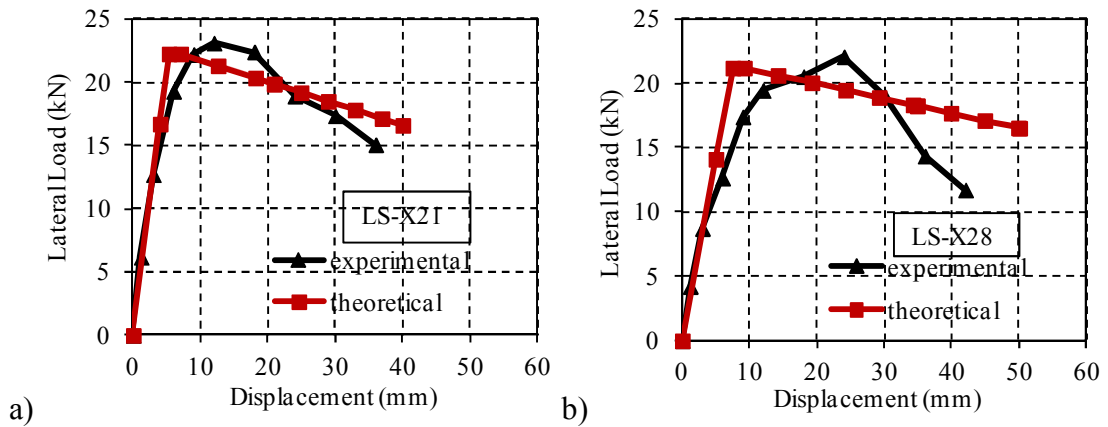


Figure 8.5 : Experimental and analytical considerations of the first type specimens.

The analytical and experimental moment-curvature relationships at the plastic hinge zone, the stress-strain relationships of confined concrete and tensile reinforcing bars are presented in Table 8.1 and Table 8.2. In these tables, the experimental moment-curvature relationship is obtained within 150 mm length from the bottom of the column. In Table 8.1 and Table 8.2, ϵ_{cc} compressive strain of core concrete, ϵ_s is the tension strain of reinforcing bar, respectively. As seen in these tables, the values of moments, curvatures and strains are given for two damage levels, namely A and B. These points are assumed to correspond to different structural performance levels of the column, such as moderate damage and severe damage, which correspond to maximum and ultimate points in the experimental moment-curvature relationship, respectively. When the experimental and analytical values of moments, curvatures and strains at these two different damage levels are compared, it is seen that there is a good agreement between experimental and predicted values. This comparison shows that as well as global load-drift relationship of the column, the local deformations and failure mechanism could also be predicted quite accurately by the algorithm presented.

Table 8.1 : Moment-curvature and stress-strain relationships of Point A and B of Specimen LS-X21.

		Point A	Point B
Analytical	Moment-curvature relationship		
	Concrete stress-strain relationship		
	Steel stress-strain relationship		
Experimental	Moment-curvature relationship		

Table 8.2 : Moment-curvature and stress-strain relationships of Point A and B of Specimen LS-X28.

		Point A	Point B
Analytical	Moment-curvature relationship		
	Concrete stress-strain relationship		
	Steel stress-strain relationship		
Experimental	Moment-curvature relationship		

The response predictions obtained using the proposed model are compared with the experimental results. Test data available on the corrosion of smooth bars is very limited. Fang et al. (2004) carried out pullout tests to evaluate the effects of corrosion on bond-slip behavior. The smooth reinforcing bars used in the study had yield strength of 289.6 MPa, tensile strength of 440 MPa with 20 mm diameter and 420 mm length. The strength of concrete is 52.1 MPa. The actual degree of corrosion was measured as the loss of weight of the reinforcement steel bar to that of the

reinforcing bars. The proposed model is used for the section loss of 6.8%. The comparison of proposed model with the experimental results are shown in Figure 8.6. As seen from Figure 8.6, the proposed model is capable of incorporating the force and slip behavior.

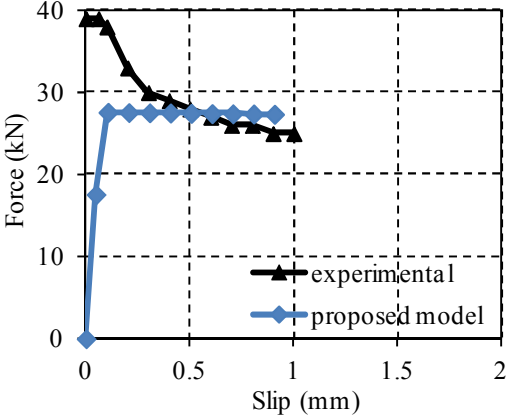


Figure 8.6 : Comparison of proposed model with the experimental results.

8.2 Analytical Study on the Seismic Performance of Normal Strength RC Columns with Corroded Deformed Reinforcing Bars

In the analytical phase of the study, the observed behavioral characteristics of the corroded bars are taken into account in the nonlinear analyses of RC columns to investigate the effects of corrosion of reinforcing bars on the inelastic behavior of RC columns subjected to lateral loads. The analysis results are then compared with experimental data. This comparison showed that the nonlinear behavior of RC columns with the corroded bars can accurately be predicted by the presented analytical algorithm up to very large displacement levels.

For studying the effects of behavior of corroded reinforcing bars on the flexural performance of RC columns, a sample column is analyzed by utilizing fiber element approach and plastic hinge concept.

8.2.1 Analyzed member

The analyzed RC column is rectangular in cross-section, the depth and width of the column are 300 and 200 mm, respectively. The cantilever column with the total height of 1400 mm is supported by a singular footing, which is assumed to be a fixed support in the analyses (Figure 8.7).

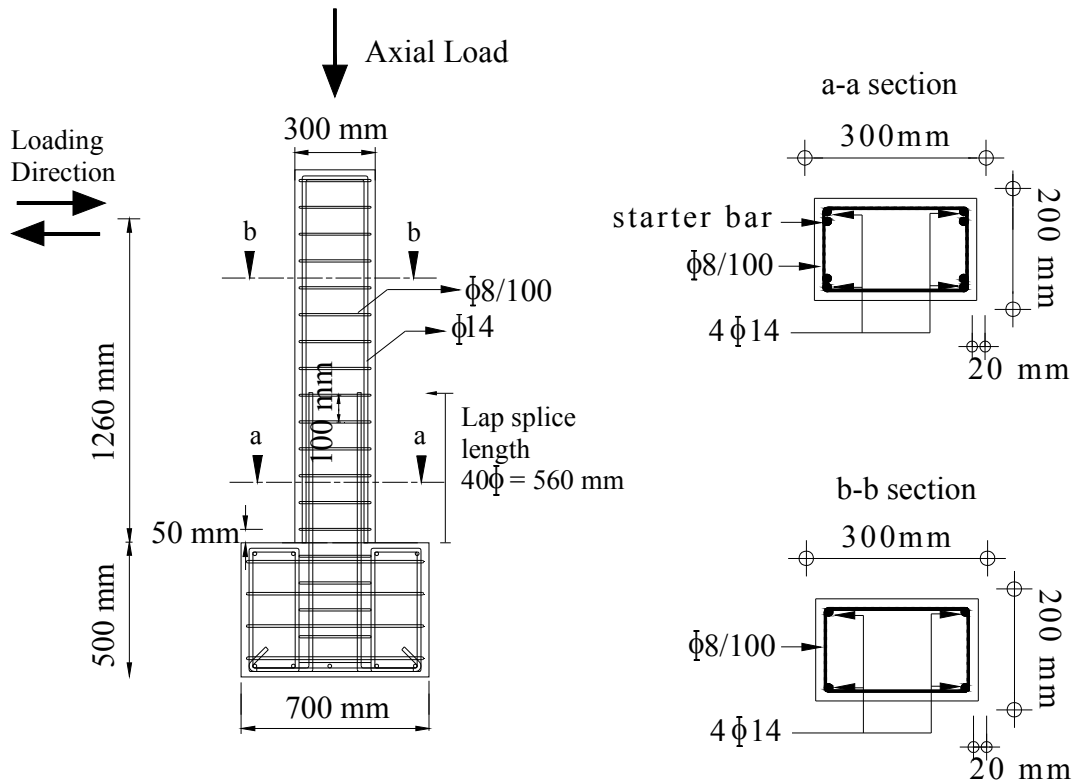


Figure 8.7 : Column model taken into account for parametric analysis.

The concrete strength is assumed to be 25.5 MPa, while the yield strengths of longitudinal and transverse bars are assumed to be 460 and 420 MPa, respectively. The diameters of longitudinal and transverse deformed bars are 14 and 8 mm, respectively. Clear cover is 20 mm from transverse bar. The transverse load is assumed to be acting at the free end of cantilever column at the height of 1200 mm from the column base. Axial load on the columns is 282 kN, which corresponds to 20% of the gross axial capacity of the column. C0 is the reference column, while the C1, C2 and C3 columns have maximum loss of cross-section of 10%, 20% and 30%, respectively. Columns are named with the first and second letters symbolizing the level of corrosion (C0, C1, C2, C3) and the third character symbolizing the number of the pits: such as 1, 3 and 6. The length of each corrosion pit is assumed to be 14 mm, which is equal to the diameter of deformed bars. The assumed corrosion patterns of the reinforcing bars are presented in Figure 8.8. It should be noted that all the pits are assumed to occur within the plastic hinge length of columns.

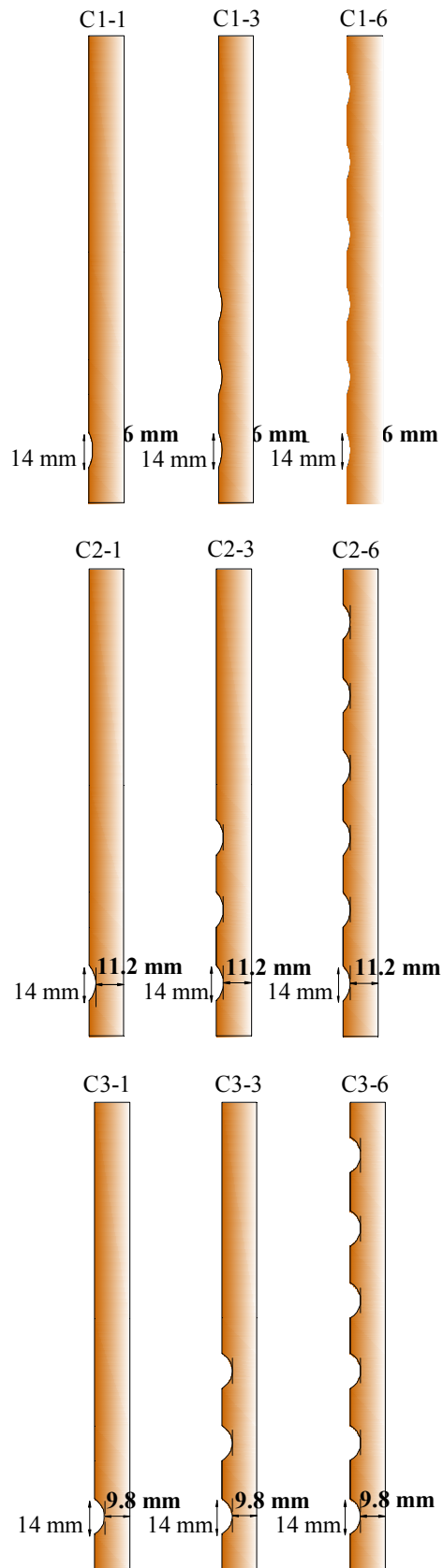


Figure 8.8 : Idealized corrosion patterns of the columns.

8.2.2 Analytical procedure

The properties of the hypothetical columns are shown in Table 8.3.

Table 8.3 : Elastic and plastic deformations of the hypothetical columns.

Columns	Cross-section loss	Number of pits	Pit length (mm)	Plastic hinge length ¹ (mm)	P ² (kN)	$\delta_{elastic}$ ³ (mm)	$\delta_{plastic}$ ⁴ (mm)	$\delta_{elastic} + \delta_{plastic}$ (mm)
C0	-	-		150	48.4	2.3	21.6	23.9
C1-1	10%	1	14	14	43.6	2.1	2.0	4.1
C1-3	10%	3	14	42	43.6	2.1	6.0	8.1
C1-6	10%	6	14	84	43.6	2.1	11.9	14.0
C2-1	20%	1	14	14	39.5	1.9	2.0	3.9
C2-3	20%	3	14	42	39.5	1.9	5.9	7.8
C2-6	20%	6	14	84	39.5	1.9	11.7	13.7
C3-1	30%	1	14	14	35.3	1.7	2.0	3.7
C3-3	30%	3	14	42	35.3	1.7	6.0	7.7
C3-6	30%	6	14	84	35.3	1.7	11.9	13.7

¹Potential plastic hinge length is assumed to be 50% of column depth for reference specimen, while it is considered as 14, 42 and 84 mm for the columns with corroded reinforcement of 1, 3 and 6 pits, respectively.

²P is the theoretical ultimate lateral load.

³ $\delta_{elastic}$ is the elastic contribution to the total top displacement at ultimate lateral load.

⁴ $\delta_{plastic}$ is the plastic contribution to the total top displacement at ultimate lateral load.

It should be noted that the plastic hinge lengths of the columns with corroded reinforcement are assumed to be equal to the lengths of the corrosion pits on the bars. The moment-curvature relationships of the critical base sections of the columns are calculated by using BAKE (2000) computer program. Moment-curvature relationships of the hypothetical columns for the cross-section losses of 10, 20, 30%, representing different levels of pitting are shown in Figure 8.9.

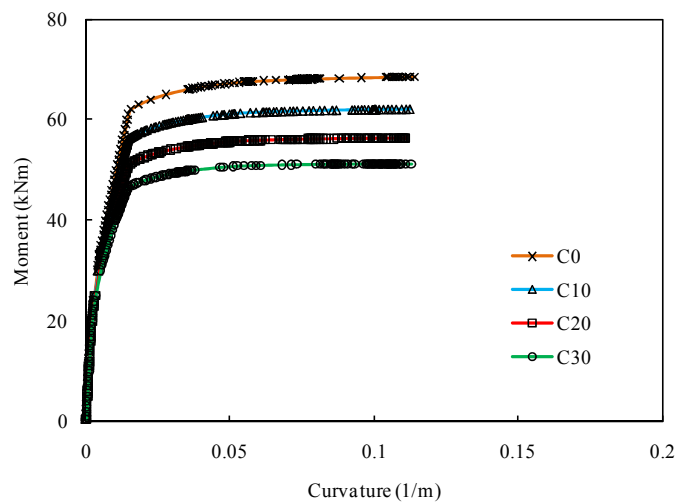


Figure 8.9 : Moment-curvature relationships of the hypothetical columns by BAKE (2000).

The ultimate point of the curvature is selected as the point at which strain of the reinforcing bar (ε_s) reaches 0.022 in tension. As seen in Figure 8.9, and as expected, the strengths of the specimens decrease as the cross-section losses increase. For obtaining analytical lateral load-lateral displacement relationships of the columns, the elastic and plastic components of the top displacement of the column ($\delta_{elastic}$ and $\delta_{plastic}$) are calculated by Eqs. (8.4)-(8-7).

In the equations L (mm) is the height of the column, θ_{PL} is the plastic rotation of the assumed plastic hinge corresponding to tensile strain of 2.2% on the reinforcing bars in tension, x_{PL} is the average plastic curvature assumed to be uniformly distributed over the assumed plastic hinge length, E_c (MPa) is the elasticity modulus of concrete, f_{ck} (MPa) is the characteristic compressive strength of concrete, $\delta_{elastic}$ (mm) is the elastic contribution to the total top displacement at ultimate lateral load, P (kN) is the lateral load, I (mm⁴) is the moment of inertia of the member, l_{PL} (mm) is the plastic hinge length of the column and $\delta_{plastic}$ is the plastic contribution to the total top displacement at ultimate lateral load (mm).

$$\delta_{elastic} = \frac{PL^3}{3E_c I} \quad (8.4)$$

$$\theta_{PL} = x_{PL} \cdot l_{PL} \quad (8.5)$$

$$\delta_{plastic} = \theta_{PL} \cdot L \quad (8.6)$$

$$\delta_{total} = \delta_{elastic} + \delta_{plastic} \quad (8.7)$$

It should be noted for the case of corroded reinforcing bars all the column is assumed to behave elastically with the exception of the total length of pits of where all plastic deformations are assumed to occur. For the uncorroded case, the plastic hinge length is assumed as 150 mm, which is equal to the half of column depth.

The theoretical load-displacement relationships obtained following the approached summarized above are presented in Figure 8.10.

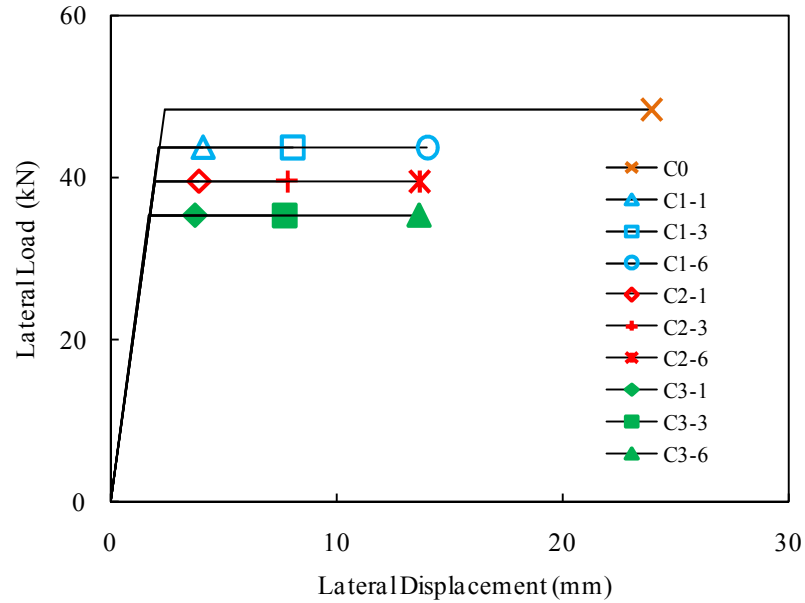


Figure 8.10 : Theoretical load-displacement relationships of the hypothetical columns.

As seen in Figure 8.10, as expected the lateral strength of the column is reduced proportional to the loss of cross-section in corrosion pits. More importantly, since all the plastic deformations are concentrated at the pits, the plastic-lateral drift capacity of the columns is significantly reduced. The drift capacity further decreases with the decrease of number of pits. The increase of drift capacity in case of higher number of pits is due to better distribution of plastic deformations throughout the reinforcing bars. Consequently, interestingly, more pits with approximately similar depths lead to a higher drift capacity than a single pit of approximately same depth. As seen in Figure 8.10, the strength reduces 27% for C3 type corrosion with 6 pits where drift capacity reduces 42%. On the other hand, drift capacity is reduced by 84% for C3 type corrosion with only 1 pit. This finding indicates a very critical concern for the drift capacities of columns of existing RC structures which are normally expected to behave in a ductile manner against earthquakes, exhibiting large drifts. It appears to be vitally important to account for reductions both in strength and more importantly in deformation capacity, in seismic safety assessment of existing structures with corroded reinforcement.

8.2.3 Comparison with experimental data

For verifying the analysis approach presented above, the behavior of specimens NS-X0 and NS-X54 were studied analytically. The geometrical and mechanical

characteristics of the tested columns are exactly same as the hypothetical column taken into account in the parametric study. For the analytical study, the bottom 150 mm part of the reinforcement was taken out from the column, divided into 10 mm long pieces, the cross-section losses were measured and the pieces were grouped according to the levels of corrosion (L1, L2, L3 and L4). The average characteristics of these groups are shown in Table 8.4.

Table 8.4 : Properties of the tested pieces.

Pieces ^{*1}	Distance from base (mm)	Corrosion groups	Section loss (%)	Number of pits	Pit length (mm)	Assumed plastic hinge length (mm)	$P_{at\ first\ yield}$ (kN)	$P_{maximum}$ (kN)	$P_{ultimate}$ (kN)
Piece 1	0-150	L1	8	2	10	20	52.15	54.48	52.40
		L2	17	2	10	20	49.84	51.98	49.70
		L3	32	4	10	40	45.74	47.81	44.48
		L4	48	7	10	70	41.53	43.32	38.91
Piece 2	150-372	L3	32	*2	*2	222	Remain elastic		
Piece 3	372-594	L2	17	*2	*2	222			
Piece 4	594-816	L2	17	*2	*2	222			
Piece 5	816-1038	L1	8	*2	*2	222			
Piece 6	1038-1260	L1	8	*2	*2	222			

1 The definition of pieces can be seen in Fig. 11.

2 In these pieces, the corrosion is assumed to form in a uniform manner (based on observations).

While calculating the load-displacement relationship of this column analytically, the plastic hinge length was assumed as half of the cross-section depth during all phase of the loadings ($l_{PL}=0.5h$). The parts of the column outside the plastic hinge are considered to remain elastic. The elastic rotations are lumped at five different heights while calculating the elastic lateral displacement component (Figure 8.11).

The deepest corrosion pits of the reinforcing bars were in the plastic hinge zone, since this part was the main target of accelerated corrosion in this thesis. On the other hand, this corrosion pattern is also in agreement with the corrosion pattern of existing columns, for most of which, the most severe effects of reinforcement corrosion are observed at and around the bases or in the vicinity of potential plastic hinge zone. In the analysis, it is assumed that there were 7 pits of 10 mm length with a cross-section loss of 48% in the plastic hinge zone (piece 1 within 150 mm distance from the bottom of the column). Since, the parts of the reinforcement above the potential plastic hinge zone are also subjected to corrosion to a lesser extent, the corrosion of these parts is assumed to be uniformly distributed over each piece. The assumed

uniform section losses for each piece are given in Table 8.4. It should be noted that these assumptions are based on observations on the column. The theoretical moment-curvature relationships are then simplified to obtain trilinear moment-curvature relationships. By utilizing the procedure outlined above in the parametric analysis paragraph, the inelastic and elastic rotations are determined. And by multiplying the rotations with the respective lengths, along which the rotations take place, the displacement of each piece is calculated. Then carrying out an incremental analysis approach load-displacement relationship of the column is obtained up to the theoretical fracture of tensile longitudinal bars at around 2% drift ratio. It should be mentioned that shear deformations, which are calculated and found to have marginal contribution to the lateral drift are neglected. This can also be proved by the fact that there was no shear damage could be observed on the specimens.

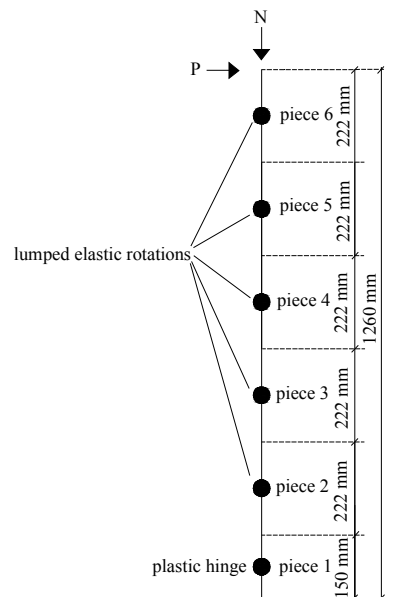


Figure 8.11 : Locations of the plastic hinge and lumped elastic rotations.

Experimental and the predicted lateral load-displacement relationships of the columns are presented in Figure 8.12. The mode of corroded column failure was with the rupture of the reinforcing bar after the crushing of concrete cover at 2% drift ratio while the mode of uncorroded column failure was with the rupture of the reinforcing bar after the crushing of concrete cover at 8% drift ratio.

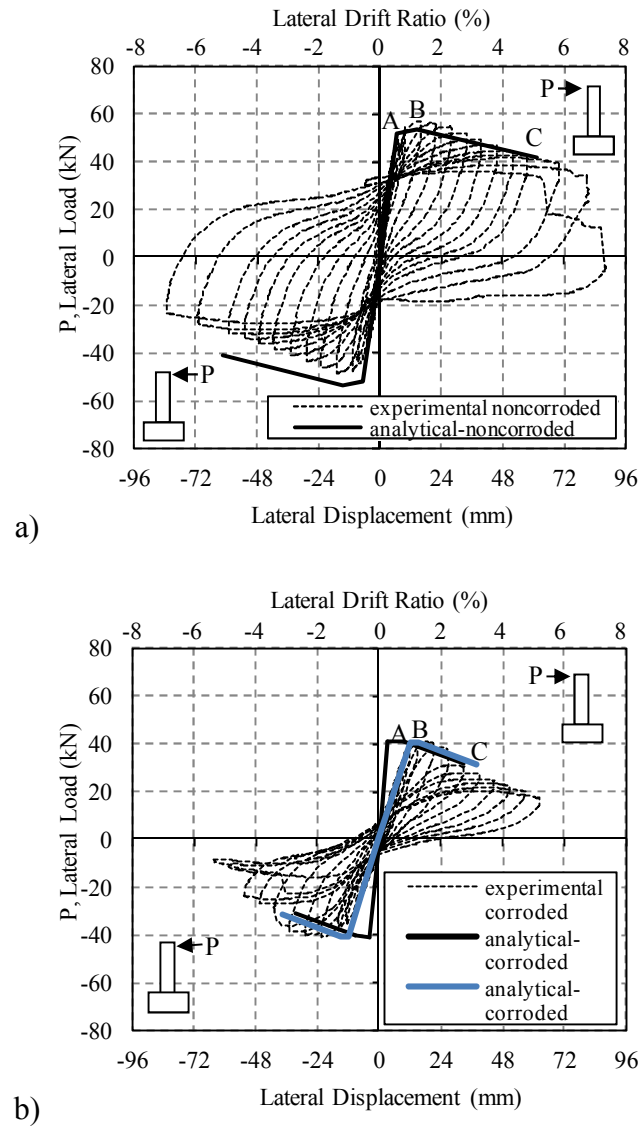


Figure 8.12 : Analytical and experimental lateral load-displacement relationships of a) Uncorroded and b) Corroded specimens.

As seen in these figures, there is a good agreement between the measured and predicted overall load-displacement behavior of the columns up to large drifts. Flexural stiffness reduced due to reversed cyclic loads during the test. As seen from Figure 8.12b, analytical behavior with blue line is the calculation with the cracked section consideration while black line is the calculation without cracked section consideration. As the specimen NS-X54 had horizontal and vertical cracks along the reinforcing bars due to corrosion, the figure presents good agreement when the cracked section was taken into consideration. The analytical moment-curvature relationships at the plastic hinge zone and the stress-strain relationships of concrete at the extreme compression failure and tensile reinforcing bars are presented in Table

8.5.

Table 8.5 : Analytical moment-curvature and stress-strain relationships of Point A, B and C.

	Point A	Point B	Point C
Moment	<p>Moment : 49.21 kNm Curvature : 0.0167 1/m</p>	<p>Moment : 51.33 kNm Curvature : 0.0579 1/m</p>	<p>Moment : 47.20 kNm Curvature : 0.2440 1/m</p>
Concrete stress-strain relationship	<p>σ_c : -24.93 MPa ϵ_c : -0.0016</p>	<p>σ_{cc} : -28.43 MPa ϵ_{cc} : -0.0026</p>	<p>σ_{cc} : -17.03 MPa ϵ_{cc} : -0.0015</p>
Steel stress-strain relationship	<p>σ_s : 460 MPa ϵ_s : 0.0028</p>	<p>σ_s : 464.1 MPa ϵ_s : 0.0116</p>	<p>σ_s : 560.0 MPa ϵ_s : 0.0429</p>

In this table, the experimental moment-curvature relationship is obtained within 150 mm length from the bottom of the column. In Table 8.5, σ_c and ϵ_c are the compressive stress and strain of concrete, σ_{cc} and ϵ_{cc} are compressive stress and strain of core concrete, σ_s and ϵ_s are tension stress and strain of reinforcing bar, respectively. As seen in this table, the values of moments, curvatures and strains are given for three damage levels, namely A, B and C. These points are assumed to correspond to different structural performance levels of the column, such as minimum damage, moderate damage and severe damage, which correspond to yielding, maximum and ultimate points in the experimental moment-curvature relationship, respectively. When the experimental and analytical values of moments, curvatures and strains at these three different damage levels are compared, it is seen that there is a good agreement between experimental and predicted values. This comparison shows that as well as global load-drift relationship of the column, the local deformations and failure mechanism could also be predicted quite accurately by the presented algorithm. In Table 8.5, it is interesting to note that while concrete loses its strength with increasing drifts, the moment capacity of the column is not influenced in the

same extent. The reason of this kind of behavior is the hardening of steel reinforcing bars after yielding. The high tensile strains in reinforcing bars are evident both through experimental measurements and through analytical study (Table 8.5).

The experimental moment-curvature relationships at the plastic hinge zone and the stress-strain relationships of concrete at the extreme compression failure and tensile reinforcing bars are presented in Figure 8.13.

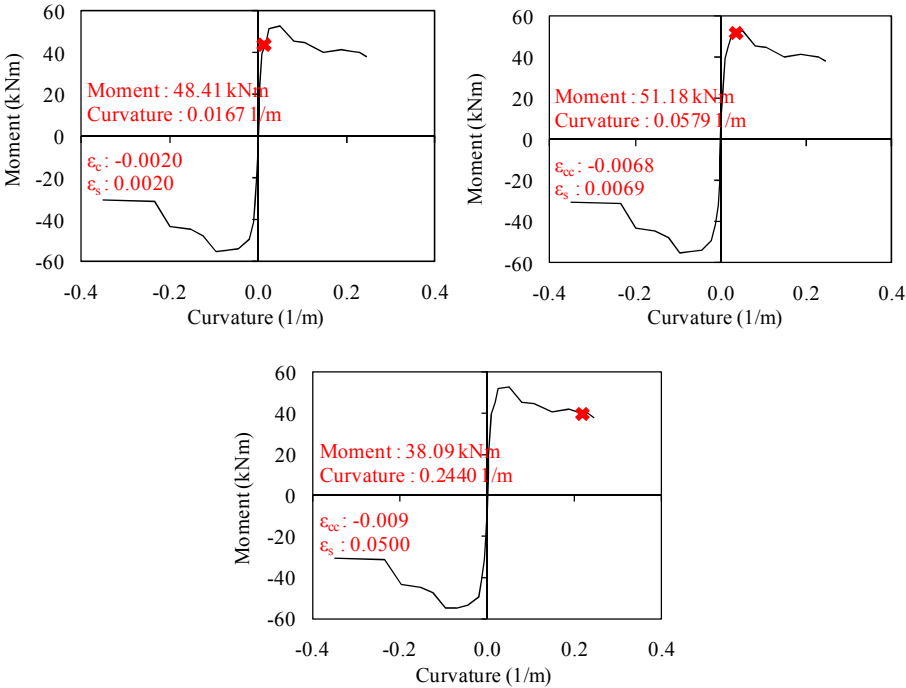


Figure 8.13 : Experimental moment-curvature and stress-strain relationships corresponding to Point A, B and C.

Finally, as explained above in the parametric analysis and through the investigation of the behavior of tested column, the corrosion of reinforcing bars has a major influence on the drift capacity of the columns under lateral loads. This is particularly a very important problem, which should be carefully taken into account in seismic assessment of existing buildings, whose structural members may have corroded reinforcing bars. In order to set forth a more reliable and general conclusion, test data are required to verify the predictions of the proposed method since the literature contains scarce information.

8.3 An Analytical study on RC Frame Building with Corroded Deformed Reinforcing Bars

For assessing the effects of extent of corrosion, distribution of the corrosion damage, ground motion and soil types on the performance of the existing RC building, a numerical study is carried out on a typical regular RC building. The seismic performance of the building is examined through nonlinear pushover analysis and nonlinear time history analyses and considered with TSDC (2007). The plan of the building and the cross-sections of the structural members are presented in Figure 8.14.

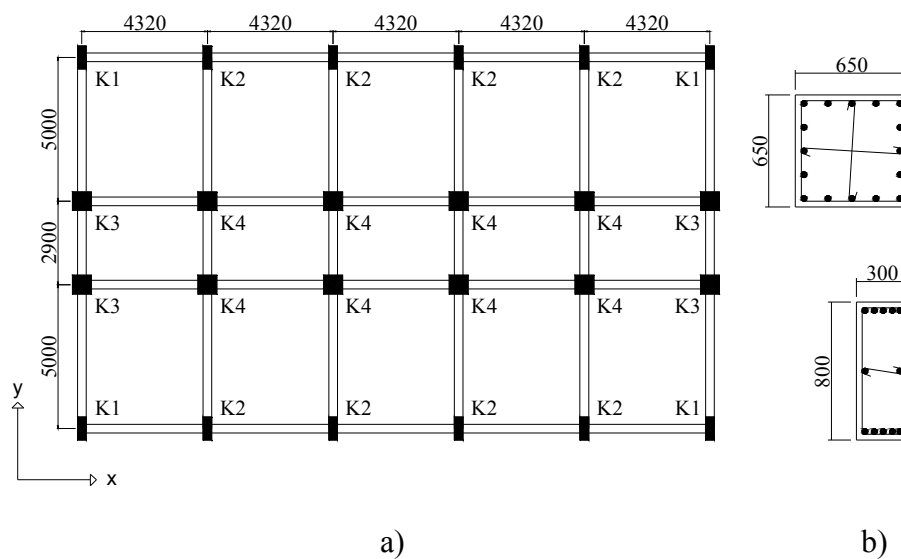


Figure 8.14 : a) A typical floor plan of the building, b) Properties and reinforcing cage of columns (Note: Dimensions are in mm units).

8.3.1 Analyzed building

The RC frame building analyzed was selected on the highest seismic risk zone. TSDC (2007) states the design horizontal acceleration as 0.4g for such zones with high seismicity. Note that, the seismic load reduction factor of 1 is taken into account as mostly done in practice for this type of RC frame structures. Consequently, the periods of structure for x and y directions were determined as 0.39 and 0.33 s, respectively. According to Figure 8.14, it can be seen that, structural system is symmetrical in x and y directions, the dimensions of the columns are 650×650 mm and 300×800 mm that are connected to each other with 300×800 mm beams. The characteristic compressive strength of concrete is 16 MPa. Both longitudinal and transverse reinforcement are deformed bars with characteristic yield strength of 420

MPa. The transverse reinforcement of the hypothetical building, consist of 8 mm bars at 200 mm spacing. It should be noted that the overall weight of the structure, which is also regular in elevation, is 17800 kN ($G+nQ$). G , n and Q are dead load, live load participation factor and live load, respectively.

8.3.2 Analytical procedure

8.3.2.1 Moment-rotation relationships

Nonlinear analysis is a deformation based method that needs moment-rotation relationships of each element of structure. For determining these features firstly, analytical model of hypothetical structure was analyzed under gravity loads to determine the axial load levels of columns; 5% and 10%. The effect of changes in column axial load level due to the lateral loads was neglected for determining moment-rotation relationships of the columns. The properties of the columns are shown in Table 8.6. According to Table 8.6, the first, the second, the third and the fourth characters of the column types denote the maximum section loss (%), dimension, axial load level (%) and number of the pits, respectively. The moment-curvature relationships of the columns were calculated for these 5% and %10 axial load levels by XTRACT (2007) computer program. The cross-sections of the columns consist of 3 components which were cover concrete, confined concrete and reinforcement. Material models that were defined in XTRACT (2007) were used to determine the nonlinear load-deformation capacity of these components for analytical model. Unconfined concrete model for cover concrete, confined concrete model for confined concrete and stress-strain relationship for reinforcing bars used by XTRACT (2007) are proposed by Mander et al. (1988).

Table 8.6 : Properties of the columns.

Building notation	Column notation	Column Type	Dimension (mm)	Axial load level (%)	Number of pits	Pit length (mm)	Plastic hinge length (mm)
S0	K1	C0-30×80-5-0	300×800	5	0	0	400
	K2	C0-30×80-10-0	300×800	10	0	0	400
	K3	C0-65×65-5-0	650×650	5	0	0	325
	K4	C0-65×65-5-0	650×650	10	0	0	325
S10-3	K1	C10-30×80-5-3	300×800	5	3	16	48
	K2	C10-30×80-10-3	300×800	10	3	16	48
	K3	C10-65×65-5-3	650×650	5	3	16	48
	K4	C10-65×65-10-3	650×650	10	3	16	48
S10-6	K1	C10-30×80-5-6	300×800	5	6	16	96
	K2	C10-30×80-10-6	300×800	10	6	16	96
	K3	C10-65×65-5-6	650×650	5	6	16	96
	K4	C10-65×65-10-6	650×650	10	6	16	96
S10-12	K1	C10-30×80-5-12	300×800	5	12	16	192
	K2	C10-30×80-10-12	300×800	10	12	16	192
	K3	C10-65×65-5-12	650×650	5	12	16	192
	K4	C10-65×65-10-12	650×650	10	12	16	192
S20-3	K1	C20-30×80-5-3	300×800	5	3	16	48
	K2	C20-30×80-10-3	300×800	10	3	16	48
	K3	C20-65×65-5-3	650×650	5	3	16	48
	K4	C20-65×65-10-3	650×650	10	3	16	48
S20-6	K1	C20-30×80-5-6	300×800	5	6	16	96
	K2	C20-30×80-10-6	300×800	10	6	16	96
	K3	C20-65×65-5-6	650×650	5	6	16	96
	K4	C20-65×65-10-6	650×650	10	6	16	96
S20-12	K1	C20-30×80-5-12	300×800	5	12	16	192
	K2	C20-30×80-10-12	300×800	10	12	16	192
	K3	C20-65×65-5-12	650×650	5	12	16	192
	K4	C20-65×65-10-12	650×650	10	12	16	192
S30-3	K1	C30-30×80-5-3	300×800	5	3	16	48
	K2	C30-30×80-10-3	300×800	10	3	16	48
	K3	C30-65×65-5-3	650×650	5	3	16	48
	K4	C30-65×65-10-3	650×650	10	3	16	48
S30-6	K1	C30-30×80-5-6	300×800	5	6	16	96
	K2	C30-30×80-10-6	300×800	10	6	16	96
	K3	C30-65×65-5-6	650×650	5	6	16	96
	K4	C30-65×65-10-6	650×650	10	6	16	96
S30-12	K1	C30-30×80-5-12	300×800	5	12	16	192
	K2	C30-30×80-10-12	300×800	10	12	16	192
	K3	C30-65×65-5-12	650×650	5	12	16	192
	K4	C30-65×65-10-12	650×650	10	12	16	192

According to the results of the program, the failure of the columns is dominated by tensile fracture. Moment at first yield and ultimate moment significantly decreased due to the cross-sectional loss (Figure 8.15).

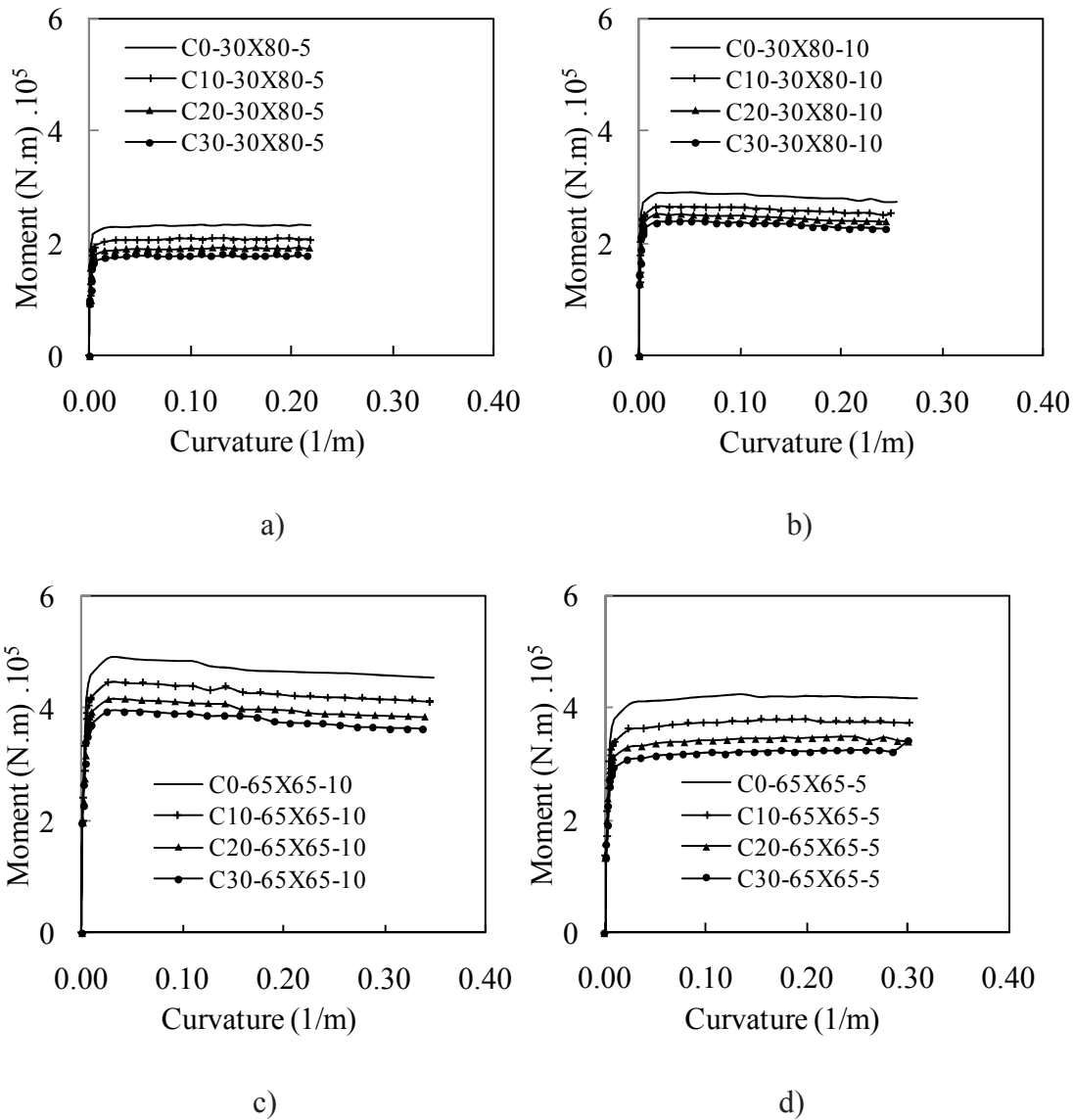


Figure 8.15 : Moment-curvature relationships of cross sections of (a) 30x80 cm for 10% axial load level, (b) 30x80 cm for 5% axial load level, (c) 65x65 cm for 10% axial load level, (d) 65x65 cm for 5% axial load level with different cross-section losses.

Rotations were obtained by multiplying curvatures with plastic hinge length of the columns to carry out an incremental analysis approach for nonlinear load-displacement relationship of the column. For uncorroded columns, plastic hinge length is assumed to be $h/2$ as proposed by TSDC (2007), where h represents effective depth of cross-section of column in bending. For corroded columns, as all plastic deformations are concentrated at the pits, the plastic hinge length is taken as the total of the lengths of the pits. The assumed dimensions of the pits are shown in Figure 8.16.

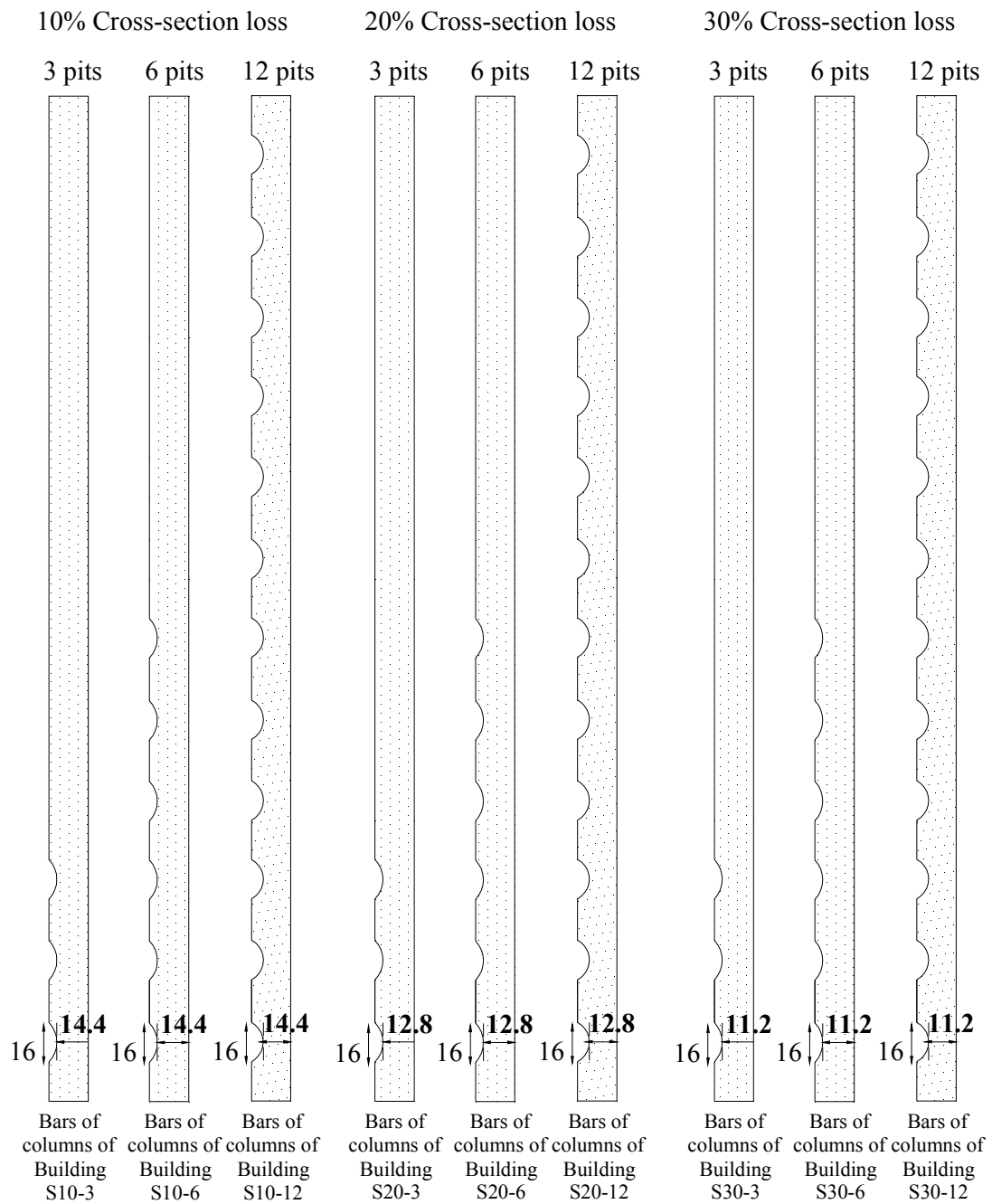


Figure 8.16 : The assumed dimensions of the pits on a typical reinforcing bar of column (Dimension units in mm).

The moment-rotation relationships of the corroded columns with different number of pits are shown in Figure 8.17. According to the Figure 8.17, the increase of rotation capacity with increasing number of pits is due to uniform distribution of plastic deformations throughout the reinforcing bar.

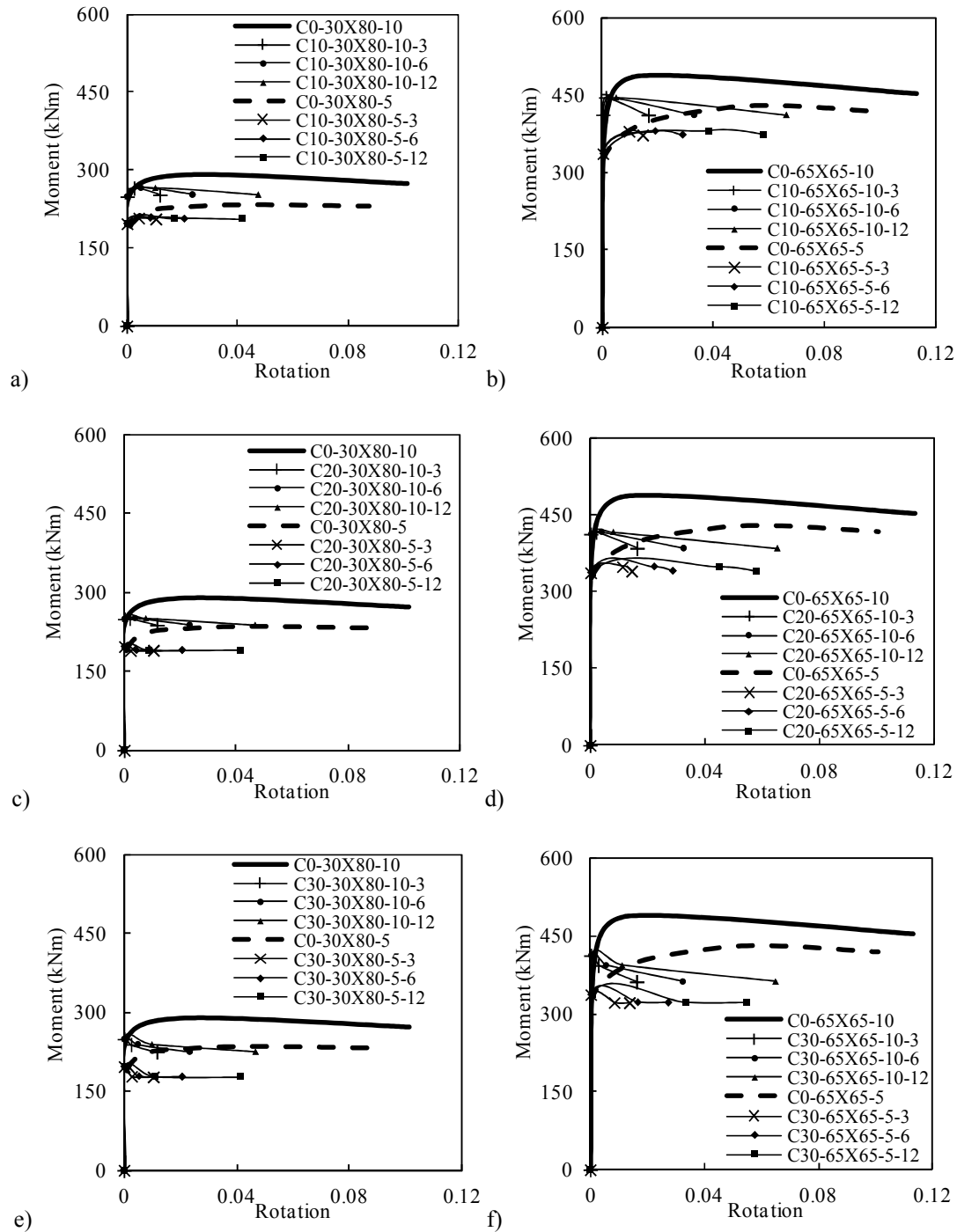


Figure 8.17 : Moment-rotation relationships for the plastic hinges of the columns.

8.3.2.2 Pushover analysis

The pushover analysis was carried out to examine the nonlinear behavior of structure. In analysis procedure, gravity loads and lateral loads which increase monotonically were executed together. After the structure was subjected to the gravity loads, the analysis progressed with the lateral loads. The lateral load distribution of the stories of structure was proportional to equivalent seismic load

distribution as defined in TSDC (2007). Nonlinear behavior of structure was related to the nonlinear load-deformation capacity of individual members of structure. Observations from earthquake areas and existing buildings in Turkey show that beams are stronger than columns as describing weak column-strong beam cases. Therefore, all the beams were assumed to behave elastically and the nonlinear load-deformation capacity of structure was affected from the nonlinear load-deformation characteristics of the columns that were combined in the form of moment-rotation relationships. All of the longitudinal bars of the columns at the basement level are assumed to be affected from corrosion. Analyses were performed according to all the reinforcement of the base columns of the hypothetical RC structure which had cross-section losses of 10%, 20%, 30% with 3 pits, 6 pits and 12 pits due to corrosion. The assumptions of the level of corrosion, pit distribution and existence of corrosion based on existing structure stock.

Base shear-drift ratio relationships for the structure with cross-section losses of 10%, 20%, 30% with different numbers of pits of the reinforcement of the base columns and uncorroded structure is shown in Figure 8.18. According to the figure, as expected, the lateral load capacity of the structure is reduced proportional to the loss of cross-section at corrosion pits. Interestingly, since all the plastic deformations are located at and around pits, the lateral deformation capacity of the structure is significantly reduced. The deformation capacity increases with the increasing number of pits due to uniform distribution of plastic deformations throughout the reinforcing bars.

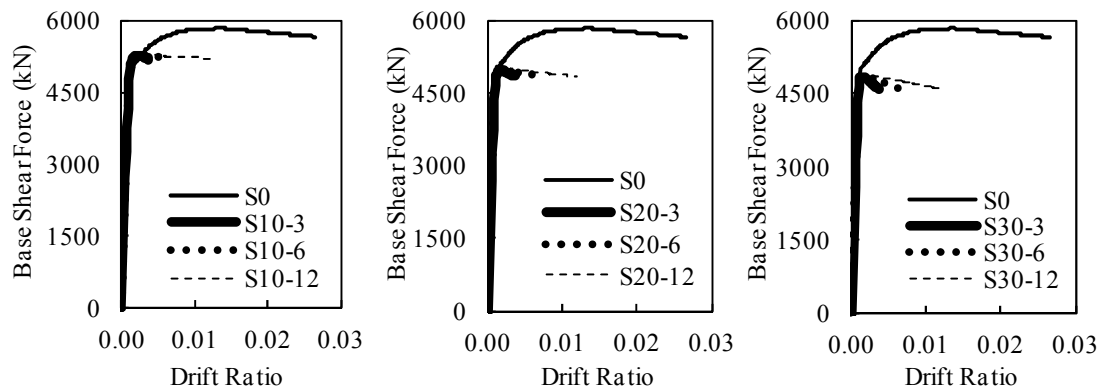


Figure 8.18 : Base shear-drift ratio relationships for the structures as a function of section loss of reinforcing bars and number of corrosion pits.

8.3.2.3 Determination of the Seismic Performance Level of the Building

The performance levels of the buildings were determined using performance criteria given by TSDC (2007). Base shear-top displacement relationships were calculated by PERFORM-3D (2007) computer program by using nonlinear pushover analysis only in “y” direction. Modal capacity diagram (modal acceleration-modal displacement) was obtained from base shear-top displacement diagram by using Eqs. (8.8a) and (8.8b).

$$a_1 = \frac{V_{y1}}{M_{y1}} \quad (8.8a)$$

In Eq. (8.8a), a_1 represents modal acceleration, V_{y1} represents base shear force, M_{y1} represents the effective modal mass for the first mode. M_{y1} is obtained as follows;

$$M_{y1} = \frac{\left(\sum_{N=1}^n m_N \phi_{yN1} \right)^2}{\left(\sum_{N=1}^n m_N \phi_{yN1}^2 \right)} \quad (8.8b)$$

In Eq. (8.8b), m_N represents lumped story mass, ϕ_{yN1} represents N^{th} component of the mode shape vector for the first mode.

$$d_1 = \frac{U_{yN}}{\phi_{yN1} \cdot \Gamma_{y1}} \quad (8.9a)$$

In Eq. (8.9a), d_1 represents modal displacement, U_{yN} represents top displacement, Γ_{y1} represents participation factor for the first mode. Γ_{y1} is obtained by Eq. (8.9b).

$$\Gamma_{y1} = \frac{\sum_{N=1}^n m_N \phi_{yN1}}{\sum_{N=1}^n m_N \phi_{yN1}^2} \quad (8.9b)$$

After obtaining modal capacity diagram, elastic demand spectrum was calculated by using elastic design acceleration spectrum for calculating elastic spectral displacement demand. Elastic design acceleration spectrum ($S(T)$ - T) was obtained by using Eq. (8.10a-c).

$$S(T) = 1 + 1.5 \cdot (T / T_A) \quad 0 \leq T \leq T_A \quad (8.10a)$$

$$S(T) = 2.5 \quad T_A \leq T \leq T_B \quad (8.10b)$$

$$S(T) = 2.5 \cdot (T_B / T)^{0.8} \quad T_B \leq T \quad (8.10c)$$

In Eq. (8.10), $S(T)$ represents spectrum coefficient, T represents period of a building for the first mode. After obtaining elastic design acceleration spectrum, elastic demand spectrum was obtained by using Eqs. (8.11a-8.12a-b).

$$S_{ae}(T) = A(T) \cdot g \quad (8.11)$$

$$A(T) = A_0 \cdot I \cdot S(T) \quad (8.11a)$$

$$S_{de}(T) = \frac{S_{ae}}{(\omega_1^{(1)})^2} \quad (8.12a)$$

$$\omega_1^{(1)} = \frac{2\pi}{T_1^{(1)}} \quad (8.12b)$$

In Eq. (8.11), S_{ae} represents elastic spectral acceleration, $A(T)$ represents spectral acceleration coefficient, A_0 represents effective ground acceleration coefficient and I represent building importance factor. In Eq. (8.12a), S_{de} represents elastic spectral displacement demand and ω_1 represents circular frequency.

For estimating elastic spectral displacement demand, the modal capacity diagram (modal acceleration-modal displacement) and elastic demand spectrum diagram (elastic spectral acceleration-elastic spectral displacement) were combined together in a diagram. Elastic spectral displacement demand was the abscissa of point where the initial tangent of the modal capacity diagram and elastic demand spectrum intersects. Eq. (8.13a-c) were used for calculating inelastic spectral displacement demand.

$$S_{di} = C_{R1} \cdot S_{de1} \quad (8.13a)$$

$$C_{R1} = 1 \quad T_1 \geq T_B \quad (8.13b)$$

$$C_{R1} = \frac{1 + (R_{y1} - 1) \cdot \frac{T_B}{T_1^{(1)}}}{R_{y1}} \quad T_1 < T_B \quad (8.13c)$$

In Eq. (8.13), S_{di} represents nonlinear spectral displacement demand for the first mode, C_{R1} represents spectral displacement amplification factor for the first mode, R_y represents seismic load reduction factor.

Top displacement demand (U_{yN}) was calculated by using Eq. (8.14).

$$U_{yN} = \Gamma_y \cdot \phi_{yN} \cdot S_{di} \quad (8.14)$$

Plastic rotation demands ($\theta_{plastic}$) of the columns correspond to top displacement demand obtained from pushover analysis by using PERFORM-3D computer program. Plastic curvature demands (χ_p) were obtained by dividing the plastic hinge length (L_{pl}) with $\theta_{plastic}$ (Eq. (8.15)).

$$\theta_{plastic} / L_{pl} = \chi_p \quad (8.15)$$

Total curvature demand (χ_T) is the sum of equivalent yield curvature (χ_y) obtained from moment-curvature relationship by using XTRACT /2007) computer programme and plastic curvature (Eq. (8.16)).

$$\chi_T = \chi_y + \chi_p \quad (8.16)$$

Strain demands are determined from moment-curvature analysis for total curvature demand. Three limit conditions have been defined for ductile elements on the cross-section. These are minimum damage limit (MN), safety limit (GV) and collapsing limit (GC). Minimum damage limit defines the beginning of the behavior beyond elasticity, safety limit defines the limit of the behavior beyond elasticity that the section is capable of safely ensuring the strength, and collapsing limit defines the limit of the behavior before collapsing (Figure 8.19).

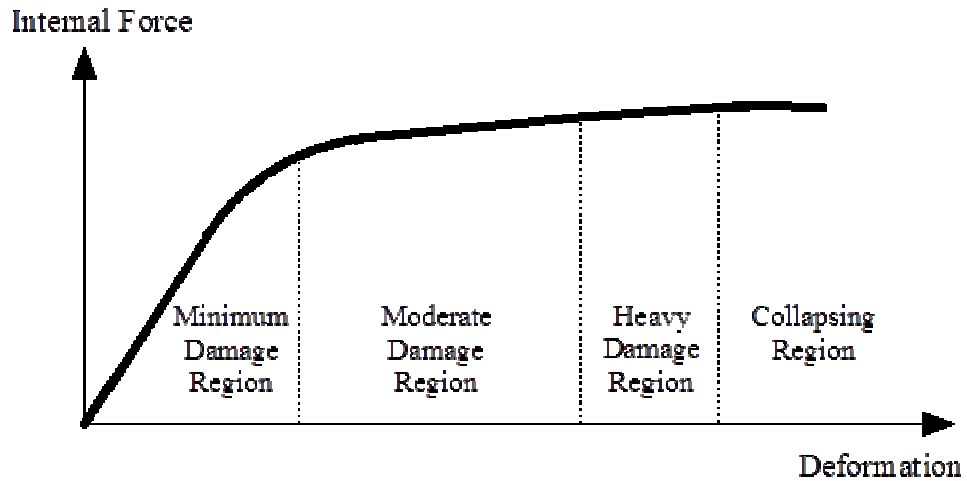


Figure 8.19 : The damage regions of sections (TSDC, 2007).

Strain capacities for MN is taken as the upper bounds of the concrete strain in the outmost fiber of the section, for GV and GC are taken as the upper bounds of the concrete strain in the outmost fiber of hoop are introduced in TSDC (2007) (Table 8.7). In Table 8.7, ρ_s and ρ_{sm} represent the existing and the required volumetric ratios of transverse reinforcement of columns, respectively. The parameters used for determining performance levels of buildings are given in Table 8.8.

Table 8.7 : Definition of damage limits (TSDC, 2007).

Damage Limits	Upper limit for reinforcement strain (ϵ_s)	Upper limit for concrete strain (ϵ_c)
<i>MN</i>	0.010	0.0035
<i>GV</i>	0.040	$0.0035 + 0.01 (\rho_s / \rho_{sm}) \leq 0.0135$
<i>GC</i>	0.060	$0.004 + 0.014 (\rho_s / \rho_{sm}) \leq 0.018$

Table 8.8 : The parameters used in determining of performance levels of buildings.

Earthquake Region	1
A_0	0.4
Soil Class	Z1
T (in y direction)	0.33 s
I	1
m_N	445.49 kN.s ² /m
$\phi_{11}, \phi_{21}, \phi_{31}, \phi_{41}$	0.0033m, 0.0078 m, 0.0116 m, 0.0139 m
M_{y1}	1495.2 kN.s ² /m
\tilde{A}_{y1}	91.61

Modal capacity diagram and elastic demand spectrum for buildings are obtained for S0 for 5% damping ratio (Figure 8.20).

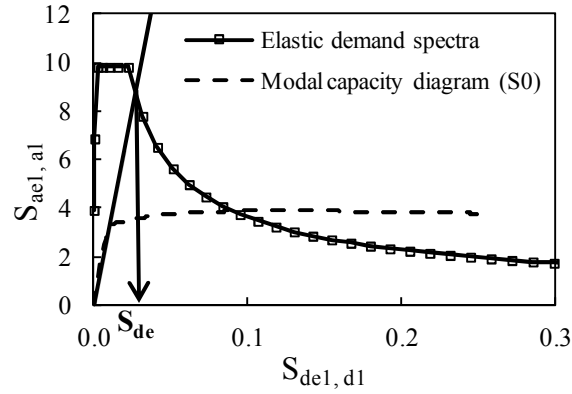


Figure 8.20 : Modal capacity diagram and elastic demand spectrum relationship.

S_{de1} of S0 building is found as 0.033 from the modal capacity diagram-elastic demand spectrum relationship. As the initial tangent of modal capacity diagram of S0 and S10-12 buildings show the slope of modal capacity-modal displacement relationship in the elastic region, the abscissa of the intersection of the modal capacity diagram and the elastic demand spectrum is (S_{de1}) 0.033 in buildings which have corroded base columns similar to building S0. As the corrosion has adverse effect on strength and drift capacity of the buildings on inelastic region after yielding point, the effect of corrosion on the period, mass participation rate and modal amplitude in elastic region is neglected in modal analysis.

As $T_1=0.33 \text{ s} \geq T_B=0.3 \text{ s}$, CR is taken as 1 (TSDC, 2007), nonlinear spectral displacement (S_{di}) is equal to linear spectral displacement (S_{del}). The target displacement (U_{yNI}) is found as 0.042. Capacity curve of buildings S0 is shown in Figure 8.21. The total curvature demand of base columns of S0 building and Damage regions for base columns of S0 building are shown in Table 8.9 and Table 8.10, respectively. Rotations were found from the pushover analysis by using target displacement (PERFORM-3D, 2007). In case of obtaining total curvature demand, elastic and plastic curvature which is found by using Eq. 8.15 were summed. The damage levels of columns are shown on plan of the building for defining the effect of level and distribution of corrosion on the total curvature and strain demands of columns are shown in Appendix J. As seen in figures in Appendix J, the damage level of columns (K2, K3, K4) does not change but strain demand values of columns decreases due to corrosion.

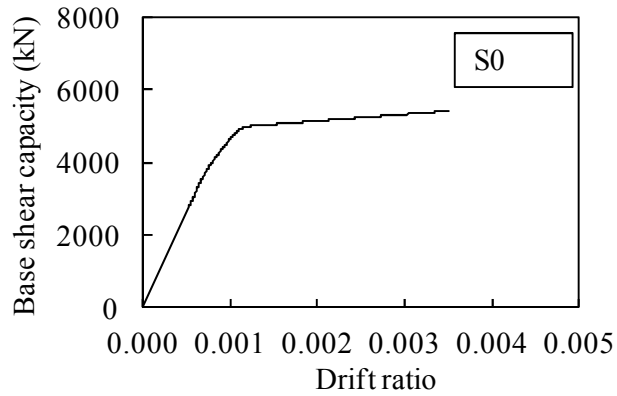


Figure 8.21 : Capacity curve of S0 building.

Table 8.9 : Total curvature demand of base columns of S0 building.

Column notation	Column type	Plastic Rotation (rad/m)	Plastic Hinge Length (L_p) (m)	Plastic Curvature (K_p) (1/m)	Elastic Curvature (K_y) (1/m)	Total Curvature (K_t) (1/m)
K1	C0-30×80-5	0.0097	0.4	0.0242500	0.002036	0.0262860
K2	C0-30×80-10	0.0098	0.4	0.0245000	0.002216	0.0267160
K2	C0-30×80-10	0.0098	0.4	0.0245000	0.002216	0.0267160
K2	C0-30×80-10	0.0098	0.4	0.0245000	0.002216	0.0267160
K2	C0-30×80-10	0.0098	0.4	0.0245000	0.002216	0.0267160
K1	C0-30×80-5	0.0097	0.4	0.0242500	0.002036	0.0262860
K3	C0-65×65-5	0.0097	0.325	0.0298462	0.004605	0.0344512
K4	C0-65×65-10	0.0096	0.325	0.0295385	0.004927	0.0344655
K4	C0-65×65-10	0.0096	0.325	0.0295385	0.004927	0.0344655
K4	C0-65×65-10	0.0096	0.325	0.0295385	0.004927	0.0344655
K4	C0-65×65-10	0.0096	0.325	0.0295385	0.004927	0.0344655
K3	C0-65×65-5	0.0097	0.325	0.0298462	0.004605	0.0344512
K3	C0-65×65-5	0.0097	0.325	0.0298462	0.004605	0.0344512
K4	C0-65×65-10	0.0096	0.325	0.0295385	0.004927	0.0344655
K4	C0-65×65-10	0.0096	0.325	0.0295385	0.004927	0.0344655
K4	C0-65×65-10	0.0096	0.325	0.0295385	0.004927	0.0344655
K4	C0-65×65-10	0.0096	0.325	0.0295385	0.004927	0.0344655
K3	C0-65×65-5	0.0097	0.325	0.0298462	0.004605	0.0344512
K1	C0-30×80-5	0.0097	0.4	0.0242500	0.002036	0.0262860
K2	C0-30×80-10	0.0098	0.4	0.0245000	0.002216	0.0267160
K2	C0-30×80-10	0.0098	0.4	0.0245000	0.002216	0.0267160
K2	C0-30×80-10	0.0098	0.4	0.0245000	0.002216	0.0267160
K2	C0-30×80-10	0.0098	0.4	0.0245000	0.002216	0.0267160
K1	C0-30×80-5	0.0097	0.4	0.0242500	0.002036	0.0262860

Table 8.10: Damage regions for base columns of S0 building.

Column notation	Column type	Unconfined concrete	Confined concrete	Steel	MN		GV		GC		Damage region
		ϵ_c	ϵ_{cc}	ϵ_{su}	ϵ_c	ϵ_{su}	ϵ_{cc}	ϵ_{su}	ϵ_{cc}	ϵ_{su}	
K1	C0-30×80-5	0.0018	0.0012	0.0175	0.0035	0.01	0.008434	0.04	0.010907	0.06	Marked Damage Region
K2	C0-30×80-10	0.0032	0.0024	0.0191	0.0035	0.01	0.008434	0.04	0.010907	0.06	Marked Damage Region
K2	C0-30×80-10	0.0032	0.0024	0.0191	0.0035	0.01	0.008434	0.04	0.010907	0.06	Marked Damage Region
K2	C0-30×80-10	0.0032	0.0024	0.0191	0.0035	0.01	0.008434	0.04	0.010907	0.06	Marked Damage Region
K2	C0-30×80-10	0.0032	0.0024	0.0191	0.0035	0.01	0.008434	0.04	0.010907	0.06	Marked Damage Region
K1	C0-30×80-5	0.0018	0.0012	0.0175	0.0035	0.01	0.008434	0.04	0.010907	0.06	Marked Damage Region
K3	C0-65×65-5	0.0026	0.0018	0.0160	0.0035	0.01	0.006852	0.04	0.008693	0.06	Marked Damage Region
K4	C0-65×65-10	0.0041	0.0030	0.0172	0.0035	0.01	0.006852	0.04	0.008693	0.06	Marked Damage Region
K4	C0-65×65-10	0.0041	0.0030	0.0172	0.0035	0.01	0.006852	0.04	0.008693	0.06	Marked Damage Region
K4	C0-65×65-10	0.0041	0.0030	0.0172	0.0035	0.01	0.006852	0.04	0.008693	0.06	Marked Damage Region
K4	C0-65×65-10	0.0041	0.0030	0.0172	0.0035	0.01	0.006852	0.04	0.008693	0.06	Marked Damage Region
K3	C0-65×65-5	0.0026	0.0018	0.0160	0.0035	0.01	0.006852	0.04	0.008693	0.06	Marked Damage Region
K3	C0-65×65-5	0.0026	0.0018	0.0160	0.0035	0.01	0.006852	0.04	0.008693	0.06	Marked Damage Region
K4	C0-65×65-10	0.0041	0.0030	0.0172	0.0035	0.01	0.006852	0.04	0.008693	0.06	Marked Damage Region
K4	C0-65×65-10	0.0041	0.0030	0.0172	0.0035	0.01	0.006852	0.04	0.008693	0.06	Marked Damage Region
K4	C0-65×65-10	0.0041	0.0030	0.0172	0.0035	0.01	0.006852	0.04	0.008693	0.06	Marked Damage Region
K4	C0-65×65-10	0.0041	0.0030	0.0172	0.0035	0.01	0.006852	0.04	0.008693	0.06	Marked Damage Region
K3	C0-65×65-5	0.0026	0.0018	0.0160	0.0035	0.01	0.006852	0.04	0.008693	0.06	Marked Damage Region
K1	C0-30×80-5	0.0018	0.0012	0.0175	0.0035	0.01	0.008434	0.04	0.010907	0.06	Marked Damage Region
K2	C0-30×80-10	0.0032	0.0024	0.0191	0.0035	0.01	0.008434	0.04	0.010907	0.06	Marked Damage Region
K2	C0-30×80-10	0.0032	0.0024	0.0191	0.0035	0.01	0.008434	0.04	0.010907	0.06	Marked Damage Region
K2	C0-30×80-10	0.0032	0.0024	0.0191	0.0035	0.01	0.008434	0.04	0.010907	0.06	Marked Damage Region
K2	C0-30×80-10	0.0032	0.0024	0.0191	0.0035	0.01	0.008434	0.04	0.010907	0.06	Marked Damage Region
K1	C0-30×80-5	0.0018	0.0012	0.0175	0.0035	0.01	0.008434	0.04	0.010907	0.06	Marked Damage Region

The steps for obtaining damage regions of S0 building are repeated for each building. Modal capacity diagram-elastic demand spectrum relationship of building S10-3 is shown in Figure 8.22. As the initial tangent of modal capacity diagram of all buildings show the slope of modal capacity-modal displacement relationship in the elastic region, the abscissa of the intersection of the modal capacity diagram and the elastic demand spectrum (S_{del}) is 0.033 in buildings which have corroded base columns similar to building S0. As the corrosion has adverse effect on strength and drift capacity of the buildings in inelastic region beyond yielding point, the effect of corrosion on the period, mass participation rate and modal amplitude in elastic region is neglected during modal analysis. The capacity curve of S10-3 for $U_{yNI}=0.042$ m is shown in Figure 8.23. Total curvature demand and damage regions for base columns of S10-3 building are shown in Table 8.11 and Table 8.12.

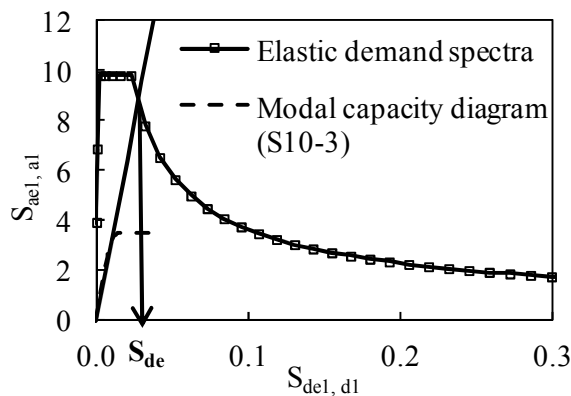


Figure 8.22 : Modal capacity diagram and elastic demand spectrum relationship.

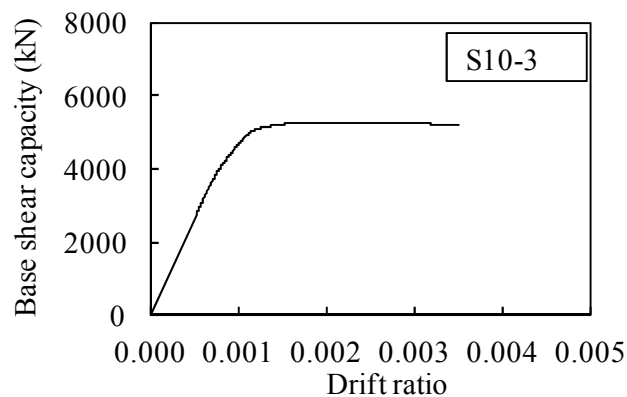


Figure 8.23 : Capacity curve of S10-3.

Table 8.11: Total curvature demand of base columns of S10-3 building.

Column notation	Column type	Plastic Rotation (rad/m)	Plastic Hinge Length (L_p) (m)	Plastic Curvature (K_p) (1/m)	Elastic Curvature (K_e) (1/m)	Total Curvature (K_t) (1/m)
K1	C10-30×80-5-3	0.01	0.048	0.2083333	0.002036	0.2103693
K2	C10-30×80-10-3	0.01	0.048	0.2083333	0.002216	0.2105493
K2	C10-30×80-10-3	0.01	0.048	0.2083333	0.002216	0.2105493
K2	C10-30×80-10-3	0.01	0.048	0.2083333	0.002216	0.2105493
K2	C10-30×80-10-3	0.01	0.048	0.2083333	0.002216	0.2105493
K1	C10-30×80-5-3	0.01	0.048	0.2083333	0.002036	0.2103693
K3	C10-65×65-5-3	0.01	0.048	0.2083333	0.004605	0.2129383
K4	C10-65×65-10-3	0.01	0.048	0.2083333	0.004927	0.2132603
K4	C10-65×65-10-3	0.01	0.048	0.2083333	0.004927	0.2132603
K4	C10-65×65-10-3	0.01	0.048	0.2083333	0.004927	0.2132603
K4	C10-65×65-10-3	0.01	0.048	0.2083333	0.004927	0.2132603
K3	C10-65×65-5-3	0.01	0.048	0.2083333	0.004605	0.2129383
K3	C10-65×65-5-3	0.01	0.048	0.2083333	0.004605	0.2129383
K4	C10-65×65-10-3	0.01	0.048	0.2083333	0.004927	0.2132603
K4	C10-65×65-10-3	0.01	0.048	0.2083333	0.004927	0.2132603
K4	C10-65×65-10-3	0.01	0.048	0.2083333	0.004927	0.2132603
K4	C10-65×65-10-3	0.01	0.048	0.2083333	0.004927	0.2132603
K4	C10-65×65-10-3	0.01	0.048	0.2083333	0.004927	0.2132603
K3	C10-65×65-5-3	0.01	0.048	0.2083333	0.004605	0.2129383
K1	C10-30×80-5-3	0.01	0.048	0.2083333	0.002036	0.2103693
K2	C10-30×80-10-3	0.01	0.048	0.2083333	0.002216	0.2105493
K2	C10-30×80-10-3	0.01	0.048	0.2083333	0.002216	0.2105493
K2	C10-30×80-10-3	0.01	0.048	0.2083333	0.002216	0.2105493
K2	C10-30×80-10-3	0.01	0.048	0.2083333	0.002216	0.2105493
K1	C10-30×80-5-3	0.01	0.048	0.2083333	0.002036	0.2103693

Table 8.12: Damage regions for base columns of S10-3 building.

Column notation	Column type	Unconfined	Confined	Steel	<i>MN</i>		<i>GV</i>		<i>GC</i>		Damage region
		concrete	concrete	ϵ_{su}	ϵ_c	ϵ_{su}	ϵ_{cc}	ϵ_{su}	ϵ_{cc}	ϵ_{su}	
		ϵ_c	ϵ_{cc}								
K1	C10-30×80-5-3	0.0148	0.0094	0.1500	0.0035	0.01	0.008434	0.04	0.010907	0.06	Collapsing Region
K2	C10-30×80-10-3	0.0305	0.0270	0.1400	0.0035	0.01	0.008434	0.04	0.010907	0.06	Collapsing Region
K2	C10-30×80-10-3	0.0305	0.0270	0.1400	0.0035	0.01	0.008434	0.04	0.010907	0.06	Collapsing Region
K2	C10-30×80-10-3	0.0305	0.0270	0.1400	0.0035	0.01	0.008434	0.04	0.010907	0.06	Collapsing Region
K2	C10-30×80-10-3	0.0305	0.0270	0.1400	0.0035	0.01	0.008434	0.04	0.010907	0.06	Collapsing Region
K1	C10-30×80-5-3	0.0148	0.0094	0.1500	0.0035	0.01	0.008434	0.04	0.010907	0.06	Collapsing Region
K3	C10-65×65-5-3	0.0234	0.0176	0.1200	0.0035	0.01	0.006852	0.04	0.008693	0.06	Collapsing Region
K4	C10-65×65-10-3	0.0344	0.0287	0.1000	0.0035	0.01	0.006852	0.04	0.008693	0.06	Collapsing Region
K4	C10-65×65-10-3	0.0344	0.0287	0.1000	0.0035	0.01	0.006852	0.04	0.008693	0.06	Collapsing Region
K4	C10-65×65-10-3	0.0344	0.0287	0.1000	0.0035	0.01	0.006852	0.04	0.008693	0.06	Collapsing Region
K4	C10-65×65-10-3	0.0344	0.0287	0.1000	0.0035	0.01	0.006852	0.04	0.008693	0.06	Collapsing Region
K3	C10-65×65-5-3	0.0234	0.0176	0.1200	0.0035	0.01	0.006852	0.04	0.008693	0.06	Collapsing Region
K3	C10-65×65-5-3	0.0234	0.0176	0.1200	0.0035	0.01	0.006852	0.04	0.008693	0.06	Collapsing Region
K4	C10-65×65-10-3	0.0344	0.0287	0.1000	0.0035	0.01	0.006852	0.04	0.008693	0.06	Collapsing Region
K4	C10-65×65-10-3	0.0344	0.0287	0.1000	0.0035	0.01	0.006852	0.04	0.008693	0.06	Collapsing Region
K4	C10-65×65-10-3	0.0344	0.0287	0.1000	0.0035	0.01	0.006852	0.04	0.008693	0.06	Collapsing Region
K4	C10-65×65-10-3	0.0344	0.0287	0.1000	0.0035	0.01	0.006852	0.04	0.008693	0.06	Collapsing Region
K3	C10-65×65-5-3	0.0234	0.0176	0.1200	0.0035	0.01	0.006852	0.04	0.008693	0.06	Collapsing Region
K1	C10-30×80-5-3	0.0148	0.0094	0.1500	0.0035	0.01	0.008434	0.04	0.010907	0.06	Collapsing Region
K2	C10-30×80-10-3	0.0305	0.0270	0.1400	0.0035	0.01	0.008434	0.04	0.010907	0.06	Collapsing Region
K2	C10-30×80-10-3	0.0305	0.0270	0.1400	0.0035	0.01	0.008434	0.04	0.010907	0.06	Collapsing Region
K2	C10-30×80-10-3	0.0305	0.0270	0.1400	0.0035	0.01	0.008434	0.04	0.010907	0.06	Collapsing Region
K2	C10-30×80-10-3	0.0305	0.0270	0.1400	0.0035	0.01	0.008434	0.04	0.010907	0.06	Collapsing Region
K1	C10-30×80-5-3	0.0148	0.0094	0.1500	0.0035	0.01	0.008434	0.04	0.010907	0.06	Collapsing Region

Modal capacity diagram-elastic demand spectrum relationship, capacity curve of building S10-6, total curvature demand and damage regions for base columns of S10-6 building are shown in Figure 8.24a-b, Table 8.13, and Table 8.14, respectively.

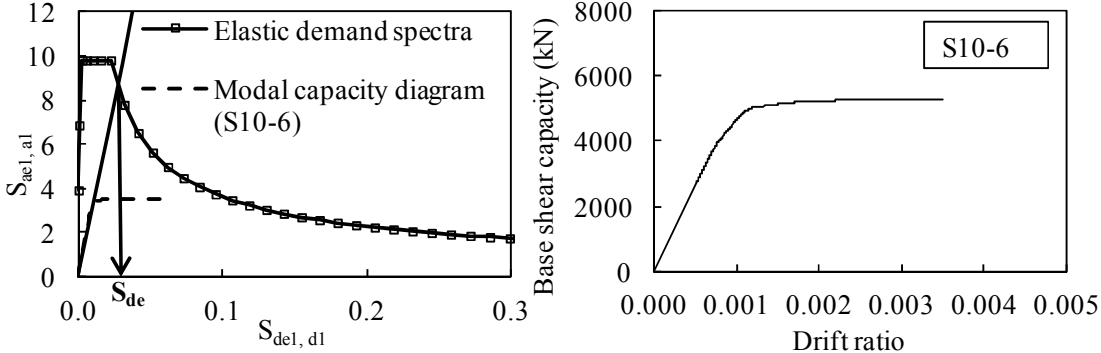


Figure 8.24 : a) Modal capacity diagram and elastic demand spectrum relationship, b) Capacity curve of S10-6.

Table 8.13: Total curvature demand of base columns of S10-6 building.

Column notation	Column type	Plastic Rotation (rad/m)	Plastic Hinge Length (L_p) (m)	Plastic Curvature (K_p) (1/m)	Elastic Curvature (K_e) (1/m)	Total Curvature (K_t) (1/m)
K1	C10-30×80-5-6	0.01	0.096	0.1041667	0.002036	0.1062027
K2	C10-30×80-10-6	0.01	0.096	0.1041667	0.002216	0.1063827
K2	C10-30×80-10-6	0.01	0.096	0.1041667	0.002216	0.1063827
K2	C10-30×80-10-6	0.01	0.096	0.1041667	0.002216	0.1063827
K1	C10-30×80-5-6	0.01	0.096	0.1041667	0.002036	0.1062027
K3	C10-65×65-5-6	0.01	0.096	0.1041667	0.004605	0.1087717
K4	C10-65×65-10-6	0.01	0.096	0.1041667	0.004927	0.1090937
K4	C10-65×65-10-6	0.01	0.096	0.1041667	0.004927	0.1090937
K4	C10-65×65-10-6	0.01	0.096	0.1041667	0.004927	0.1090937
K4	C10-65×65-10-6	0.01	0.096	0.1041667	0.004927	0.1090937
K3	C10-65×65-5-6	0.01	0.096	0.1041667	0.004605	0.1087717
K3	C10-65×65-5-6	0.01	0.096	0.1041667	0.004605	0.1087717
K4	C10-65×65-10-6	0.01	0.096	0.1041667	0.004927	0.1090937
K4	C10-65×65-10-6	0.01	0.096	0.1041667	0.004927	0.1090937
K4	C10-65×65-10-6	0.01	0.096	0.1041667	0.004927	0.1090937
K3	C10-65×65-5-6	0.01	0.096	0.1041667	0.004605	0.1087717
K1	C10-30×80-5-6	0.01	0.096	0.1041667	0.002036	0.1062027
K2	C10-30×80-10-6	0.01	0.096	0.1041667	0.002216	0.1063827
K2	C10-30×80-10-6	0.01	0.096	0.1041667	0.002216	0.1063827
K2	C10-30×80-10-6	0.01	0.096	0.1041667	0.002216	0.1063827
K1	C10-30×80-5-6	0.01	0.096	0.1041667	0.002036	0.1062027

Table 8.14: Damage regions for base columns of S10-6 building.

Column notation	Column type	Unconfined concrete ϵ_c	Confined concrete ϵ_{cc}	Steel ϵ_{su}	<i>MN</i>		<i>GV</i>		<i>GC</i>		Damage region
					ϵ_c	ϵ_{cc}	ϵ_{su}	ϵ_{cc}	ϵ_{su}	ϵ_{cc}	
K1	C10-30×80-5-6	0.0069	0.0041	0.0770	0.0035	0.01	0.00843	0.04	0.010907	0.06	Collapsing Region
K2	C10-30×80-10-6	0.0128	0.0099	0.0750	0.0035	0.01	0.00843	0.04	0.010907	0.06	Collapsing Region
K2	C10-30×80-10-6	0.0128	0.0099	0.0750	0.0035	0.01	0.00843	0.04	0.010907	0.06	Collapsing Region
K2	C10-30×80-10-6	0.0128	0.0099	0.0750	0.0035	0.01	0.00843	0.04	0.010907	0.06	Collapsing Region
K2	C10-30×80-10-6	0.0128	0.0099	0.0750	0.0035	0.01	0.00843	0.04	0.010907	0.06	Collapsing Region
K1	C10-30×80-5-6	0.0069	0.0041	0.0770	0.0035	0.01	0.00843	0.04	0.010907	0.06	Collapsing Region
K3	C10-65×65-5-6	0.0086	0.0056	0.0590	0.0035	0.01	0.00685	0.04	0.008693	0.06	Advanced Damage Region
K4	C10-65×65-10-6	0.0136	0.0106	0.0530	0.0035	0.01	0.00685	0.04	0.008693	0.06	Collapsing Region
K4	C10-65×65-10-6	0.0136	0.0106	0.0530	0.0035	0.01	0.00685	0.04	0.008693	0.06	Collapsing Region
K4	C10-65×65-10-6	0.0136	0.0106	0.0530	0.0035	0.01	0.00685	0.04	0.008693	0.06	Collapsing Region
K4	C10-65×65-10-6	0.0136	0.0106	0.0530	0.0035	0.01	0.00685	0.04	0.008693	0.06	Collapsing Region
K3	C10-65×65-5-6	0.0086	0.0056	0.0590	0.0035	0.01	0.00685	0.04	0.008693	0.06	Advanced Damage Region
K3	C10-65×65-5-6	0.0086	0.0056	0.0590	0.0035	0.01	0.00685	0.04	0.008693	0.06	Advanced Damage Region
K4	C10-65×65-10-6	0.0136	0.0106	0.0530	0.0035	0.01	0.00685	0.04	0.008693	0.06	Collapsing Region
K4	C10-65×65-10-6	0.0136	0.0106	0.0530	0.0035	0.01	0.00685	0.04	0.008693	0.06	Collapsing Region
K4	C10-65×65-10-6	0.0136	0.0106	0.0530	0.0035	0.01	0.00685	0.04	0.008693	0.06	Collapsing Region
K4	C10-65×65-10-6	0.0136	0.0106	0.0530	0.0035	0.01	0.00685	0.04	0.008693	0.06	Collapsing Region
K3	C10-65×65-5-6	0.0086	0.0056	0.0590	0.0035	0.01	0.00685	0.04	0.008693	0.06	Advanced Damage Region
K1	C10-30×80-5-6	0.0069	0.0041	0.0770	0.0035	0.01	0.00843	0.04	0.010907	0.06	Collapsing Region
K2	C10-30×80-10-6	0.0128	0.0099	0.0750	0.0035	0.01	0.00843	0.04	0.010907	0.06	Collapsing Region
K2	C10-30×80-10-6	0.0128	0.0099	0.0750	0.0035	0.01	0.00843	0.04	0.010907	0.06	Collapsing Region
K2	C10-30×80-10-6	0.0128	0.0099	0.0750	0.0035	0.01	0.00843	0.04	0.010907	0.06	Collapsing Region
K2	C10-30×80-10-6	0.0128	0.0099	0.0750	0.0035	0.01	0.00843	0.04	0.010907	0.06	Collapsing Region
K1	C10-30×80-5-6	0.0069	0.0041	0.0770	0.0035	0.0100	0.00843	0.04	0.010907	0.06	Collapsing Region

Modal capacity diagram and elastic demand spectrum relationship, capacity curve of building S10-12, total curvature demand and damage regions for base columns of building S10-12 are shown in Figure 8.25a-b, Table 8.15, and Table 8.16, respectively.

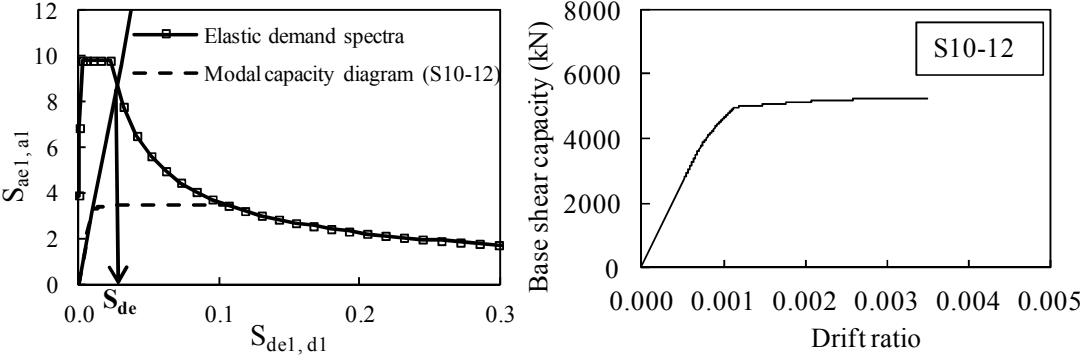


Figure 8.25 : a) Modal capacity diagram and elastic demand spectrum relationship, b) Capacity curve of S10-12.

Table 8.15: Total curvature demand of base columns of S10-12 building.

Column notation	Column type	Plastic Rotation (rad/m)	Plastic Hinge Length (L_p) (m)	Plastic Curvature (K_p) (1/m)	Elastic Curvature (K_e) (1/m)	Total Curvature (K_t) (1/m)
K1	C10-30×80-5-12	0.01	0.192	0.0520833	0.002036	0.0541193
K2	C10-30×80-10-12	0.01	0.192	0.0520833	0.002216	0.0542993
K2	C10-30×80-10-12	0.01	0.192	0.0520833	0.002216	0.0542993
K2	C10-30×80-10-12	0.01	0.192	0.0520833	0.002216	0.0542993
K2	C10-30×80-10-12	0.01	0.192	0.0520833	0.002216	0.0542993
K1	C10-30×80-5-12	0.01	0.192	0.0520833	0.002036	0.0541193
K3	C10-65×65-5-12	0.01	0.192	0.0520833	0.004605	0.0566883
K4	C10-65×65-10-12	0.01	0.192	0.0520833	0.004927	0.0570103
K4	C10-65×65-10-12	0.01	0.192	0.0520833	0.004927	0.0570103
K4	C10-65×65-10-12	0.01	0.192	0.0520833	0.004927	0.0570103
K4	C10-65×65-10-12	0.01	0.192	0.0520833	0.004927	0.0570103
K3	C10-65×65-5-12	0.01	0.192	0.0520833	0.004605	0.0566883
K3	C10-65×65-5-12	0.01	0.192	0.0520833	0.004605	0.0566883
K4	C10-65×65-10-12	0.01	0.192	0.0520833	0.004927	0.0570103
K4	C10-65×65-10-12	0.01	0.192	0.0520833	0.004927	0.0570103
K4	C10-65×65-10-12	0.01	0.192	0.0520833	0.004927	0.0570103
K4	C10-65×65-10-12	0.01	0.192	0.0520833	0.004927	0.0570103
K3	C10-65×65-10-12	0.01	0.192	0.0520833	0.004605	0.0566883
K1	C10-65×65-10-12	0.01	0.192	0.0520833	0.002036	0.0541193
K2	C10-65×65-10-12	0.01	0.192	0.0520833	0.002216	0.0542993
K2	C10-65×65-10-12	0.01	0.192	0.0520833	0.002216	0.0542993
K2	C10-65×65-10-12	0.01	0.192	0.0520833	0.002216	0.0542993
K2	C10-65×65-10-12	0.01	0.192	0.0520833	0.002216	0.0542993
K1	C10-65×65-10-12	0.01	0.192	0.0520833	0.002036	0.0541193

Table 8.16: Damage regions for base columns of S10-12 building.

Column notation	Column type	Unconfined concrete	Confined concrete	Steel	<i>MN</i>		<i>GV</i>		<i>GC</i>		Damage region
		ϵ_c	ϵ_{cc}	ϵ_{su}	ϵ_c	ϵ_{su}	ϵ_{cc}	ϵ_{su}	ϵ_{cc}	ϵ_{su}	
K1	C10-30×80-5-12	0.0035	0.0020	0.0400	0.0035	0.01	0.008434	0.04	0.010907	0.06	Advanced Damage Region
K2	C10-30×80-10-12	0.0057	0.0043	0.0343	0.0035	0.01	0.008434	0.04	0.010907	0.06	Marked Damage Region
K2	C10-30×80-10-12	0.0057	0.0043	0.0343	0.0035	0.01	0.008434	0.04	0.010907	0.06	Marked Damage Region
K2	C10-30×80-10-12	0.0057	0.0043	0.0343	0.0035	0.01	0.008434	0.04	0.010907	0.06	Marked Damage Region
K2	C10-30×80-10-12	0.0057	0.0043	0.0343	0.0035	0.01	0.008434	0.04	0.010907	0.06	Marked Damage Region
K1	C10-30×80-5-12	0.0035	0.0020	0.0400	0.0035	0.01	0.008434	0.04	0.010907	0.06	Advanced Damage Region
K3	C10-65×65-5-12	0.0039	0.0024	0.0272	0.0035	0.01	0.006852	0.04	0.008693	0.06	Marked Damage Region
K4	C10-65×65-10-12	0.0068	0.0051	0.0301	0.0035	0.01	0.006852	0.04	0.008693	0.06	Marked Damage Region
K4	C10-65×65-10-12	0.0068	0.0051	0.0301	0.0035	0.01	0.006852	0.04	0.008693	0.06	Marked Damage Region
K4	C10-65×65-10-12	0.0068	0.0051	0.0301	0.0035	0.01	0.006852	0.04	0.008693	0.06	Marked Damage Region
K4	C10-65×65-10-12	0.0068	0.0051	0.0301	0.0035	0.01	0.006852	0.04	0.008693	0.06	Marked Damage Region
K3	C10-65×65-5-12	0.0039	0.0024	0.0272	0.0035	0.01	0.006852	0.04	0.008693	0.06	Marked Damage Region
K3	C10-65×65-5-12	0.0039	0.0024	0.0272	0.0035	0.01	0.006852	0.04	0.008693	0.06	Marked Damage Region
K4	C10-65×65-10-12	0.0068	0.0051	0.0301	0.0035	0.01	0.006852	0.04	0.008693	0.06	Marked Damage Region
K4	C10-65×65-10-12	0.0068	0.0051	0.0301	0.0035	0.01	0.006852	0.04	0.008693	0.06	Marked Damage Region
K4	C10-65×65-10-12	0.0068	0.0051	0.0301	0.0035	0.01	0.006852	0.04	0.008693	0.06	Marked Damage Region
K4	C10-65×65-10-12	0.0068	0.0051	0.0301	0.0035	0.01	0.006852	0.04	0.008693	0.06	Marked Damage Region
K3	C10-65×65-10-12	0.0039	0.0024	0.0272	0.0035	0.01	0.006852	0.04	0.008693	0.06	Marked Damage Region
K1	C10-65×65-10-12	0.0035	0.0020	0.0400	0.0035	0.01	0.008434	0.04	0.010907	0.06	Advanced Damage Region
K2	C10-65×65-10-12	0.0057	0.0043	0.0343	0.0035	0.01	0.008434	0.04	0.010907	0.06	Marked Damage Region
K2	C10-65×65-10-12	0.0057	0.0043	0.0343	0.0035	0.01	0.008434	0.04	0.010907	0.06	Marked Damage Region
K2	C10-65×65-10-12	0.0057	0.0043	0.0343	0.0035	0.01	0.008434	0.04	0.010907	0.06	Marked Damage Region
K2	C10-65×65-10-12	0.0057	0.0043	0.0343	0.0035	0.01	0.008434	0.04	0.010907	0.06	Marked Damage Region
K1	C10-65×65-10-12	0.0035	0.0020	0.0400	0.0035	0.01	0.008434	0.04	0.010907	0.06	Advanced Damage Region

Modal capacity diagram-elastic demand spectrum relationship, capacity curve of building S20-3, total curvature demand and damage regions for base columns of S20-3 building are shown in Figure 8.26a-b, Table 8.17, and Table 8.18, respectively.

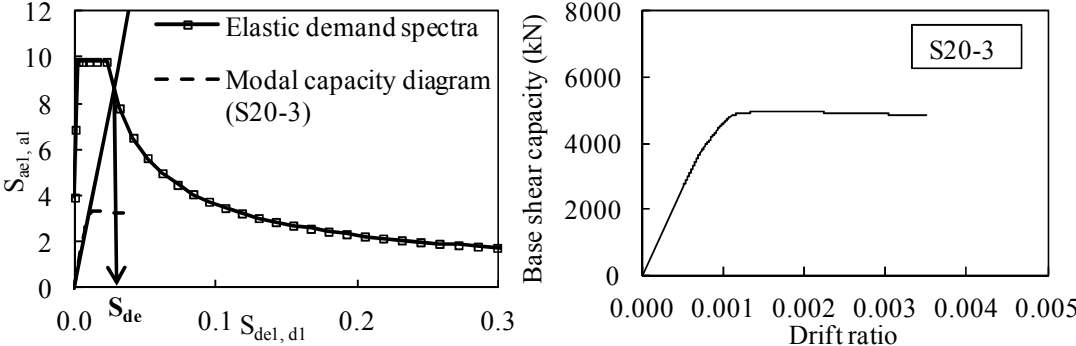


Figure 8.26 : a) Modal capacity diagram and elastic demand spectrum relationship, b) Capacity curve of S20-3.

Table 8.17: Total curvature demand of base columns of S20-3 building.

Column notation	Column type	Plastic Rotation (rad/m)	Plastic Hinge Length (L_p) (m)	Plastic Curvature (K_p) (1/m)	Elastic Curvature (K_y) (1/m)	Total Curvature (K_t) (1/m)
K1	C20-30×80-5-3	0.01	0.048	0.2083333	0.002036	0.2103693
K2	C20-30×80-10-3	0.01	0.048	0.2083333	0.002216	0.2105493
K2	C20-30×80-10-3	0.01	0.048	0.2083333	0.002216	0.2105493
K2	C20-30×80-10-3	0.01	0.048	0.2083333	0.002216	0.2105493
K2	C20-30×80-10-3	0.01	0.048	0.2083333	0.002216	0.2105493
K1	C20-30×80-5-3	0.01	0.048	0.2083333	0.002036	0.2103693
K3	C20-65×65-5-3	0.01	0.048	0.2083333	0.004605	0.2129383
K4	C20-65×65-10-3	0.01	0.048	0.2083333	0.004927	0.2132603
K4	C20-65×65-10-3	0.01	0.048	0.2083333	0.004927	0.2132603
K4	C20-65×65-10-3	0.01	0.048	0.2083333	0.004927	0.2132603
K4	C20-65×65-10-3	0.01	0.048	0.2083333	0.004927	0.2132603
K3	C20-65×65-5-3	0.01	0.048	0.2083333	0.004605	0.2129383
K3	C20-65×65-5-3	0.01	0.048	0.2083333	0.004605	0.2129383
K4	C20-65×65-10-3	0.01	0.048	0.2083333	0.004927	0.2132603
K4	C20-65×65-10-3	0.01	0.048	0.2083333	0.004927	0.2132603
K4	C20-65×65-10-3	0.01	0.048	0.2083333	0.004927	0.2132603
K4	C20-65×65-10-3	0.01	0.048	0.2083333	0.004927	0.2132603
K3	C20-65×65-5-3	0.01	0.048	0.2083333	0.004605	0.2129383
K1	C20-30×80-5-3	0.01	0.048	0.2083333	0.002036	0.2103693
K2	C20-30×80-10-3	0.01	0.048	0.2083333	0.002216	0.2105493
K2	C20-30×80-10-3	0.01	0.048	0.2083333	0.002216	0.2105493
K2	C20-30×80-10-3	0.01	0.048	0.2083333	0.002216	0.2105493
K2	C20-30×80-10-3	0.01	0.048	0.2083333	0.002216	0.2105493
K1	C20-30×80-5-3	0.01	0.048	0.2083333	0.002036	0.2103693

Table 8.18: Damage regions for base columns of S20-3 building.

Column notation	Column type	Unconfined	Confined	Steel	<i>MN</i>		<i>GV</i>		<i>GC</i>		Damage region
		concrete	concrete	ϵ_{su}	ϵ_c	ϵ_{su}	ϵ_{cc}	ϵ_{su}	ϵ_{cc}	ϵ_{su}	
		ϵ_c	ϵ_{cc}								
K1	C20-30×80-5-3	0.0139	0.0086	0.1500	0.0035	0.01	0.008434	0.04	0.010907	0.06	Collapsing Region
K2	C20-30×80-10-3	0.0299	0.0246	0.1300	0.0035	0.01	0.008434	0.04	0.010907	0.06	Collapsing Region
K2	C20-30×80-10-3	0.0299	0.0246	0.1300	0.0035	0.01	0.008434	0.04	0.010907	0.06	Collapsing Region
K2	C20-30×80-10-3	0.0299	0.0246	0.1300	0.0035	0.01	0.008434	0.04	0.010907	0.06	Collapsing Region
K2	C20-30×80-10-3	0.0299	0.0246	0.1300	0.0035	0.01	0.008434	0.04	0.010907	0.06	Collapsing Region
K1	C20-30×80-5-3	0.0139	0.0086	0.1500	0.0035	0.01	0.008434	0.04	0.010907	0.06	Collapsing Region
K3	C20-65×65-5-3	0.0170	0.0123	0.1000	0.0035	0.01	0.006852	0.04	0.008693	0.06	Collapsing Region
K4	C20-65×65-10-3	0.0317	0.0261	0.0607	0.0035	0.01	0.006852	0.04	0.008693	0.06	Collapsing Region
K4	C20-65×65-10-3	0.0317	0.0261	0.0607	0.0035	0.01	0.006852	0.04	0.008693	0.06	Collapsing Region
K4	C20-65×65-10-3	0.0317	0.0261	0.0607	0.0035	0.01	0.006852	0.04	0.008693	0.06	Collapsing Region
K4	C20-65×65-10-3	0.0317	0.0261	0.0607	0.0035	0.01	0.006852	0.04	0.008693	0.06	Collapsing Region
K3	C20-65×65-5-3	0.0170	0.0123	0.1000	0.0035	0.01	0.006852	0.04	0.008693	0.06	Collapsing Region
K3	C20-65×65-5-3	0.0170	0.0123	0.1000	0.0035	0.01	0.006852	0.04	0.008693	0.06	Collapsing Region
K4	C20-65×65-10-3	0.0317	0.0261	0.0607	0.0035	0.01	0.006852	0.04	0.008693	0.06	Collapsing Region
K4	C20-65×65-10-3	0.0317	0.0261	0.0607	0.0035	0.01	0.006852	0.04	0.008693	0.06	Collapsing Region
K4	C20-65×65-10-3	0.0317	0.0261	0.0607	0.0035	0.01	0.006852	0.04	0.008693	0.06	Collapsing Region
K4	C20-65×65-10-3	0.0317	0.0261	0.0607	0.0035	0.01	0.006852	0.04	0.008693	0.06	Collapsing Region
K4	C20-65×65-10-3	0.0317	0.0261	0.0607	0.0035	0.01	0.006852	0.04	0.008693	0.06	Collapsing Region
K3	C20-65×65-5-3	0.0170	0.0123	0.1000	0.0035	0.01	0.006852	0.04	0.008693	0.06	Collapsing Region
K1	C20-30×80-5-3	0.0139	0.0086	0.1500	0.0035	0.01	0.008434	0.04	0.010907	0.06	Collapsing Region
K2	C20-30×80-10-3	0.0299	0.0246	0.1300	0.0035	0.01	0.008434	0.04	0.010907	0.06	Collapsing Region
K2	C20-30×80-10-3	0.0299	0.0246	0.1300	0.0035	0.01	0.008434	0.04	0.010907	0.06	Collapsing Region
K2	C20-30×80-10-3	0.0299	0.0246	0.1300	0.0035	0.01	0.008434	0.04	0.010907	0.06	Collapsing Region
K2	C20-30×80-10-3	0.0299	0.0246	0.1300	0.0035	0.01	0.008434	0.04	0.010907	0.06	Collapsing Region
K2	C20-30×80-10-3	0.0299	0.0246	0.1300	0.0035	0.01	0.008434	0.04	0.010907	0.06	Collapsing Region
K1	C20-30×80-5-3	0.0139	0.0086	0.1500	0.0035	0.01	0.008434	0.04	0.010907	0.06	Collapsing Region

Modal capacity diagram-elastic demand spectrum relationship, capacity curve of building S20-6, total curvature demand and damage regions for base columns of building S20-6 are shown in Figure 8.27a-b, Table 8.19, and Table 8.20, respectively.

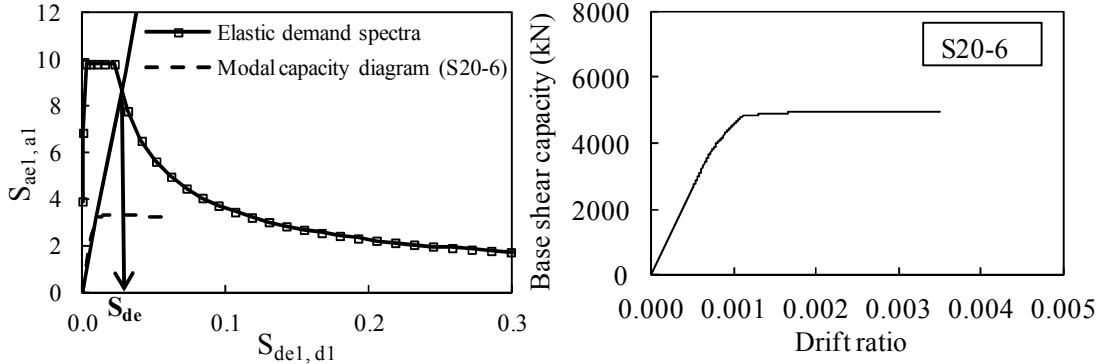


Figure 8.27 : a) Modal capacity diagram and elastic demand spectrum relationship, b) Capacity curve of S20-6.

Table 8.19: Total curvature demand of base columns of S20-6 building.

Column notation	Column type	Plastic Rotation (rad/m)	Plastic Hinge Length (L_p) (m)	Plastic Curvature (K_p) (1/m)	Elastic Curvature (K_y) (1/m)	Total Curvature (K_t) (1/m)
K1	C20-30×80-5-6	0.01	0.096	0.1041667	0.002036	0.1062027
K2	C20-30×80-10-6	0.01	0.096	0.1041667	0.002216	0.1063827
K2	C20-30×80-10-6	0.01	0.096	0.1041667	0.002216	0.1063827
K2	C20-30×80-10-6	0.01	0.096	0.1041667	0.002216	0.1063827
K2	C20-30×80-10-6	0.01	0.096	0.1041667	0.002216	0.1063827
K1	C20-30×80-5-6	0.01	0.096	0.1041667	0.002036	0.1062027
K3	C20-65×65-5-6	0.01	0.096	0.1041667	0.004605	0.1087717
K4	C20-65×65-10-6	0.01	0.096	0.1041667	0.004927	0.1090937
K4	C20-65×65-10-6	0.01	0.096	0.1041667	0.004927	0.1090937
K4	C20-65×65-10-6	0.01	0.096	0.1041667	0.004927	0.1090937
K4	C20-65×65-10-6	0.01	0.096	0.1041667	0.004927	0.1090937
K3	C20-65×65-5-6	0.01	0.096	0.1041667	0.004605	0.1087717
K3	C20-65×65-5-6	0.01	0.096	0.1041667	0.004605	0.1087717
K4	C20-65×65-10-6	0.01	0.096	0.1041667	0.004927	0.1090937
K4	C20-65×65-10-6	0.01	0.096	0.1041667	0.004927	0.1090937
K4	C20-65×65-10-6	0.01	0.096	0.1041667	0.004927	0.1090937
K4	C20-65×65-10-6	0.01	0.096	0.1041667	0.004927	0.1090937
K3	C20-65×65-5-6	0.01	0.096	0.1041667	0.004605	0.1087717
K1	C20-30×80-5-6	0.01	0.096	0.1041667	0.002036	0.1062027
K2	C20-30×80-10-6	0.01	0.096	0.1041667	0.002216	0.1063827
K2	C20-30×80-10-6	0.01	0.096	0.1041667	0.002216	0.1063827
K2	C20-30×80-10-6	0.01	0.096	0.1041667	0.002216	0.1063827
K2	C20-30×80-10-6	0.01	0.096	0.1041667	0.002216	0.1063827
K1	C20-30×80-5-6	0.01	0.096	0.1041667	0.002036	0.1062027

Table 8.20: Damage regions for base columns of S20-6 building.

Column notation	Column type	Unconfined	Confined	Steel	<i>MN</i>		<i>GV</i>		<i>GC</i>		Damage region
		concrete	concrete	ϵ_{su}	ϵ_c	ϵ_{su}	ϵ_{cc}	ϵ_{su}	ϵ_{cc}	ϵ_{su}	
		ϵ_c	ϵ_{cc}								
K1	C20-30×80-5-6	0.0067	0.0040	0.0769	0.0035	0.01	0.008434	0.04	0.010907	0.06	Collapsing Region
K2	C20-30×80-10-6	0.0124	0.0100	0.0743	0.0035	0.01	0.008434	0.04	0.010907	0.06	Collapsing Region
K2	C20-30×80-10-6	0.0124	0.0100	0.0743	0.0035	0.01	0.008434	0.04	0.010907	0.06	Collapsing Region
K2	C20-30×80-10-6	0.0124	0.0100	0.0743	0.0035	0.01	0.008434	0.04	0.010907	0.06	Collapsing Region
K2	C20-30×80-10-6	0.0124	0.0100	0.0743	0.0035	0.01	0.008434	0.04	0.010907	0.06	Collapsing Region
K1	C20-30×80-5-6	0.0067	0.0040	0.0769	0.0035	0.01	0.008434	0.04	0.010907	0.06	Collapsing Region
K3	C20-65×65-5-6	0.0077	0.0049	0.0576	0.0035	0.01	0.006852	0.04	0.008693	0.06	Advanced Damage Region
K4	C20-65×65-10-6	0.0133	0.0103	0.0528	0.0035	0.01	0.006852	0.04	0.008693	0.06	Collapsing Region
K4	C20-65×65-10-6	0.0133	0.0103	0.0528	0.0035	0.01	0.006852	0.04	0.008693	0.06	Collapsing Region
K4	C20-65×65-10-6	0.0133	0.0103	0.0528	0.0035	0.01	0.006852	0.04	0.008693	0.06	Collapsing Region
K4	C20-65×65-10-6	0.0133	0.0103	0.0528	0.0035	0.01	0.006852	0.04	0.008693	0.06	Collapsing Region
K3	C20-65×65-5-6	0.0077	0.0049	0.0576	0.0035	0.01	0.006852	0.04	0.008693	0.06	Advanced Damage Region
K3	C20-65×65-5-6	0.0077	0.0049	0.0576	0.0035	0.01	0.006852	0.04	0.008693	0.06	Advanced Damage Region
K4	C20-65×65-10-6	0.0133	0.0103	0.0528	0.0035	0.01	0.006852	0.04	0.008693	0.06	Collapsing Region
K4	C20-65×65-10-6	0.0133	0.0103	0.0528	0.0035	0.01	0.006852	0.04	0.008693	0.06	Collapsing Region
K4	C20-65×65-10-6	0.0133	0.0103	0.0528	0.0035	0.01	0.006852	0.04	0.008693	0.06	Collapsing Region
K4	C20-65×65-10-6	0.0133	0.0103	0.0528	0.0035	0.01	0.006852	0.04	0.008693	0.06	Collapsing Region
K4	C20-65×65-10-6	0.0133	0.0103	0.0528	0.0035	0.01	0.006852	0.04	0.008693	0.06	Collapsing Region
K3	C20-65×65-5-6	0.0077	0.0049	0.0576	0.0035	0.01	0.006852	0.04	0.008693	0.06	Advanced Damage Region
K1	C20-30×80-5-6	0.0067	0.0040	0.0769	0.0035	0.01	0.008434	0.04	0.010907	0.06	Collapsing Region
K2	C20-30×80-10-6	0.0124	0.0100	0.0743	0.0035	0.01	0.008434	0.04	0.010907	0.06	Collapsing Region
K2	C20-30×80-10-6	0.0124	0.0100	0.0743	0.0035	0.01	0.008434	0.04	0.010907	0.06	Collapsing Region
K2	C20-30×80-10-6	0.0124	0.0100	0.0743	0.0035	0.01	0.008434	0.04	0.010907	0.06	Collapsing Region
K2	C20-30×80-10-6	0.0124	0.0100	0.0743	0.0035	0.01	0.008434	0.04	0.010907	0.06	Collapsing Region
K1	C20-30×80-5-6	0.0067	0.0040	0.0769	0.0035	0.01	0.008434	0.04	0.010907	0.06	Collapsing Region

Modal capacity diagram-elastic demand spectrum relationship, capacity curve of building S20-12, total curvature demand and damage regions for base columns of S20-12 building are shown in Figure 8.28a-b, Table 8.21, and 0, respectively.

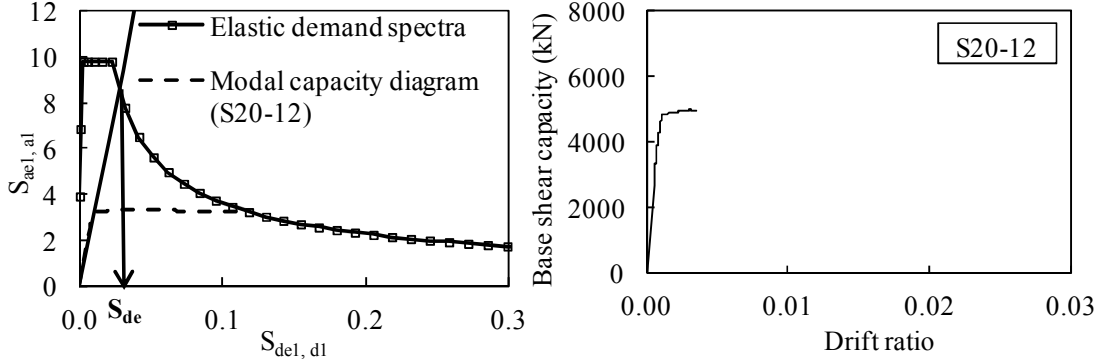


Figure 8.28 : a) Modal capacity diagram and elastic demand spectrum relationship, b) Capacity curve of S20-12.

Table 8.21: Total curvature demand of base columns of S20-12 building.

Column notation	Column type	Plastic Rotation (rad/m)	Plastic Hinge Length (L_p) (m)	Plastic Curvature (K_p) (1/m)	Elastic Curvature (K_e) (1/m)	Total Curvature (K_t) (1/m)
K1	C20-30×80-5-12	0.01	0.192	0.0520833	0.002036	0.0541193
K2	C20-30×80-10-12	0.01	0.192	0.0520833	0.002216	0.0542993
K2	C20-30×80-10-12	0.01	0.192	0.0520833	0.002216	0.0542993
K2	C20-30×80-10-12	0.01	0.192	0.0520833	0.002216	0.0542993
K2	C20-30×80-10-12	0.01	0.192	0.0520833	0.002216	0.0542993
K1	C20-30×80-5-12	0.01	0.192	0.0520833	0.002036	0.0541193
K3	C20-65×65-5-12	0.01	0.192	0.0520833	0.004605	0.0566883
K4	C20-65×65-10-12	0.01	0.192	0.0520833	0.004927	0.0570103
K4	C20-65×65-10-12	0.01	0.192	0.0520833	0.004927	0.0570103
K4	C20-65×65-10-12	0.01	0.192	0.0520833	0.004927	0.0570103
K4	C20-65×65-10-12	0.01	0.192	0.0520833	0.004927	0.0570103
K3	C20-65×65-5-12	0.01	0.192	0.0520833	0.004605	0.0566883
K3	C20-65×65-5-12	0.01	0.192	0.0520833	0.004605	0.0566883
K4	C20-65×65-10-12	0.01	0.192	0.0520833	0.004927	0.0570103
K4	C20-65×65-10-12	0.01	0.192	0.0520833	0.004927	0.0570103
K4	C20-65×65-10-12	0.01	0.192	0.0520833	0.004927	0.0570103
K4	C20-65×65-10-12	0.01	0.192	0.0520833	0.004927	0.0570103
K3	C20-65×65-5-12	0.01	0.192	0.0520833	0.004605	0.0566883
K1	C20-30×80-5-12	0.01	0.192	0.0520833	0.002036	0.0541193
K2	C20-30×80-10-12	0.01	0.192	0.0520833	0.002216	0.0542993
K2	C20-30×80-10-12	0.01	0.192	0.0520833	0.002216	0.0542993
K2	C20-30×80-10-12	0.01	0.192	0.0520833	0.002216	0.0542993
K2	C20-30×80-10-12	0.01	0.192	0.0520833	0.002216	0.0542993
K1	C20-30×80-5-12	0.01	0.192	0.0520833	0.002036	0.0541193

Table 8.22: Damage regions for base columns of S20-12 building.

Column notation	Column type	Unconfined	Confined	Steel	<i>MN</i>		<i>GV</i>		<i>GC</i>		Damage region
		concrete	concrete	ϵ_{su}	ϵ_c	ϵ_{su}	ϵ_{cc}	ϵ_{su}	ϵ_{cc}	ϵ_{su}	
		ϵ_c	ϵ_{cc}								
K1	C20-30×80-5-12	0.0034	0.0020	0.0399	0.0035	0.01	0.008434	0.04	0.010907	0.06	Marked Damage Region
K2	C20-30×80-10-12	0.0054	0.0041	0.0349	0.0035	0.01	0.008434	0.04	0.010907	0.06	Marked Damage Region
K2	C20-30×80-10-12	0.0054	0.0041	0.0349	0.0035	0.01	0.008434	0.04	0.010907	0.06	Marked Damage Region
K2	C20-30×80-10-12	0.0054	0.0041	0.0349	0.0035	0.01	0.008434	0.04	0.010907	0.06	Marked Damage Region
K2	C20-30×80-10-12	0.0054	0.0041	0.0349	0.0035	0.01	0.008434	0.04	0.010907	0.06	Marked Damage Region
K1	C20-30×80-5-12	0.0034	0.0020	0.0399	0.0035	0.01	0.008434	0.04	0.010907	0.06	Marked Damage Region
K3	C20-65×65-5-12	0.0036	0.0022	0.0276	0.0035	0.01	0.006852	0.04	0.008693	0.06	Marked Damage Region
K4	C20-65×65-10-12	0.0046	0.0035	0.0295	0.0035	0.01	0.006852	0.04	0.008693	0.06	Marked Damage Region
K4	C20-65×65-10-12	0.0046	0.0035	0.0295	0.0035	0.01	0.006852	0.04	0.008693	0.06	Marked Damage Region
K4	C20-65×65-10-12	0.0046	0.0035	0.0295	0.0035	0.01	0.006852	0.04	0.008693	0.06	Marked Damage Region
K4	C20-65×65-10-12	0.0046	0.0035	0.0295	0.0035	0.01	0.006852	0.04	0.008693	0.06	Marked Damage Region
K4	C20-65×65-10-12	0.0046	0.0035	0.0295	0.0035	0.01	0.006852	0.04	0.008693	0.06	Marked Damage Region
K3	C20-65×65-5-12	0.0036	0.0022	0.0276	0.0035	0.01	0.006852	0.04	0.008693	0.06	Marked Damage Region
K3	C20-65×65-5-12	0.0036	0.0022	0.0276	0.0035	0.01	0.006852	0.04	0.008693	0.06	Marked Damage Region
K4	C20-65×65-10-12	0.0046	0.0035	0.0295	0.0035	0.01	0.006852	0.04	0.008693	0.06	Marked Damage Region
K4	C20-65×65-10-12	0.0046	0.0035	0.0295	0.0035	0.01	0.006852	0.04	0.008693	0.06	Marked Damage Region
K4	C20-65×65-10-12	0.0046	0.0035	0.0295	0.0035	0.01	0.006852	0.04	0.008693	0.06	Marked Damage Region
K4	C20-65×65-10-12	0.0046	0.0035	0.0295	0.0035	0.01	0.006852	0.04	0.008693	0.06	Marked Damage Region
K4	C20-65×65-10-12	0.0046	0.0035	0.0295	0.0035	0.01	0.006852	0.04	0.008693	0.06	Marked Damage Region
K3	C20-65×65-5-12	0.0036	0.0022	0.0276	0.0035	0.01	0.006852	0.04	0.008693	0.06	Marked Damage Region
K1	C20-30×80-5-12	0.0034	0.0020	0.0399	0.0035	0.01	0.008434	0.04	0.010907	0.06	Marked Damage Region
K2	C20-30×80-10-12	0.0054	0.0041	0.0349	0.0035	0.01	0.008434	0.04	0.010907	0.06	Marked Damage Region
K2	C20-30×80-10-12	0.0054	0.0041	0.0349	0.0035	0.01	0.008434	0.04	0.010907	0.06	Marked Damage Region
K2	C20-30×80-10-12	0.0054	0.0041	0.0349	0.0035	0.01	0.008434	0.04	0.010907	0.06	Marked Damage Region
K2	C20-30×80-10-12	0.0054	0.0041	0.0349	0.0035	0.01	0.008434	0.04	0.010907	0.06	Marked Damage Region
K2	C20-30×80-10-12	0.0054	0.0041	0.0349	0.0035	0.01	0.008434	0.04	0.010907	0.06	Marked Damage Region
K1	C20-30×80-5-12	0.0034	0.0020	0.0399	0.0035	0.01	0.008434	0.04	0.010907	0.06	Marked Damage Region

Modal capacity diagram-elastic demand spectrum relationship, capacity curve of building S30-3, total curvature demand and damage regions for base columns of S30-3 building are shown in Figure 8.29a-b, Table 8.23, and Table 8.24, respectively.

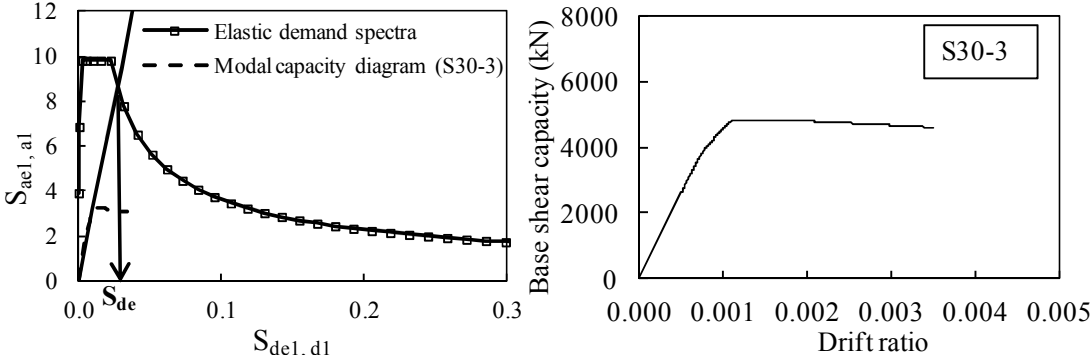


Figure 8.29 : a) Modal capacity diagram and elastic demand spectrum relationship, b) Capacity curve of S30-3.

Table 8.23 : Total curvature demand of base columns of S30-3 building.

Column notation	Column type	Plastic Rotation (rad/m)	Plastic Hinge Length (L_p) (m)	Plastic Curvature (K_p) (1/m)	Elastic Curvature (K_y) (1/m)	Total Curvature (K_t) (1/m)
K1	C30-30×80-5-3	0.01	0.048	0.2083333	0.002036	0.2103693
K2	C30-30×80-10-3	0.01	0.048	0.2083333	0.002216	0.2105493
K2	C30-30×80-10-3	0.01	0.048	0.2083333	0.002216	0.2105493
K2	C30-30×80-10-3	0.01	0.048	0.2083333	0.002216	0.2105493
K2	C30-30×80-10-3	0.01	0.048	0.2083333	0.002216	0.2105493
K1	C30-30×80-5-3	0.01	0.048	0.2083333	0.002036	0.2103693
K3	C30-65×65-5-3	0.01	0.048	0.2083333	0.004605	0.2129383
K4	C30-65×65-10-3	0.01	0.048	0.2083333	0.004927	0.2132603
K4	C30-65×65-10-3	0.01	0.048	0.2083333	0.004927	0.2132603
K4	C30-65×65-10-3	0.01	0.048	0.2083333	0.004927	0.2132603
K4	C30-65×65-10-3	0.01	0.048	0.2083333	0.004927	0.2132603
K3	C30-65×65-5-3	0.01	0.048	0.2083333	0.004605	0.2129383
K3	C30-65×65-5-3	0.01	0.048	0.2083333	0.004605	0.2129383
K4	C30-65×65-10-3	0.01	0.048	0.2083333	0.004927	0.2132603
K4	C30-65×65-10-3	0.01	0.048	0.2083333	0.004927	0.2132603
K4	C30-65×65-10-3	0.01	0.048	0.2083333	0.004927	0.2132603
K4	C30-65×65-10-3	0.01	0.048	0.2083333	0.004927	0.2132603
K3	C30-65×65-5-3	0.01	0.048	0.2083333	0.004605	0.2129383
K1	C30-30×80-5-3	0.01	0.048	0.2083333	0.002036	0.2103693
K2	C30-30×80-10-3	0.01	0.048	0.2083333	0.002216	0.2105493
K2	C30-30×80-10-3	0.01	0.048	0.2083333	0.002216	0.2105493
K2	C30-30×80-10-3	0.01	0.048	0.2083333	0.002216	0.2105493
K2	C30-30×80-10-3	0.01	0.048	0.2083333	0.002216	0.2105493
K1	C30-30×80-5-3	0.01	0.048	0.2083333	0.002036	0.2103693

Table 8.24: Damage regions for base columns of S30-3 building.

Column notation	Column type	Unconfined	Confined	Steel	<i>MN</i>		<i>GV</i>		<i>GC</i>		Damage region
		concrete	concrete	ϵ_{su}	ϵ_c	ϵ_{su}	ϵ_{cc}	ϵ_{su}	ϵ_{cc}	ϵ_{su}	
		ϵ_c	ϵ_{cc}								
K1	C30-30×80-5-3	0.0136	0.0082	0.1500	0.0035	0.01	0.008434	0.04	0.010907	0.06	Collapsing Region
K2	C30-30×80-10-3	0.0309	0.0255	0.1400	0.0035	0.01	0.008434	0.04	0.010907	0.06	Collapsing Region
K2	C30-30×80-10-3	0.0309	0.0255	0.1400	0.0035	0.01	0.008434	0.04	0.010907	0.06	Collapsing Region
K2	C30-30×80-10-3	0.0309	0.0255	0.1400	0.0035	0.01	0.008434	0.04	0.010907	0.06	Collapsing Region
K2	C30-30×80-10-3	0.0309	0.0255	0.1400	0.0035	0.01	0.008434	0.04	0.010907	0.06	Collapsing Region
K1	C30-30×80-5-3	0.0136	0.0082	0.1500	0.0035	0.01	0.008434	0.04	0.010907	0.06	Collapsing Region
K3	C30-65×65-5-3	0.0177	0.0119	0.1100	0.0035	0.01	0.006852	0.04	0.008693	0.06	Collapsing Region
K4	C30-65×65-10-3	0.0338	0.0278	0.1000	0.0035	0.01	0.006852	0.04	0.008693	0.06	Collapsing Region
K4	C30-65×65-10-3	0.0338	0.0278	0.1000	0.0035	0.01	0.006852	0.04	0.008693	0.06	Collapsing Region
K4	C30-65×65-10-3	0.0338	0.0278	0.1000	0.0035	0.01	0.006852	0.04	0.008693	0.06	Collapsing Region
K4	C30-65×65-10-3	0.0338	0.0278	0.1000	0.0035	0.01	0.006852	0.04	0.008693	0.06	Collapsing Region
K3	C30-65×65-5-3	0.0177	0.0119	0.1100	0.0035	0.01	0.006852	0.04	0.008693	0.06	Collapsing Region
K3	C30-65×65-5-3	0.0177	0.0119	0.1100	0.0035	0.01	0.006852	0.04	0.008693	0.06	Collapsing Region
K4	C30-65×65-10-3	0.0338	0.0278	0.1000	0.0035	0.01	0.006852	0.04	0.008693	0.06	Collapsing Region
K4	C30-65×65-10-3	0.0338	0.0278	0.1000	0.0035	0.01	0.006852	0.04	0.008693	0.06	Collapsing Region
K4	C30-65×65-10-3	0.0338	0.0278	0.1000	0.0035	0.01	0.006852	0.04	0.008693	0.06	Collapsing Region
K4	C30-65×65-10-3	0.0338	0.0278	0.1000	0.0035	0.01	0.006852	0.04	0.008693	0.06	Collapsing Region
K3	C30-65×65-5-3	0.0177	0.0119	0.1100	0.0035	0.01	0.006852	0.04	0.008693	0.06	Collapsing Region
K1	C30-30×80-5-3	0.0136	0.0082	0.1500	0.0035	0.01	0.008434	0.04	0.010907	0.06	Collapsing Region
K2	C30-30×80-10-3	0.0309	0.0255	0.1400	0.0035	0.01	0.008434	0.04	0.010907	0.06	Collapsing Region
K2	C30-30×80-10-3	0.0309	0.0255	0.1400	0.0035	0.01	0.008434	0.04	0.010907	0.06	Collapsing Region
K2	C30-30×80-10-3	0.0309	0.0255	0.1400	0.0035	0.01	0.008434	0.04	0.010907	0.06	Collapsing Region
K2	C30-30×80-10-3	0.0309	0.0255	0.1400	0.0035	0.01	0.008434	0.04	0.010907	0.06	Collapsing Region
K1	C30-30×80-5-3	0.0136	0.0082	0.1500	0.0035	0.01	0.008434	0.04	0.010907	0.06	Collapsing Region

Modal capacity diagram-elastic demand spectrum relationship, capacity curve of building S30-6, total curvature demand and damage regions for base columns of S30-6 building are shown in Figure 8.30a-b, Table 8.25, and Table 8.26, respectively.

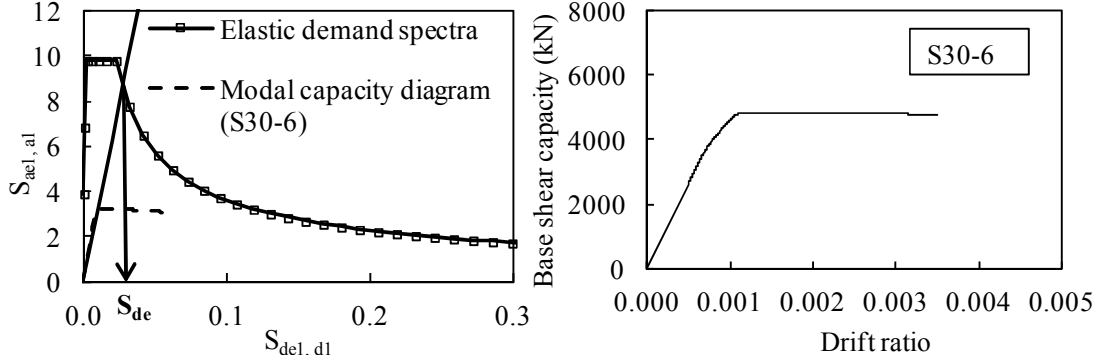


Figure 8.30 : a) Modal capacity diagram and elastic demand spectrum relationship, b) Capacity curve of S30-6.

Table 8.25: Total curvature demand of base columns of S30-6 building.

Column notation	Column type	Plastic Rotation (rad/m)	Plastic Hinge Length (L_p) (m)	Plastic Curvature (K_p) (1/m)	Elastic Curvature (K_y) (1/m)	Total Curvature (K_t) (1/m)
K1	C30-30×80-5-6	0.01	0.096	0.1041667	0.002036	0.1062027
K2	C30-30×80-10-6	0.01	0.096	0.1041667	0.002216	0.1063827
K2	C30-30×80-10-6	0.01	0.096	0.1041667	0.002216	0.1063827
K2	C30-30×80-10-6	0.01	0.096	0.1041667	0.002216	0.1063827
K2	C30-30×80-10-6	0.01	0.096	0.1041667	0.002216	0.1063827
K1	C30-30×80-5-6	0.01	0.096	0.1041667	0.002036	0.1062027
K3	C30-65×65-5-6	0.01	0.096	0.1041667	0.004605	0.1087717
K4	C30-65×65-10-6	0.01	0.096	0.1041667	0.004927	0.1090937
K4	C30-65×65-10-6	0.01	0.096	0.1041667	0.004927	0.1090937
K4	C30-65×65-10-6	0.01	0.096	0.1041667	0.004927	0.1090937
K4	C30-65×65-10-6	0.01	0.096	0.1041667	0.004927	0.1090937
K3	C30-65×65-5-6	0.01	0.096	0.1041667	0.004605	0.1087717
K3	C20-65×65-5-6	0.01	0.096	0.1041667	0.004605	0.1087717
K4	C30-65×65-10-6	0.01	0.096	0.1041667	0.004927	0.1090937
K4	C30-65×65-10-6	0.01	0.096	0.1041667	0.004927	0.1090937
K4	C30-65×65-10-6	0.01	0.096	0.1041667	0.004927	0.1090937
K4	C30-65×65-10-6	0.01	0.096	0.1041667	0.004927	0.1090937
K3	C30-65×65-5-6	0.01	0.096	0.1041667	0.004605	0.1087717
K1	C30-30×80-5-6	0.01	0.096	0.1041667	0.002036	0.1062027
K2	C30-30×80-10-6	0.01	0.096	0.1041667	0.002216	0.1063827
K2	C30-30×80-10-6	0.01	0.096	0.1041667	0.002216	0.1063827
K2	C30-30×80-10-6	0.01	0.096	0.1041667	0.002216	0.1063827
K2	C30-30×80-10-6	0.01	0.096	0.1041667	0.002216	0.1063827
K1	C30-30×80-5-6	0.01	0.096	0.1041667	0.002036	0.1062027

Table 8.26: Damage regions for base columns of S30-6 building.

Column notation	Column type	Unconfined concrete	Confined concrete	Steel	<i>MN</i>		<i>GV</i>		<i>GC</i>		Damage region
		ϵ_c	ϵ_{cc}	ϵ_{su}	ϵ_c	ϵ_{su}	ϵ_{cc}	ϵ_{su}	ϵ_{cc}	ϵ_{su}	
K1	C30-30×80-5-6	0.0067	0.0039	0.0767	0.0035	0.01	0.008434	0.04	0.010907	0.06	Collapsing Region
K2	C30-30×80-10-6	0.0120	0.0092	0.0728	0.0035	0.01	0.008434	0.04	0.010907	0.06	Collapsing Region
K2	C30-30×80-10-6	0.0120	0.0092	0.0728	0.0035	0.01	0.008434	0.04	0.010907	0.06	Collapsing Region
K2	C30-30×80-10-6	0.0120	0.0092	0.0728	0.0035	0.01	0.008434	0.04	0.010907	0.06	Collapsing Region
K2	C30-30×80-10-6	0.0120	0.0092	0.0728	0.0035	0.01	0.008434	0.04	0.010907	0.06	Collapsing Region
K1	C30-30×80-5-6	0.0067	0.0039	0.0767	0.0035	0.01	0.008434	0.04	0.010907	0.06	Collapsing Region
K3	C30-65×65-5-6	0.0843	0.0052	0.0643	0.0035	0.01	0.006852	0.04	0.008693	0.06	Collapsing Region
K4	C30-65×65-10-6	0.0123	0.0094	0.0534	0.0035	0.01	0.006852	0.04	0.008693	0.06	Collapsing Region
K4	C30-65×65-10-6	0.0123	0.0094	0.0534	0.0035	0.01	0.006852	0.04	0.008693	0.06	Collapsing Region
K4	C30-65×65-10-6	0.0123	0.0094	0.0534	0.0035	0.01	0.006852	0.04	0.008693	0.06	Collapsing Region
K4	C30-65×65-10-6	0.0123	0.0094	0.0534	0.0035	0.01	0.006852	0.04	0.008693	0.06	Collapsing Region
K3	C30-65×65-5-6	0.0843	0.0052	0.0643	0.0035	0.01	0.006852	0.04	0.008693	0.06	Collapsing Region
K3	C20-65×65-5-6	0.0843	0.0052	0.0643	0.0035	0.01	0.006852	0.04	0.008693	0.06	Collapsing Region
K4	C30-65×65-10-6	0.0123	0.0094	0.0534	0.0035	0.01	0.006852	0.04	0.008693	0.06	Collapsing Region
K4	C30-65×65-10-6	0.0123	0.0094	0.0534	0.0035	0.01	0.006852	0.04	0.008693	0.06	Collapsing Region
K4	C30-65×65-10-6	0.0123	0.0094	0.0534	0.0035	0.01	0.006852	0.04	0.008693	0.06	Collapsing Region
K4	C30-65×65-10-6	0.0123	0.0094	0.0534	0.0035	0.01	0.006852	0.04	0.008693	0.06	Collapsing Region
K4	C30-65×65-10-6	0.0123	0.0094	0.0534	0.0035	0.01	0.006852	0.04	0.008693	0.06	Collapsing Region
K3	C30-65×65-5-6	0.0843	0.0052	0.0643	0.0035	0.01	0.006852	0.04	0.008693	0.06	Collapsing Region
K1	C30-30×80-5-6	0.0067	0.0039	0.0767	0.0035	0.01	0.008434	0.04	0.010907	0.06	Collapsing Region
K2	C30-30×80-10-6	0.0120	0.0092	0.0728	0.0035	0.01	0.008434	0.04	0.010907	0.06	Collapsing Region
K2	C30-30×80-10-6	0.0120	0.0092	0.0728	0.0035	0.01	0.008434	0.04	0.010907	0.06	Collapsing Region
K2	C30-30×80-10-6	0.0120	0.0092	0.0728	0.0035	0.01	0.008434	0.04	0.010907	0.06	Collapsing Region
K2	C30-30×80-10-6	0.0120	0.0092	0.0728	0.0035	0.01	0.008434	0.04	0.010907	0.06	Collapsing Region
K2	C30-30×80-10-6	0.0120	0.0092	0.0728	0.0035	0.01	0.008434	0.04	0.010907	0.06	Collapsing Region
K1	C30-30×80-5-6	0.0067	0.0039	0.0767	0.0035	0.01	0.008434	0.04	0.010907	0.06	Collapsing Region

Modal capacity diagram-elastic demand spectrum relationship, capacity curve of building S30-12, total curvature demand and damage regions for base columns of S30-12 building are shown in Figure 8.31a-b, Table 8.27, and Table 8.28, respectively.

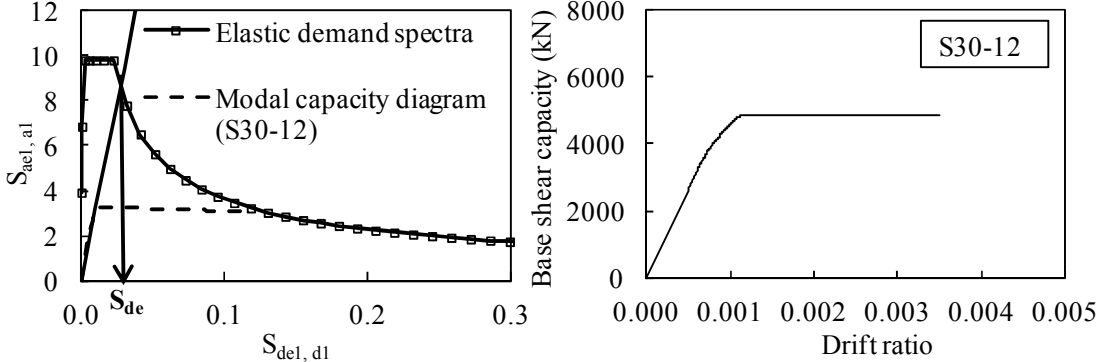


Figure 8.31 : a) Modal capacity diagram and elastic demand spectrum relationship, b) Capacity curve of S30-12.

Table 8.27: Total curvature demand of base columns of S30-12 building.

Column notation	Column type	Plastic Rotation (rad/m)	Plastic Hinge Length (L_p) (m)	Plastic Curvature (K_p) (1/m)	Elastic Curvature (K_e) (1/m)	Total Curvature (K_t) (1/m)
K1	C30-30×80-5-12	0.01	0.192	0.0520833	0.002036	0.0541193
K2	C30-30×80-10-12	0.01	0.192	0.0520833	0.002216	0.0542993
K2	C30-30×80-10-12	0.01	0.192	0.0520833	0.002216	0.0542993
K2	C30-30×80-10-12	0.01	0.192	0.0520833	0.002216	0.0542993
K2	C30-30×80-10-12	0.01	0.192	0.0520833	0.002216	0.0542993
K1	C30-30×80-5-12	0.01	0.192	0.0520833	0.002036	0.0541193
K3	C30-65×65-5-12	0.01	0.192	0.0520833	0.004605	0.0566883
K4	C30-65×65-10-12	0.01	0.192	0.0520833	0.004927	0.0570103
K4	C30-65×65-10-12	0.01	0.192	0.0520833	0.004927	0.0570103
K4	C30-65×65-10-12	0.01	0.192	0.0520833	0.004927	0.0570103
K4	C30-65×65-10-12	0.01	0.192	0.0520833	0.004927	0.0570103
K3	C30-65×65-5-12	0.01	0.192	0.0520833	0.004605	0.0566883
K3	C30-65×65-5-12	0.01	0.192	0.0520833	0.004605	0.0566883
K4	C30-65×65-10-12	0.01	0.192	0.0520833	0.004927	0.0570103
K4	C30-65×65-10-12	0.01	0.192	0.0520833	0.004927	0.0570103
K4	C30-65×65-10-12	0.01	0.192	0.0520833	0.004927	0.0570103
K4	C30-65×65-10-12	0.01	0.192	0.0520833	0.004927	0.0570103
K3	C30-65×65-5-12	0.01	0.192	0.0520833	0.004605	0.0566883
K1	C30-30×80-5-12	0.01	0.192	0.0520833	0.002036	0.0541193
K2	C30-30×80-10-12	0.01	0.192	0.0520833	0.002216	0.0542993
K2	C30-30×80-10-12	0.01	0.192	0.0520833	0.002216	0.0542993
K2	C30-30×80-10-12	0.01	0.192	0.0520833	0.002216	0.0542993
K2	C30-30×80-10-12	0.01	0.192	0.0520833	0.002216	0.0542993
K1	C30-30×80-5-12	0.01	0.192	0.0520833	0.002036	0.0541193

Table 8.28: Damage regions for base columns of S30-12 building.

Column notation	Column type	Unconfined	Confined	Steel	<i>MN</i>		<i>GV</i>		<i>GC</i>		Damage region
		concrete	concrete	ϵ_{su}	ϵ_c	ϵ_{su}	ϵ_{cc}	ϵ_{su}	ϵ_{cc}	ϵ_{su}	
		ϵ_c	ϵ_{cc}								
K1	C30-30×80-5-12	0.0032	0.0018	0.0400	0.0035	0.01	0.008434	0.04	0.010907	0.06	Advanced Damage Region
K2	C30-30×80-10-12	0.0053	0.0040	0.0343	0.0035	0.01	0.008434	0.04	0.010907	0.06	Marked Damage Region
K2	C30-30×80-10-12	0.0053	0.0040	0.0343	0.0035	0.01	0.008434	0.04	0.010907	0.06	Marked Damage Region
K2	C30-30×80-10-12	0.0053	0.0040	0.0343	0.0035	0.01	0.008434	0.04	0.010907	0.06	Marked Damage Region
K2	C30-30×80-10-12	0.0053	0.0040	0.0343	0.0035	0.01	0.008434	0.04	0.010907	0.06	Marked Damage Region
K1	C30-30×80-5-12	0.0032	0.0018	0.0400	0.0035	0.01	0.008434	0.04	0.010907	0.06	Advanced Damage Region
K3	C30-65×65-5-12	0.0035	0.0021	0.0272	0.0035	0.01	0.006852	0.04	0.008693	0.06	Marked Damage Region
K4	C30-65×65-10-12	0.0057	0.0041	0.0301	0.0035	0.01	0.006852	0.04	0.008693	0.06	Marked Damage Region
K4	C30-65×65-10-12	0.0057	0.0041	0.0301	0.0035	0.01	0.006852	0.04	0.008693	0.06	Marked Damage Region
K4	C30-65×65-10-12	0.0057	0.0041	0.0301	0.0035	0.01	0.006852	0.04	0.008693	0.06	Marked Damage Region
K4	C30-65×65-10-12	0.0057	0.0041	0.0301	0.0035	0.01	0.006852	0.04	0.008693	0.06	Marked Damage Region
K4	C30-65×65-10-12	0.0057	0.0041	0.0301	0.0035	0.01	0.006852	0.04	0.008693	0.06	Marked Damage Region
K3	C30-65×65-5-12	0.0035	0.0021	0.0272	0.0035	0.01	0.006852	0.04	0.008693	0.06	Marked Damage Region
K3	C30-65×65-5-12	0.0035	0.0021	0.0272	0.0035	0.01	0.006852	0.04	0.008693	0.06	Marked Damage Region
K4	C30-65×65-10-12	0.0057	0.0041	0.0301	0.0035	0.01	0.006852	0.04	0.008693	0.06	Marked Damage Region
K4	C30-65×65-10-12	0.0057	0.0041	0.0301	0.0035	0.01	0.006852	0.04	0.008693	0.06	Marked Damage Region
K4	C30-65×65-10-12	0.0057	0.0041	0.0301	0.0035	0.01	0.006852	0.04	0.008693	0.06	Marked Damage Region
K4	C30-65×65-10-12	0.0057	0.0041	0.0301	0.0035	0.01	0.006852	0.04	0.008693	0.06	Marked Damage Region
K3	C30-65×65-5-12	0.0035	0.0021	0.0272	0.0035	0.01	0.006852	0.04	0.008693	0.06	Marked Damage Region
K1	C30-30×80-5-12	0.0032	0.0018	0.0400	0.0035	0.01	0.008434	0.04	0.010907	0.06	Advanced Damage Region
K2	C30-30×80-10-12	0.0053	0.0040	0.0343	0.0035	0.01	0.008434	0.04	0.010907	0.06	Marked Damage Region
K2	C30-30×80-10-12	0.0053	0.0040	0.0343	0.0035	0.01	0.008434	0.04	0.010907	0.06	Marked Damage Region
K2	C30-30×80-10-12	0.0053	0.0040	0.0343	0.0035	0.01	0.008434	0.04	0.010907	0.06	Marked Damage Region
K2	C30-30×80-10-12	0.0053	0.0040	0.0343	0.0035	0.01	0.008434	0.04	0.010907	0.06	Marked Damage Region
K1	C30-30×80-5-12	0.0032	0.0018	0.0400	0.0035	0.01	0.008434	0.04	0.010907	0.06	Advanced Damage Region

The effect of level and distribution of corrosion on the behavior of RC columns under lateral load is obtained with nonlinear pushover analysis by damage determination. The damage levels of columns are shown on plan of the building for defining the effect of level and distribution of corrosion on the total curvature and strain demands of columns. The damage levels of building S10, S20 and S30 with 3, 6 and 12 number of pits with the consideration of building S0 are shown in Figure 8.32, Figure 8.33, and Figure 8.34, respectively. As seen in these figures, the level of the damages of the columns increases as the level of the corrosion increases. As it can be seen clearly in this table, the higher strains caused higher damages for the structural members with corroded reinforcement. However, the damage level of the columns affected positively with increasing number of pits is due to uniform distribution of plastic deformations throughout the reinforcing bar. The strain of columns increases with the increase of corrosion. The damage level of buildings S30-3 and S30-6 does not change but strain values of K1 columns decreases as the number of pits increases (Table 8.29).

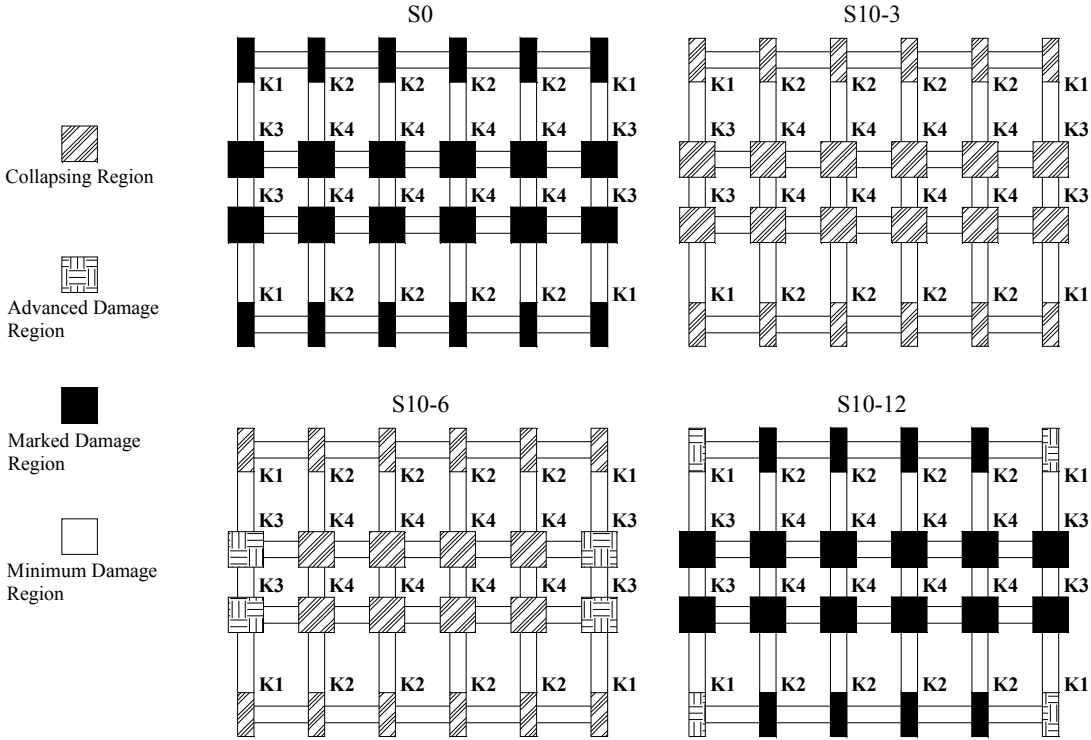


Figure 8.32 : Damage levels of base columns of S0, S10-3, S10-6 and S10-12 buildings.

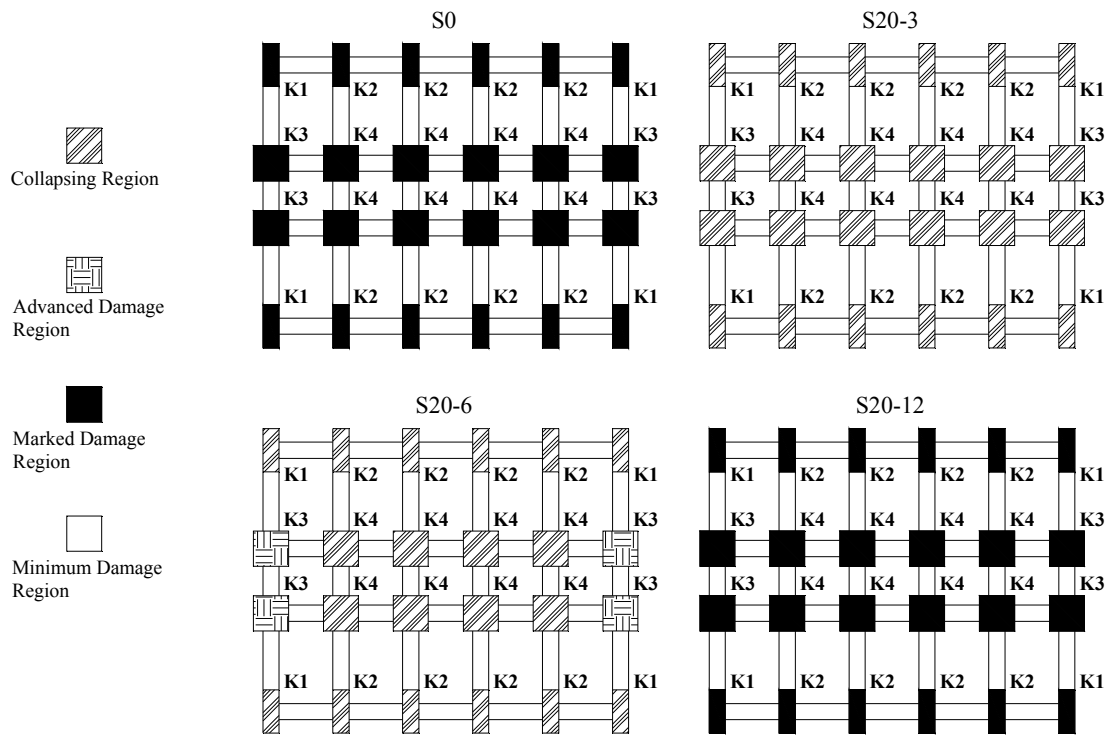


Figure 8.33 : Damage levels of base columns of S0, S20-3, S20-6 and S20-12 buildings.

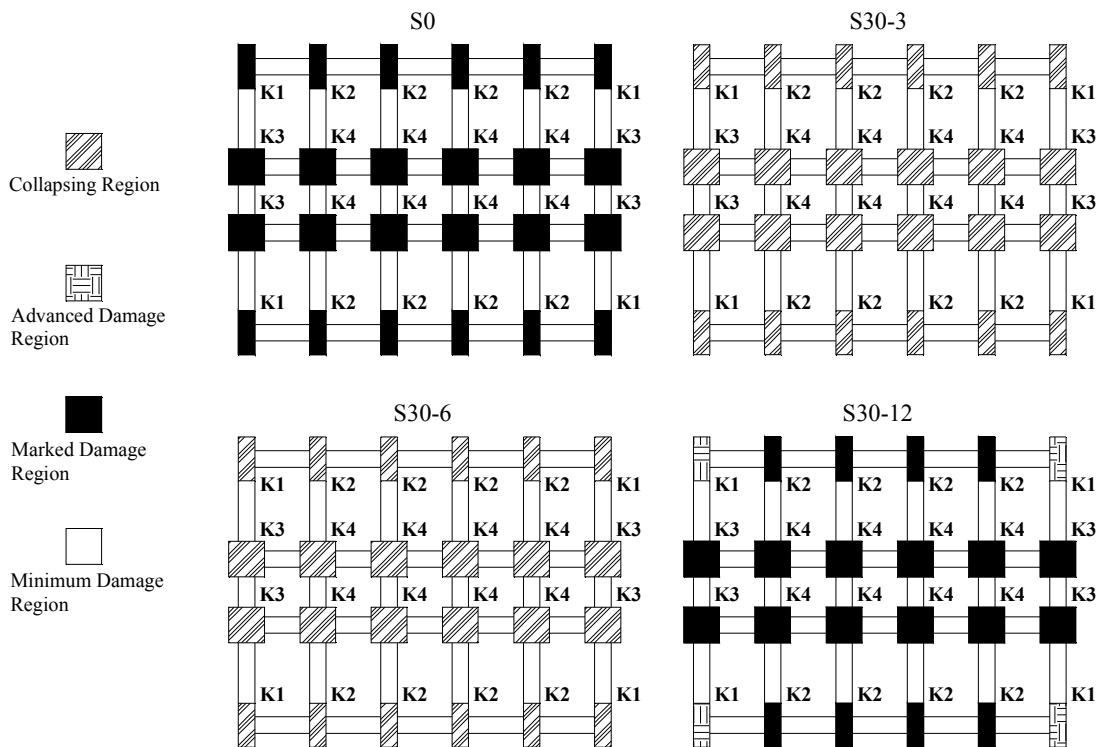


Figure 8.34 : Damage levels of base columns of S0, S30-3, S30-6 and S30-12 buildings.

Table 8.29: Strain values of K1 and K2 columns of S30-3 and S30-6 buildings.

Building notation	Column notation	Column type	Unconfined concrete	Confined concrete	Steel
			ϵ_c	ϵ_{cc}	ϵ_{su}
S30-3	K1	C30-30×80-5-3	0.0136	0.0082	0.1500
	K2	C30-30×80-10-3	0.0309	0.0255	0.1400
S30-6	K1	C30-30×80-5-6	0.0067	0.0039	0.0767
	K2	C30-30×80-10-6	0.0120	0.0092	0.0728

8.3.2.4 Nonlinear Time History Analysis

In case of nonlinear time history analysis, the RC structure is analysed under earthquake excitations and the deformations and internal forces are obtained as a function of time. All the beams were assumed to behave elastically during time history analysis as in nonlinear pushover analysis. The damage levels of base columns of buildings S0 and S10-12 under certain earthquake motions were investigated with nonlinear time history analysis. The earthquake records are presented in Table 8.30. The acceleration-time relationships of earthquake records are given in Appendix G. The acceleration records are scaled to 0.95g which corresponds to elastic demand acceleration for S0 and S10-12 buildings. Nonlinear time history analysis was performed for 6 earthquake records for S0 and S10-12 buildings by PERFORM-3D and drift ratio-time relationships for first stories were obtained (Appendix H). While using this software package, cyclic member behavior is modeled through the cyclic moment-rotation relationships as shown in Figure 8.35. In this software, the stiffness degradation at any rotation level can be modeled through the reductions of the dissipated energy (the area enclosed by the hysteresis loops) as a ratio of the energy to be dissipated through the assumption of an ideal elastic-plastic behavior. In this study, the stiffness degradation is modeled through the reductions of energy dissipations of 0.8, 0.6 and 0.4 depending on the ranges of the plastic rotations. Curvature of each column is determined by dividing the maximum rotation of each column with plastic hinge length. The damage levels were determined according to the values of unconfined concrete strain, confined concrete strain and steel strain which are calculated from XTRACT (2007). Damage regions of base columns of S0 and S10-12 buildings are given in Appendix I, respectively.

The damage levels of base columns of S0 and S10-12 buildings which were obtained for 6 earthquake records are given in Appendix J. As seen from the tables and figures, the strains of S10-12 building is more than S0 building.

Table 8.30: Earthquake records.

Earthquake	Location	Direction	Date	PGA (g)	PGV (cm/s)	PGD (cm)
Mexico	Victoria	CPE045	06.Sept.1980	0.62	31.60	13.20
Northridge	Sylmar	SYL360	17.Jan.1994	0.84	129.60	32.68
Japan	Kobe	KJM000	16.Jan.1995	0.82	81.30	17.68
Turkey	Kocaeli	CNA000	17.Aug.1999	0.18	18.40	18.24
Turkey	Duzce	DZC270	12.Nov.1999	0.52	83.50	42.09
Turkey	Bingöl	EW	01.May.2003	0.56	29.11	15.22

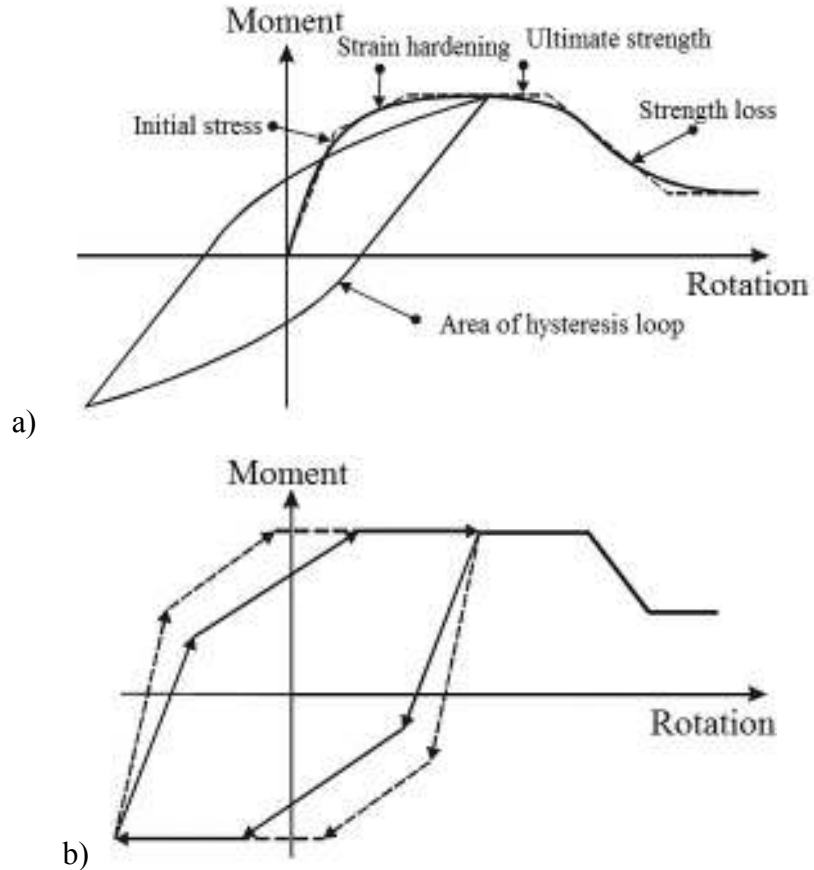


Figure 8.35 : a) Main aspects of inelastic behavior, b) Pattern of cyclic moment-rotation relationships assigned to potential plastic hinges (PERFORM-3D, 2007).

9. CONCLUSIONS

This dissertation contains experimental and theoretical studies on the effect of reinforcement corrosion on seismic behavior of the columns. Thirteen specimens, which were classified into three types were produced, subjected to accelerated corrosion process and then tested under constant axial load and reversed cyclic loads. The first type specimens were constructed using low strength concrete and plain reinforcing bars and with insufficient lap splices at column-footing connection to represent the existing relatively old structures built without complying the design codes. One of the six specimens of this type was the reference specimen without reinforcement corrosion while the other five were subjected to different levels of accelerated corrosion. The second type specimens were designed and constructed according to current seismic design codes in Turkey. One of the six specimens of this type was the reference specimen without reinforcement corrosion while the other five were subjected to different levels of accelerated corrosion. The third type specimen had the same characteristics with the first type specimens with an additional hook at ends of longitudinal bars lapped over at the column-footing connection. All specimens were tested to failure (or until large lateral drifts) and the performances of these columns were studied through their strength, deformation capacity, strain distribution along reinforcing bars, displacement components, moment-curvature relationships of critical sections and failure mode characteristics.

According to the autopsy made after the tests and failure modes, corrosion was observed to be distributed on reinforcing bars of the first and the third type specimens almost uniformly, probably due to high permeability of low strength concrete and large number of voids, while corrosion concentrated on few locations of reinforcing bars of the second type specimens, probably due to local deficiencies around these regions.

None of the specimens of the first type reached their theoretical capacity considering uncorroded reinforcing bar cross-sections. The reference specimen, survived without a strength loss up to relatively larger drift ratios when compared to specimens with

corroded reinforcing bars. The slip of longitudinal bars dominated the behavior of specimens without corrosion and with low level corrosion. The bond strengths of heavily corroded specimens (LS-X21 and LS-X28) increased due to better bond conditions (friction) by rust products on the surface of the plain bars and these specimens reached their theoretical capacity determined considering corroded reinforcing bar cross-sectional area, which is less than the theoretical capacity considering uncorroded reinforcing bar cross-sectional area.

An analytical study was carried out in order to predict the seismic performance of low strength RC columns with corroded plain reinforcing bars. A bond-slip model is proposed by using the results of the experimental data for determining the bond-slip behavior of columns with corroded plain reinforcing bars. The model showed a good agreement compared to experimentally observed behavior and measured characteristics. The bond stress calculated according to CEB-FIB (1990) is seen to be lower than actual case in case of corroded reinforcing bars. While, the proposed model originates from CEB-FIB (1990) bond stress-slip model, a modification factor is introduced for the second branch to consider the effect of corrosion. The nonlinear lateral load-displacement behavior of the structural members can be predicted with the proposed model as a function of the corrosion level.

The failure of the heavily corroded second type specimens were due to fracture of the starter bars. Corrosion of reinforcing bars mainly caused a significant reduction in drift capacity of the tested columns. While the reference specimen could reach 8% drift ratio without a significant loss in strength, the starter bars of the specimens with corrosion fractured at drift ratios of as small as 2% causing a significant sudden loss in strength. Localization of corrosion (pit type) of reinforcing bars was seen to have a significant adverse effect on the inelastic behavior of columns under lateral loads, particularly in terms of drift capacity (together with its better known effect on the strength). This is due to concentration of plastic deformations of reinforcing bars only at the most heavily corroded sections rather than occurring all through the potential plastic hinge length. It is known that the displacement capacity is as important as strength, particularly for the buildings, which are designed to exhibit a ductile behavior during earthquakes. Another finding is the relatively reduced energy dissipation capacity of specimens with corroded reinforcement, reflected with relatively higher pinched hysteresis curves with respect to the reference specimen.

This deficiency is attributed to the reduced bond of reinforcing bars due to damage of concrete in the form of cracks aligned in the direction of longitudinal bars.

An analytical study was carried out on the hypothetical columns with corroded deformed reinforcing bars in different patterns in terms of magnitude and distribution of corrosion pits. The presented analytical algorithm on the seismic performance of normal strength RC columns with corroded deformed reinforcing bars successfully predicted the global lateral load-displacement relationship of a column with corroded reinforcing bars. Furthermore, the predicted curvatures, concrete compressive strains at the cover and at the core and the steel strains were in good agreement with the experimental results.

Even though the concrete was low strength and lap splice length (40 times the diameter of longitudinal bars) is remarkably less than it should be according to design documents (97ϕ), the third type specimen with hook detailing at the end of lap splices reached its theoretical capacity considering corroded reinforcing bar and sustained its capacity until 3% drift ratio.

Nonlinear pushover analyses and nonlinear time history analyses are carried out for ten hypothetical buildings with different scenarios of corrosion. It should be noted that the theoretical assumptions and the considered corrosion scenarios are based on the results of the experimental study and practical observations. When the actual plastic hinge lengths are considered in the analyses (either by pushover or nonlinear time history analysis), the deformations and correspondingly the member damages increase remarkably, leading to significantly poorer overall seismic performance. It is also worth to note that the predicted member damages (based on strains of concrete and steel) were remarkably different at the performance point obtained in the pushover and the nonlinear time history analyses. Furthermore, different earthquake excitations in case of the nonlinear time history analyses lead to the similar overall seismic performance levels.

Considering the widespread problem of corrosion in existing structures in Turkey, these findings are deemed as valuable information for the seismic performance assessment of buildings with corrosion damaged structural members. By evaluating the test results and improving the analytical methods, effective retrofit strategies can also be developed for such weak existing structural members.

REFERENCES

- ACI-222R** (2001). Protection of metals in concrete against corrosion, *American Concrete Institute*, Detroit, USA.
- Al-Sulaimani, G.J., Kaleemullah, M., Basunbul, I.A., and Rasheeduzzaffar** (1990). Influence of corrosion and cracking on bond behavior and strength of reinforced concrete members. *Proceedings American Concrete Institute*, Vol.87, no. 2, pp. 220-231.
- Apostolopoulos, C.A., and Michalopoulos, D.** (2006). Mechanical properties of reinforcing steel and fatigue behavior in corrosive environment. *Journal of Materials Engineering and Performance*, Vol. 16, no.5, pp. 559-566.
- Apostolopoulos, C.A.** (2008). The influence of corrosion and cross-section diameter on the mechanical properties of S500_c steel. *Journal of Materials Engineering and Performance*, Vol.18, no. 2, pp. 190-195.
- Apostolopoulos, C.A., and Papadakis, V.G.** (2008). Consequences of steel corrosion on the ductility properties of reinforcement bar. *Construction and Building Materials*, Vol. 22, pp. 2316-2324.
- ASCE/SEI 41** (2007). Seismic Rehabilitation of Existing Buildings, American Society of Civil Engineers, Reston, VA.
- ASTM A370**, 2010: Standard test methods and definitions for mechanical testing of steel products." *ASTM*, West Conshohocken, PA, USA.
- ASTM C876** (1999). Standard test method for half-cell potentials of uncoated reinforcing steel in concrete." *ASTM*, West Conshohocken, PA, USA.
- ASTM G1** (2003). Standard practice for preparing, cleaning and evaluating corrosion test specimens." *ASTM*, West Conshohocken, PA, USA.
- ASTM G15** (2004). Standard Terminology Relating to Corrosion and Corrosion Testing." *ASTM*, West Conshohocken, PA, USA.
- ASTM G46** (1994). Standard Guide for Examination and Evaluation of Pitting Corrosion." *ASTM*, West Conshohocken, PA, USA.
- Auyeung, Y., Balaguru, P., and Chung, L.** (2000). Bond Behavior of Corroded Reinforcement Bars, *ACI Materials Journal*, Vol.97, no.2, pp. 214-221.
- Bae, S.W., and Belarbi, A.** (2009). Effects of Corrosion of Steel on RC Columns Wrapped with FRP Sheets. *Journal of Performance of Constructed Facilities*, Vol. 23, no. 1, pp. 20-31.

- BAKE** (2000). Cross-Sectional Structural Analysis of Components, developed by A. Ilki during his PhD thesis, Nonlinear behavior of concrete members under reversed cyclic loads, Istanbul Technical University, Istanbul, Turkey.
- Balazs, G.** (2007). Connecting Reinforcement to Concrete by Bond, *Beton-und Stahlbetonbau Special Edition*, Vol.102, Ernst & Sohn Verlag für Architektur und technische Wissenschaften GmbH & Co. KG, Berlin.
- Bhargava, K., Ghosh, A.K., Mori, Y., and Ramanujam, S.** (2007). Corrosion-Induced Bond Strength Degradation in Reinforced Concrete-Analytical and Empirical Models, *Nuclear Engineering and Design*, Vol. 237, pp. 1140-1157.
- Bousias, S.N., Spathis, L.A., Triantafillou, T.C., and Fardis, M.N.** (2002). Seismic Retrofitting of Corrosion Damaged RC Columns, *12th European Conference on Earthquake Engineering*, Paper Reference 431, London, 9-13 September.
- Cairns, J., and Abdullah, R.B.** (1996). Bond Strength of Black and Epoxy-Coated Reinforcement-A Theoretical Approach, *ACI Materials Journal*, Vol.93, no.4, pp.362-369.
- Cairns, J., Plizzari, G., Du, Y., Law, D.W., and Franzoni, C.** (2005). Mechanical Properties of Corrosion-Damaged Reinforcement, *ACI Materials Journal*, Vol.102, no.4.
- Castel, A., Francois, R., and Arliguie, G.,** 2000: Mechanical Behavior of Corroded Reinforced Concrete Beams-Part 2: Bond and notch effects.” *Materials and Structures*, Vol. 33, 545-551.
- CEB-FIP** (1990). Model Code for Concrete Structures, Lausanne, Switzerland.
- CEB-FIB** (2000). Bond of Reinforcement in Concrete. State of Art Report, Bulletin 10.
- Cho, J.Y., and Pincheira, J.A.** (2006). Inelastic Analysis of Reinforced Concrete Columns with Short Lap Splices Subjected to Reversed Cyclic Loads, *ACI Structural Journal*, Vol. 103, no. 2, 280-290.
- Coronelli, D.** (2002). Corrosion Cracking and Bond Strength Modeling for Corroded Bars in Reinforced Concrete, *ACI Structural Journal*, Vol. 99, no. 3.
- Coronelli, D., and Gambarova, P.** (2004). Structural Assessment of Corroded Reinforced Concrete Beams: Modeling Guidelines, *Journal of Structural Engineering*, Vol.130, no.8.
- Demirtaş, B.** (2008). The Effect of Corrosion on Reinforced Concrete Columns in regard of Seismic Performance, MSc. Thesis, Istanbul Technical University, Istanbul, Turkey.
- DIN 488** (1986). Reinforcing Steel; Reinforcing Steel Bars; Dimensions and Masses, Deutsches Institut Fur Normung E.V. (German National Standard).
- Eurocode8** (2005). Design of Structures for Earthquake Resistance, European Standard, Brussels, Belgium.
- Fang, C., Lundgren, K., Chen, L., and Zhu C.** (2004). Corrosion Influence on Bond in Reinforced Concrete, *Cement and Concrete Research*, Vol. 34, pp. 2159–2167.

- Fang, C., Gylltoft, K., Lundgren, and Plos, M.**, (2006a). Effect of Corrosion on Bond in Reinforced Concrete under Cyclic Loading, *Cement and Concrete Research*, Vol. **36**, pp. 548–555.
- Fang, C., Lundgren, K., Chen, L., and Zhu C.** (2006b). Bond Behavior of Corroded Reinforcing Steel Bars in Concrete. *Cement and Concrete Research*, Vol. **36**, pp. 1931-1938.
- FEMA 356** (2000). Prestandard and Commentary for the Seismic Rehabilitation of Buildings, Washington, U.S.A.
- Feliu, S., Gonzales, J.A., Feliu, S., Jr., and Andrade, M.C.** (1990). Confinement of the Electrical Signal for in Situ Measurement of Polarization Resistance in Reinforced Concrete. *ACI Materials Journal*, Vol. **87**, no. 5.
- Graeff, A.G., Silva Filho, and L.C.P.** (2008). Analysis of rebar cross sectional area loss by effect of reinforced concrete corrosion, *IIDBMC International Conference on Durability of Building Materials and Components*, Istanbul, Turkey, May 11-14.
- Harajli, M. H., Hamad, B. S., and Rteil, A.** (2004). Effect of confinement on bond strength between steel bars and concrete. *ACI Structural Journal*, Vol. **101**, no.5, pp.595-603.
- Lehman, D.E., and Moehle, J.P.** (2000). Seismic Performance of Well-Confined Concrete Bridge Columns, *PEER report*, Pacific Earthquake Engineering Research Center College of Engineering, University of California, Berkeley, USA.
- Lundgren, K.** (2001). Bond between corroded reinforcement and concrete, *Report No 3*, Chalmers University of Technology, Department of Structural Engineering and Concrete Structures, Goteborg, Sweden.
- Lundgren, K., Kettil, P., Hanjari, K.Z., Schulune, H., and Soto San Roman, A.** (2009). Analytical Model for the Bond-Slip Behavior of Corroded Ribbed Reinforcement, *Structure and Infrastructure Engineering*, Vol.8, No.2, pp.157-169.
- Maaddawy, T.E., Soudki, K. and Topper, T.**, (2005). Computer Based Mathematical Model for the Performance Prediction of Corroded Beams Repaired With FRP, *Journal of Composites for Construction*, Vol. **9**, no. 3.
- Mander, J.B., Priestley, M.J.N., and Park, R.** (1988). Observed Stress-Strain Behavior for Confined Concrete, *ASCE Journal of Structural Engineering*, V.114, No.8, 1827-1849.
- Mangat, P.S., and Elgarf, M.S.** (1999). Flexural Strength of Concrete Beams with Corroding Reinforcement, *ACI Structural Journal*, Vol. **96**, no.1.
- Mansfeld F.** (1981). Recording and analysis of AC impedance data for corrosion studies”, *Corrosion*, Vol. **37**, no. 5, pp. 301-307.
- Melek, M.** (2006). Experimental and analytical assessment of columns with short lap splices subjected to cyclic loads, *PhD thesis*, Department of Civil Engineering, University of California, Los Angeles, U.S.A..

- Mo, Y.L., and Chan, J.** (1996). Bond and slip of plain rebars in concrete, *ASCE Journal of Materials in Civil Engineering*, Vol.8, no.4, pp. 208-211.
- Pantazopoulou, S. J., Bonacci J. F., Sheikh, S., Thomas, M. D. A., and Hearn, N.** (2001). Repair of Corrosion-Damaged Columns with FRP Wraps. *Journal of Composites for Construction*, Vol. 5, no. 1.
- PEER Structural and Performance Database** (2004). University of California, Berkley, USA.
- PERFORM-3D** (2007). Nonlinear Analysis and Performance Assessment for 3D Structures, Computers and Structures Inc., Berkeley, California, USA.
- Pregartner, T., Cairns, J., and Ozbolt, J.** (2004). Modelling Effect of Corrosion on Bond Strength of Plain Bar Reinforcement, *Fib Structural Concrete*, Vol.5, No.3.
- Reyes, O.** (1999). Modelling of Reinforced Concrete Columns with Short Lap Splices Subjected to Earthquakes, *MS Thesis*, University of Wisconsin, Madison.
- Rodriguez, J., Ortega, L.M., and Garcia, A.M.** (1994a). Assessment of Structural Elements with Corroded Reinforcement, *Corrosion and Corrosion of Steel Protection of Steel in Concrete*. Ed Swamy, R.N. Sheffield Academic Press, pp. 171-185.
- Rodriguez J., Ortega L.M., and Casal J.** (1994b). Corrosion of Reinforcing Bars and Service Life of Reinforced Concrete Structures: Corrosion on Bond Deterioration. International Conference on Concrete Across Borders, Odense, Denmark, Vol.2, pp. 315-326.
- Sezen, H., and Moehle, J.P.** (2004). Shear Strength Model for Lightly Reinforced Concrete Columns, *ASCE Journal of Structural Engineering*, Vol. 130, no.11, pp. 1692-1703.
- Song, H.W., and Saraswathy V.** (2007). Corrosion Monitoring of Reinforced Concrete Structures-A Review, *International Journal of Electrochemical Science*, Vol. 2, pp. 1-28.
- Stanish, K., Hooton, R.D., and Pantazopoulou, S.J.** (1999). Corrosion Effects on Bond Strength in Reinforced Concrete”, *ACI Structural Journal*, Vol.96, no.6.
- Tastani, S.P., and Pantazopoulou, S.J.** (2007). Behavior of Corroded bar Anchorages, *ACI Structural Journal*, Vol.104, no.6.
- TSDC** (2007). Regulations for Buildings to be Constructed in Earthquake Prone Areas, *Turkish Seismic Design Code*, Ankara, Turkey.
- TS708** (1996). Steel bars for concrete, *Turkish Standards Institute*, Ankara, Turkey.
- TS500** (2000). Requirements for design and construction of reinforced concrete structures, *Turkish Standards Institute*, Ankara, Turkey.
- Wang C.Y., Shih, C.C., Hong S.C., and Hwang, W.C.** (2004). Rehabilitation of Cracked and Corroded Reinforced Concrete Beams with Fiber-Reinforced Plastic Patches. *Journal of Composites for Construction*, Vol. 8, no. 3.

Wang, X., and Liu, X. (2004). Bond Strength Modelling for Corroded Reinforcement in Reinforced Concrete, *Structural Engineering and Mechanics*, Vol.17, no.6, pp.863-878.

XTRACT (2007). Cross-sectional structural analysis of components.

Xu, G., Wei, J., Tan, T., and Liu, H.Q. (2007). Modelling Bond Strength of Corroded Plain Bar Reinforcement, *Fib Structural Concrete*, Vol.8, No.3.

Youlin, X., Zhijun, C., Xiaofeng, Liu, L., Pinwu, G., and Shuhui, Y. (2003). Experimental Research on Mechanical Properties of Corroded Steel Bars, *International Symposium 2003 on the reserach and application of high strength reinforcing bar*, 96-103.

APPENDICES

APPENDIX A: Reinforcing cage of specimens.

APPENDIX B: Distance between the concrete surface of the columns and the LVDTs.

APPENDIX C: Crack propagation of specimens while pulling and pushing.

APPENDIX D: The strain-drift ratio relationship of specimens.

APPENDIX E: The views and crack patterns of specimens.

APPENDIX F: The general appearance of a typical corroded reinforcing bar taken out from the column, the surface condition of the reinforcement bars observed through an optical stereo microscope and scan view of the reinforcement bar with 3D optical scanner.

APPENDIX G: Earthquake records scaled due to 0.95g.

APPENDIX H : Drift ratio-time relationship for first stories of S0, S10-12 buildings.

APPENDIX I : Damage regions of base columns of S0 and S10-12 buildings.

APPENDIX J: The damage levels of base columns of S0 and S10-12 buildings on plan for different earthquake records.

APPENDIX A

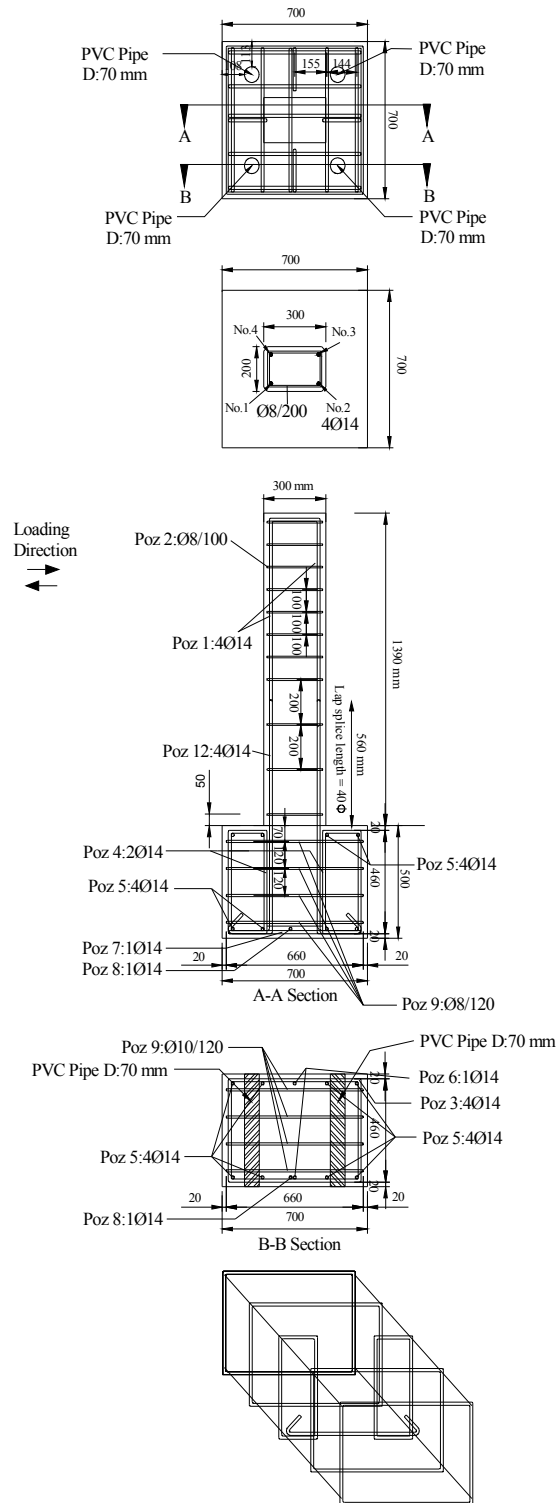


Figure A.1 : Reinforcing cage of the first type specimens (south side).

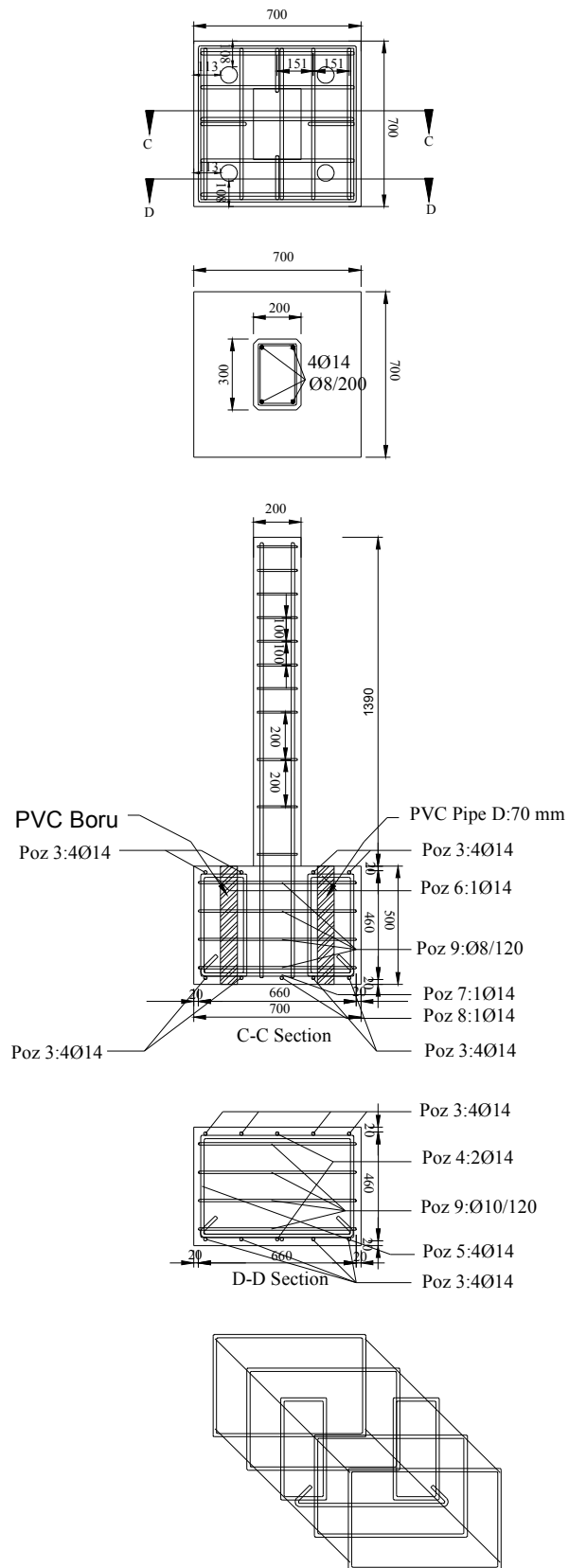


Figure A.2 : Reinforcing cage of the first type specimens (east side).

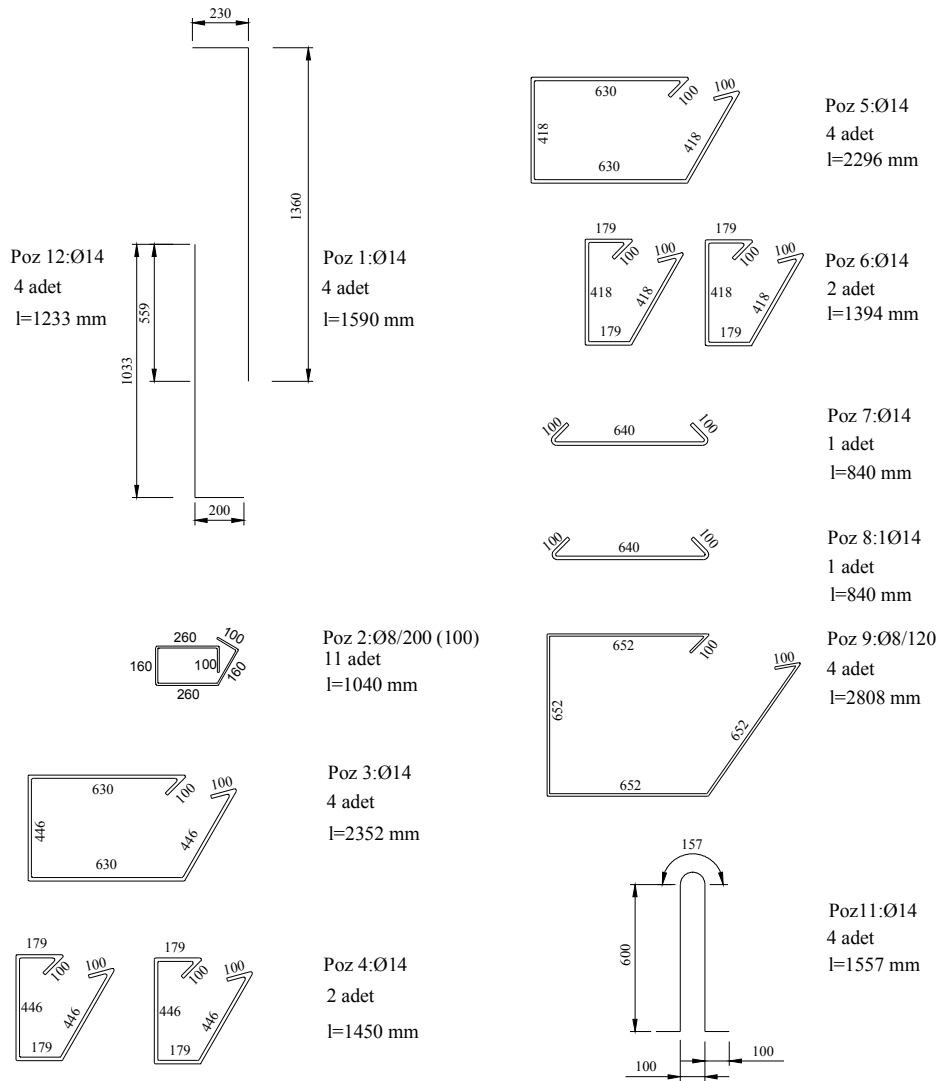


Figure A.3 : Details of reinforcing cage of the first type specimens.

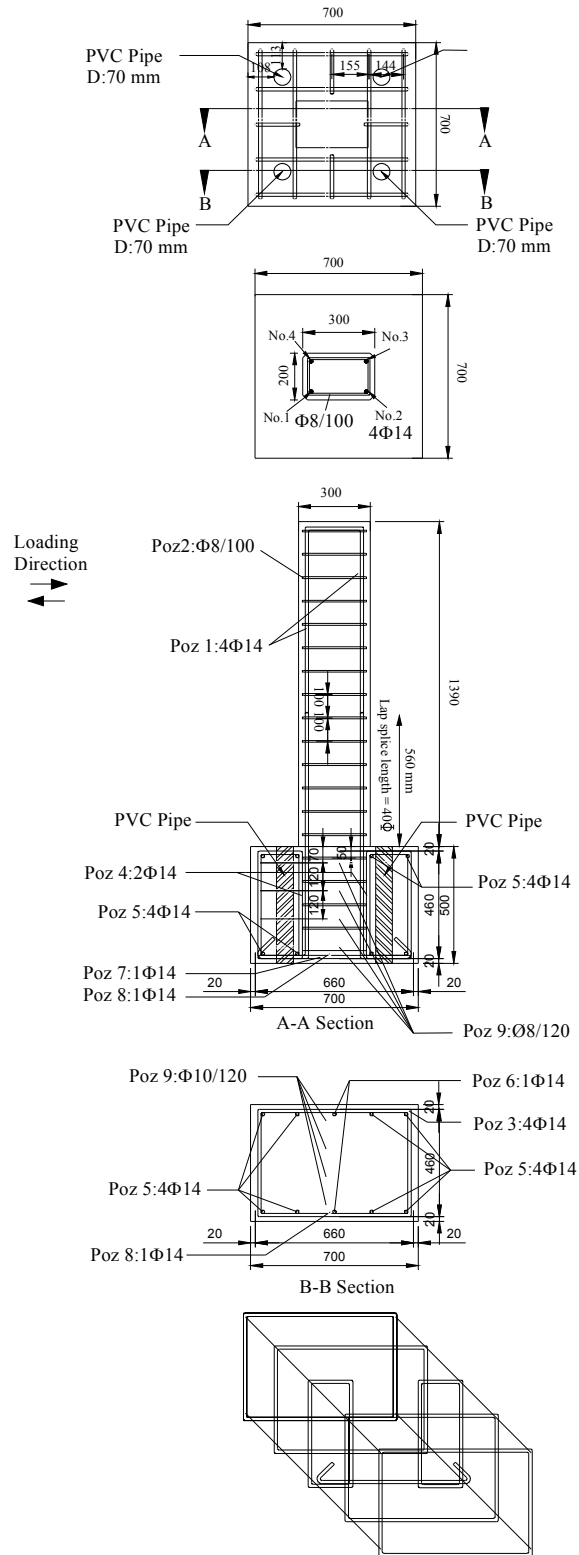


Figure A.4 : Reinforcing cage of the second type specimens (south side).

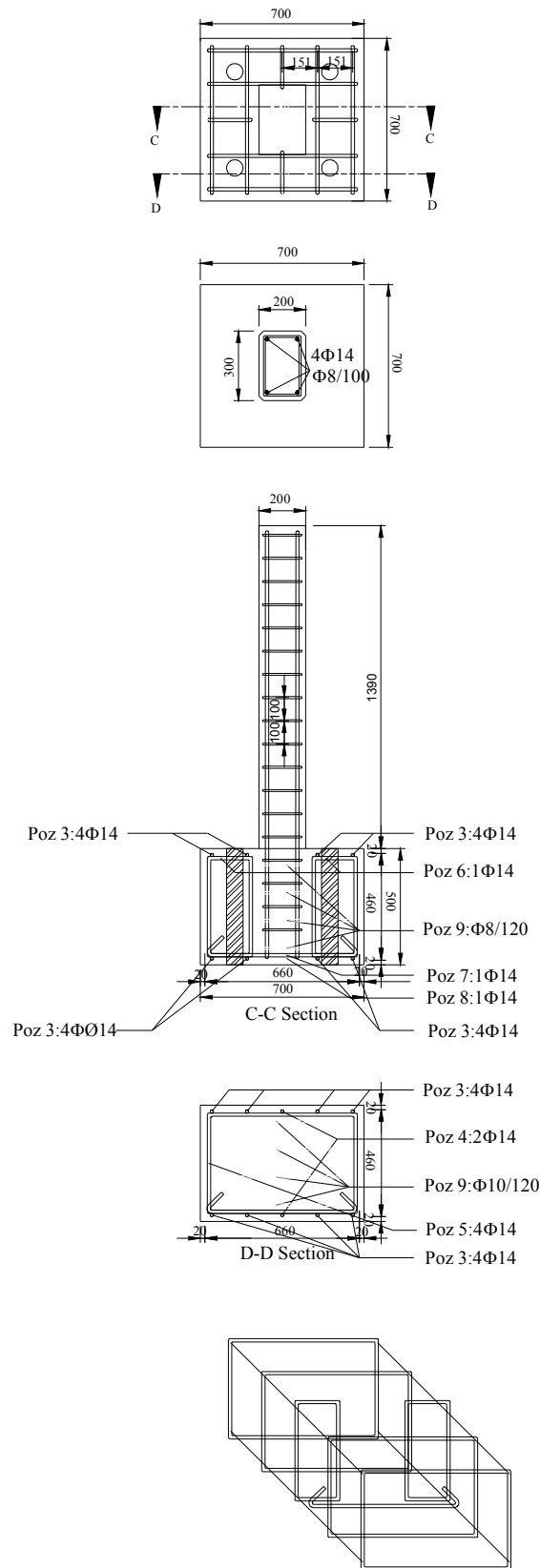


Figure A.5 : Reinforcing cage of the second type specimens (east side).

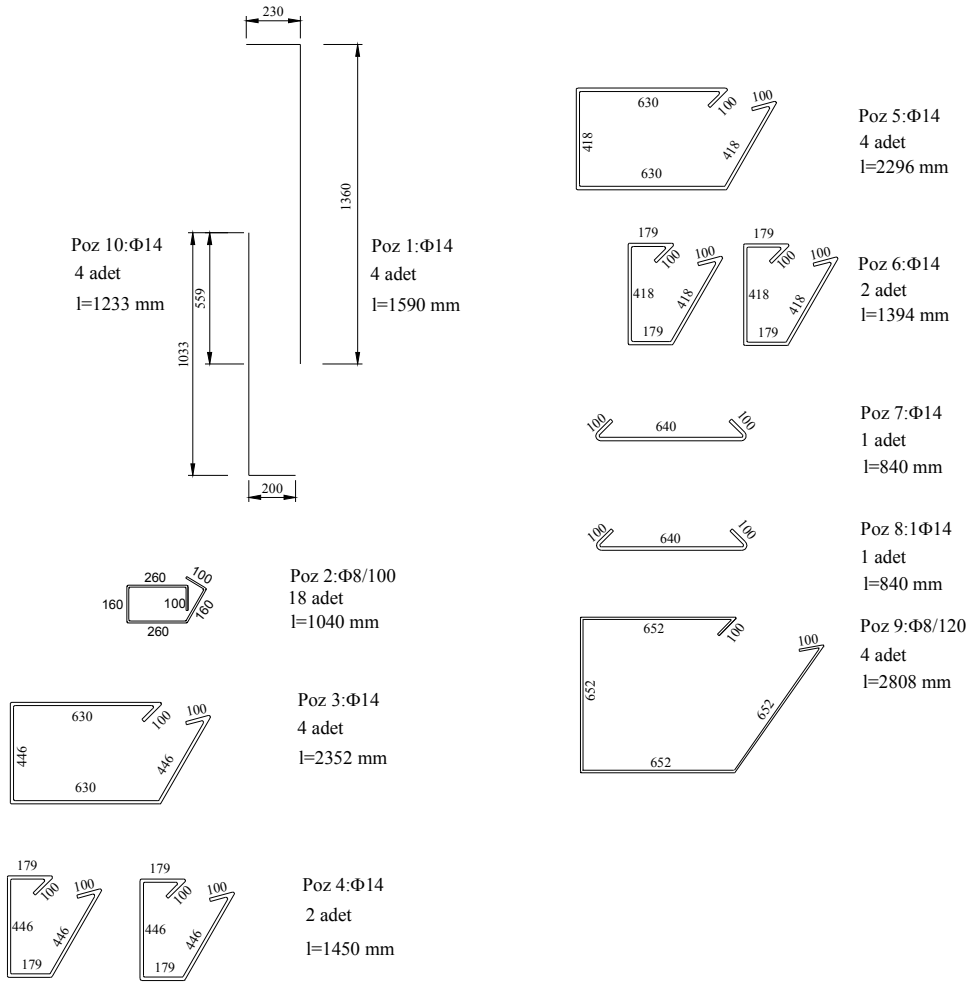


Figure A.6 : Details of reinforcing cage of the second type specimens.

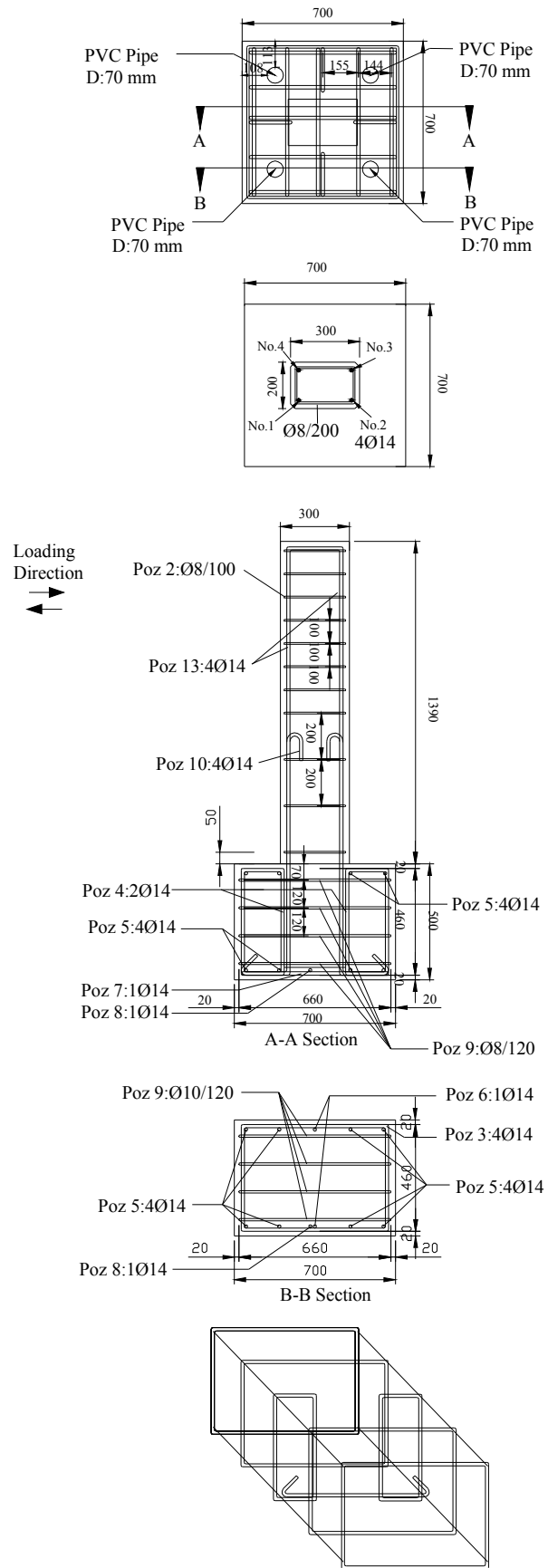


Figure A.7 : Reinforcing cage of the third type specimens (south side).

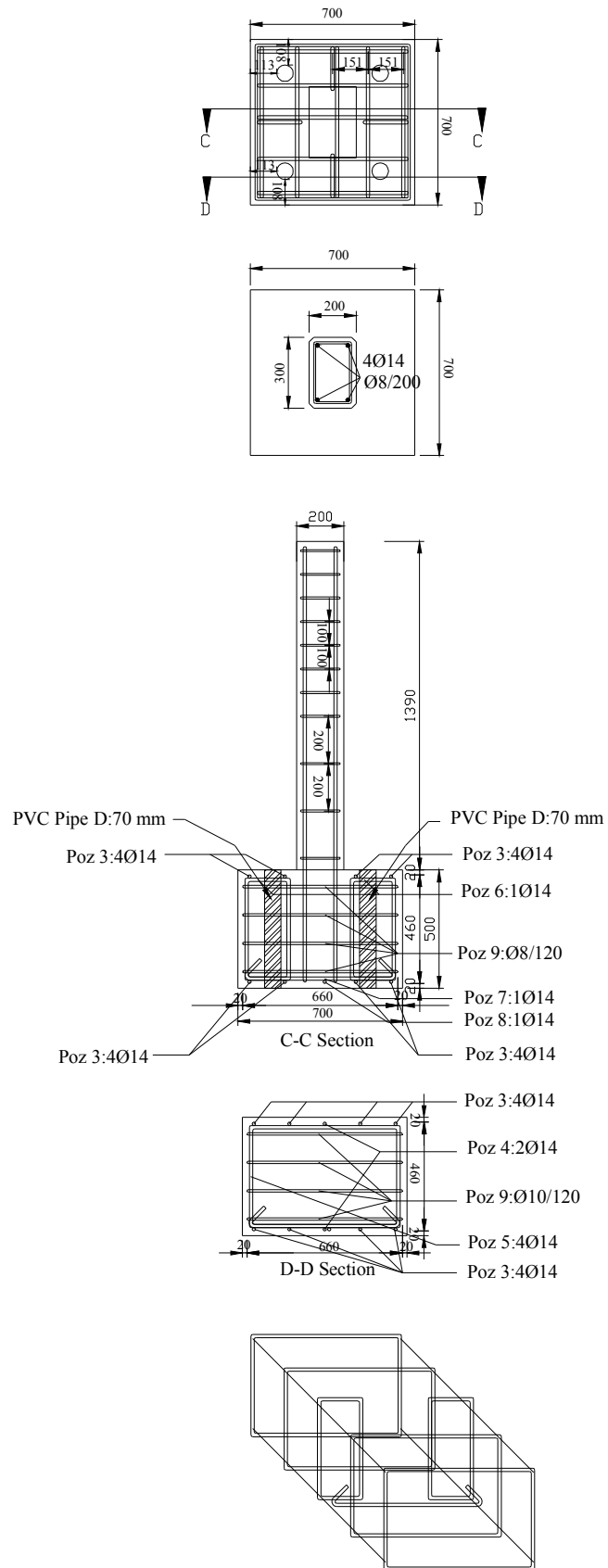


Figure A.8 : Reinforcing cage of the third type specimens (east side).

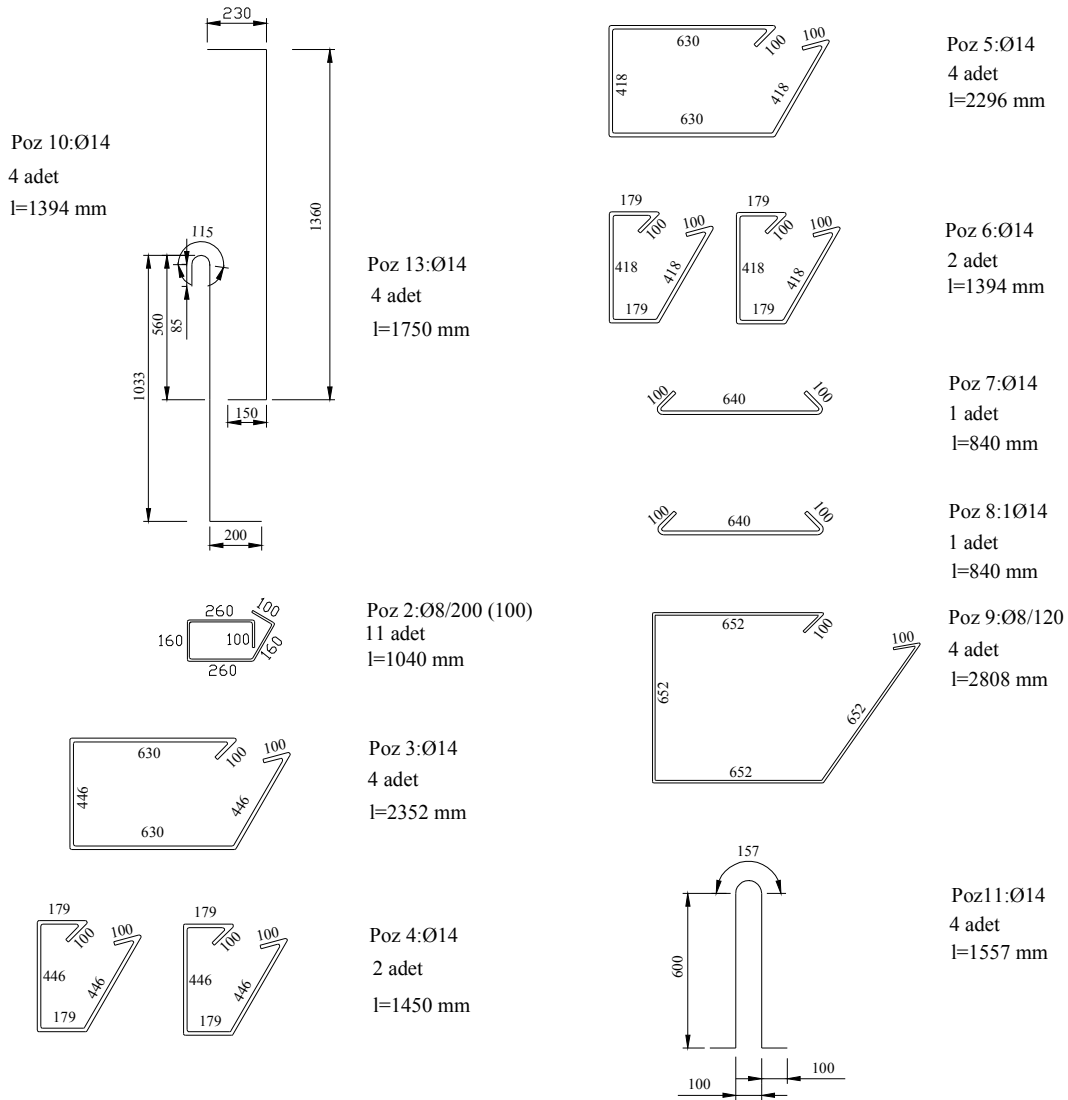


Figure A.9 : Details of reinforcing cage of the third type specimens.

APPENDIX B

Table B.1: Distance between the concrete surface of the columns and the LVDTs.

Specimen	Distances					
	X11 (mm)	X21 (mm)	X31 (mm)	X12 (mm)	X22 (mm)	X32 (mm)
LS-X0	42	42	41	40	40	41
LS-X6	38	39	39	42	41	40
LS-X8	40	40	40	38	40	38
LS-X12	30	48	45	35	42	43
LS-X21	38	42.5	47	35	41	42.5
LS-X28	35	42	45	40	40	50
NS-X0	38	39	48	42	42	41
NS-X9	37	44	43	37	43	52
NS-X13	33	40	41	46	40	39
NS-X16	41	41	55	34	46	43
NS-X22	40	40	36	30	40	38
NS-X54	46	53	47	40	42	56
LS-X19-H	42	46	51	38	50	54

APPENDIX C

Table C.1 : Crack propagation of LS-X0 while pushing.

Drift ratio (%)	North		South	
	Crack	Explanation	Crack	Explanation
0.10	-	-	-	-
0.25	-	-	-	-
0.50	A : 0.1	A : Crack at the column-footing interface.	A : 0.1	A : Crack at the column-footing interface.
0.75	A : 0.2 B : 0.1	B : Flexural crack 250 mm from above the top of the footing.	A : 0.4 B : 0.1	B : Flexural crack 250 mm from above the top of the footing.
1.00	A : 0.6 B : 0.2		A : 1.0 B : 0.3	
1.50	A : 1.2 B : 0.4 A : 1.2 B : 0.6 BL ₁ : 0.2 BL ₂ : 0.1 BL ₃ : 0.3	BL ₁ : Vertical crack between 0-100 mm from above the top of the footing. BL ₂ : Vertical crack between 0-200 mm from above the top of the footing. BL ₃ : Vertical crack between 500-650 mm from above the top of the footing.	A : 1.6 B : 0.3 A : 3.0 B : 0.7	
2.00				
2.50	A : 1.6 B : 0.8	BL ₁ : 0.5 BL ₂ : 0.1 BL ₃ : 0.3	A : 3.5 B : 0.8	
3.00	A : 2.0 B : 0.9	BL ₁ : 1.2 BL ₂ : 0.2 BL ₃ : 0.3	A : 3.7 B : 1.6 BL ₁ : 0.1	BL ₁ : Vertical crack between 250-300 mm from above the top of the footing.
3.50	A : 3.0 B : 1.2	BL ₁ : 1.4 BL ₂ : 0.3 BL ₃ : 0.4	A : 4.0 B : 2.5 BL ₁ : 0.3	
4.00	A : 3.5 B : 1.4 BL ₁ > 1.4 BL ₂ : 0.6	BL ₃ : 0.5 BL ₄ < 0.1 BL ₄ : Vertical crack between 250-350 mm from above the top of the footing.	A : 4.1 B : 2.5 BL ₁ : 0.3	
4.50	A > 3.5 B : 1.6 BL ₁ > 1.4 BL ₂ : 0.8	BL ₃ : 0.5 BL ₄ : 0.1	A : 5.3 B : 2.5 BL ₁ : 0.3	
5.00	A > 3.5 B : 2.0 BL ₁ > 1.4	BL ₂ : 1.2 BL ₃ : 0.5 BL ₄ : 0.1	A > 5.3 B : 2.5 BL ₁ : 0.3 BL ₂ : 0.1	BL ₂ : Vertical crack between 100-200 mm from above the top of the footing.

Table C.2 : Crack propagation of LS-X0 while pulling.

Drift ratio (%)	North		South	
	Crack	Explanation	Crack	Explanation
0.10	-	-	-	-
0.25	-	-	-	-
	A' : 0.1 B' : 0.2	A' : Crack at the column-footing interface.	A' : 0.1 B' : 0.1	A' : Crack at the column-footing interface.
0.50		B' : Flexural crack 250 mm from above the top of the footing.		B' : Flexural crack 250 mm from above the top of the footing.
0.75	A' : 0.3 B' : 0.3		A' : 0.4 B' : 0.2	
1.00	A' : 0.8 B' : 0.4		A' : 0.6 B' : 0.4	
1.50	A' : 1.4 B' : 0.9		A' : 1.4 B' : 0.6	
	A' : 2.5 B' : 0.9	BL ₁ ' : Vertical crack between 0-150 mm	A' : 2.0 B' : 0.8	
2.00	BL ₁ ' : 0.2	from above the top of the footing at compression zone while pushing.		
	A' : 2.8 B' : 0.9 BL ₁ ' : 0.5 BL ₂ ' : 0.1 BL ₃ ' : 0.2	BL ₂ ' : Vertical crack between 550-600 mm from above the top of the footing at compression zone while pulling.	A' : 3.0 B' : 0.8 BL ₁ ' : 0.2	BL ₁ ' : Vertical crack between 0-150 mm from above the top of the footing at compression zone while pushing.
2.50		BL ₃ ' : Vertical crack between 450-600 mm from above the top of the footing at compression zone while pulling.		
	A' : 3.0 B' : 0.9 BL ₁ ' : 0.5 BL ₂ ' : 0.1 BL ₃ ' : 0.2		A' : 3.0 B' : 0.8 BL ₁ ' : 0.2	
3.00	A' : 3.5 B' : 1.2		A' : 5.5 B' : 1.0	
3.50	BL ₁ ' : 0.5 BL ₂ ' : 0.1 BL ₃ ' : 0.2		BL ₁ ' : 0.4	
	A' : 5.5 B' : 1.2	BL ₁ ' : 0.5 BL ₂ ' : 0.1 BL ₃ ' : 0.3	A' > 5.5 B' : 1.0 BL ₁ ' : 0.5	
4.00				

Table C.3 : Crack propagation of LS-X6 while pushing.

Drift ratio (%)	North		South	
	Crack	Explanation	Crack	Explanation
0.09	-	-	-	-
0.23	-	-	-	-
	A : 0.1 B : 0.1	A : Crack at the column-footing interface.	A : 0.2 B : 0.3	A : Crack at the column-footing interface. B : Shear crack between 150-250 mm from above the top of the footing.
0.60		B : Flexural crack 250 mm from above the top of the footing.		
1.00	A : 1.0 B : 0.2		A : 1.0 B : 0.5	
1.50	A : 1.0 B : 0.3		A : 1.8 B : 0.5	
2.00	A : 1.0 B : 0.4		A : 2.0 B : 0.6 C : 0.4	C : Flexural crack 50 mm from above the top of the footing.
	A : 4.0		A : 4.0	
2.50	B : 0.3		B : 0.6 C : 0.85	
	A : 5.0		A : 5.0	
3.00	B : 0.2		B : 0.5 C : 0.9	
	A : 7.0		A : 7.0	
3.50	B : 0.2		B : 0.3 C : 1.6	
	A : 8.0		A : 7.0	
4.00	B : 0.1		B : 0.3 C : 1.7	
	A : 10.0		A : 10.0	
4.50	B : 0.1		B : 0.3 C : 2.2	
	A : 10.0		A : 10.0	
5.00	B : 0.1		B : 0.3 C : 5.0	

Table C.4 : Crack propagation of LS-X6 while pulling.

Drift ratio (%)	North		South	
	Crack	Explanation	Crack	Explanation
0.10	-	-	-	-
0.25	-	-	-	-
	A' : 0.1 B' : 0.1	A' : Crack at the column-footing interface.	A' < 0.1 B' < 0.1	A' : Flexural crack 50 mm from above the top of the footing.
0.50		B' : Flexural crack 250 mm from above the top of the footing.		B' : Flexural crack 150 mm from above the top of the footing.
1.00	A' : 0.2 B' : 0.1		A' : 0.1 B' : 0.5 C' : 0.1	C' : Crack at the column-footing interface.
	A' : 1.8 B' : 0.1 C' : 0.4 D' : 0.25	C' : Shear crack between 100-150 mm from above the top of the footing. D' : Shear crack between 120-170 mm from above the top of the footing.	A' : 0.8 B' : 0.95 C' : 1.8 D' : 2.1	D' : Shear crack between 150-250 mm from above the top of the footing.
1.50		E' : Flexural crack 50 mm from above the top of the footing.		
2.00	A' : 2.0 B' : 0.1 C' : 0.6 D' : 0.25 E' : 0.5		A' : 1.5 B' : 1.1 C' : 2.0 D' : 0.1	
	A' : 3.2 B' : 0.1	C' : 0.8 D' : 0.2 E' : 2.5	A' : 2.6 B' : 1.0 C' : 3.2 D' : 0.1	
2.50				
3.00	A' : 3.5 B' : 0.1	C' : 1.0 D' : 0.5 E' : 3.5	A' : 3.0 B' : 0.4	C' : 3.5 D' : 0.1
	A' > 3.5 B' : 0.1	C' : 1.0 D' : 0.2 E' : 3.7	A' : 5.0 B' : 0.5	C' > 3.5 D' : 0.1
3.50				
4.00	A' > 3.5 B' : 0.1 C' : 1.1	D' : 0.2 E' : 3.8	A' : 7.0 B' : 0.5	C' > 3.5 D' : 0.1
	A' > 3.5 B' : 0.1 C' : 1.2	D' : 0.2 E' > 3.8	A' : 10.0 B' : 0.5	C' > 3.5 D' : 0.1
4.50				

Table C.5 : Crack propagation of LS-X8 while pushing.

Drift ratio (%)	North		South	
	Crack	Explanation	Crack	Explanation
0.10	-	-	-	-
0.25	-	-	-	-
0.50	A : 0.2	A : Shear crack between 50-250 mm from above the top of the footing.	A : 0.2	A : Shear crack between 50-250 mm from above the top of the footing.
			B : 0.2	
0.75	A : 0.4	B : Vertical crack between 50-150 mm from above the top of the footing.	A : 0.4	C : Crack at the column-footing interface.
	B : 0.1		B : 0.4	
1.00	A : 0.4		C : 0.1	D : Vertical crack between 100-150 mm from above the top of the footing.
	B : 0.2		D : 0.1	
1.50	A : 0.6	D : Flexural crack 50 mm from above the top of the footing.	A : 0.4	E : Vertical crack between 100-150 mm from above the top of the footing.
	B : 0.4		B : 0.5	
2.00	D : 0.5		C : 0.1	F : Shear crack between 250-300 mm from above the top of the footing.
			D : 0.3	
2.50			E : 0.1	G : Shear crack between 350-450 mm from above the top of the footing. H : Vertical crack between 550-600 mm from above the top of the footing.
			F : 0.1	
3.00			G : 0.1	I : Flexural crack 20 mm from above the top of the footing.
			H : 0.1	
3.00			I : 0.1	J : Shear crack between 150-250 mm from above the top of the footing.
			F : 0.1	
3.00	A : 0.6	E : Vertical crack between 50-100 mm from above the top of the footing.	A : 0.6	G : 0.1
	B : 0.9		B : 0.6	
3.00	D : 1.8		C : 0.9	H : 0.2
	E : 0.5		D : 0.6	
3.00			E : 0.2	I : 1.0
			F : 0.1	
3.00	A : 0.6		A : 0.7	J : 0.1
	B : 1.6		B : 0.6	
3.00	D : 2.5		C : 2.0	F : 0.1
	E : 1.6		D : 0.4	
3.00			E : 0.1	G : 0.1
			A : 1.0	
3.00			B : 0.6	H : 0.2
			C : 2.5	
3.00			D : 0.4	I : 3.0
			E : 0.2	
3.00				J : 0.1

Table C.5 (contd.) : Crack propagation of LS-X8 while pushing.

Drift ratio (%)	North		South	
	Crack	Explanation	Crack	Explanation
3.50	A : 2.0		A: 1.2	F : 0.1
	B > 1.6		B : 0.8	G : 0.1
	D : 2.5		C : 3.0	H : 0.4
	E > 1.6		D : 0.5	I : 3.5
			E : 0.3	J : 0.1
4.00	A > 2.0		A : 1.0	F : 0.1
	B > 1.6		B : 0.8	G : 0.1
	D : 2.5		C > 3.0	H : 0.5
	E > 1.6		D > 0.5	I : 3.5
			E > 0.3	J : 0.1

Table C.6 : Crack propagation of LS-X8 while pulling.

Drift ratio (%)	North		South	
	Crack	Explanation	Crack	Explanation
-0.10	-	-	-	-
-0.25	-	-	-	-
-0.50	A' : 0.2	A' : Shear crack between 100-200 mm from above the top of the footing.	A' : 0.2	A' : Shear crack between 50-250 mm from above the top of the footing.
-0.75	A' : 0.5 B' : 0.1	B' : Crack at the column-footing interface.	A' : 1.0	
-1.00	A' : 0.6 B' : 0.2 C' : 0.1	C' : Flexural crack 30 mm from above the top of the footing.	A' : 0.9 B' : 0.3 C' : 0.1 D' : 0.1 E' : 0.1 F' : 0.1	B' : Shear crack between 50-100 mm from above the top of the footing. C' : Shear crack between 500-650 mm from above the top of the footing.
-1.50	A' : 0.8 B' : 0.4 C' : 0.5 D' : 0.1 E' : 0.1 F' : 0.1 G' : 0.1	D' : Vertical crack between 80-120 mm from above the top of the footing. E' : Vertical crack between 100-150 mm from above the top of the footing. F' : Vertical crack between 550-600 mm from above the top of the footing. G' : Vertical crack between 650-700 mm from above the top of the footing.	A' : 1.0 B' : 0.9 C' : 0.1 D' : 0.1 E' : 0.1 F' : 0.1	
-2.00	A' : 0.6 B' : 1.0 C' : 1.2 D' : 0.4 E' : 0.3 F' : 0.2 G' : 0.1 H' : 0.1	H' : Flexural crack 100 mm from above the top of the footing. I' : Shear crack between 200-250 mm from above the top of the footing.	A' : 1.0 B' : 1.2 C' : 0.1 D' : 0.1 E' : 0.1 F' : 0.1	
-2.50	A' : 0.6 B' : 2.0 C' : 1.8 D' : 0.9 E' : 0.9	F' : 0.2 G' < 0.1 H' : 0.1 I' : 0.1	A' : 1.6 B' : 2.5 C' : 0.2 D' : 0.2	E' < 0.1 F' : 0.1 G' : 0.7 G' : Flexural crack 50 mm from above the top of the footing.

Table C.6 (contd.) : Crack propagation of LS-X8 while pulling.

Drift ratio (%)	North		South	
	Crack	Explanation	Crack	Explanation
-3.00	A' : 0.7	I' > 0.1	A' > 1.6	E' : 0.1
	B' > 1.0	J' : 1.0	B' : 2.5	F' : 0.1
	C' > 1.2	K' : 0.7	C' : 0.2	G' : 1.4
	D' : 2.5	J' : Shear crack	D' : 0.2	H' : 0.7
	E' : 3.0	between 550-650 mm		I' : 0.1
	F' : 0.1	from above the top of		
	G' < 0.1	the footing.		
-3.50	H' > 0.1	K' : Vertical crack		
		between 500-600 mm		
		from above the top of		
		the footing.	A' > 1.6	E' : 0.1
			B' > 2.5	F' : 0.1
-4.00			C' : 0.1	G' : 1.0
			D' : 0.6	H' : 0.8
				I' : 0.1
			A' > 1.6	E' : 0.1
			B' > 2.5	F' : 0.1
		C' : 0.1	G' < 1.0	
		D' : 0.6	H' : 0.8	
			I' : 0.1	

Table C.7 : Crack propagation of LS-X12 while pushing.

Drift ratio (%)	North		South	
	Crack	Explanation	Crack	Explanation
0.10	-	-	A: 0.1	A: Vertical crack between 550-650 mm from above the top of the footing.
0.25	-	-	A: 0.1	
0.50	A < 0.1	A: Shear crack between 50-100 mm from above the top of the footing.	A: 0.2	B: Shear crack between 100-150 mm from above the top of the footing.
	A < 0.1 B: 0.3 C: 0.1 D: 0.1 E < 0.1 F < 0.1	B: Shear crack between 100-250 mm from above the top of the footing. C: Shear crack between 300-450 mm from above the top of the footing. D: Crack at the column-footing interface. E: Flexural crack 300 mm from above the top of the footing. F: Vertical crack between 500-700 mm from above the top of the footing.	A: 0.4 B: 0.1 C: 0.1 D: 0.1 E: ezilme F: 0.2 G: 0.1 H < 0.1 I < 0.1	C: Crack at the column-footing interface. D: Shear crack between 50-250 mm from above the top of the footing. E: Vertical crack between 50-150 mm from above the top of the footing. F: Shear crack between 250-350 mm from above the top of the footing. G: Shear crack between 450-500 mm from above the top of the footing. H: Vertical crack between 500-650 mm from above the top of the footing. I: Vertical crack between 850-950 mm from above the top of the footing.
0.75				
1.00	A < 0.1 B: 0.4 C: 0.2 D: 0.1	E: 0.2 F: 0.1 G: 0.2 G: Flexural crack 350 mm from above the top of the footing.	A: 0.5 B: 0.1 C: 0.3 D: 0.1 E: ezilme F: 0.2 G: 0.1	H < 0.1 I < 0.1 J: 0.1 J: Shear crack between 700-750 mm from above the top of the footing.
	A < 0.1 B: 0.8 C: 0.4 D: 0.4 E: 0.2 F: 0.2 G: 0.3 H: 0.4 I: 0.1 J: 0.1	H: Shear crack between 0-50 mm from above the top of the footing. I: Vertical crack between 700-800 mm from above the top of the footing. J: Vertical crack between 750-900 mm from above the top of the footing.	A: 0.7 B: 0.1 C: 0.6 D: 0.1 E: ezilme F: 0.3 G: 0.1 H: 0.2 I < 0.1 J: 0.1	

Table C.7 (contd.) : Crack propagation of LS-X12 while pushing.

Drift ratio (%)	North		South	
	Crack	Explanation	Crack	Explanation
2.00	A < 0.1	L: 0.5	A: 0.9	H:0.3
	B: 0.9	M: 0.3	B: 0.1	I < 0.1
	C: 0.4	N: 0.2	C: 1.8	J: 0.1
	D: 0.4	K: Shear crack	D: 0.3	K: 0.1
	E: 0.2	between 500-650 mm	E: ezilme	K: Vertical crack between
	F: 0.3	from above the top of	F: 0.3	650-700 mm from above
	G: 0.3	the footing.	G: 0.1	the top of the footing.
	H: 0.9	L: Flexural crack 50		
	I: 0.2	mm from above the		
	J: 0.1	top of the footing.		
	K: 0.1	M: Vertical crack		
		between 50-100 mm		
		from above the top of		
	the footing.			
	N: Shear crack			
	between 150-250 mm			
	from above the top of			
	the footing.			
2.50	A < 0.1	J : 0.1	A : 1.6	G : 0.1
	B : 1.0	K : 0.1	B : 0.1	H :0.5
	C : 0.5	L : 1.6	C : 3.5	I < 0.1
	D : 3.0	M : 1.6	D : 0.5	J : 0.1
	E : 0.2	N : 0.6	E : ezilme	K : 0.1
	F : 0.3		F : 0.3	
	G : 0.3			
	H : 2.5			
	I : 0.5			
		A < 0.1	J : 0.1	A : 1.8
	B : 1.0	K < 0.1	B : 0.3	H :0.6
	C : 0.5	L : 3.0	C > 1.8	I < 0.1
	D : 3.5	M : 4.0	D : 1.0	J : 0.1
	E : 0.2	N : 1.6	E : ezilme	K : 0.1
	F : 0.3	O : 0.3	F : 0.1	L < 0.1
	G < 0.1	O: Vertical crack		M : 0.2
3.00	H > 2.5	between 250-350 mm		L: Vertical crack between
	I : 0.5	from above the top of		400-450 mm from above
	the footing.			the top of the footing.
				M: Vertical crack between
				400-500 mm from above
				the top of the footing.

Table C.8 : Crack propagation of LS-X12 while pulling.

Drift ratio (%)	North		South	
	Crack	Explanation	Crack	Explanation
-0.10	A' : 0.1 B' < 0.1	A': Vertical crack between 700-750 mm from above the top of the footing. B': Vertical crack between 800-900 mm from above the top of the footing.	-	-
	-0.25	A' : 0.1 B' < 0.1		
-0.50	A' : 0.1 B' < 0.1	C': Flexural crack 450 mm from above the top of the footing.	A' < 0.1	A': Flexural crack 100 mm from above the top of the footing.
	A' : 0.1 B' < 0.1	D': Flexural crack 250 mm from above the top of the footing.		
	E' < 0.1 F' < 0.1	E': Vertical crack between 350-450 mm from above the top of the footing.		
		F': Vertical crack between 250-350 mm from above the top of the footing.		
	A' : 0.1 B' : 0.1	G' : 0.1 H': 0.1	A' < 0.1 B' < 0.1	B': Flexural crack 50 mm from above the top of the footing.
	C' : 0.1 D' : 0.1	G': Vertical crack between 600-650 mm from above the top of the footing.	C' : 0.1 D' < 0.1	C': Shear crack between 250-400 mm from above the top of the footing.
	E' < 0.1 F' : 0.1	H': Crack at the column-footing interface.	E' < 0.1 F' : 0.1	D': Vertical crack between 450-600 mm from above the top of the footing.
	-0.75		G' < 0.1	E': Crack at the column-footing interface. F': Vertical crack between 650-750 mm from above the top of the footing.

Table C.8 (contd.) : Crack propagation of LS-X12 while pulling.

Drift ratio (%)	North		South	
	Crack	Explanation	Crack	Explanation
-1.00	A': 0.1	F': 0.1	A' <0.1	G': Shear crack between
	B': 0.1	G': 0.2	B': 0.3	500-600 mm from above
	C': 0.1	H': 0.2	C': 0.1	the top of the footing.
	D': 0.1	I': 0.2	D' <0.1	H': Vertical crack between
	E' < 0.1	I': Shear crack	E': 0.1	350-450 mm from above
		between 300-450 mm	F': 0.1	the top of the footing.
		from above the top of	G' <0.1	I': Vertical crack between
		the footing.	H': 0.2	450-700 mm from above
			I': 0.2	the top of the footing.
			J': ezilme	J': Vertical crack between
-1.50			K': 0.1	50-200 mm from above the
			L': 0.1	top of the footing.
			M' < 0.1	K': Shear crack between
				450-500 mm from above
				the top of the footing.
				L': Vertical crack between
				750-850 mm from above
				the top of the footing.
				M': Vertical crack between
				800-850 mm from above
-2.00				the top of the footing.
	A': 0.1	L': 0.1	A' <0.1	K': 0.1
	B': 0.1	M': ezilme	B': 0.8	L': 0.1
	C': 0.1	K': Shear crack	C': 0.1	M' < 0.1
	D': 0.1	between 330-380 mm	D': 0.1	N' < 0.1
	E' < 0.1	from above the top of	E': 0.3	O': 0.1
	F': 0.1	the footing.	F': 0.2	P': 0.1
	G': 0.3	L': Shear crack	G' <0.1	N': Shear crack between
	H': 1.0	between 500-550 mm	H': 0.3	350-450 mm from above
	I': 0.4	from above the top of	I': 0.3	the top of the footing.
K': 0.1	the footing.	J': ezilme		
	M': Flexural crack			
	350 mm from above			
	the top of the footing.			
	A': 0.3	G': 0.4	A' < 0.1	K': 0.1
	B': 0.1	H': 1.4	B': 3.5	L': 0.2
	C': 0.1	I': 0.4	C': 0.1	M' < 0.1
	D': 0.2	K': 0.1	D': 0.3	N' < 0.1
	E' < 0.1	L': 0.1	E': 1.2	O': 0.1
	F': 0.2	M': ezilme	F': 0.2	P': 0.2
			G' <0.1	O': Shear crack between
			H': 0.5	300-350 mm from above
			I': 0.4	the top of the footing. P':
			J': ezilme	Shear crack between 300-
				350 mm from above the top
				of the footing.

Table C.9 : Crack propagation of LS-X21 while pushing.

Drift ratio (%)	North		South	
	Crack	Explanation	Crack	Explanation
0.10	-	-	-	-
0.25	-	-	-	-
0.50	-	-	-	-
0.75	A : 0.1	A : Shear crack between 150-250 mm from above the top of the footing. B : Shear crack between 250-400 mm from above the top of the footing. C : Vertical crack between 600-650 mm from above the top of the footing.	A : 0.1	A : Shear crack between 150-400 mm from above the top of the footing. B : Shear crack between 350-400 mm from above the top of the footing. C : Vertical crack between 100-150 mm from above the top of the footing.
	B : 0.1		B : 0.1	
	C : 0.1		C : 0.2	
1.00	A : 0.2	D : Shear crack between 0-50 mm from above the top of the footing	A : 0.2	D : Flexural crack 250 mm from above the top of the footing. E : Shear crack between 450-500 mm from above the top of the footing. F : Vertical crack between 850-950 mm from above the top of the footing.
	B : 0.2		B : 0.2	
	C : 0.2		C : 0.4	
	D : 0.3		D : 0.1 E : 0.2 F : 0.1	
1.50	A : 0.3	E : Shear crack between 500-550 mm from above the top of the footing. F : Vertical crack between 150-250 mm from above the top of the footing.	A : 0.6	D : 0.6 E : 0.2 F : 0.1
	B : 0.4		B : 0.2	
	C : 0.4		C : 1.8	
	D : 0.5			
2.00	E : 0.1	F : Vertical crack between 150-250 mm from above the top of the footing. F < 0.1 G : 0.9	A : 0.8	F : 0.1 G < 0.1 G : Shear crack between 650-750 mm from above the top of the footing.
	F : 0.1		B : 0.2	
			C : 10.0	
			D : 1.8	
2.50	A : 0.8	E : 0.1 F < 0.1 G : 0.9	E : 0.2	E : 0.2 F : 0.1 G < 0.1
	B : 0.5		A : 3.0	
	C : 0.4		B < 0.2	
	D : 3.5		C > 10.0	
3.00	A : 0.9	E : 0.3 F : 0.1 G : 2.5	D > 1.8	E : 0.1 F < 0.1 G < 0.1
	B : 0.9		A : 2.5	
	C : 0.7		B : 0.1	
	D : 7.0		C > 10.0 D > 1.8	

Table C.10 : Crack propagation of LS-X21 while pulling.

Drift ratio (%)	North		South	
	Crack	Explanation	Crack	Explanation
-0.10	-	-	-	-
-0.25	-	-	-	-
-0.50	-	-	-	-
	A' : 0.1	A' : Flexural crack 250 mm from above the top of the footing.	A' : 0.1 B' : 0.1	A' : Flexural crack 250 mm from above the top of the footing.
-0.75				B' : Vertical crack between 100-200 mm from above the top of the footing.
	A' : 0.1 B' : 0.1 C' : 0.1	B' : Shear crack between 300-450 mm from above the top of the footing.	A' : 0.1 B' : 0.1 C' : 0.1	C' : Shear crack between 600-650 mm from above the top of the footing.
-1.00		C' : Shear crack between 500-650 mm from above the top of the footing.	D' : 0.1	D' : Vertical crack between 650-850 mm from above the top of the footing.
	A' : 0.2 B' : 0.2 C' : 0.1		A' : 0.1 B' < 0.1 C' : 0.1	E' : Vertical crack between 600-700 mm from above the top of the footing.
-1.50			D' : 0.1 E' : 0.4 F' : 0.2 G' : 0.2	F' : Vertical crack between 250-400 mm from above the top of the footing.
				G' : Vertical crack between 200-300 mm from above the top of the footing.
-2.00	A' : 0.2 B' : 0.2 C' : 0.1 D' : 0.2	D' : Shear crack between 250-450 mm from above the top of the footing.	A' : 0.1 B' < 0.1 C' : 0.2	D' : 0.1 E' : 0.5 F' : 0.5 G' : ezilme
-2.50	A' : 0.2 B' : 0.2 C' : 0.1 D' : 0.7		A' < 0.1 B' < 0.1 C' : 0.2	D' : 0.1 E' : 0.7 F' : 0.6 G' : ezilme

Table C.11 : Crack propagation of LS-X28 while pushing.

Drift ratio (%)	North		South	
	Crack	Explanation	Crack	Explanation
0.10	-		-	
0.25	-		-	
0.50	-		-	
0.75	A : 0.1	A : Crack at the column-footing interface.	A : 0.1	A : Crack at the column-footing interface.
1.00	A : 0.4		A : 0.4	
1.50	A : 1.3 A : 1.8 B : 0.1 C : 0.1 D : 0.2	B : Vertical crack between 100-250 mm from above the top of the footing. C : Shear crack between 250-400 mm from above the top of the footing. D : Shear crack between 450-600 mm from above the top of the footing..	A : 1.4 A : 1.5 B : 0.8 C : 0.3	B : Shear crack between 50-100 mm from above the top of the footing. C : Vertical crack between 100-200 mm from above the top of the footing.
2.00				
2.50	A : 3.5 B : 0.3 C : 0.3 D : 0.3 A : 7.0		A > 1.5 B > 0.8 C : 0.2	
3.00	B : 0.2 C : 0.2 D : 0.1			
3.50	A > 7.0 B : 0.2 C : 0.3 D : 0.2		A > 1.5 B > 0.8 C > 0.2	

Table C.12 : Crack propagation of LS-X28 while pulling.

Drift ratio (%)	North		South	
	Crack	Explanation	Crack	Explanation
-0.10	-		-	
-0.25	-		-	
-0.50	-		-	
-0.75	A' : 0.1	A' : Crack at the column-footing interface.	A' : 0.1	A' : Crack at the column-footing interface.
-1.00	A' : 0.2		A' : 0.2	
-1.50	A' : 0.5 A' : 2.2 B' : 0.2 C' : 0.3	B' : Flexural crack 250 mm from above the top of the footing. C' : Flexural crack 450 mm from above the top of the footing.	A' : 1.3 A' : 2.2 B' : 0.2 C' : 0.1	B' : Vertical crack between 250-450 mm from above the top of the footing. C' : Vertical crack between 150-200 mm from above the top of the footing.
-2.00				
-2.50	A' : 1.3 B' : 0.3 C' : 0.5		A' > 2.2 B' : 0.2 C' > 0.1	
-3.00	A' : 1.2 B' : 0.2 C' : 0.2		A' > 2.2 B' : 0.5 C' > 0.1	

Table C.13 : Crack propagation of NS-X0 while pushing.

Drift ratio (%)	North		South	
	Crack	Explanation	Crack	Explanation
0.10	-	-	-	-
0.25	-	-	-	-
0.50	A : 0.4	A : Crack at the column-footing interface.	A : 0.4	A : Crack at the column-footing interface.
	A : 0.5 B : 0.1 C < 0.1 D < 0.2	B : Flexural crack 350 mm from above the top of the footing. C : Flexural crack 450 mm from above the top of the footing. D : Flexural crack 550 mm from above the top of the footing.	A : 0.5 B : 0.1 C : 0.1 D < 0.1	B : Flexural crack 150 mm from above the top of the footing. C : Flexural crack 350 mm from above the top of the footing. D : Flexural crack 550 mm from above the top of the footing.
0.75				
1.00	A : 0.6 B : 0.2 C : 0.1 D : 0.2		A : 0.5 B : 0.1 C : 0.1 D : 0.1	
1.50	A : 0.9 B : 0.2 C : 0.1 D : 0.2		A : 0.8 B : 0.1 C : 0.1 D : 0.1	
2.00	A : 1.6 B : 0.2 C : 0.1 D : 0.2		A : 1.0 B : 0.1 C : 0.1 D : 0.1	
2.50	A : 2.5 B : 0.2 C : 0.1 D : 0.2		A : 1.6 B : 0.2 C : 0.2 D : 0.1	
3.00	A : 3.0 B : 0.1 C < 0.1 D : 0.1	Crack: Vertical crack between 50-200 mm from above the top of the footing.	A : 3.0 B : 0.2 C : 0.2 D : 0.15	
3.50	A : 3.5 B : 0.2 C < 0.1 D : 0.2		A > 3.0 B : 0.2 C : 0.2 D : 0.2	Crack: Vertical crack between 0-150 mm from above the top of the footing.
4.00	A : 5.0 B : 0.1 C < 0.1 D : 0.2		A > 3.0 B : 0.2 C : 0.2 D : 0.2	
4.50	A > 5.0 B : 0.2 C < 0.1 D : 0.25		A > 3.0 B : 0.3 C : 0.2 D : 0.2	
5.00	A > 5.0 B : 0.2 C < 0.1 D : 0.25		A > 3.0 B : 0.3 C : 0.2 D : 0.2	
6.00	A > 5.0 B : 0.2 C < 0.1 D : 0.25		A > 3.0 B > 0.3 C : 0.2 D : 0.2	

Table C.14 : Crack propagation of NS-X0 while pulling.

Drift ratio (%)	North		South	
	Crack	Explanation	Crack	Explanation
-0.10	-	-	-	-
-0.25	-	-	-	-
-0.50	A' : 0.3	A': Crack at the column-footing interface.	A' : 0.3	A': Crack at the column-footing interface.
	A' : 0.4 B' : 0.1 C' : 0.1 D' : 0.1 E' < 0.1 F' < 0.1	B': Flexural crack 150 mm from above the top of the footing. C': Flexural crack 250 mm from above the top of the footing. D': Flexural crack 350 mm from above the top of the footing. E': Flexural crack 450 mm from above the top of the footing. F': Flexural crack 550 mm from above the top of the footing.	A' : 0.3 B' : 0.1 C' : 0.1 D' : 0.1 E' < 0.1 F' < 0.1	B': Flexural crack 150 mm from above the top of the footing. C': Flexural crack 250 mm from above the top of the footing. D': Flexural crack 350 mm from above the top of the footing. E': Flexural crack 450 mm from above the top of the footing. F': Flexural crack 550 mm from above the top of the footing.
-0.75				
-1.00	A' : 0.6 B' : 0.1 C' : 0.1	D' : 0.1 E' : 0.1 F' : 0.1	A' : 0.3 B' : 0.1 C' : 0.1	D' : 0.1 E' : 0.1 F' : 0.1
-1.50	A' : 0.8 B' : 0.1 C' : 0.1	D' : 0.1 E' : 0.1 F' : 0.1	A' : 0.5 B' : 0.8 C' : 0.1 D' : 0.1 E' : 0.1	G': Shear crack between 300-400 mm from above the top of the footing. F' : 0.1 G' < 0.1
-2.00%	A' : 0.9 B' : 0.1 C' : 0.1	D' : 0.1 E' : 0.1 F' : 0.2	A' : 0.9 B' : 0.1 C' : 0.2 D' : 0.1	E' : 0.1 F' : 0.2 G' : 0.1
-2.50	A' : 1.8 B' : 0.1 C' : 0.1	D' : 0.1 E' : 0.1 F' : 0.2	A' : 1.8 B' : 0.1 C' : 0.2 D' : 0.1	E' : 0.1 F' : 0.2 G' : 0.1
-3.00	A' > 1.8 B' < 0.1 C' : 0.1	D' : 0.1 E' : 0.1 F' : 0.2	A' > 1.8 B' : 0.2 C' : 0.2	D' : 0.1 E' : 0.1 F' : 0.2 G' : 0.1
-3.50	A' > 1.8 B' < 0.1 C' : 0.1	D' : 0.1 E' : 0.15 F' : 0.2	A' > 1.8 B' : 0.2 C' : 0.2 D' : 0.1	E' : 0.1 F' : 0.2 G' : 0.1
-4.00	A' > 1.8 B' : 0.1 C' : 0.1	D' : 0.1 E' : 0.15 F' : 0.2	A' > 1.8 B' : 0.2 C' : 0.2 D' : 0.1	E' : 0.1 F' : 0.2 G' : 0.1
-5.00	A' > 1.8 B' : 0.1 C' : 0.1	D' : 0.1 E' : 0.15 F' : 0.2	A' > 1.8 B' : 0.2 C' : 0.2 D' : 0.1	E' : 0.1 F' : 0.2 G' : 0.1
-6.00	A' > 1.8 B' : 0.1 C' : 0.1	D' : 0.1 E' : 0.15 F' : 0.2	A' > 1.8 B' : 0.2 C' : 0.2 D' : 0.1	E' : 0.1 F' : 0.2 G' : 0.1

Table C.15 : Crack propagation of NS-X9 while pushing.

Drift ratio (%)	North		South	
	Crack	Explanation	Crack	Explanation
0.10	-	-	-	-
0.25	-	-	-	-
	A : 0.1 B : 0.1	A : Crack at the column-footing interface.	A : 0.1	A : Crack at the column-footing interface.
0.50		B : Flexural crack 150 mm from above the top of the footing.		
	A : 0.1 B : 0.1		A : 0.2 B : 0.1	B : Flexural crack 150 mm from above the top of the footing.
0.75		C : Flexural crack 550 mm from above the top of the footing.		C : Flexural crack 350 mm from above the top of the footing.
	A : 0.5 B : 0.2 C : 0.1 D < 0.1 E : 0.1	D : Flexural crack 450 mm from above the top of the footing.	A : 0.6 B < 0.1 C < 0.1 D : 0.1 E < 0.1 F < 0.1	D : Flexural crack 550 mm from above the top of the footing.
1.00		E : Flexural crack 350 mm from above the top of the footing.		E : Flexural crack 650 mm from above the top of the footing.
				F : Flexural crack 750 mm from above the top of the footing.
	A : 1.2 B : 0.2 C : 0.1	D < 0.1 E : 0.1	A : 1.0 B < 0.1 C < 0.1	D : 0.1 E < 0.1 F < 0.1
1.50				
	A : 1.8 B : 0.2 C : 0.1 D < 0.1 E : 0.1		A : 1.6 B < 0.1 C < 0.1 D : 0.1 E < 0.1	F : 0.1 G : 0.1 G : Vertical crack between 0-100 mm from above the top of the footing.
2.00				
	A : 3.5 B : 0.2 C : 0.2 D < 0.1 E : 0.1 F : 0.1	F : Vertical crack between 0-100 mm from above the top of the footing.	A : 2.8 B < 0.1 C < 0.1 D : 0.1	E < 0.1 F : 0.1 G : 0.1
2.50				
	A : 5.0 B : 0.2 C : 0.2 D : 0.1 E : 0.1 F : 0.1	G : Vertical crack between 0-50 mm from above the top of the footing.	A : 3.0 B < 0.1 C < 0.1 D : 0.1	E < 0.1 F : 0.1 G : 0.3
3.00				
	A : 10.0 B : 0.2 C : 0.2 D : 0.1	E : 0.1 F : 1.0 G : 0.2	A : 3.5 B < 0.1 C < 0.1 D : 0.1 E < 0.1 H : 0.3	F : 0.1 G : 0.5 H : Vertical crack between 0-100 mm from above the top of the footing.
3.50				
	A : 12.0 B : 0.2 C : 0.2 D : 0.1	E : 0.1 F : 2.5 G : 0.4	A : 3.5 B < 0.1 C < 0.1 D : 0.1	E < 0.1 F : 0.1 G : 2.0 H : 0.7
4.00				

Table C.15 (contd.) : Crack propagation of NS-X9 while pushing.

Drift ratio (%)	North		South	
	Crack	Explanation	Crack	Explanation
4.50	A : 15.0	E : 0.1	A > 3.5	E < 0.1
	B : 0.2	F : 3.5	B < 0.1	F : 0.1
	C : 0.2	G : 0.8	C < 0.1	G > 2.0
	D : 0.1		D : 0.1	H > 0.7
5.00	A > 15.0	E : 0.1	A > 3.5	E < 0.1
	B : 0.2	F : 5.0	B < 0.1	F : 0.1
	C : 0.2	G > 0.8	C < 0.1	G > 2.0
	D : 0.1		D : 0.1	H > 0.7
6.00	A > 15.0	E : 0.1	A > 3.5	E < 0.1
	B : 0.2	F > 5.0	B < 0.1	F : 0.1
	C : 0.2	G > 0.8	C < 0.1	G > 2.0
	D : 0.1		D : 0.2	H > 0.7

Table C.16 : Crack propagation of NS- X9 while pulling.

Drift ratio (%)	North		South	
	Crack	Explanation	Crack	Explanation
-0.10	-	-	-	-
-0.25	-	-	-	-
	A' : 0.1	A': Crack at the column-footing interface.	A' : 0.1 B' <0.1	A': Crack at the column-footing interface.
-0.50		B': Flexural crack 250 mm from above the top of the footing.		B': Flexural crack 250 mm from above the top of the footing.
	A' : 0.1 B' : 0.1 C' : 0.1 D' < 0.1 E' < 0.1 F' < 0.1	C': Vertical crack between 0-100 mm from above the top of the footing. D': Flexural crack 350 mm from above the top of the footing.	A' : 0.1 B' <0.1 C' < 0.1 D' <0.1 E' <0.1	C': Flexural crack 150 mm from above the top of the footing. D': Flexural crack 350 mm from above the top of the footing.
-0.75		E': Flexural crack 450 mm from above the top of the footing. F': Flexural crack 600 mm from above the top of the footing.		E': Flexural crack 500 mm from above the top of the footing.
	A' : 0.5 B' : 0.1 C' : 0.3 D' : 0.1 E' < 0.1 F' < 0.1 G:0.1	G': Flexural crack 150 mm from above the top of the footing.	A' :0.5 B' < 0.1 C' : 0.1 D' <0.1 E' < 0.1 F' : 0.2	F': Vertical crack between 0-100 mm from above the top of the footing.
-1.00	A' : 1.8 B' : 0.1 C' : 0.5 D' : 0.1	E' < 0.1 F' < 0.1 G':0.1	A' :1.4 B' : 0.1 C' : 0.1 D' <0.1 E' < 0.1	F' : 0.4 G':0.1
-1.50			C' : 0.1 D' <0.1 E' < 0.1	G': Vertical crack between 0-150 mm from above the top of the footing.
	A' : 3.5 B' : 0.1 C' : 0.7 D' : 0.1 E' < 0.1 F' : 0.1 G' : 0.1 H' < 0.1	H': Flexural crack 650 mm from above the top of the footing.	A' :3.5 B' : 0.1 C' : 0.3 D' <0.1 E' < 0.1 F' : 0.7 G':0.4 H':0.2 I':0.1	H': Vertical crack between 0-100 mm from above the top of the footing. I': Flexural crack 550 mm from above the top of the footing..
-2.00				
	A' : 3.5 B' : 0.1 C' : 0.7 D' : 0.1 E' < 0.1	F' : 0.1 G': 0.1 H' < 0.1 I: 0.1	A' >3.5 B' : 0.1 C' : 0.4 D' <0.1 E' < 0.1	F' : 0.7 G' >0.4 H' >0.2 I':0.1
-2.50				
	A' : 6.0 B' : 0.1 C' : 1.0 D' : 0.1 E' < 0.1	F' : 0.1 G': 0.1 H' < 0.1 I: 0.1	A' >3.5 B' : 0.1 C' : 0.6 D' <0.1 E' < 0.1	F' > 0.7 G' >0.4 H' >0.2 I':0.1
-3.00				
	A' > 6.0 B' : 0.1 C' : 0.4 D' : 0.1 E' < 0.1	F' : 0.1 G': 0.1 H' < 0.1 I: 0.1	A' >3.5 B' : 0.1 C' : 0.9 D' <0.1 E' < 0.1	F' > 0.7 G' >0.4 H' >0.2 I':0.1
-3.50				

Table C.16 (contd.) : Crack propagation of NS- X9 while pulling.

Drift ratio (%)	North		South	
	Crack	Explanation	Crack	Explanation
-4.00	A' > 6.0	F' : 0.1	A' > 3.5	F' > 0.7
	B' : 0.1	G' : 0.1	B' : 0.1	G' > 0.4
	C' ₂ > 0.4	H < 0.1	C' : 1.0	H' > 0.2
	D' : 0.1	I : 0.1	D' < 0.1	I' : 0.1
	E' < 0.1		E' < 0.1	
-4.50	A' > 6.0	F' : 0.1	A' > 3.5	F' > 0.7
	B' : 0.1	G' : 0.1	B' : 0.1	G' > 0.4
	C' ₂ > 0.4	H < 0.1	C' : 2.0	H' > 0.2
	D' : 0.1	I : 0.1	D' < 0.1	I' : 0.1
	E' < 0.1		E' < 0.1	
-5.00	A' > 6.0	F' : 0.1	A' > 3.5	F' > 0.7
	B' : 0.1	G' : 0.1	B' : 0.1	G' > 0.4
	C' ₂ > 0.4	H < 0.1	C' : 3.5	H' > 0.2
	D' : 0.1	I : 0.1	D' < 0.1	I' : 0.1
	E' < 0.1		E' < 0.1	
-6.00	A' > 6.0	F' : 0.1	A' > 3.5	F' > 0.7
	B' : 0.1	G' : 0.1	B' : 0.1	G' > 0.4
	C' ₂ > 0.4	H < 0.1	C' : 10.0	H' > 0.2
	D' : 0.1	I : 0.1	D' < 0.1	I' : 0.1
	E' < 0.1		E' < 0.1	
-7.00	A' > 6.0	F' : 0.1	A' > 3.5	F' > 0.7
	B' : 0.1	G' : 0.1	B' : 0.1	G' > 0.4
	C' ₂ > 0.4	H < 0.1	C' : 12.0	H' > 0.2
	D' : 0.1	I : 0.1	D' < 0.1	I' : 0.1
	E' < 0.1		E' < 0.1	

Table C.17 : Crack propagation of NS-X13 while pushing.

Drift ratio (%)	North		South	
	Crack	Explanation	Crack	Explanation
0.10	-	-	-	-
0.25	-	-	-	-
0.50			A : 0.1	A : Crack at the column-footing interface.
0.75	A : 0.5	A : Crack at the column-footing interface.	A : 0.2	
	A : 0.7		A : 0.3 B : 0.4 BL ₁ : 0.1	B : Flexural crack 50 mm from above the top of the footing. BL₁ : Vertical crack between 0-50 mm from above the top of the footing.
1.00				
1.50	A : 0.9 B : 0.2	B : Vertical crack between 0-50 mm from above the top of the footing.	A : 0.4 B : 0.4 BL ₁ : 0.2	
2.00	A : 1.2 B : 0.4		A > 0.4 B : 0.8 BL ₁ : 0.5	
2.50	A > 1.2 B : 0.6 BL ₁ : 0.3 C < 0.1	C : Flexural crack 250 mm from above the top of the footing. BL₁ : Vertical crack between 0-100 mm from above the top of the footing.	A > 0.4 B : 1.2 BL ₁ : 0.9	
3.00	A > 1.2 B : 0.7 BL ₁ : 1.0 C < 0.1			
	A > 1.2 B : 0.7 BL ₁ > 1.0			

Table C.18 : Crack propagation of NS-X13 while pulling.

Drift ratio (%)	North		South	
	Crack	Explanation	Crack	Explanation
-0.10	-	-	-	-
-0.25	-	-	-	-
-0.50	A' : 0.1	A': Crack at the column-footing interface.	A' : 0.1	A': Crack at the column-footing interface.
-0.75	A' : 0.6 BL ₁ ' : 0.2	BL ₁ ': Vertical crack between 0-50 mm from above the top of the footing.	A' : 0.4 BL ₁ ' : 0.3	BL ₁ ': Vertical crack between 0-100 mm from above the top of the footing.
-1.00	A' : 0.8 BL ₁ ' : 0.4		A' : 0.4 BL ₁ ' : 0.7	
-1.50	A' : 0.8 BL ₁ ' : 1.0	Crack': Vertical crack between 0-100 mm from above the top of the footing.	A' : 0.7 BL ₁ ' : 1.4	
-2.00	A' : 1.2 BL ₁ ' : 1.2		A' : 1.2 BL ₁ ' : 3.0 B' : 0.2	B': Vertical crack between 0-50 mm from above the top of the footing and flexural crack 50 mm from above the top of the footing.
-2.50			A' > 1.2 BL ₁ ' : 8.0 B' : 0.8	
-3.00			A' > 1.2 BL ₁ ' : 10.0 B' : 0.9	

Table C.19 : Crack propagation of NS-X16 while pushing.

Drift ratio (%)	North		South	
	Crack	Explanation	Crack	Explanation
0.10	-	-	-	-
0.25	-	-	A : 0.2	A : Flexural crack 50 mm from above the top of the footing.
0.50	A : 0.1	A : Flexural crack 50 mm from above the top of the footing.	A : 0.2	
0.75	A : 0.1 B : 0.2	B: Crack at the column-footing interface.	A : 0.2 B : 0.2	B: Crack at the column-footing interface.
1.00	A : 0.1 B : 0.6		A : 0.2 B : 0.6 C : 0.1	C : Vertical crack between 100-200 mm from above the top of the footing.
1.50	A : 0.1 B : 1.8 C : 0.2	C : Vertical crack between 0-100 mm from above the top of the footing.	A : 0.2 B : 1.6 C : 0.1 D : 0.1	D : Vertical crack between 0-100 mm from above the top of the footing.
2.00	A : 0.1 B : 2.5 C : 0.2		A : 0.2 B : 2.5	C : 0.1 D : 0.1
2.50	A : 0.1 B > 2.5 C : 0.3		A : 0.2 B : 3.5	C : 0.2 D : 0.2
3.00	A : 0.1 B : 3.5 C : 0.6		A : 0.2 B > 3.5	C : 0.2 D : 0.4
3.50	A : 0.1 B : 5.0 C : 0.7		A : 0.2 B > 3.5	C : 0.2 D : 0.4
4.00	A : 0.1 B > 5.0 C : 0.8		A : 0.2 B > 3.5	C : 0.2 D > 0.4
4.50	A : 0.1 B > 7.0 C > 0.8		A : 0.2 B > 3.5	C : 0.2 D > 0.4
5.00	A : 0.1 B > 10.0 C > 0.8		A : 0.2 B > 3.5	C : 0.2 D > 0.4

Table C.20 : Crack propagation of NS-X16 while pulling.

Drift ratio (%)	North		South	
	Crack	Explanation	Crack	Explanation
-0.10	-	-	-	-
-0.25	-	-	-	-
-0.50	A' : 0.2 B' : 0.1	A' : Flexural crack 50 mm from above the top of the footing. B' : Flexural crack 250 mm from above the top of the footing.	A' : 0.2 B' : 0.1	A' : Flexural crack 50 mm from above the top of the footing. B' : Flexural crack 250 mm from above the top of the footing.
	A' : 0.2 B' : 0.1 C : 0.2 D : 0.1	C' Crack at the column-footing interface. D' : Flexural crack 550 mm from above the top of the footing.	A' : 0.2 B' : 0.1 C : 0.2 D : 0.1 E' : 0.2	C' : Crack at the column-footing interface. D' : Vertical crack between 750~900 mm from above the top of the footing E' : Flexural crack 50 mm from above the top of the footing.
-1.00	A' : 0.3 B' : 0.1	C : 0.6 D : 0.1	A' : 0.3 B' : 0.1 C : 0.7 A' : 0.4 B' : 0.1	D : 0.1 E' : 0.1
-1.50	A' : 0.6 B' : 0.1 C : 1.8 D : 0.1		C : 2.0 D : 0.1 E' : 0.1 F' : 0.1	F' : Vertical crack between 50-150 mm from above the top of the footing.
-2.00	A' : 0.6 B' : 0.1	C' > 1.8 D' : 0.1	A' : 0.5 B' : 0.1 C > 2.0	D : 0.1 E' : 0.2 F' : 0.3
-2.50	A' : 1.4 B' : 0.1	C' > 1.8 D' : 0.1	A' : 0.5 B' : 0.1 C > 2.0	D : 0.1 E' : 0.5 F' : 0.6
-3.00	A' : 1.4 B' : 0.1	C' > 1.8 D' : 0.1	A' : 0.5 B' : 0.1 C > 2.0	D : 0.1 E' > 0.5 F' : 2.0
-3.50	A' : 2.0 B' : 0.1	C' > 1.8 D' : 0.1	A' : 0.5 B' : 0.1 C > 2.0	D : 0.1 E' > 0.5 F' > 2.0
-4.00	A' > 2.0 B' : 0.1	C' > 1.8 D' : 0.1	A' : 0.5 B' : 0.1 C > 2.0	D : 0.1 E' > 0.5 F' > 2.0
-4.50	A' > 2.0 B' : 0.1	C' > 1.8 D' : 0.1		

Table C.21 : Crack propagation of NS-X22 while pushing.

Drift ratio (%)	North		South	
	Crack	Explanation	Crack	Explanation
0.10	-	-	-	-
0.25	-	-	-	-
0.50	-	-	-	-
0.75	-	-	-	-
	A : 0.3 B : 0.1 C < 0.1	A: Crack at the column-footing interface. B : Flexural crack 100 mm from above the top of the footing. C: Flexural crack 350 mm from above the top of the footing.	A : 0.4 B : 0.1 C < 0.1 D : 0.1 E < 0.1	A: Crack at the column-footing interface. B : Flexural crack 100 mm from above the top of the footing. C : Flexural crack 250 mm from above the top of the footing. D : Flexural crack 350 mm from above the top of the footing. E : Flexural crack 650 mm from above the top of the footing.
1.00				
	A :0.6 B : 0.1 C < 0.1		A : 0.9 B : 0.1 C < 0.1 D : 0.1 E < 0.1	
1.50				
	A : 0.9 B : 0.1 C < 0.1 D < 0.1	D: Flexural crack 250 mm from above the top of the footing.	A : 1.8 B : 0.1 C < 0.1 D : 0.1 E < 0.1	
2.00				
	A :0.9 B : 0.2 C > 0.1 D : 0.1 E : 0.2 F : 0.2	E: Flexural crack 50 mm from above the top of the footing.	A : 1.6 B : 0.1 C < 0.1 D : 0.1 E < 0.1 F < 0.1	F: Flexural crack 550 mm from above the top of the footing.
2.50				
	A :1.2 B : 0.2 C > 0.1 D : 0.1 E : 0.2 F : 1.0	Crack: Vertical crack between 100-150 mm from above the top of the footing.	A : 1.6 B : 0.1 C < 0.1 D : 0.1 E < 0.1 F < 0.1	
3.00				
	A :1.4 B : 0.25 C : 0.1 A >1.4 B : 0.25 C : 0.1 D < 0.1	D < 0.1 E : 0.35 F : 1.8 E : 0.60 F : 2.0 G : 0.55	A : 5.0 B : 0.1 C < 0.1 A > 5.0 B : 0.1 C < 0.1 D : 0.2 E < 0.1 F : 0.2 G : 0.25	D : 0.2 E < 0.1 F : 0.1 G: Vertical crack between 0-100 mm from above the top of the footing. H: Vertical crack between 0-50 mm from above the top of the footing.
3.50				
	A >1.4 B : 0.25 C : 0.1	D < 0.1 E : 0.65 F : 2.2	A > 5.0 B : 0.1 C < 0.1 D : 0.2	E < 0.1 F : 0.2 G : 0.3
4.00				
	A >1.4 B : 0.25 C : 0.1	D < 0.1 E : 0.65 F : 2.2	A > 5.0 B : 0.1 C < 0.1 D : 0.2	E < 0.1 F : 0.2 G : 0.3
4.50				

Table C.22 : Crack propagation of NS-X22 while pulling.

Drift ratio (%)	North		South	
	Crack	Explanation	Crack	Explanation
-0.10	-	-	-	-
-0.25	-	-	-	-
-0.50	-	-	-	-
	A' : 0.4 B' : 0.2	A': Crack at the column-footing interface.	A' : 0.2 B' : 0.1	A': Crack at the column-footing interface.
-0.75		B': Vertical crack between 0-100 mm from above the top of the footing.		B': Flexural crack 100 mm from above the top of the footing.
	A' : 0.9 B' : 0.2 C' : 0.1	C': Vertical crack between 100-300 mm from above the top of the footing.	A' : 0.8 B' : 0.4 C' : 0.1	C': Vertical crack between 400-450 mm from above the top of the footing.
-1.00				
	A' : 0.9 B' : 0.4 C' : 0.3		A' : 1.0 B' : 0.4 C' : 0.1 D' : 0.3 E' : 0.4	D': Flexural crack 50 mm from above the top of the footing. E': Flexural crack 50 mm from above the top of the footing.
-1.50				
	A' : 1.4 B' : 1.0 C' : 0.9	F': Flexural crack 50 mm from above the top of the footing.	A' : 1.0 B' : 0.4 C' : 0.1 D' : 0.7 E' : 0.9 F' : 0.6	F': Vertical crack between 0-100 mm from above the top of the footing.
-2.00				
	A' : 1.8 B' : 1.4 C' : 1.3		A' : 6.0 B' : 0.4 C' : 0.2	D' : 0.5 E' : 1.8 F' : 1.2
-2.50				
	A' : 5.0 B' : 3.0 C' : 1.5		A' : 6.0 B' : 0.4 C' : 0.2 D' : 0.5	E' : 2.0 F' : 1.6 H' : 0.8
-3.00				
	A' > 5.0 B' : 1.8 C' : 1.5		A' > 6.0 B' : 0.55 C' : 0.1 D' : 0.6	E' > 2.0 F' > 1.6 H' : 1.0
-3.50				
	A' > 5.0 B' : 5.0 C' : 1.5		A' > 6.0 B' : 0.55 C' : 0.1 D' > 0.6	E' > 2.0 F' > 1.6 H' : 1.30
-4.00				
	A' > 5.0 B' > 5.0 C' : 4.0			
-4.50				

Table C.23 : Crack propagation of NS-X54 while pushing.

Drift ratio (%)	North		South	
	Crack	Explanation	Crack	Explanation
0.10	-		-	
0.25	-		-	
0.50	-		-	
0.75	A : 0.1	A: Crack at the column-footing interface.	A : 0.1	A: Crack at the column-footing interface.
	A : 0.2 B : 0.1	B : Flexural crack 50 mm from above the top of the footing.	A : 0.2 B : 0.1	B : Flexural crack 150 mm from above the top of the footing.
1.00				
1.50	A :1.3		A : 1.3	
	B : 0.4		B : 0.2	
2.00	A : 3.8		A : 3.0	
	B : 0.4		B : 0.2	
2.50	A :6.0		A : 4.0	
	B : 0.4		B : 0.2	
3.00	A :8.0		A : 5.0	
	B : 0.4		B : 0.2	
3.50	A :11.0		A > 5.0	
	B : 0.4		B : 0.2	
4.00	A :14.0		A > 5.0	
	B :0.4		B : 0.2	
4.50	A >14.0		A > 5.0	
	B : 0.4		B : 0.2	
5.00	A >14.0		A > 5.0	
	B : 0.4		B : 0.2	

Table C.24 : Crack propagation of NS-X54 while pulling.

Drift ratio (%)	North		South	
	Crack	Explanation	Crack	Explanation
-0.10	-	-	-	-
-0.25	-	-	-	-
-0.50	-	-	-	-
-0.75	-	-	-	-
-1.00	A' : 0.1	A': Crack at the column-footing interface.	A' : 0.1	A': Crack at the column-footing interface.
-1.50	A' : 2.0		A' : 2.0	
-2.00	A' : 3.8		B' : 0.2	B': Flexural crack 150 mm from above the top of the footing.
-2.50	A' : 4.0		A' : 4.0	
-3.00	A' : 2.7		B' : 0.2	
-3.50	A' : 7.0		A' : 5.0	
-4.00	A' :10.0		B' : 0.2	
-4.50	A' > 10.0		A' > 5.0	
-5.00	A' > 10.0		B' : 0.2	

Table C.25 : Crack propagation of LS-X19-H while pushing.

Drift ratio (%)	North		South	
	Crack	Explanation	Crack	Explanation
0.10	-	-	-	-
0.25	-	-	-	-
0.50	A < 0.1	A : Crack at the column-footing interface.	A < 0.1	A : Crack at the column-footing interface.
0.75	A : 0.1		A : 0.3	
1.00	A : 0.4		A : 0.7	
1.50	A : 1.0		A : 1.0	
2.00	A : 2.1	B : Vertical crack between 300-400 mm from above the top of the footing.	A : 1.3	
	B : 0.1			
2.50	A : 3.5		A : 3.5	B : Shear crack between 350-450 mm from above the top of the footing. C : Flexural crack 450 mm from above the top of the footing.
	B : 0.1		B : 0.2	
3.00			C : kabarma	
	A : 3.5	C : Vertical crack between 500-650 mm from above the top of the footing.	A > 2.5	
	B : 0.4		B : 0.4	
C : 0.2	C : kabarma			
3.50	A : 5.0		A > 2.5	D : Shear crack between 150-250 mm from above the top of the footing. E : Vertical crack between 750-950 mm from above the top of the footing.
	B : 0.4		B : 0.5	
	C : 0.2		C : 0.5	
			D : 0.2	
4.00			E : 0.2	
	A : 6.0		A > 2.5	F : Shear crack between 450-500 mm from above the top of the footing.
	B : 0.4		B : 0.4	
	C : 0.3		C : ezilme	
			D < 0.1	
		E : 0.1		
4.50			F : 0.1	
	A : 7.0		A > 2.5	
	B : 0.4		B : 0.1	
	C : 0.4		C : ezilme	
			D < 0.1	
5.00			E < 0.1	
	A : 15.0		F < 0.1	
	B : 0.5		A > 2.5	
	C : 0.8		B : 0.1	
			C : ezilme	
			D < 0.1	
		E < 0.1		
		F < 0.1		

Table C.26 : Crack propagation of LS-X19-H while pulling.

Drift ratio (%)	North		South	
	Crack	Explanation	Crack	Explanation
-0.10	-	-	-	-
-0.25	-	-	-	-
-0.50	A' : 0.1	A' : Crack at the column-footing interface.	-	-
-0.75	A' : 0.1		A' : 0.2	A' : Crack at the column-footing interface.
-1.00	A' : 0.2		A' : 0.4	
-1.50	A' : 0.7		A' : 0.4	
-2.00	A' : 2.3		A' : 1.3	B' : Vertical crack between 0-150 mm from above the top of the footing.
	A' : 2.0 B' : 0.3	B' : Shear crack between 300-400 mm from above the top of the footing.	B' : 0.3	
-2.50			A' : 3.5	C' : Shear crack between 600-650 mm from above the top of the footing. D' : Shear crack between 250-350 mm from above the top of the footing. E' : Vertical crack between 250-300 mm from above the top of the footing.
			B' : 0.5 C' : 0.2 D' : 0.2 E' : 0.2 F' : 0.1 G' : 0.1 H' : 0.1	F' : Shear crack between 500-600 mm from above the top of the footing. G' : Vertical crack between 650-750 mm from above the top of the footing. H' : Vertical crack between 650-750 mm from above the top of the footing.
-3.00	A' : 4.0 B' : 0.4		A' : 4.0 B' : 0.3 C' : 0.2 D' : 0.3	E' : 0.3 F' : 0.2 G' : 0.2 H' : 0.2
	A' > 4.0 B' : 0.5		A' > 4.0 B' : 0.3 C' : 0.2 D' : 0.3	E' : 0.2 F' : 0.2 G' : 0.2 H' : 0.2

Table C.26 (contd.) : Crack propagation of LS-X19-H while pulling.

Drift ratio (%)	North		South	
	Crack	Explanation	Crack	Explanation
-4.00	A' > 4.0	D' : Vertical crack between 100-200 mm from above the top of the footing.	A' >4.0	I' : Shear crack between 650-750 mm from above the top of the footing.
	B' < 0.5		B' <0.3	
	D' : 0.2		C' : 0.2	J' : Shear crack between 650-750 mm from above the top of the footing.
	E' : 0.1		D' < 0.3	
	F' : 0.3	E' : Vertical crack between 150-200 mm from above the top of the footing.	E' < 0.2	K1' : Shear crack between 500-600 mm from above the top of the footing.
	G' : 0.2		F' < 0.2	K2' : Vertical crack between 450-550 mm from above the top of the footing.
	H' : 0.2		G' :0.2	
	I' : 0.2	F' : Shear crack between 200-250 mm from above the top of the footing.	H' :0.2	M' : Shear crack between 350-450 mm from above the top of the footing.
		G' : Vertical crack between 500-600 mm from above the top of the footing.	I' :0.1	N' : Vertical crack between 100-250 mm from above the top of the footing.
		H' : Vertical crack between 550-650 mm from above the top of the footing.	J' : 0.1	
-4.50		I' : Vertical crack between 550-650 mm from above the top of the footing.	K1' : 0.1	
	A' > 4.0	F' : 0.6	K2' :0.1	
	B' : 0.4	G' : 0.4	M' :0.1	
	D' : 0.6	H' : 0.4	N' :0.1	
	E' : 0.2	I' : 0.8		
-5.00			A' >4.0	I' :0.1
			B' <0.3	J' : 0.2
			C' <0.2	K1' : 0.1
			D' < 0.3	K2' :0.4
			E' < 0.2	M' :0.5
			F' < 0.2	N' :0.5
			G' :0.5	
			H' :0.7	
	F' > 0.3	A' >4.0	I' :0.3	
	G' : 0.2	B' <0.3	J' : 0.4	
	H' : 0.2	C' <0.2	K1' : 1.2	
	I' > 0.8	D' < 0.3	K2' :1.2	
		E' < 0.2	M' : 0.1	
		F' < 0.2	N' < 0.5	
		G' :0.8		
		H' :0.7		

APPENDIX D

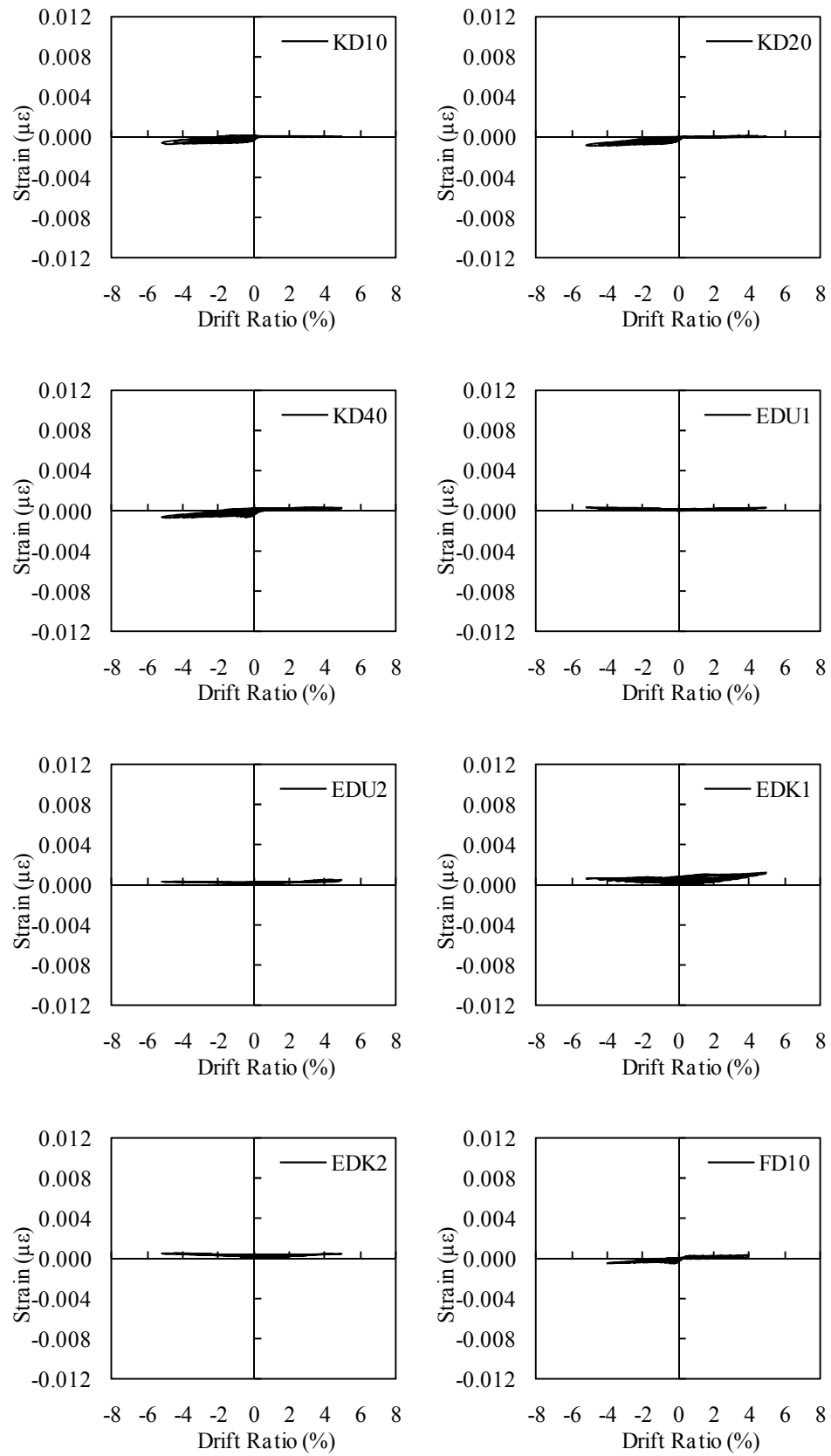


Figure D.1 : LS-X0.

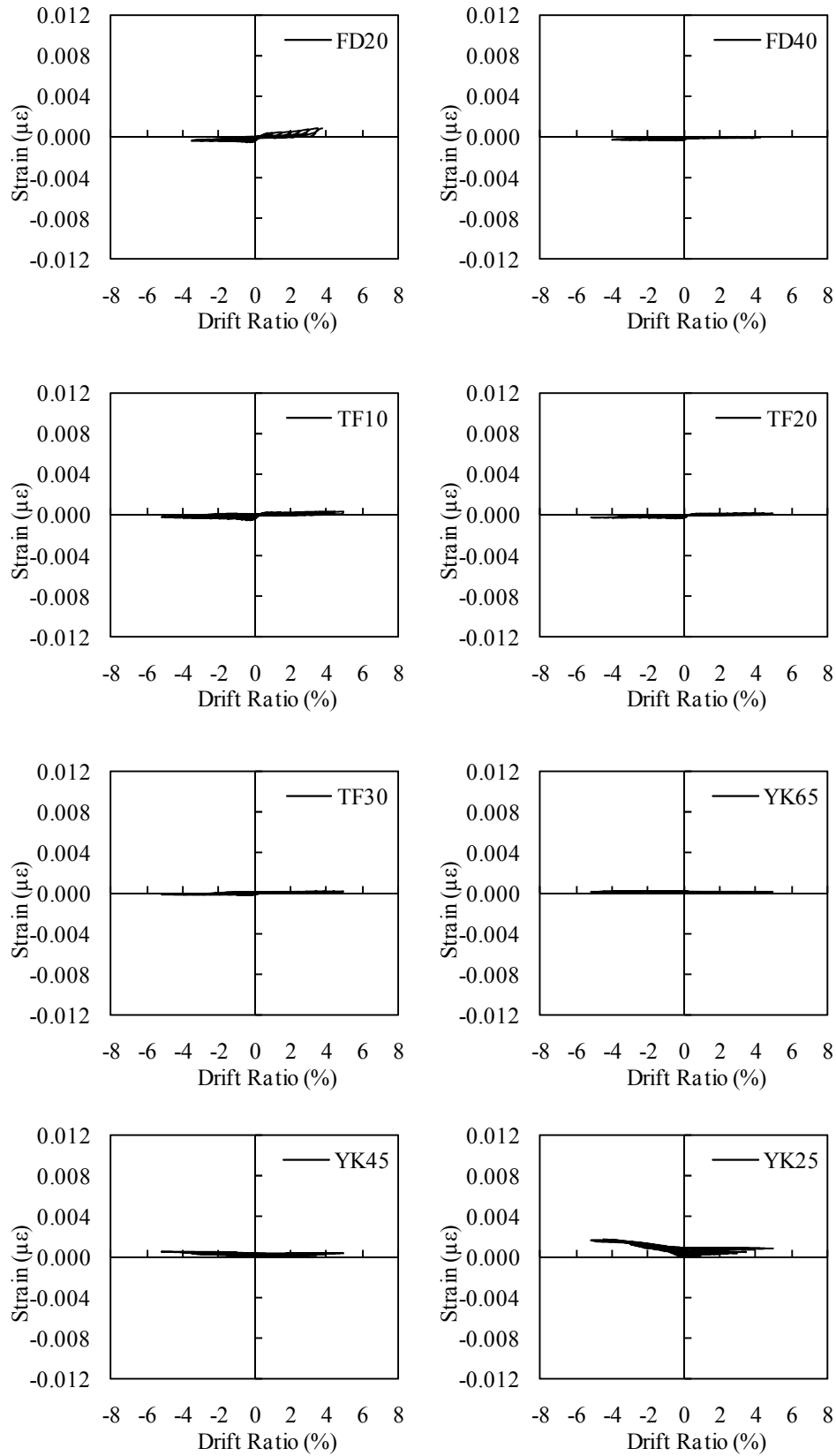


Figure D.1 (contd.) : LS-X0.

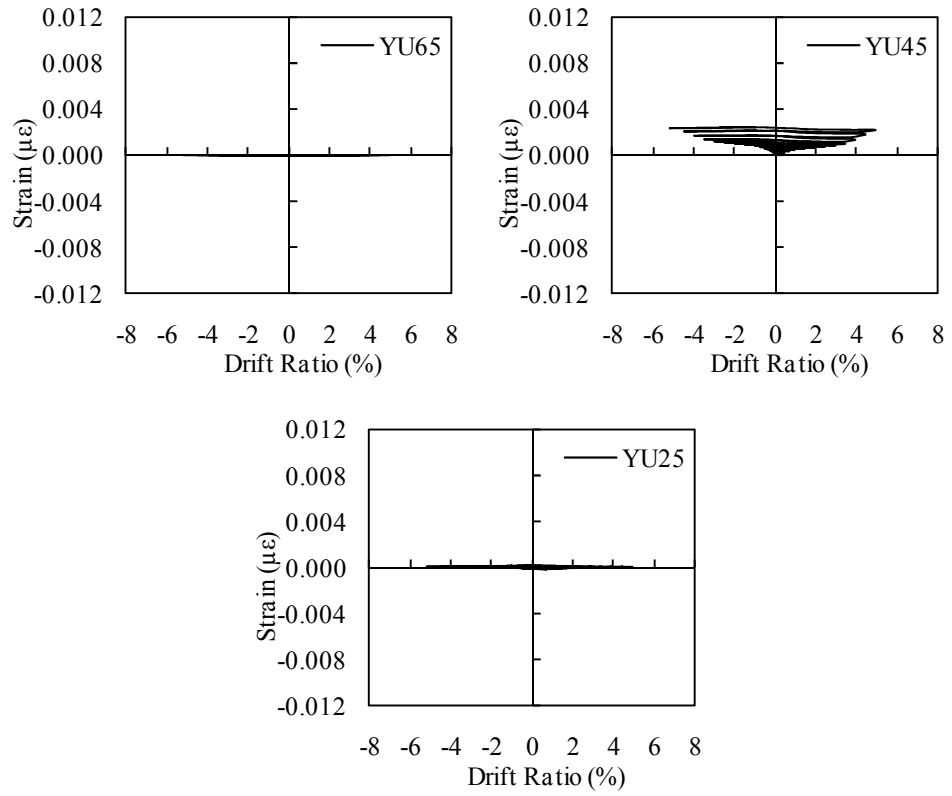


Figure D.1 (contd.) : LS-X0.

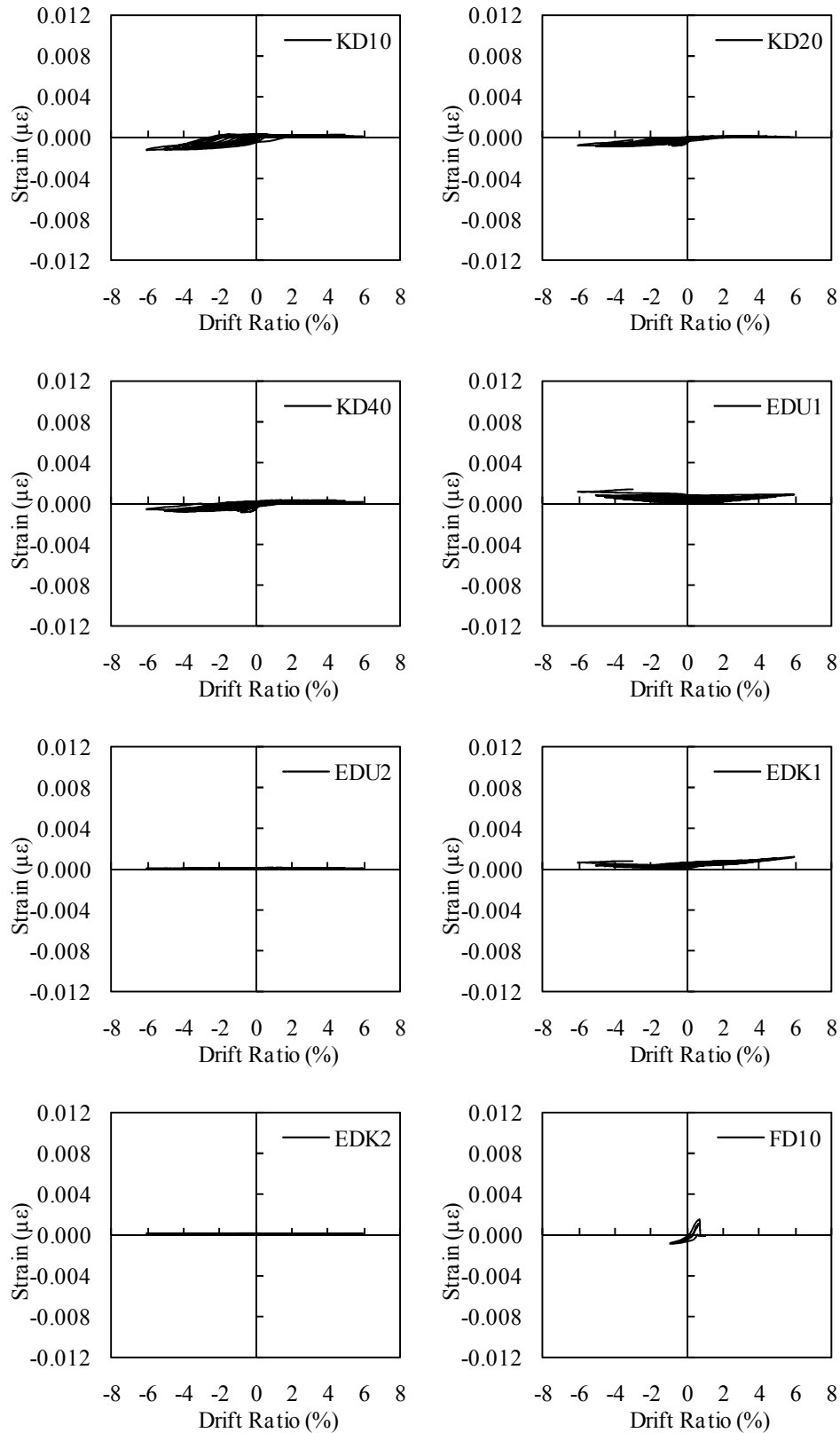


Figure D.2: LS-X6.

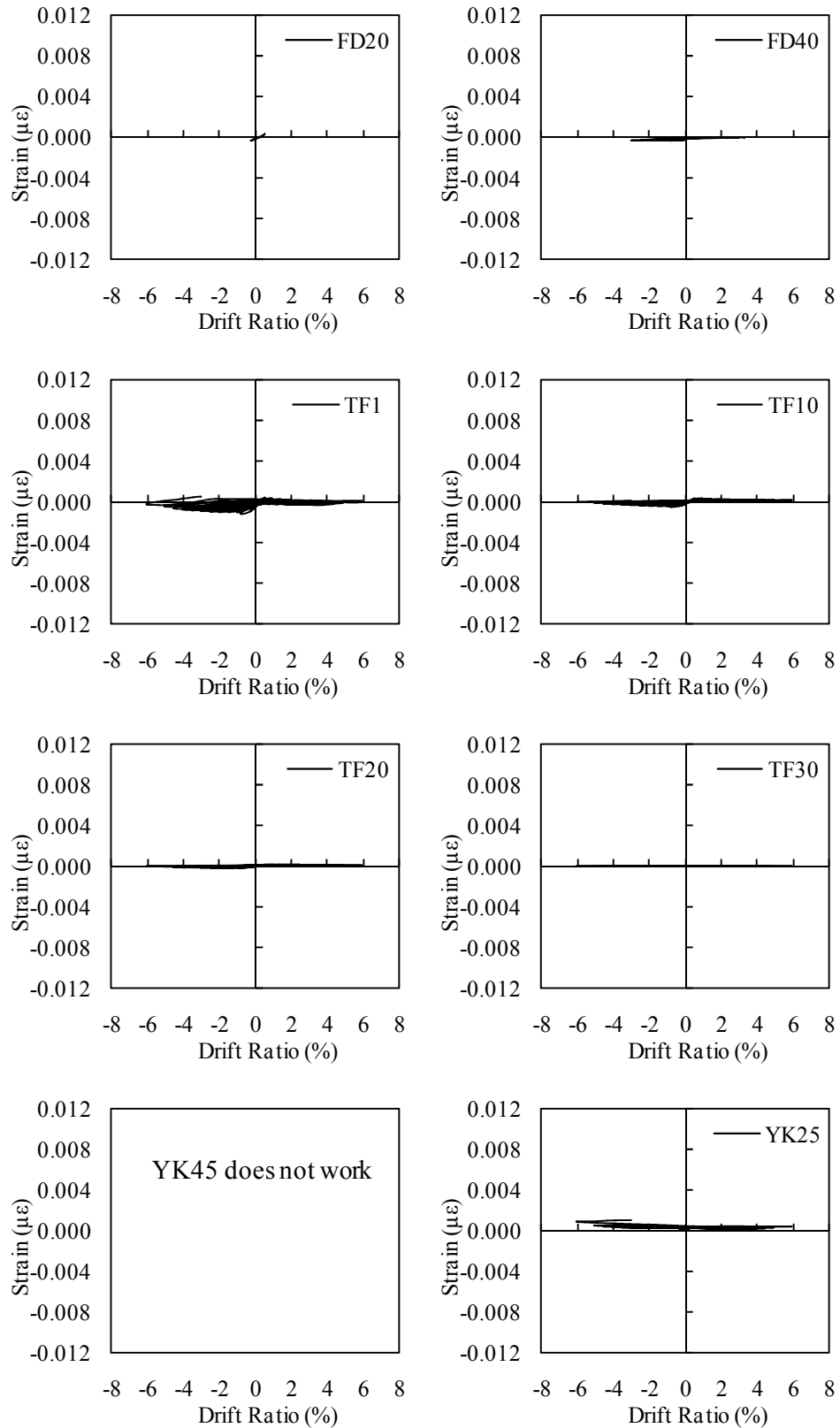


Figure D.2 (contd.) : LS-X6.

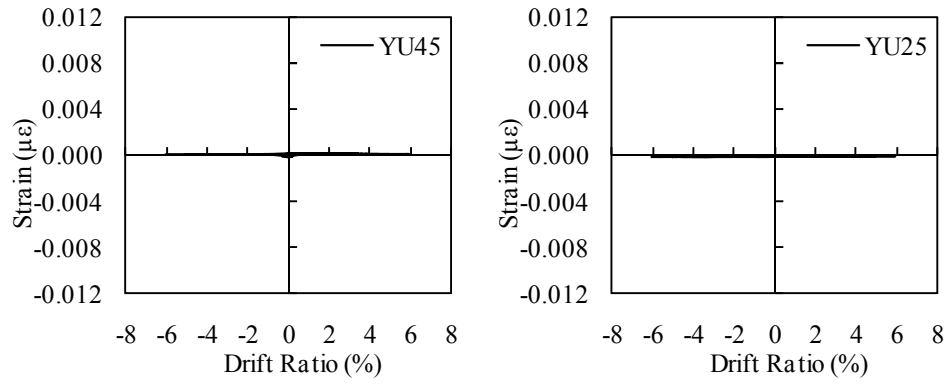


Figure D.2 (contd.) : LS-X6.

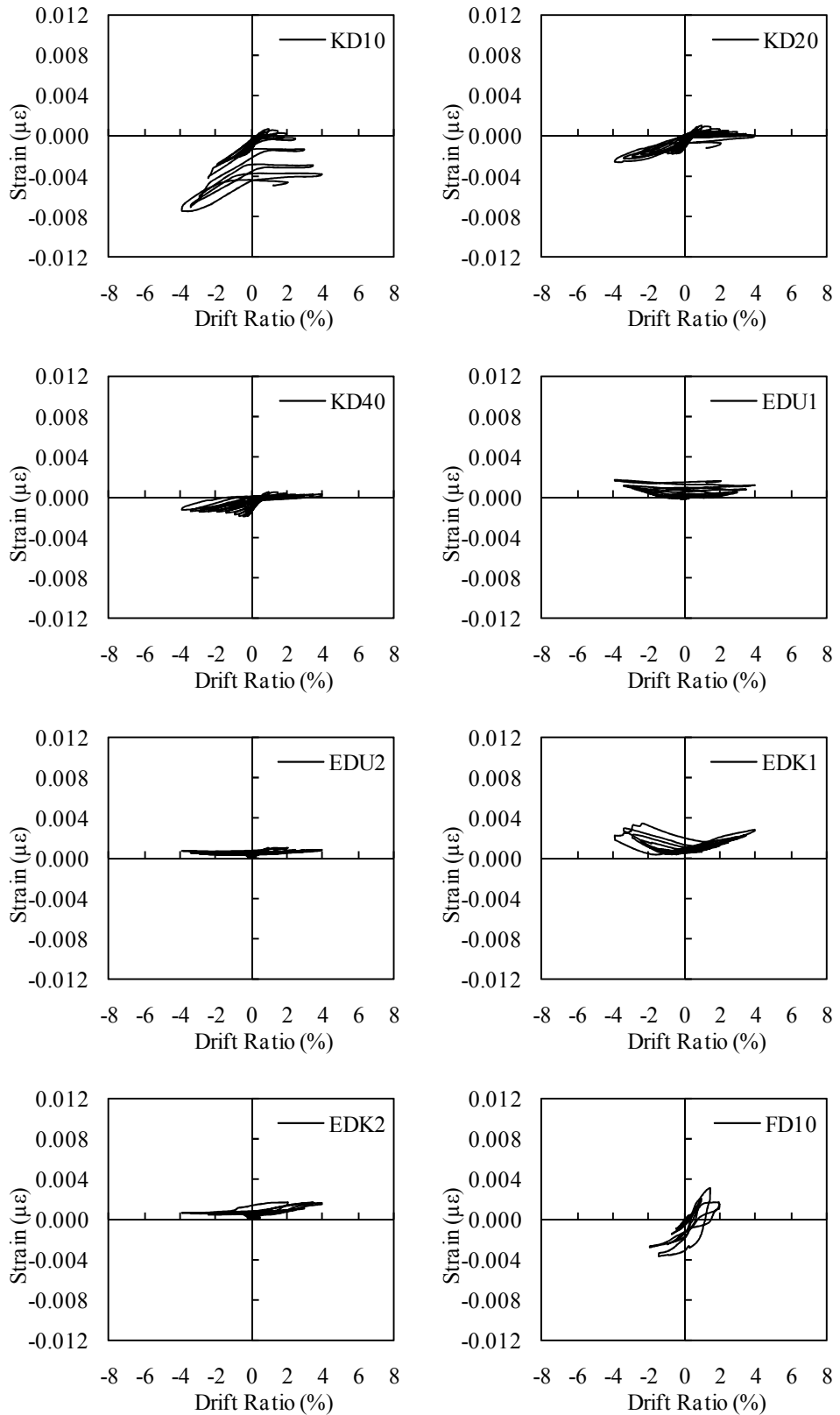


Figure D.3 : LS-X8.

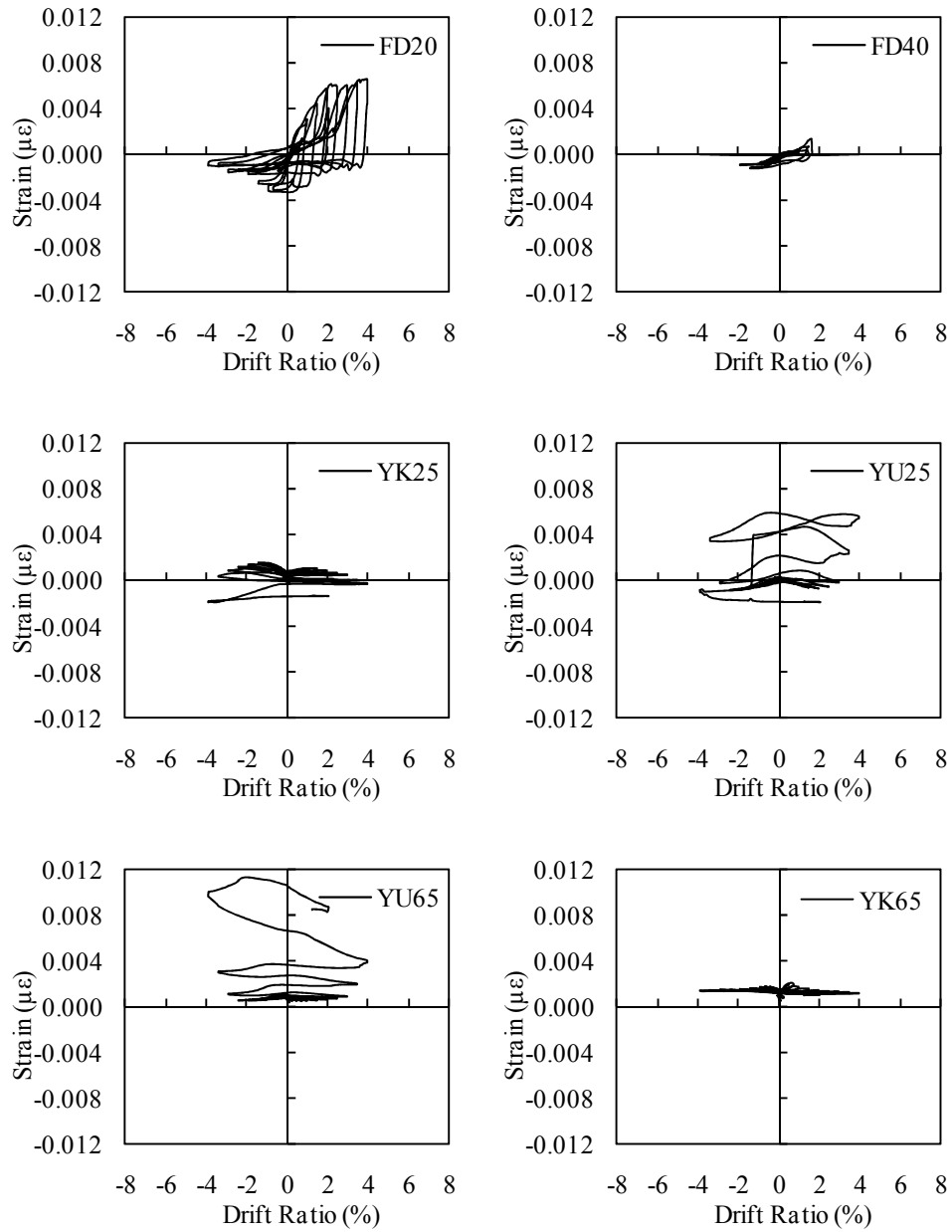


Figure D.3 (contd.) : LS-X8.

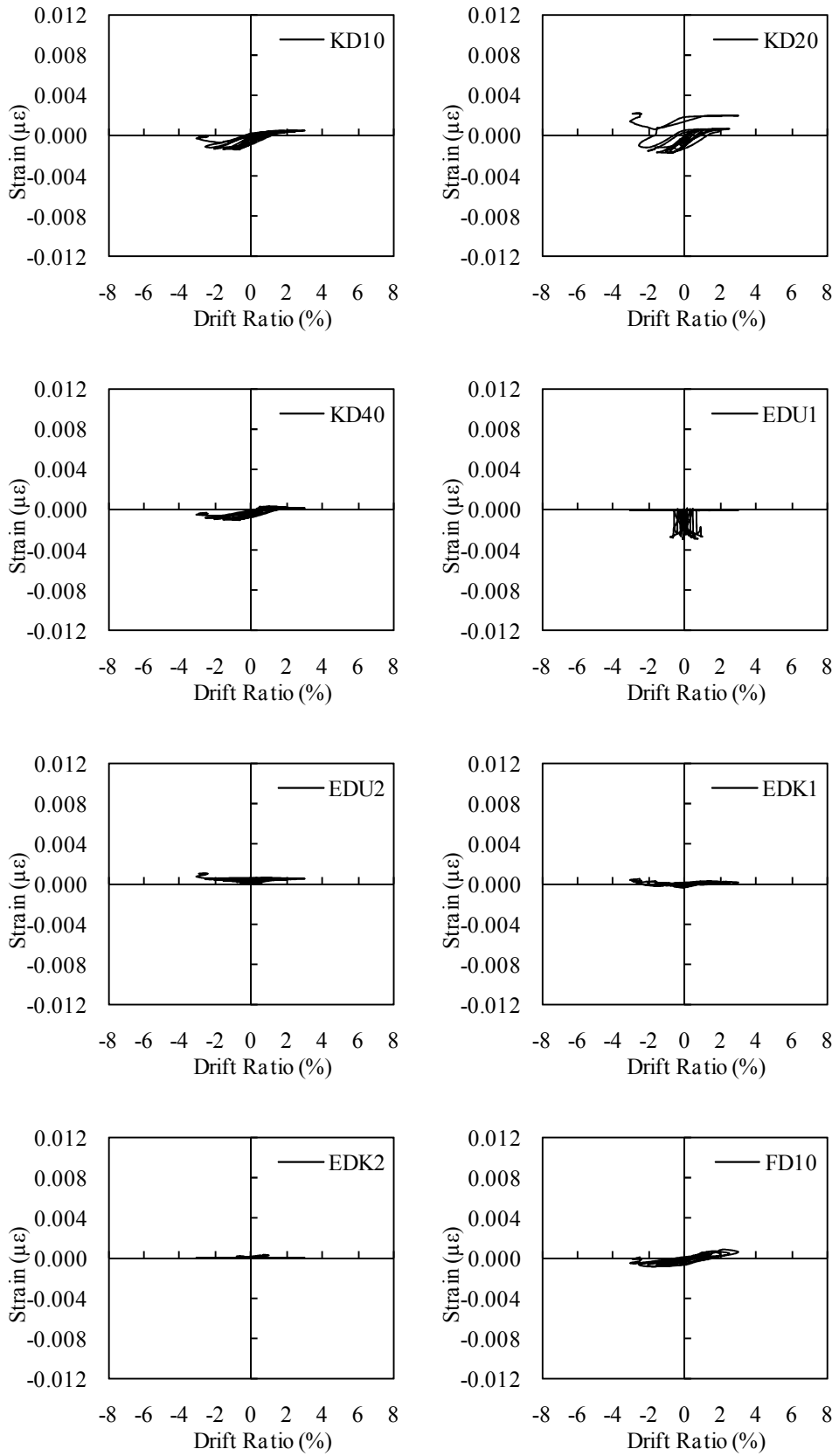


Figure D.4 : LS-X12.

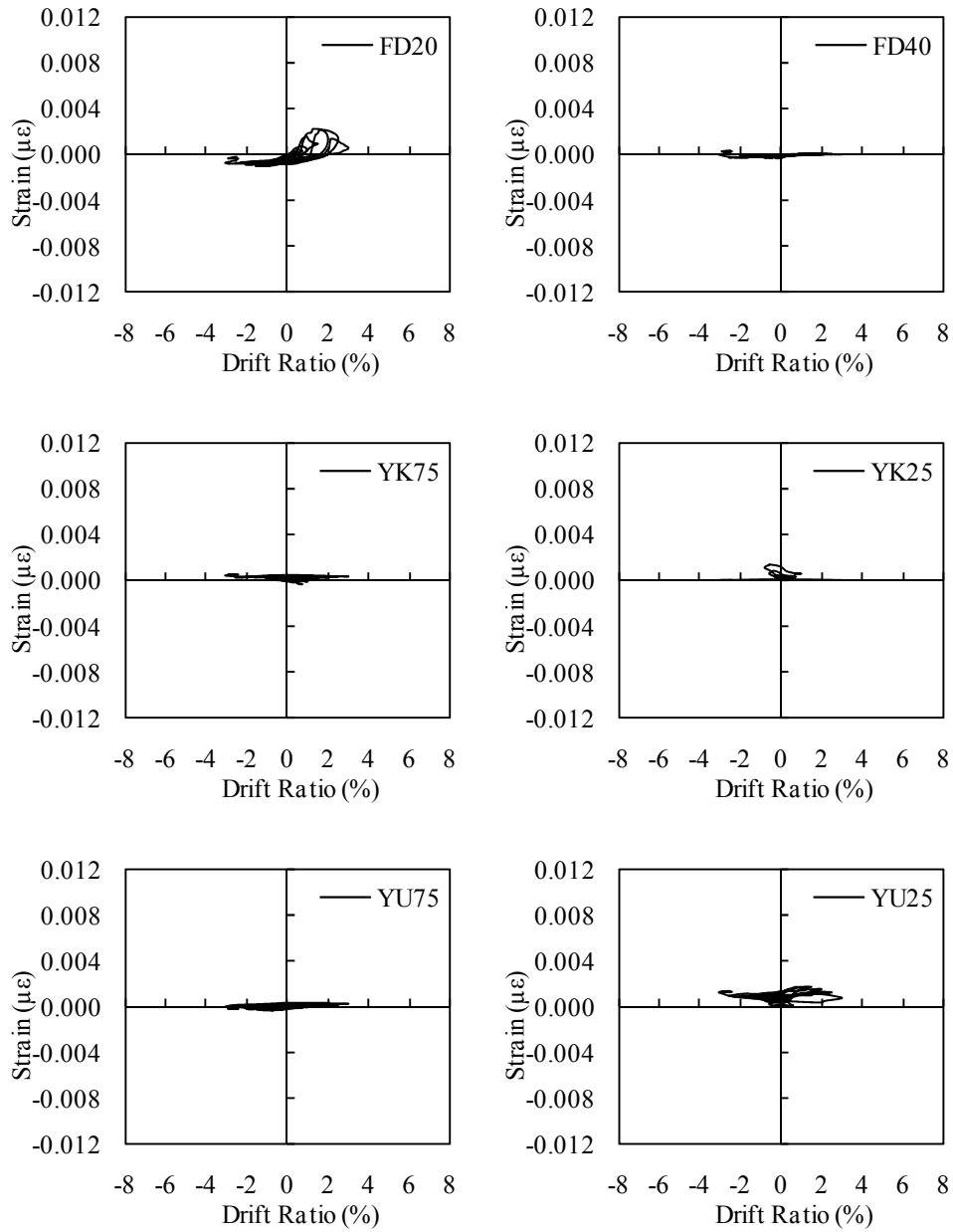


Figure D.4 (contd.) : LS-X12.

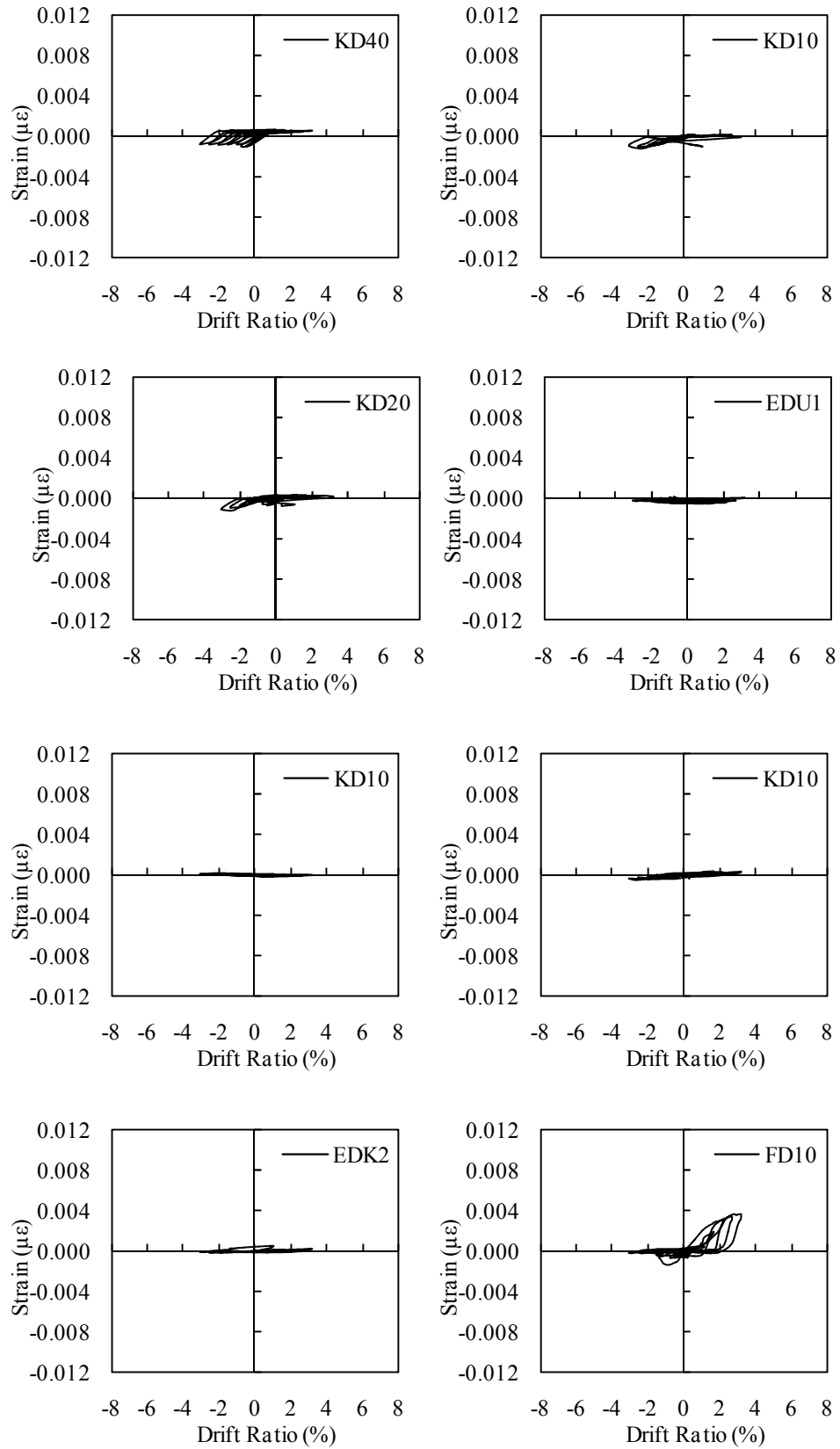


Figure D.5 : LS-X21.

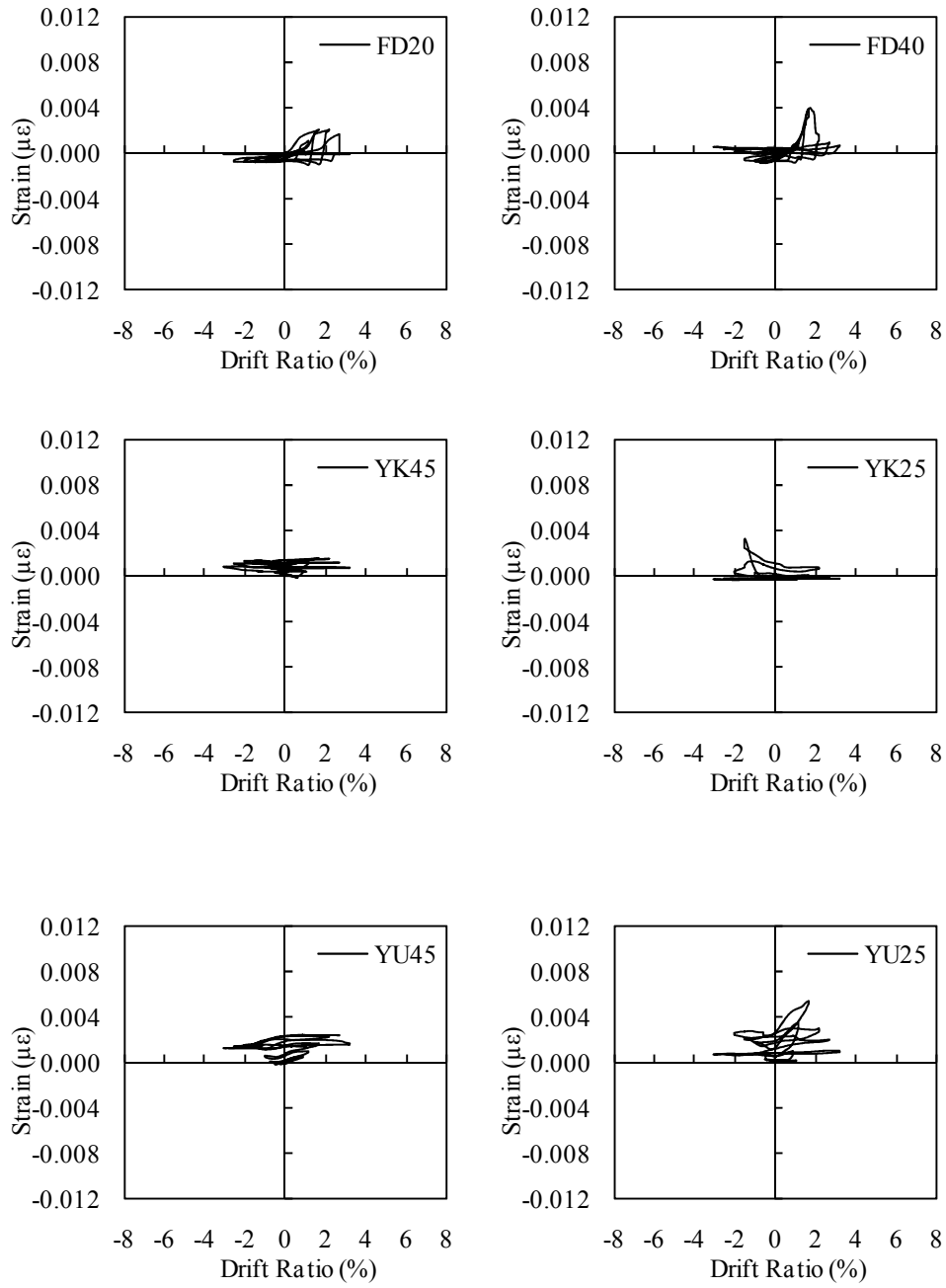


Figure D.5 (contd.) : LS-X21.

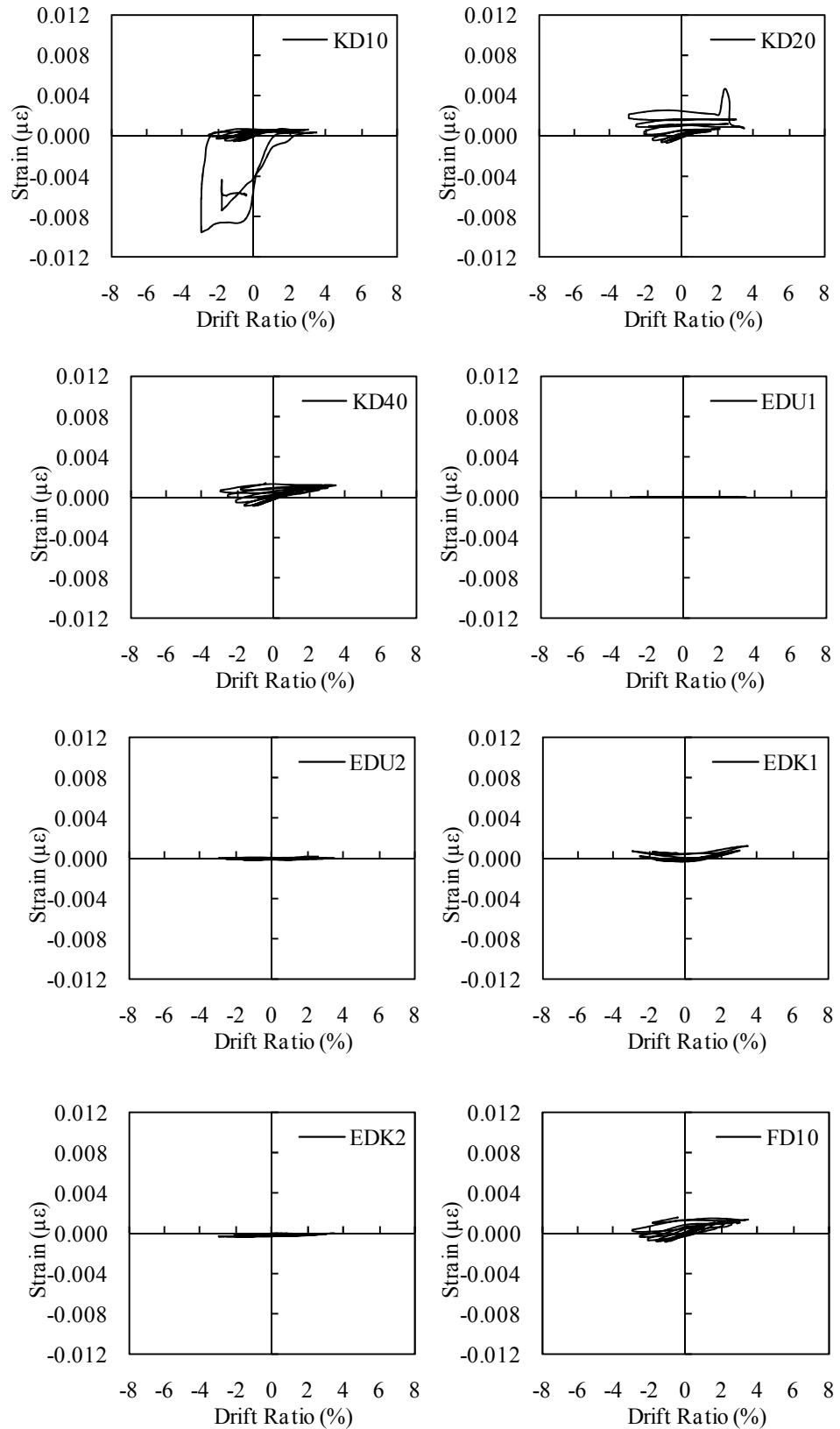


Figure D.6: LS-X28.

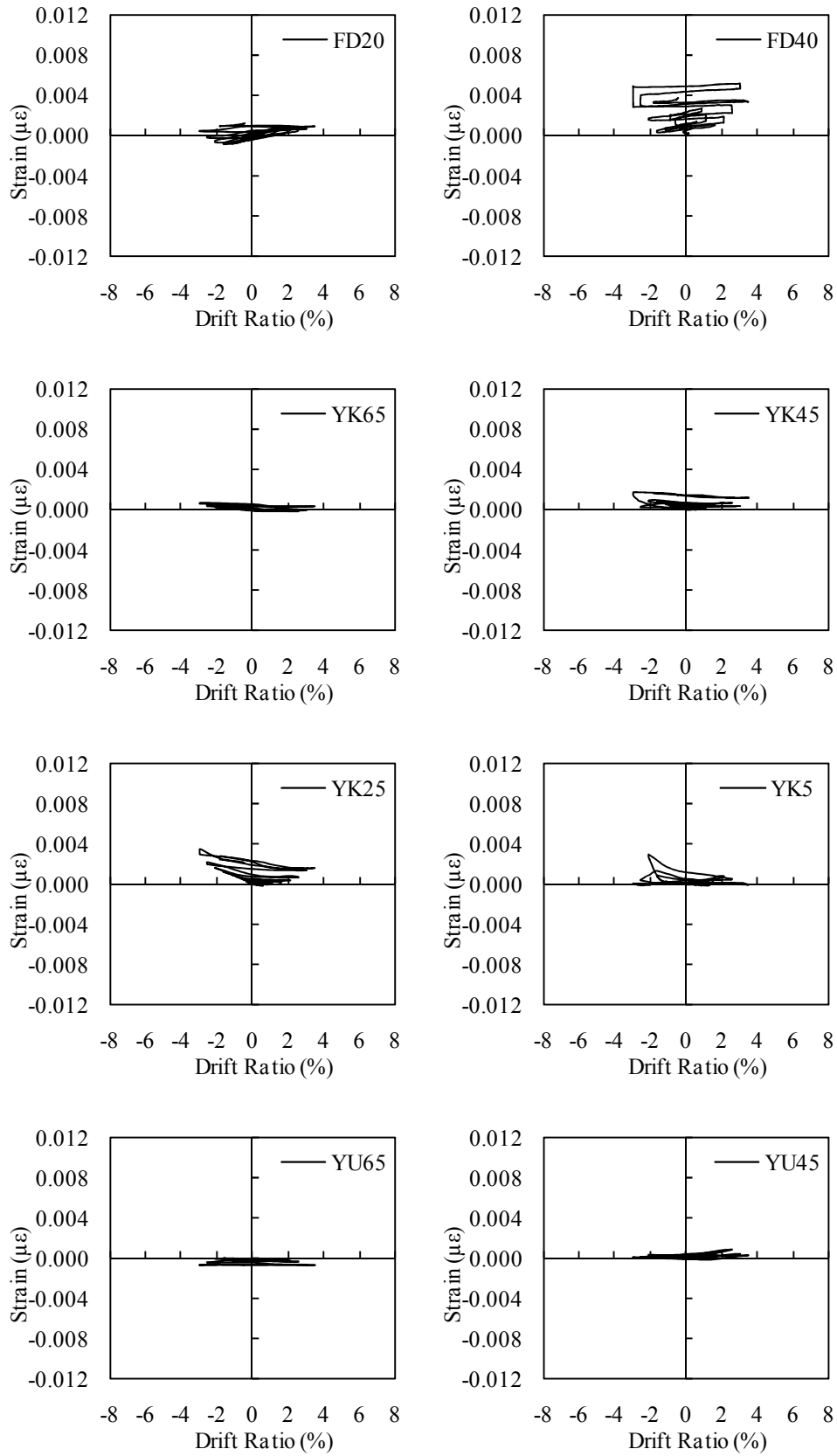


Figure D.6 (contd.) : LS-X28.

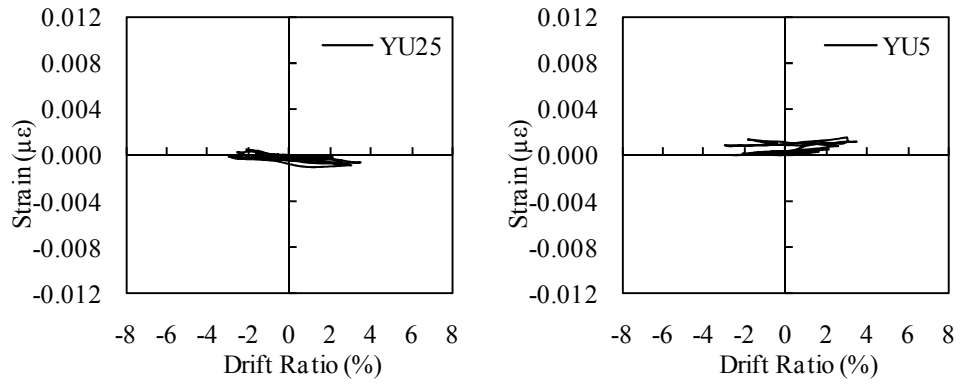


Figure D.6 (contd.) : LS-X28.

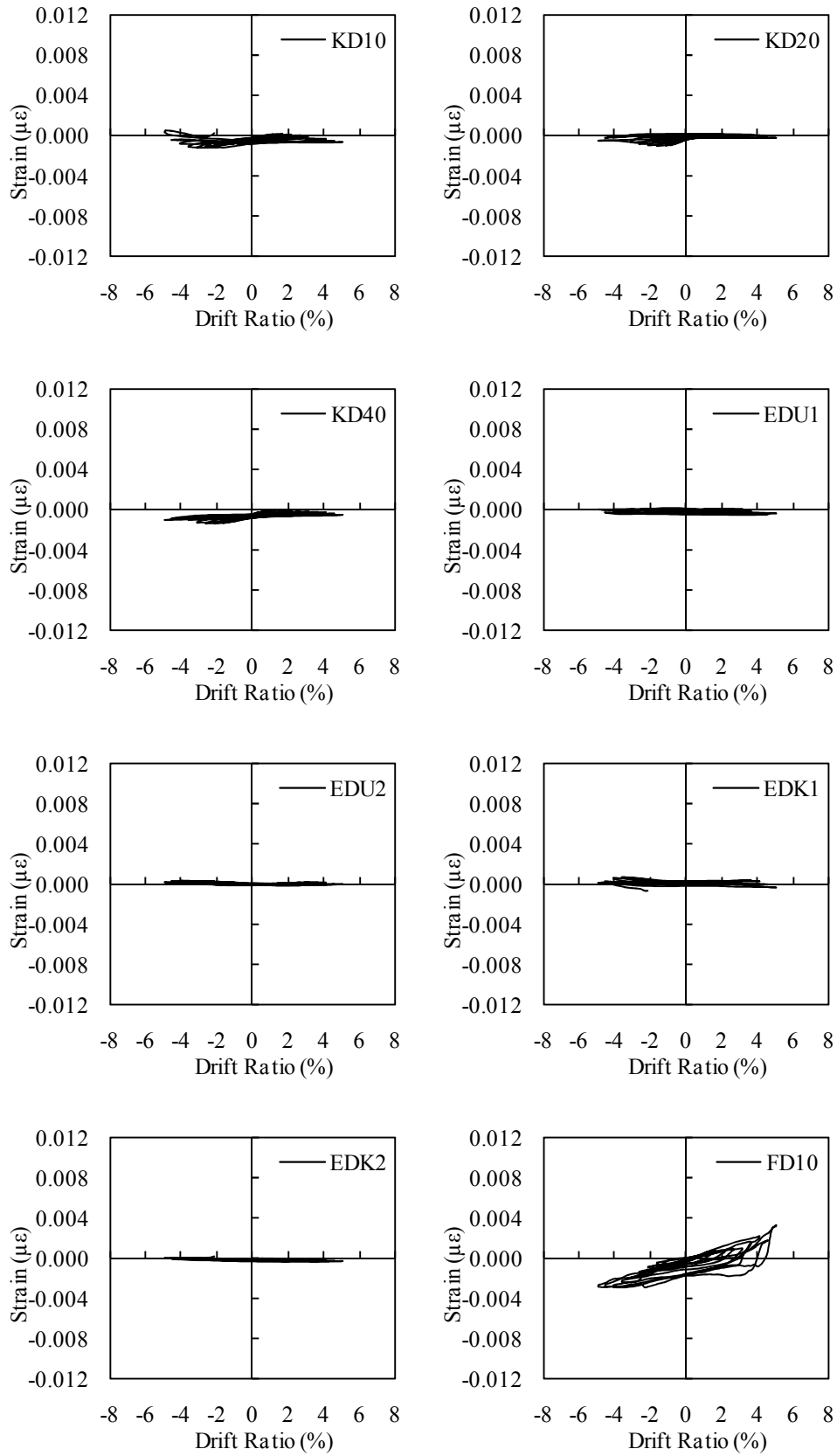


Figure D.7 : LS-X19-H.

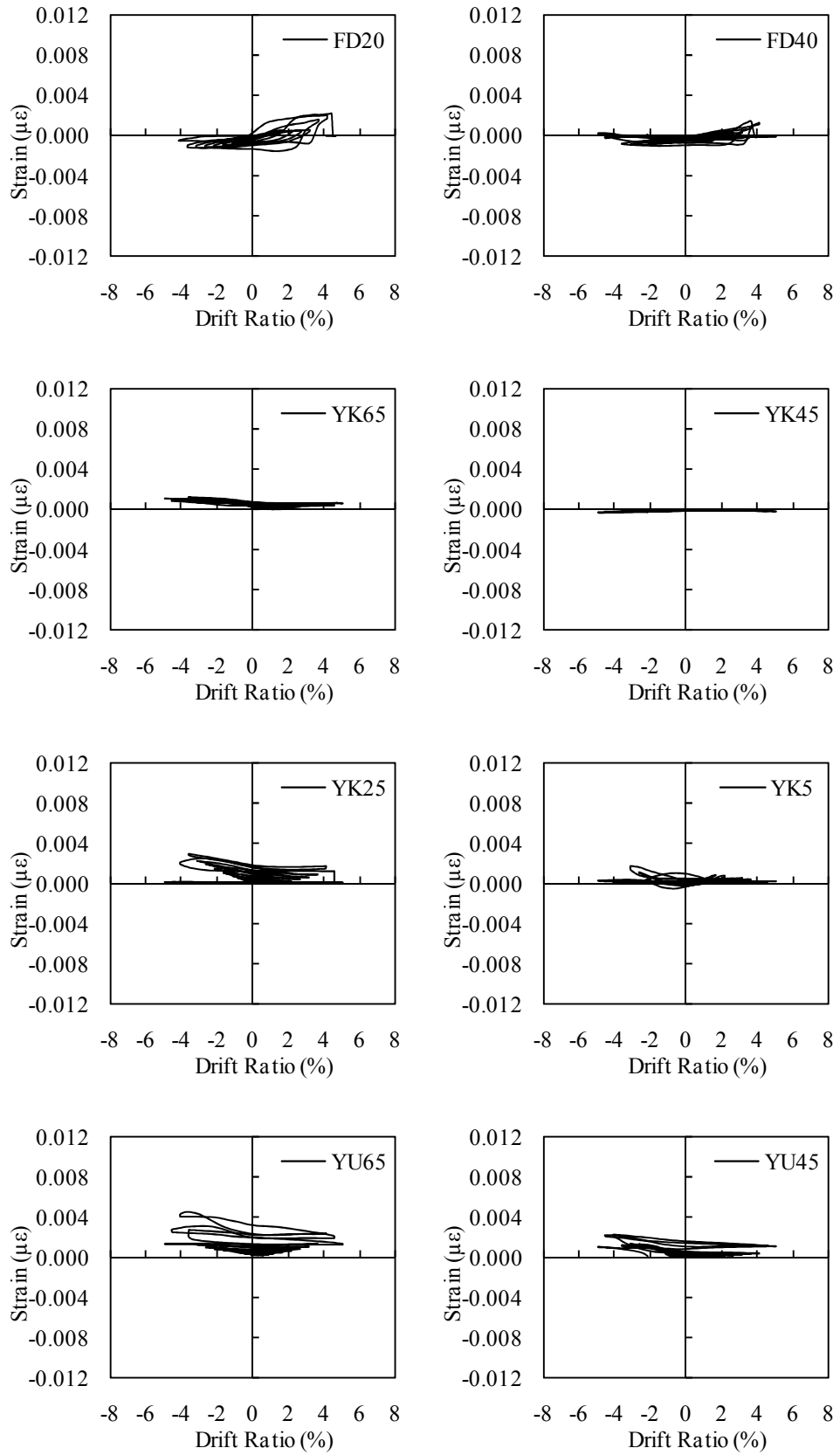


Figure D.7 (contd.) : LS-X19-H.

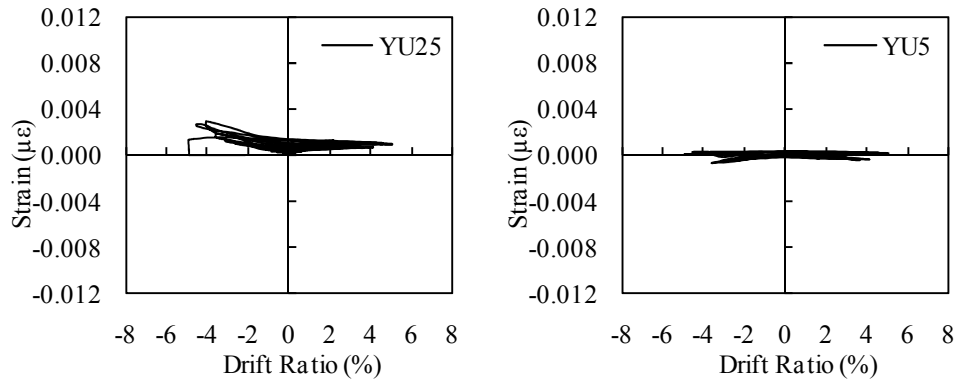


Figure D.7 (contd.) : LS-X19-H.

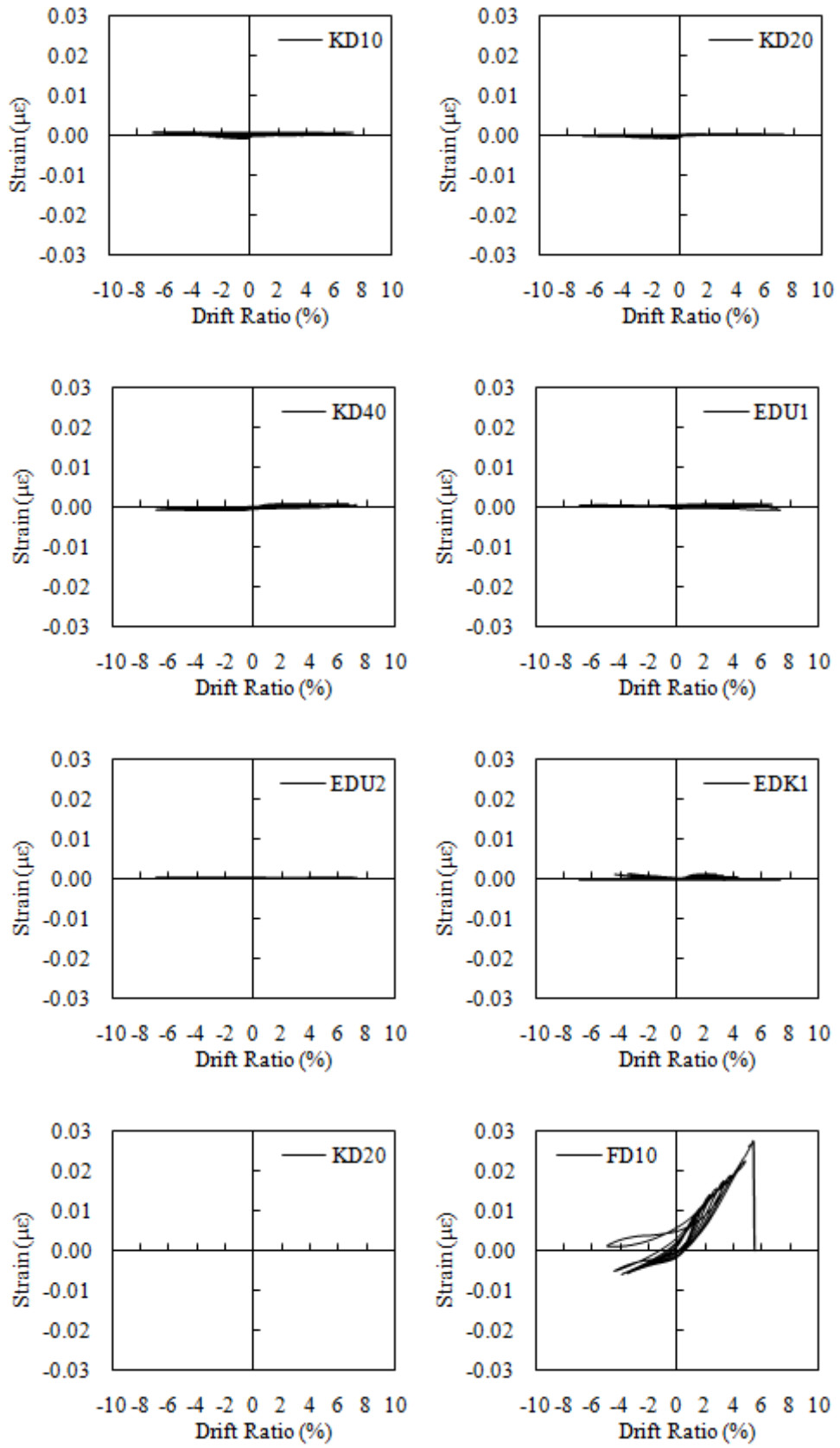


Figure D.8 : NS-X0.

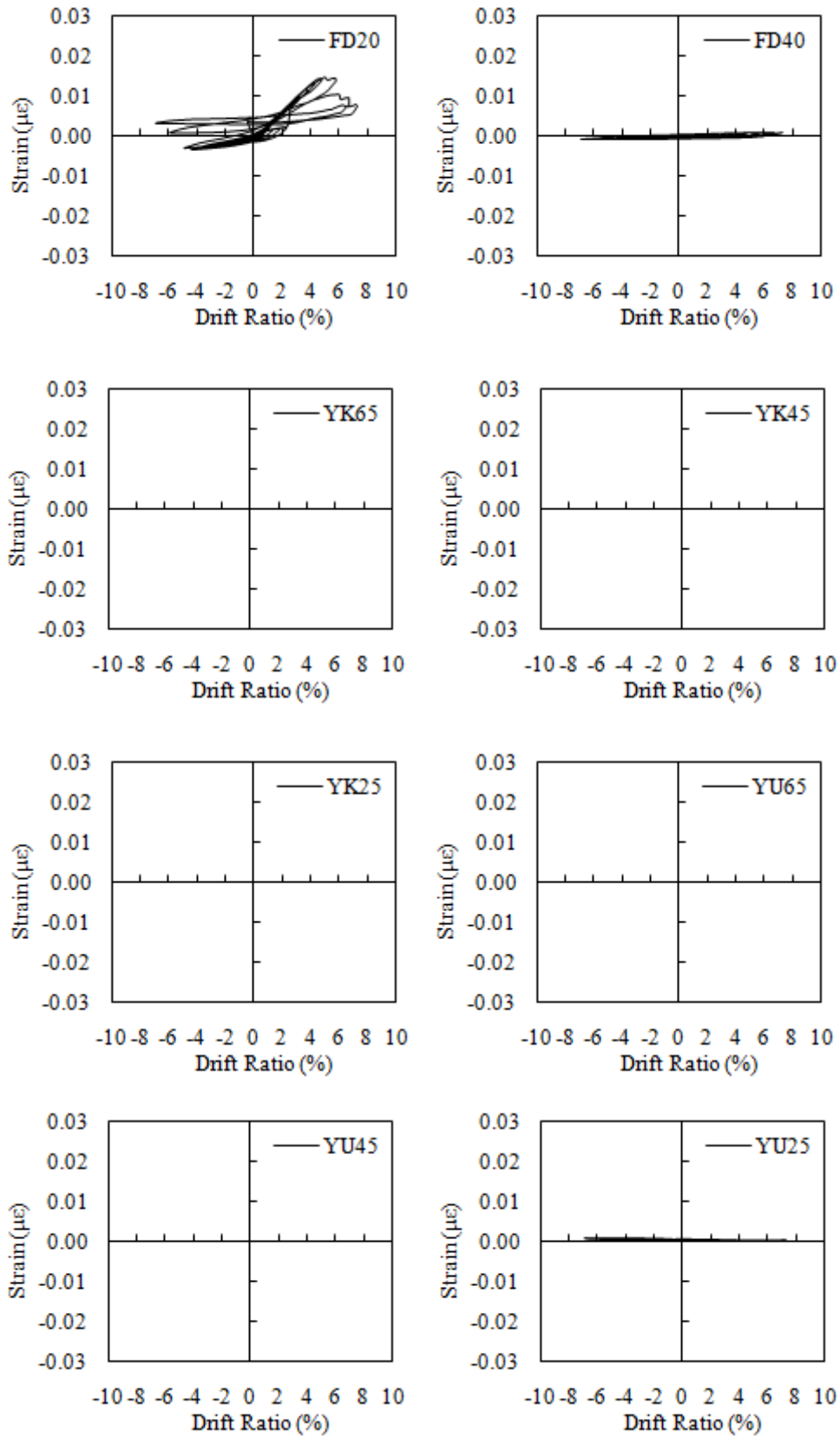


Figure D.8 (contd.) : NS-X0.

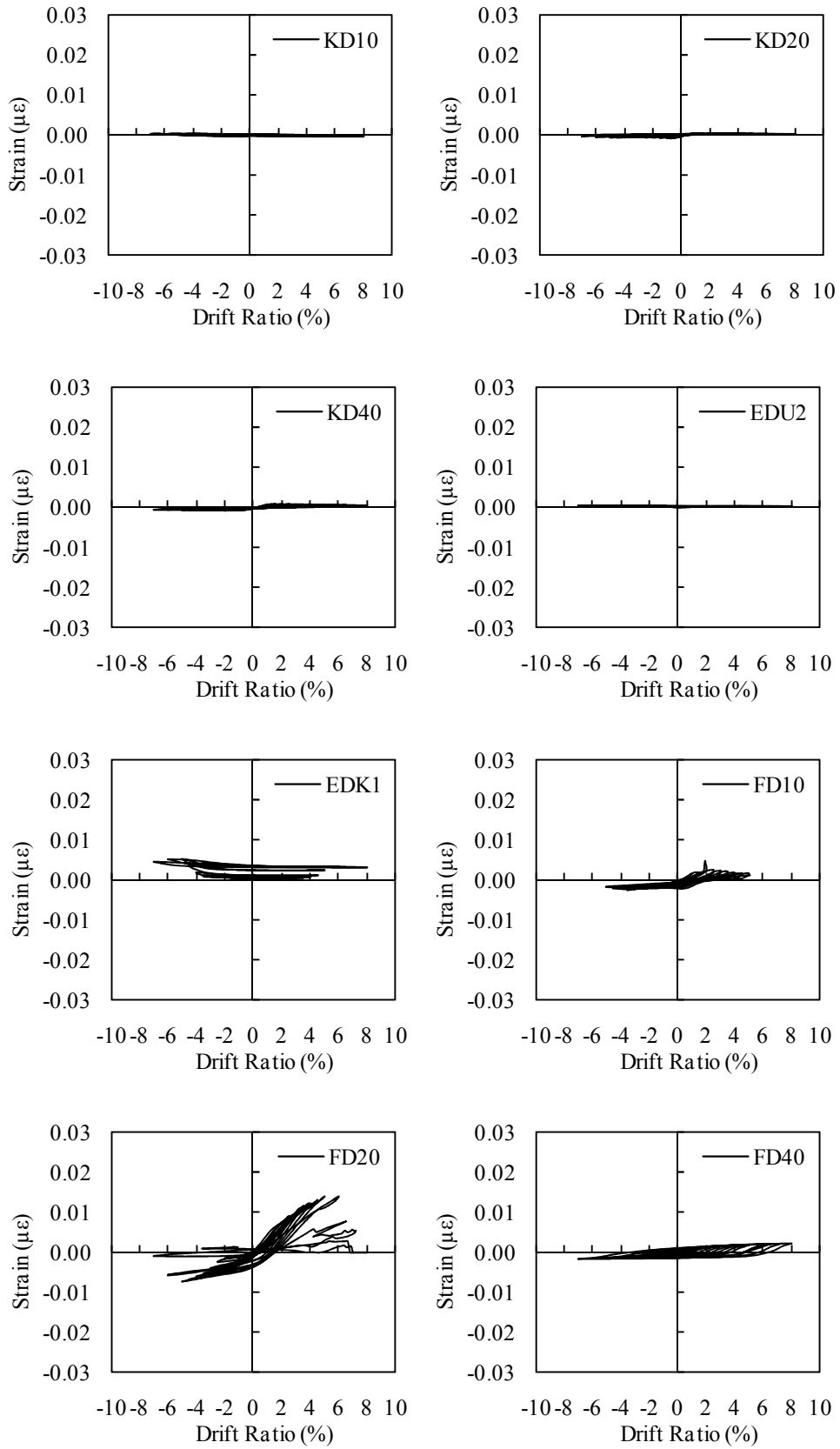


Figure D.9: NS-X9.

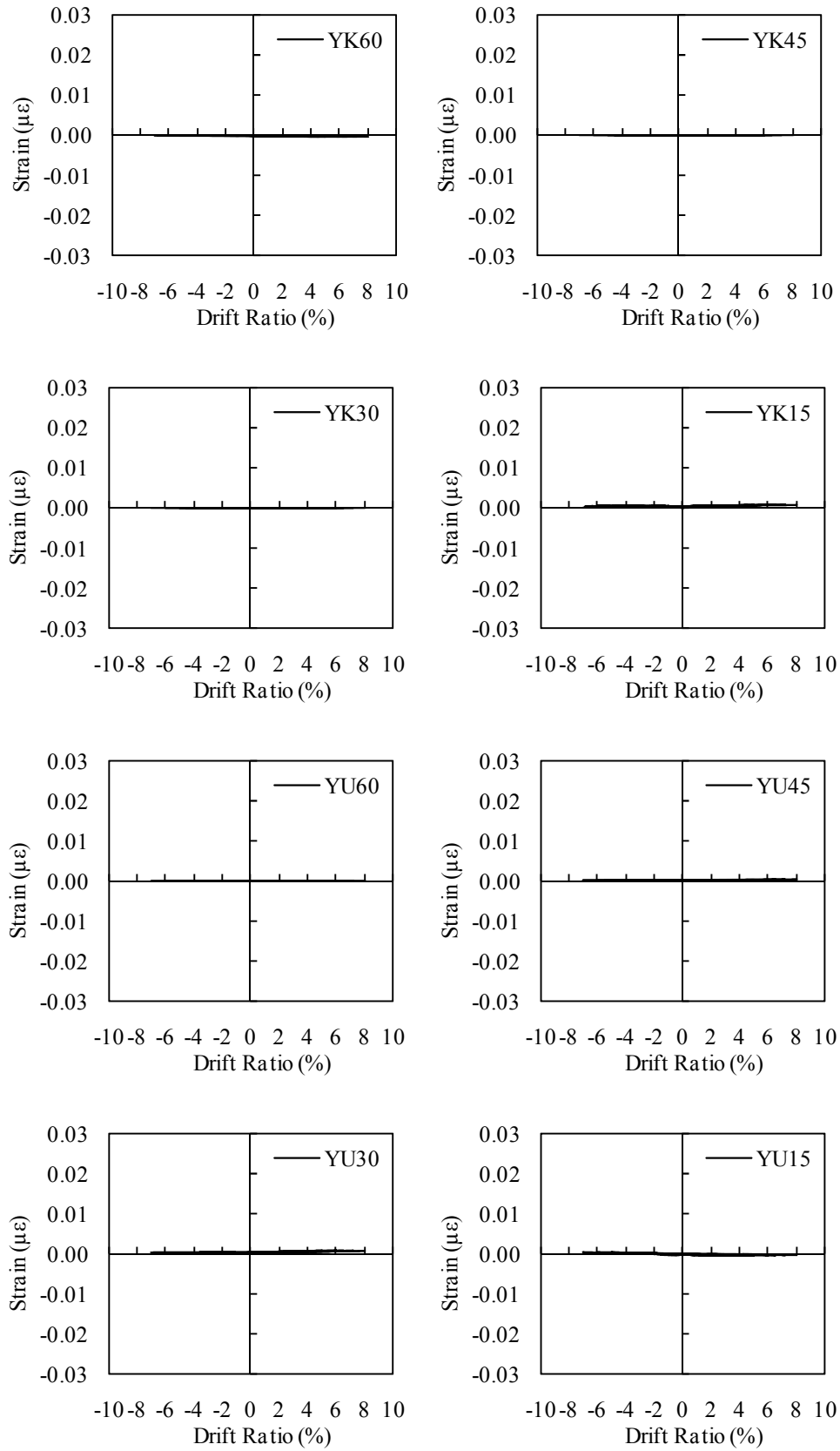


Figure D.9 (contd.) : NS-X9.

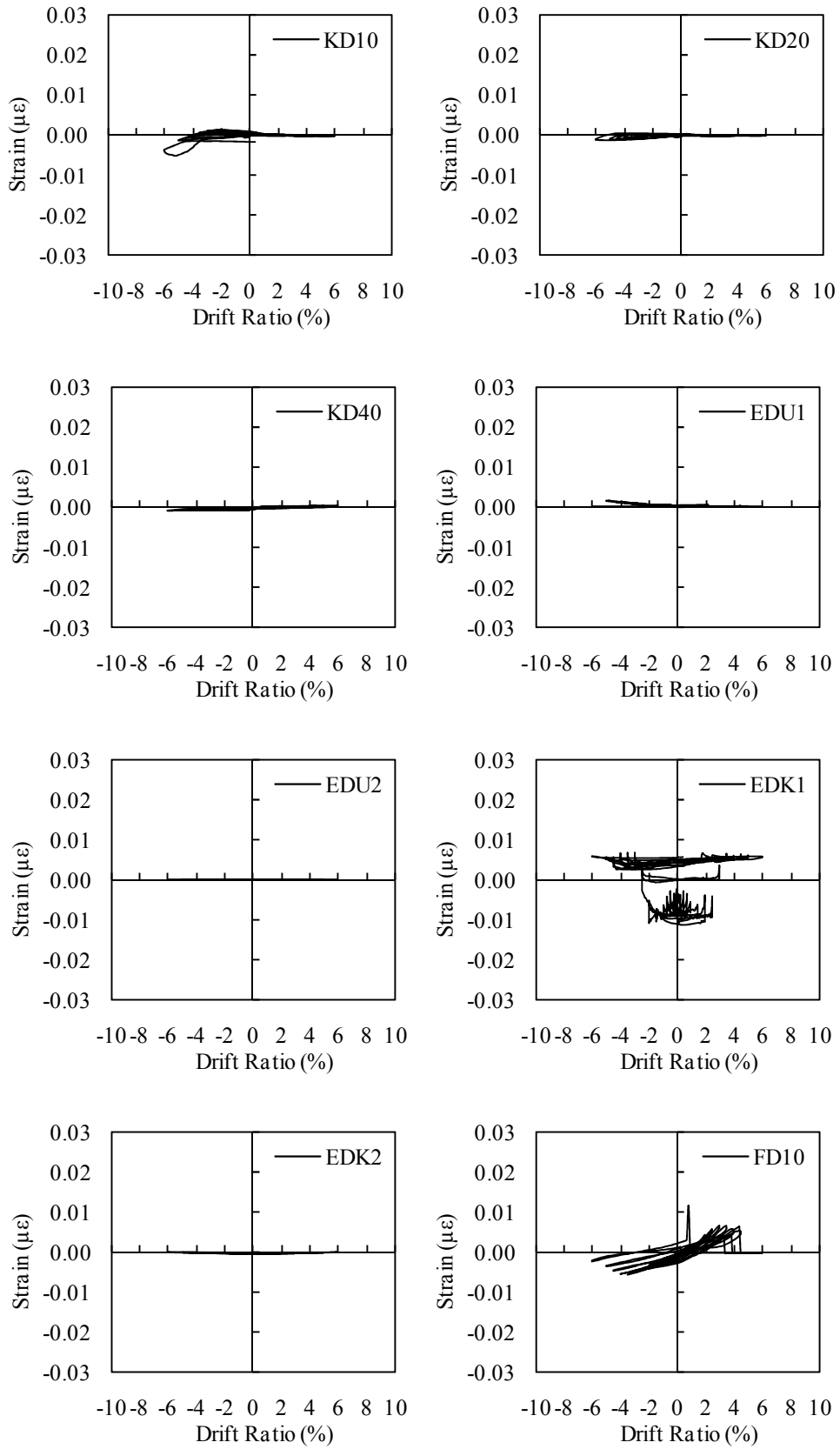


Figure D.10 : NS-X13.

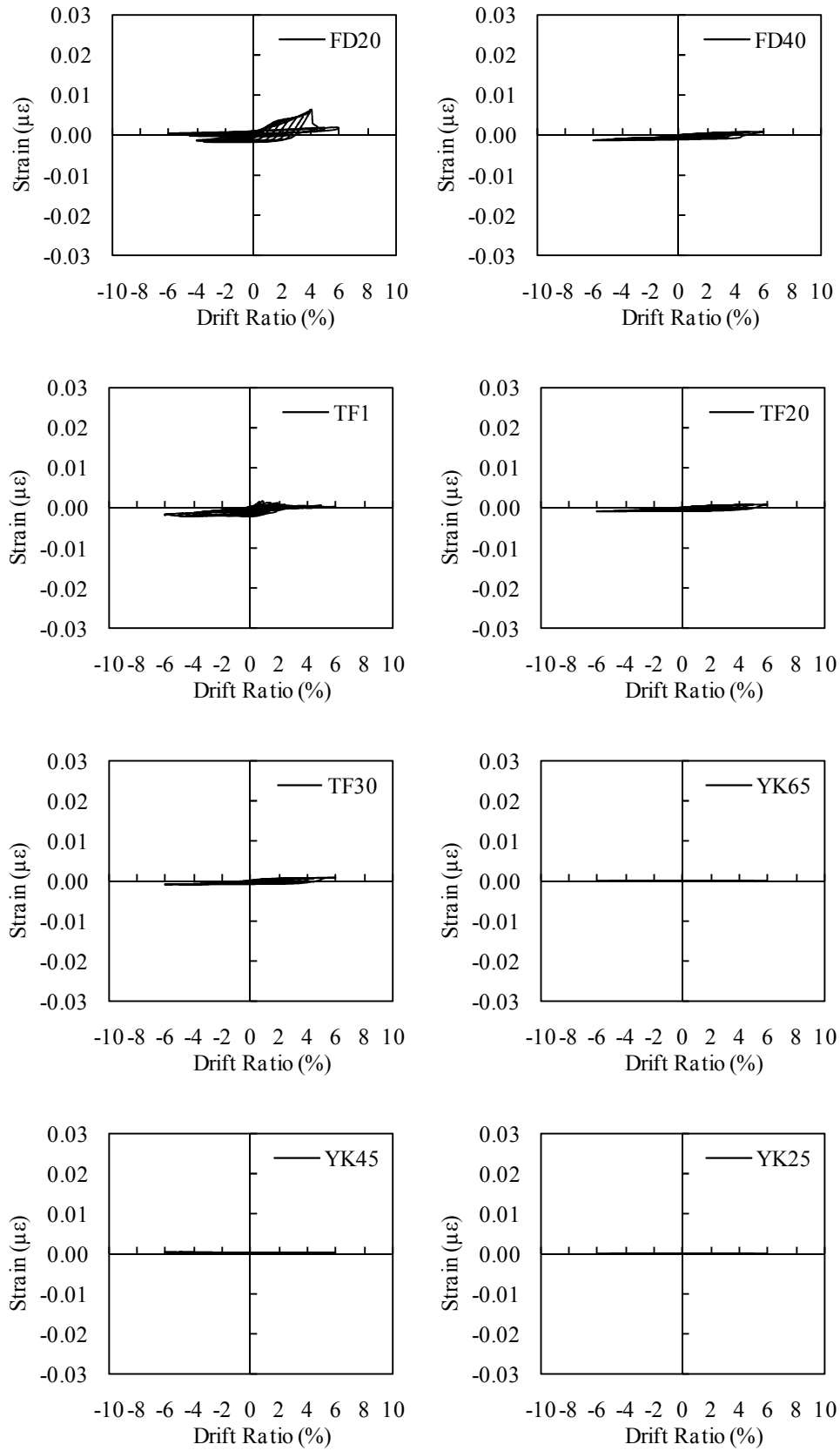


Figure D.10 (contd.) : NS-X13.

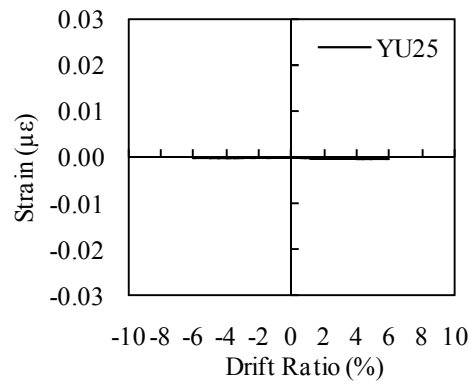
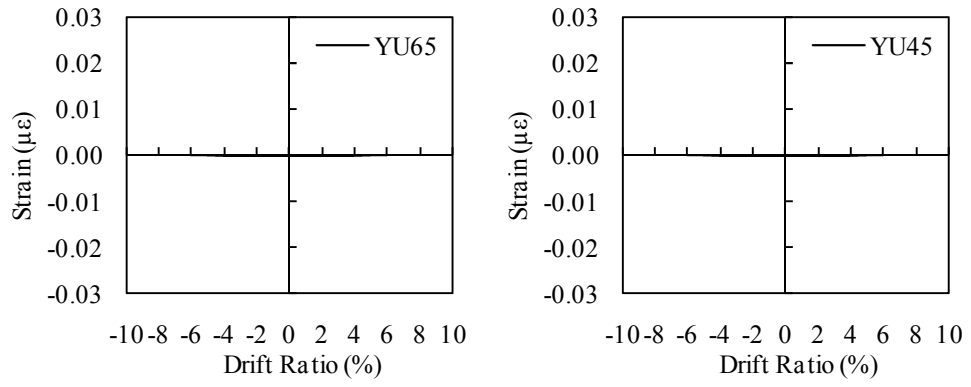


Figure D.11 (contd.) : NS-X13.

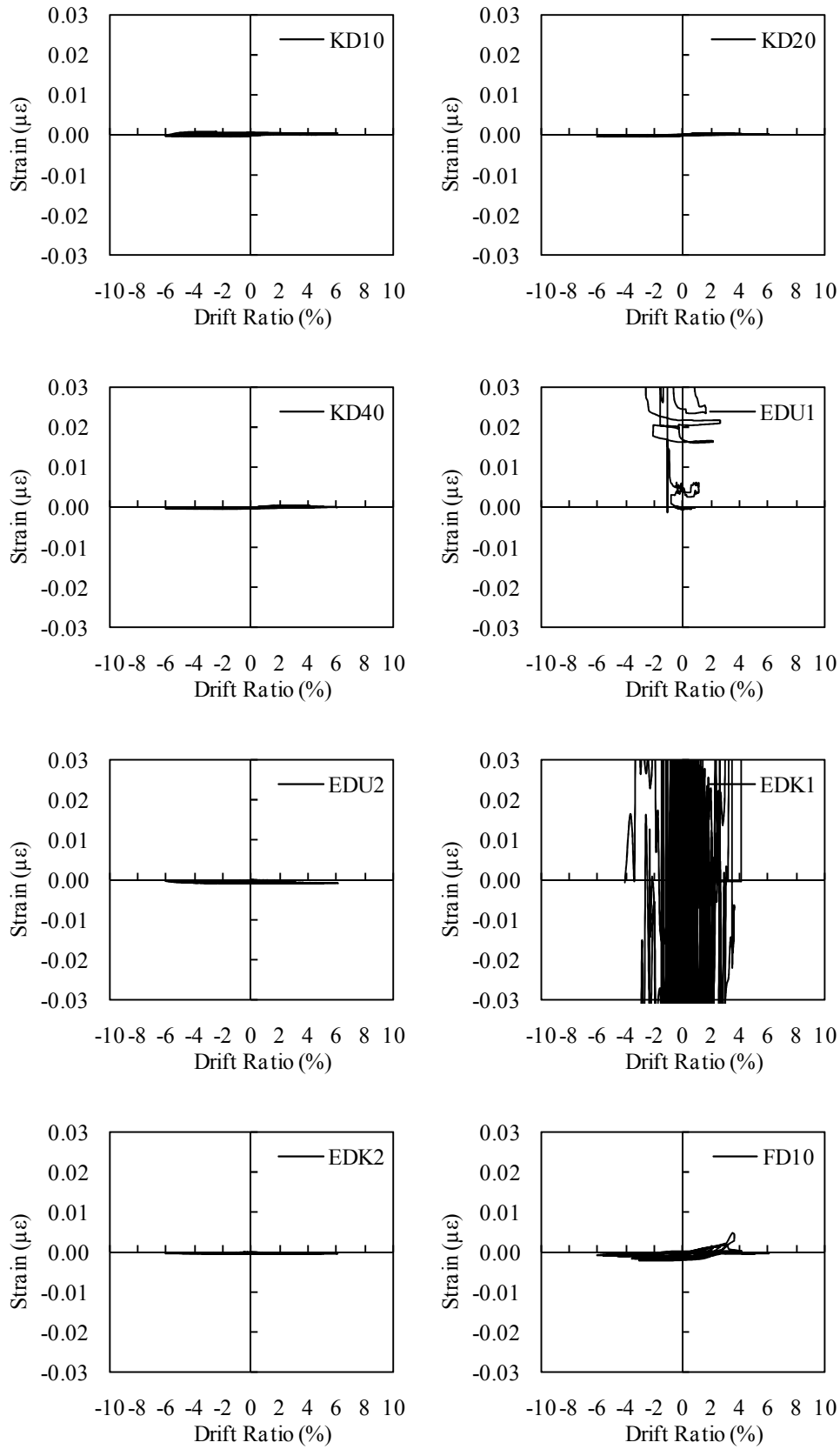


Figure D.11 : NS-X22.

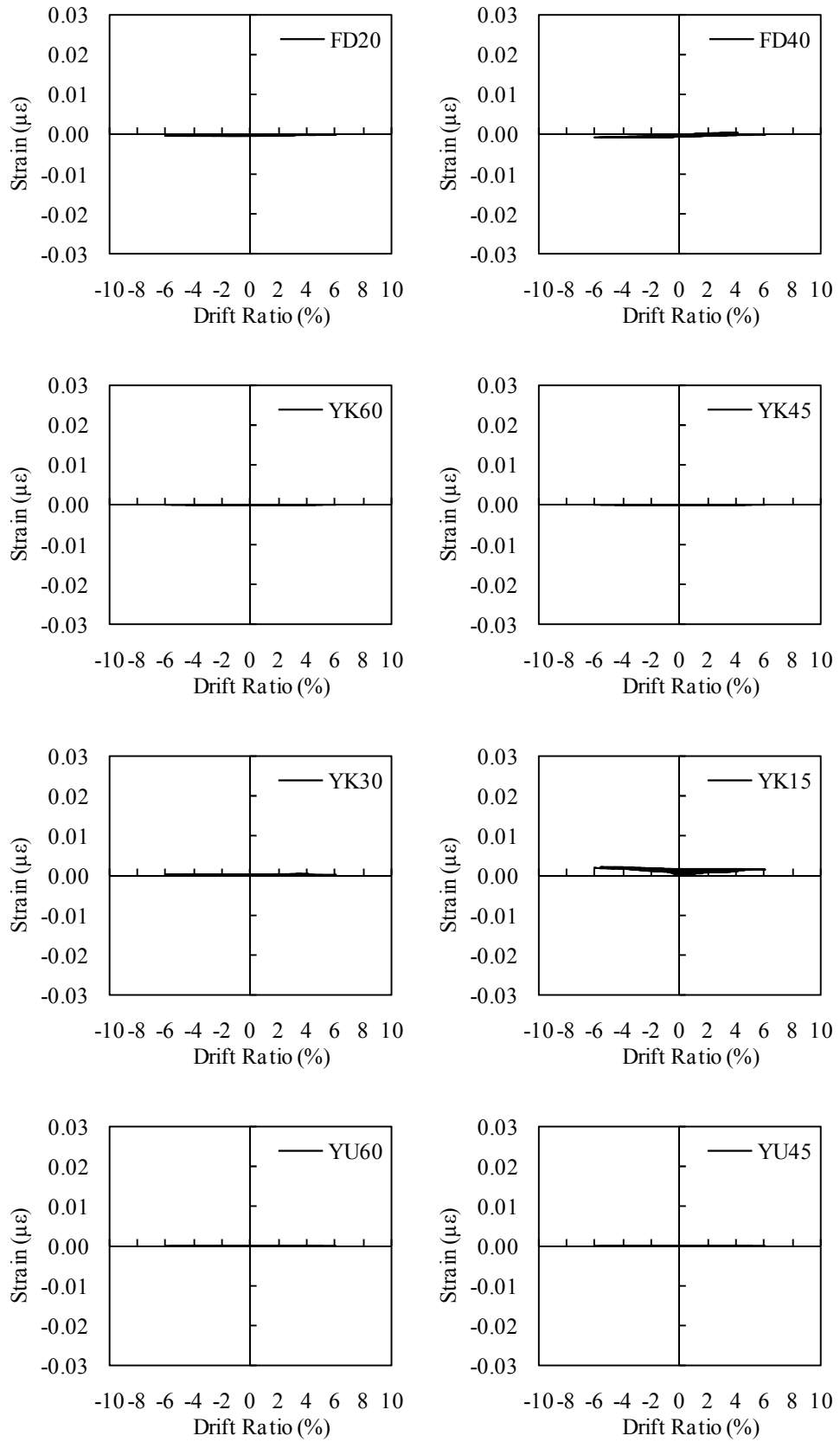


Figure D.12 (contd.) : NS-X22.

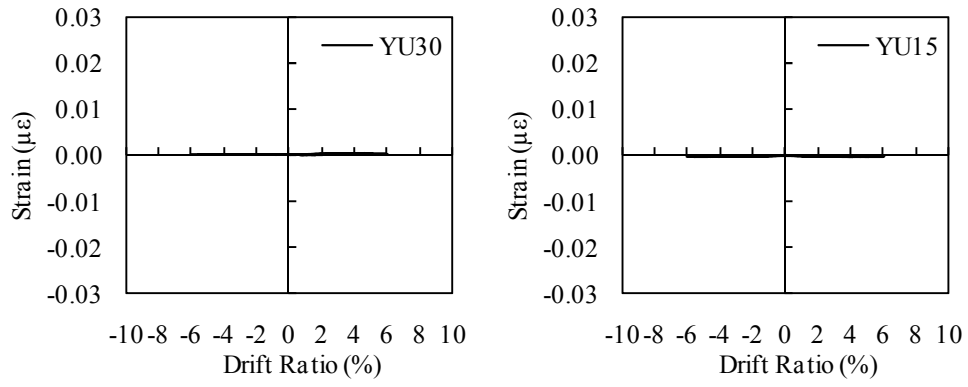


Figure D.13 (contd.) : NS-X22.

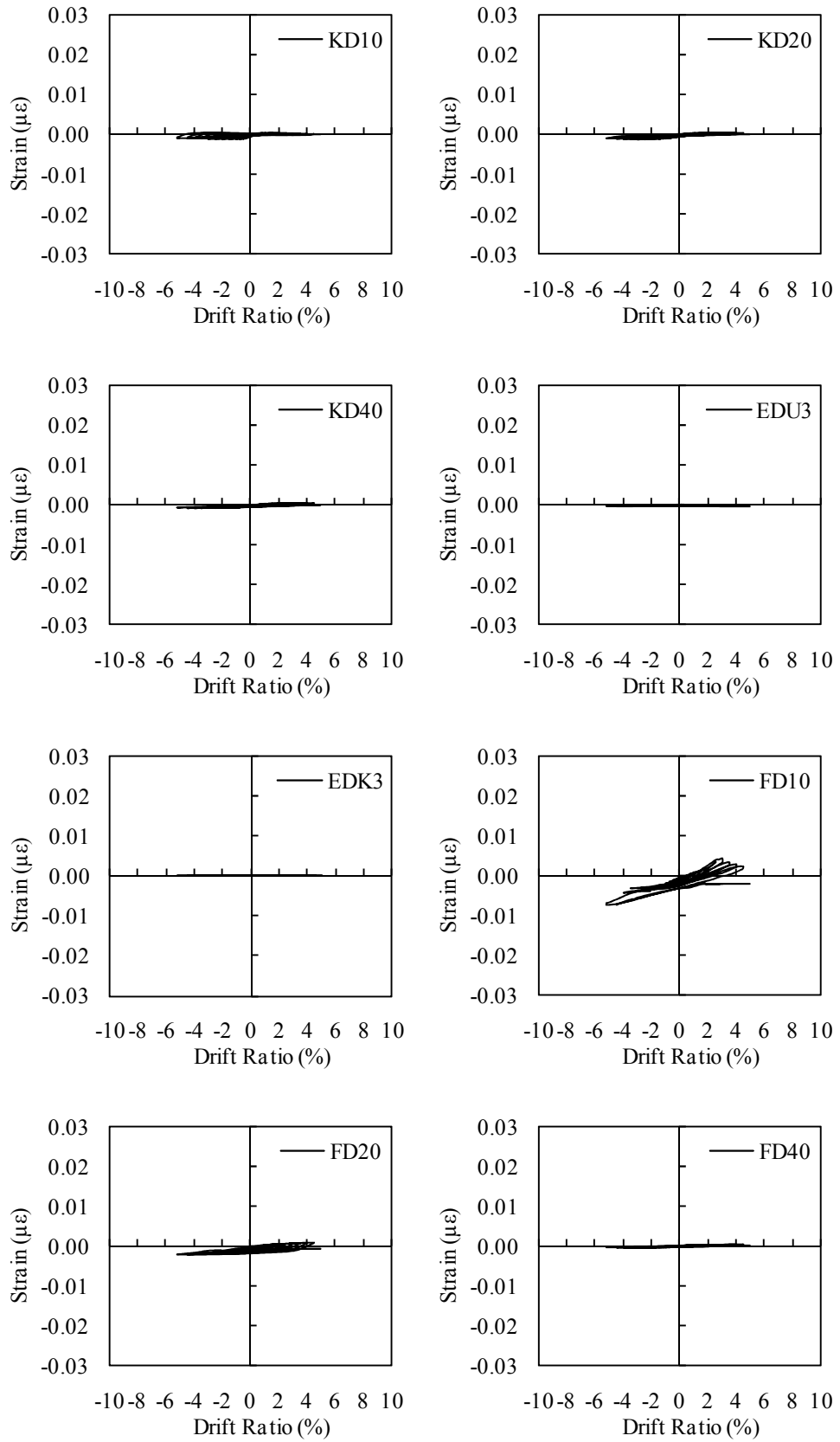


Figure D.12 : NS-X16.

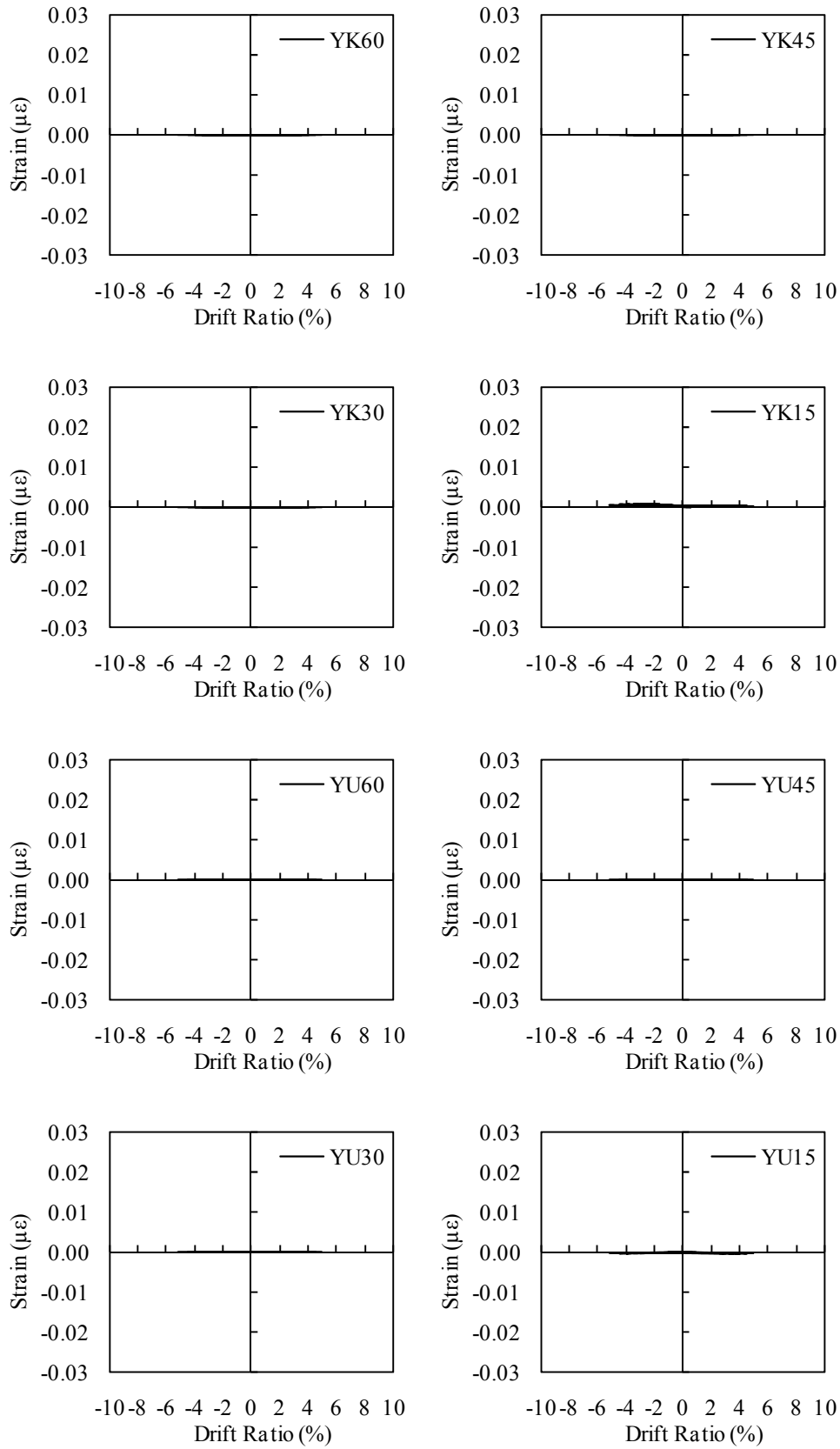


Figure D.12 (contd.) : NS-X16.

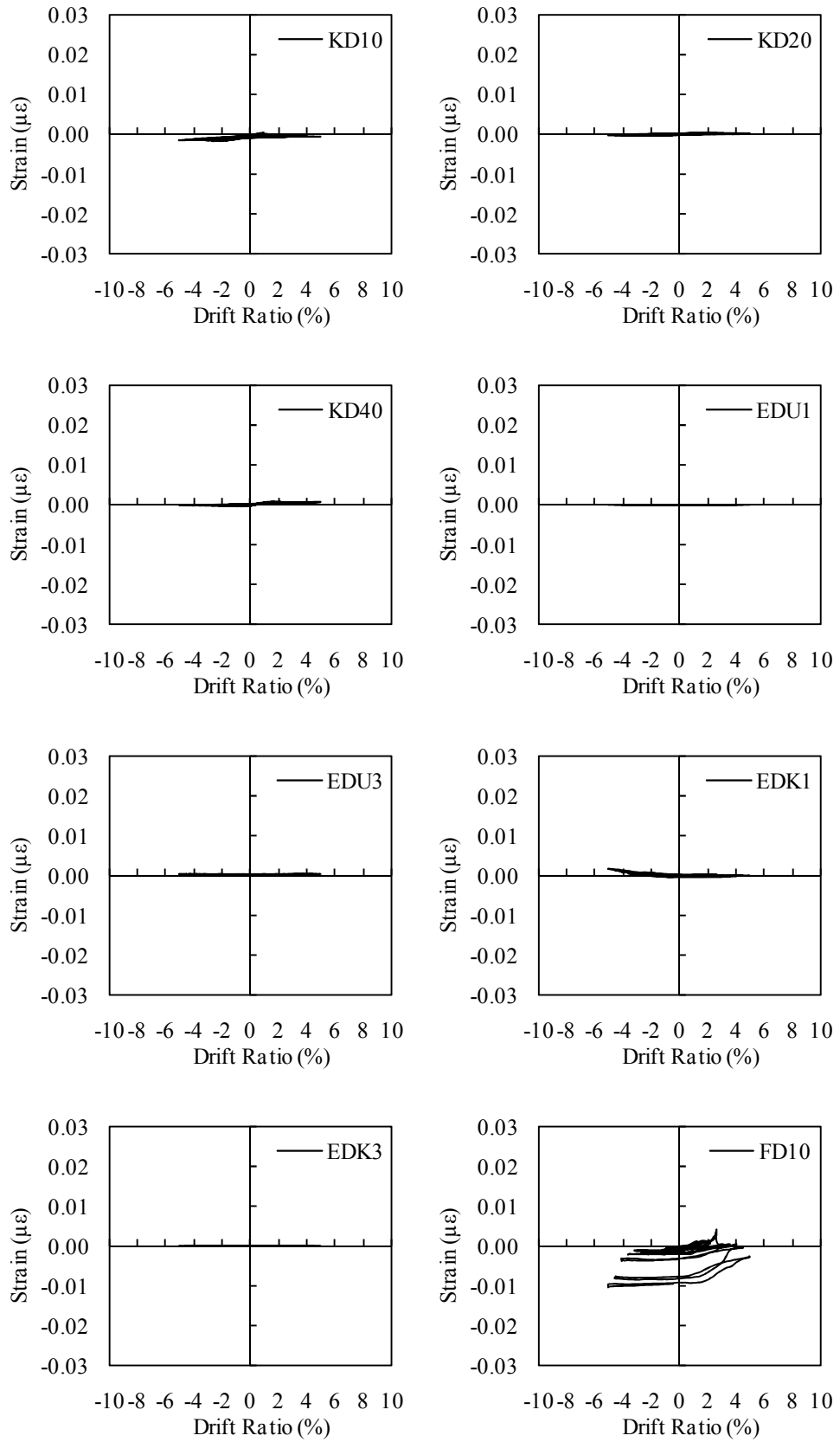


Figure D.13 : NS-X54.

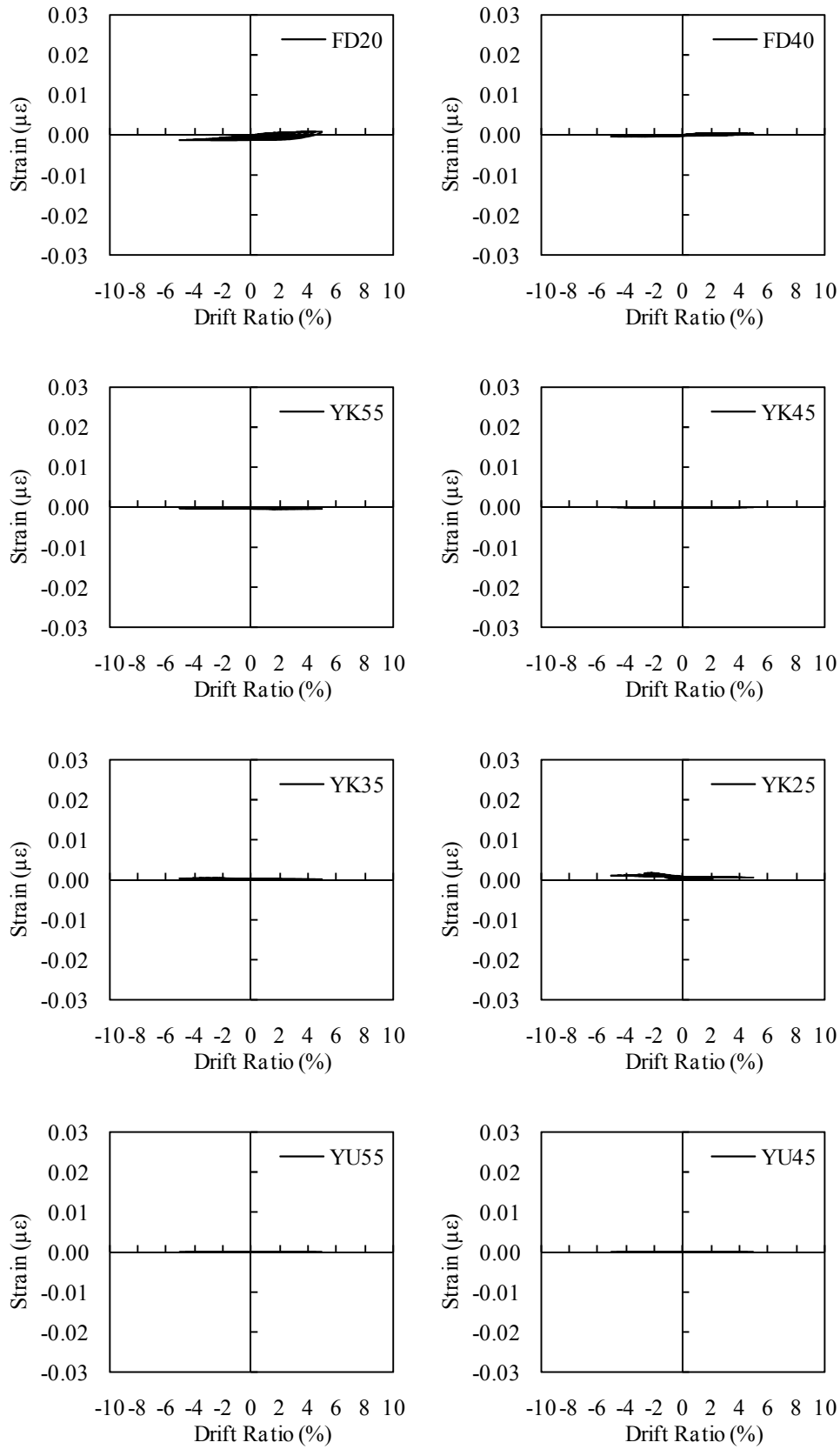


Figure D.13 (contd.) : NS-X54.

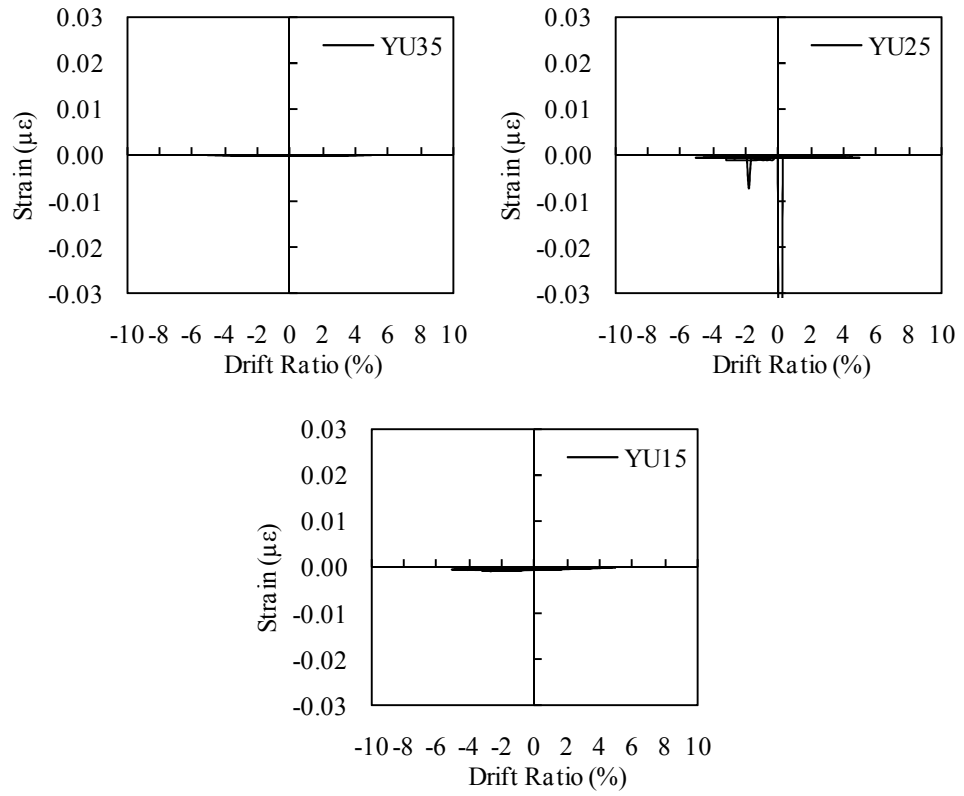


Figure D.13 (contd.) : NS-X54.

APPENDIX E

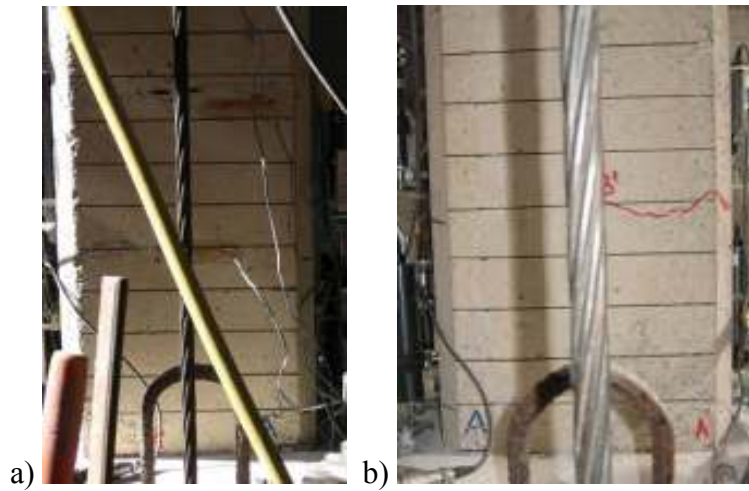


Figure E.1: a) North, and b) South view of LS-X0 after -0.5% drift ratio.

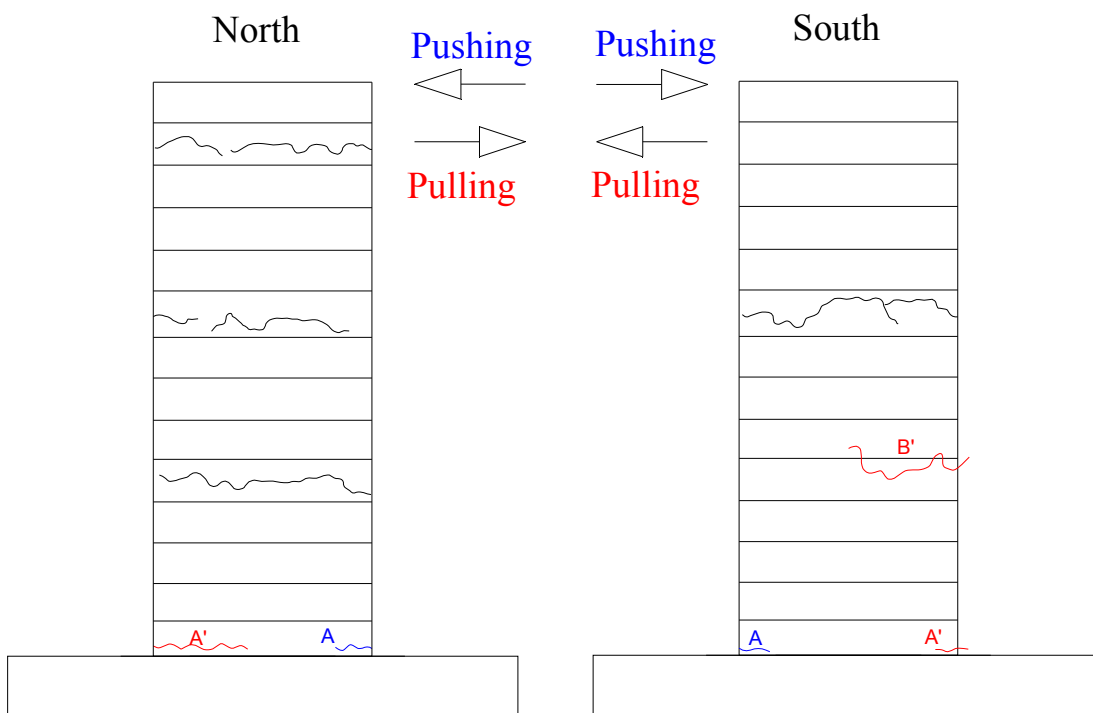


Figure E.2: Crack pattern of LS-X0 after -0.5% drift ratio.

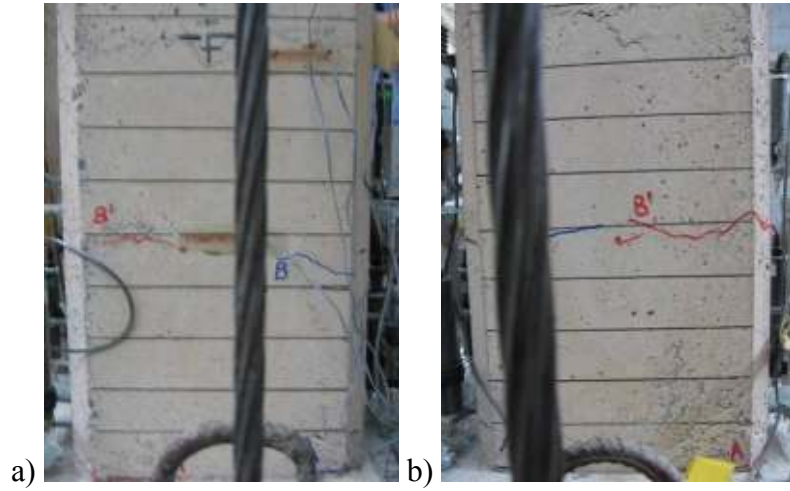


Figure E.3: a) North, and (b) south view of LS-X0 after -0.75% drift ratio.

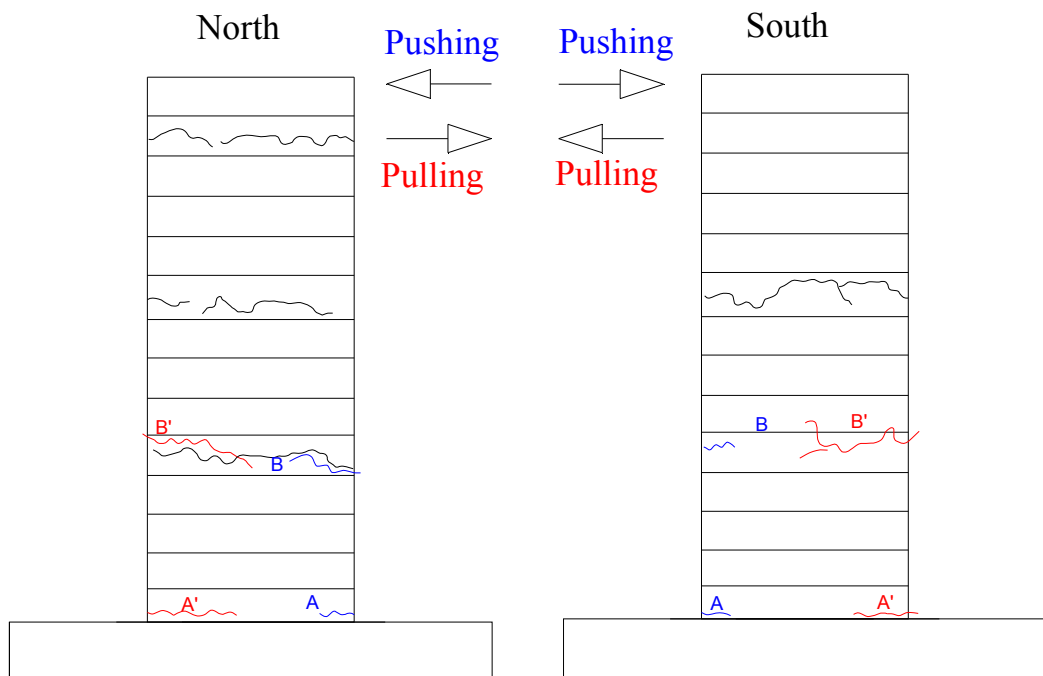


Figure E.4: Crack pattern of LS-X0 after -0.75% drift ratio.

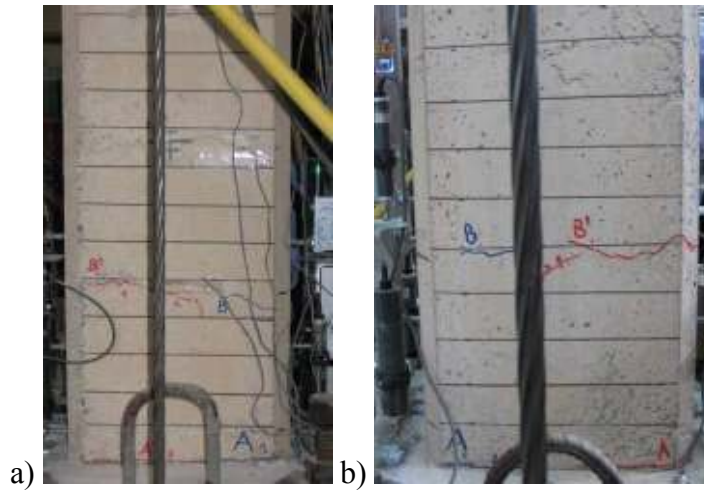


Figure E.5: a) North, and b) South view of LS-X0 after -1% drift ratio.

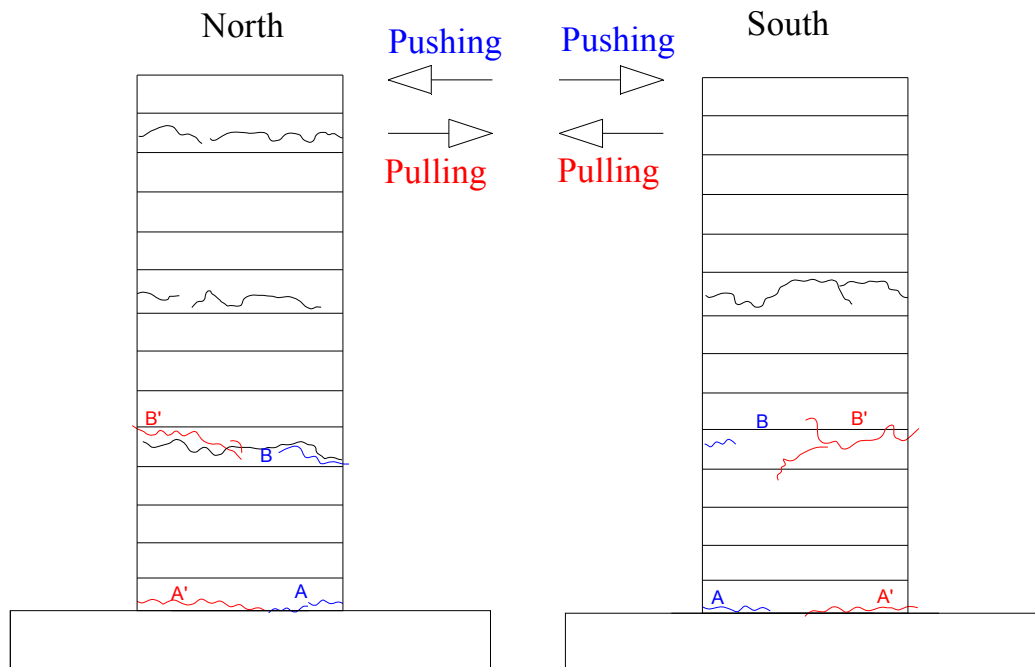


Figure E.6: Crack pattern of LS-X0 after -1% drift ratio.

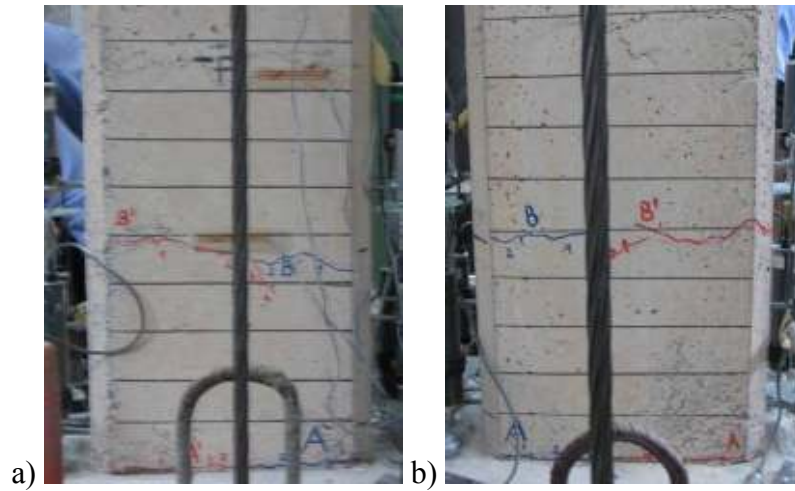


Figure E.7: a) North, and b) South view of LS-X0 after -1.5% drift ratio.

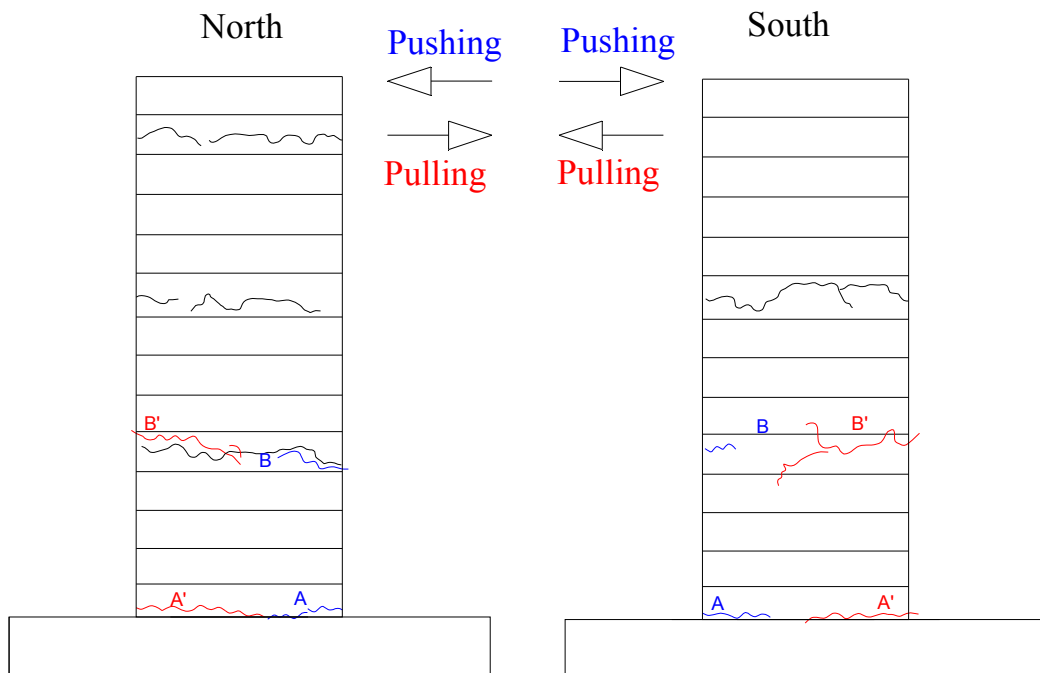


Figure E.8: Crack pattern of LS-X0 after -1.5% drift ratio.

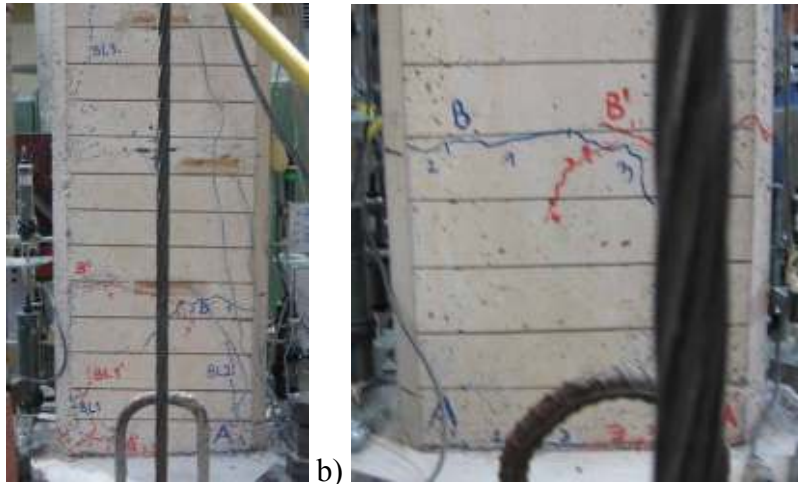


Figure E.9: a) North, and b) South view of specimen LS-X0 after -2% drift ratio.

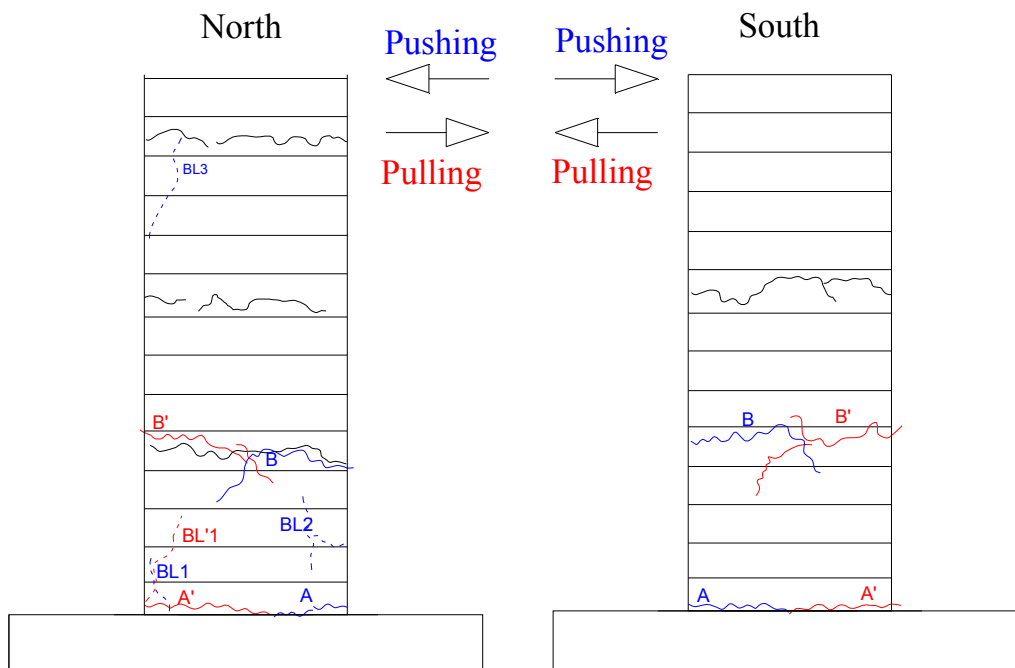


Figure E.10: Crack pattern of LS-X0 after -2% drift ratio.

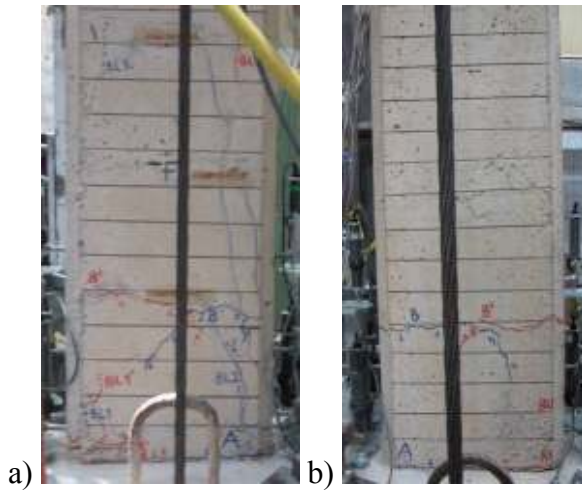


Figure E.11: a) North, and b) South view of LS-X0 after -2.5% drift ratio.

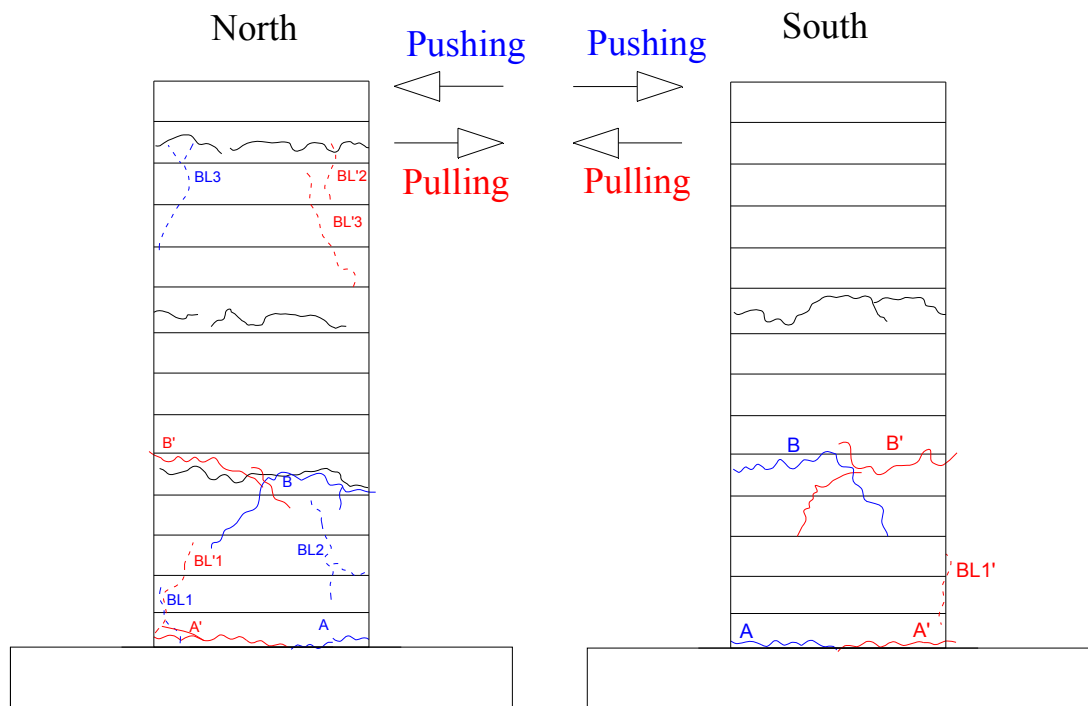


Figure E.12: Crack pattern of LS-X0 after -2.5% drift ratio.

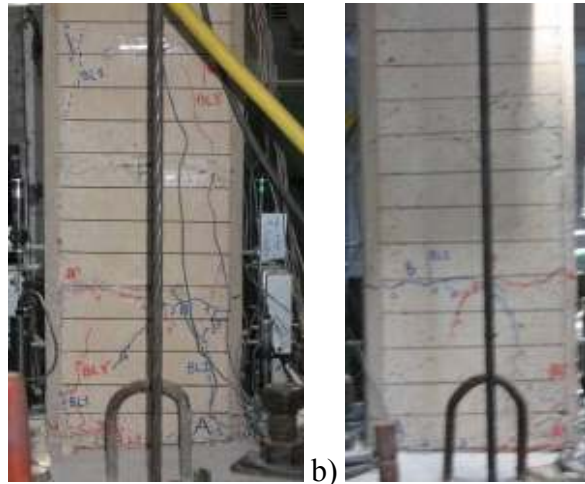


Figure E.13: a) North, and b) South view of LS-X0 after -3% drift ratio.

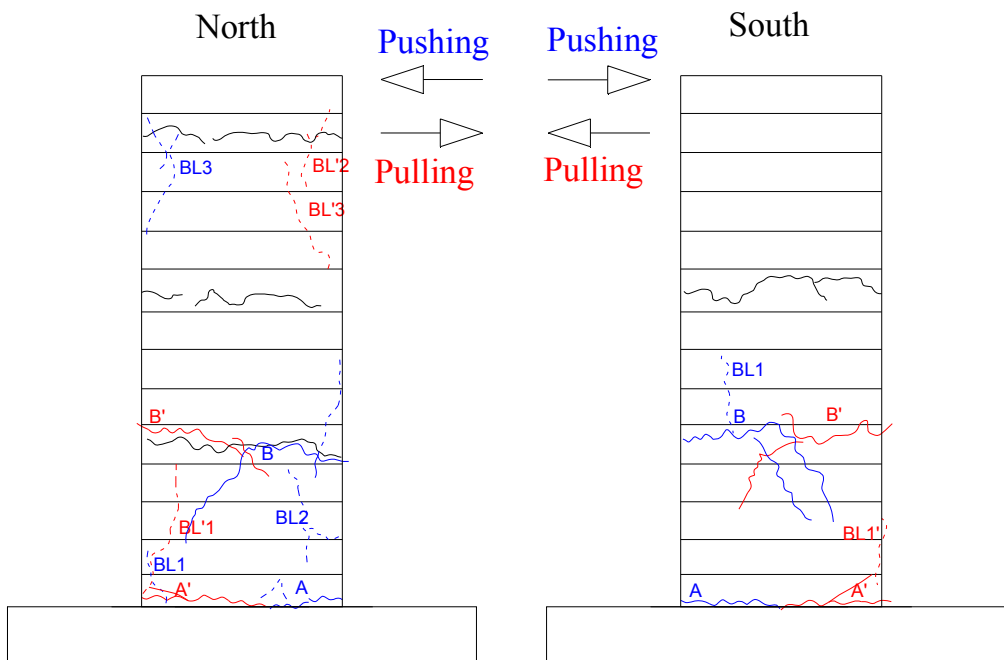


Figure E.14: Crack pattern of LS-X0 after -3% drift ratio.

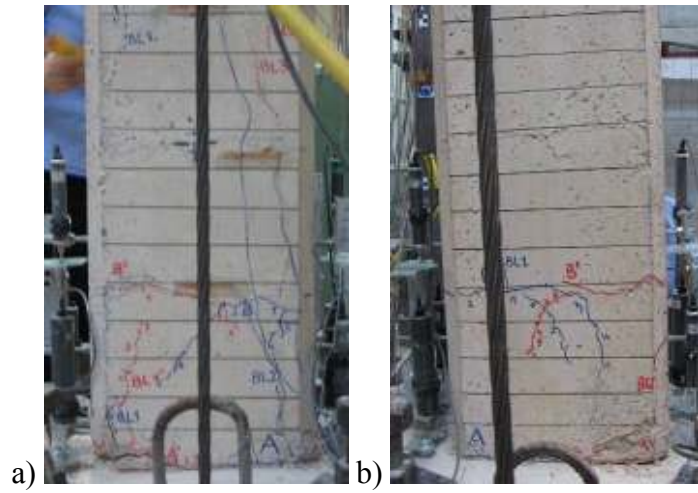


Figure E.15: a) North, and b) South view of LS-X0 after -3.5% drift ratio.

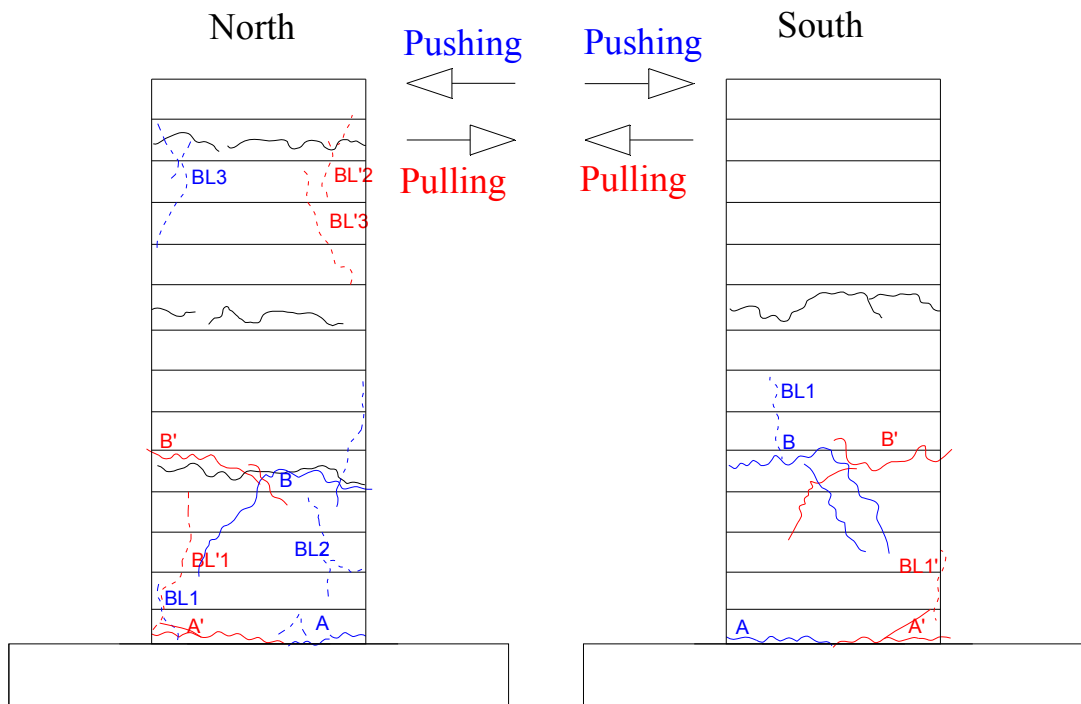


Figure E.16: Crack pattern of LS-X0 after 3.5% drift ratio.

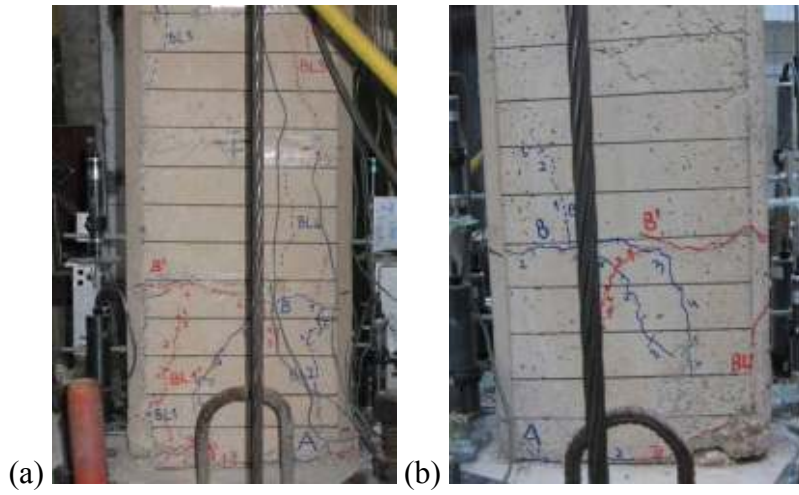


Figure E.17: a) North, and b) South view of LS-X0 after -4% drift ratio.

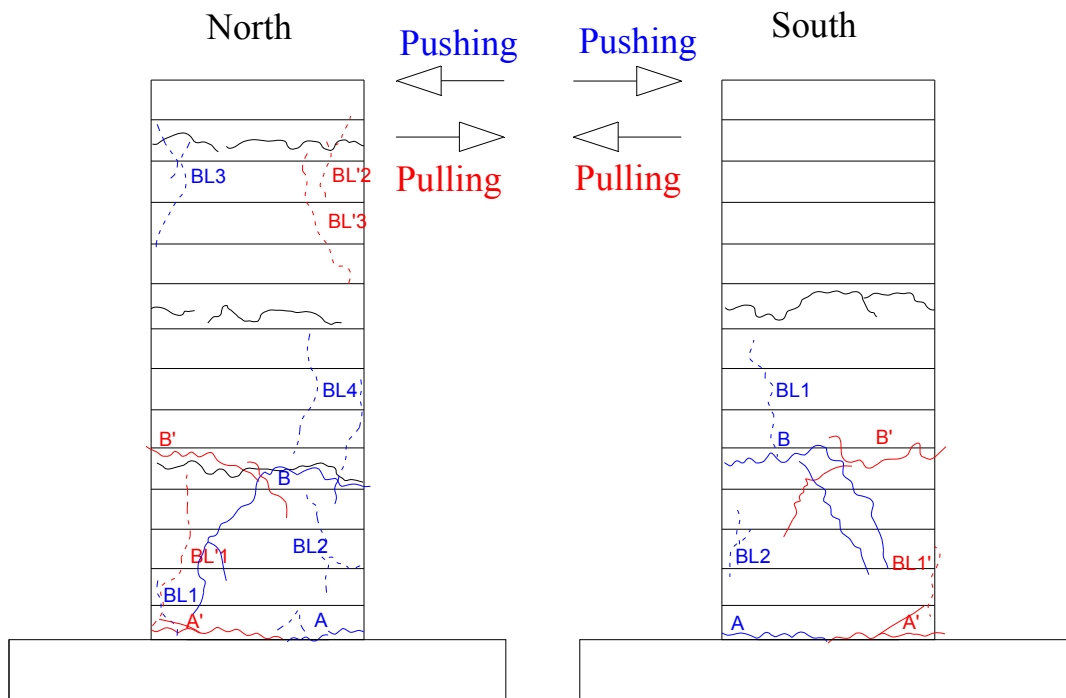


Figure E.18: Crack pattern of LS-X0 after -4% drift ratio.

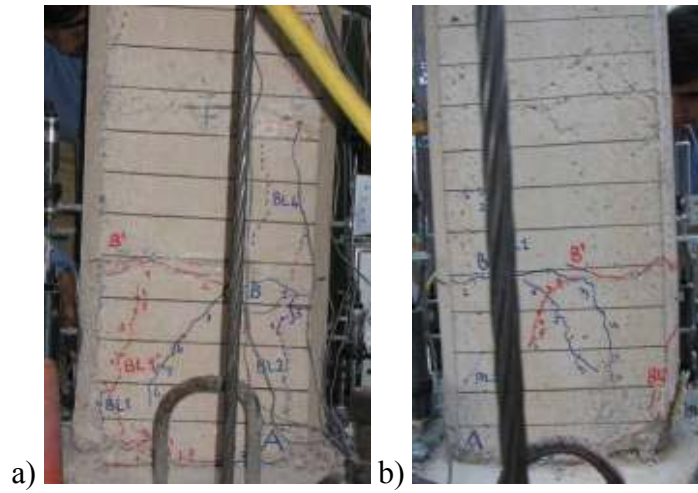


Figure E.19: a) North, and b) South view of LS-X0 after -4.5% drift ratio.

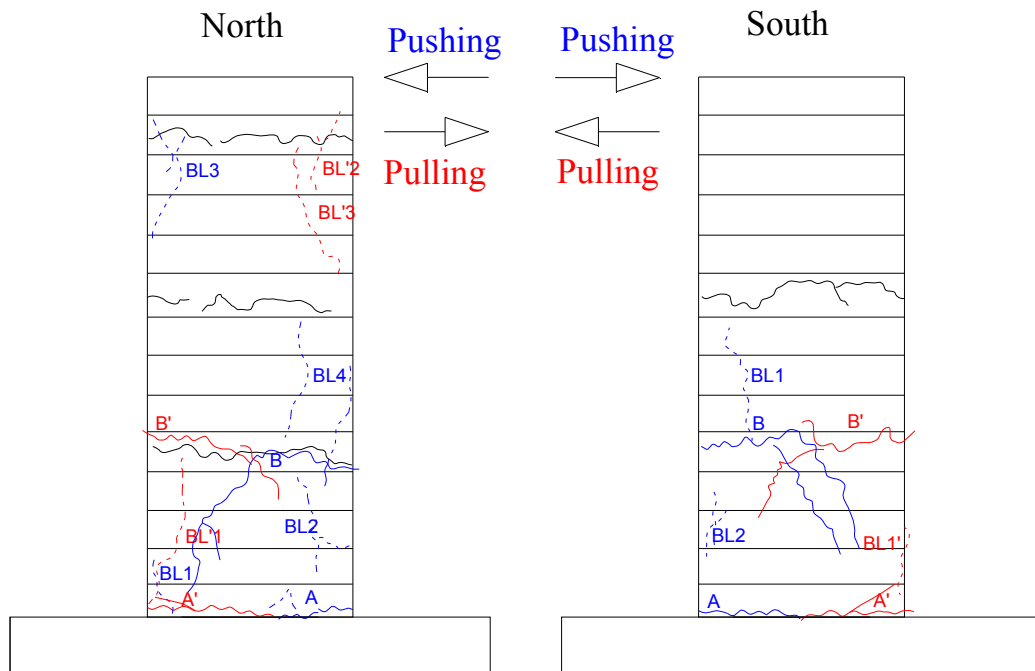


Figure E.20: Crack pattern of LS-X0 after -4.5% drift ratio.

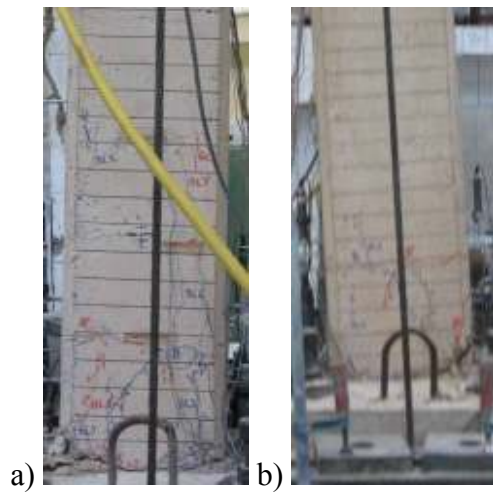


Figure E.21: a) North, and b) South view of LS-X0 after -5% drift ratio.

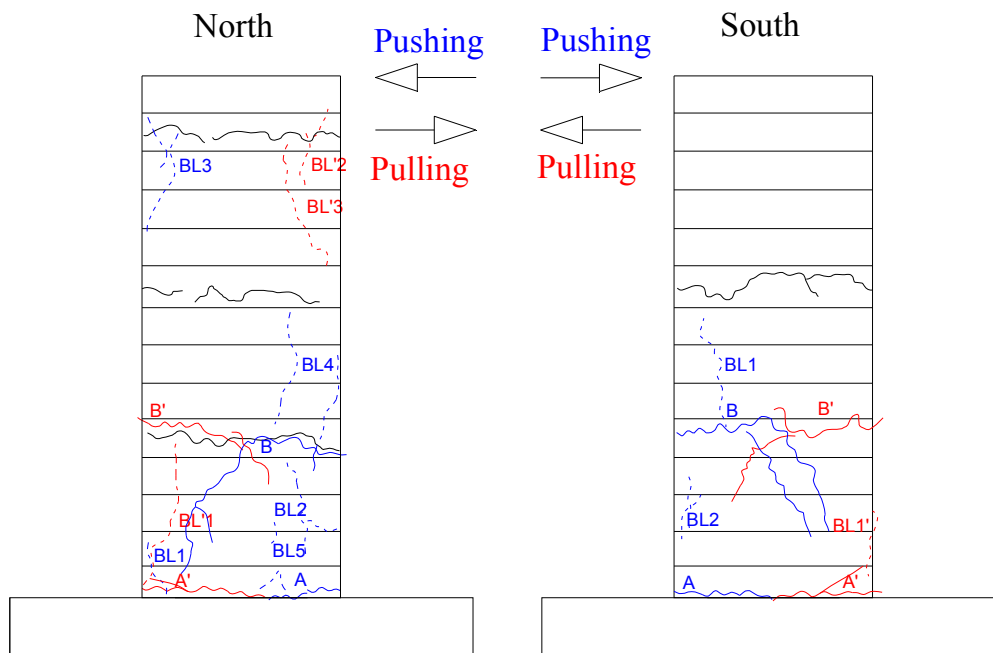


Figure E.22: Crack pattern of LS-X0 after -5% drift ratio.

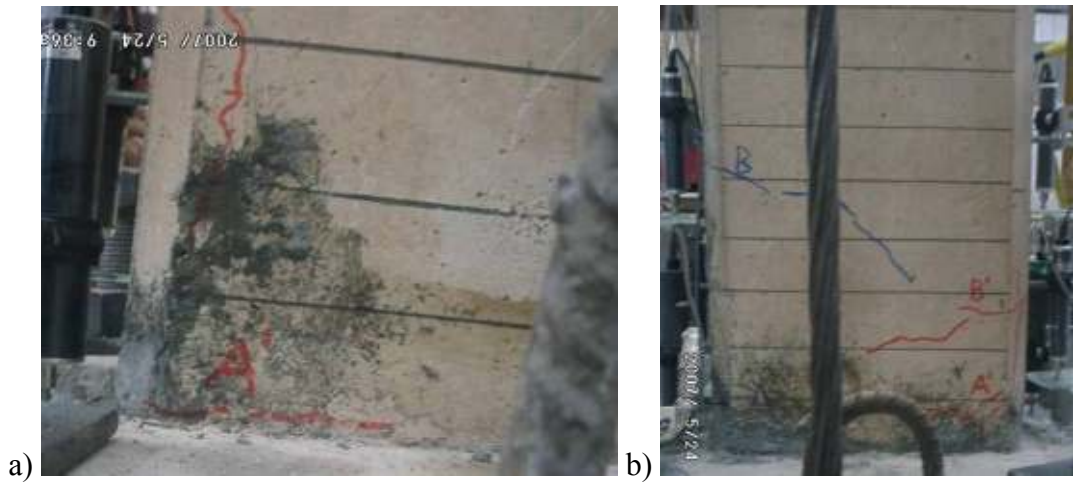


Figure E.23: a) North, and b) South view of LS-X6 after -0.5% drift ratio.

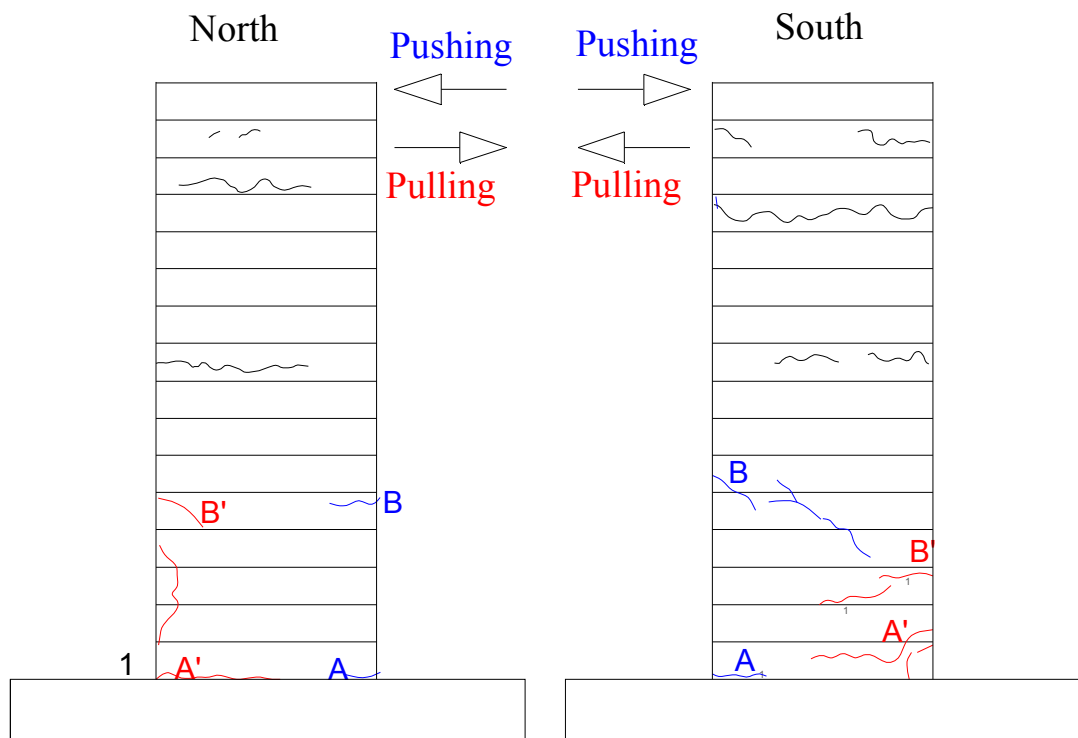


Figure E.24: Crack pattern of LS-X6 after -0.5% drift ratio.

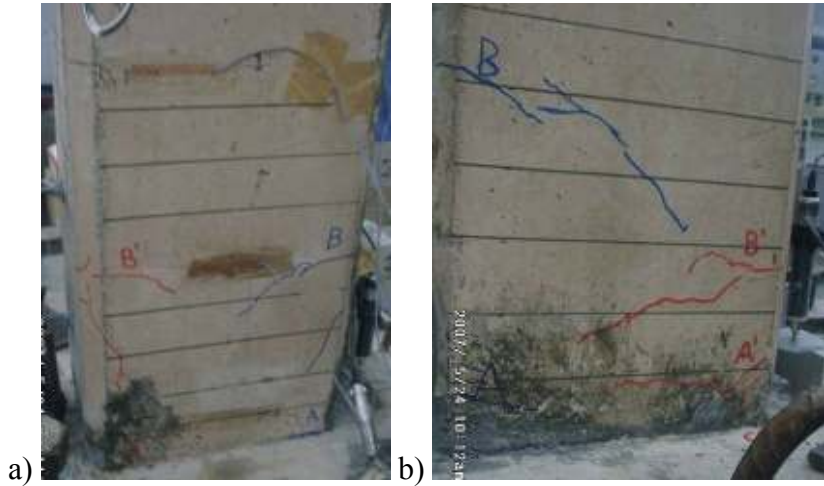


Figure E.25: a) North, and b) South view of LS-X6 after -1% drift ratio.

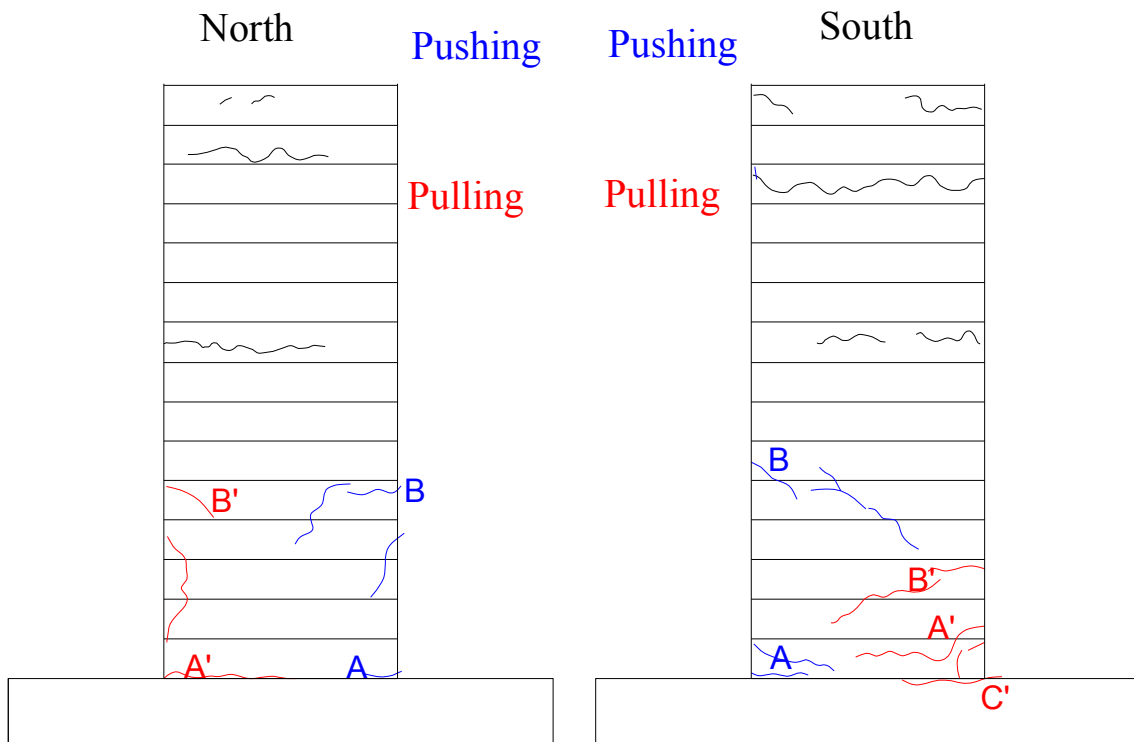


Figure E.26: Crack pattern of LS-X6 after -1% drift ratio.

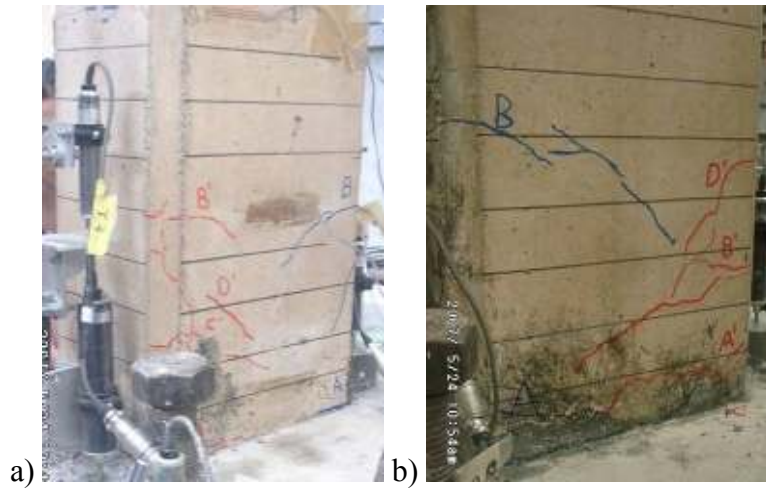


Figure E.27: a) North, and b) South view of LS-X6 after -1.5% drift ratio.

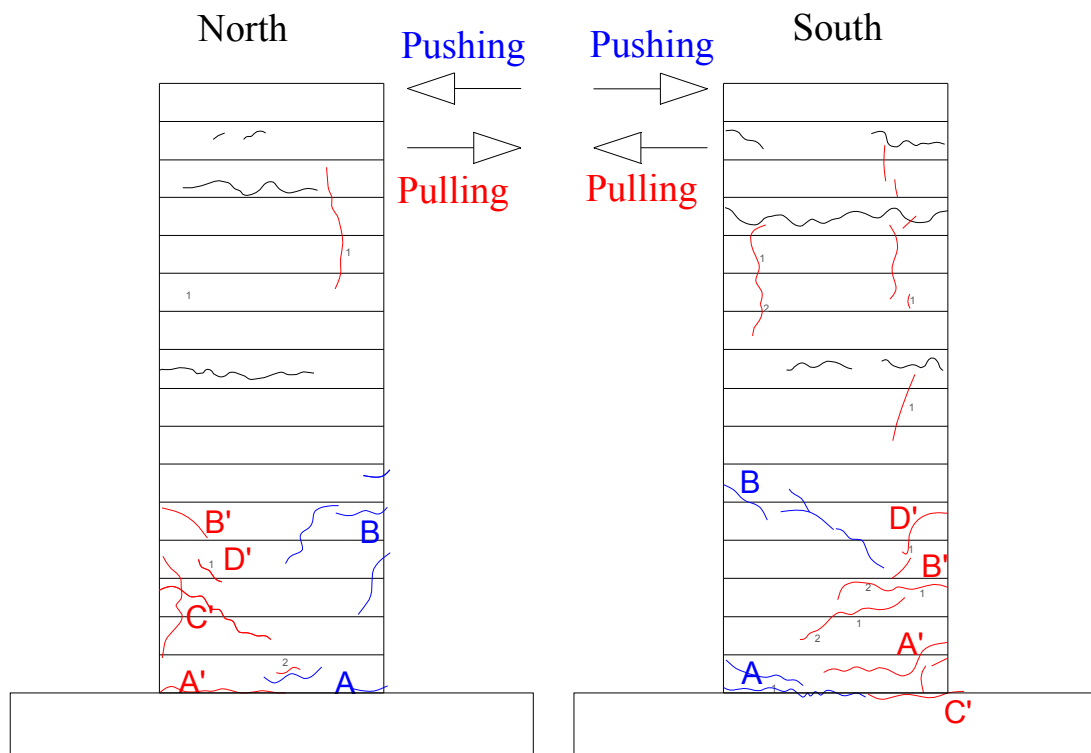


Figure E.28: Crack pattern of LS-X6 after -1.5% drift ratio.

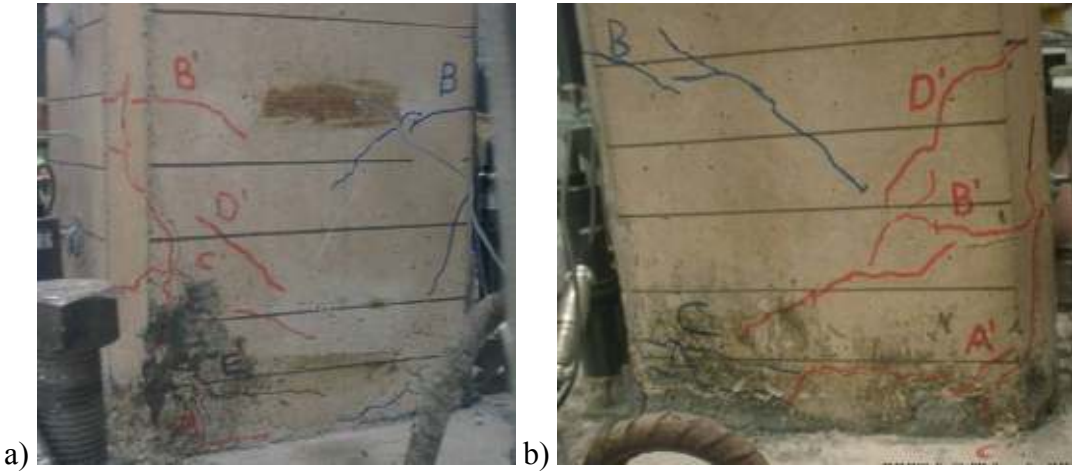


Figure E.29: a) North, and b) South view of LS-X6 after -2% drift ratio.

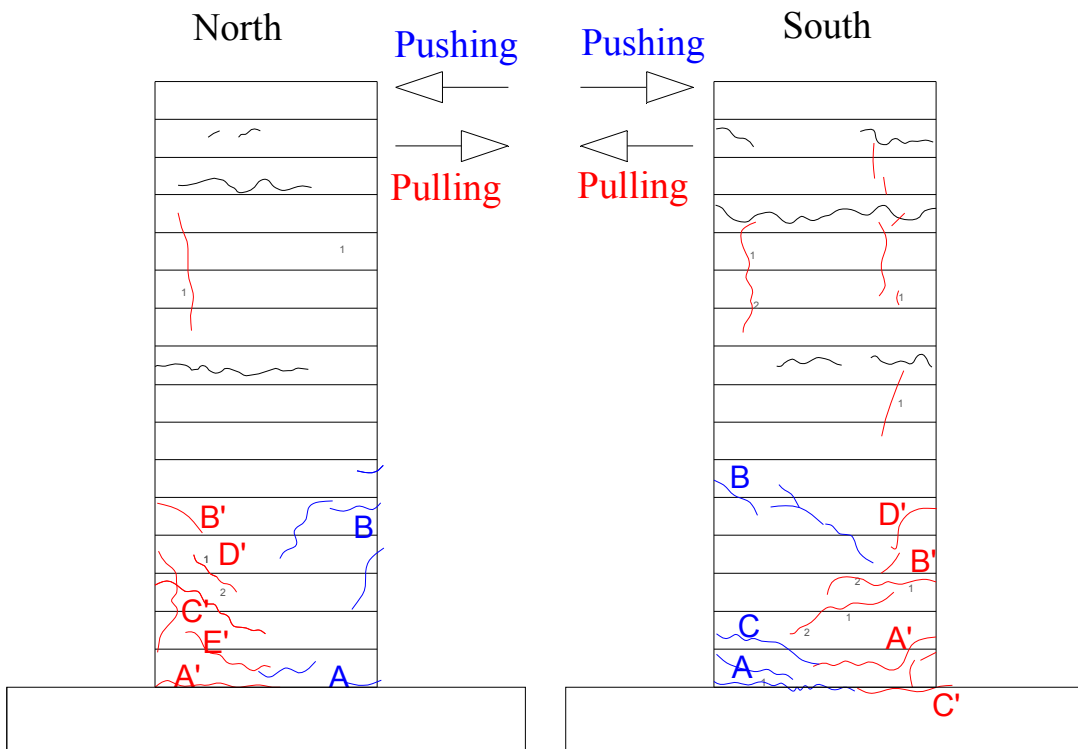


Figure E.30: Crack pattern of LS-X6 after -2% drift ratio.

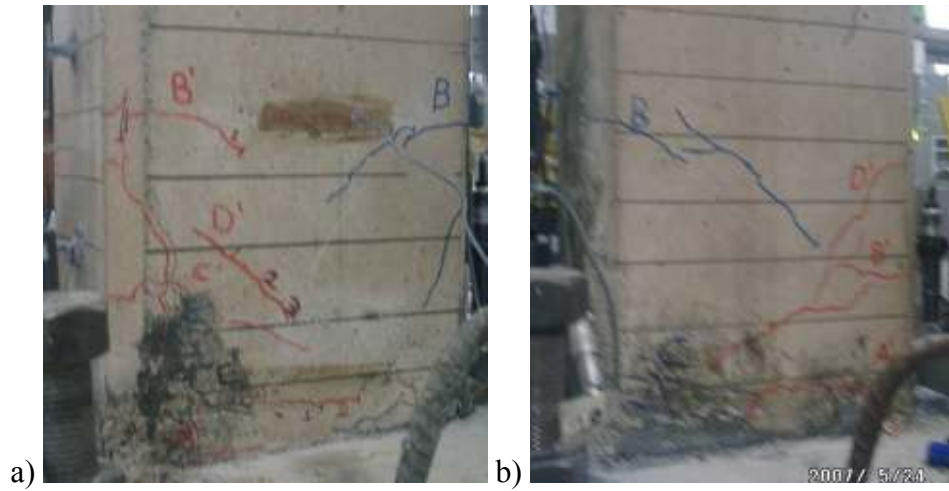


Figure E.31: a) North, and (b) South view of LS-X6 after -2.5% drift ratio.

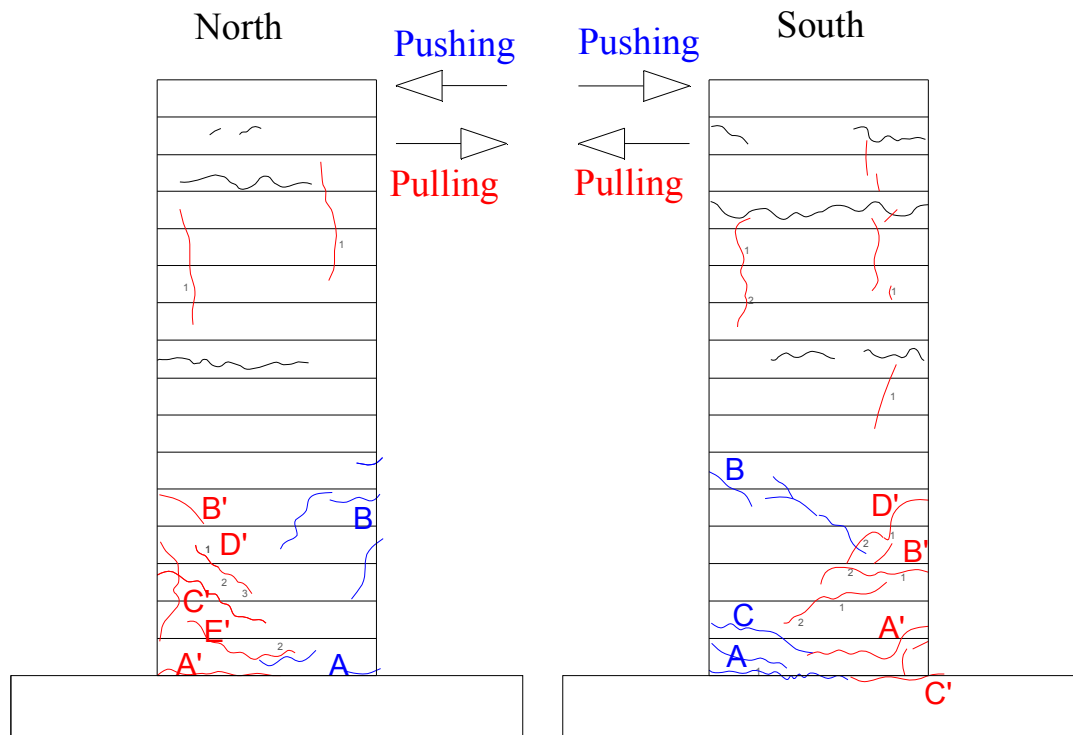


Figure E.32: Crack pattern of LS-X6 after -2.5% drift ratio.

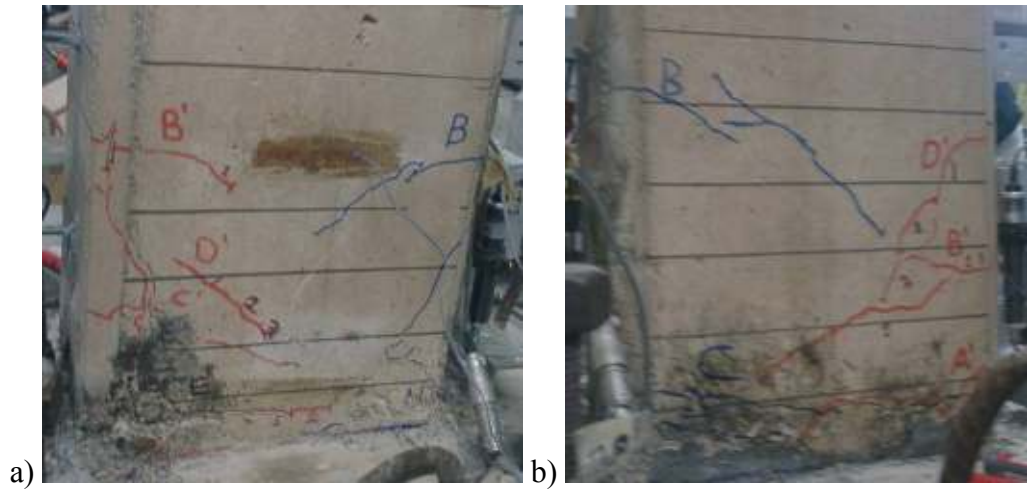


Figure E.33: a) North, and b) South view of LS-X6 after -3% drift ratio.

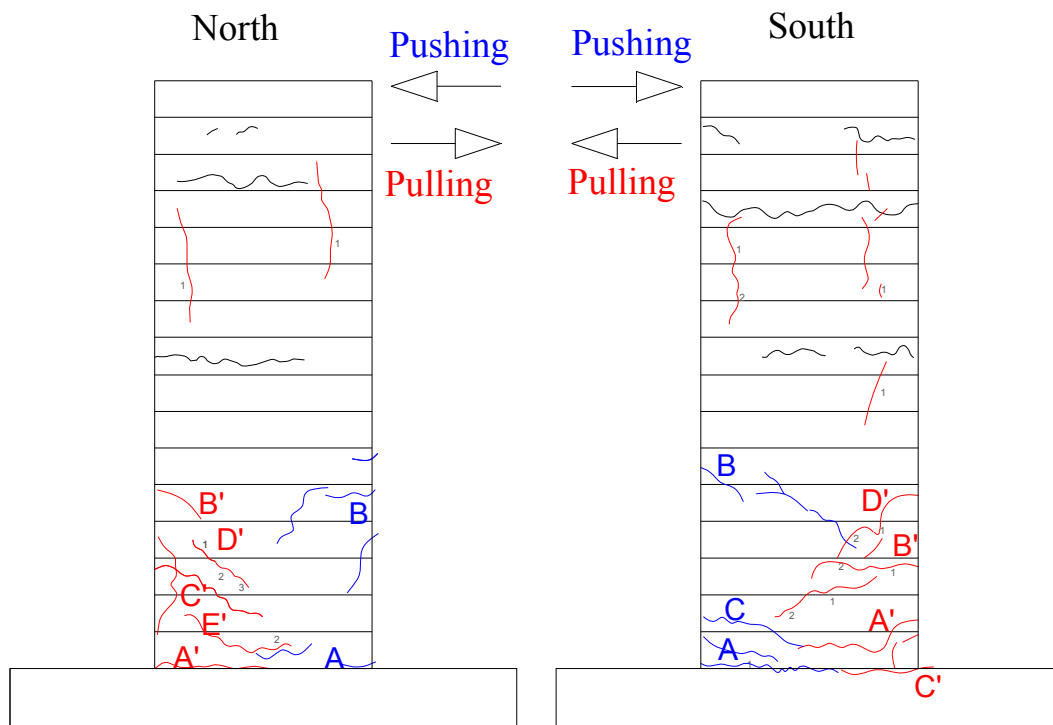


Figure E.34: Crack pattern of LS-X6 after -3% drift ratio.

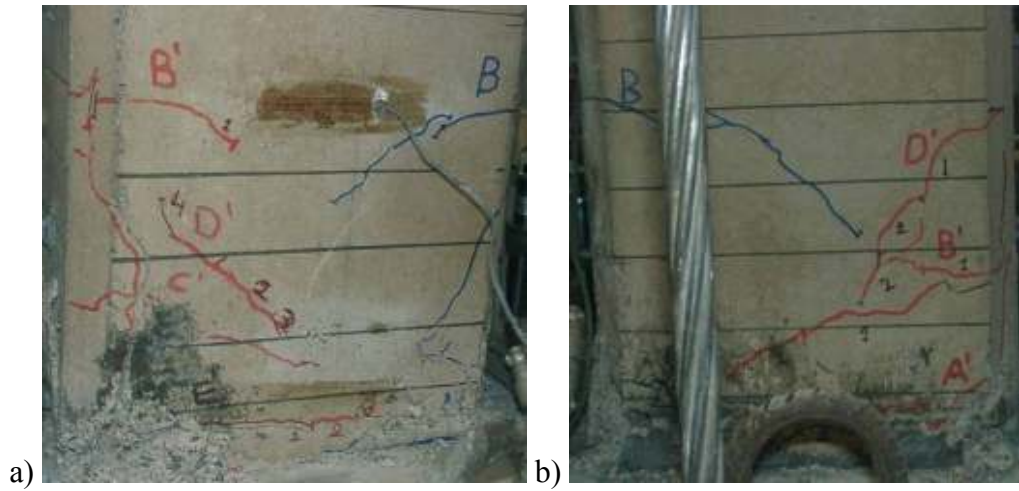


Figure E.35: a) North, and b) South view of LS-X6 after -3.5% drift ratio.

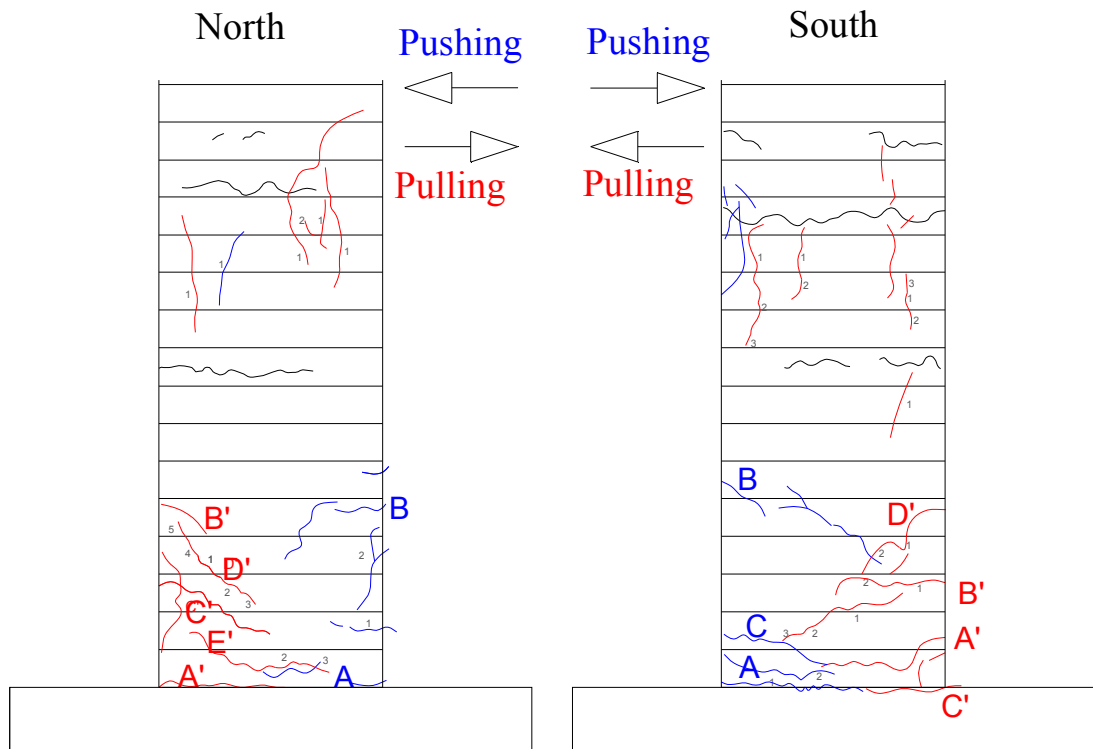


Figure E.36: Crack pattern of LS-X6 after -3.5% drift ratio.

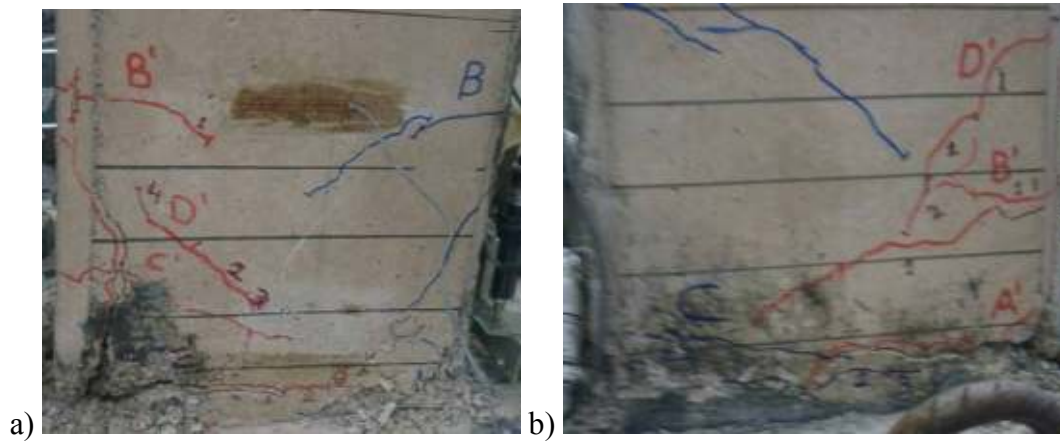


Figure E.37: a) North, and b) South view of LS-X6 after -4% drift ratio.

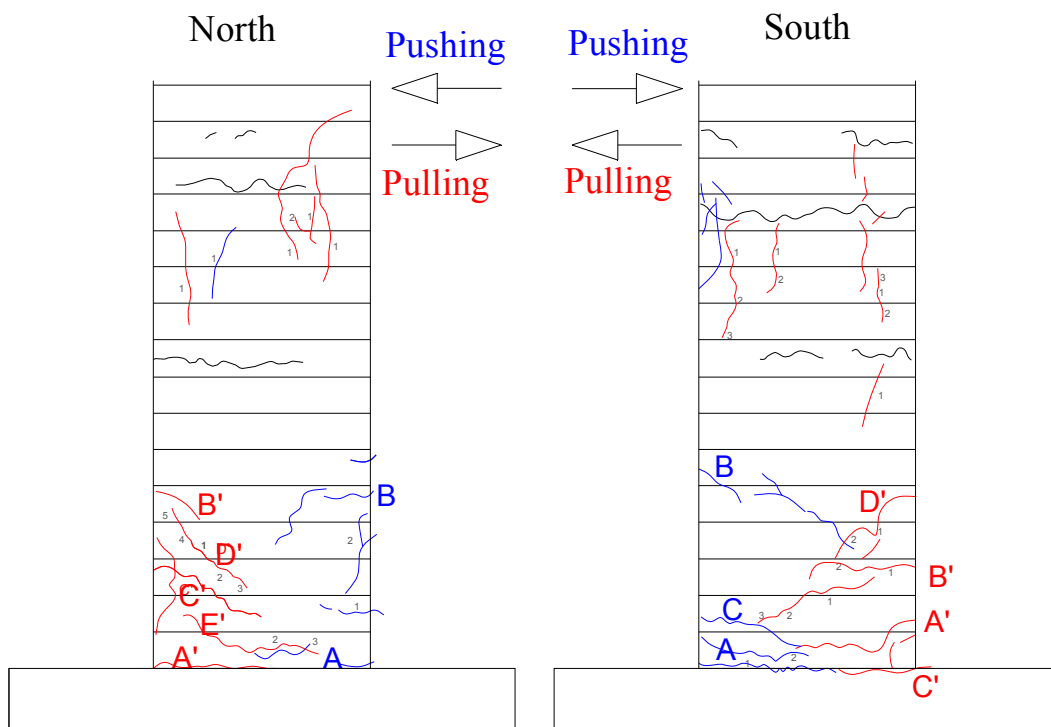


Figure E.38: Crack pattern of LS-X6 after -4% drift ratio.

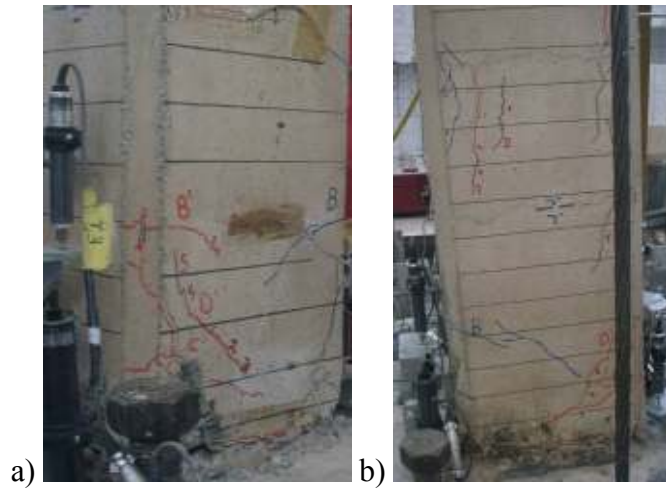


Figure E.39: a) North, and b) South view of LS-X6 after -4.5% drift ratio.

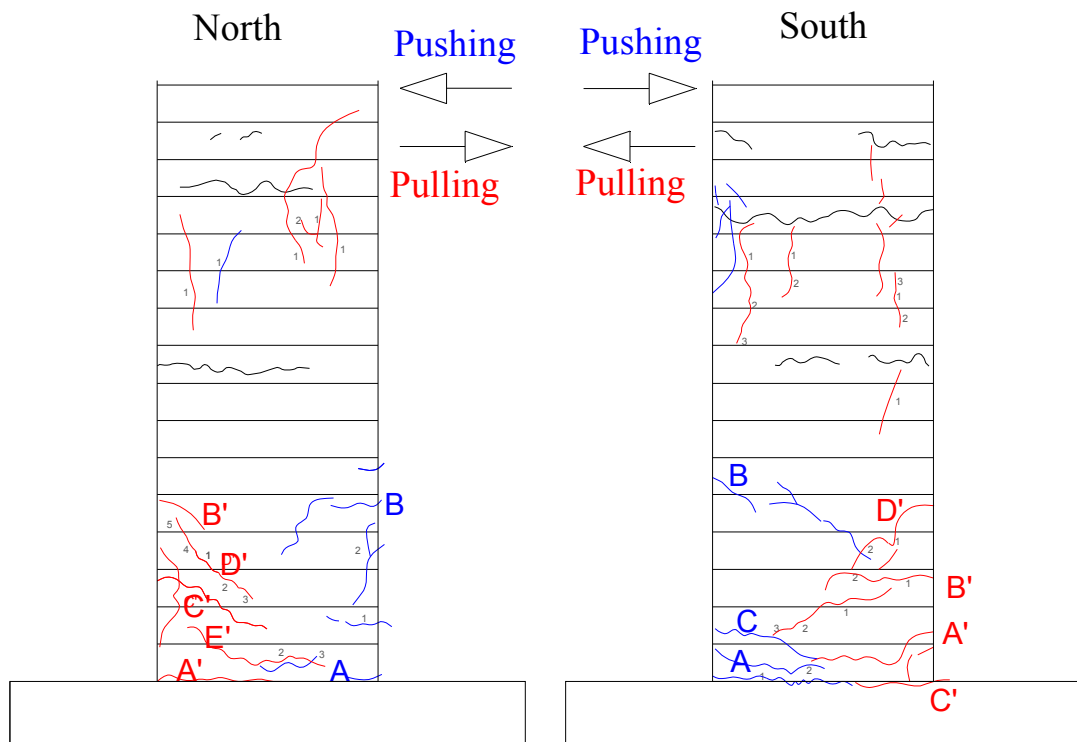


Figure E.40: Crack pattern of LS-X6 after -4.5% drift ratio.

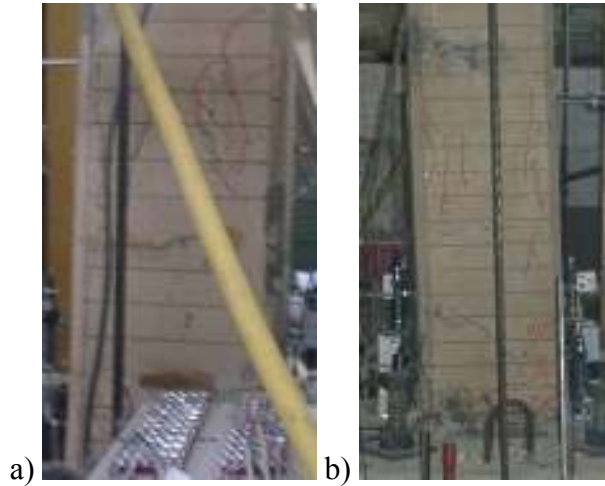


Figure E.41: a) North, and b) South view of LS-X6 after -5% drift ratio.

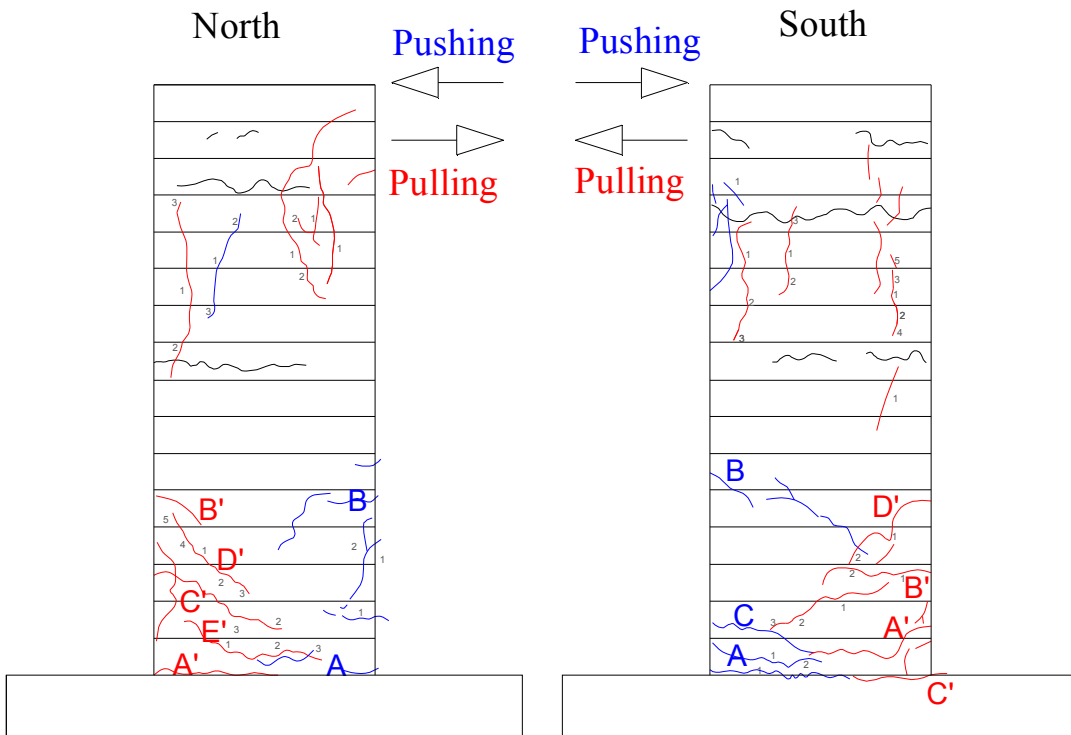


Figure E.42: Crack pattern of LS-X6 after -5% drift ratio.

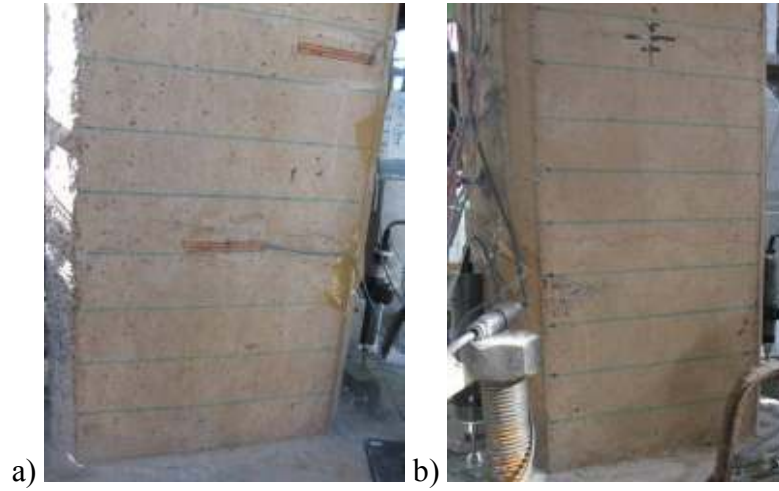


Figure E.43: a) North, and (b) South view of LS-X8 after -0.25% drift ratio.

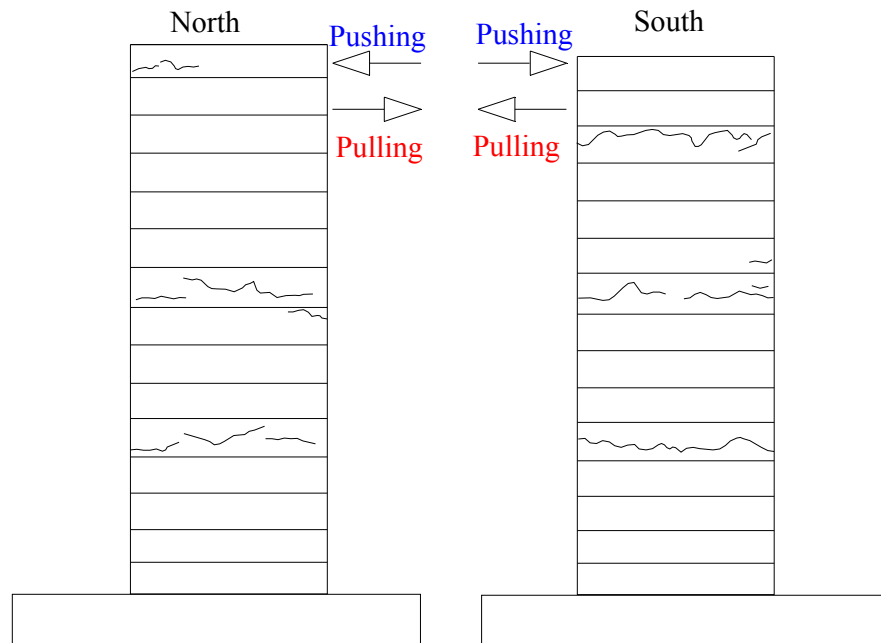


Figure E.44: Crack pattern of LS-X8 after -0.25% drift ratio.

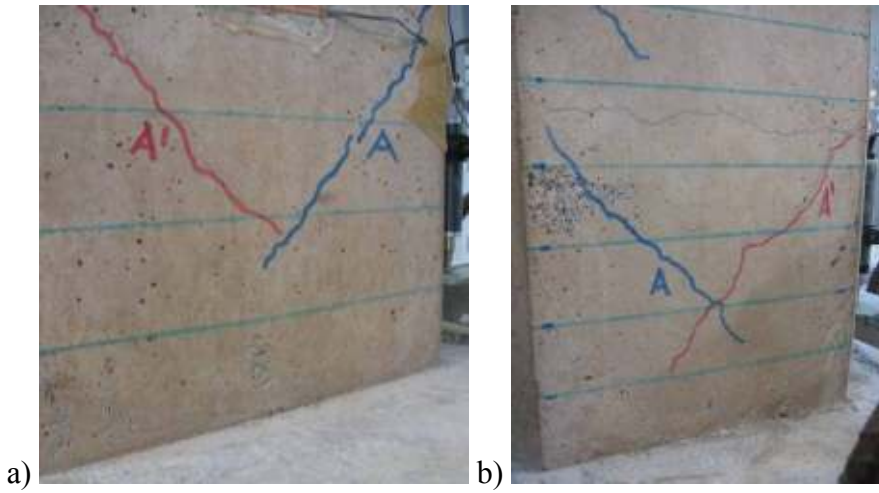


Figure E.45: (a) North, and (b) South view of LS-X8 after -0.5% drift ratio.

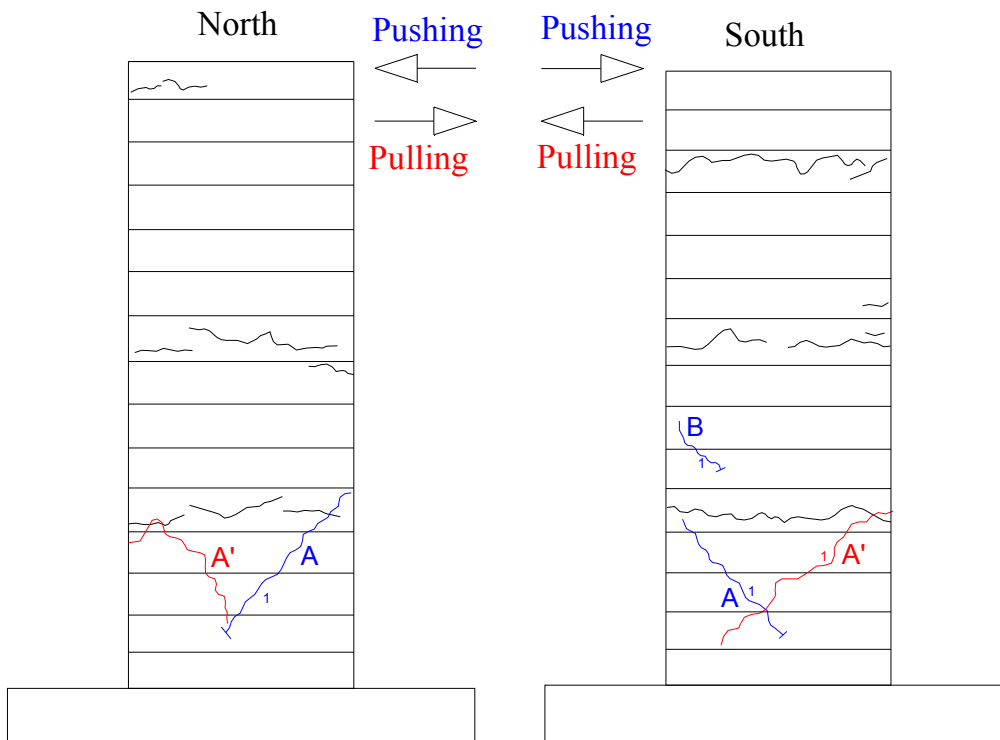


Figure E.46: Crack pattern of LS-X8 after -0.5% drift ratio.

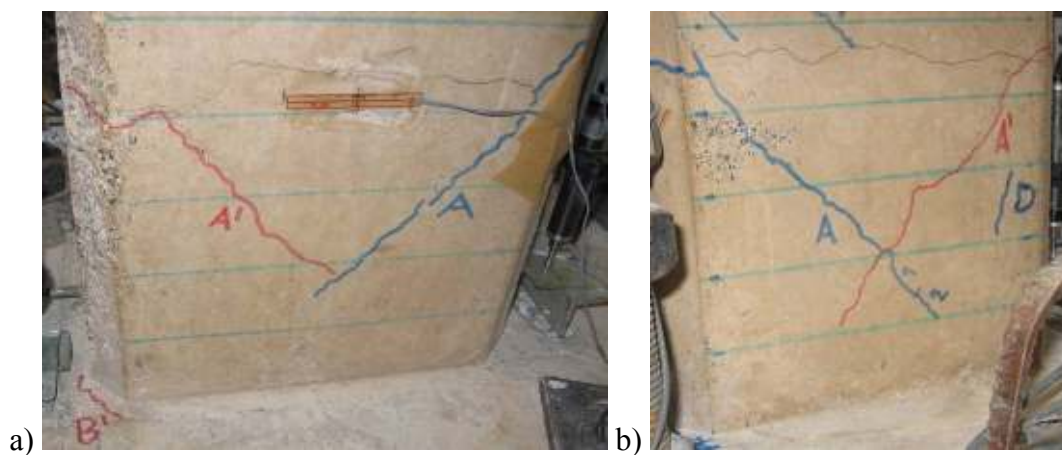


Figure E.47: a) North, and b) South view of LS-X8 after -0.75% drift ratio.

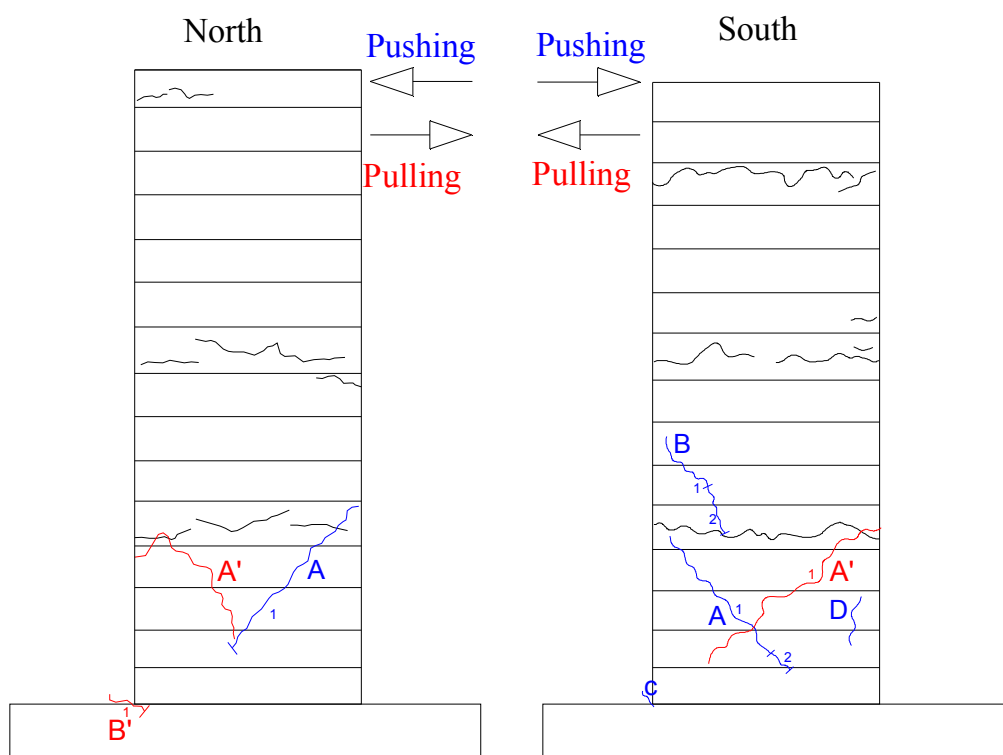


Figure E.48: Crack pattern of LS-X8 after -0.75% drift ratio.

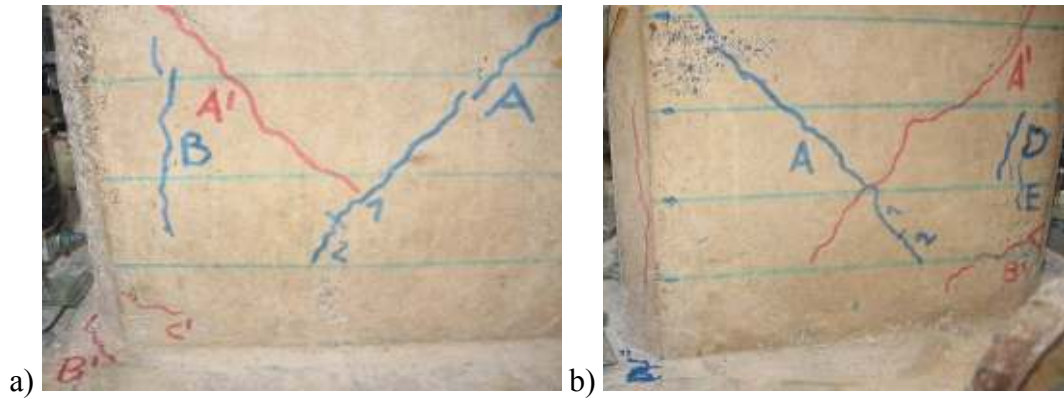


Figure E.49: a) North, and b) South view of LS-X8 after -1% drift ratio.

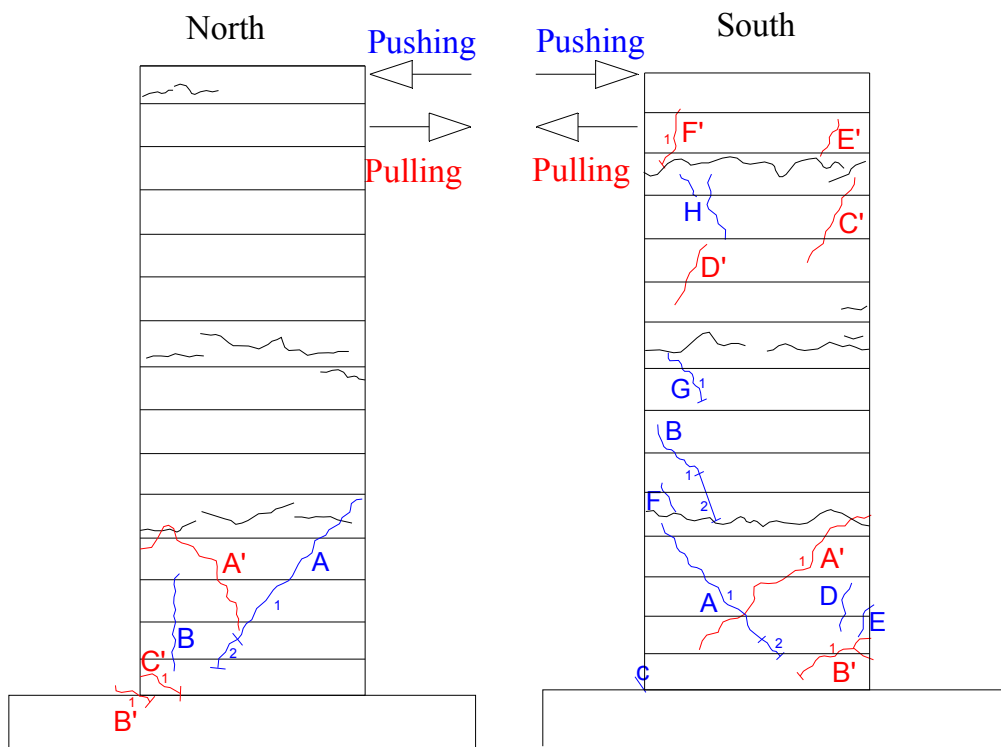


Figure E.50: Crack pattern of LS-X8 after -1% drift ratio.

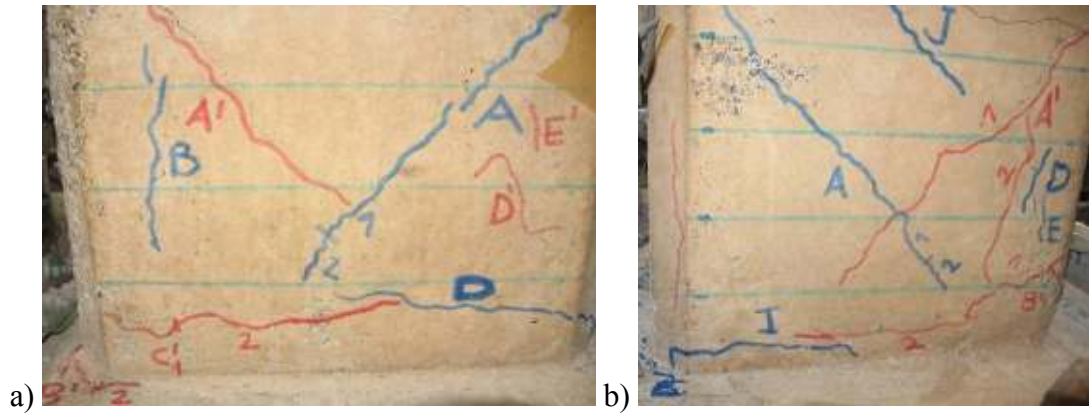


Figure E.51: (a) North, and (b) South view of LS-X8 after -1.5% drift ratio.

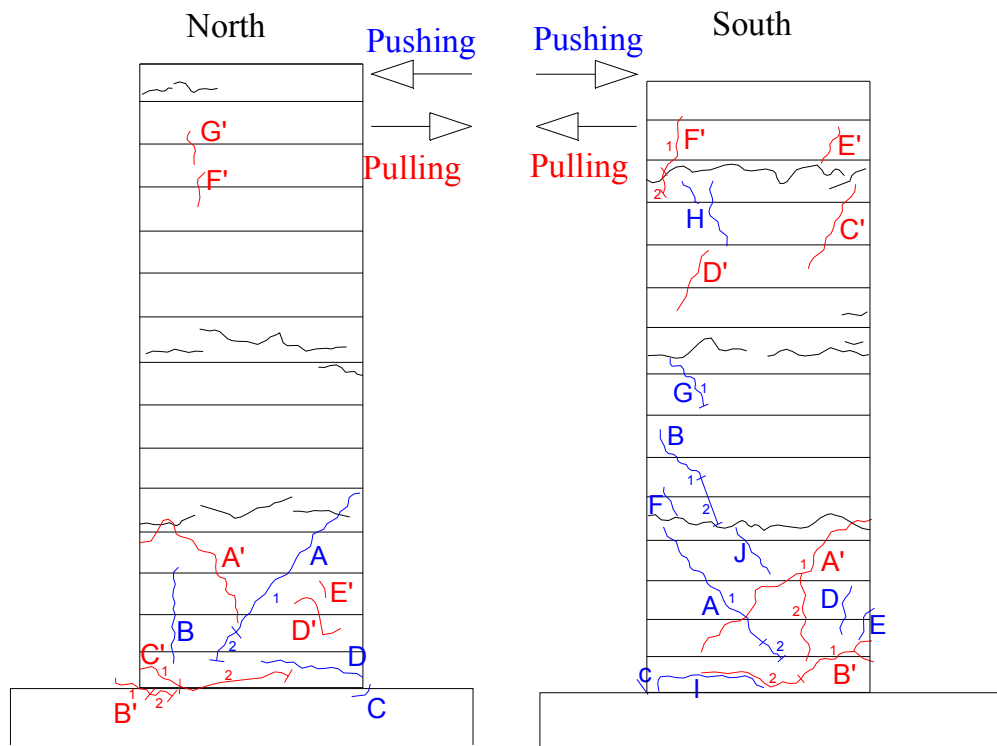


Figure E.52: Crack pattern of LS-X8 after -1.5% drift ratio.

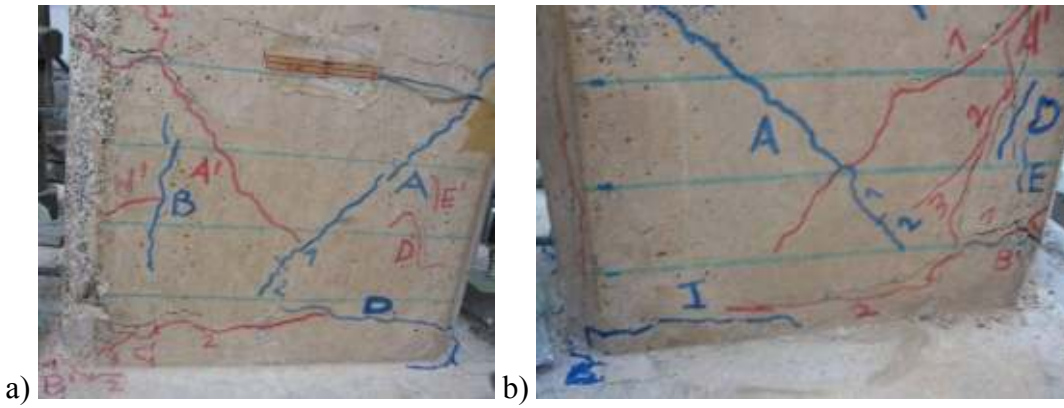


Figure E.53: (a) North, and (b) South view of LS-X8 after -2% drift ratio.

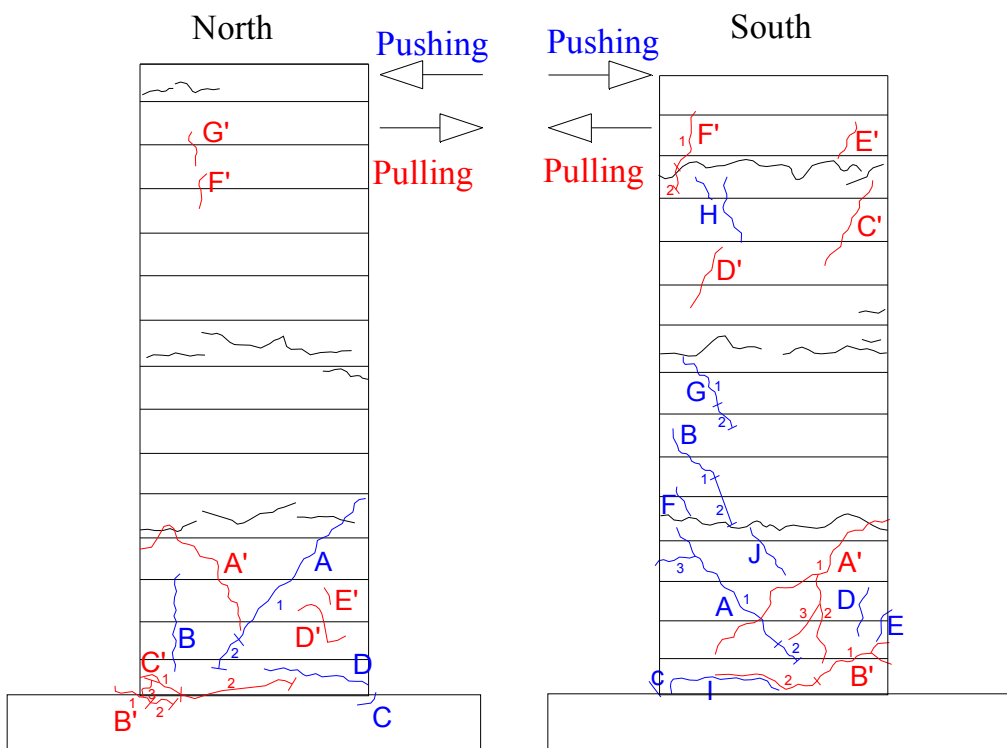


Figure E.54: Crack pattern of LS-X8 after -2% drift ratio.



Figure E.55: a) North, and b) South view of LS-X8 after -2.5% drift ratio.

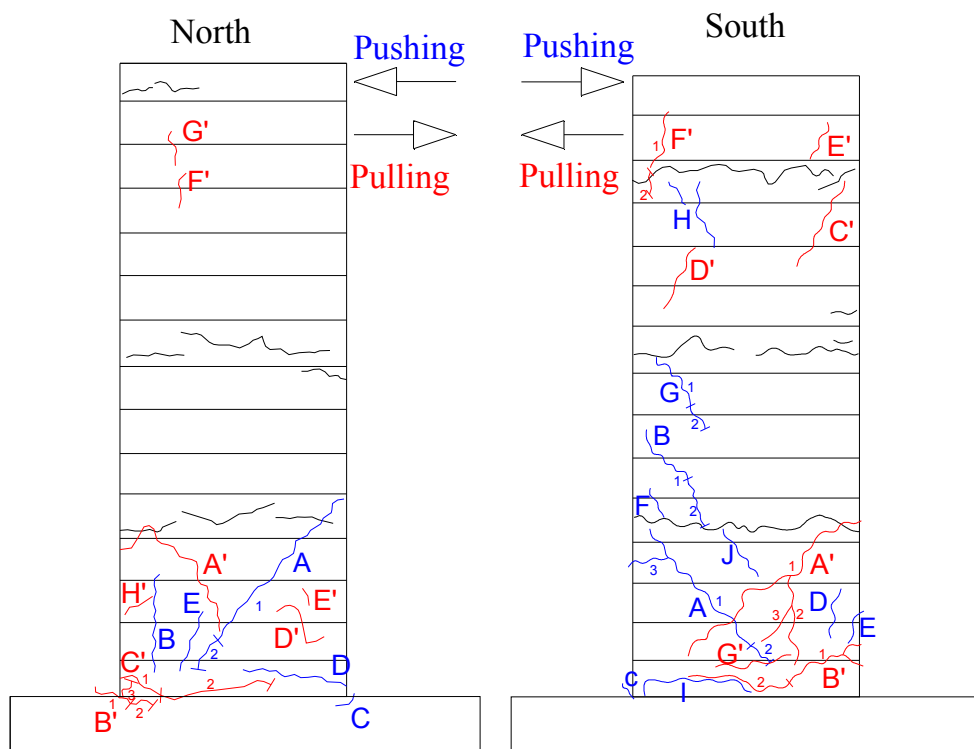


Figure E.56: Crack pattern of LS-X8 after -2.5% drift ratio.

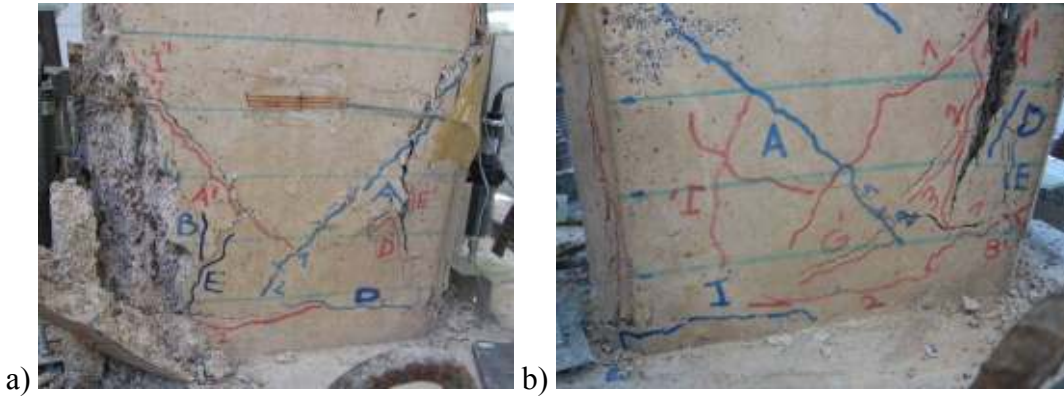


Figure E.57: a) North, and b) South view of LS-X8 after -3% drift ratio.

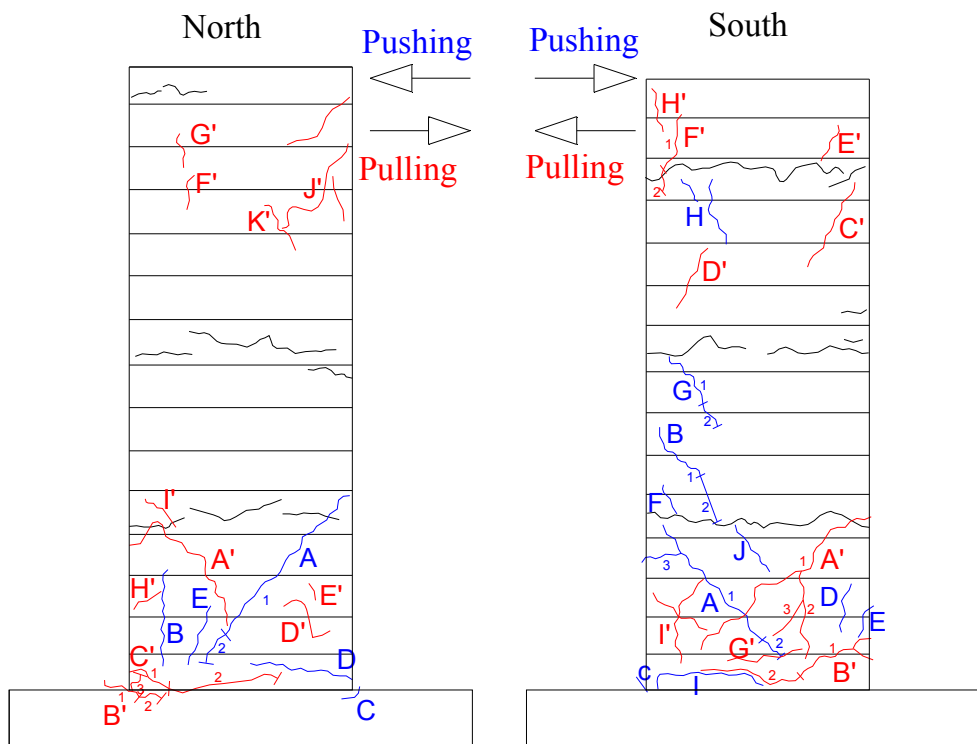


Figure E.58: Crack pattern of LS-X8 after -3% drift ratio.

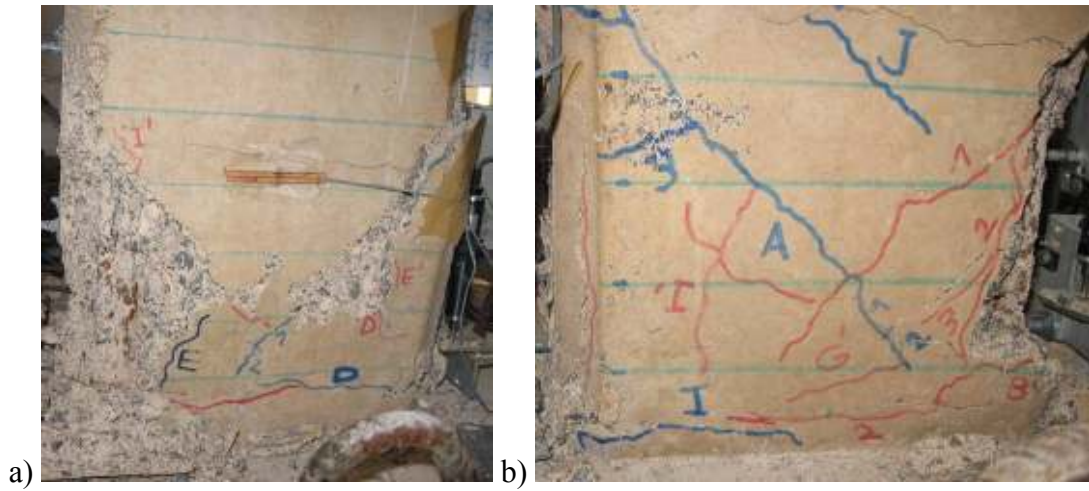


Figure E.59: a) North, and b) South view of LS-X8 after -3.5% drift ratio.

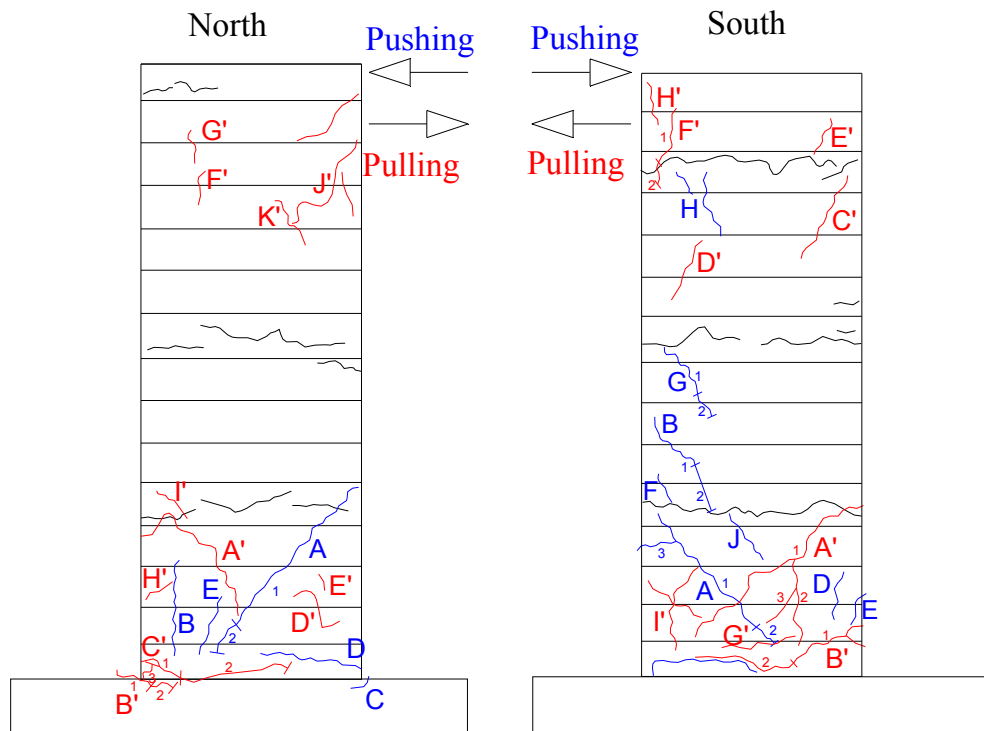


Figure E.60: Crack pattern of LS-X8 after -3.5% drift ratio.

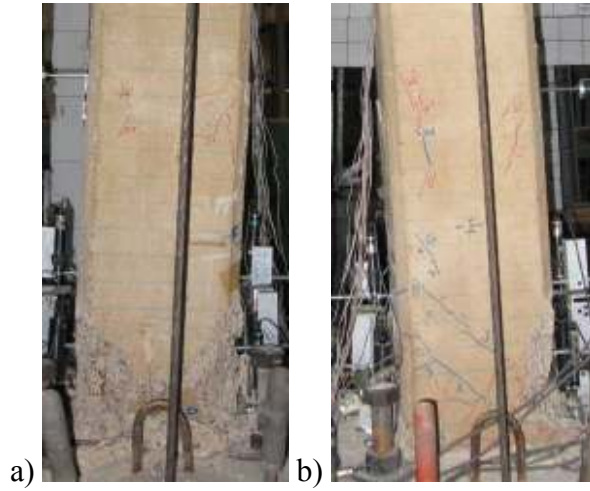


Figure E.61: a) North, and b) South view of LS-X8 after -4% drift ratio.

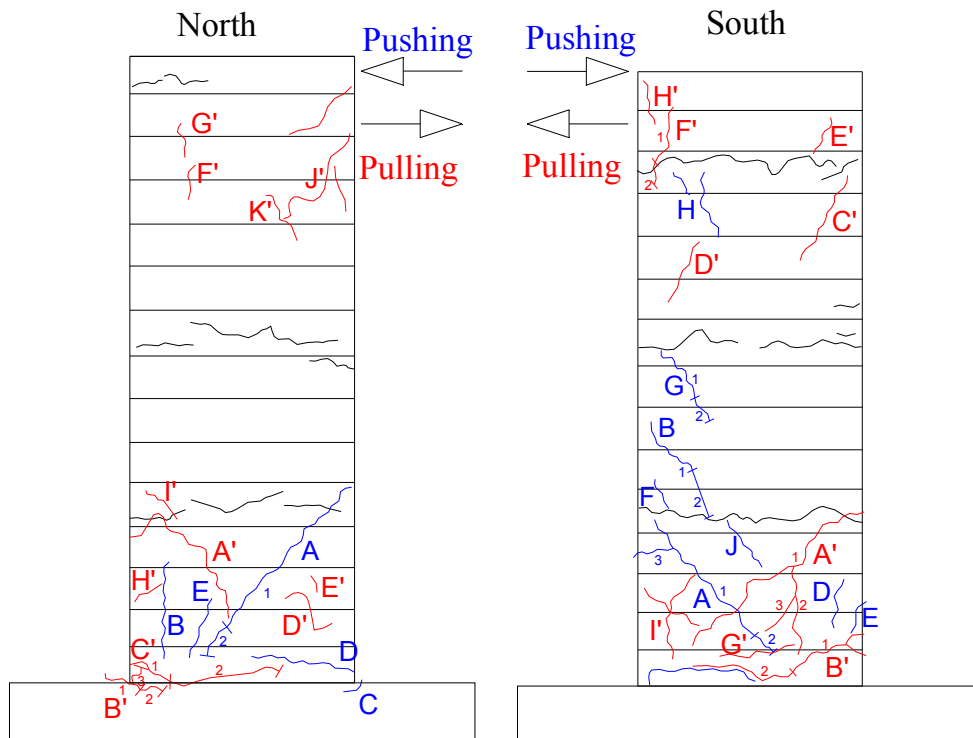


Figure E.62: Crack pattern of LS-X8 after -4% drift ratio.

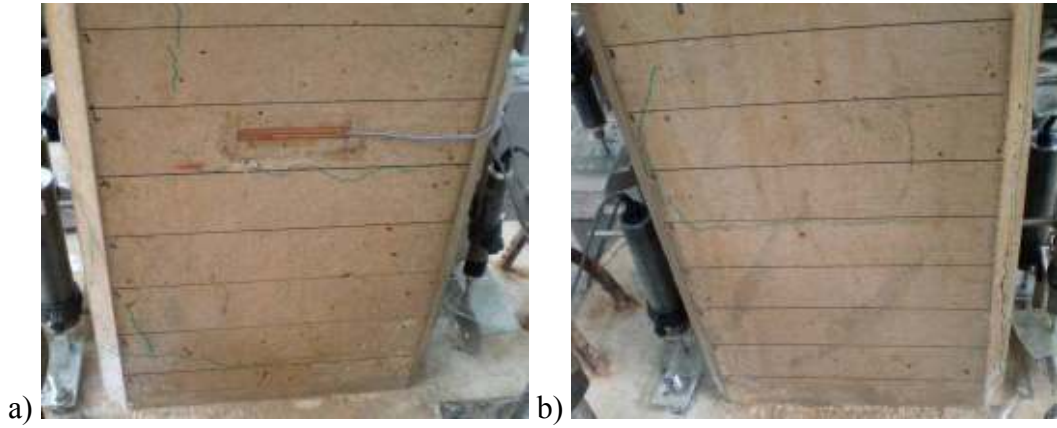


Figure E.63: a) North, and b) South view of LS-X12 after -0.1% drift ratio.

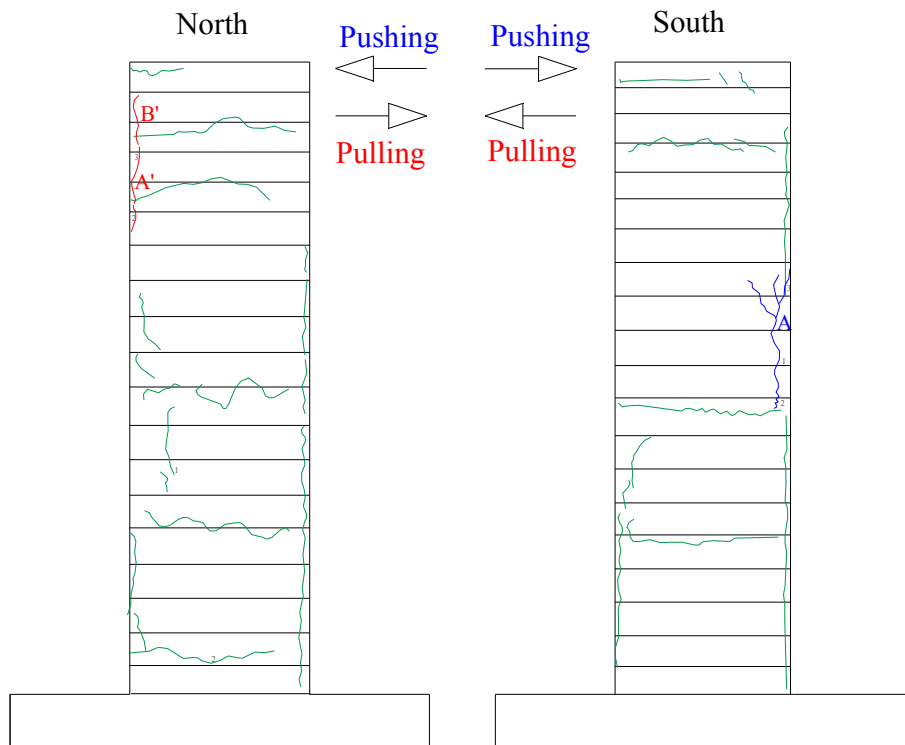


Figure E.64: Crack pattern of LS-X12 after -0.1% drift ratio.

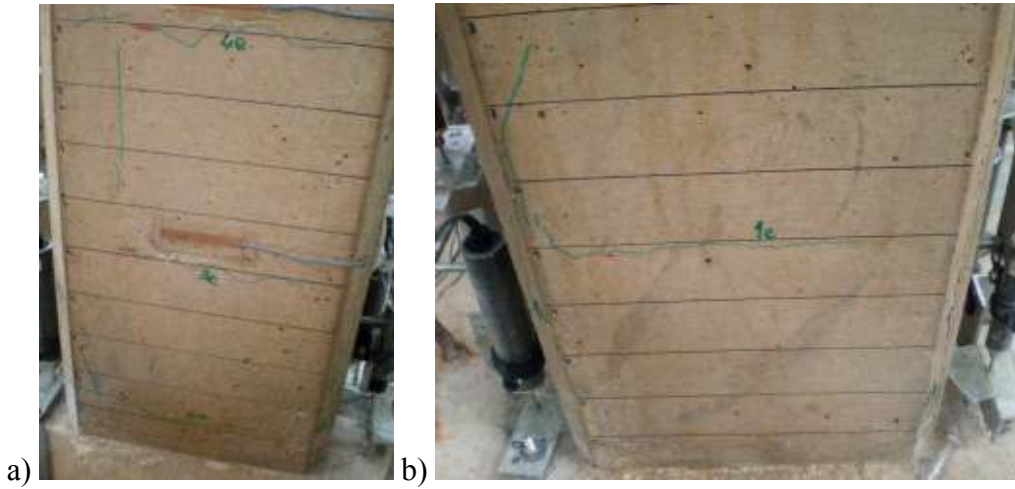


Figure E.65: a) North, and b) South view of LS-X12 after -0.25% drift ratio.

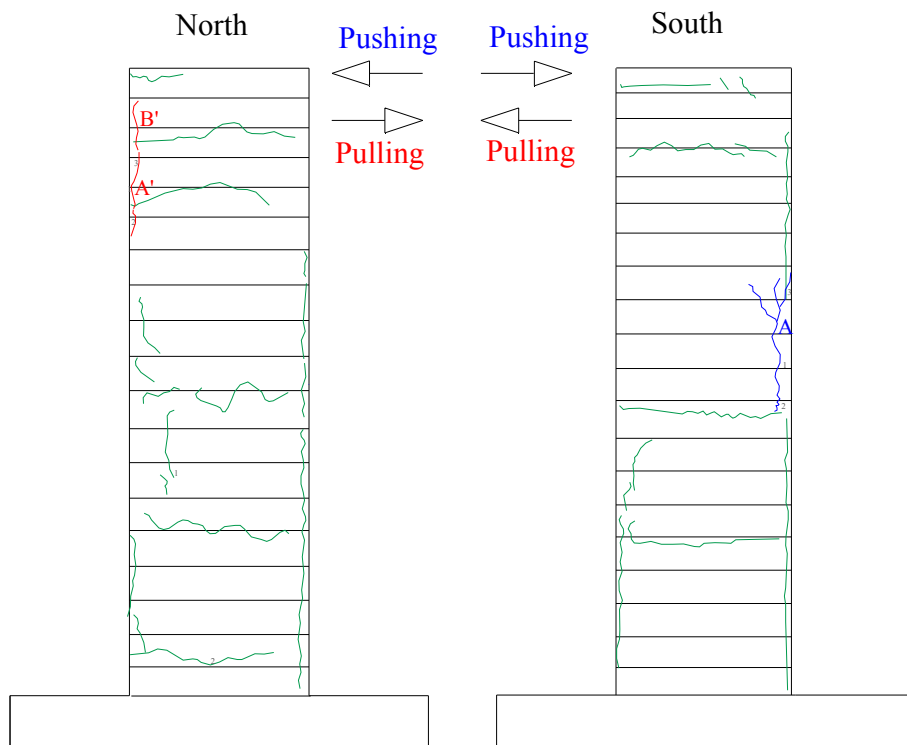


Figure E.66: Crack pattern of LS-X12 after -0.25% drift ratio.

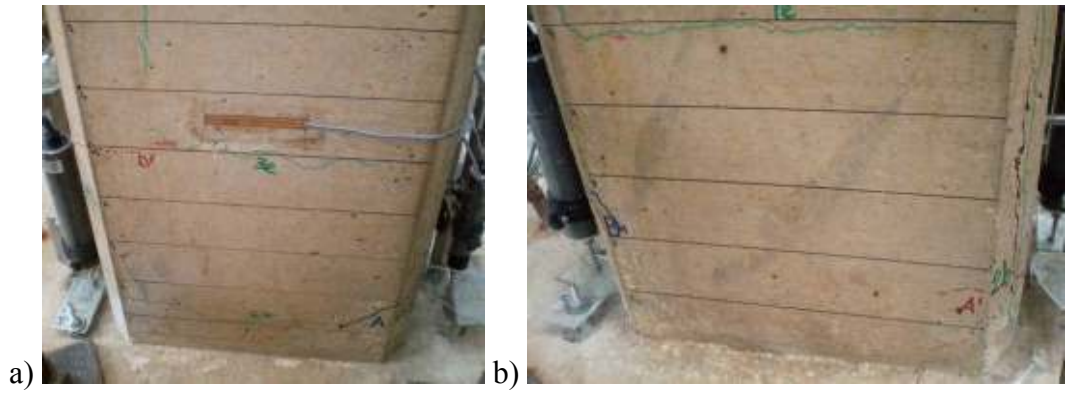


Figure E.67: a) North, and b) South view of LS-X12 after -0.5% drift ratio.

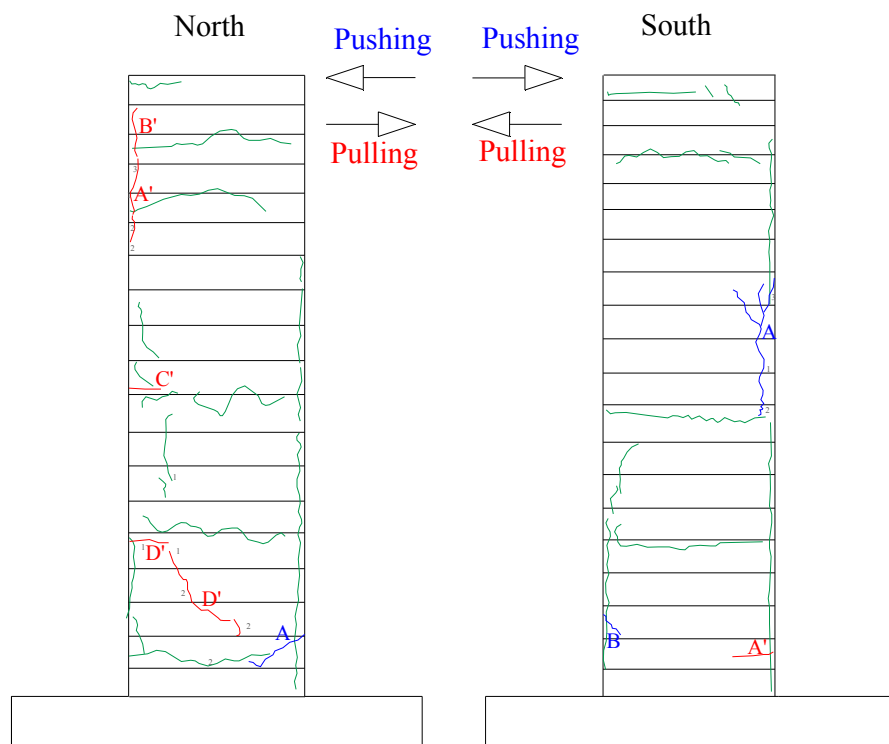


Figure E.68: Crack pattern of LS-X12 after -0.5% drift ratio.

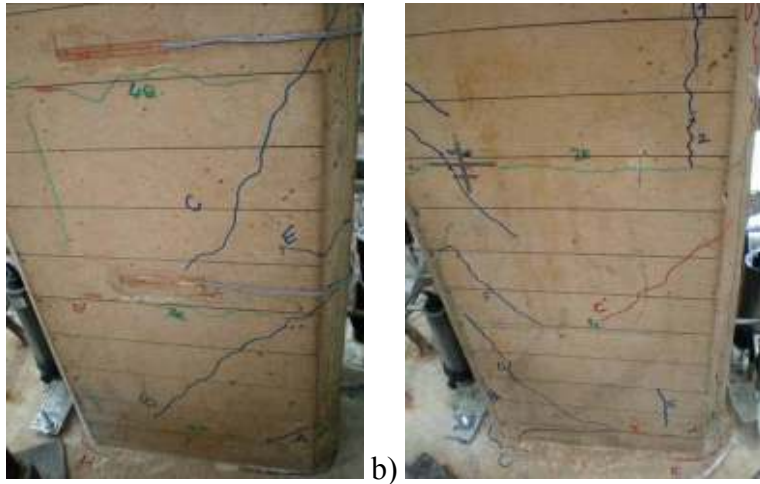


Figure E.69: a) North, and b) South view of LS-X12 after -0.75% drift ratio.

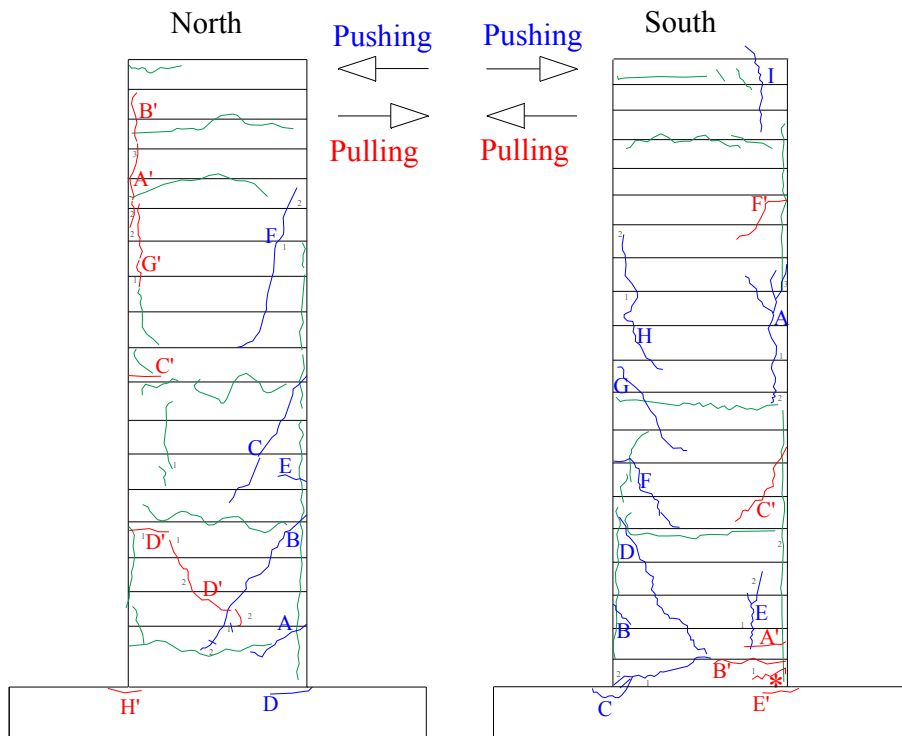


Figure E.70: Crack pattern of LS-X12 after -0.75% drift ratio.

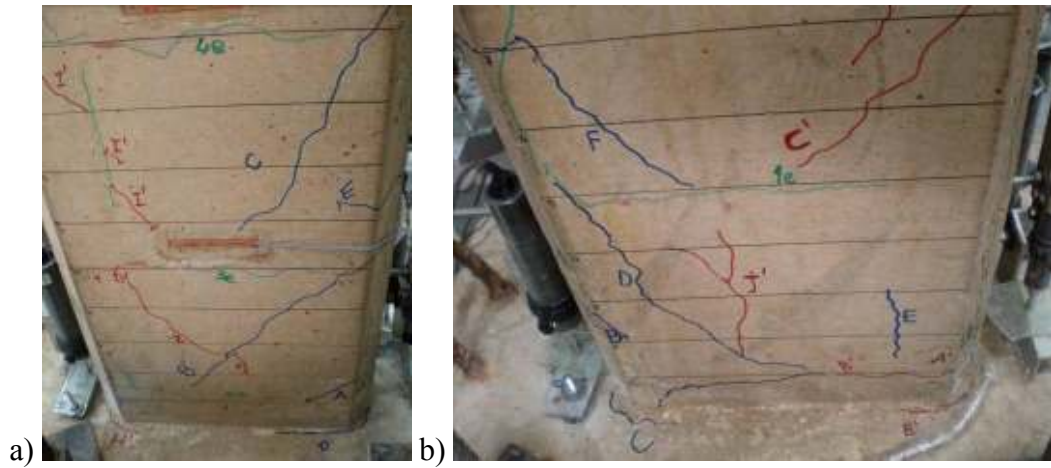


Figure E.71: a) North, and b) South view of LS-X12 after -1% drift ratio.

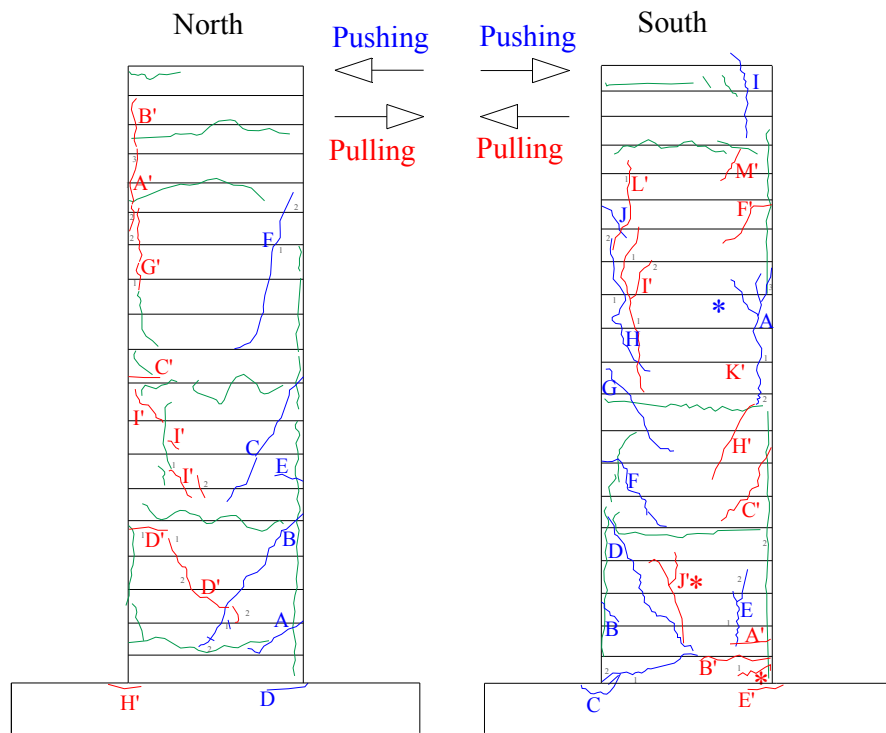


Figure E.72: Crack pattern of LS-X12 after -1% drift ratio.

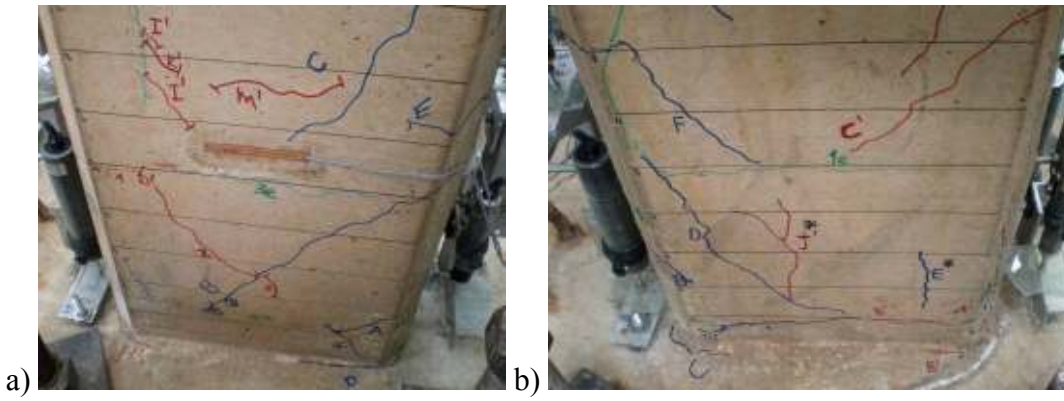


Figure E.73: a) North, and b) South view of LS-X12 after -1.5% drift ratio.

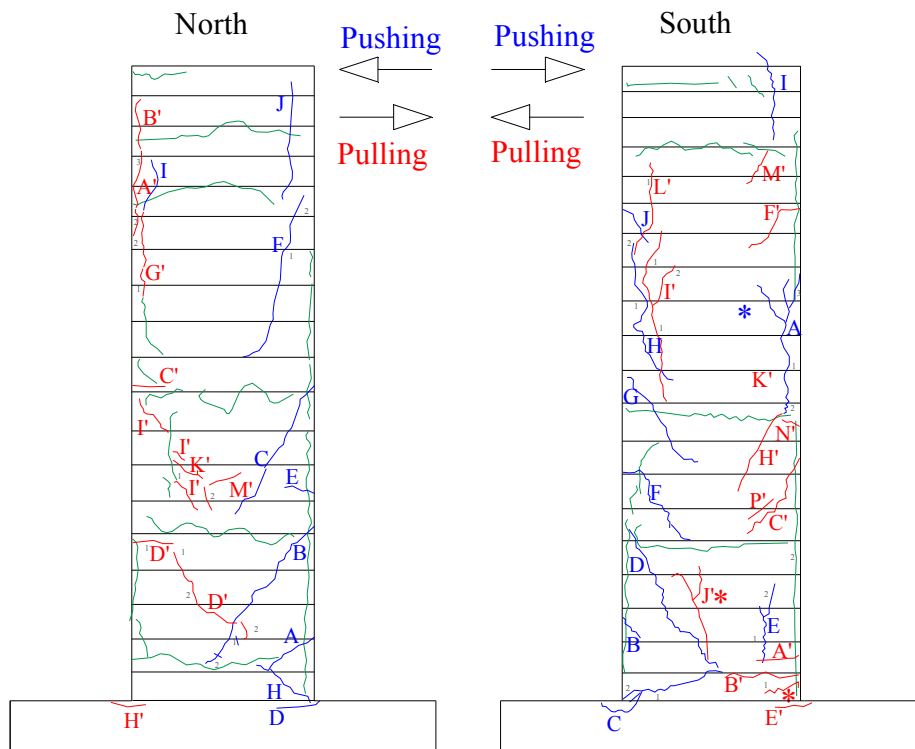


Figure E.74: Crack pattern of LS-X12 after -1.5% drift ratio.

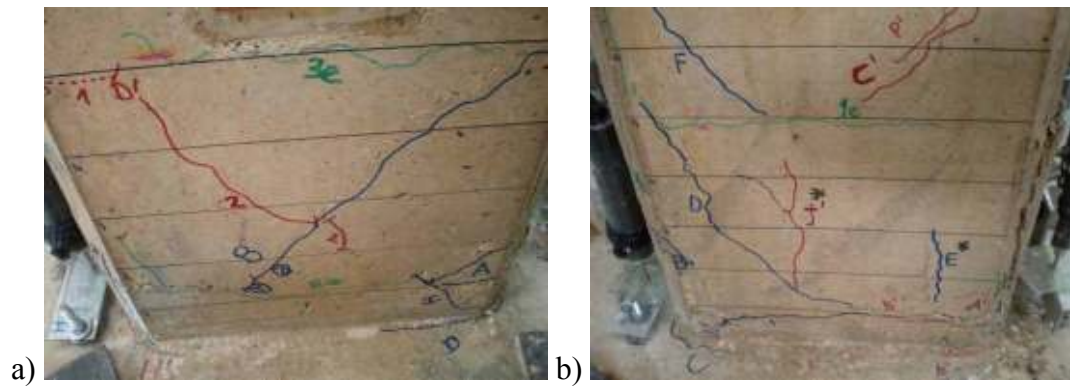


Figure E.75: a) North, and b) South view of LS-X12 after -2% drift ratio.

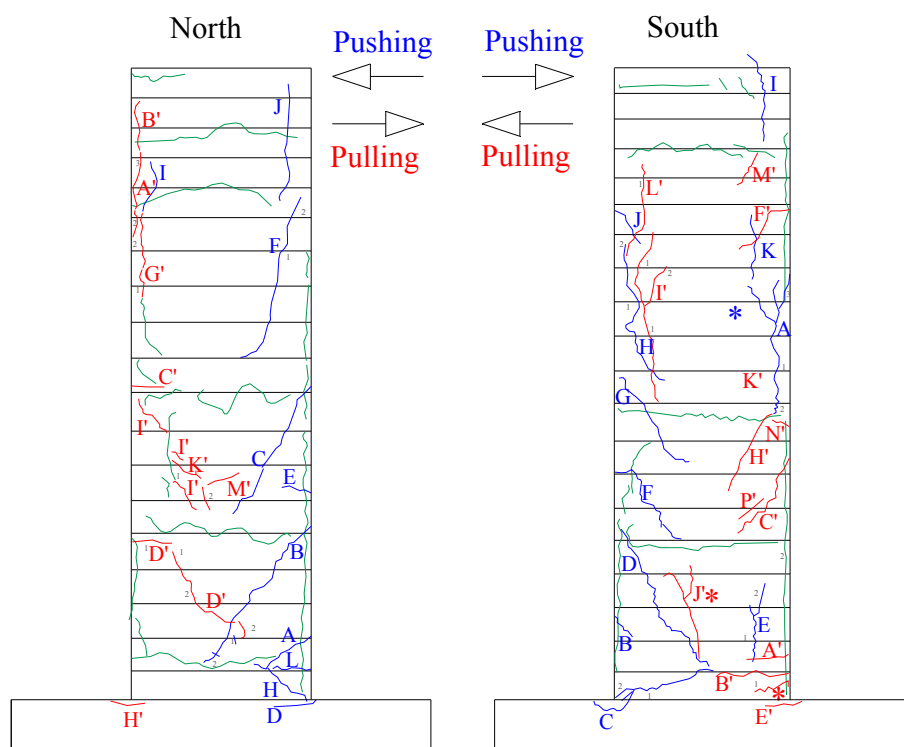


Figure E.76: Crack pattern of LS-X12 after -2% drift ratio.

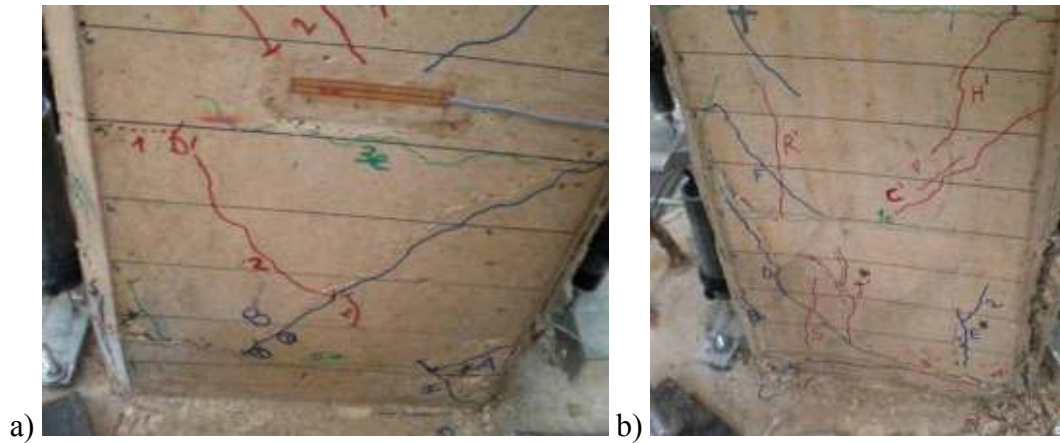


Figure E.77: a) North, and b) South view of LS-X12 after -2.5% drift ratio.

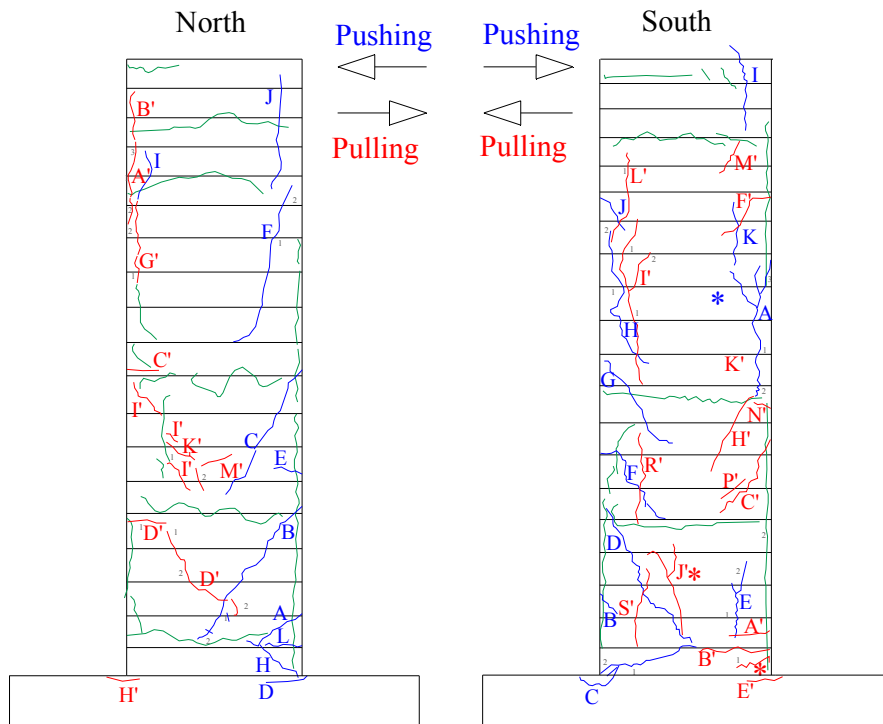


Figure E.78: Crack pattern of LS-X12 after -2.5% drift ratio.

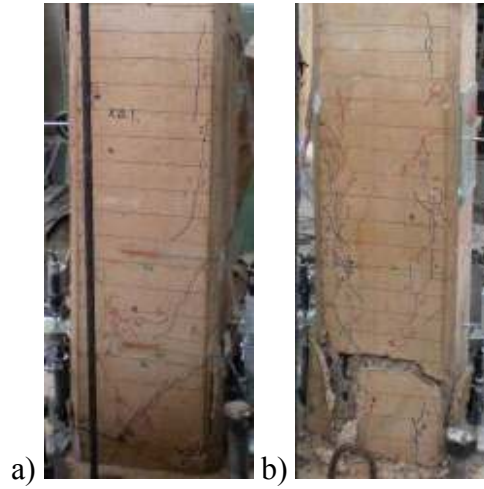


Figure E.79: a) North, and b) South view of LS-X12 after -3% drift ratio.

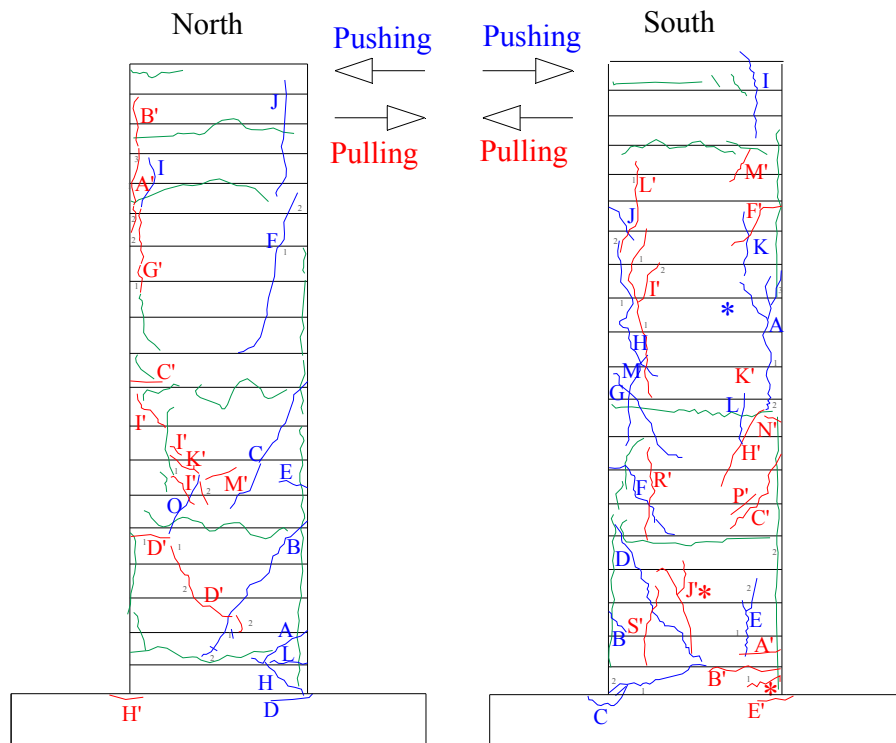


Figure E.80: Crack pattern of LS-X12 after -3% drift ratio.

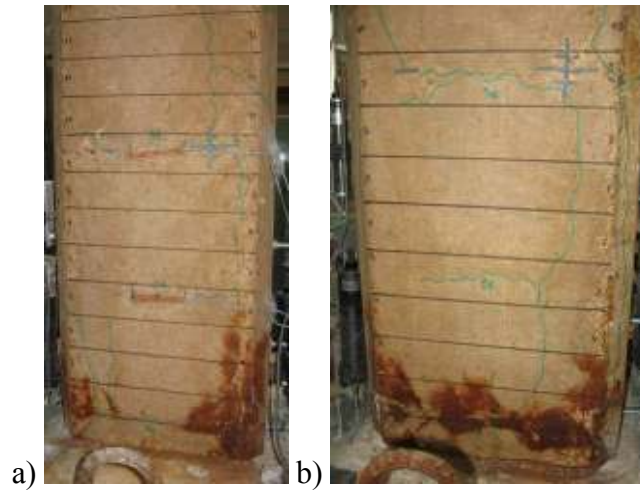


Figure E.81: a) North, and b) South view of LS-X21 after -0.1% drift ratio.

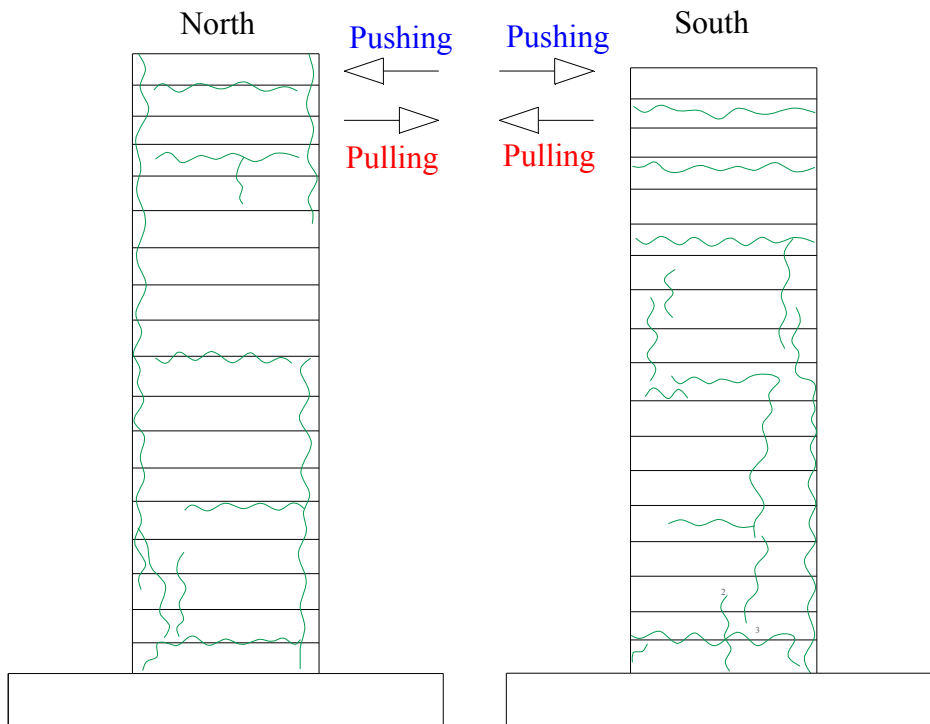


Figure E.82: Crack pattern of LS-X21 after -0.1% drift ratio.

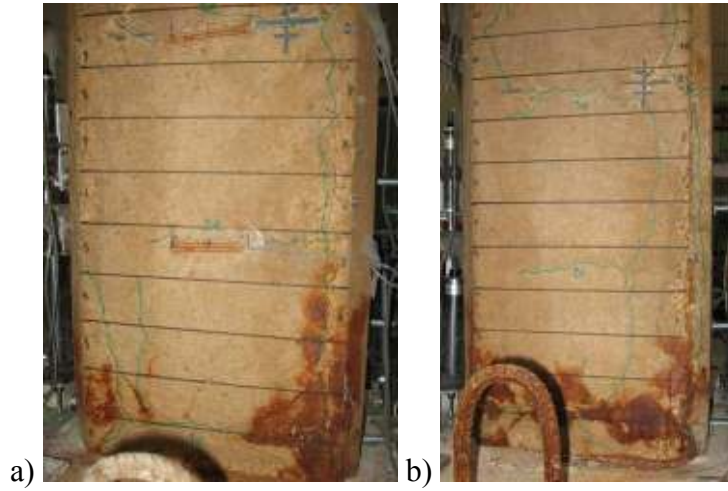


Figure E.83: a) North, and b) South view of LS-X21 after -0.25% drift ratio.

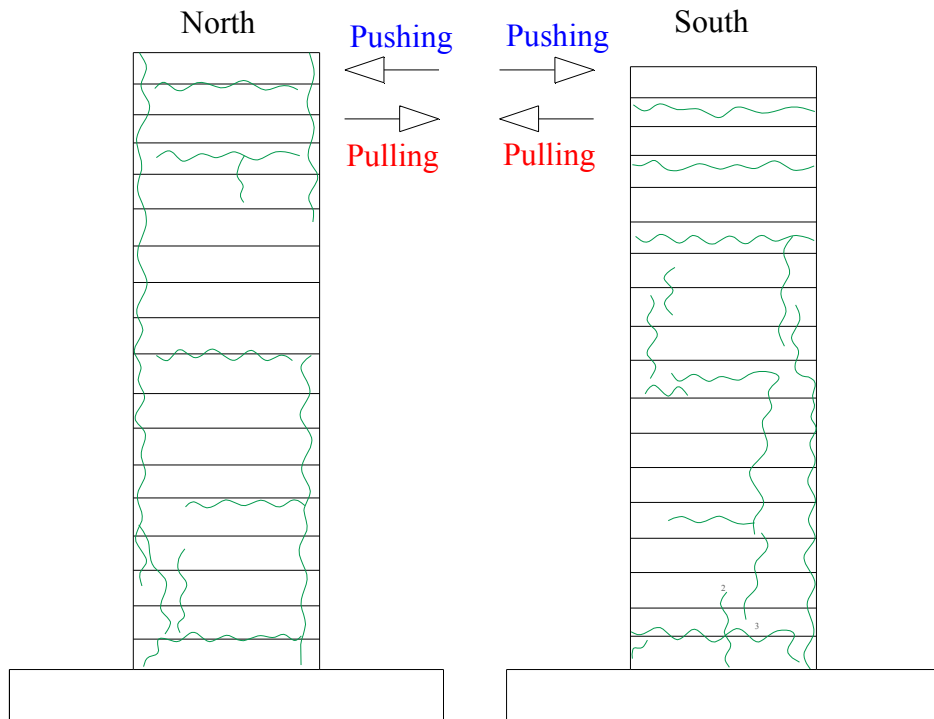


Figure E.84: Crack pattern of LS-X21 after -0.25% drift ratio.

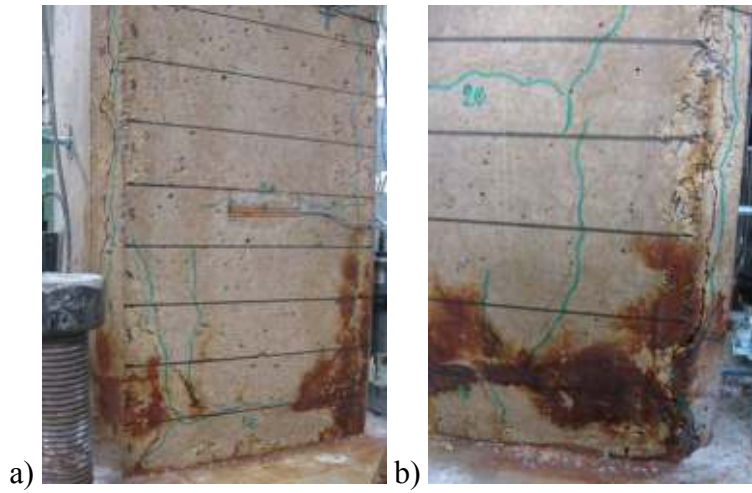


Figure E.85: a) North, and b) South view of LS-X21 after -0.5% drift ratio.

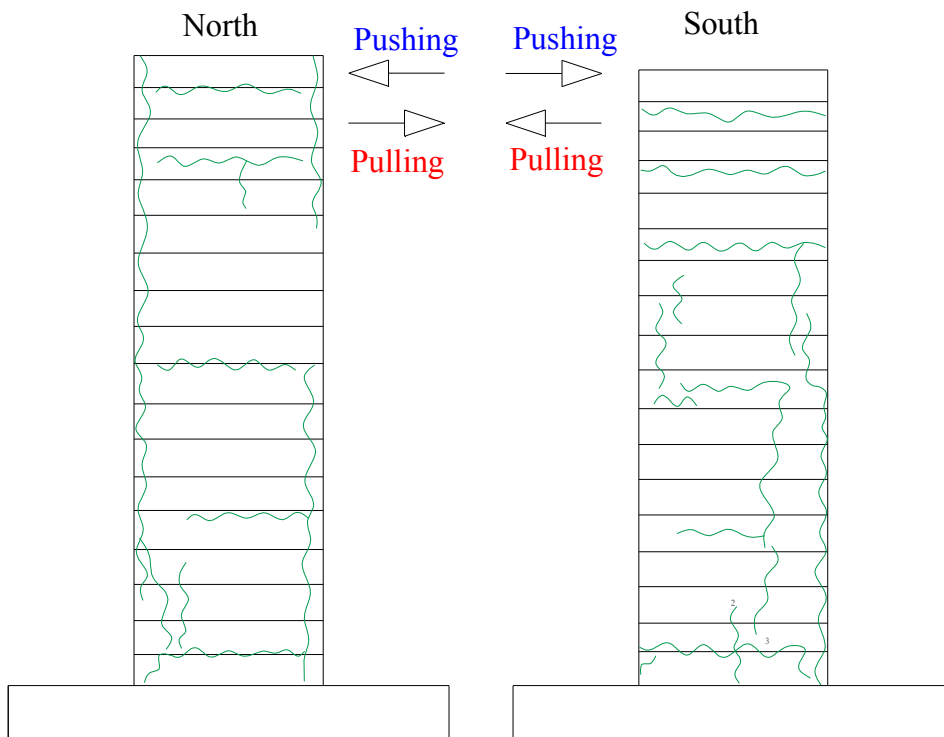


Figure E.86: Crack pattern of LS-X21 after -0.5% drift ratio.

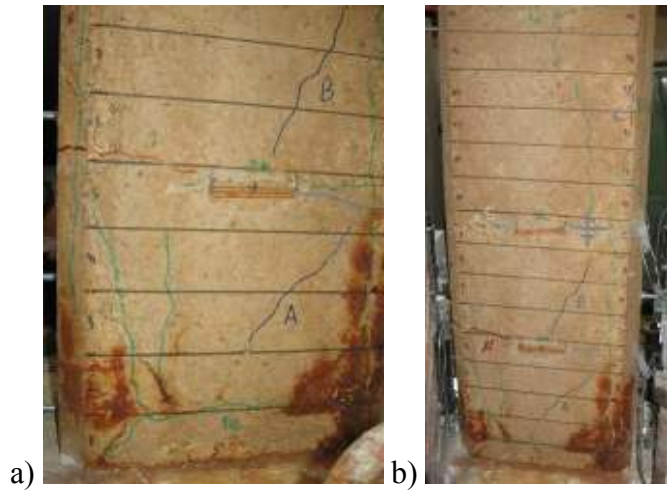


Figure E.87: a) North, and b) South view of LS-X21 after -0.75% drift ratio.

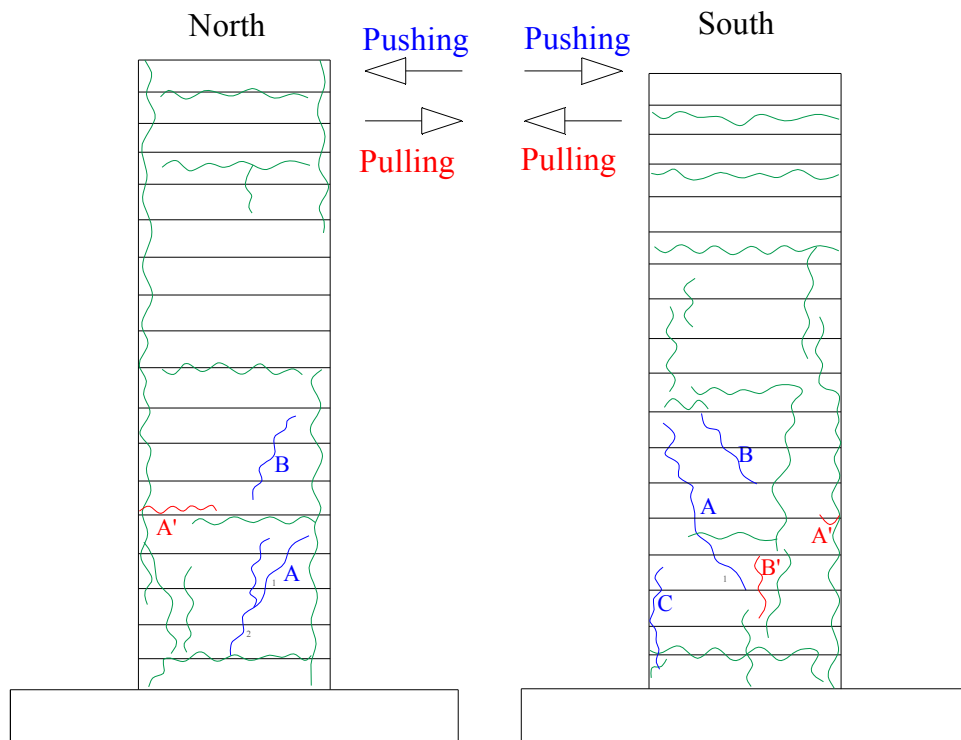


Figure E.88: Crack pattern of LS-X21 after -0.75% drift ratio.

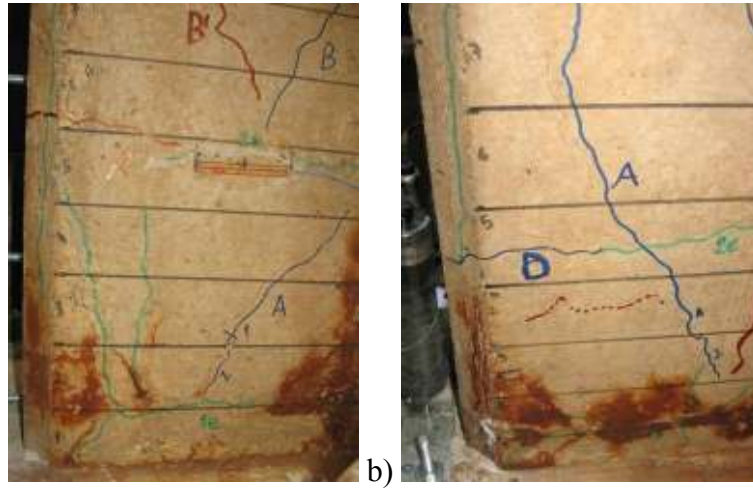


Figure E.89: a) North, and b) South view of LS-X21 after -1% drift ratio.

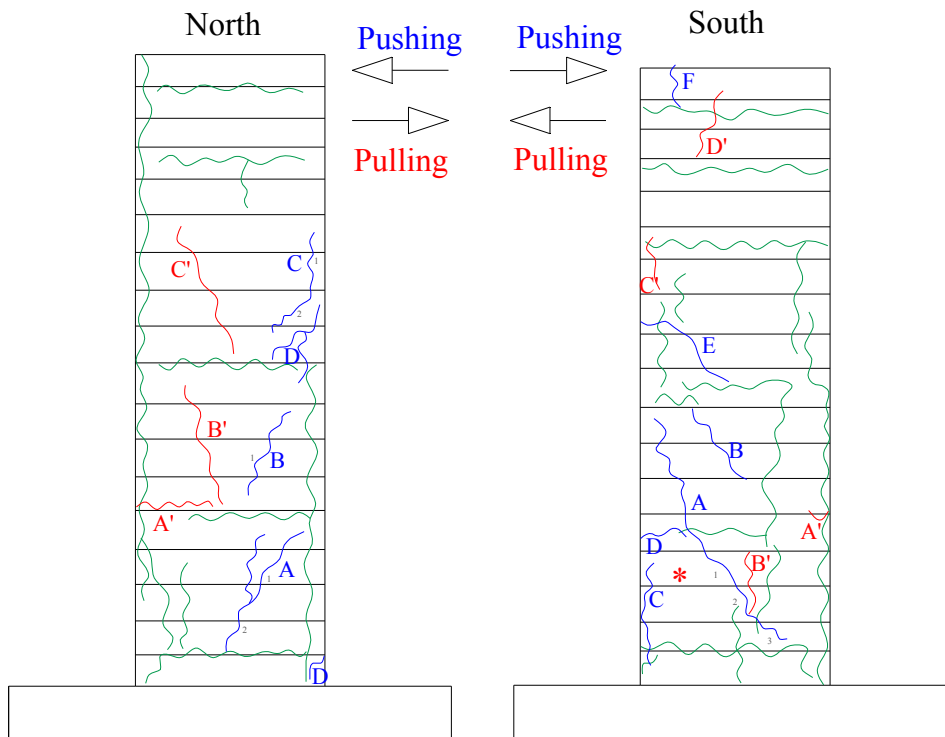


Figure E.90: Crack pattern of LS-X21 after -1% drift ratio.

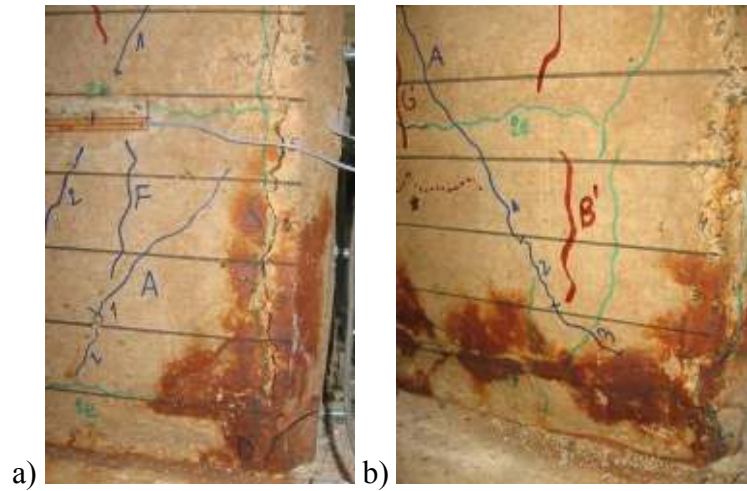


Figure E.91: (a) North, and (b) South view of LS-X21 after -1.5% drift ratio.

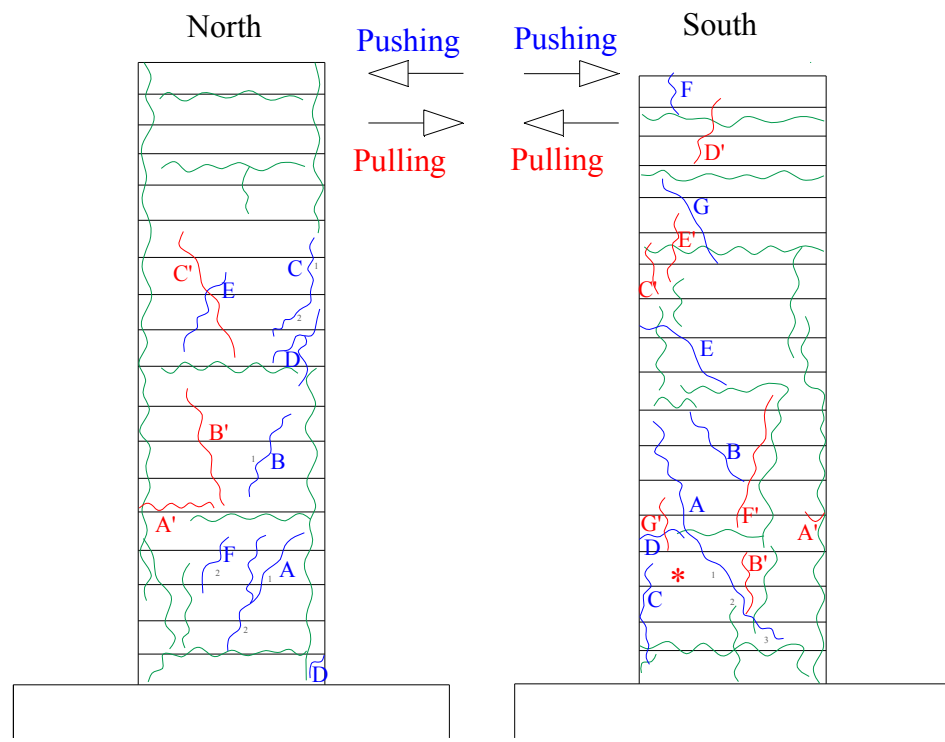


Figure E.92: Crack pattern of LS-X21 after -1.5% drift ratio.

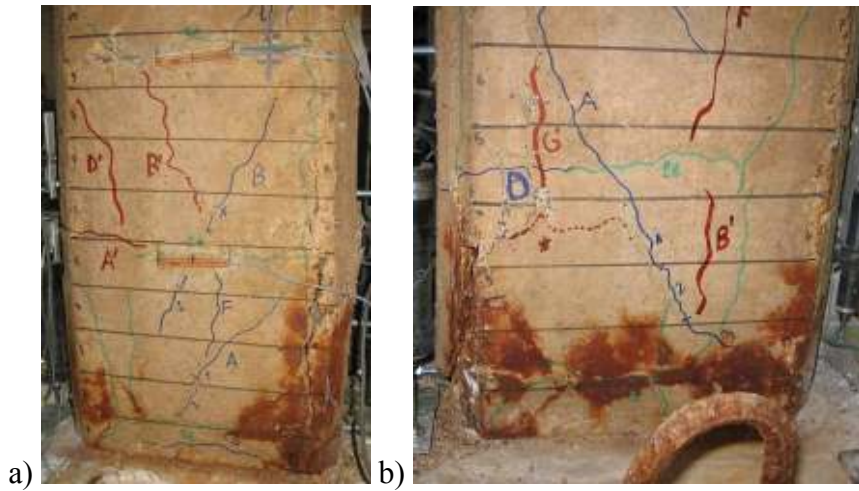


Figure E.93: a) North, and b) South view of LS-X21 after -2% drift ratio.

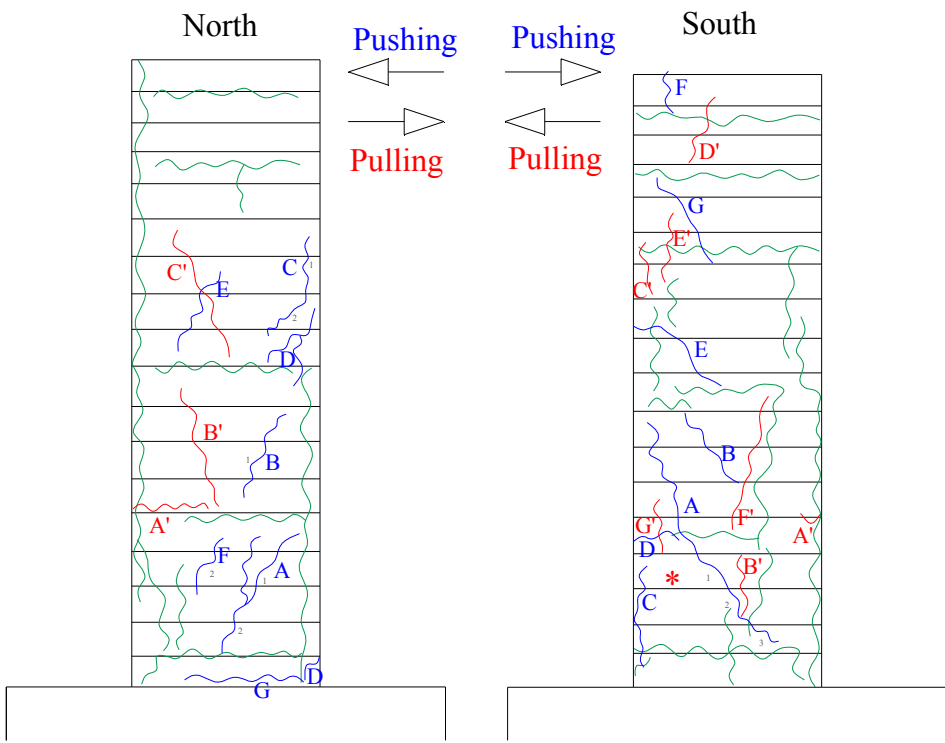


Figure E.94: Crack pattern of LS-X21 after -2% drift ratio.

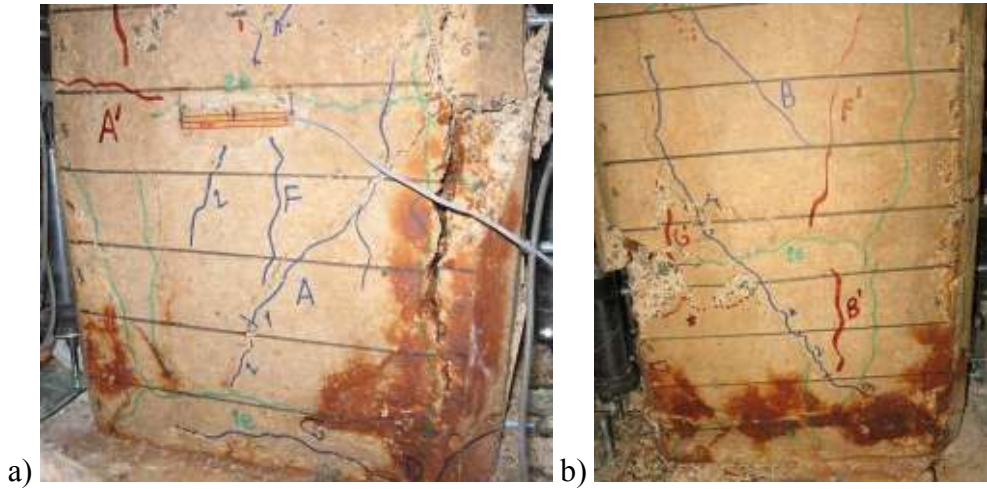


Figure E.95: a) North, and b) South view of LS-X21 after -2.5% drift ratio.

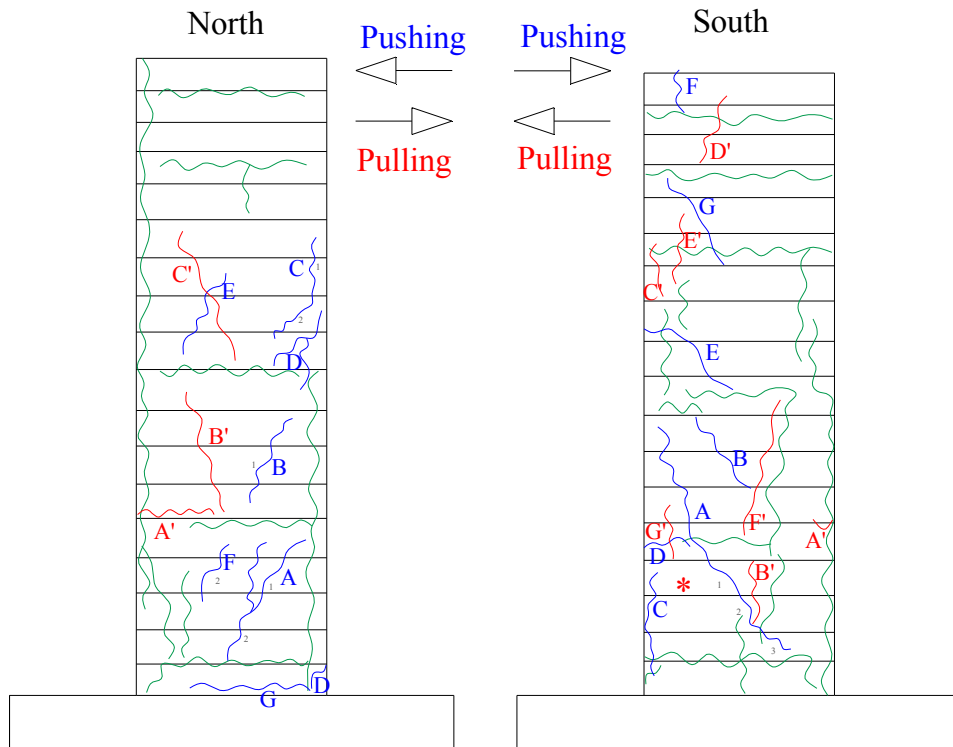


Figure E.96: Crack pattern of LS-X21 after -2.5% drift ratio.

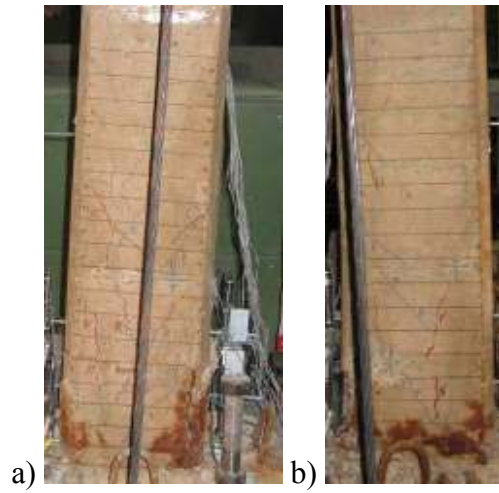


Figure E.97: a) North, and b) South view of LS-X21 after -3% drift ratio.

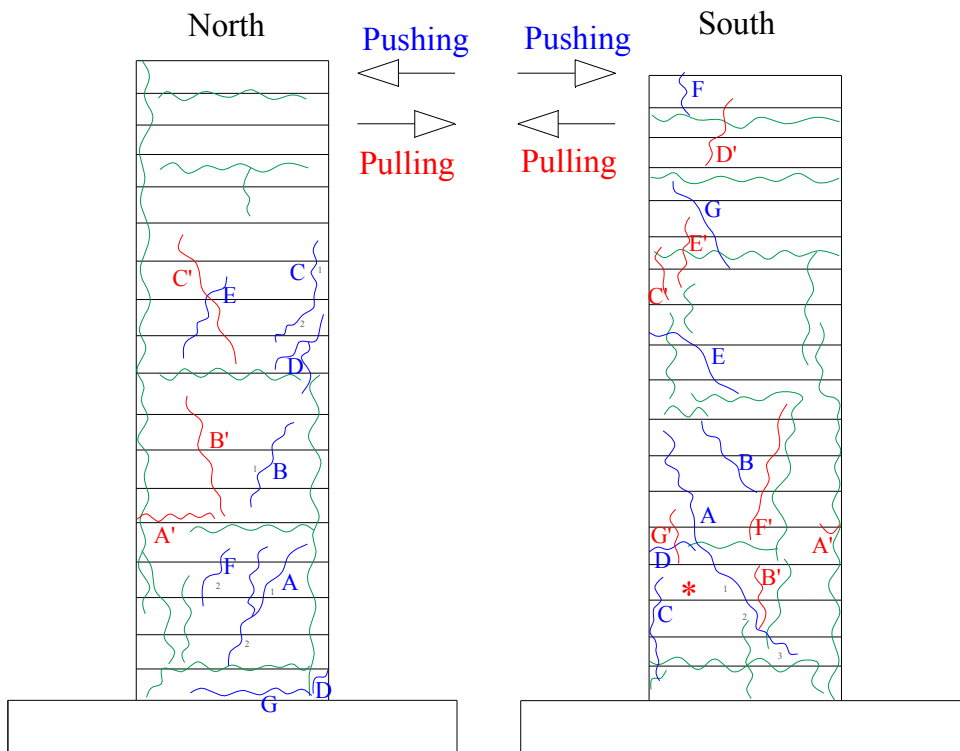


Figure E.98: Crack pattern of LS-X21 after -3% drift ratio.

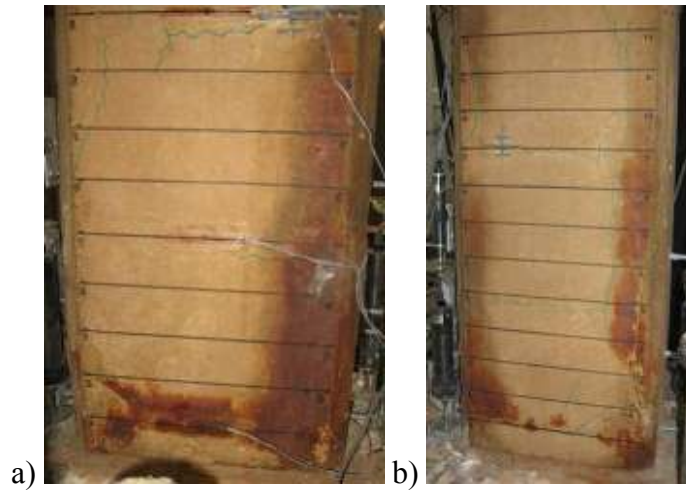


Figure E.99: a) North, and b) South view of LS-X28 after -0.1% drift ratio.

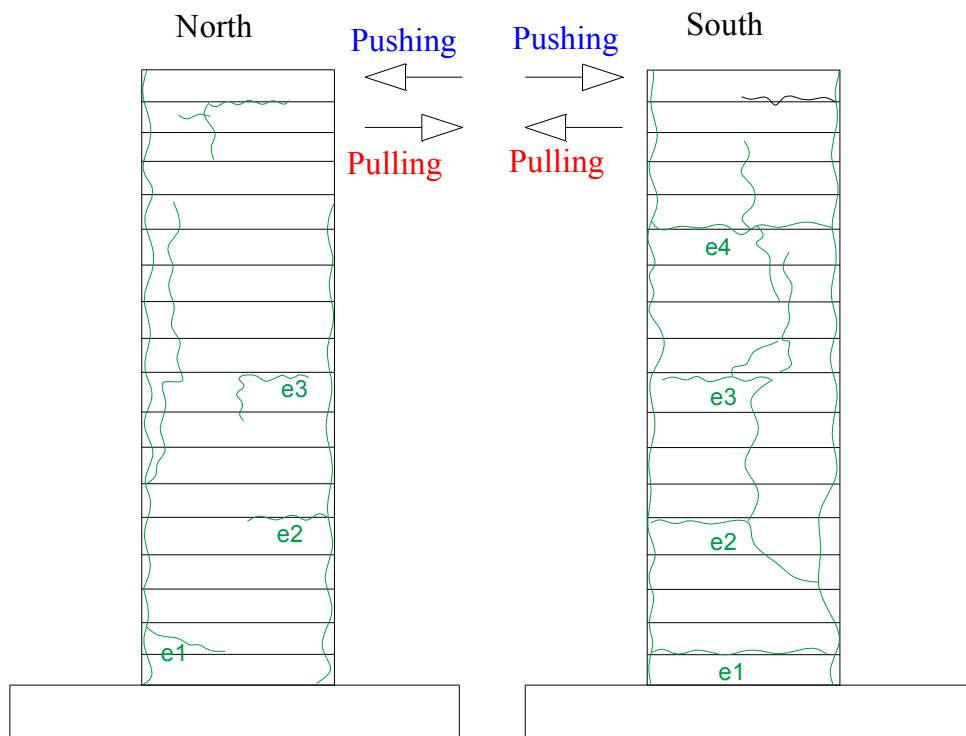


Figure E.100: Crack pattern of LS-X28 after -0.1% drift ratio.

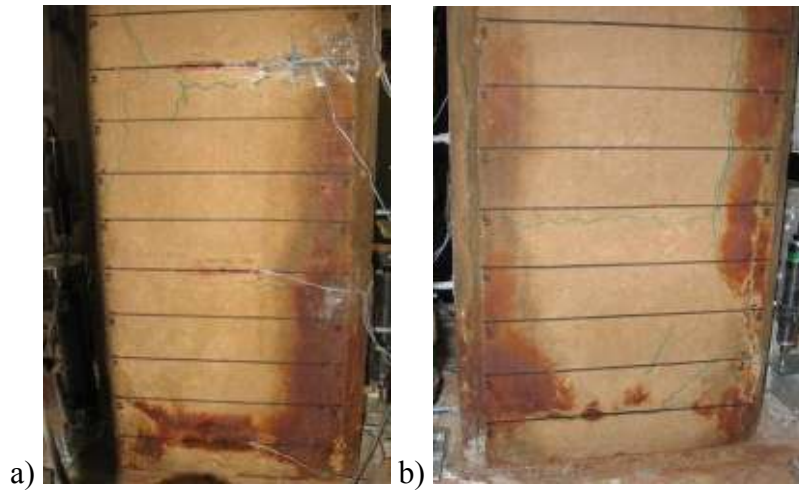


Figure E.101: a) North, and b) South view of LS-X28 after -0.25% drift ratio.

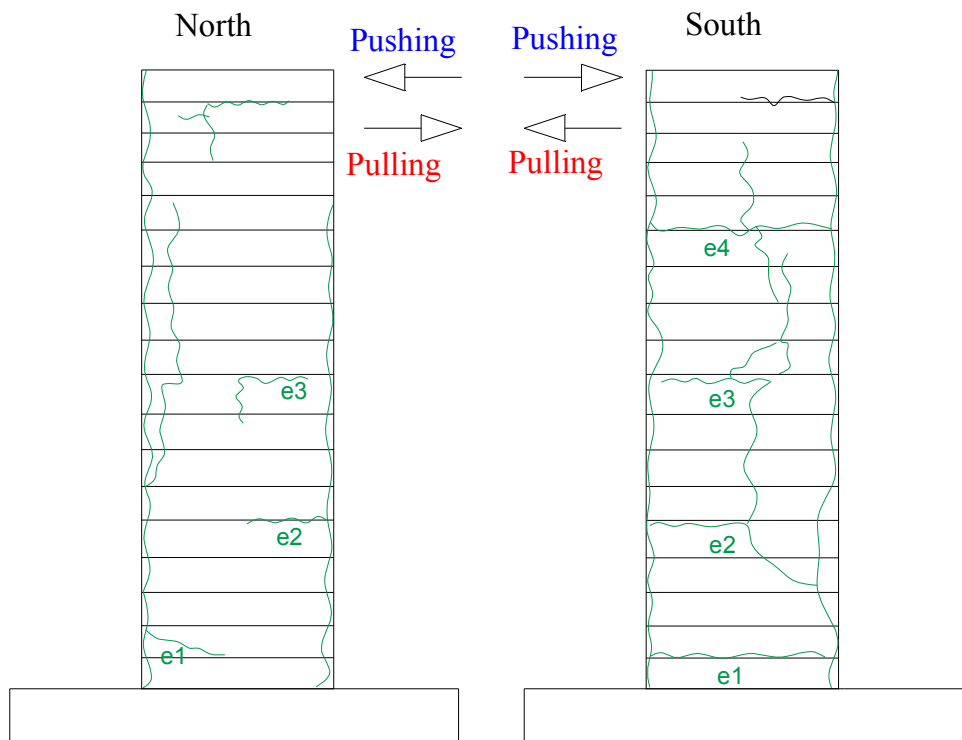


Figure E.102: Crack pattern of LS-X28 after -0.25% drift ratio.

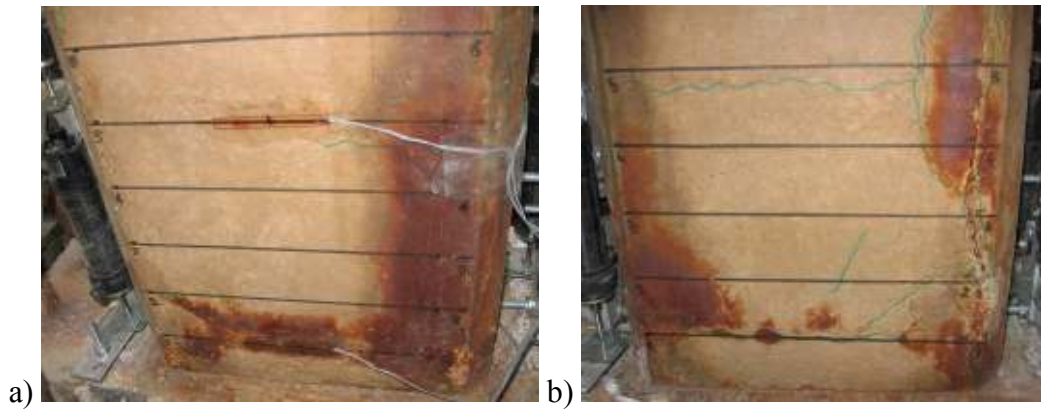


Figure E.103: a) North, and b) South view of LS-X28 after -0.5% drift ratio.

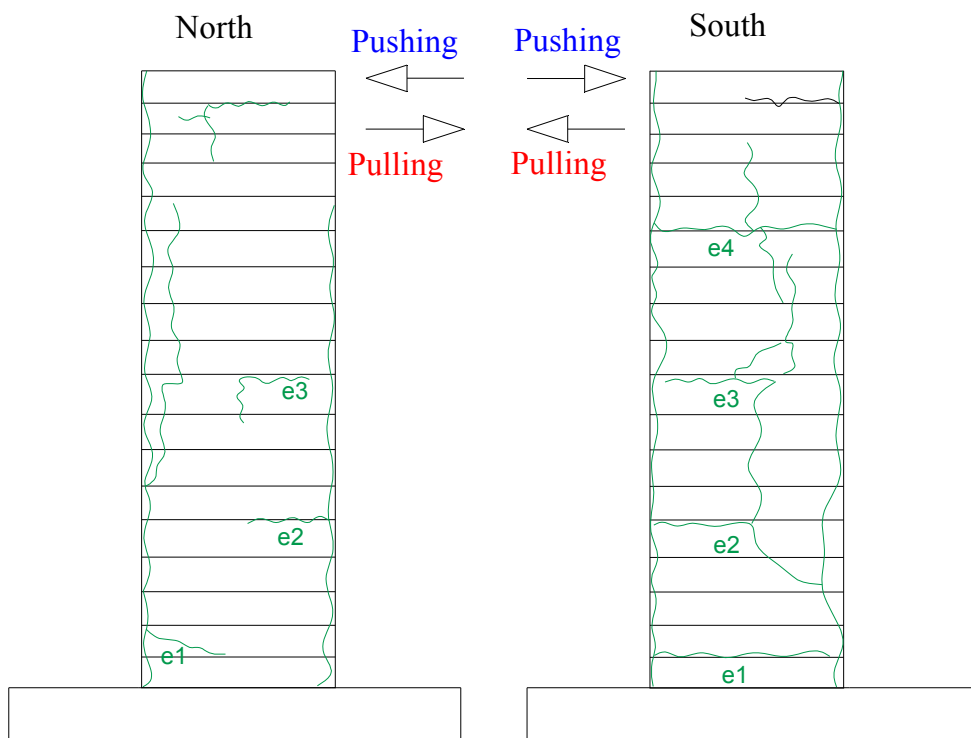


Figure E.104: Crack pattern of LS-X28 after -0.5% drift ratio.

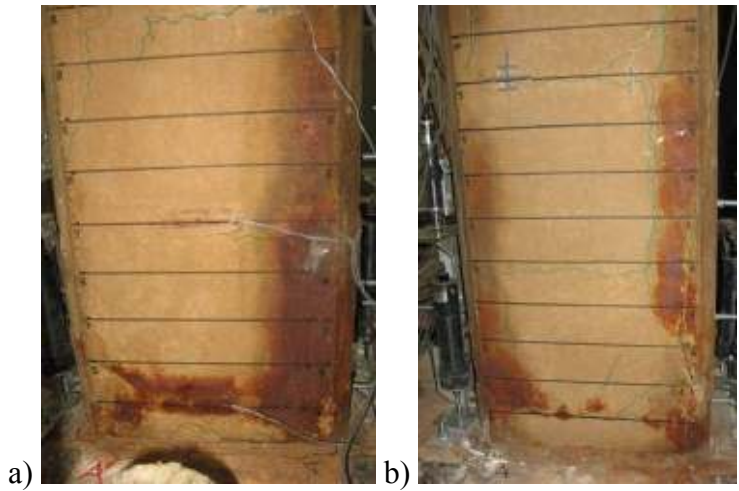


Figure E.105: a) North, and b) South view of LS-X28 after -0.75% drift ratio.

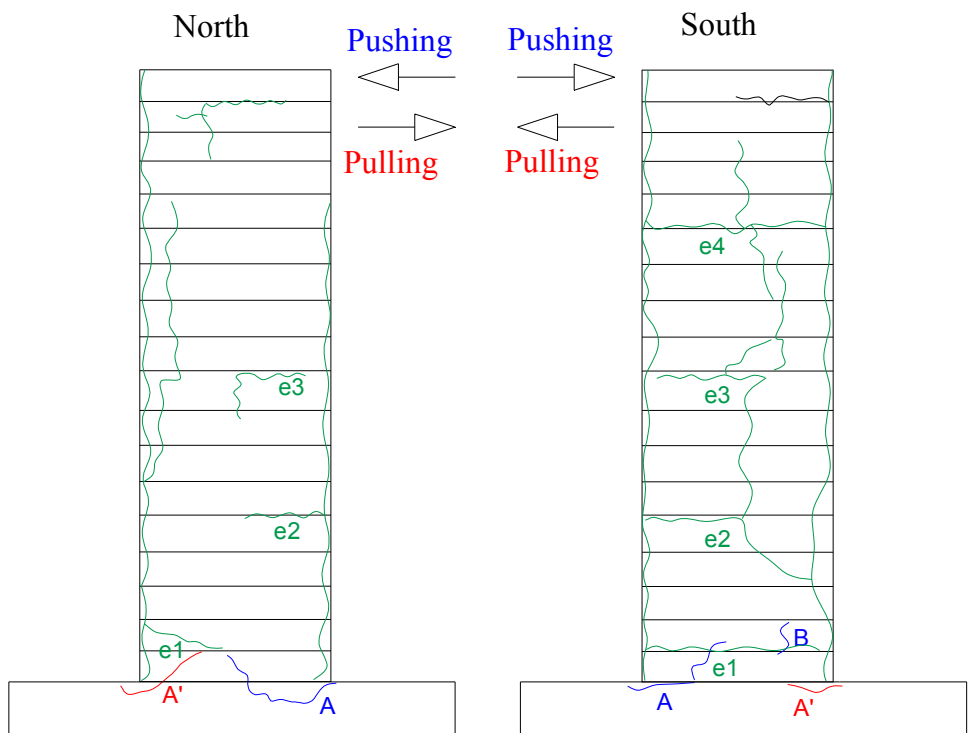


Figure E.106: Crack pattern of LS-X28 after -0.75% drift ratio.

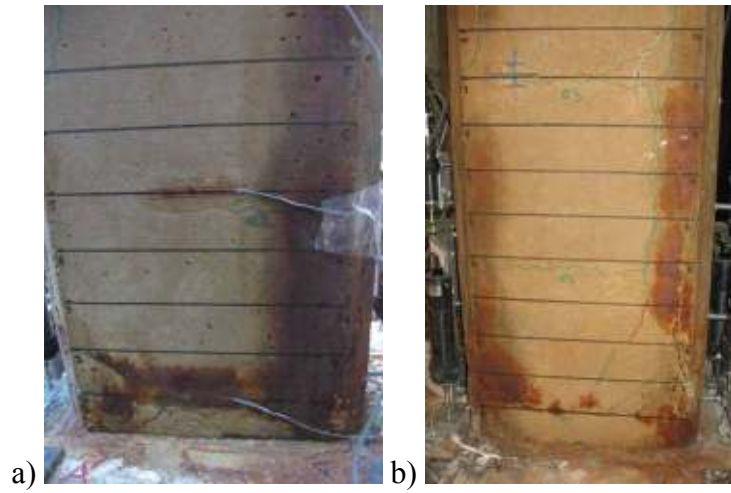


Figure E.107: a) North, and b) South view of LS-X28 after -1% drift ratio.

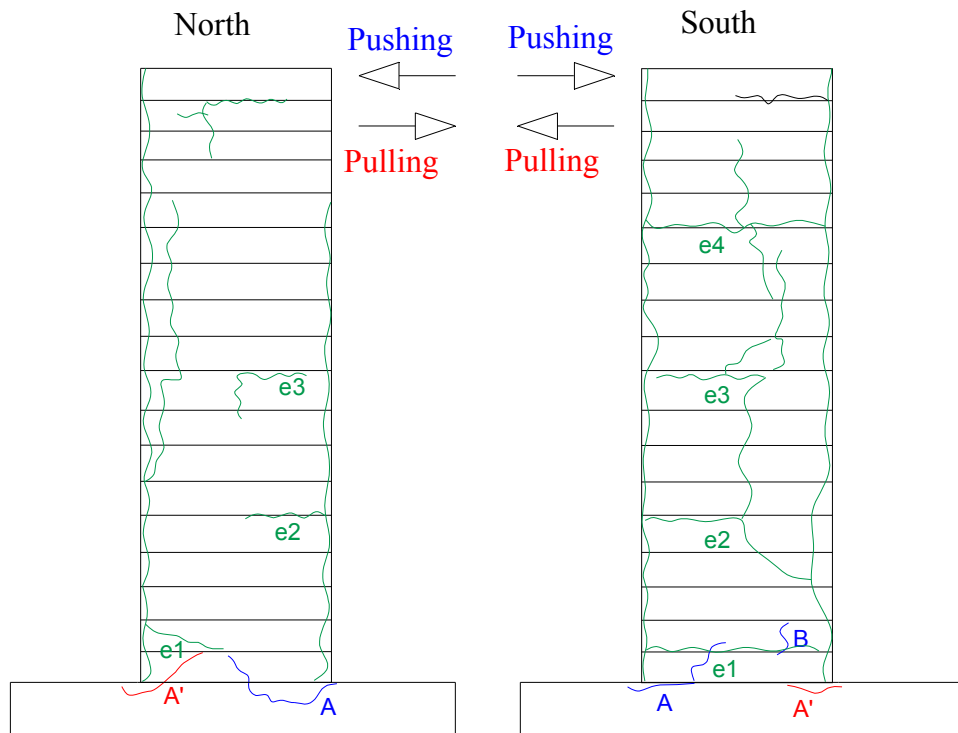


Figure E.108: Crack pattern of LS-X28 after -1% drift ratio.

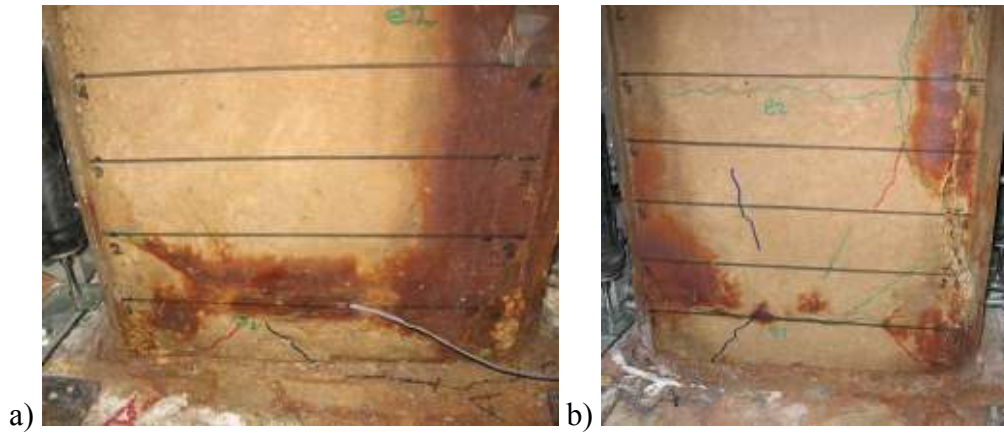


Figure E.109: a) North, and b) South view of LS-X28 after -1.5% drift ratio.

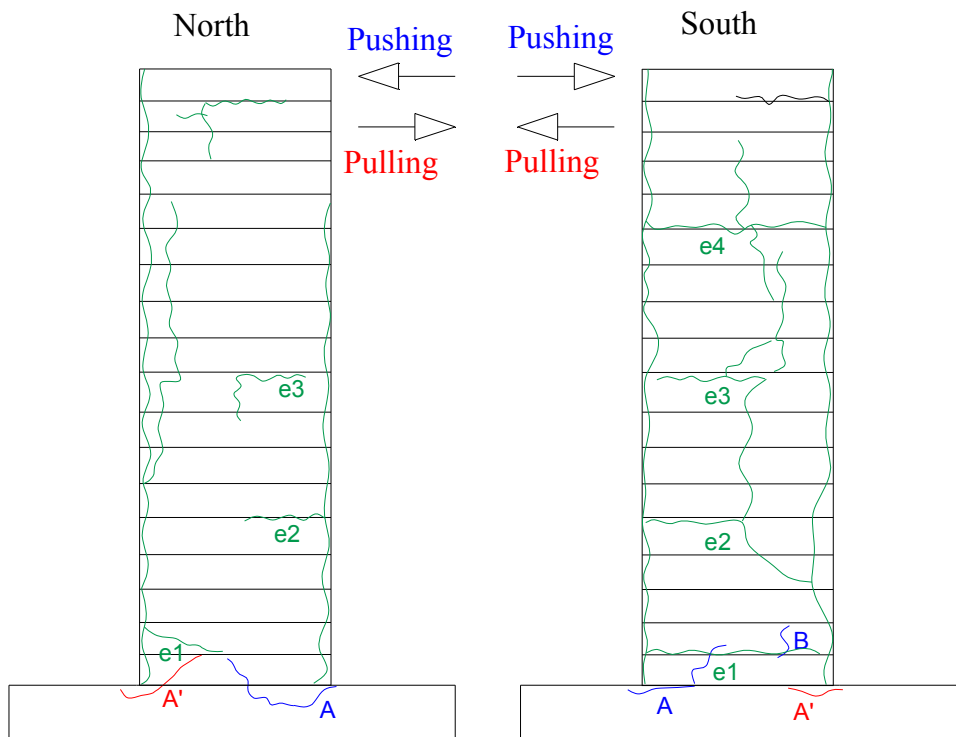


Figure E.110: Crack pattern of LS-X28 after -1.5% drift ratio.

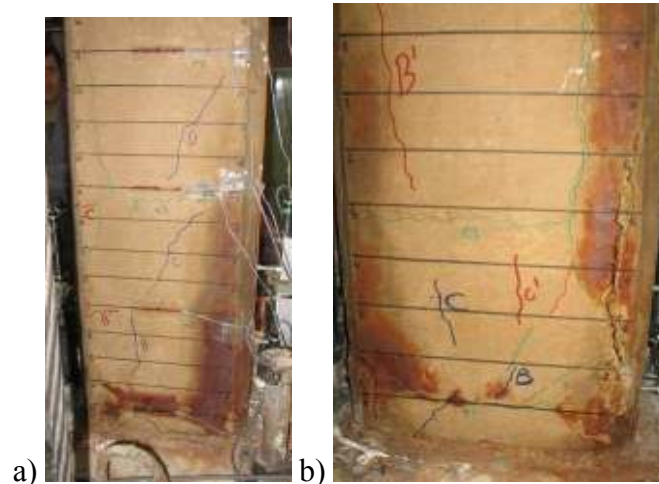


Figure E.111: a) North, and b) South view of LS-X28 after -2% drift ratio.

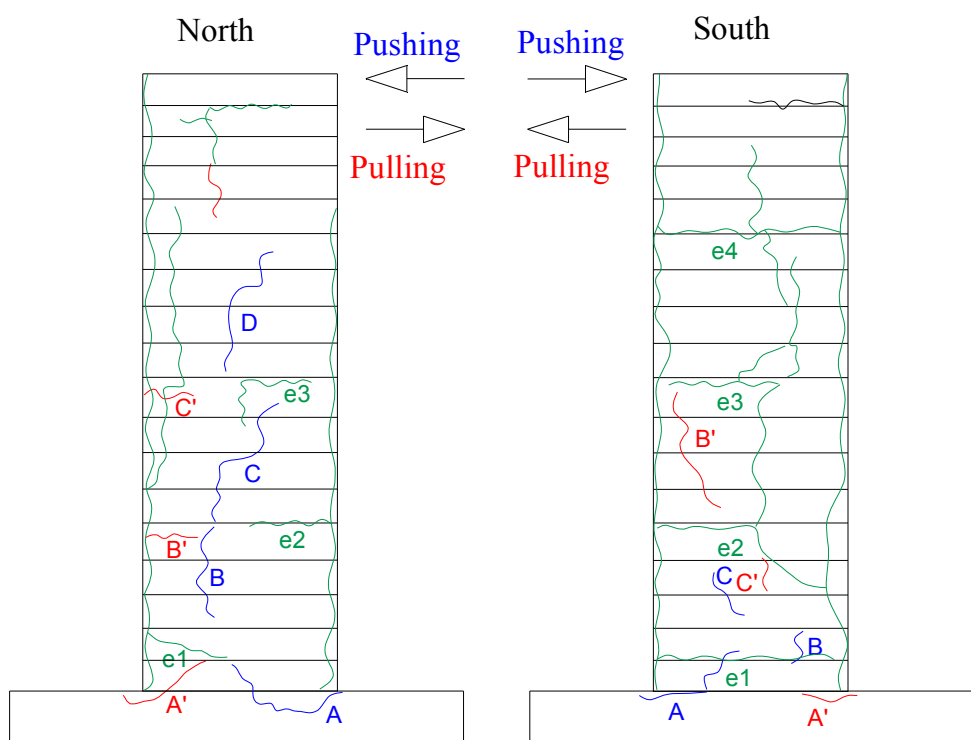


Figure E.112: Crack pattern of LS-X28 after -2% drift ratio.

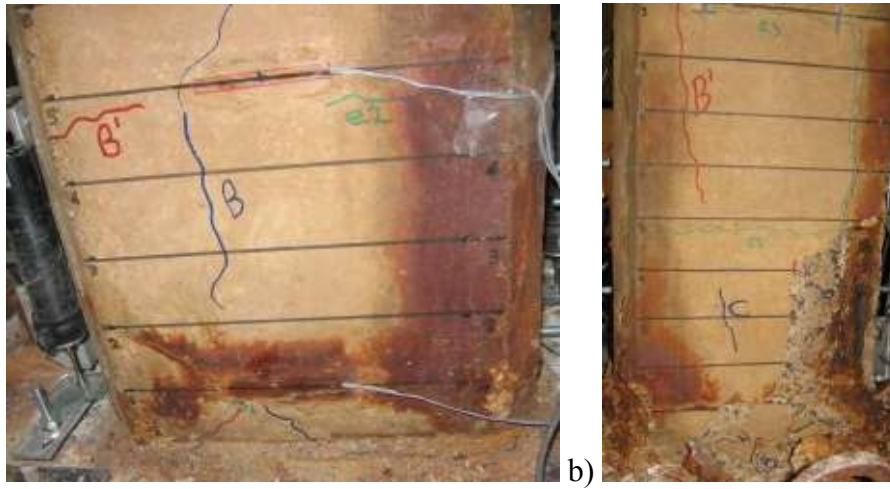


Figure E.113: a) North, and b) South view of LS-X28 after -2.5% drift ratio.

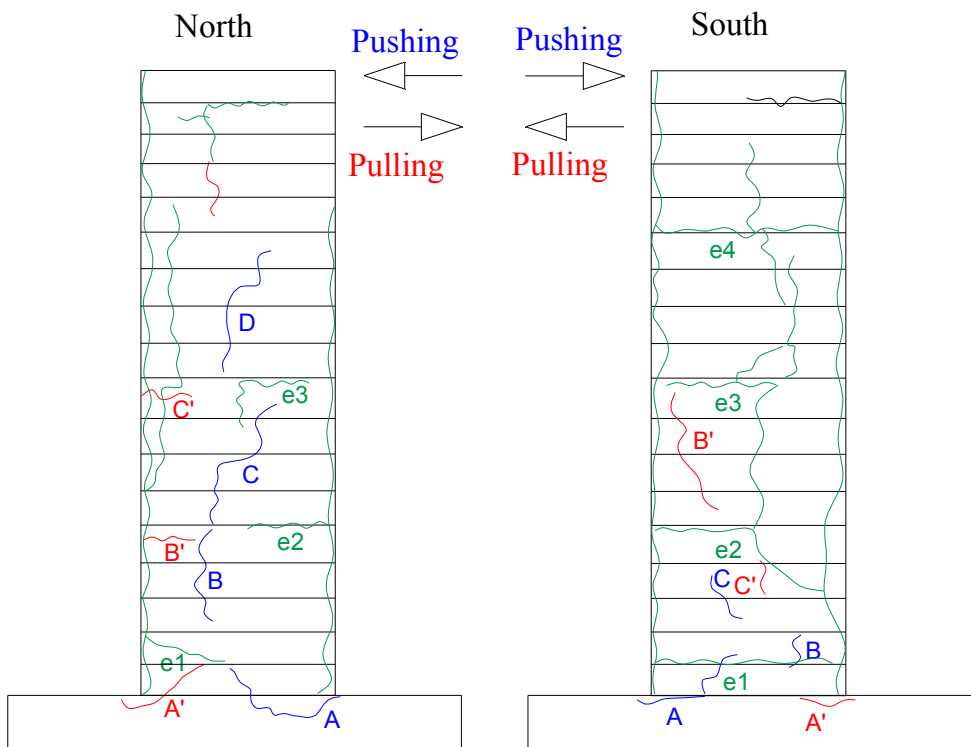


Figure E.114: Crack pattern of LS-X28 after -2.5% drift ratio.

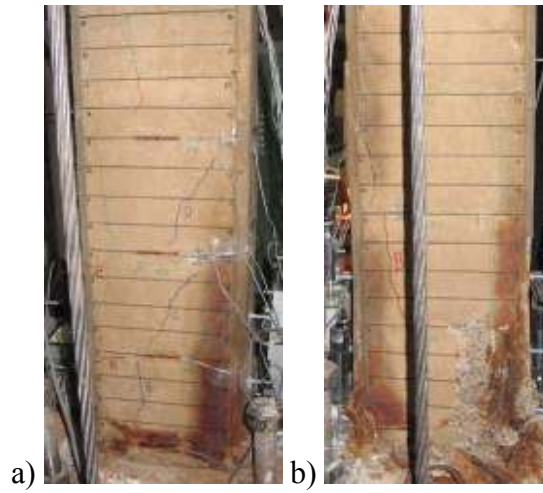


Figure E.115: a) North, and b) South view of LS-X28 after -3% drift ratio.

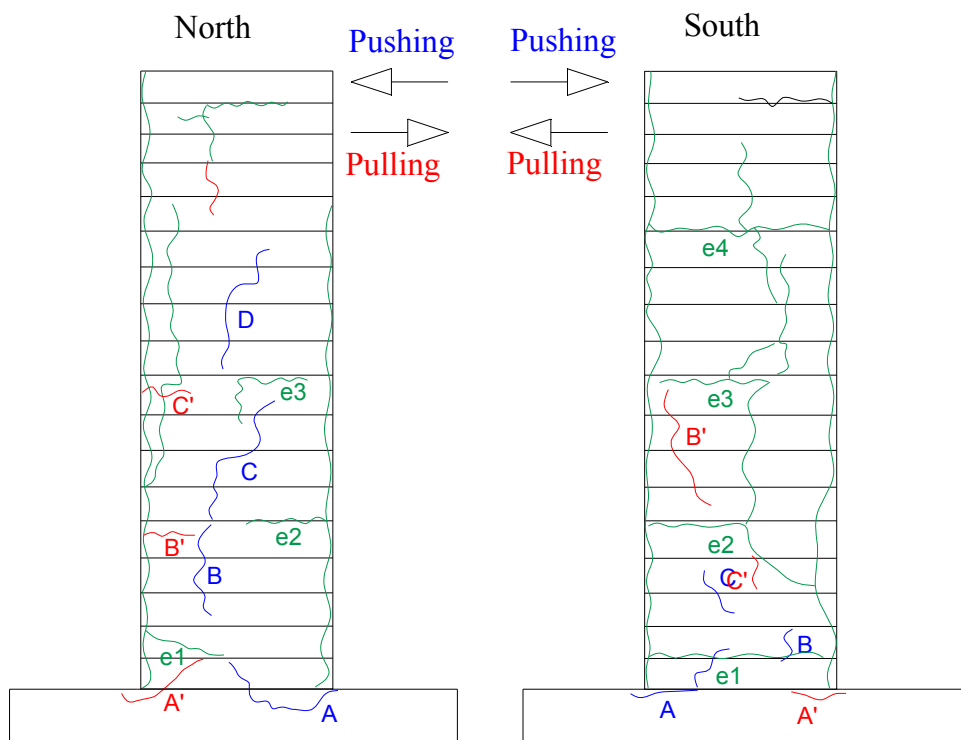


Figure E.116: Crack pattern of LS-X28 after -3% drift ratio.

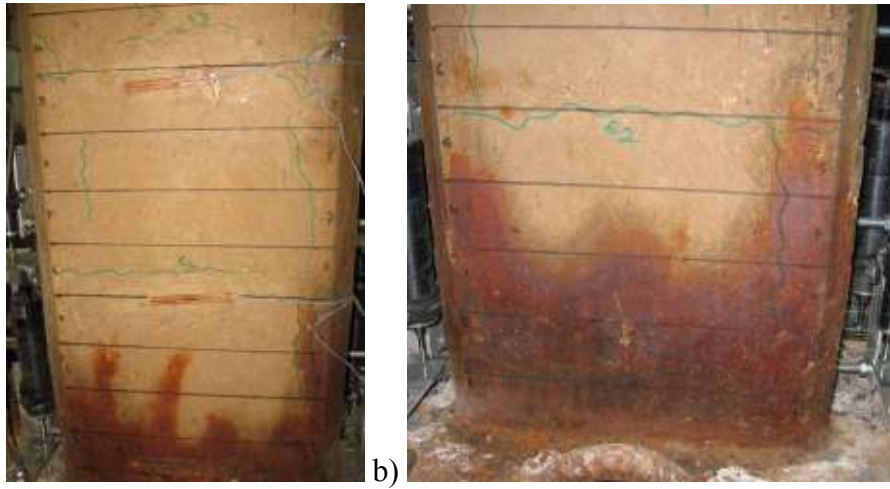


Figure E.117: a) North, and b) South view of LS-X19-H after -0.1% drift ratio.

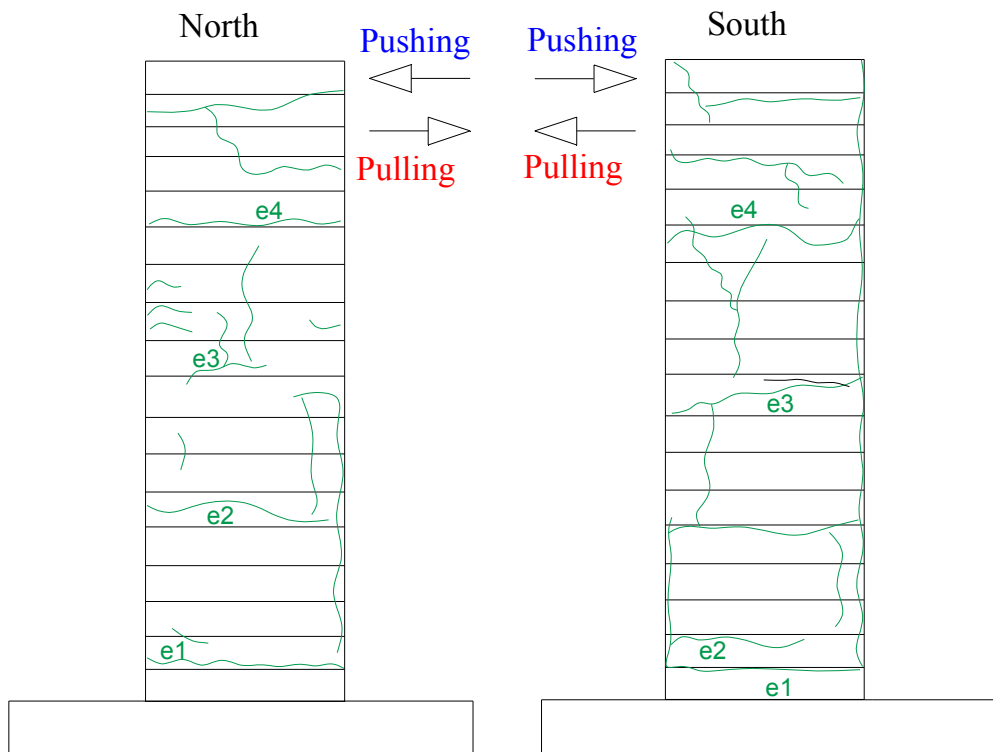


Figure E.118: Crack pattern of LS-X19-H after -0.1% drift ratio.

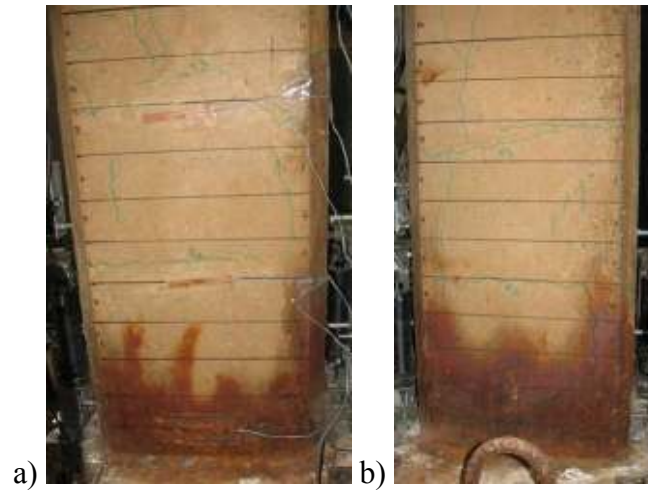


Figure E.119: a) North, and b) South view of LS-X19-H after -0.25% drift ratio.

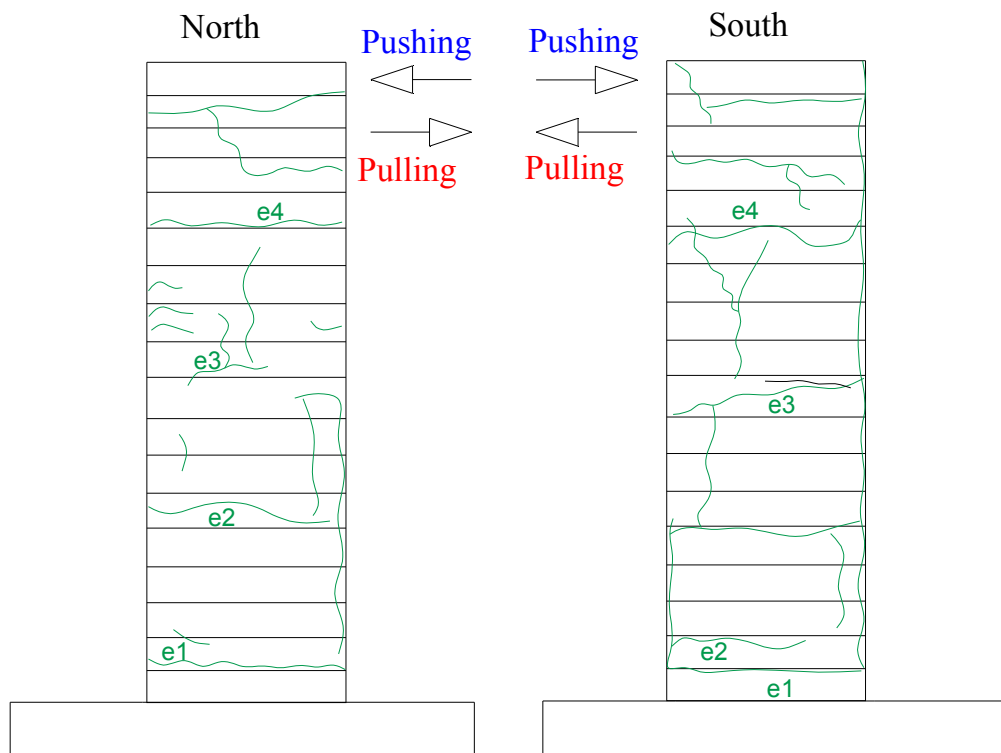


Figure E.120: Crack pattern of LS-X19-H after -0.25% drift ratio.

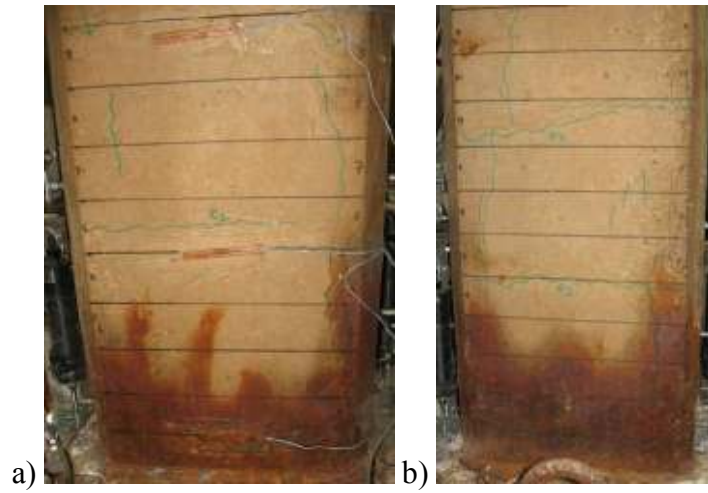


Figure E.121: a) North, and b) South view of LS-X19-H after -0.5% drift ratio.

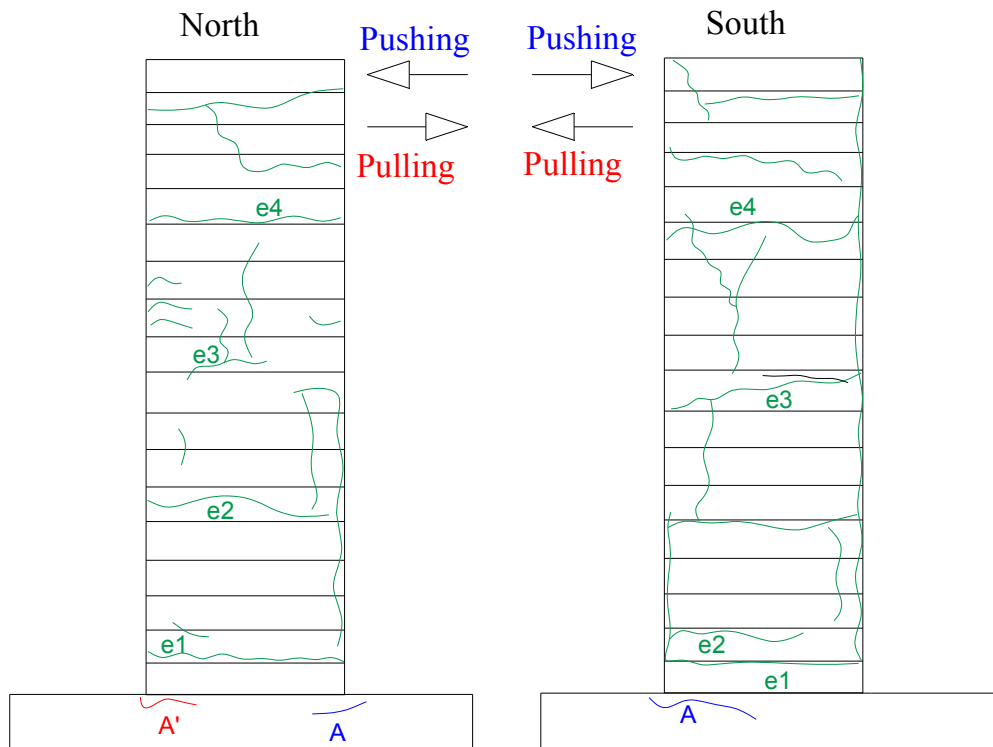


Figure E.122: Crack pattern of LS-X19-H after -0.5% drift ratio.

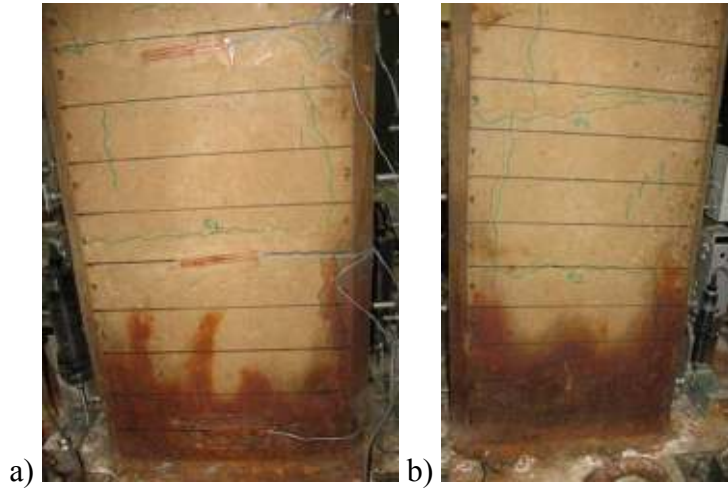


Figure E.123: a) North, and b) South view of LS-X19-H after -0.75% drift ratio.

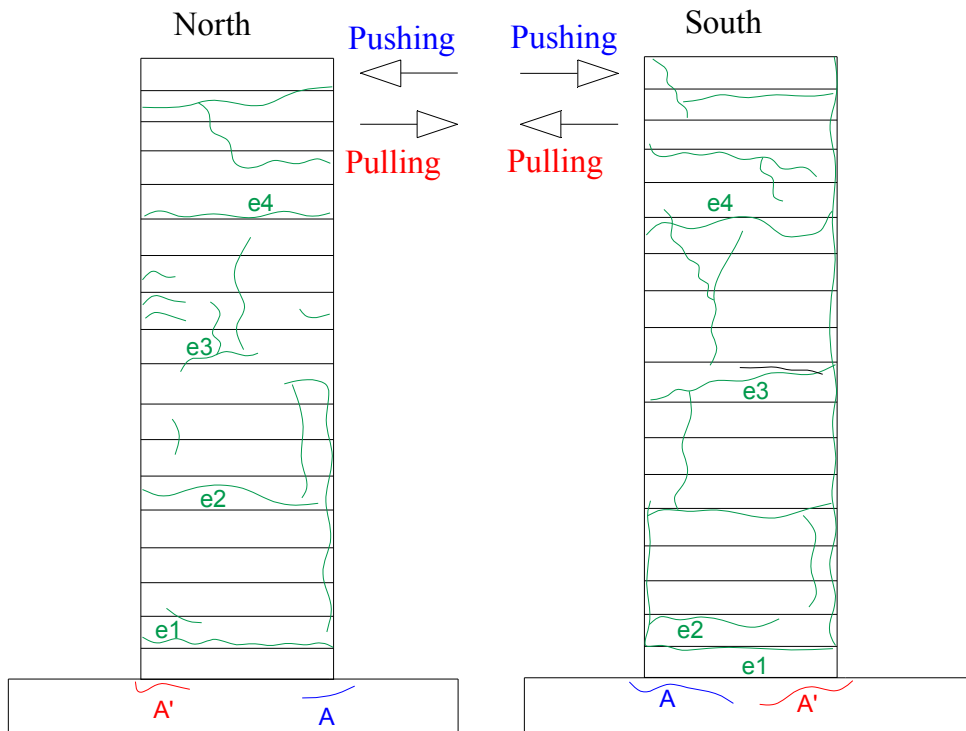


Figure E.124: Crack pattern of LS-X19-H after -0.75% drift ratio.

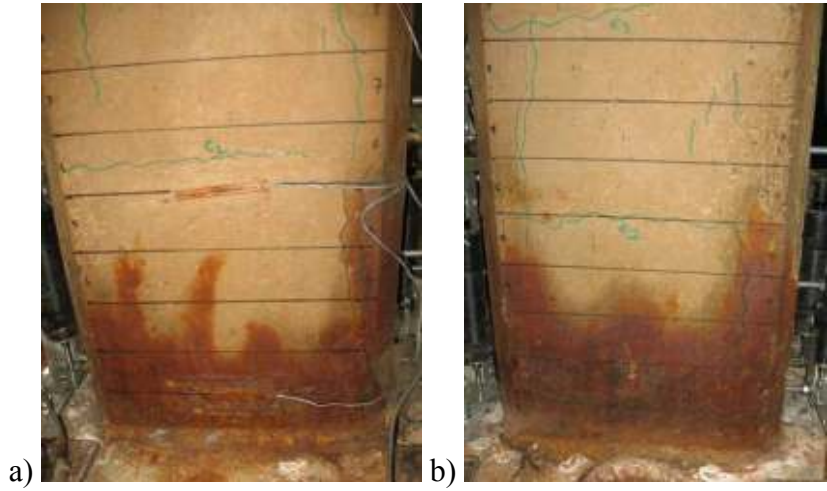


Figure E.125: a) North, and b) South view of LS-X19-H after -1% drift ratio.

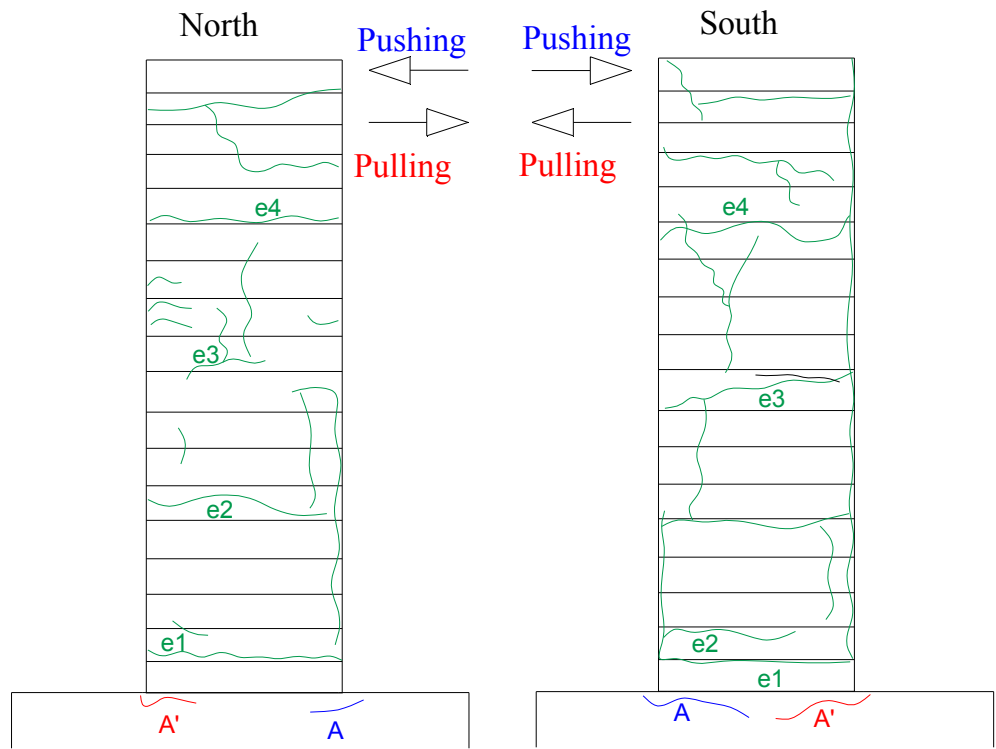


Figure E.126: Crack pattern of LS-X19-H after -1% drift ratio.

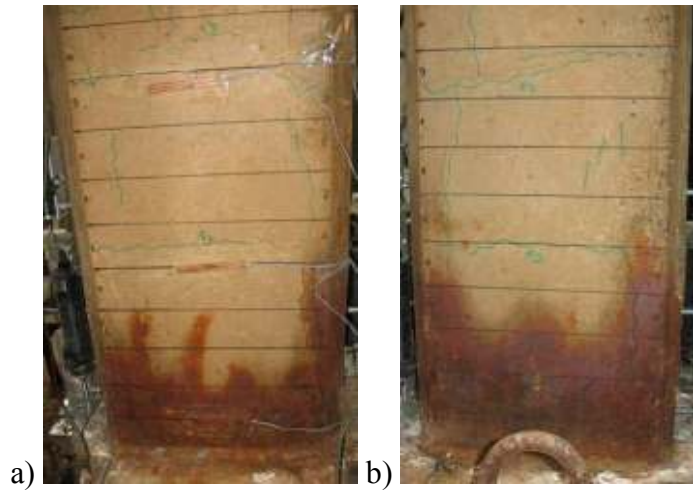


Figure E.127: a) North, and b) South view of LS-X19-H after -1.5% drift ratio.

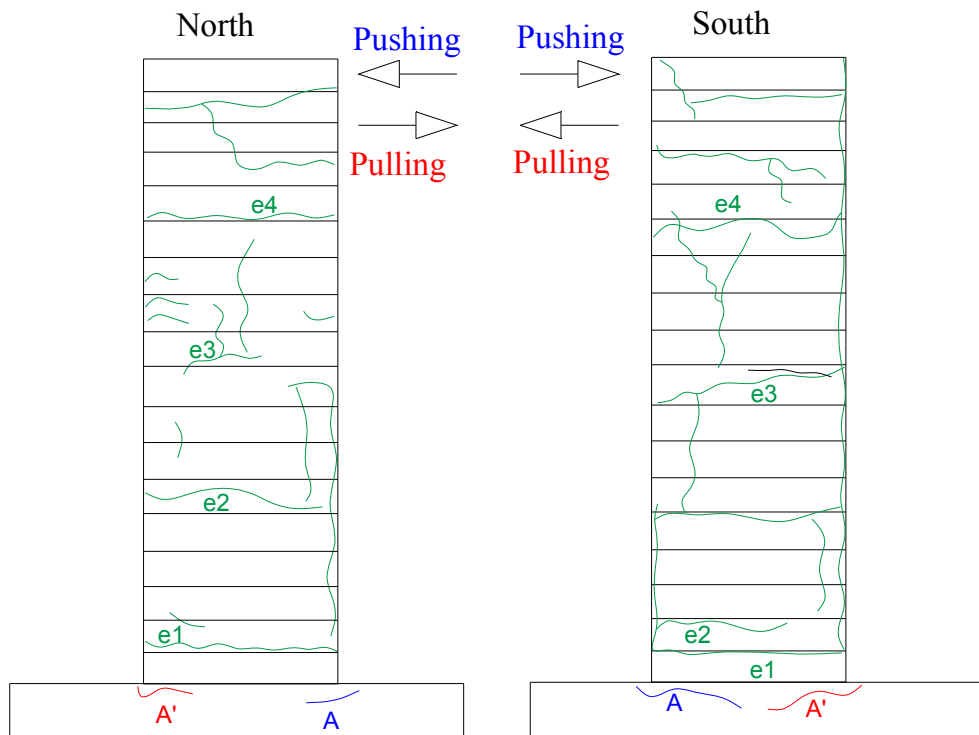


Figure E.128: Crack pattern of LS-X19-H after -1.5% drift ratio.

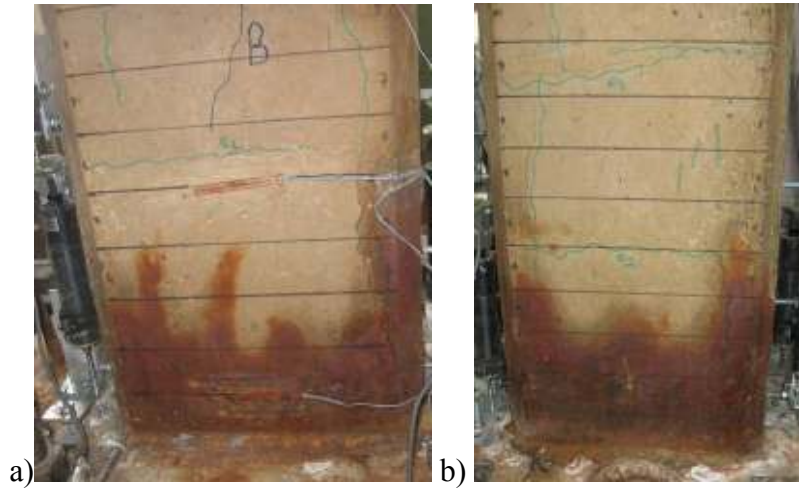


Figure E.129: a) North, and b) South view of LS-X19-H after -2% drift ratio.

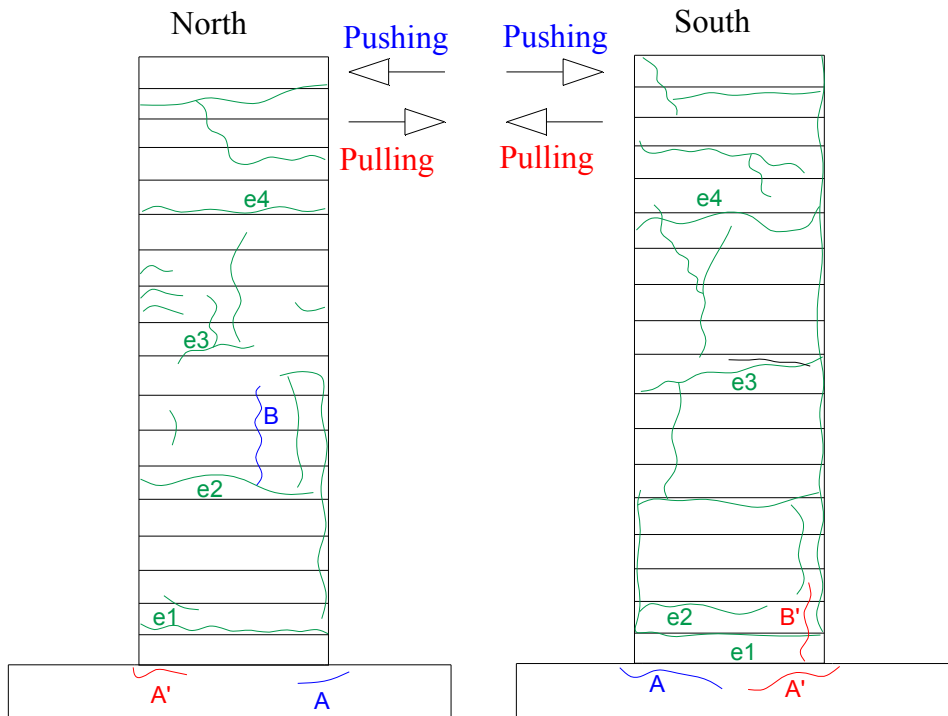


Figure E.130: Crack pattern of LS-X19-H after -2% drift ratio.

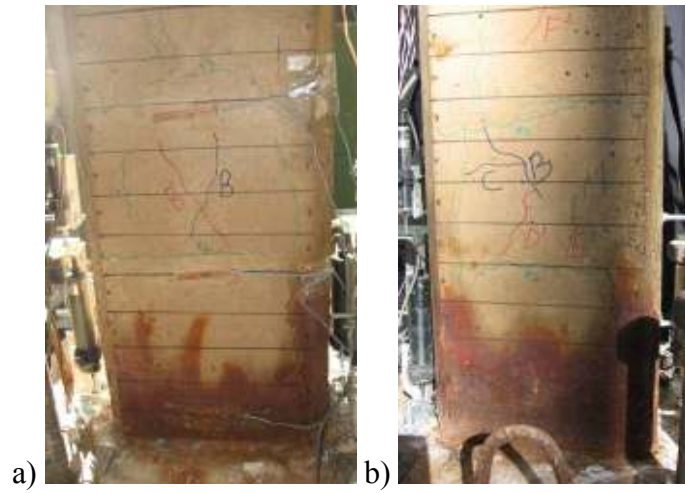


Figure E.131: a) North, and b) South view of LS-X19-H after -2.5% drift ratio.

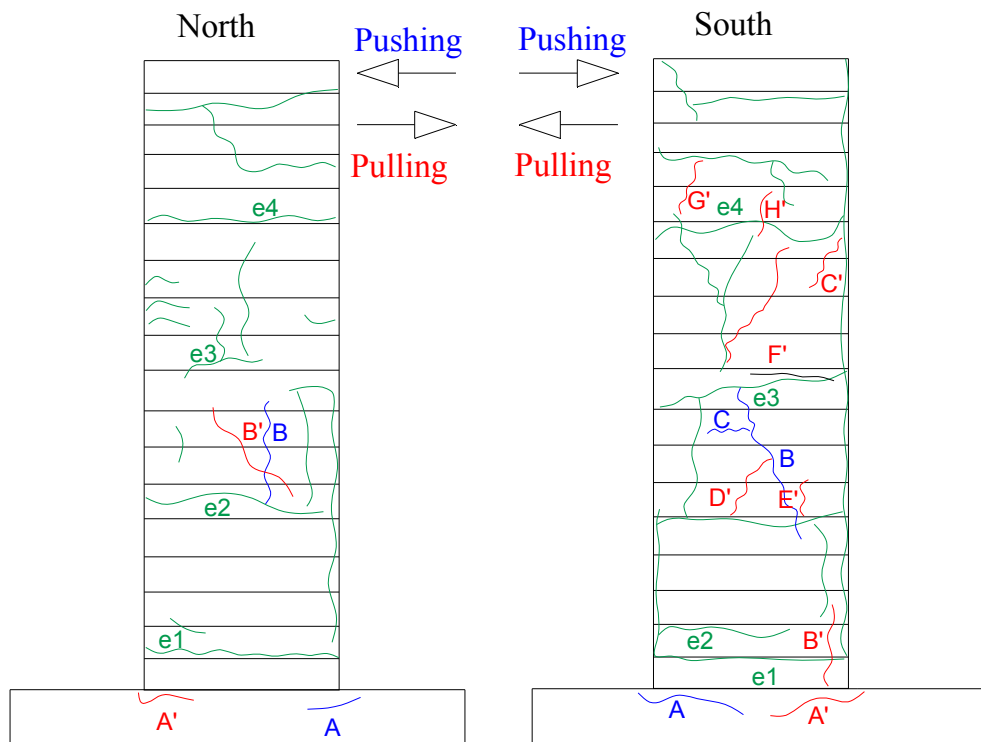


Figure E.132: Crack pattern of LS-X19-H after -2.5% drift ratio.

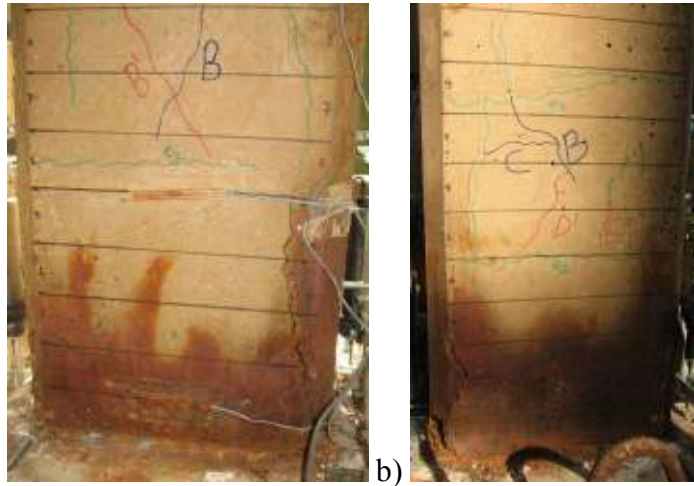


Figure E.133: a) North, and b) South view of LS-X19-H after -3% drift ratio.

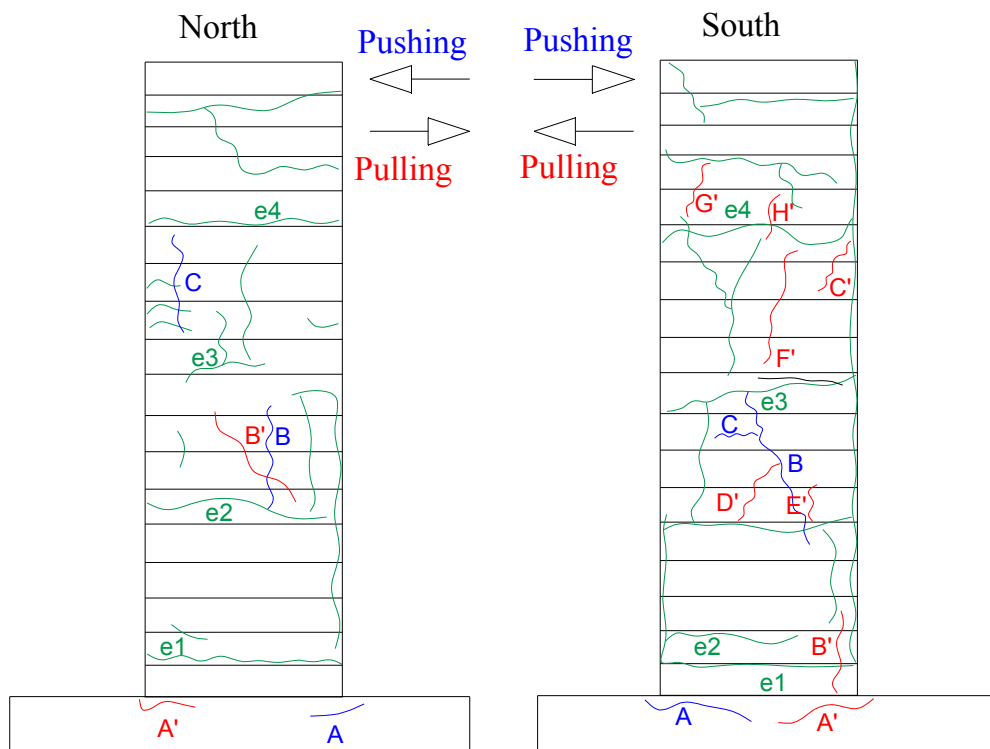


Figure E.134: Crack pattern of LS-X19-H after -3% drift ratio.



Figure E.135: a) North, and b) South view of LS-X19-H after -3.5% drift ratio.

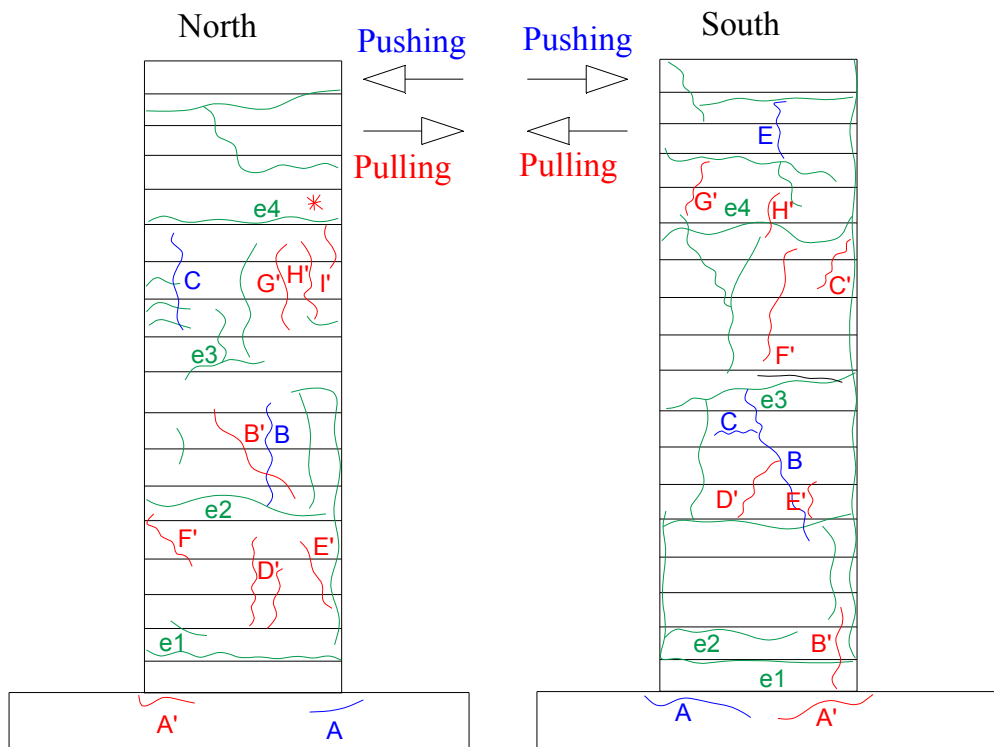


Figure E.136: Crack pattern of LS-X19-H after -3.5% drift ratio.

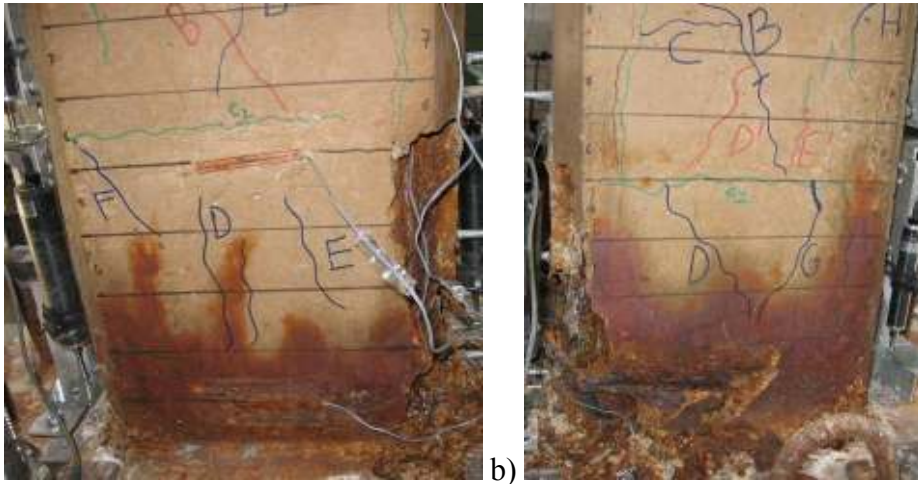


Figure E.137: a) North, and b) South view of LS-X19-H after -4% drift ratio.

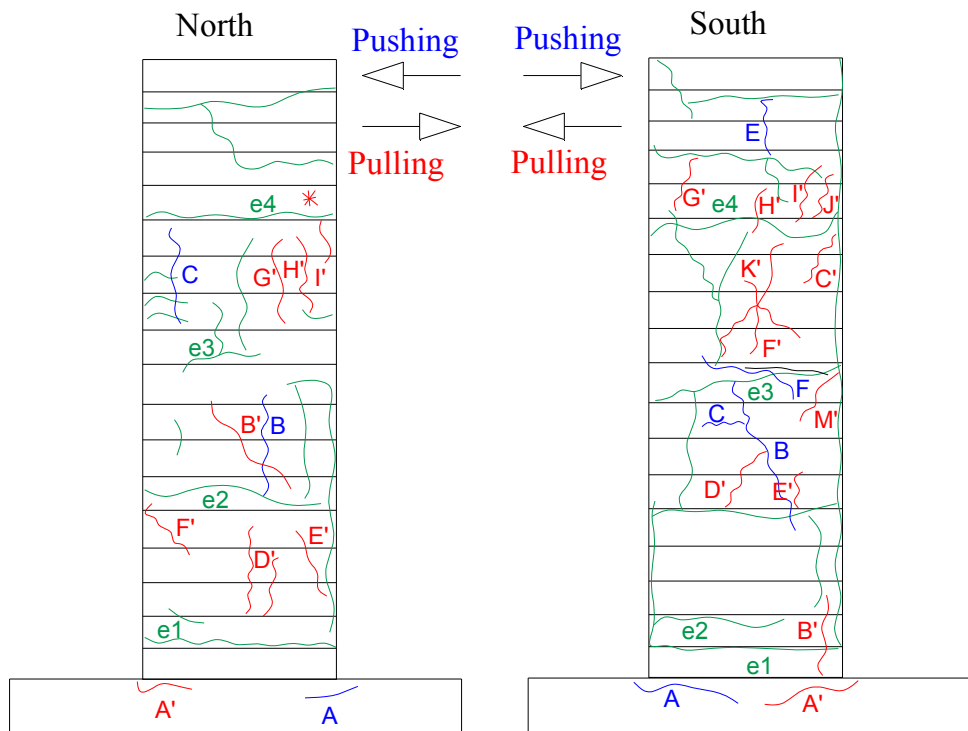


Figure E.138: Crack pattern of LS-X19-H after -4% drift ratio.

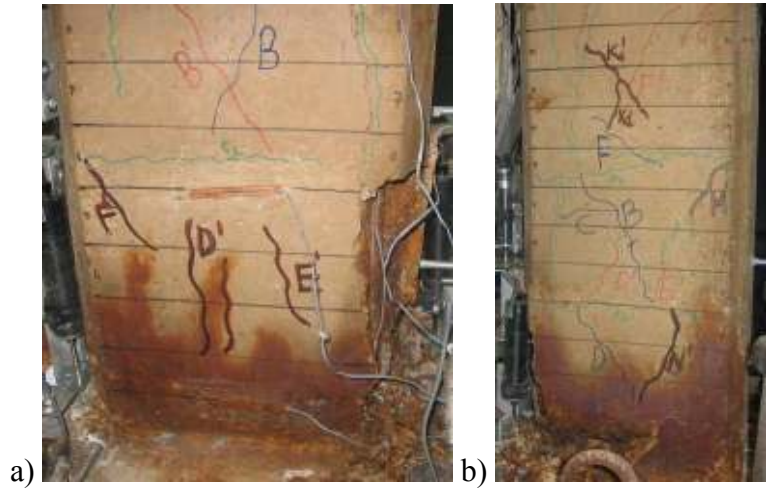


Figure E.139: a) North, and b) South view of LS-X19-H after -4.5% drift ratio.

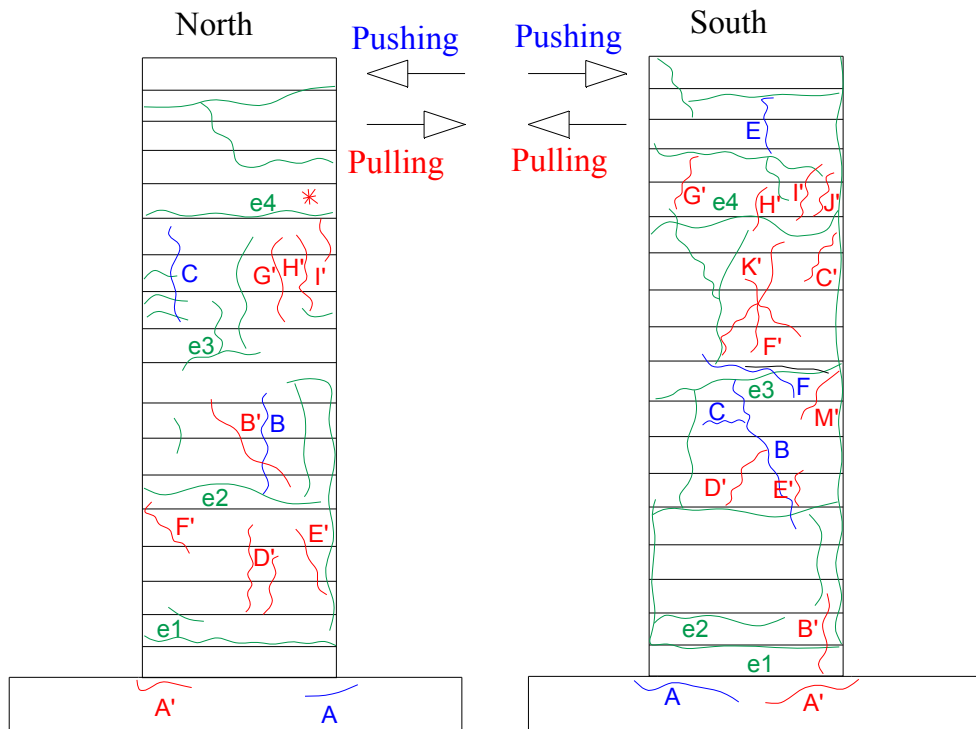


Figure E.140: Crack pattern of LS-X19-H after -4.5% drift ratio.

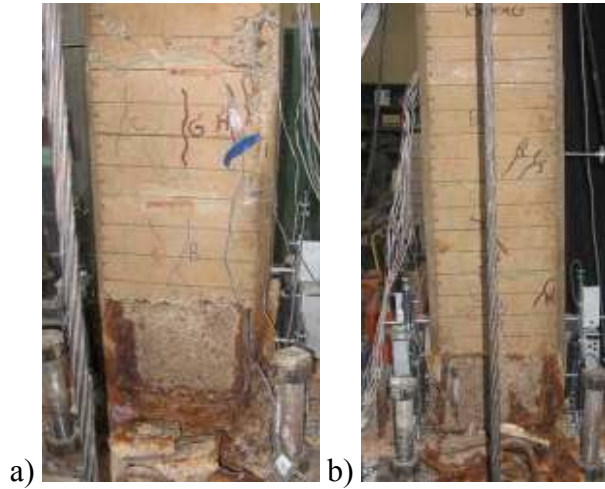


Figure E.141: a) North, and b) South view of LS-X19-H after -5% drift ratio.

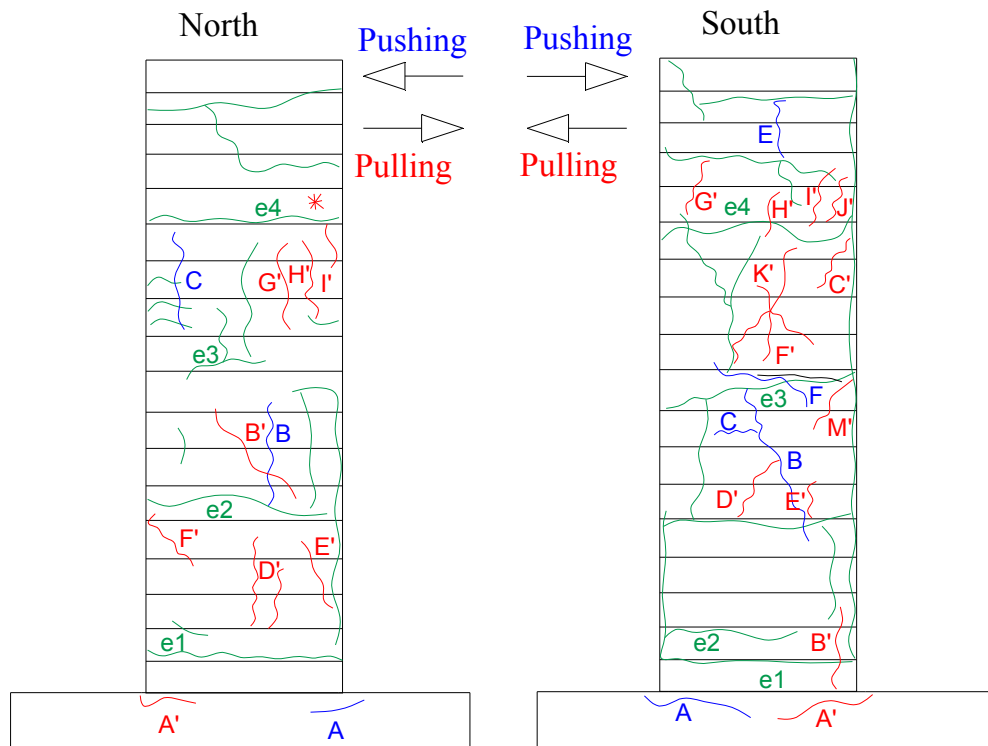


Figure E.142: Crack pattern of LS-X19-H after -5% drift ratio.

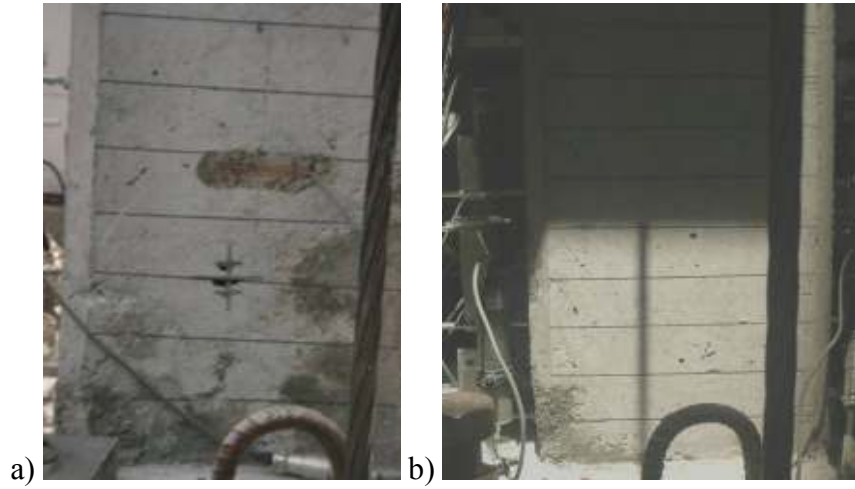


Figure E.143: (a) North, and (b) South view of NS-X0 after -0.1% drift ratio.

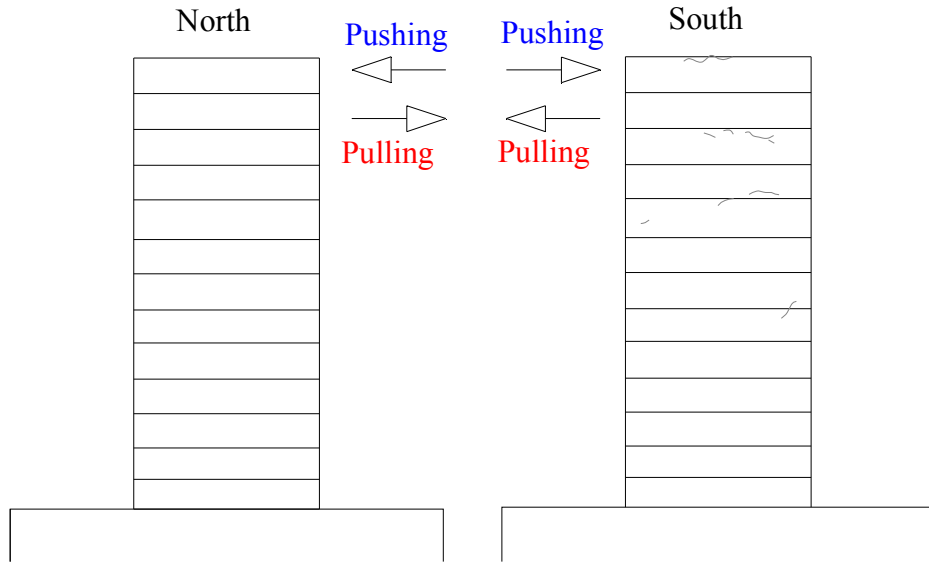


Figure E.144: Crack pattern of NS-X0 after -0.1% drift ratio.

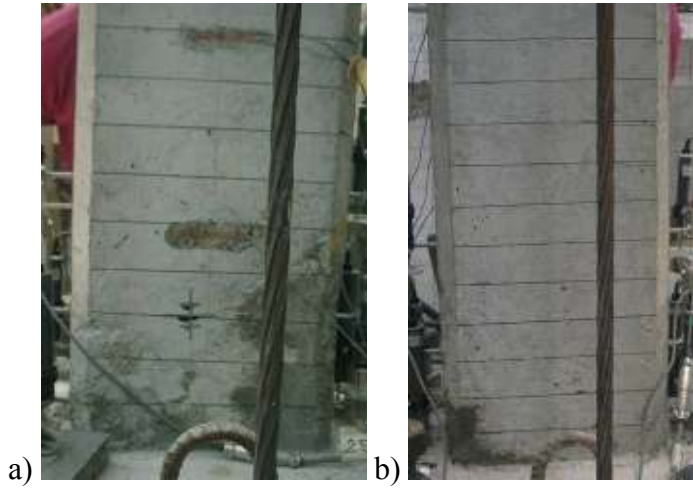


Figure E.145: a) North, and b) South view of NS-X0 after -0.25% drift ratio.

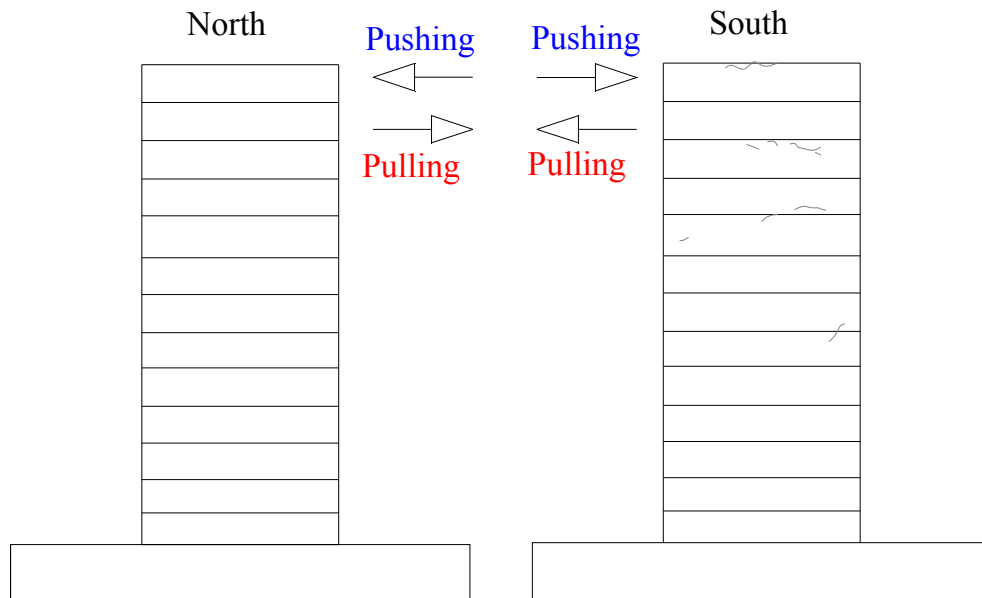


Figure E.146: Crack pattern of NS-X0 after -0.25% drift ratio.

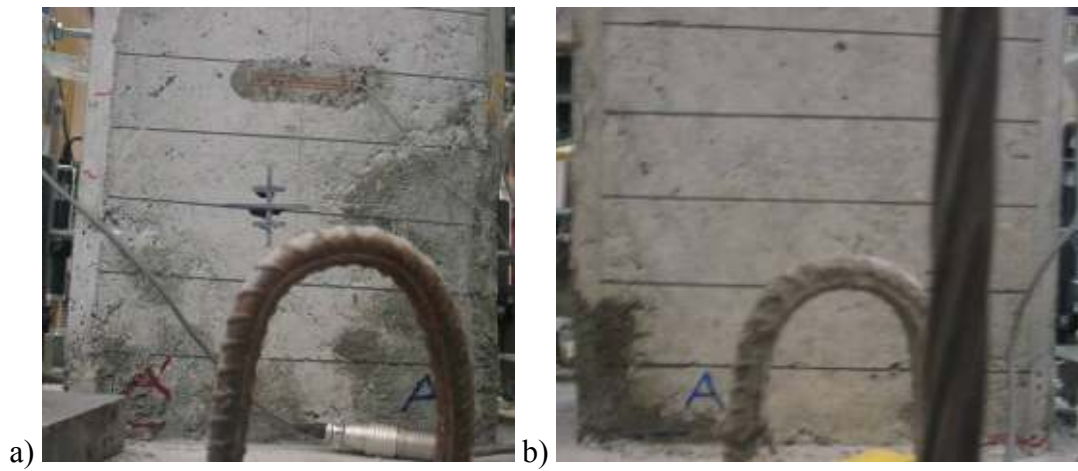


Figure E.147: a) North, and b) South view of NS-X0 after -0.5% drift ratio.

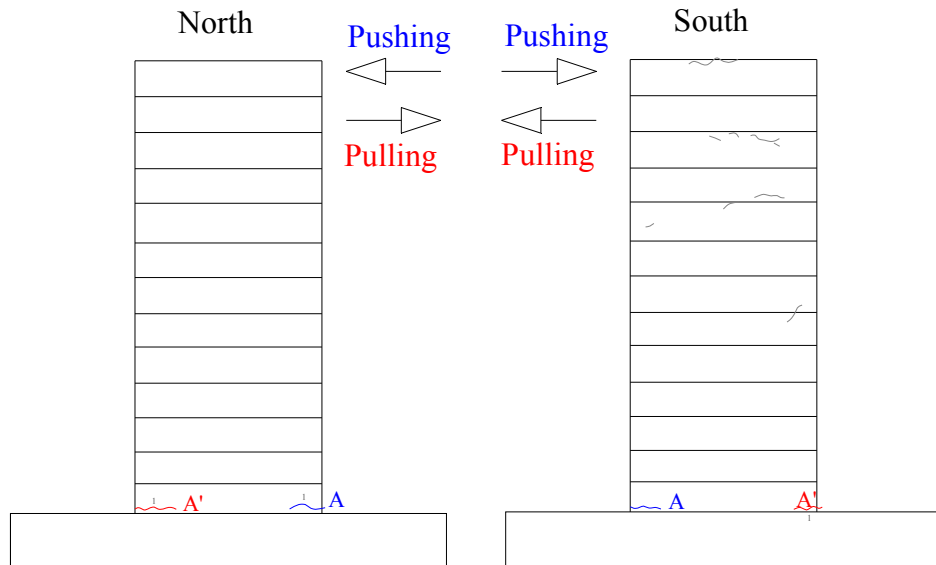


Figure E.148: Crack pattern of NS-X0 after -0.5% drift ratio.

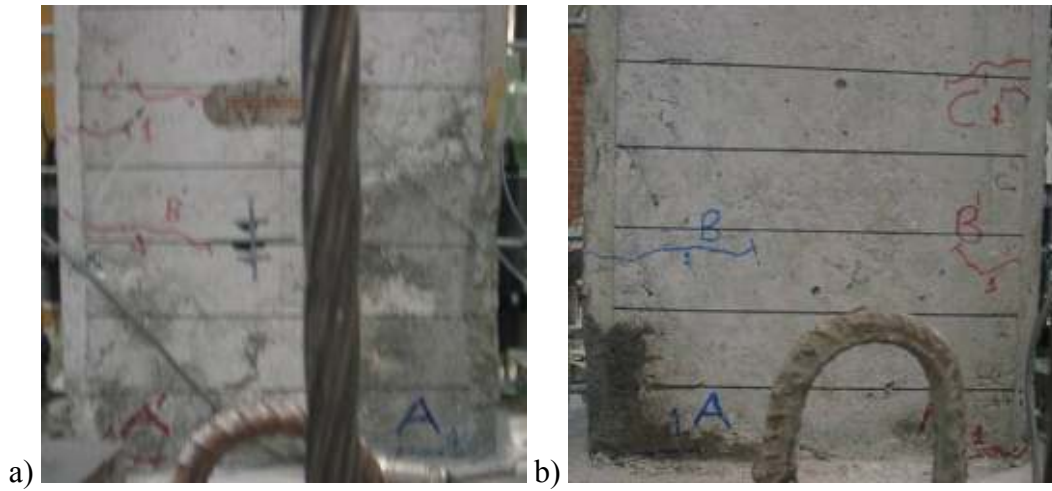


Figure E.149: a) North, and b) South view of NS-X0 after -0.75% drift ratio.

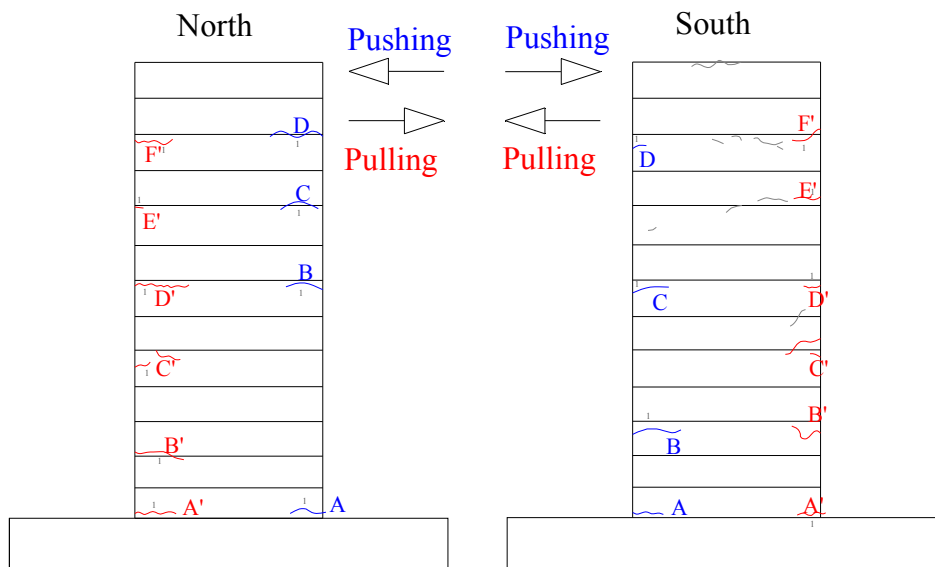


Figure E.150: Crack pattern of NS-X0 after -0.75% drift ratio.

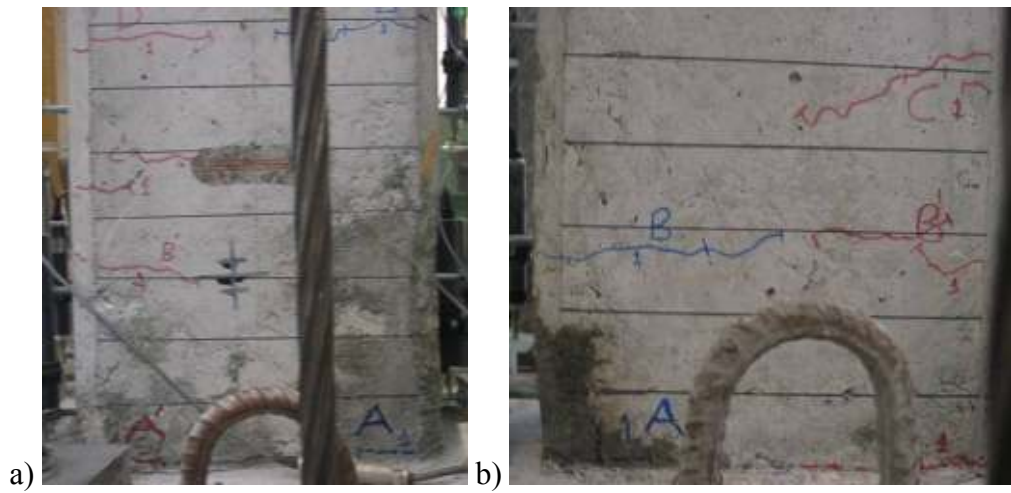


Figure E.151: a) North, and b) South view of NS-X0 after -1% drift ratio.

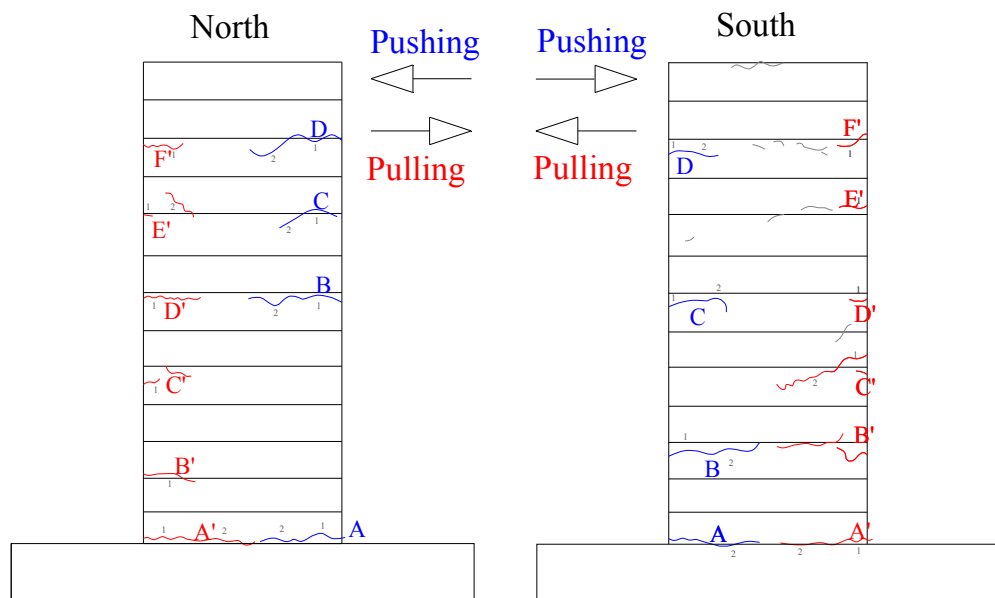


Figure E.152: Crack pattern of NS-X0 after -1% drift ratio.

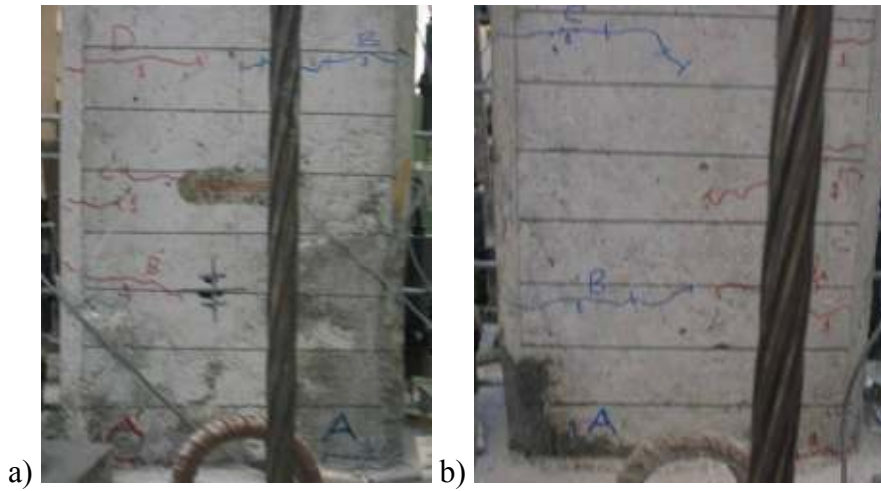


Figure E.153: a) North, and b) South view of NS-X0 after 1.5% drift ratio.

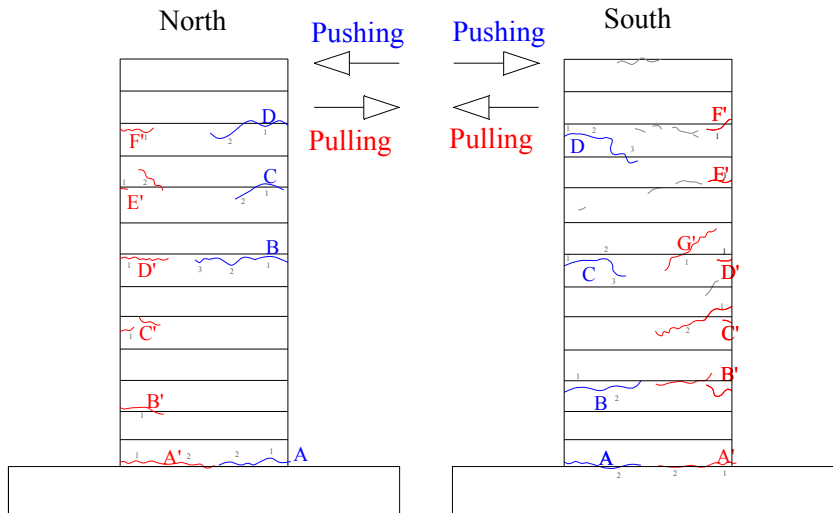


Figure E.154: Crack pattern of NS-X0 after -1.5% drift ratio.

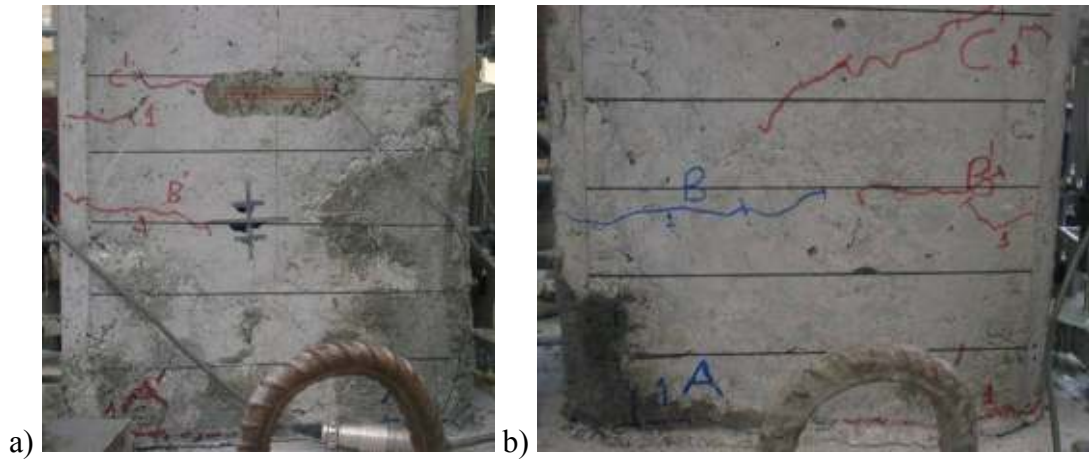


Figure E.155: a) North, and b) South view of NS-X0 after -2% drift ratio.

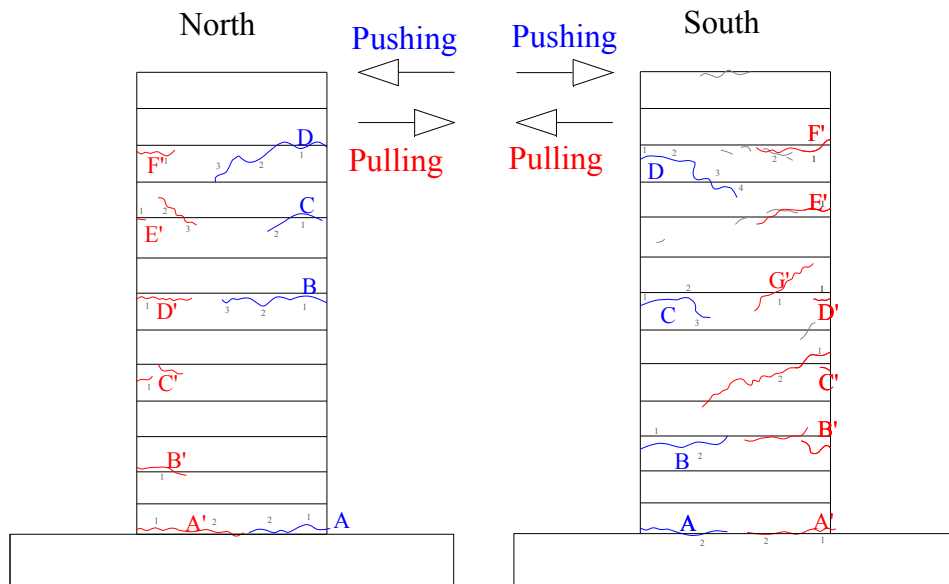


Figure E.156: Crack pattern of NS-X0 after -2% drift ratio.

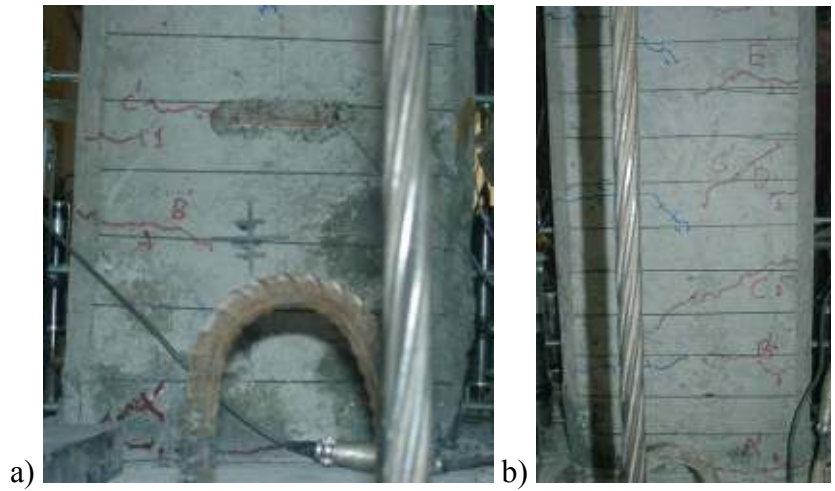


Figure E.157: a) North, and b) South view of NS-X0 after -2.5% drift ratio.

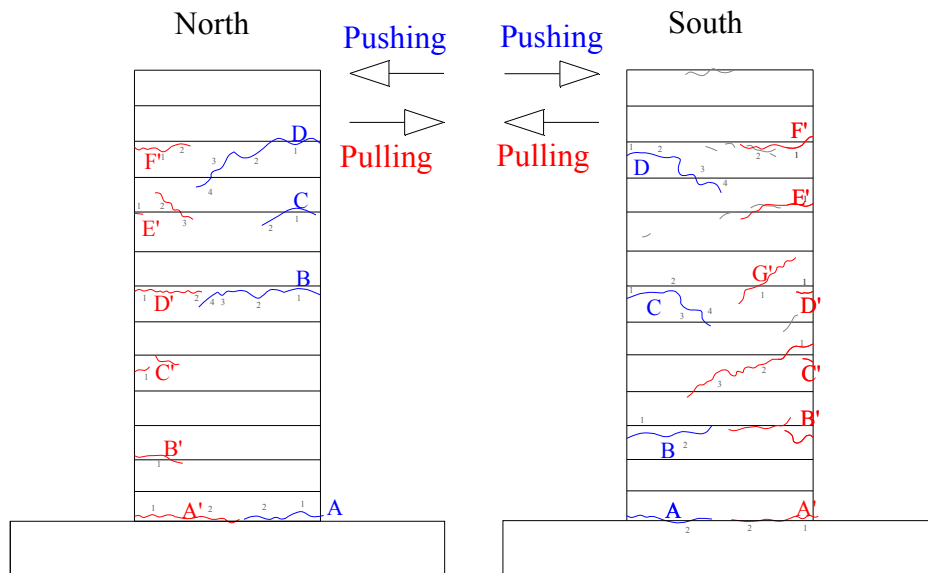


Figure E.158: Crack pattern of NS-X0 after -2.5% drift ratio.

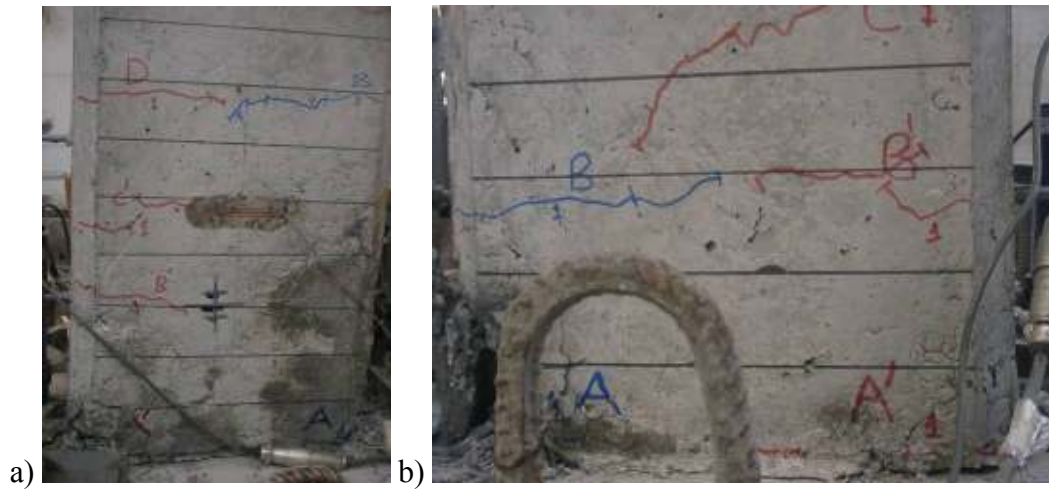


Figure E.159: a) North, and b) South view of NS-X0 after -3% drift ratio.

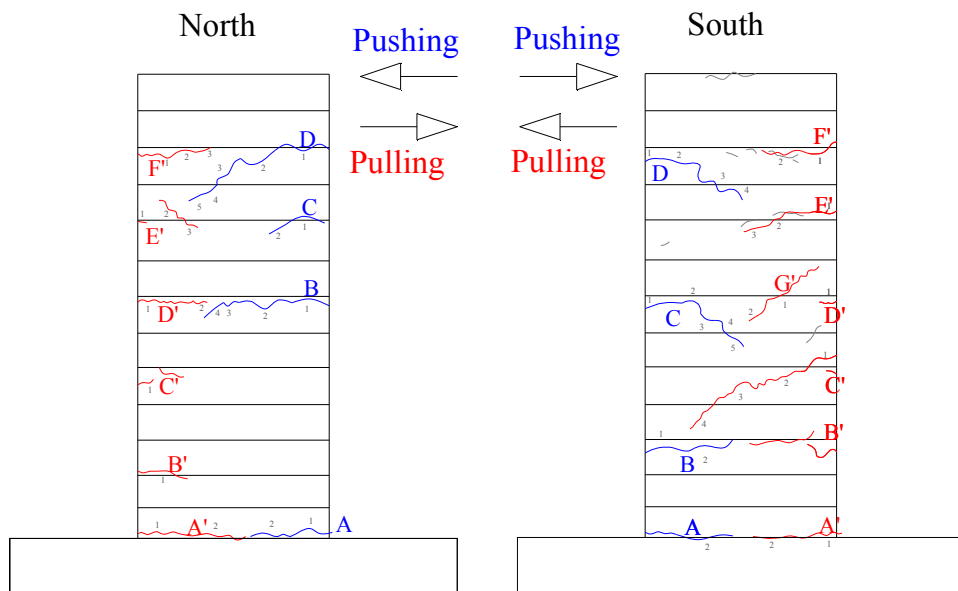


Figure E.160: Crack pattern of NS-X0 after -3% drift ratio.

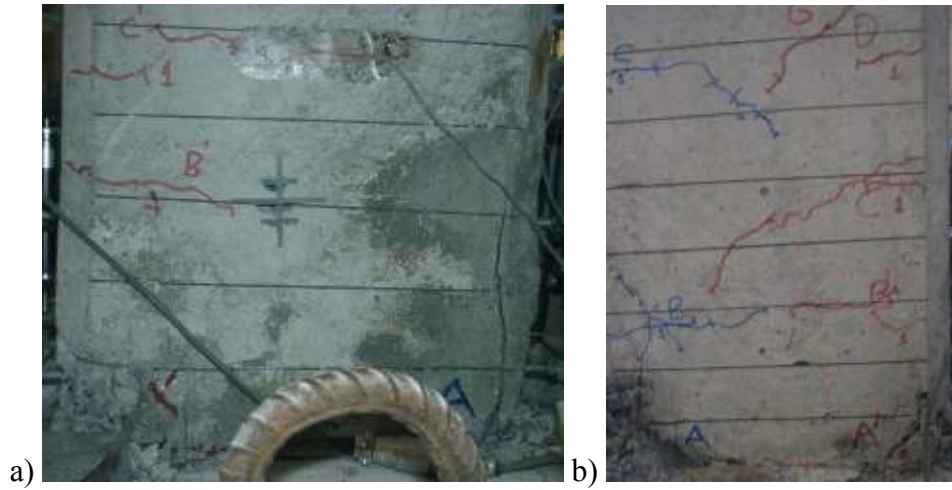


Figure E.161: a) North, and b) South view of NS-X0 after -3.5% drift ratio.

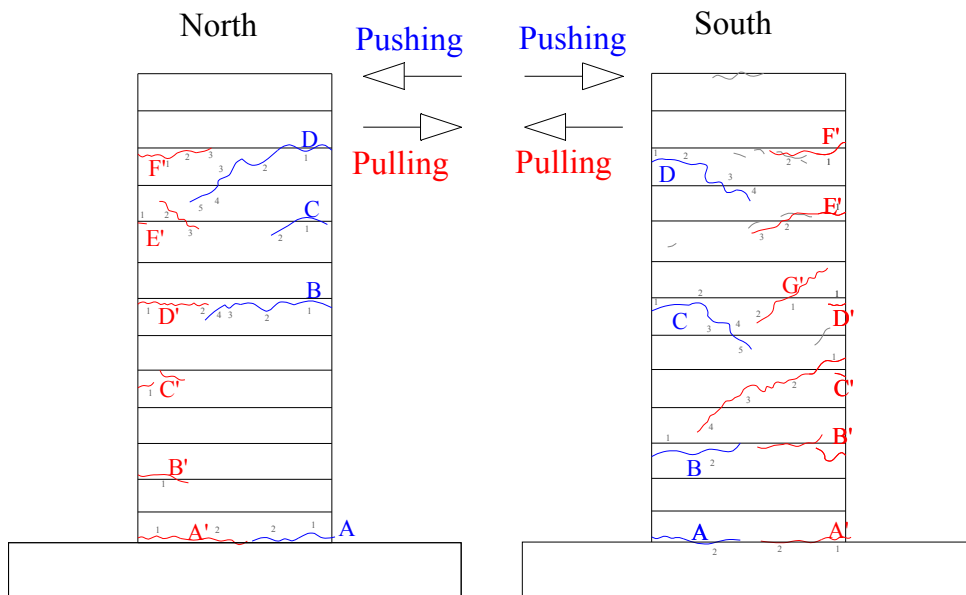


Figure E.162: Crack pattern of NS-X0 after -3.5% drift ratio.

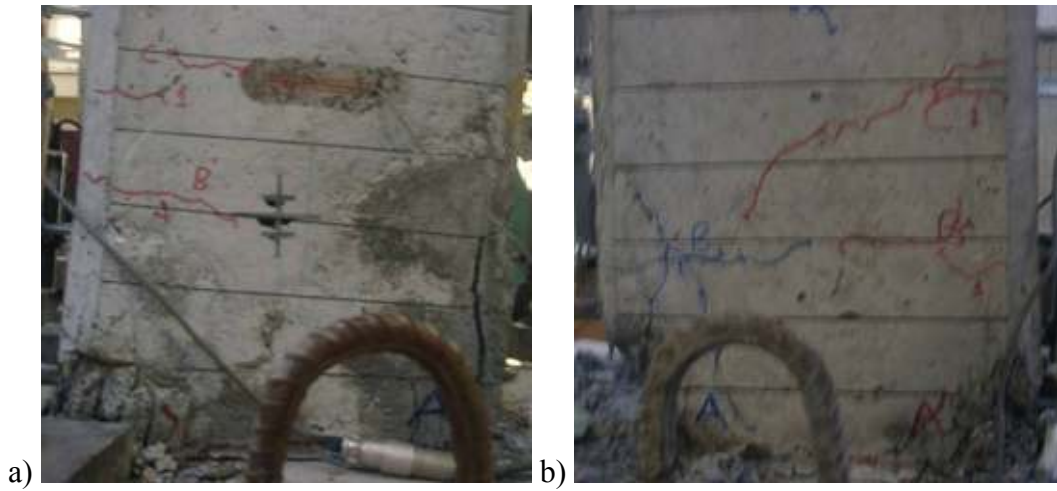


Figure E.163: a) North, and b) South view of NS-X0 after -4% drift ratio.

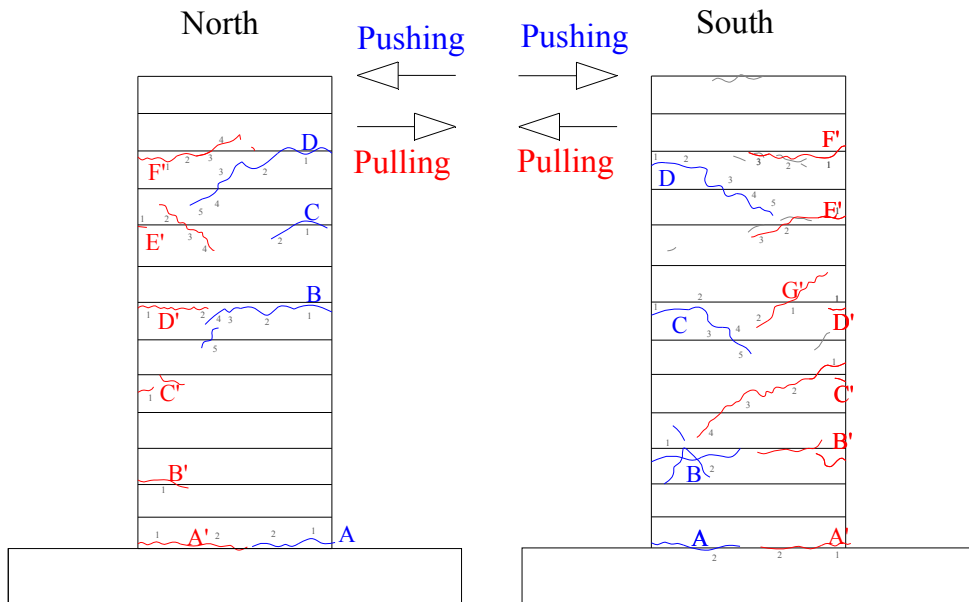


Figure E.164: Crack pattern of NS-X0 after -4% drift ratio.

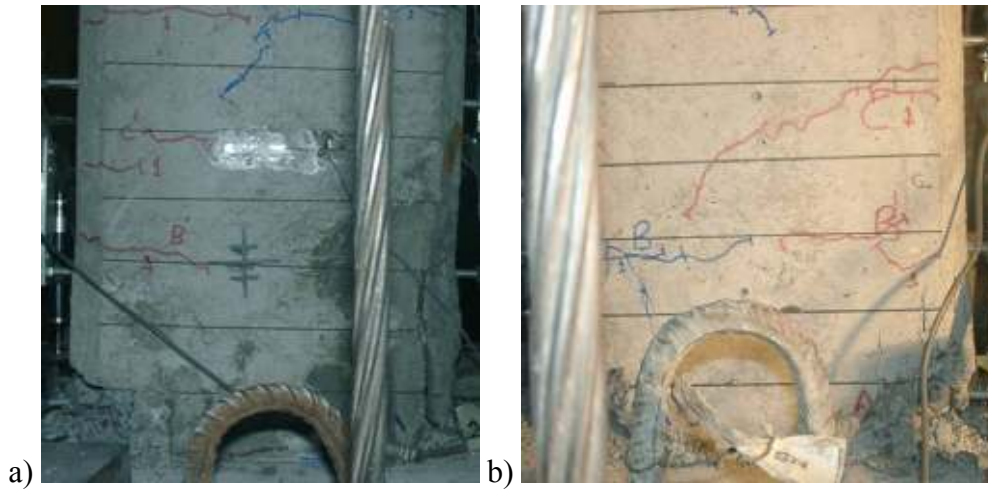


Figure E.165: a) North, and b) South view of NS-X0 after -5% drift ratio.

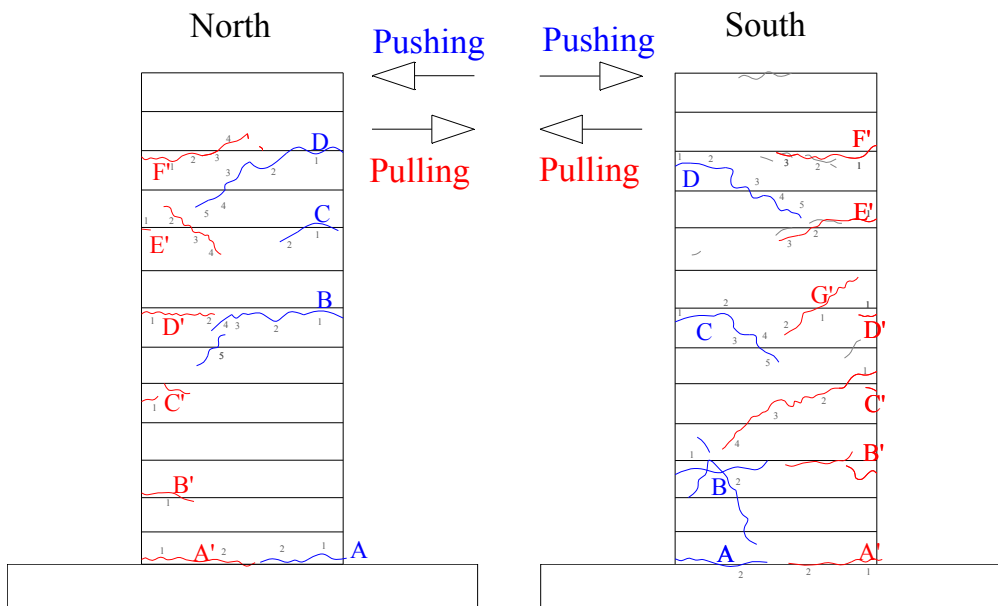


Figure E.166: Crack pattern of NS-X0 after -5% drift ratio.

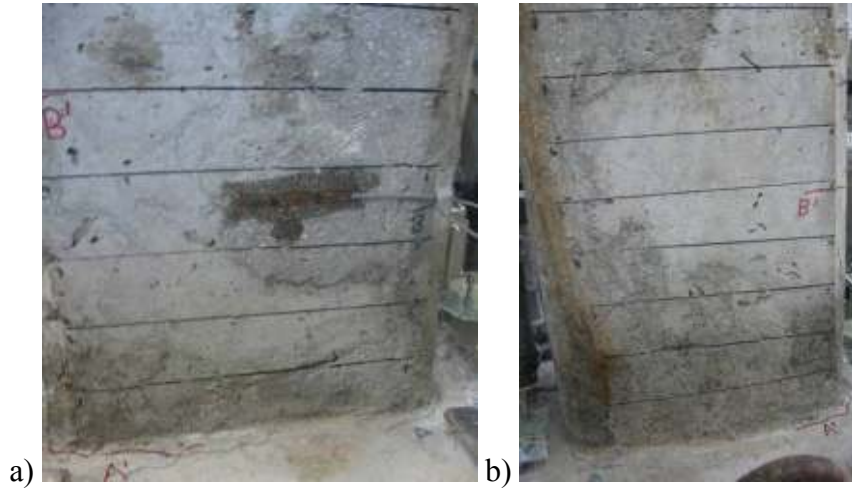


Figure E.167: a) North, and b) South view of NS-X9 after -0.5% drift ratio.

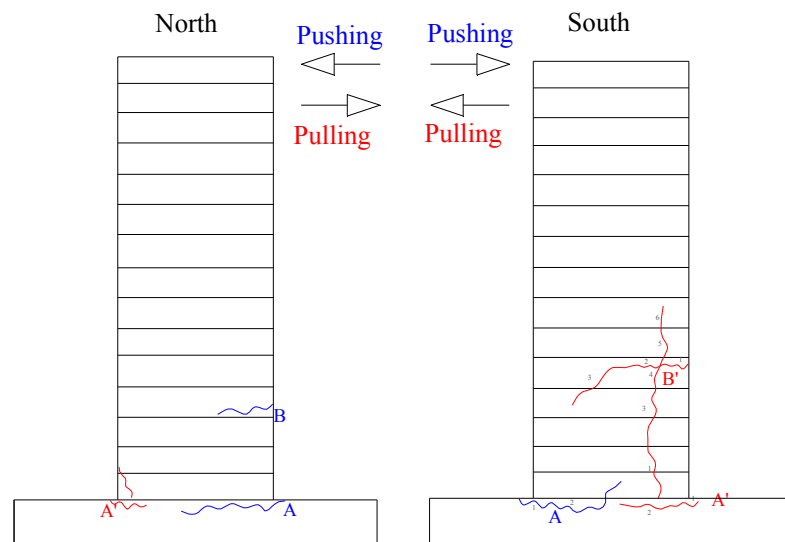


Figure E.168: Crack pattern of NS-X9 after -0.5% drift ratio.

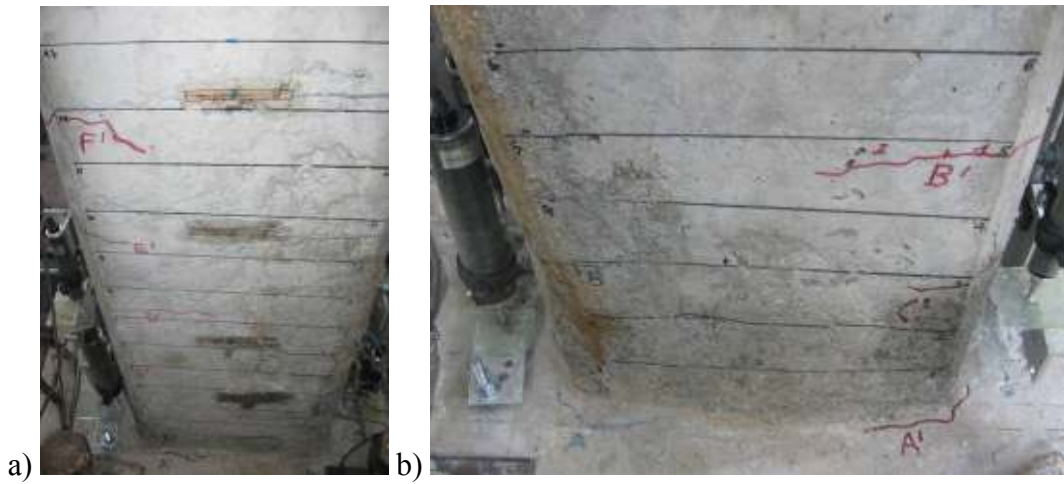


Figure E.169: a) North, and b) South view of NS-X9 after -0.75% drift ratio.

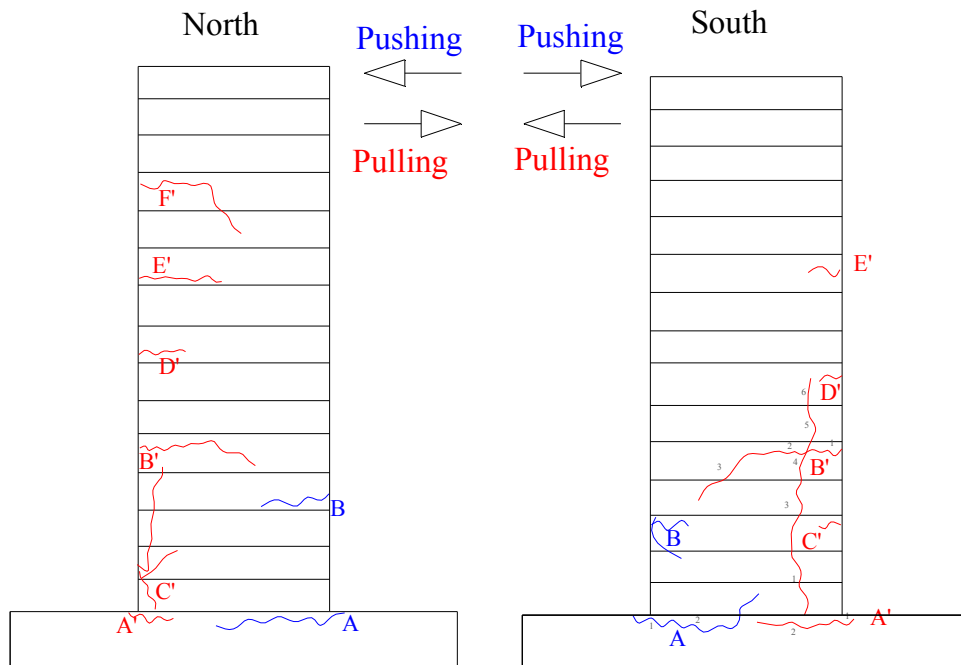


Figure E.170: Crack pattern of NS-X9 after -0.75% drift ratio.

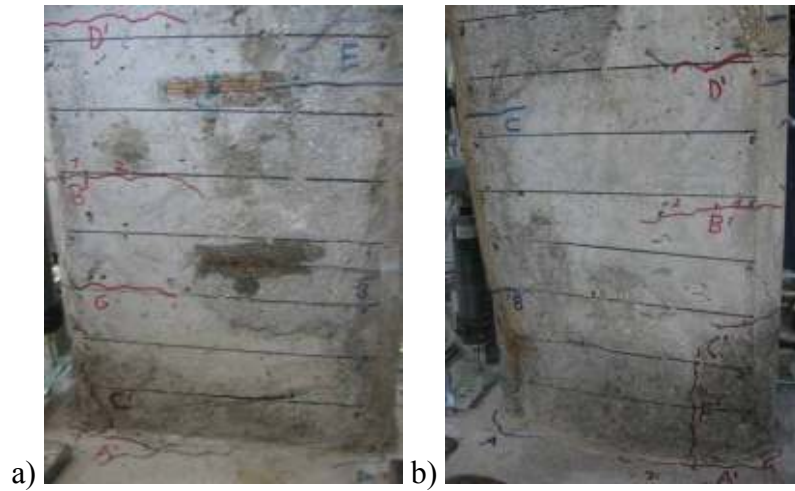


Figure E.171: a) North, and b) South view of NS-X9 after -1% drift ratio.

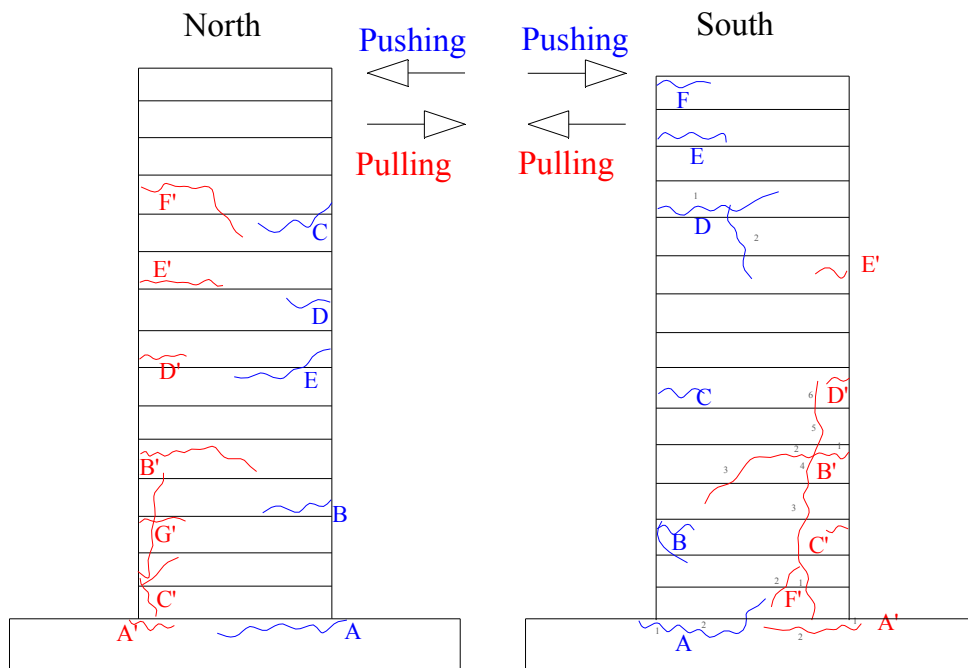


Figure E.172: Crack pattern of NS-X9 after -1% drift ratio.

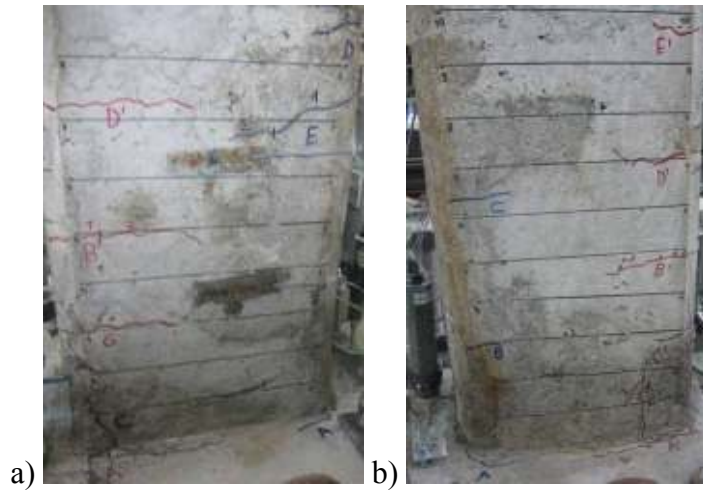


Figure E.173: a) North, and b) South view of NS-X9 after -1.5% drift ratio.

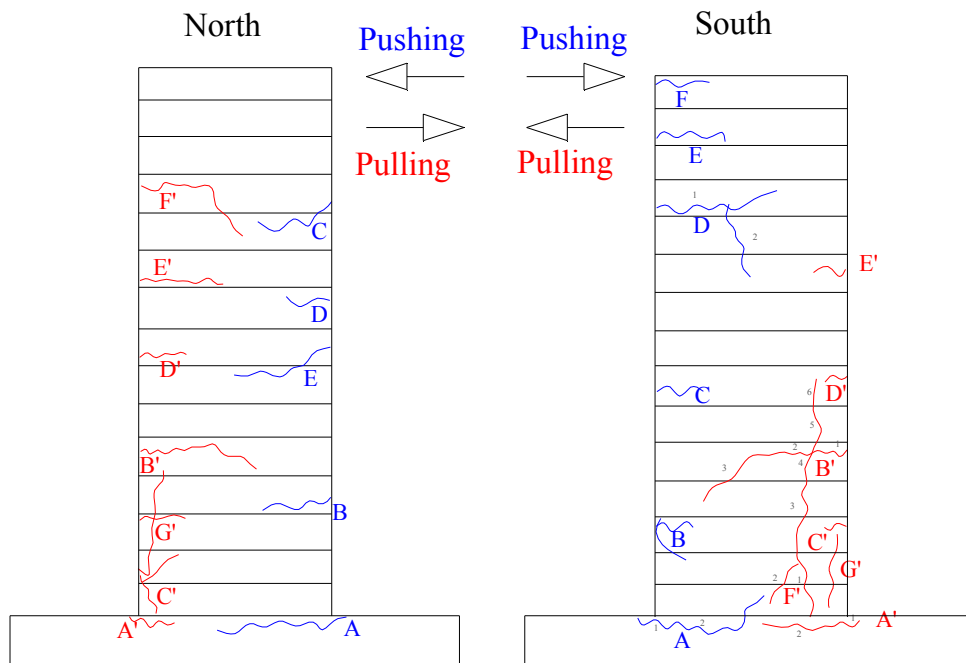


Figure E.174: Crack pattern of NS-X9 after -1.5% drift ratio.

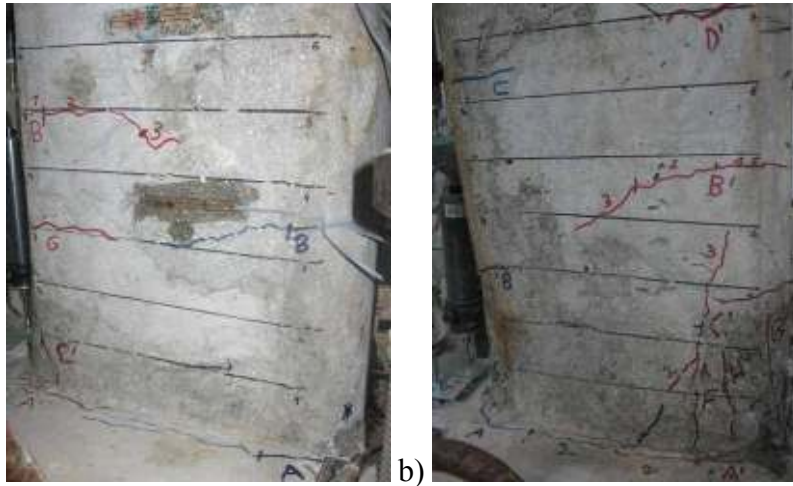


Figure E.175: a) North, and b) South view of NS-X9 after -2% drift ratio.

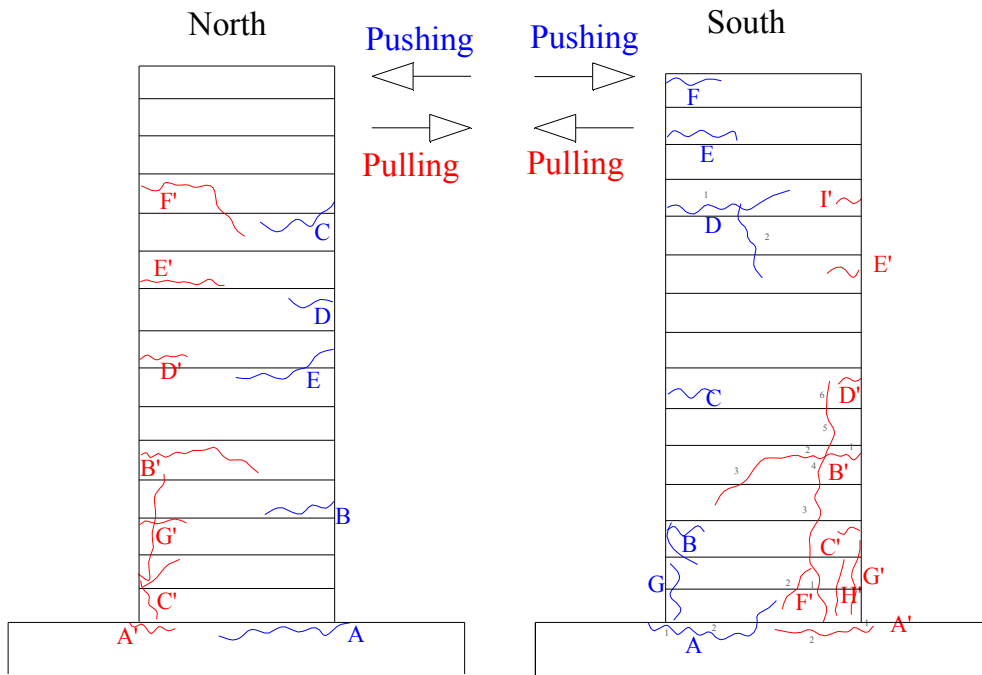


Figure E.176: Crack pattern of NS-X9 after -2% drift ratio.

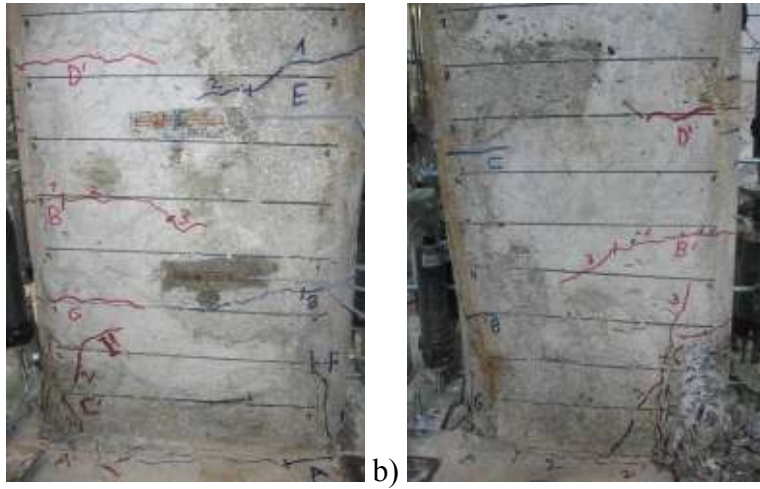


Figure E.177: a) North, and b) South view of NS-X9 after -2.5% drift ratio.

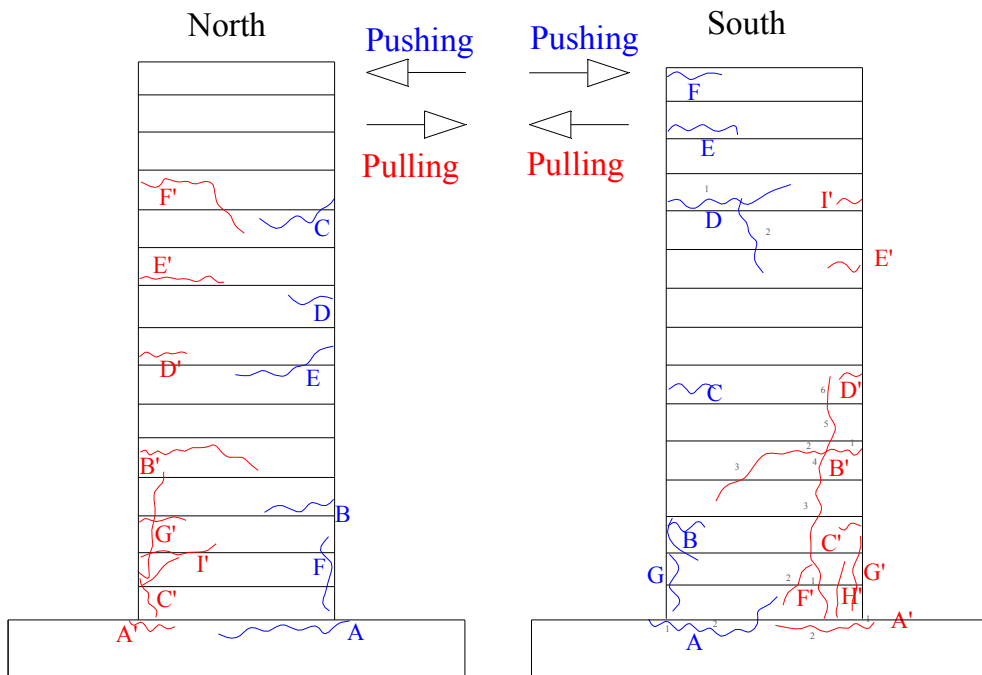


Figure E.178: Crack pattern of NS-X9 after -2.5% drift ratio.

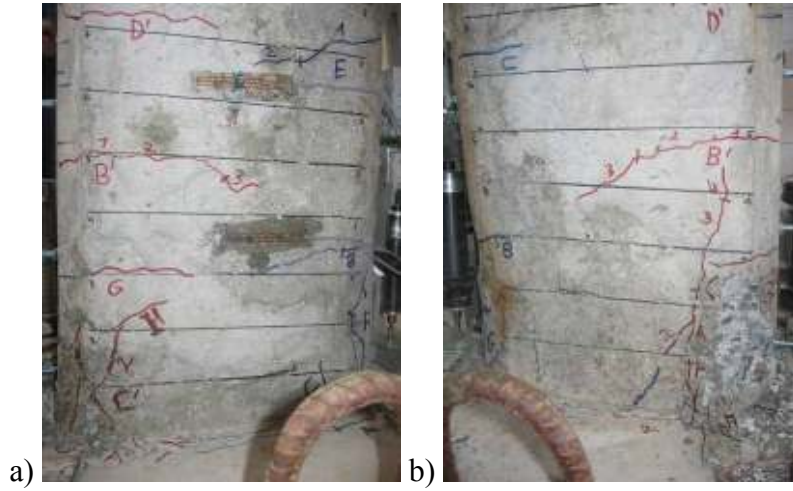


Figure E.179: a) North, and b) South view of NS-X9 after -3% drift ratio.

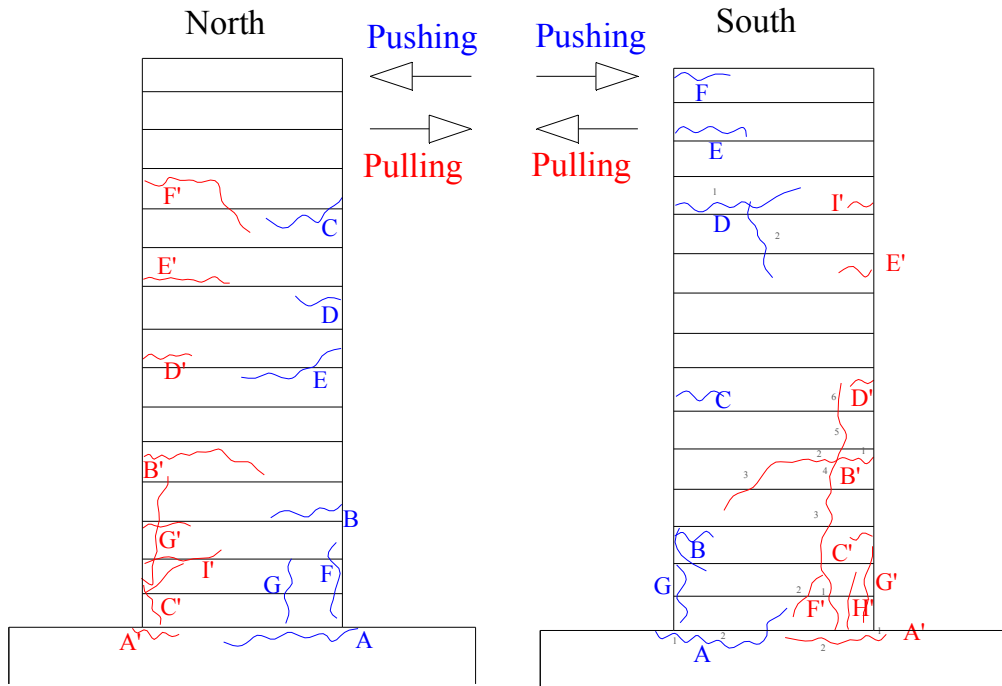


Figure E.180: Crack pattern of NS-X9 after -3% drift ratio.

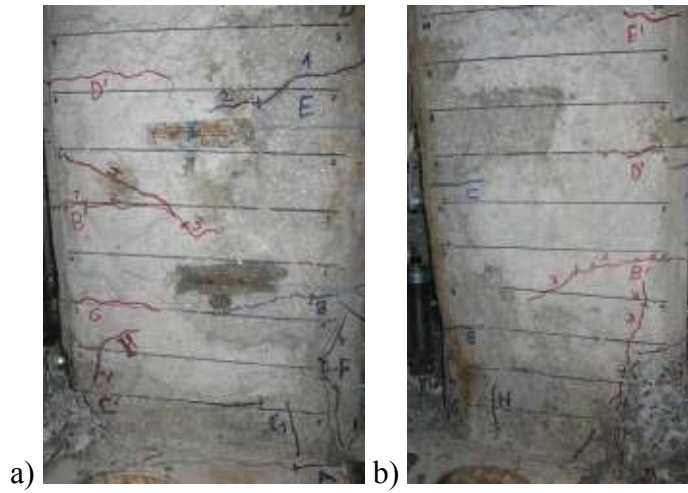


Figure E.181: a) North, and b) South view of NS-X9 after -3.5% drift ratio.

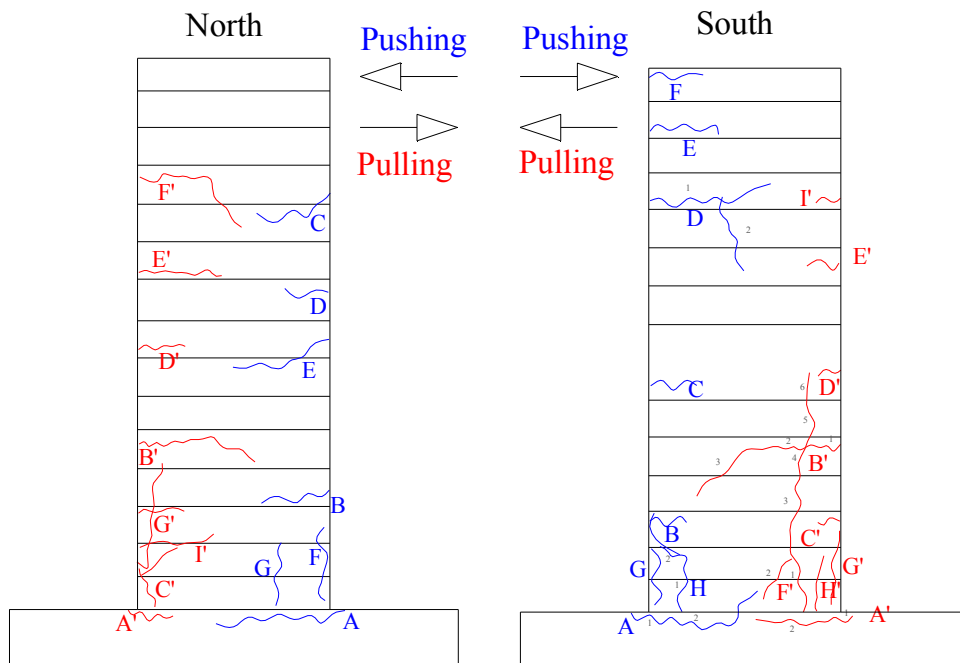


Figure E.182: Crack pattern of NS-X9 after -3.5% drift ratio.

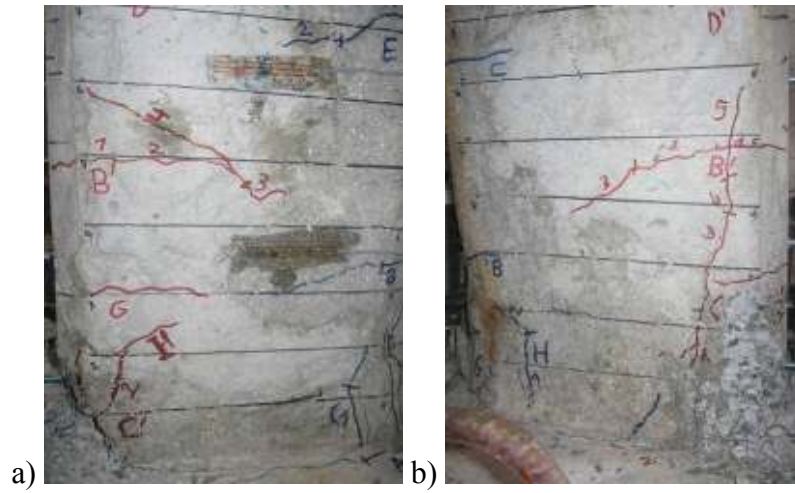


Figure E.183: a) North, and b) South view of NS-X9 after -4% drift ratio.

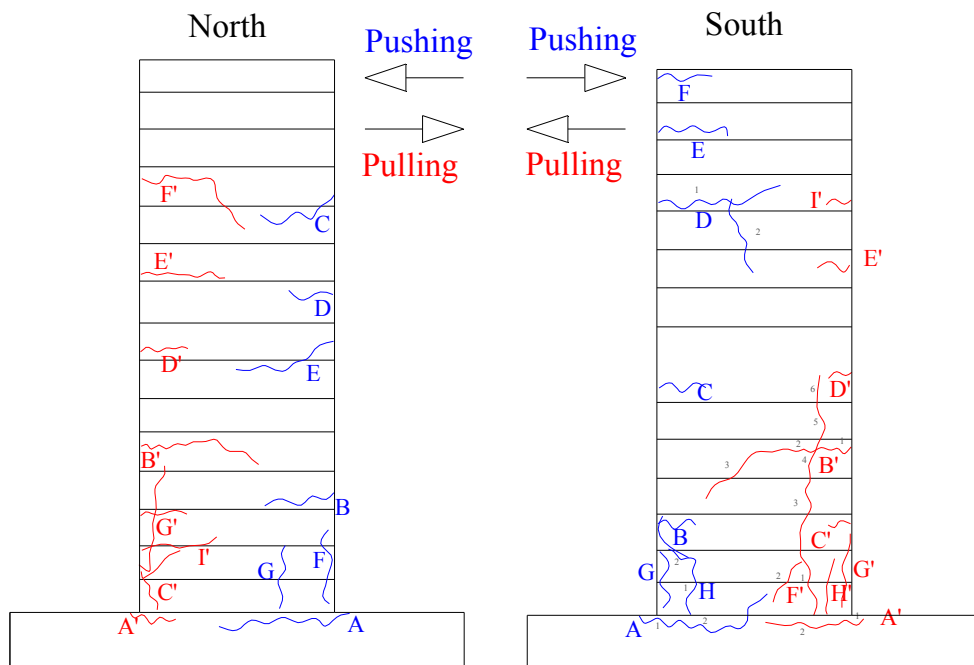


Figure E.184: Crack pattern of NS-X9 after -4% drift ratio.

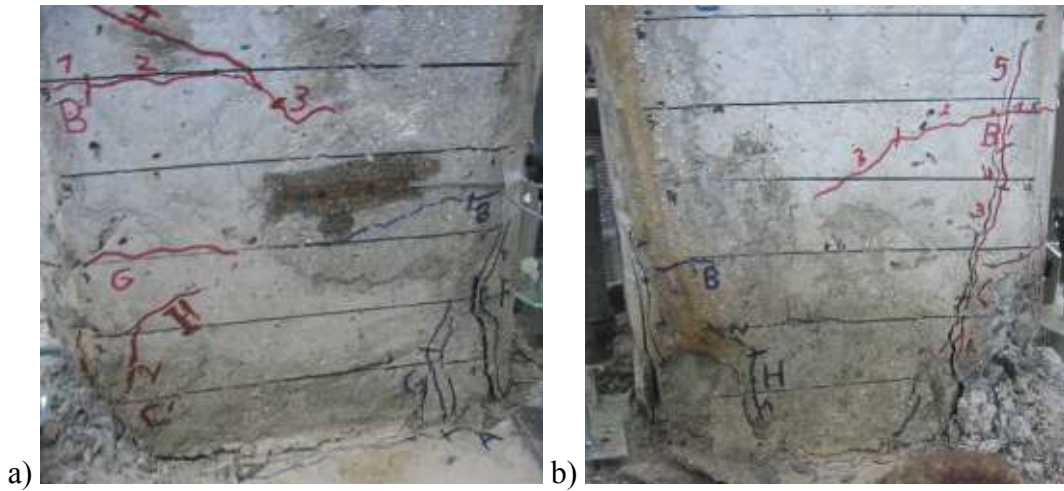


Figure E.185: a) North, and b) South view of NS-X9 after -4.5% drift ratio.

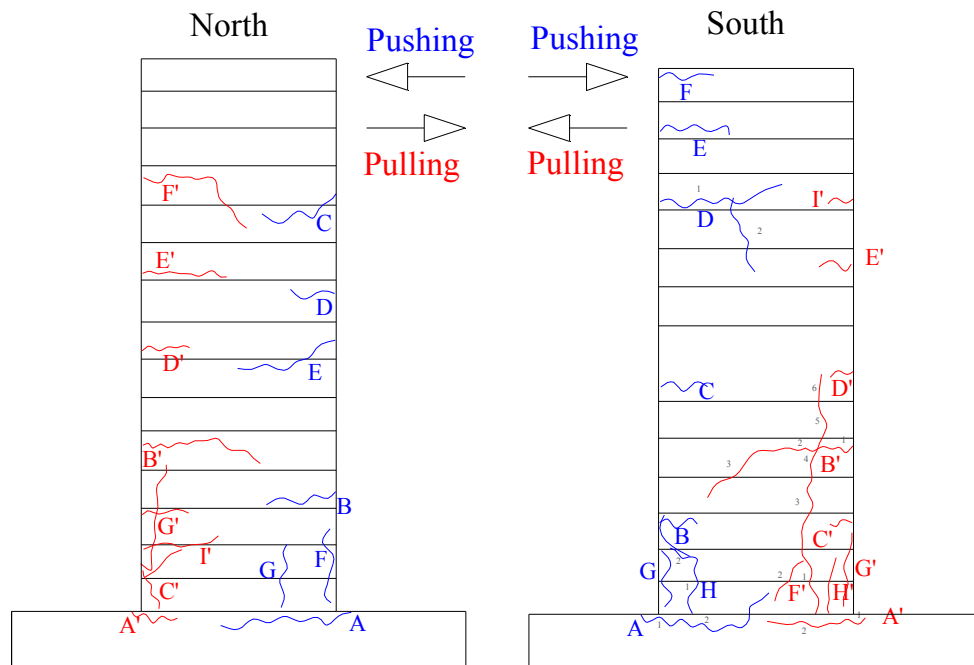


Figure E.186: Crack pattern of NS-X9 after -4.5% drift ratio.

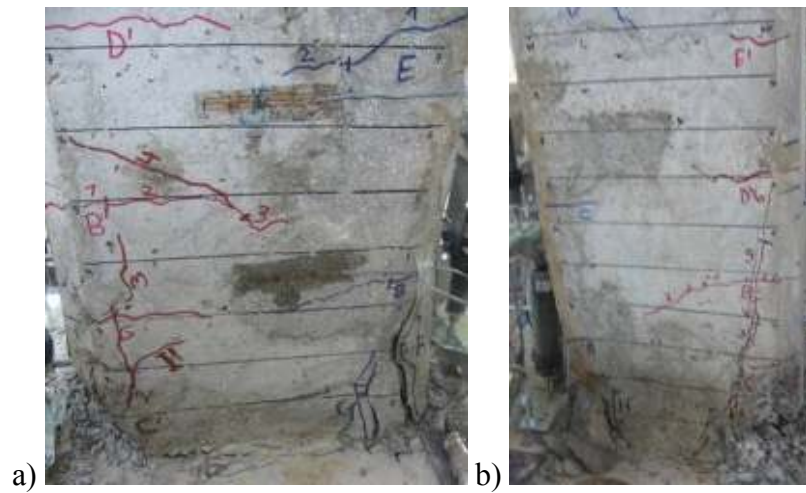


Figure E.187: a) North, and b) South view of NS-X9 after -5% drift ratio.

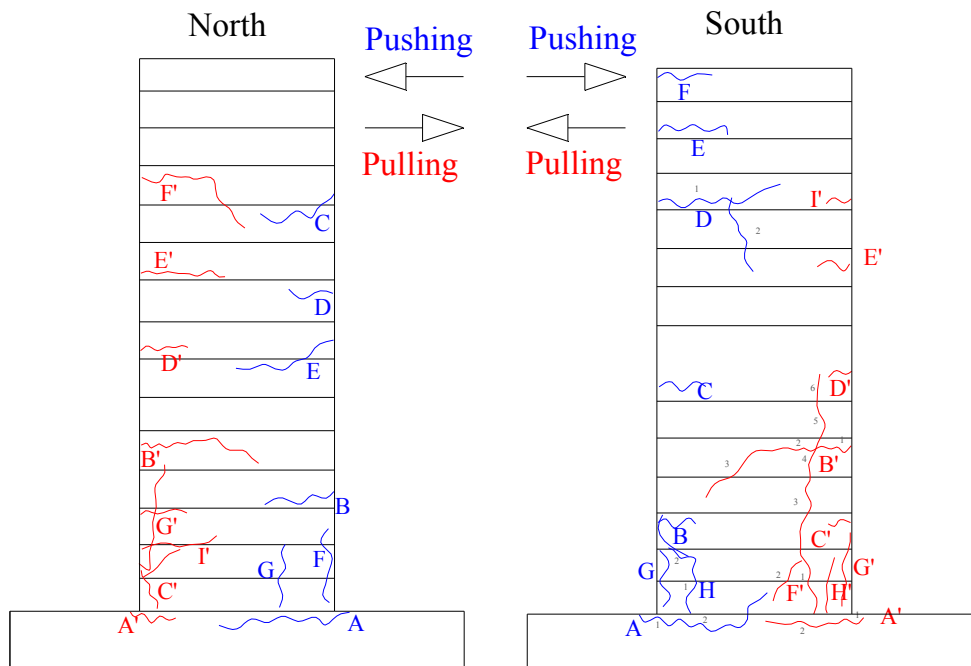


Figure E.188: Crack pattern of NS-X9 after -5% drift ratio.

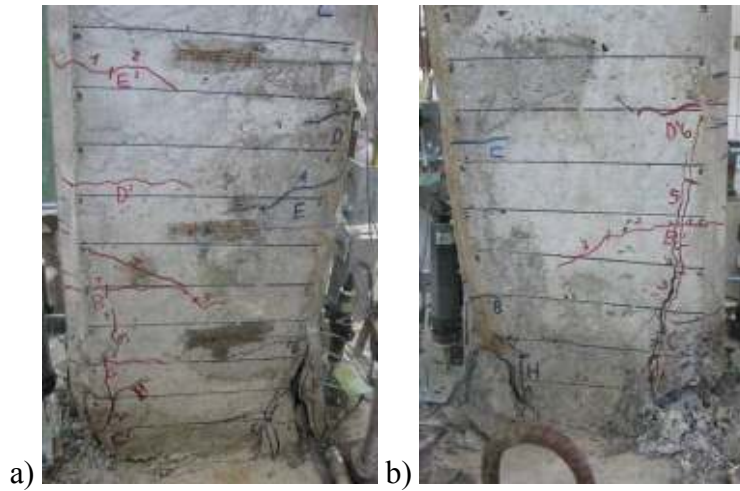


Figure E.189: a) North, and b) South view of NS-X9 after -6% drift ratio.

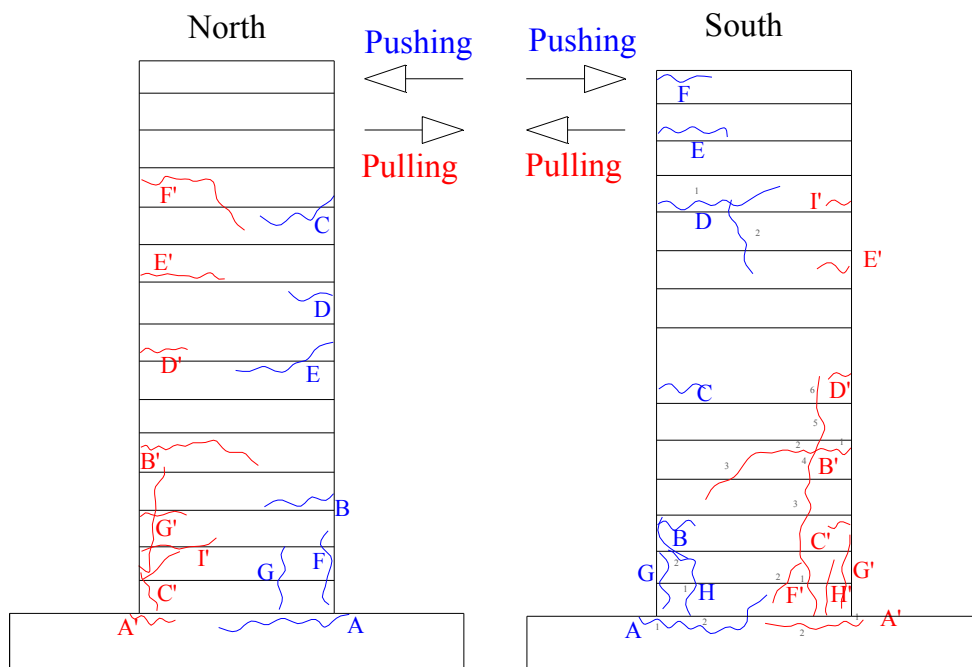


Figure E.190: Crack pattern of NS-X9 after -6% drift ratio.

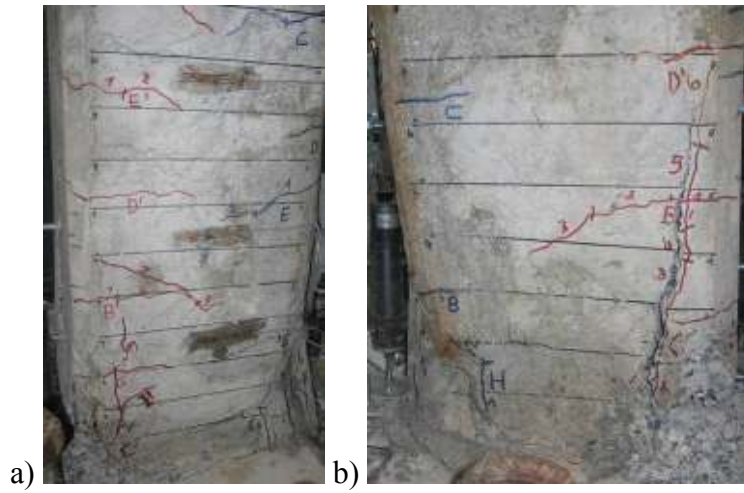


Figure E.191: a) North, and b) South view of NS-X9 after -7% drift ratio.

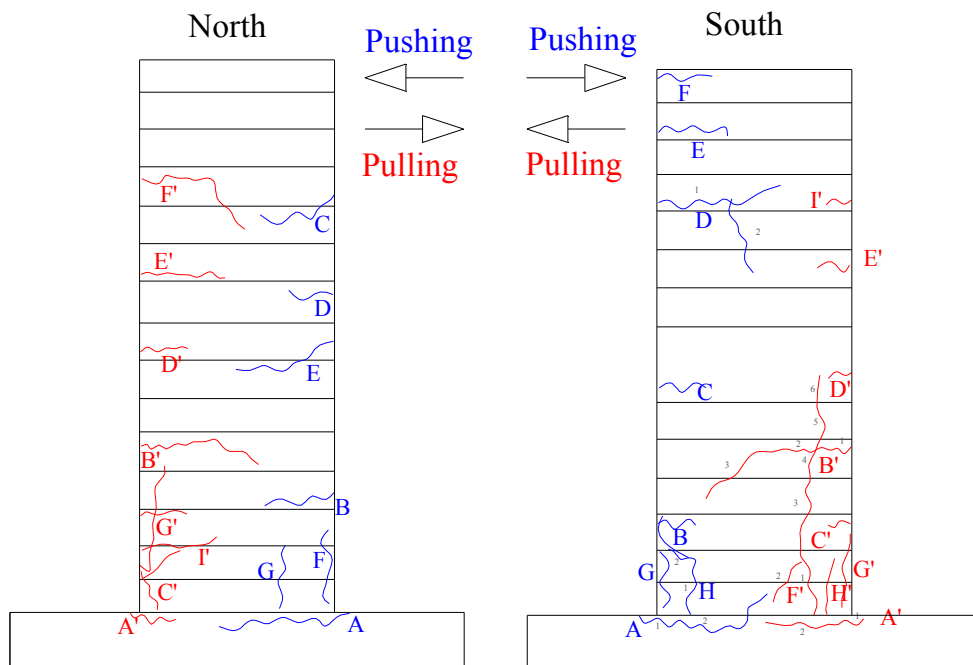


Figure E.192: Crack pattern of NS-X9 after -7% drift ratio.

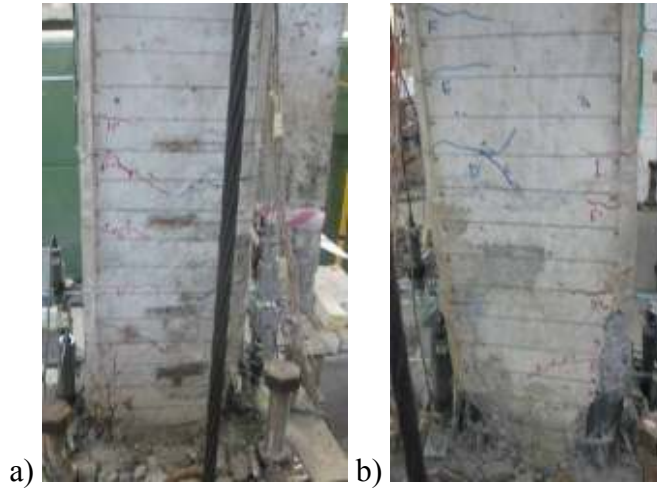


Figure E.193: a) North, and b) South view of NS-X9 after -8% drift ratio.

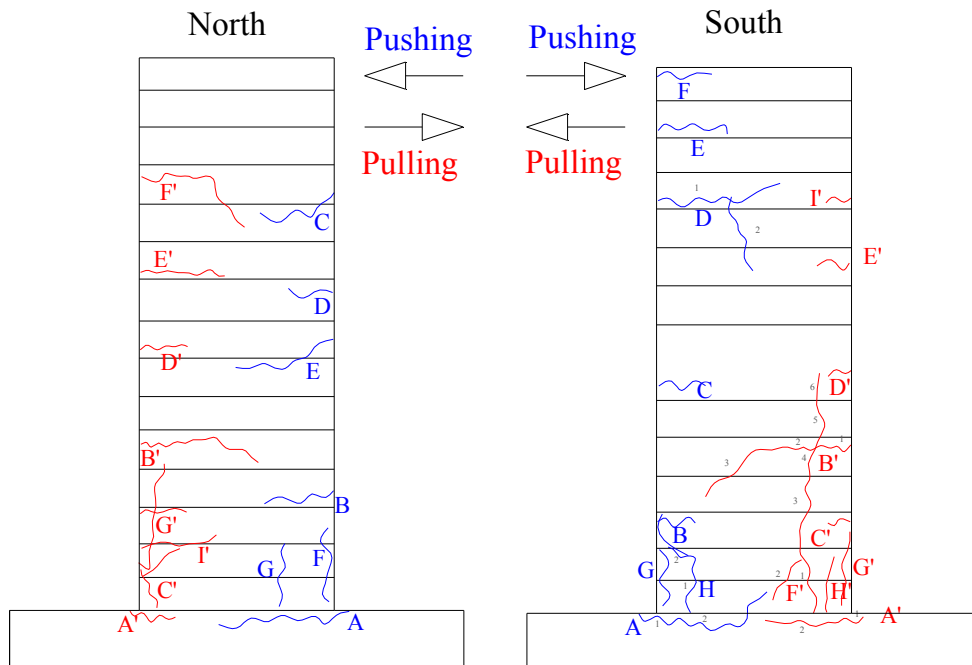


Figure E.194: Crack pattern of NS-X9 after -8% drift ratio.

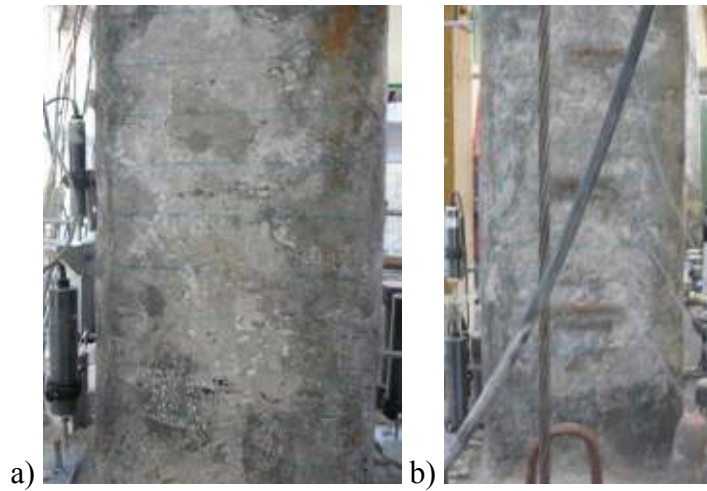


Figure E.195: a) North, and b) South view of NS-X13 after -0.1% drift ratio.

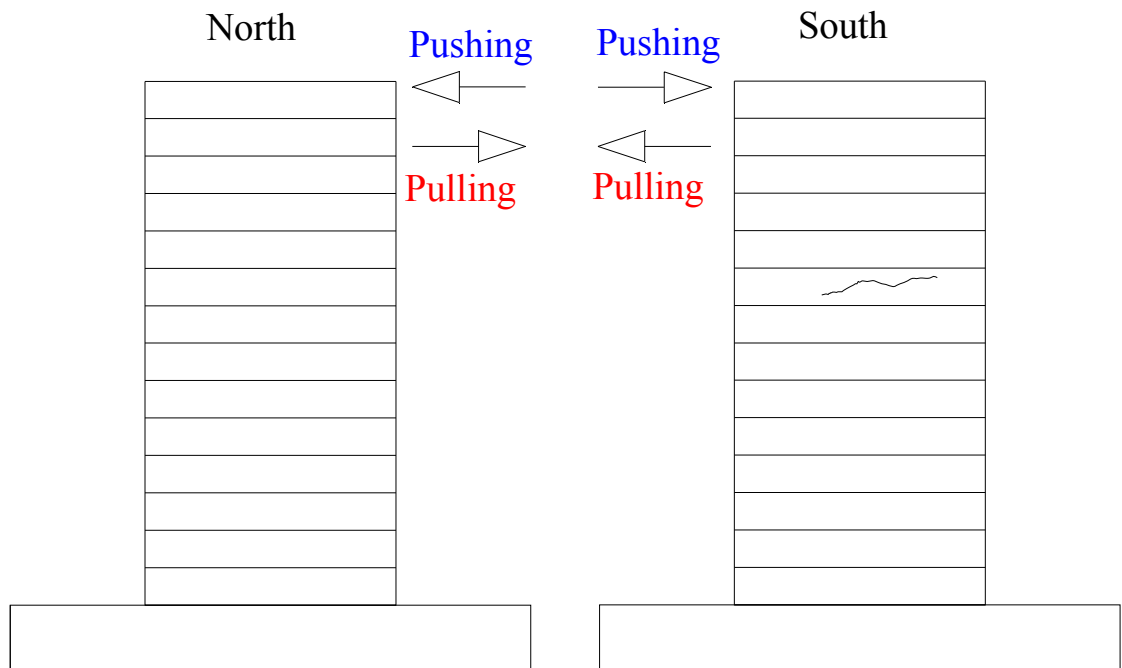


Figure E.196: Crack pattern of NS-X13 after -0.1% drift ratio.

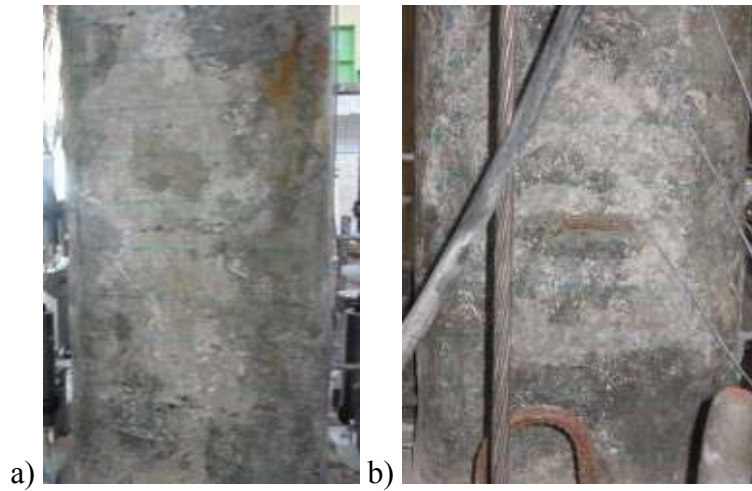


Figure E.197: a) North, and b) South view of NS-X13 after -0.25% drift ratio.

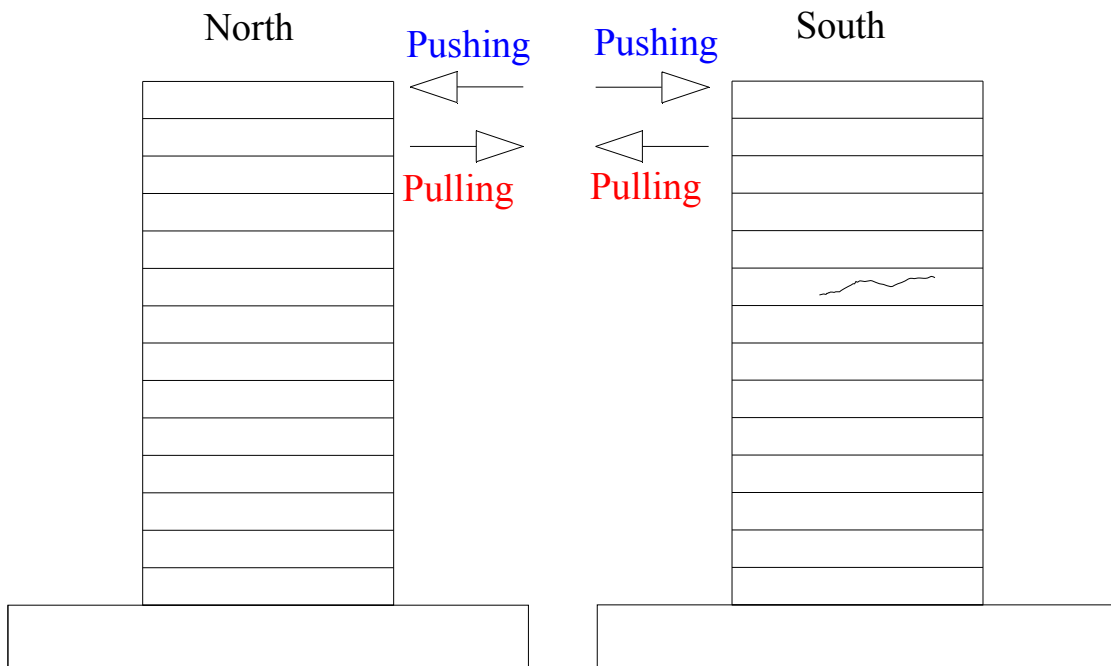


Figure E.198: Crack pattern of NS-X13 after -0.25% drift ratio.

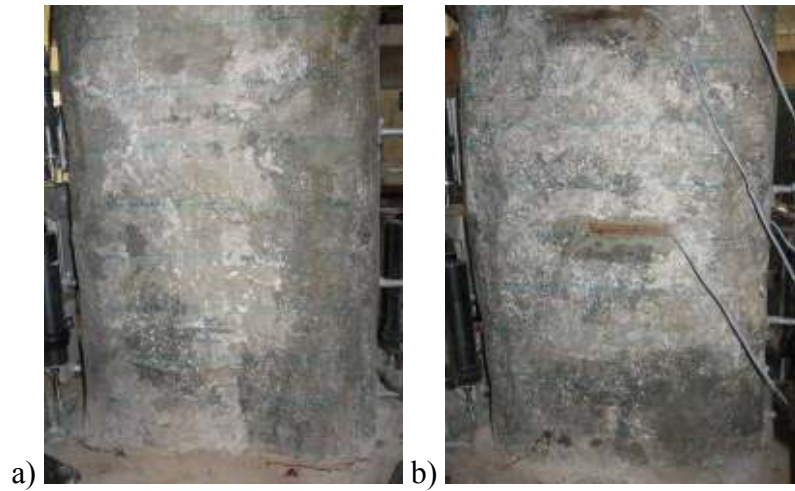


Figure E.199: a) North, and b) South view of NS-X13 after -0.5% drift ratio.

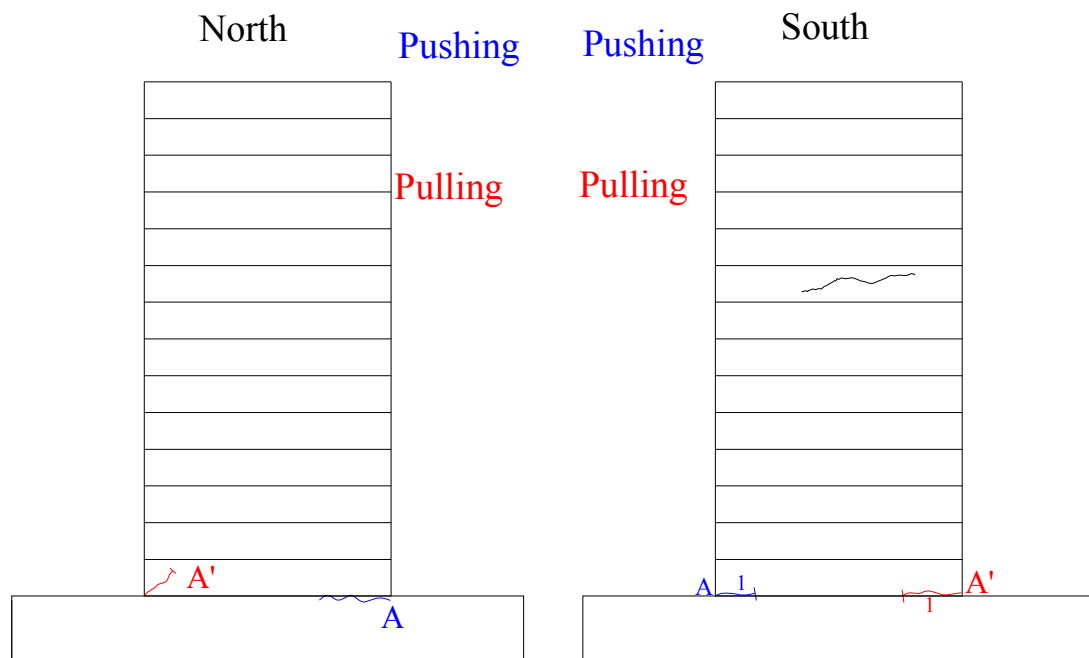


Figure E.200: Crack pattern of NS-X13 after -0.5% drift ratio.

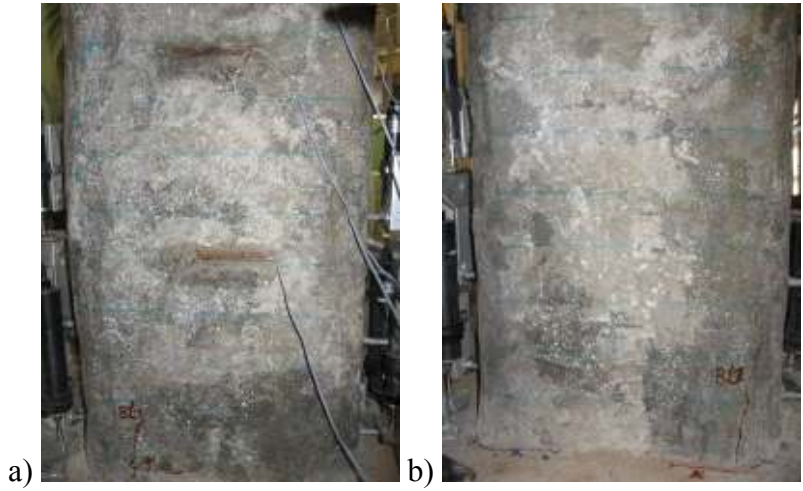


Figure E.201: a) North, and b) South view of NS-X13 after -0.75% drift ratio.

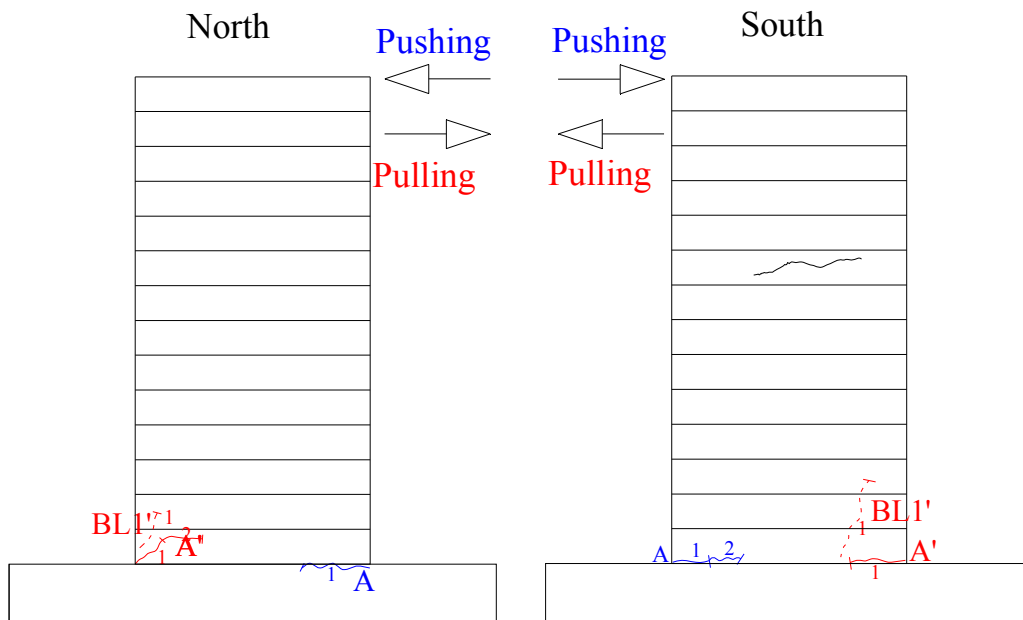


Figure E.202: Crack pattern of NS-X13 after -0.75% drift ratio.

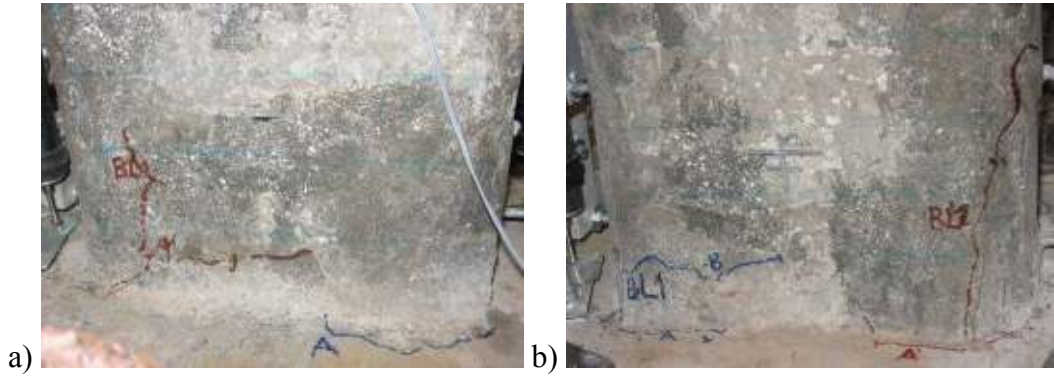


Figure E.203: a) North, and b) South view of NS-X13 after -1% drift ratio.

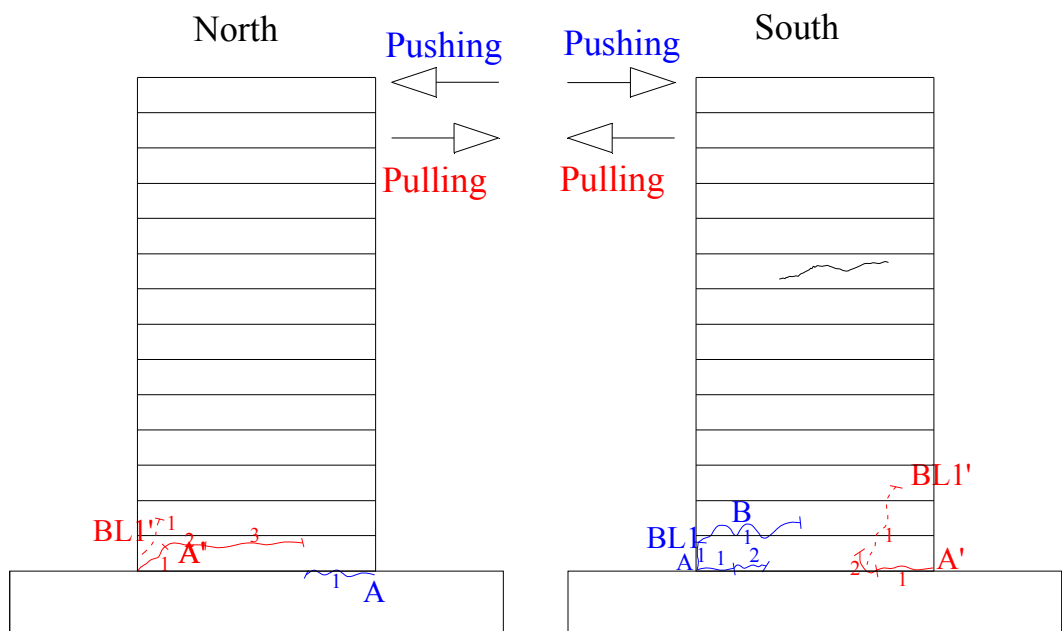


Figure E.204: Crack pattern of NS-X13 after -1% drift ratio.

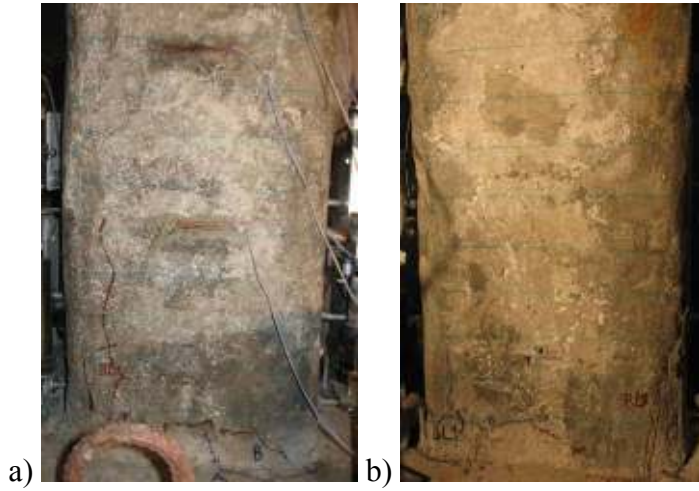


Figure E.205: a) North, and b) South view of NS-X13 after -1.5% drift ratio.

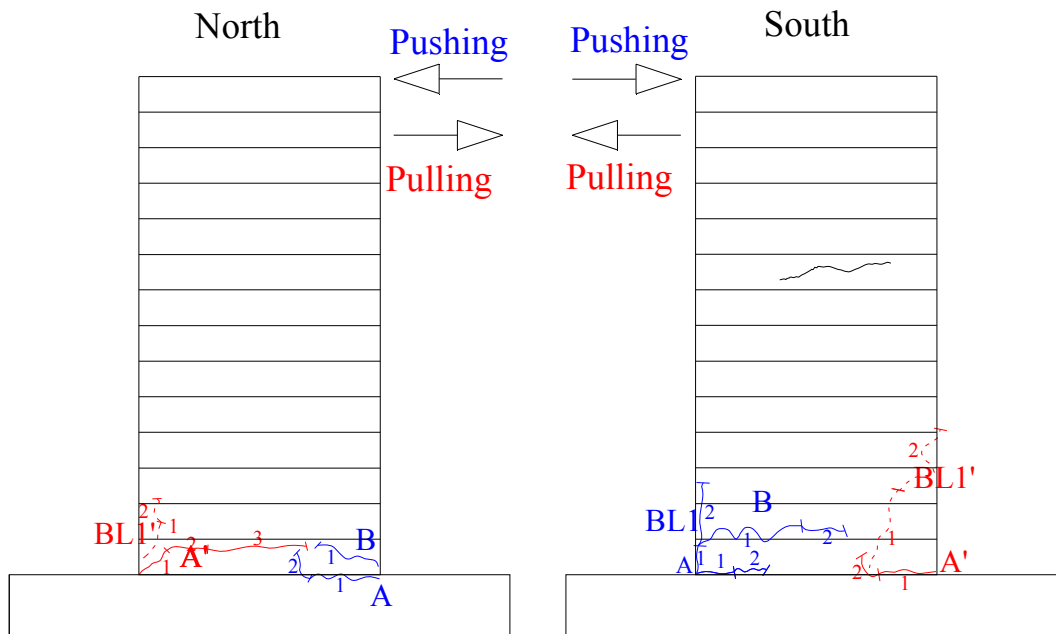


Figure E.206: Crack pattern of NS-X13 after -1.5% drift ratio.

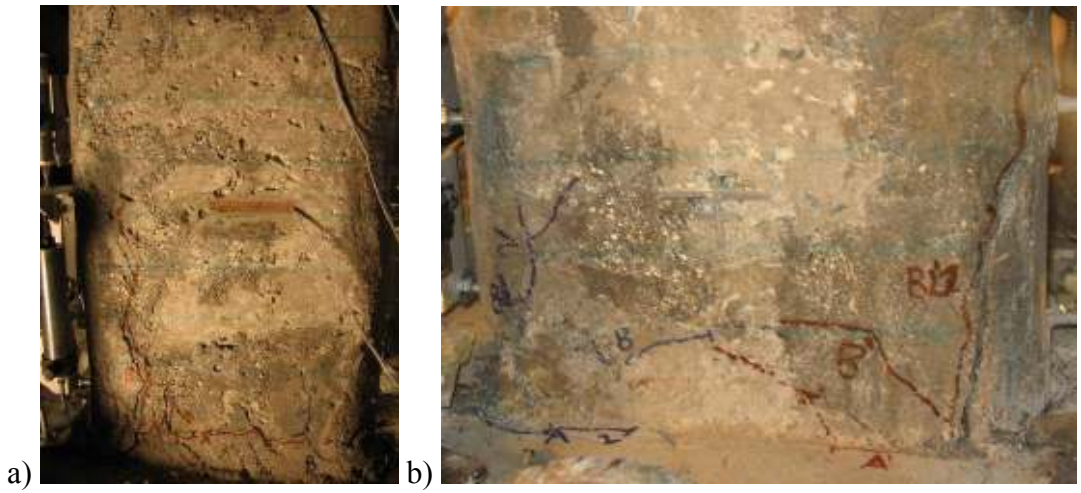


Figure E.207: a) North, and b) South view of NS-X13 after -2% drift ratio.

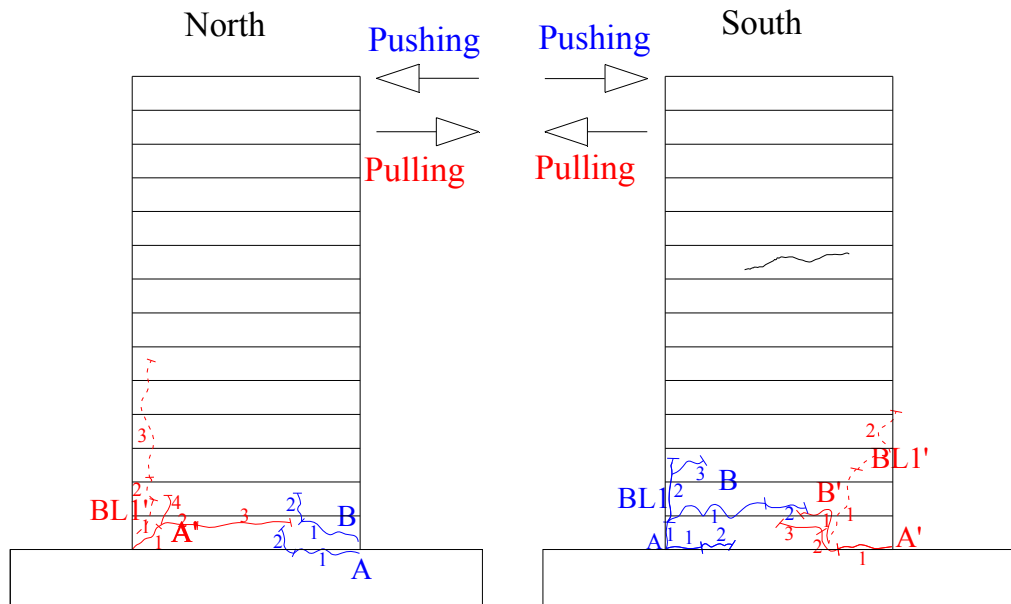


Figure E.208: Crack pattern of NS-X13 after -2% drift ratio.

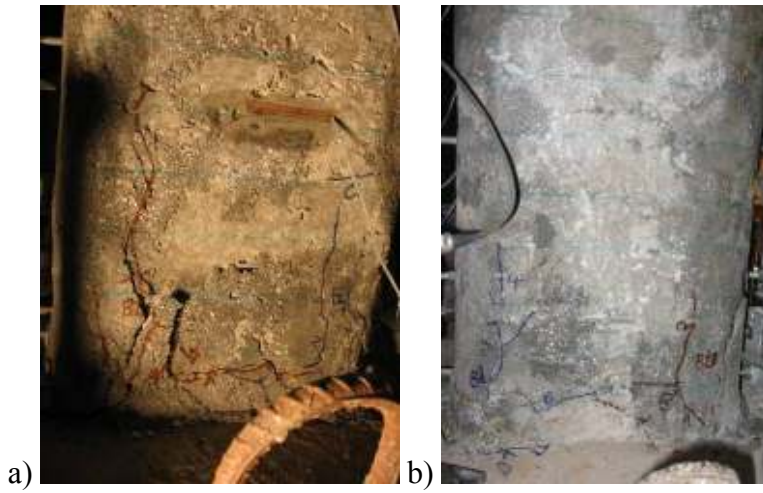


Figure E.209: a) North, and b) South view of NS-X13 after -2.5% drift ratio.

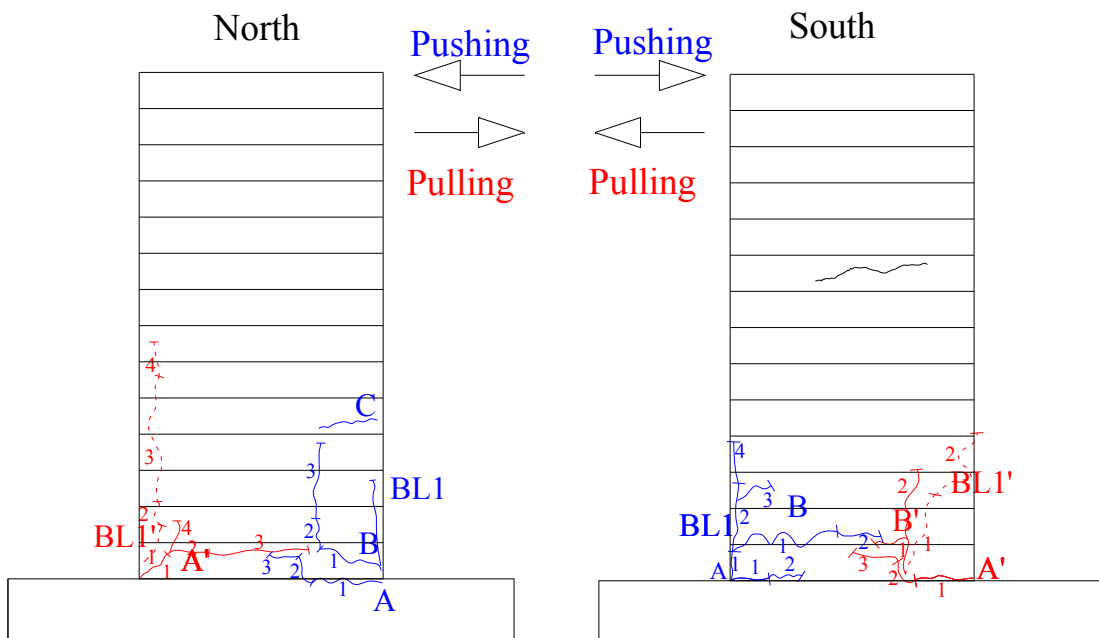


Figure E.210: Crack pattern of NS-X13 after -2.5% drift ratio.

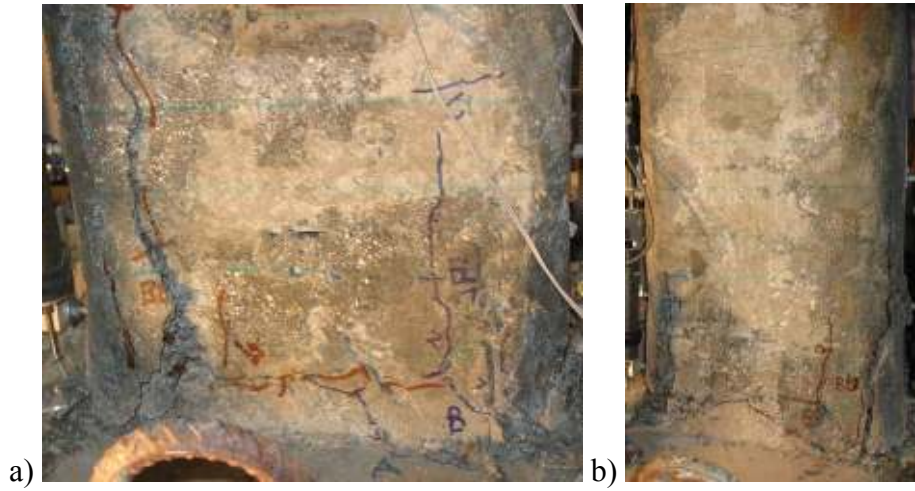


Figure E.211: a) North, and b) South view of NS-X13 after -3% drift ratio.

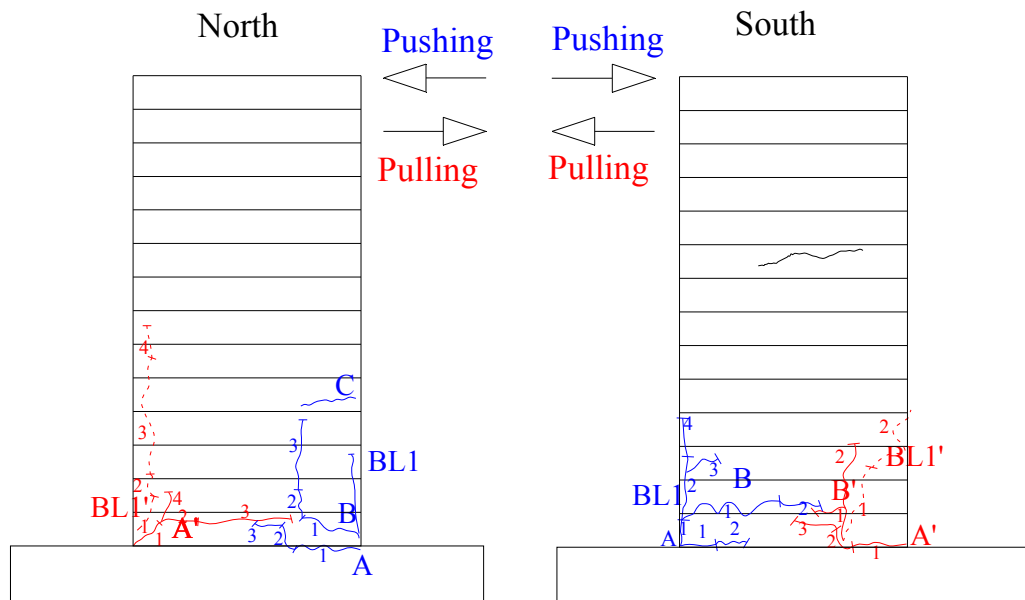


Figure E.212: Crack pattern of NS-X13 after -3% drift ratio.

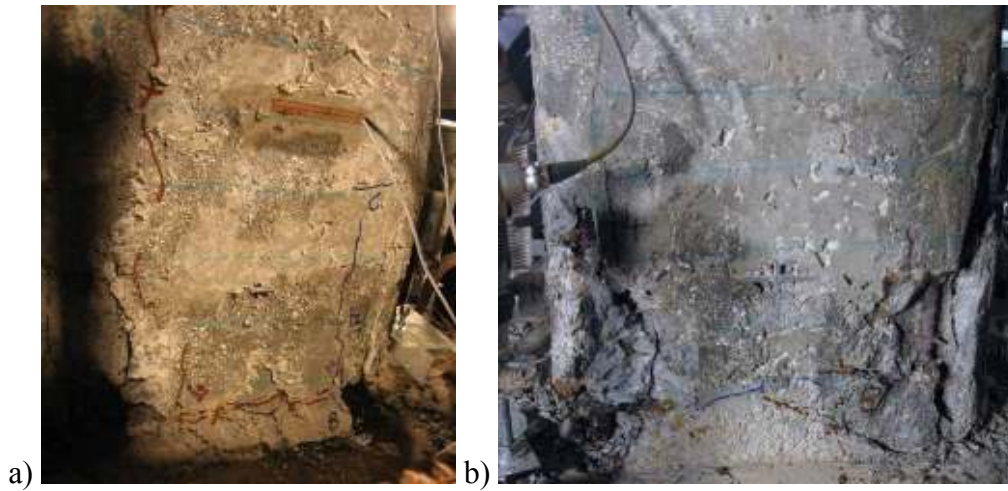


Figure E.213: a) North, and b) South view of NS-X13 after -3.5% drift ratio.

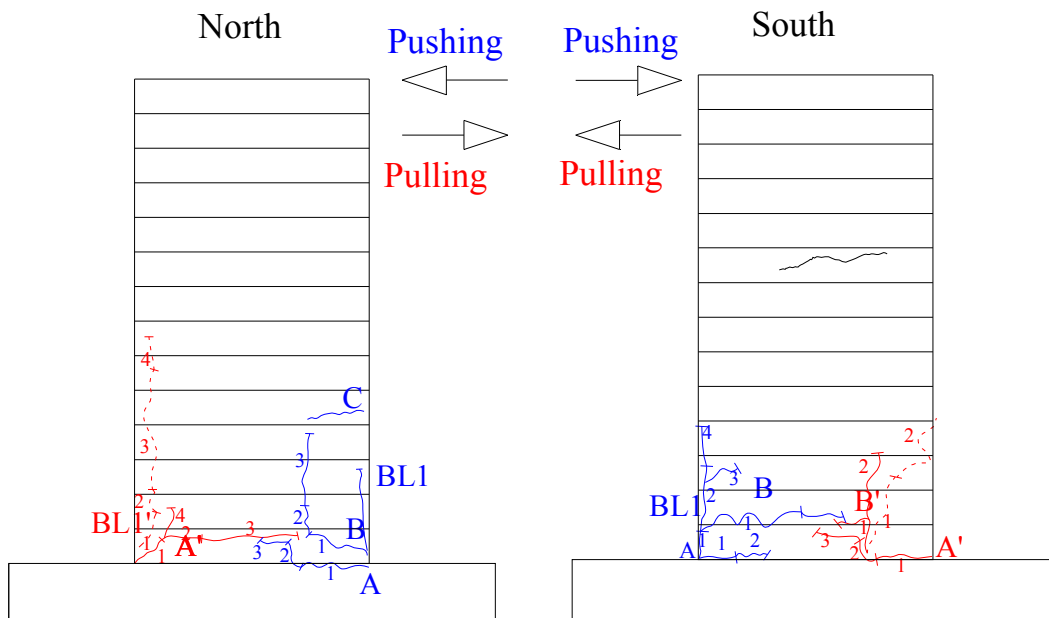


Figure E.214: Crack pattern of NS-X13 after -3.5% drift ratio.

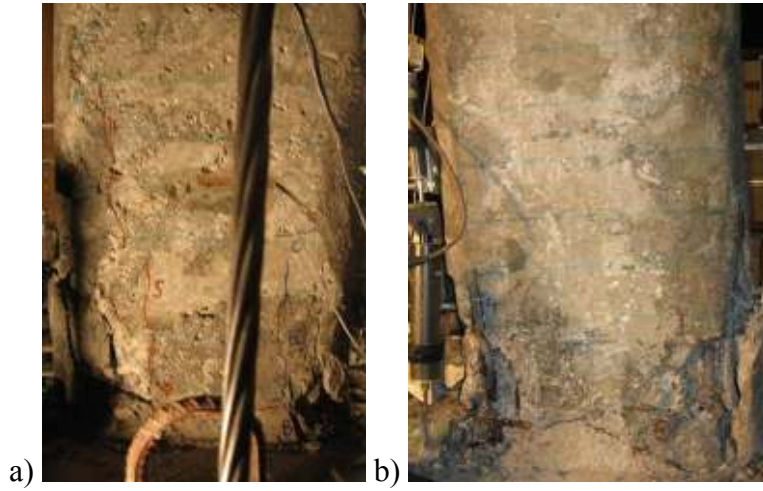


Figure E.215: (a) North, and (b) South view of NS-X13 after -4% drift ratio.

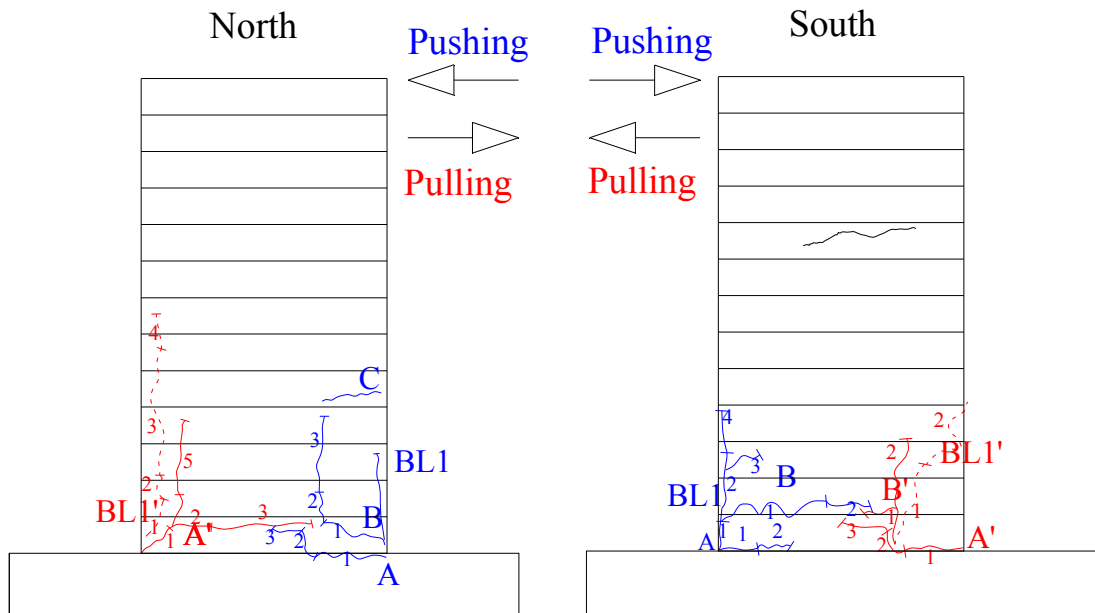


Figure E.216: Crack pattern of NS-X13 after -4% drift ratio.

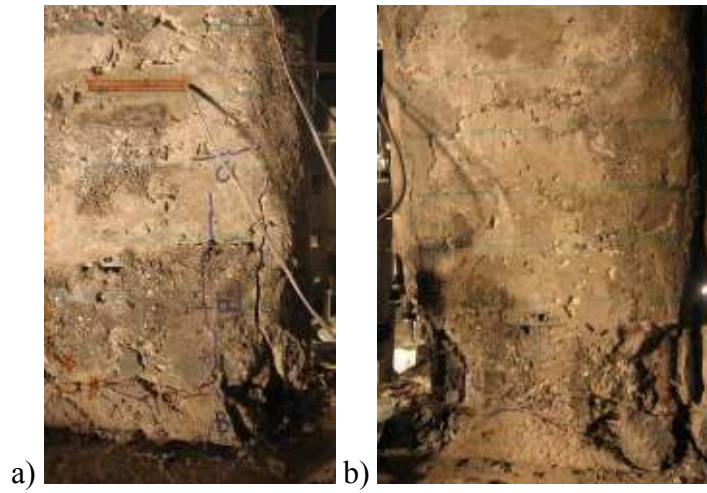


Figure E.217: (a) North, and (b) South view of NS-X13 after -4.5% drift ratio.

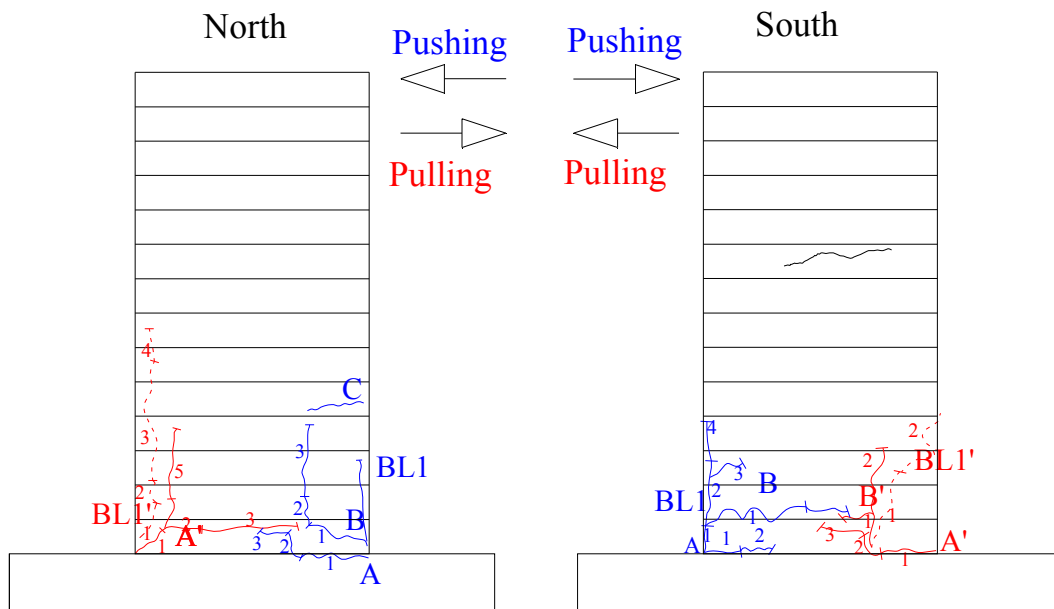


Figure E.218: Crack pattern of NS-X13 after -4.5% drift ratio.

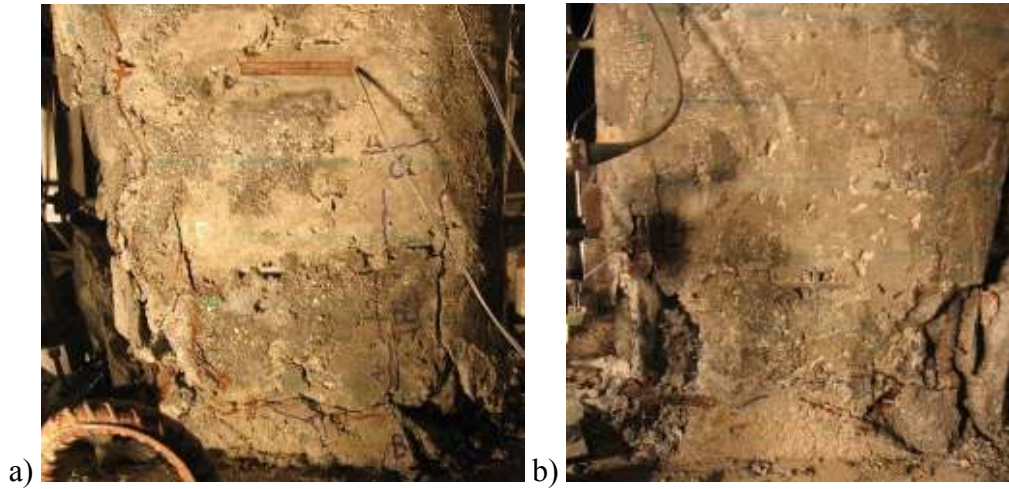


Figure E.219: a) North, and b) South view of NS-X13 after -5% drift ratio.

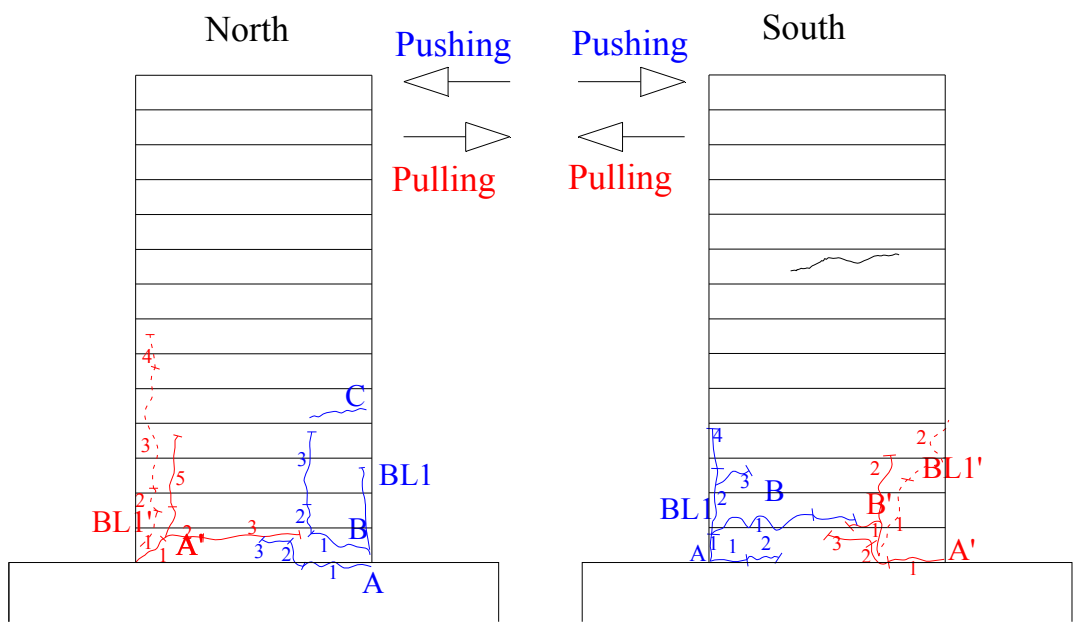


Figure E.220: Crack pattern of NS-X13 after -5% drift ratio.



Figure E.221: a) North, and b) South view of NS-X13 after -6% drift ratio.

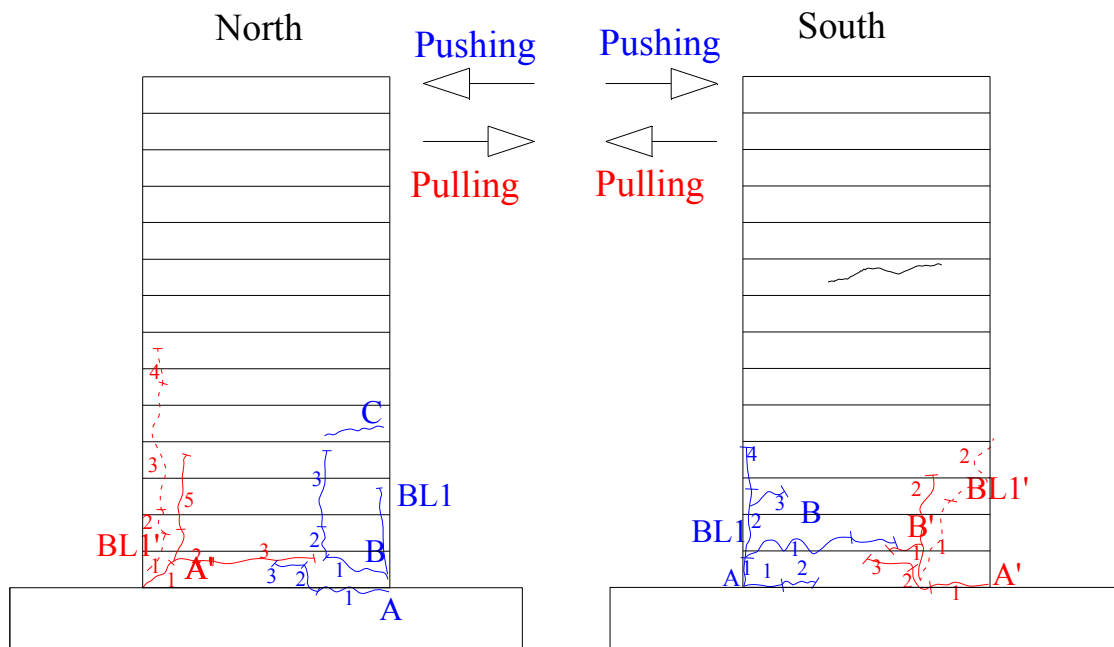


Figure E.222: Crack pattern of NS-X13 after -6% drift ratio.

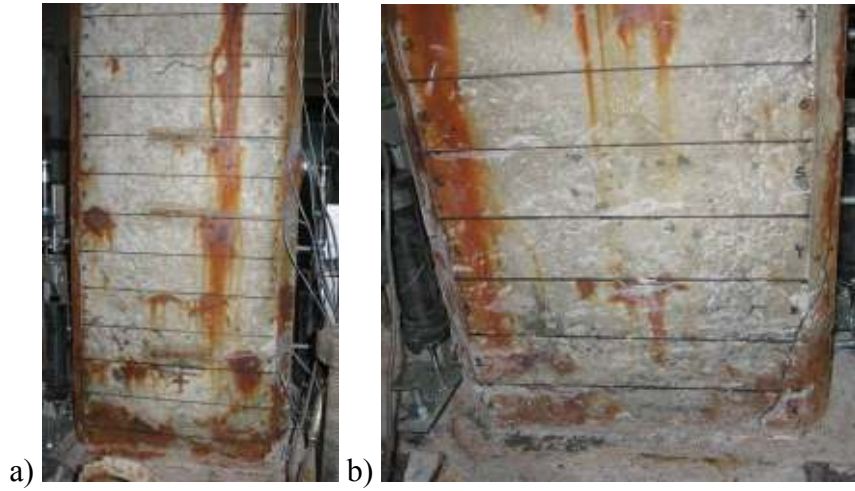


Figure E.223: a) North, and b) South view of NS-X16 after -0.1% drift ratio.

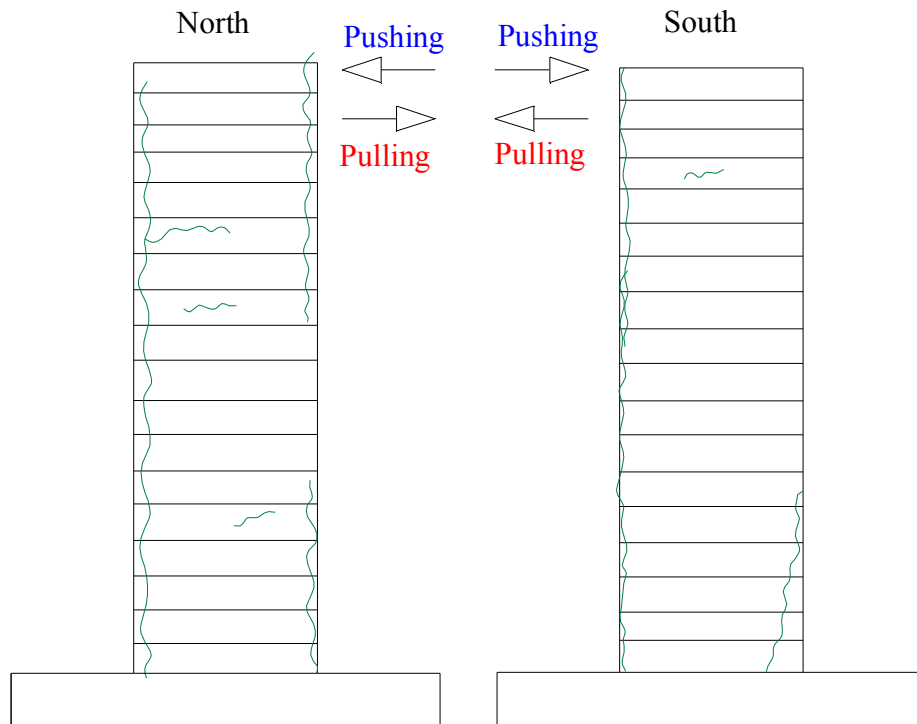


Figure E.224: Crack pattern of NS-X16 after -0.1% drift ratio.

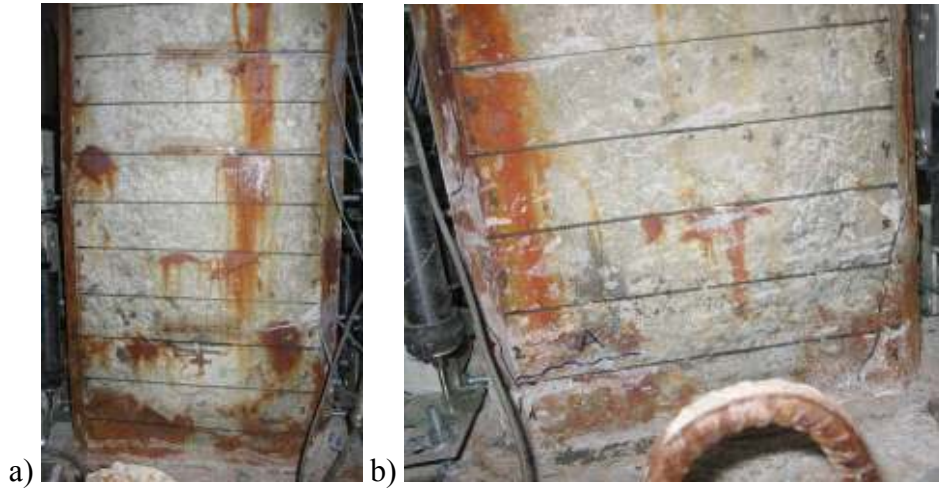


Figure E.225: a) North, and b) South view of NS-X16 after -0.25% drift ratio.

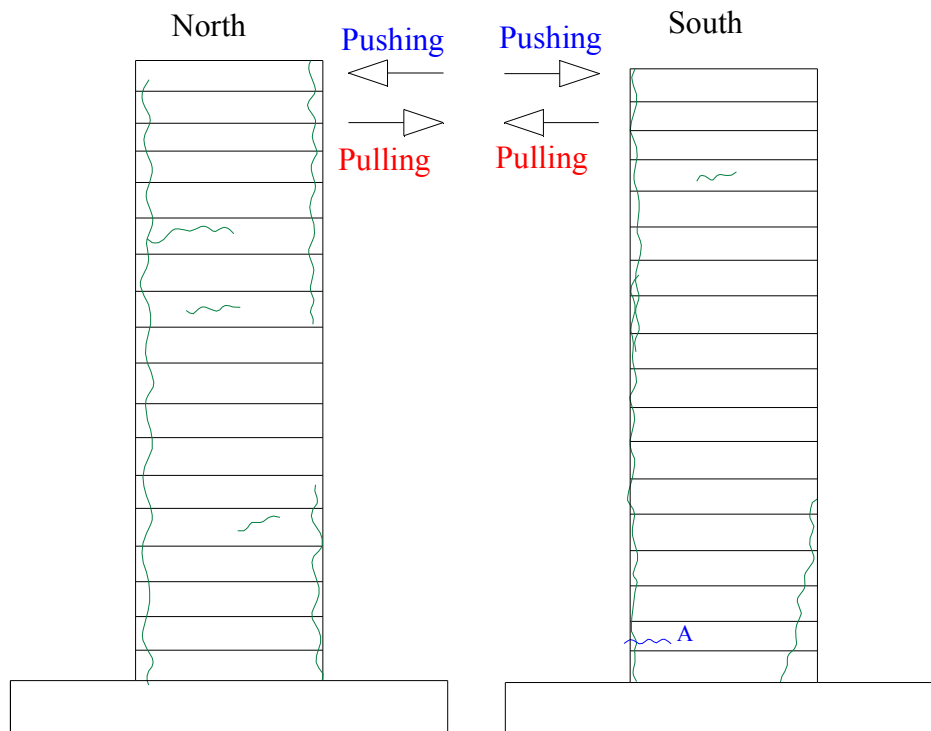


Figure E.226: Crack pattern of NS-X16 after -0.25% drift ratio.

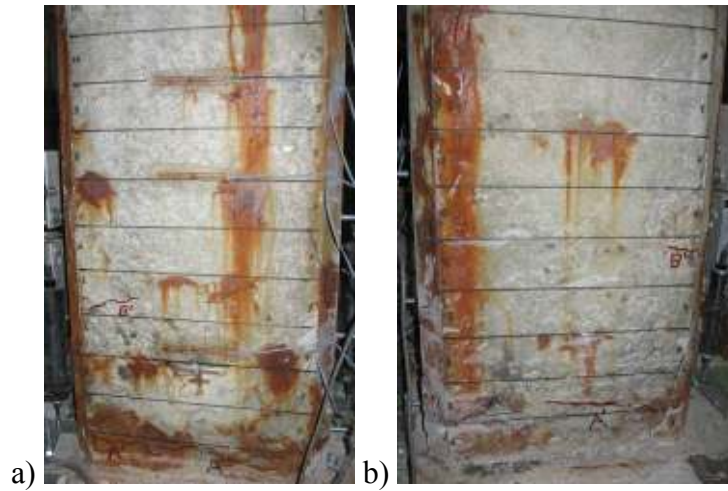


Figure E.227: a) North, and b) South view of NS-X16 after -0.5% drift ratio.

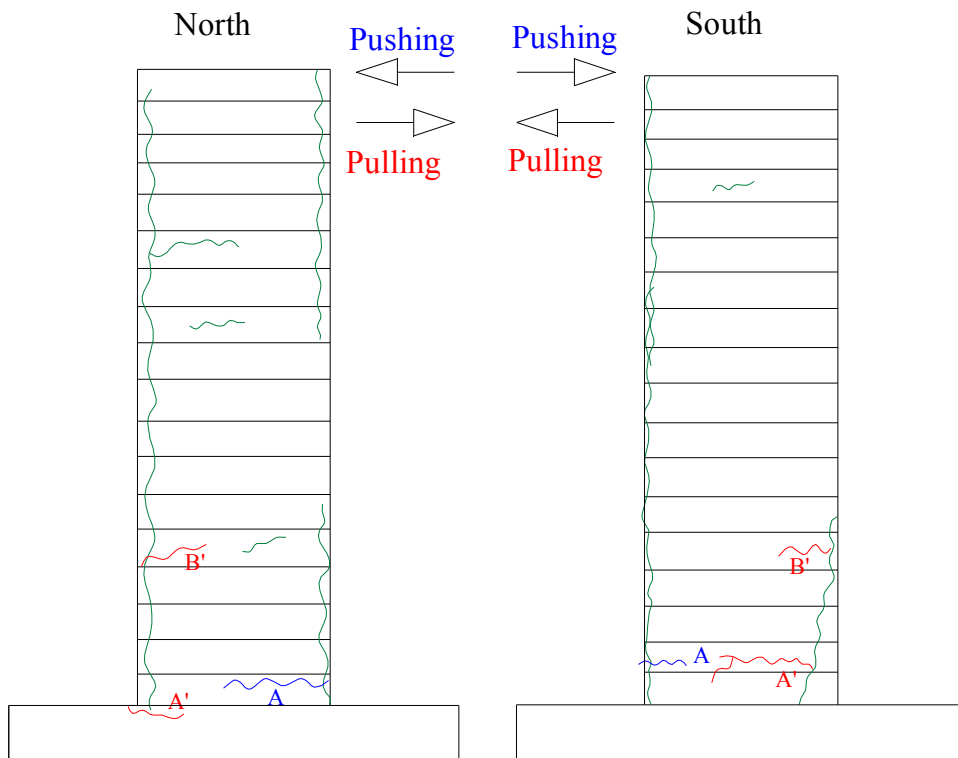


Figure E.228: Crack pattern of NS-X16 after -0.5% drift ratio.

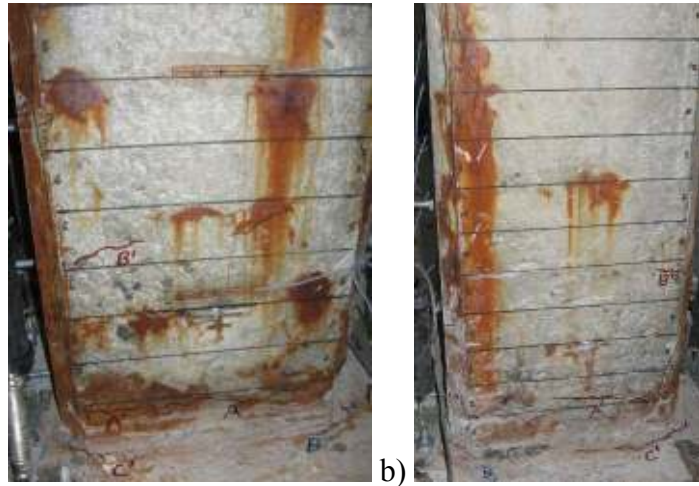


Figure E.229: a) North, and b) South view of NS-X16 after -0.75% drift ratio.

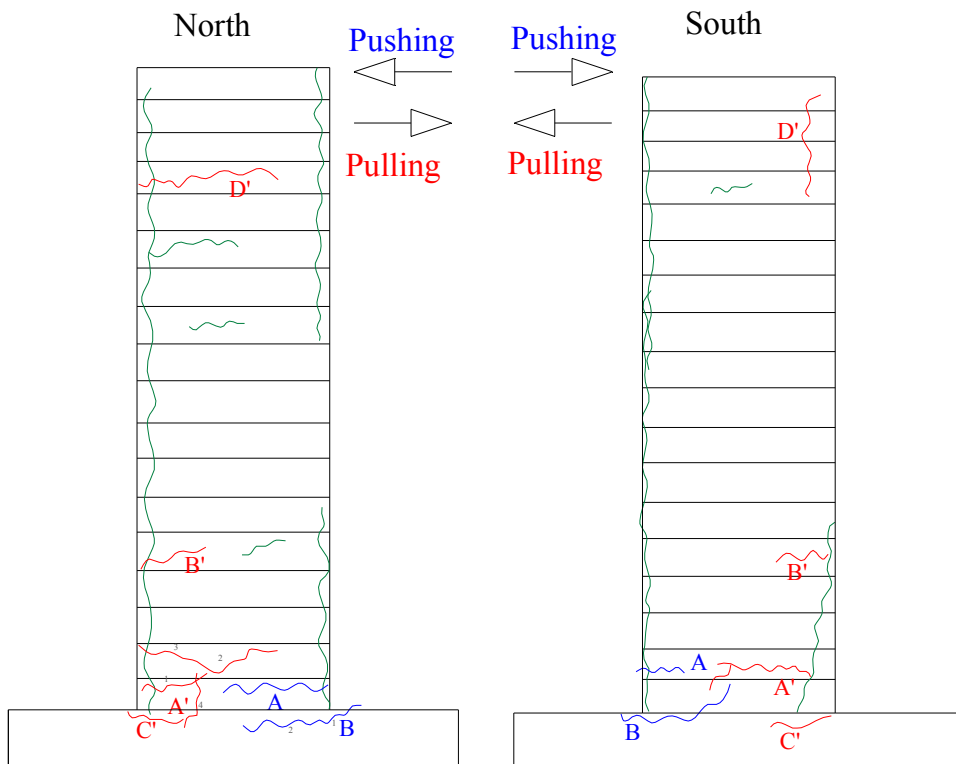


Figure E.230: Crack pattern of NS-X16 after -0.75% drift ratio.

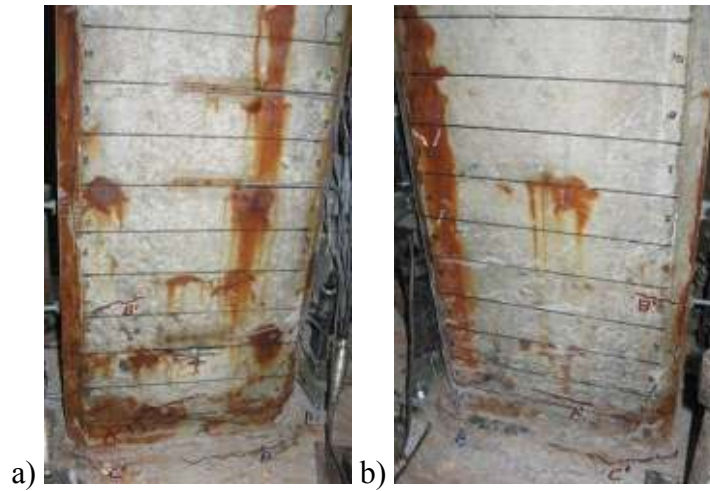


Figure E.231: (a) North, and (b) South view of NS-X16 after -1% drift ratio.

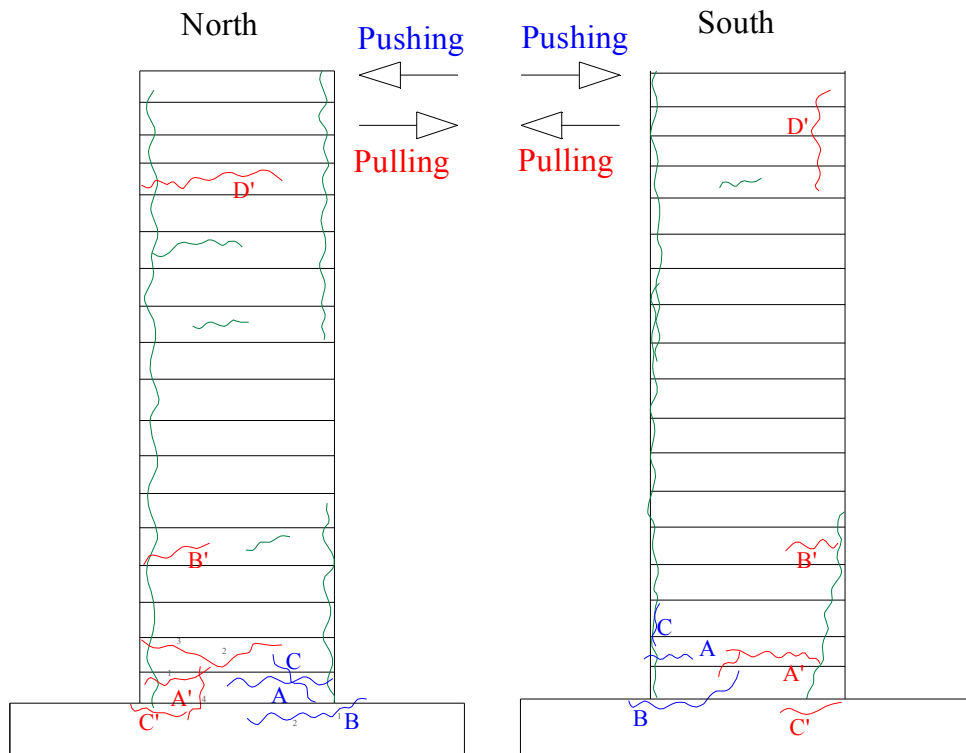


Figure E.232: Crack pattern of NS-X16 after -1% drift ratio.

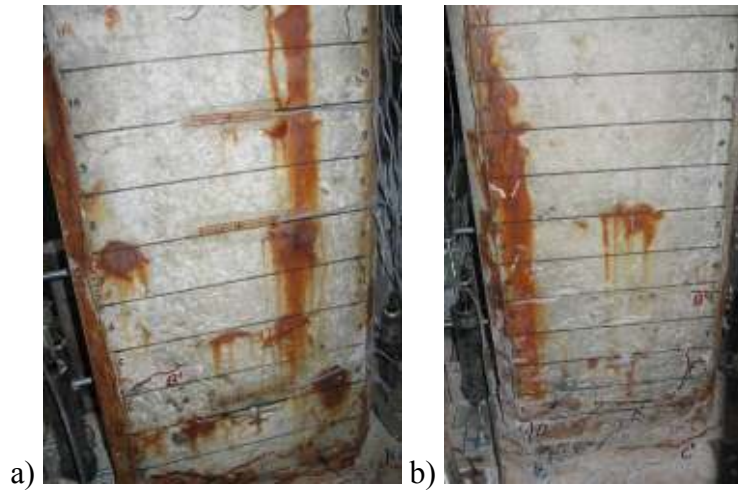


Figure E.233: a) North, and b) South view of NS-X16 after -1.5% drift ratio.

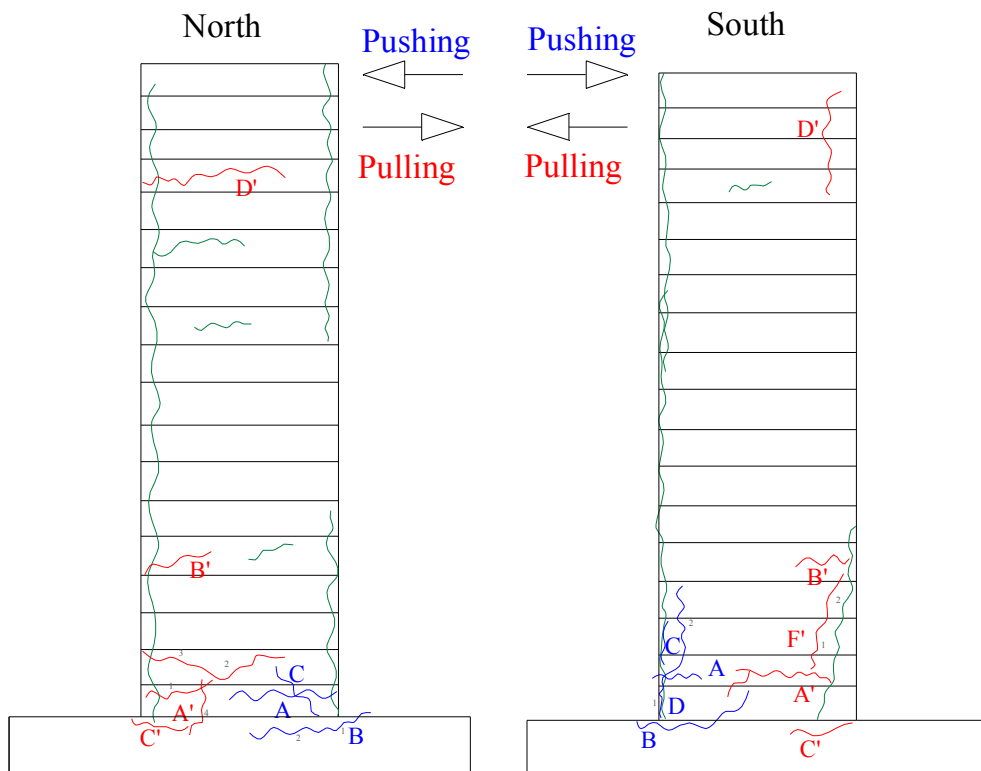


Figure E.234: Crack pattern of NS-X16 after -1.5% drift ratio.

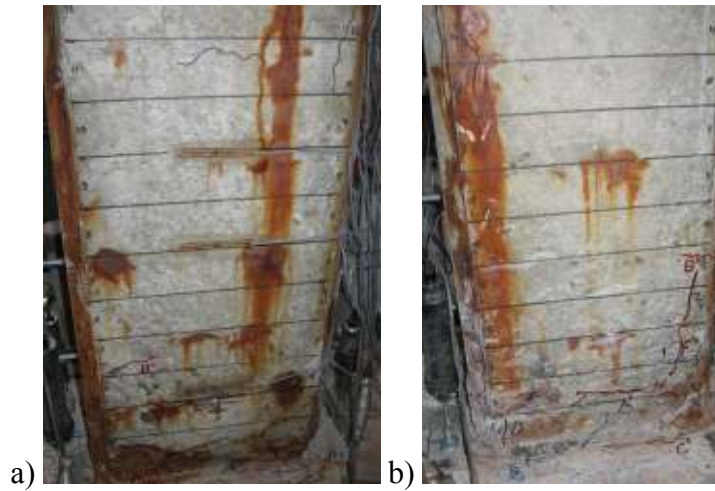


Figure E.235: a) North, and b) South view of NS-X16 after -2% drift ratio.

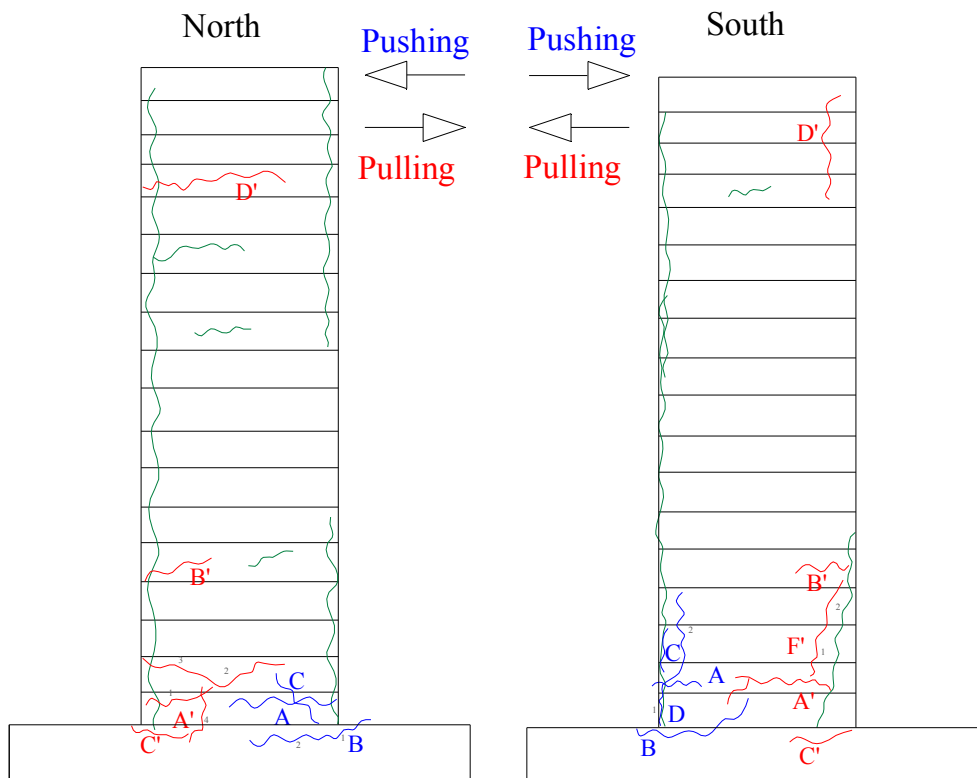


Figure E.236: Crack pattern of NS-X16 after -2% drift ratio.

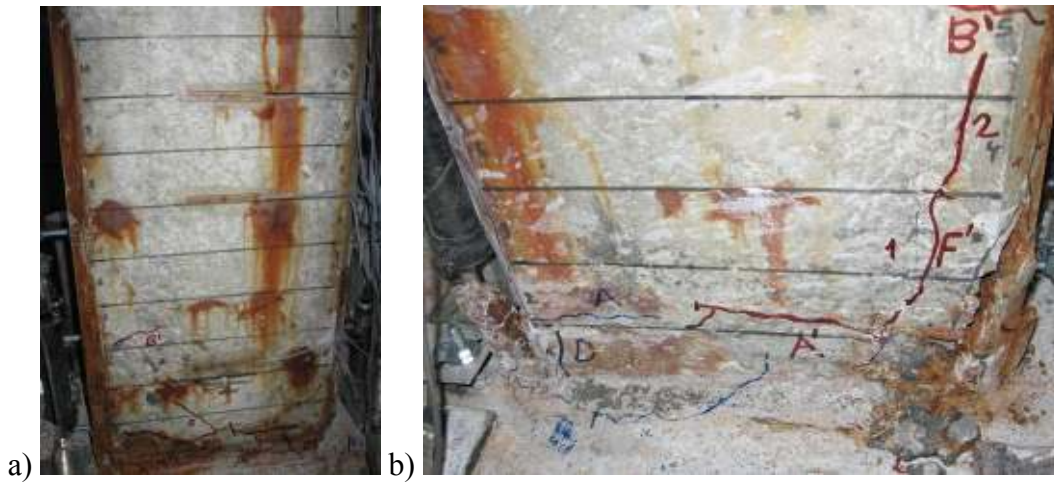


Figure E.237: a) North, and b) South view of NS-X16 after -2.5% drift ratio.

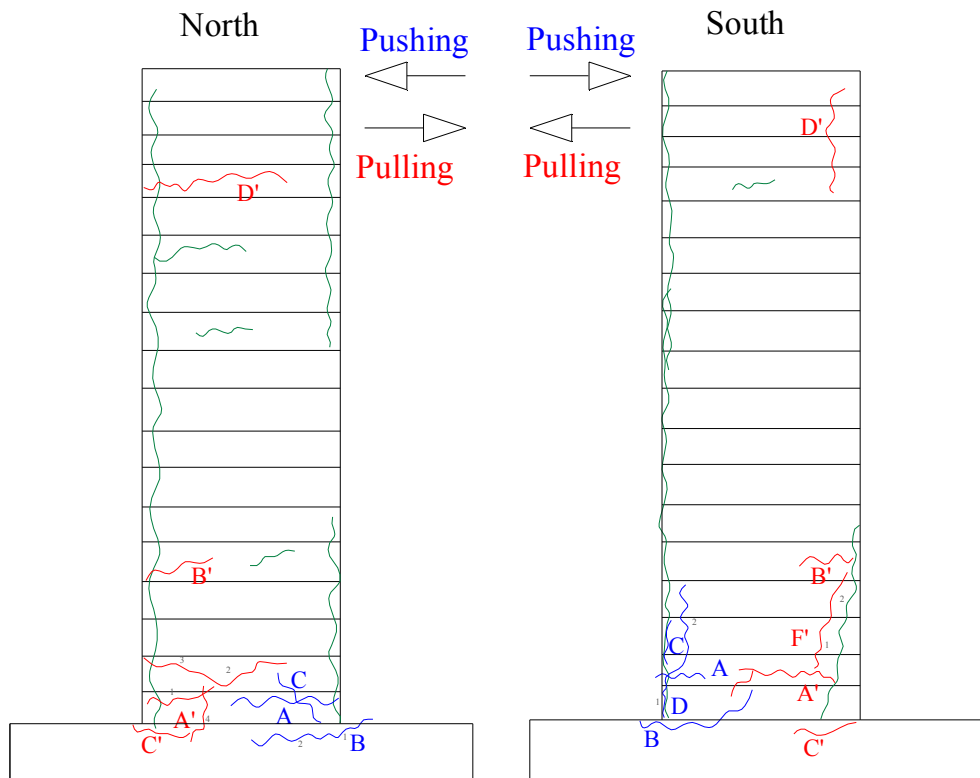


Figure E.238: Crack pattern of NS-X16 after -2.5% drift ratio.

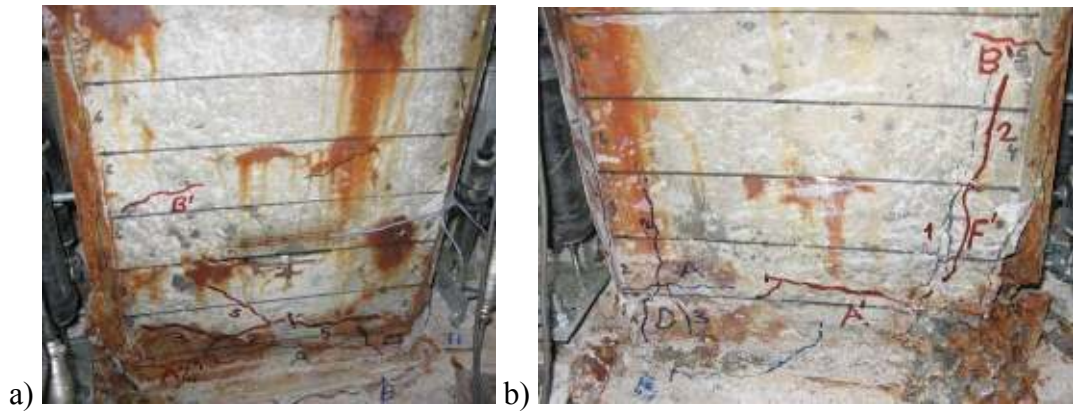


Figure E.239: a) North, and b) South view of NS-X16 after -3% drift ratio.

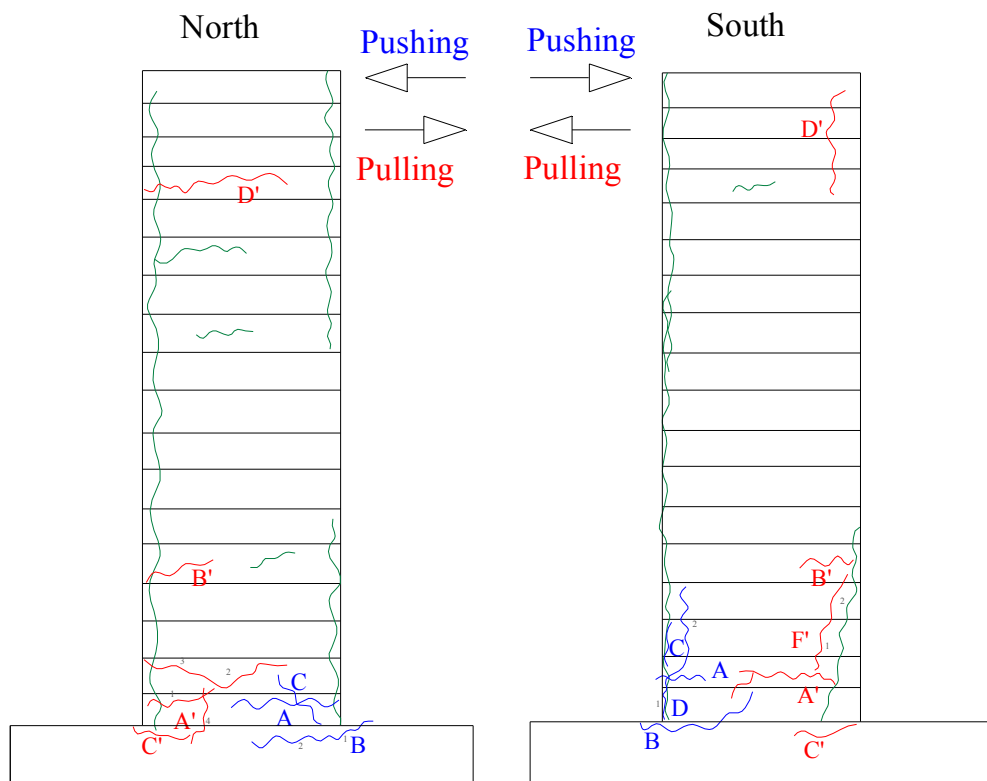


Figure E.240: Crack pattern of NS-X16 after -3% drift ratio.

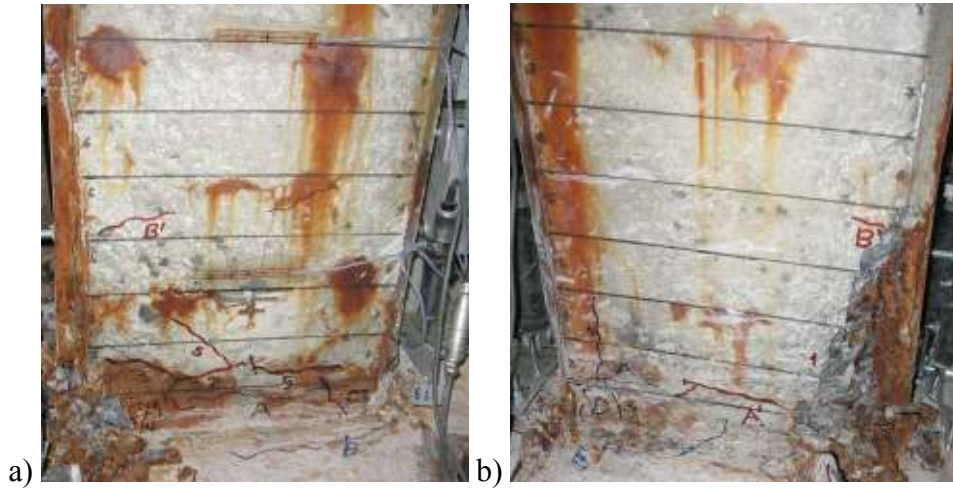


Figure E.241: a) North, and b) South view of NS-X16 after -3.5% drift ratio.

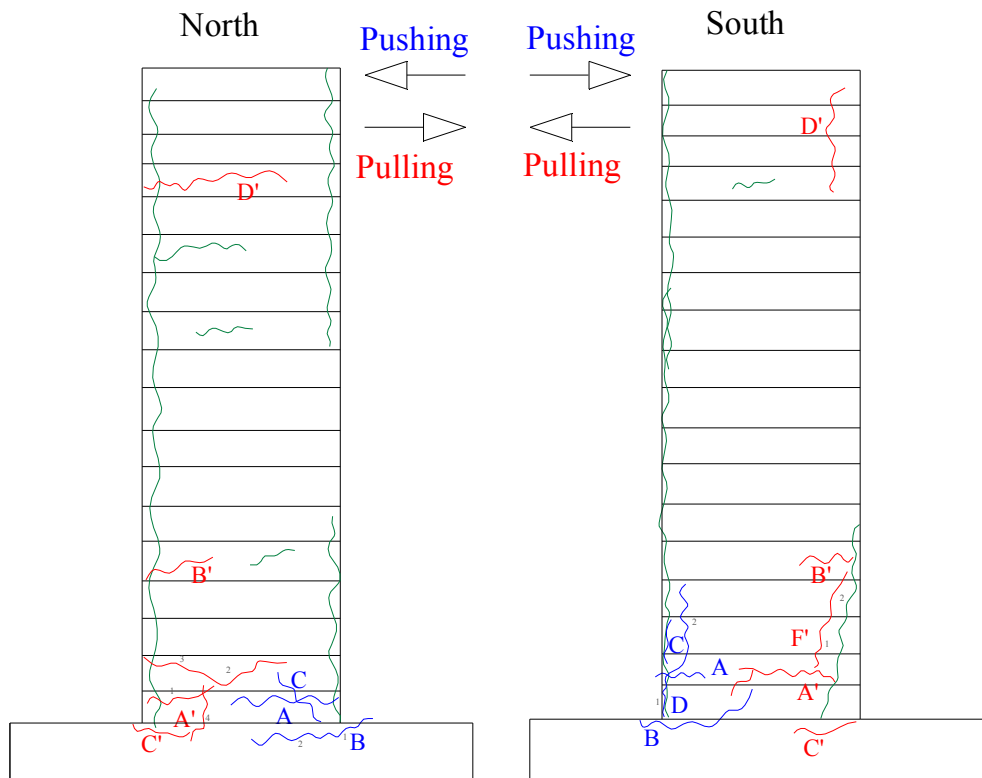


Figure E.242: Crack pattern of NS-X16 after -3.5% drift ratio.

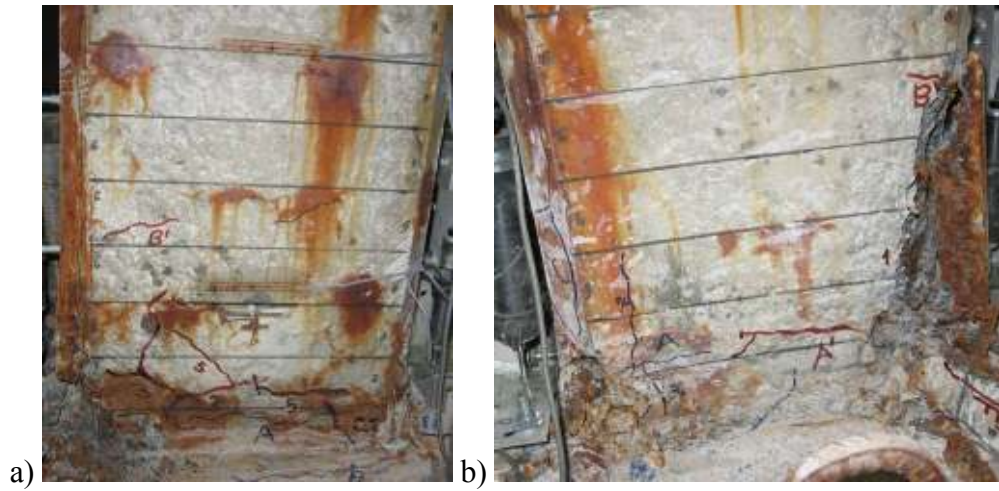


Figure E.243: a) North, and b) South view of NS-X16 after -4% drift ratio.

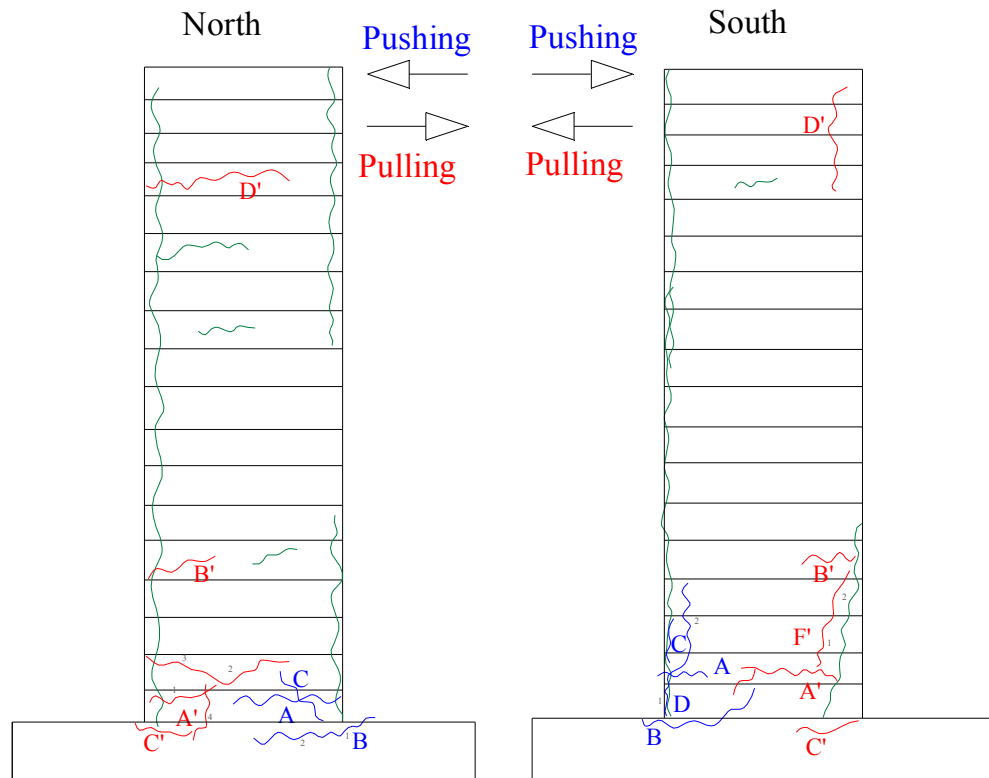


Figure E.244: Crack pattern of NS-X16 after -4% drift ratio.

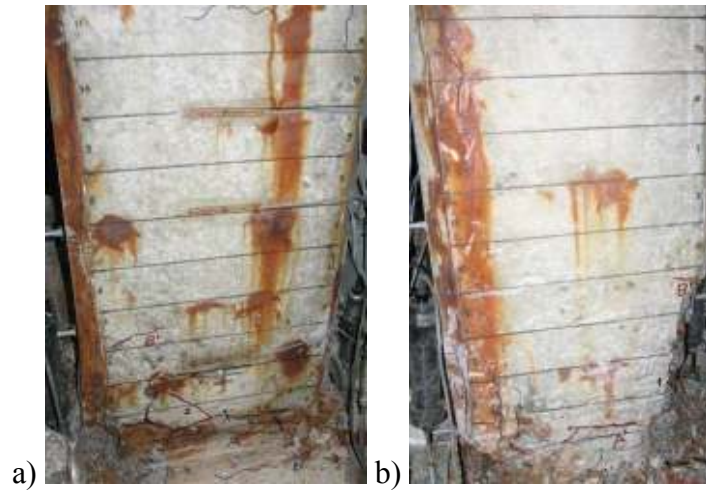


Figure E.245: a) North, and b) South view of NS-X16 after -4.5% drift ratio.

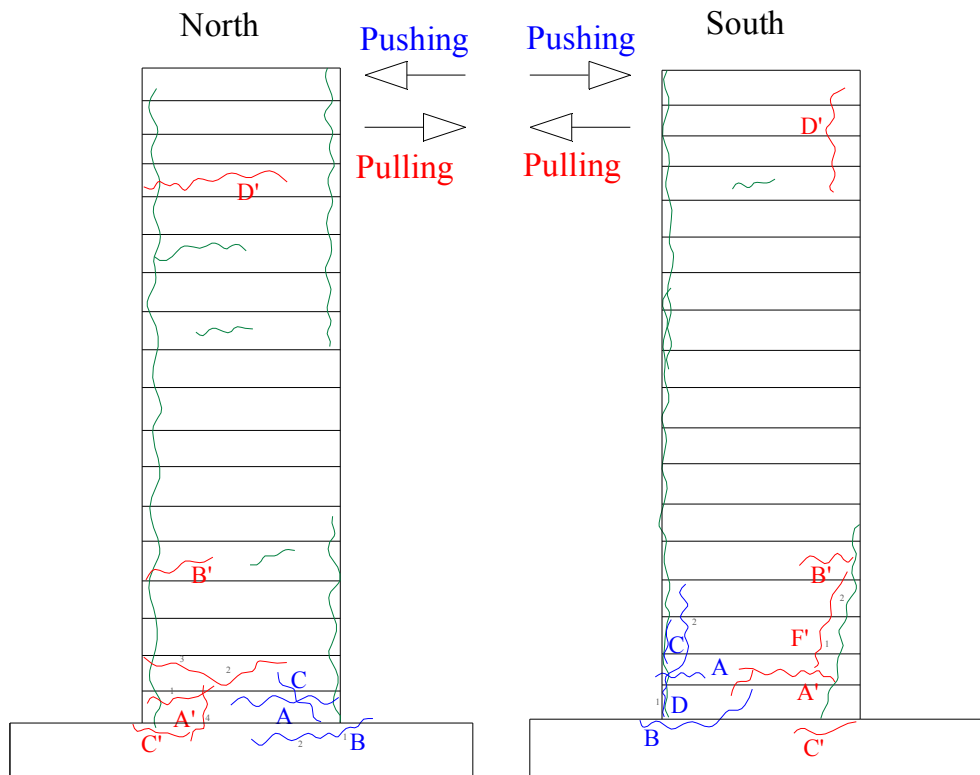


Figure E.246: Crack pattern of NS-X16 after -4.5% drift ratio.

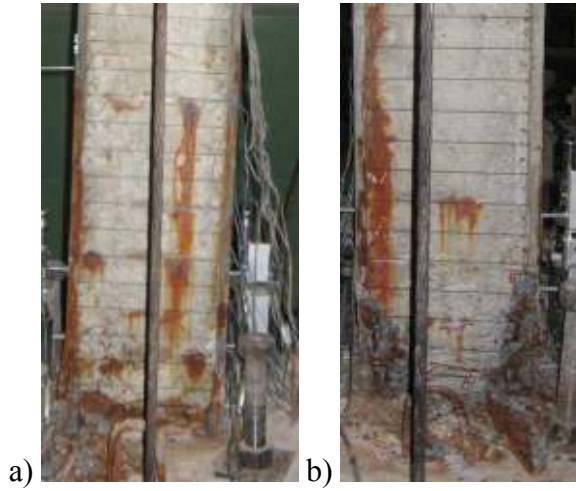


Figure E.247: a) North, and b) South view of NS-X16 after -5% drift ratio.

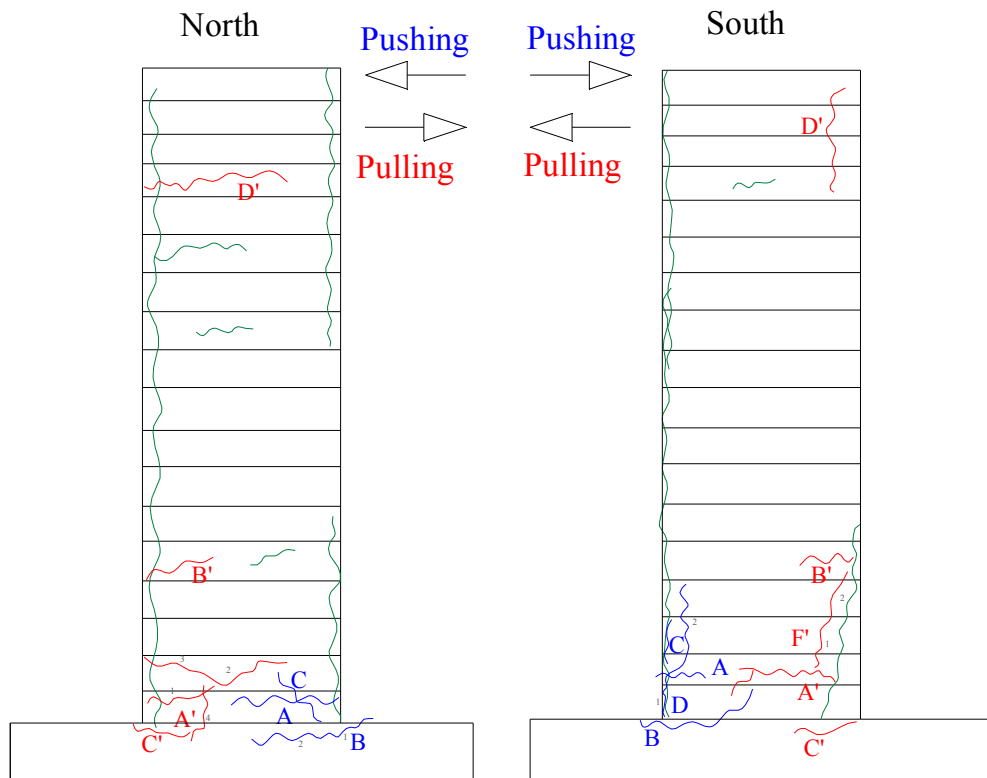


Figure E.248: Crack pattern of NS-X16 after -5% drift ratio.

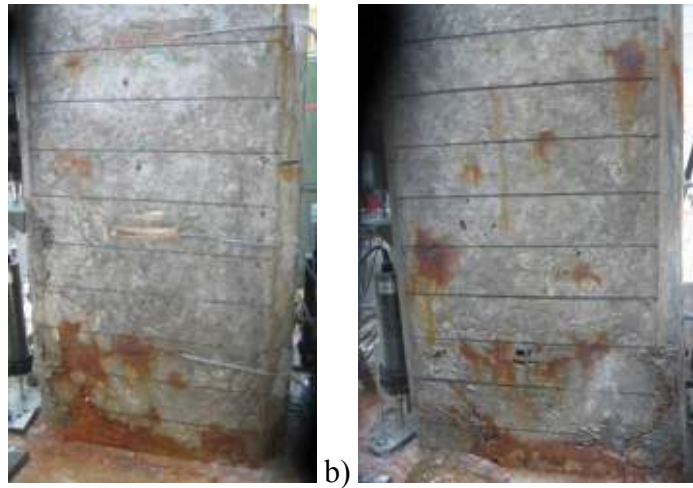


Figure E.249: a) North, and b) South view of NS-X22 after -0.1% drift ratio.

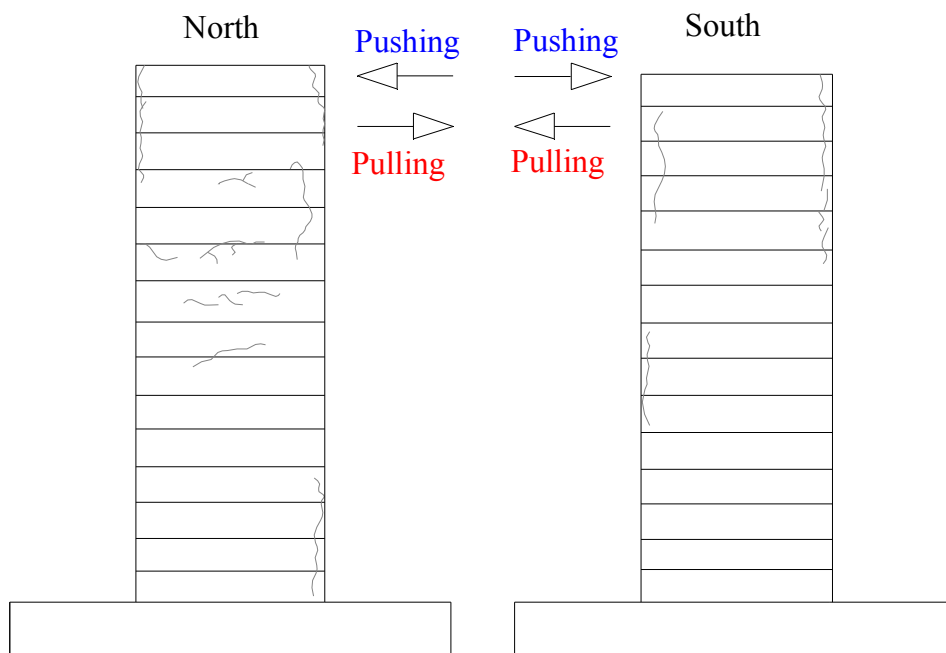


Figure E.250: Crack pattern of NS-X22 after -0.1% drift ratio.

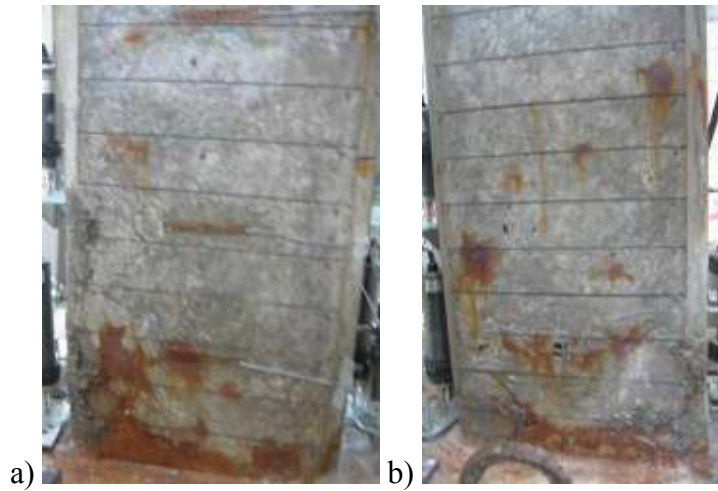


Figure E.251: a) North, and b) South view of NS-X22 after -0.25% drift ratio.

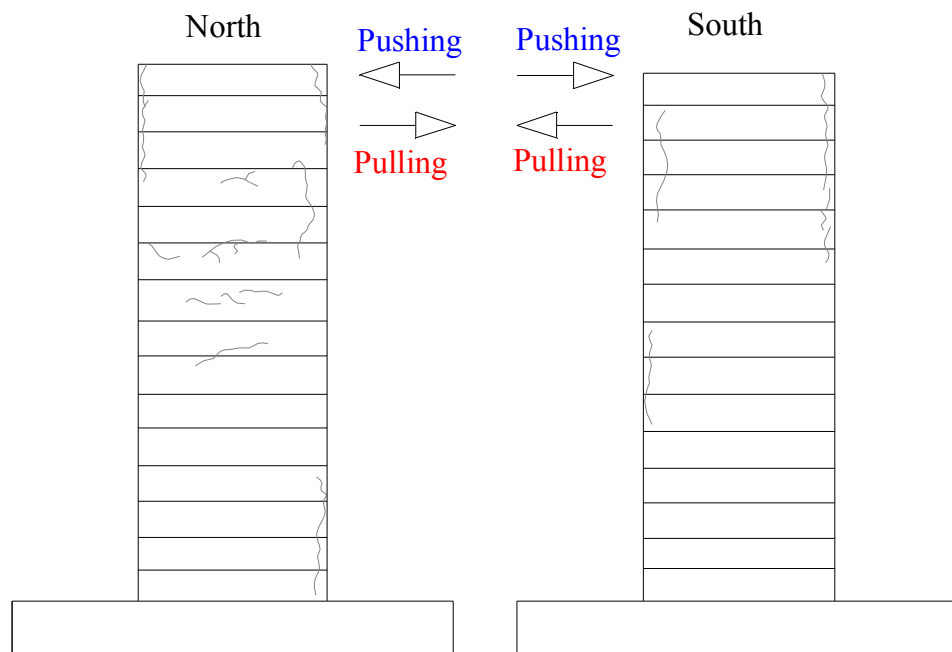


Figure E.252: Crack pattern of NS-X22 after -0.25% drift ratio.

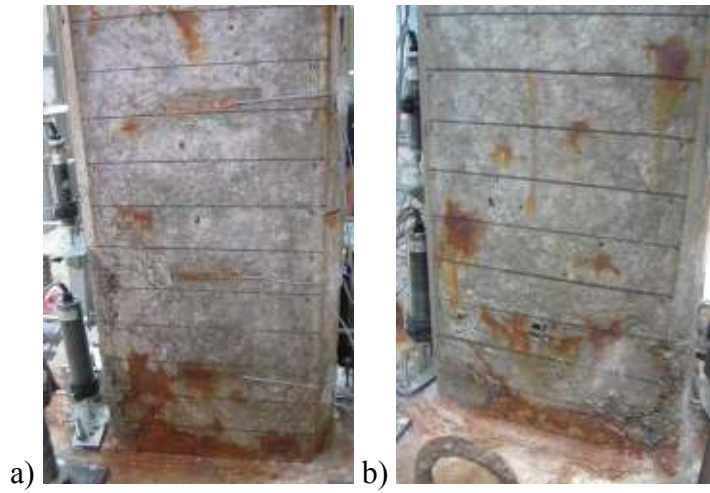


Figure E.253: (a) North, and (b) South view of NS-X22 after -0.5% drift ratio.

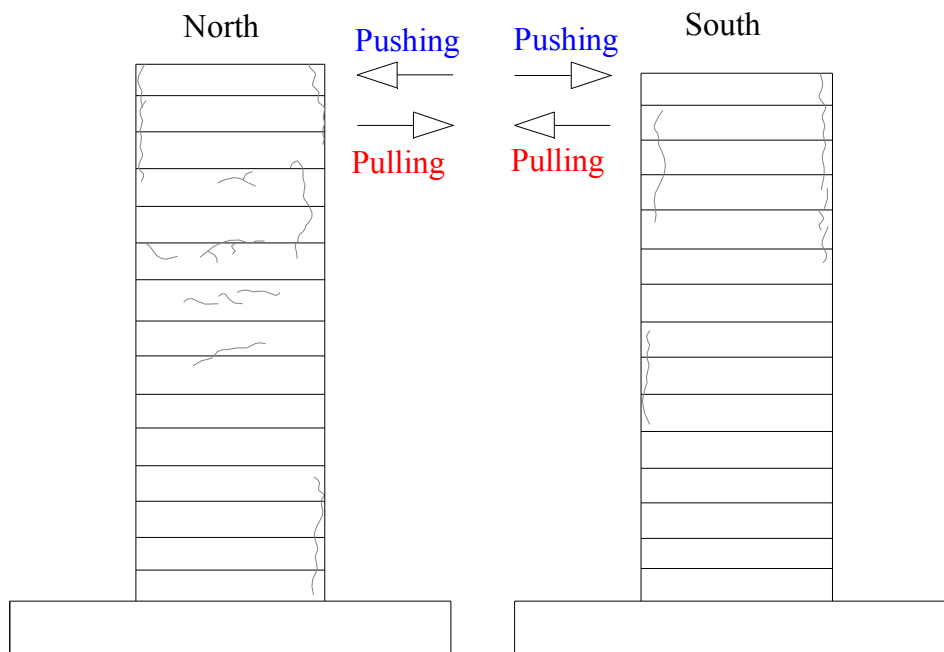


Figure E.254: Crack pattern of NS-X22 after -0.5% drift ratio.

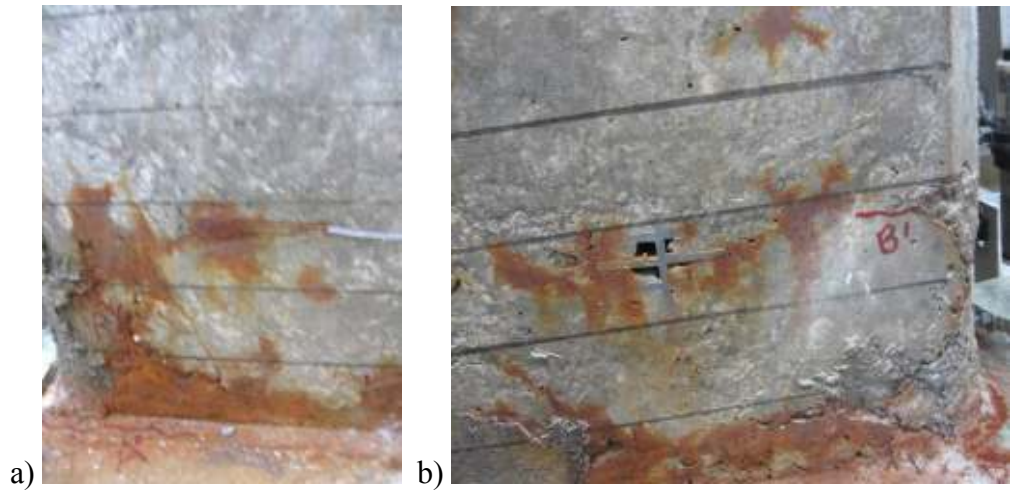


Figure E.255: a) North, and b) South view of NS-X22 after -0.75% drift ratio.

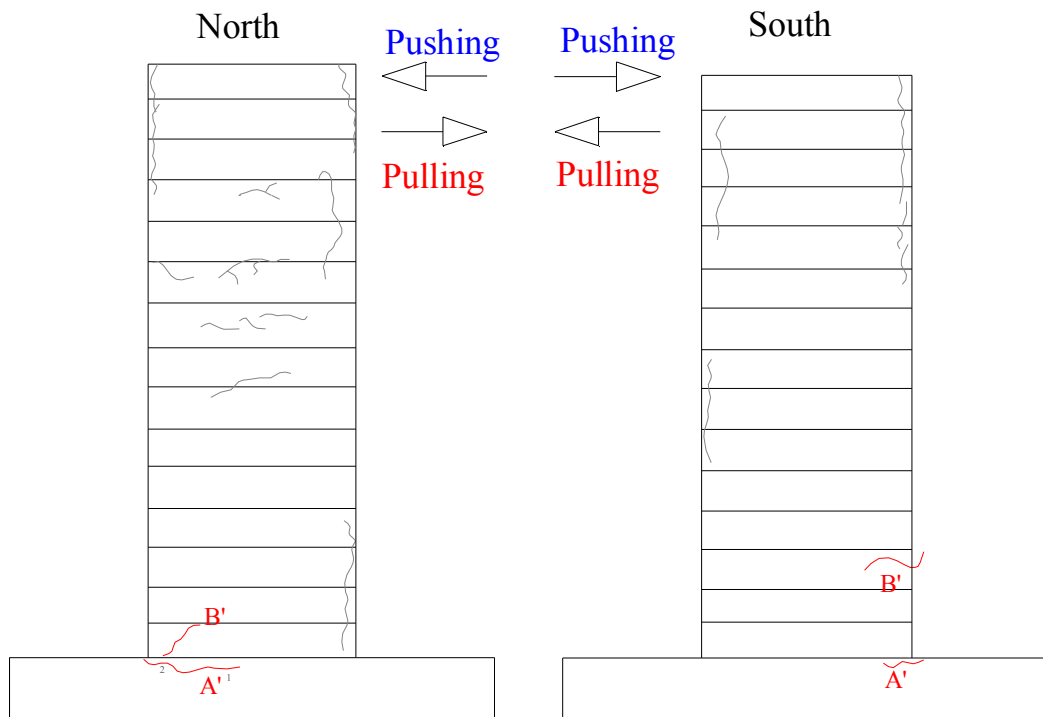


Figure E.256: Crack pattern of NS-X22 after -0.75% drift ratio.



Figure E.257: a) North, and b) South view of NS-X22 after -1% drift ratio.

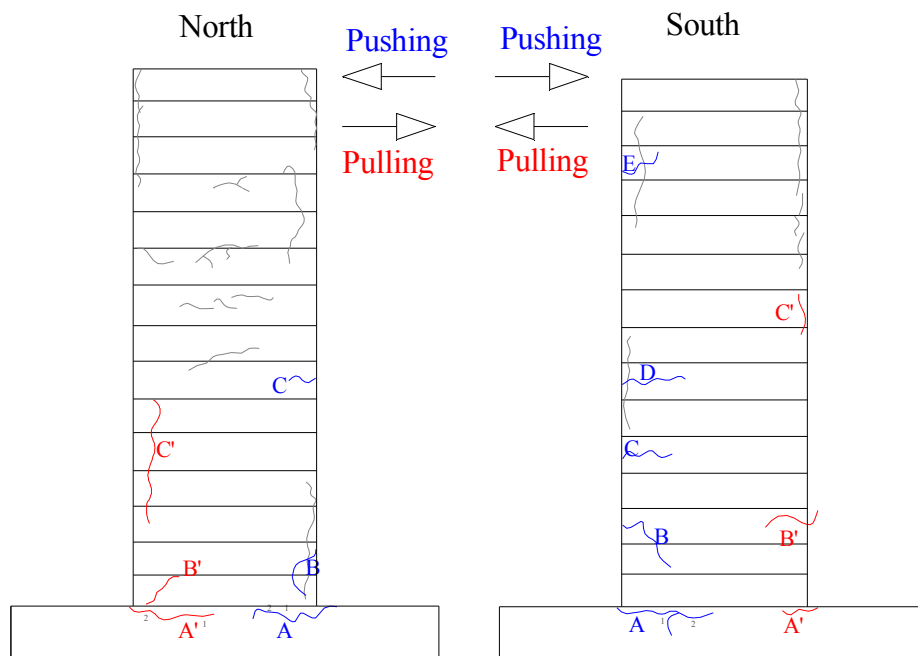


Figure E.258: Crack pattern of NS-X22 after -1% drift ratio.

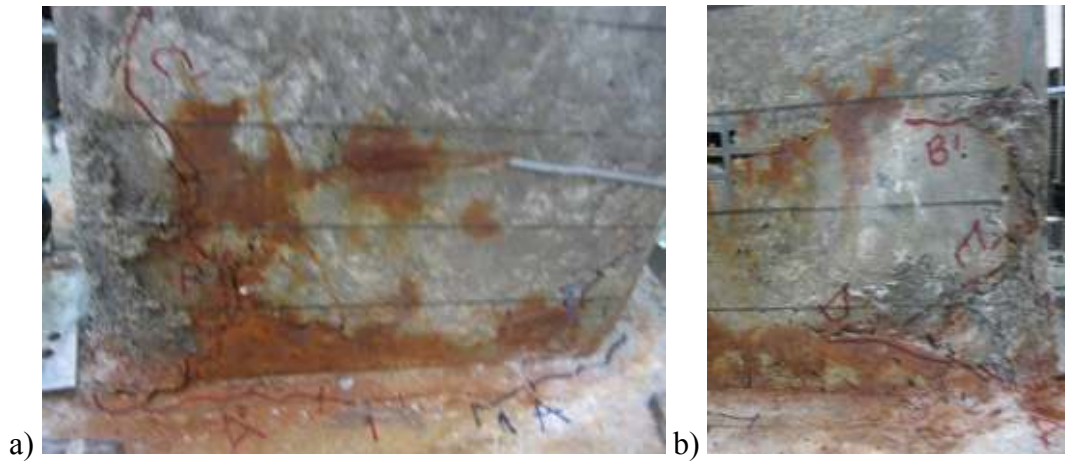


Figure E.259: a) North, and b) South view of NS-X22 after -1.5% drift ratio.

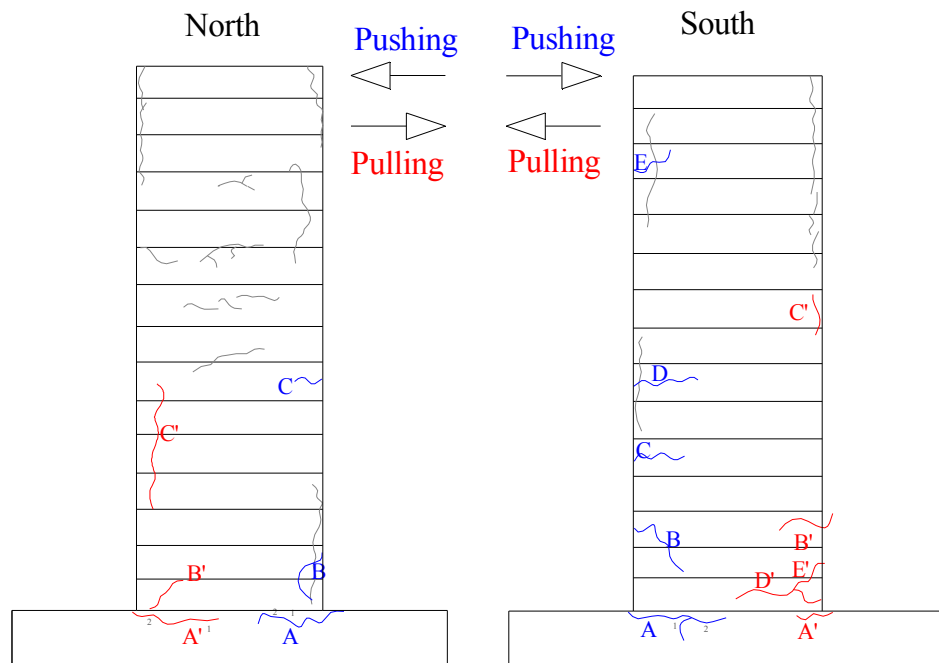


Figure E.260: Crack pattern of NS-X22 after -1.5% drift ratio.

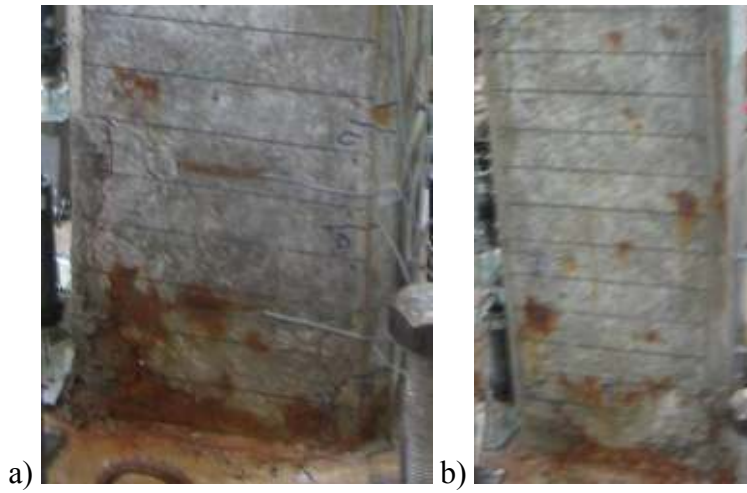


Figure E.261: a) North, and b) South view of NS-X22 after -2% drift ratio.

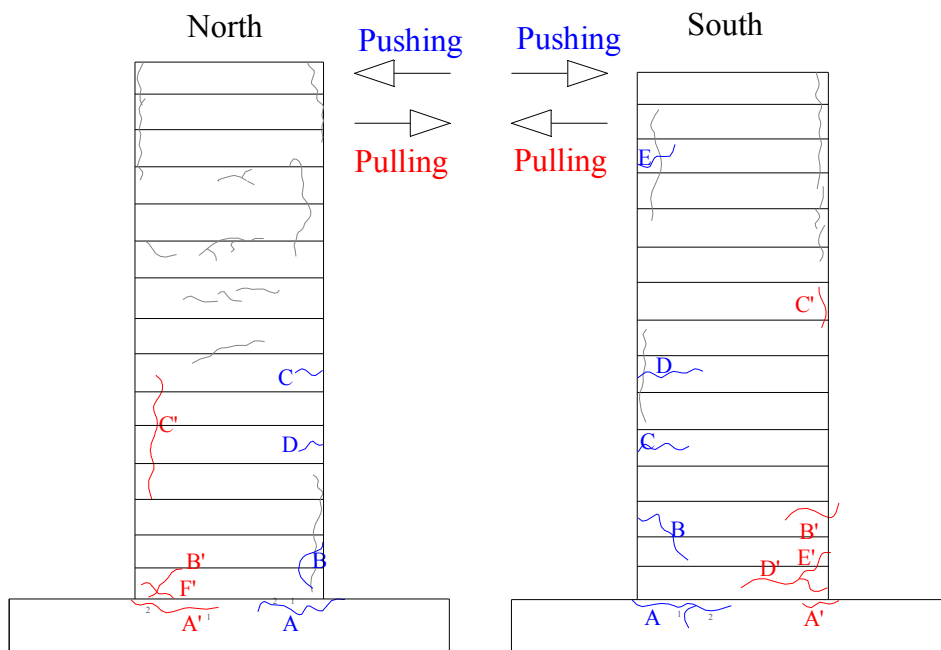


Figure E.262: Crack pattern of NS-X22 after -2% drift ratio.



Figure E.263: a) North, and b) South view of NS-X22 after -2.5% drift ratio.

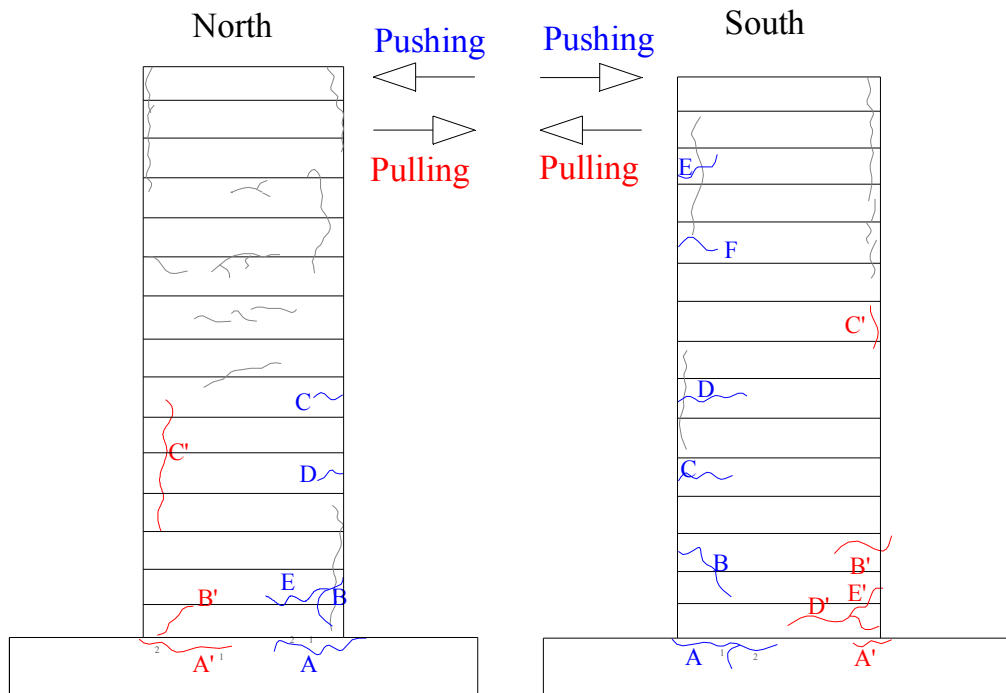


Figure E.264: Crack pattern of NS-X22 after -2.5% drift ratio.

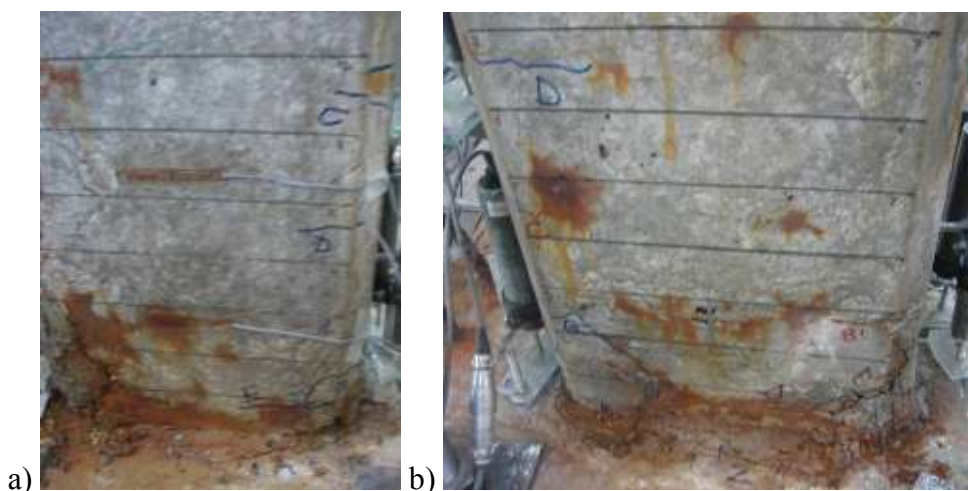


Figure E.265: a) North, and b) South view of NS-X22 after -3% drift ratio.

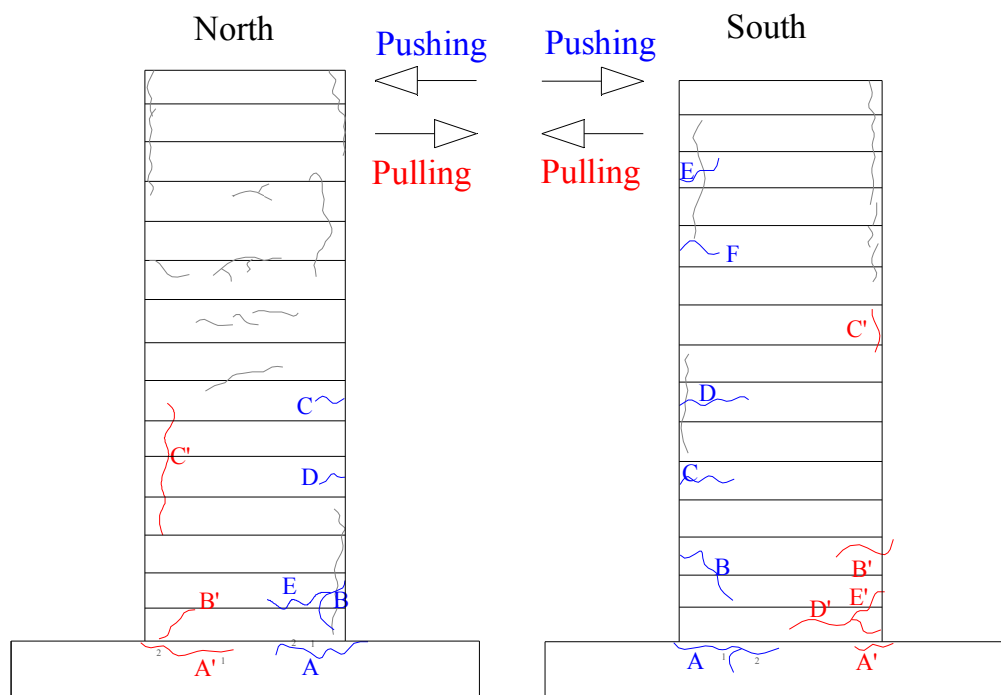


Figure E.266: Crack pattern of NS-X22 after -3% drift ratio.

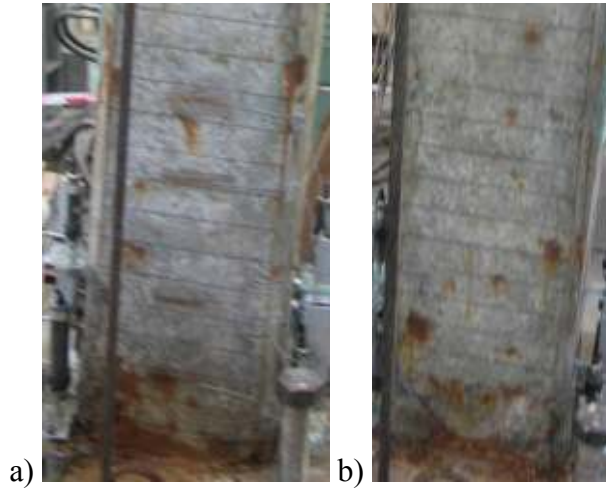


Figure E.267: a) North, and b) South view of NS-X22 after 3.5% drift ratio.

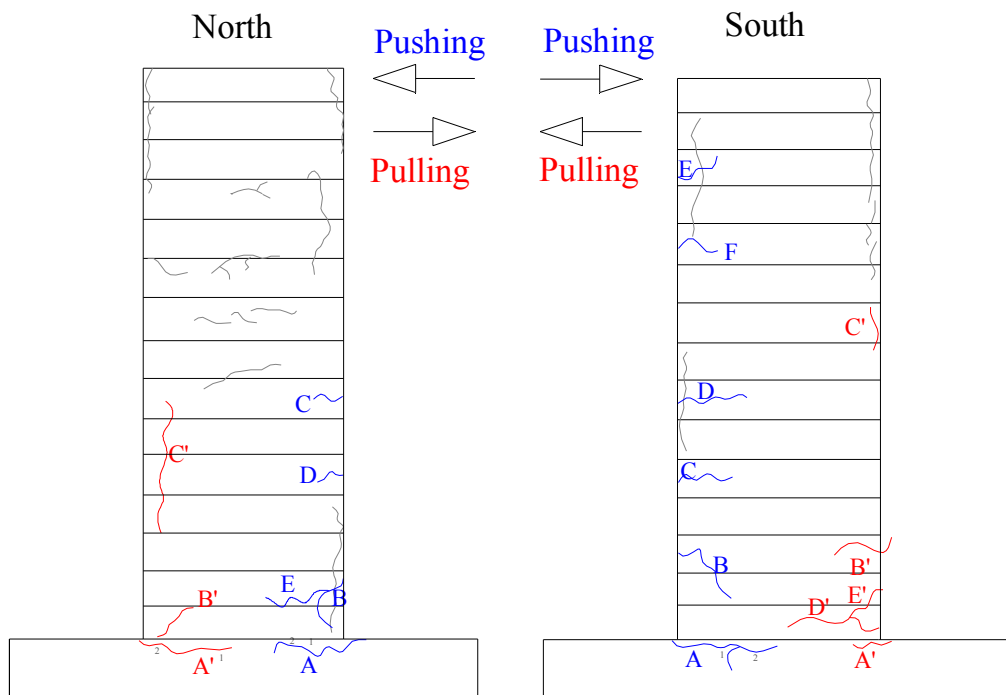


Figure E.268: Crack pattern of NS-X22 after -3.5% drift ratio.

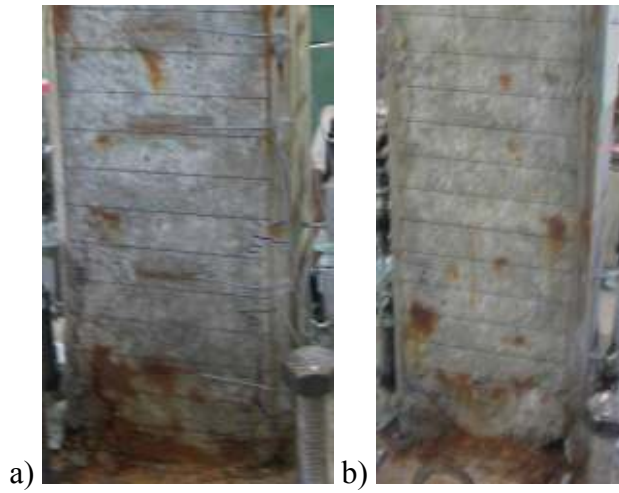


Figure E.269: a) North, and b) South view of NS-X22 after -4% drift ratio.

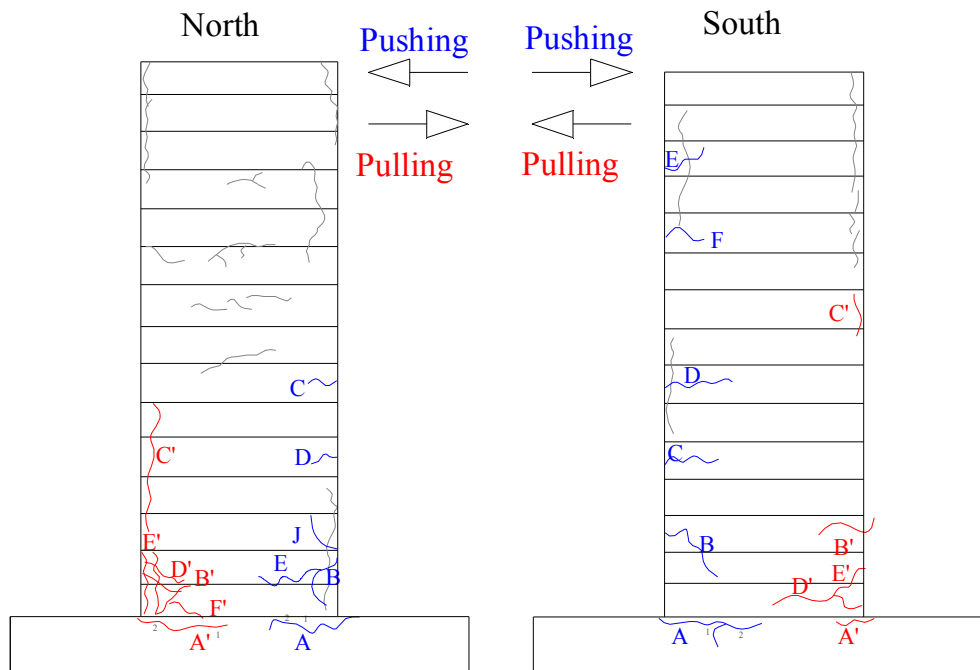


Figure E.270: Crack pattern of NS-X22 after -4% drift ratio.

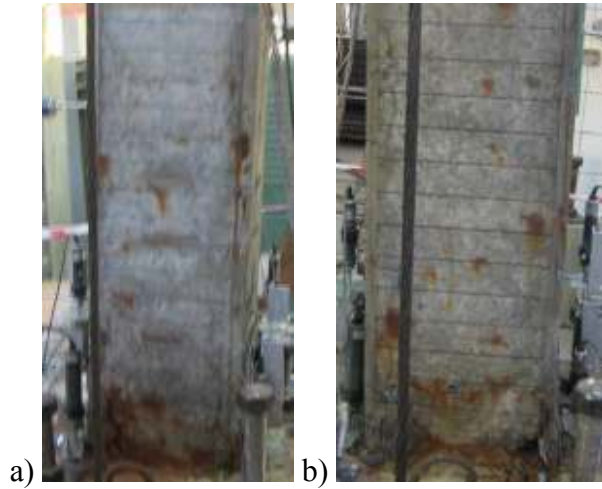


Figure E.271: a) North, and b) South view of NS-X22 after -4.5% drift ratio.

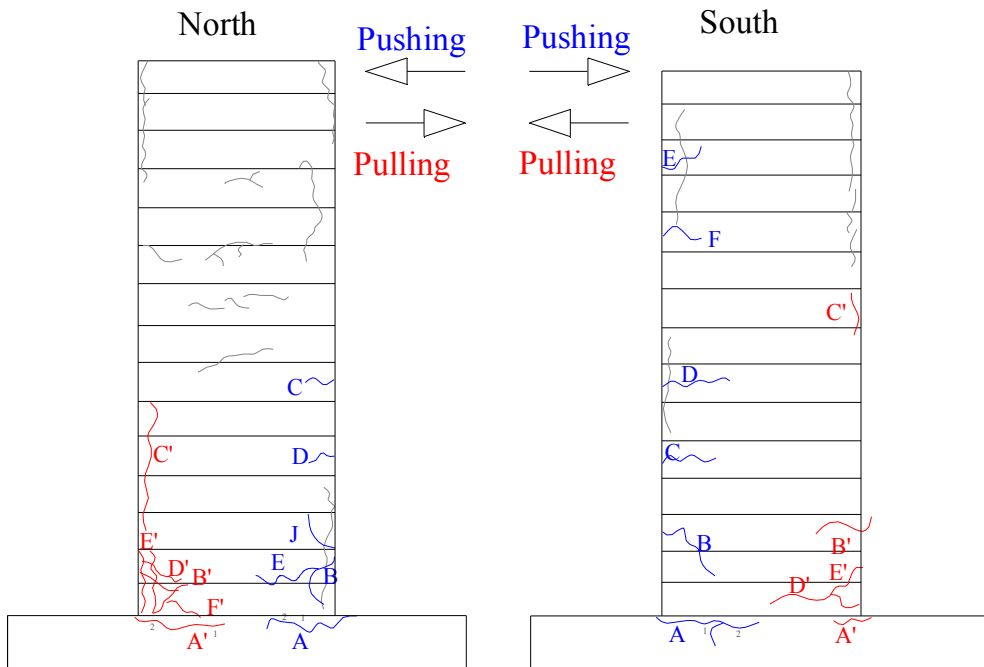


Figure E.272: Crack pattern of NS-X22 after -4.5% drift ratio.

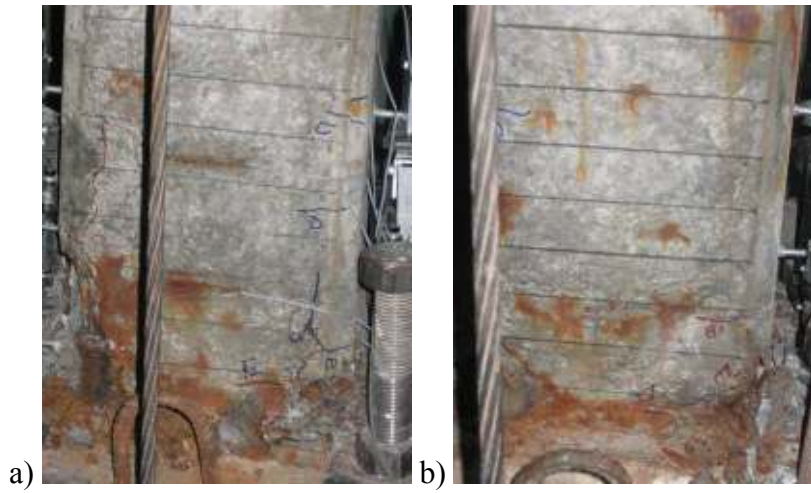


Figure E.273: a) North, and b) South view of NS-X22 after -6% drift ratio.

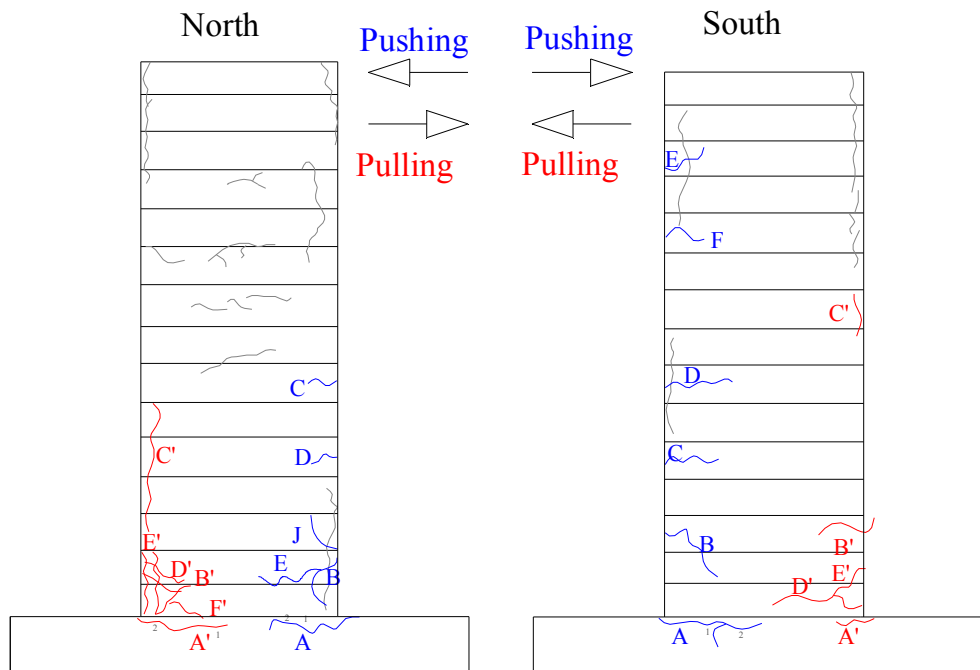


Figure E.274: Crack pattern of NS-X22 after -6% drift ratio.

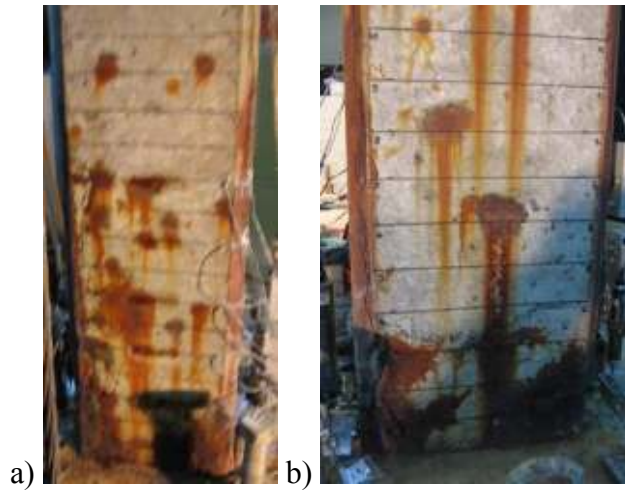


Figure E.275: (a) North, and (b) South view of NS-X54 after -0.1% drift ratio.

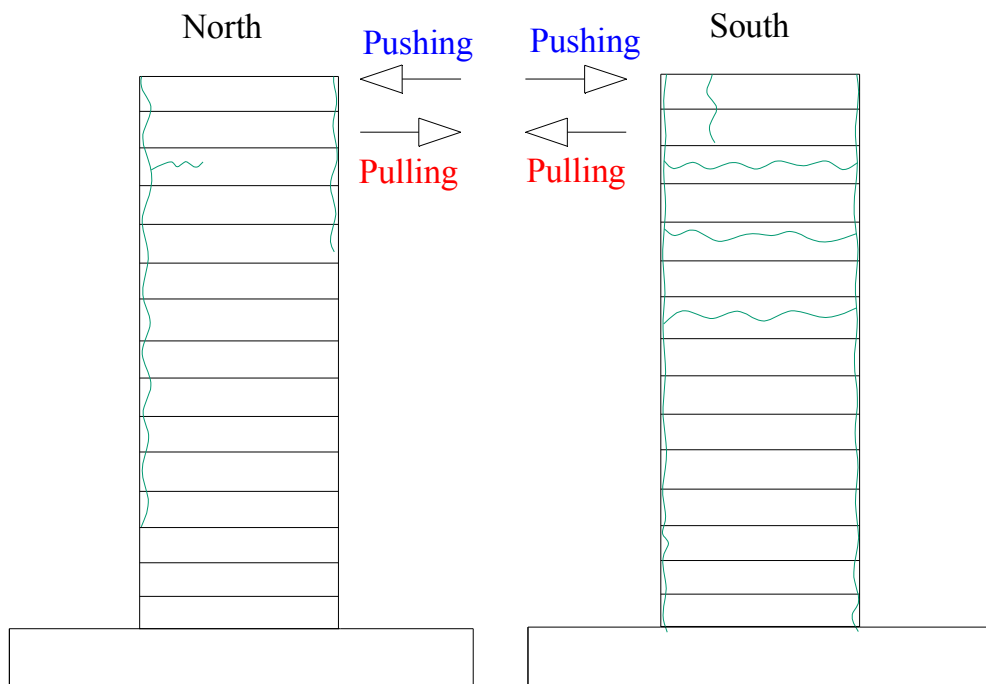


Figure E.276: Crack pattern of NS-X54 after -0.1% drift ratio.



Figure E.277: a) North, and b) South view of NS-X54 after -0.25% drift ratio.

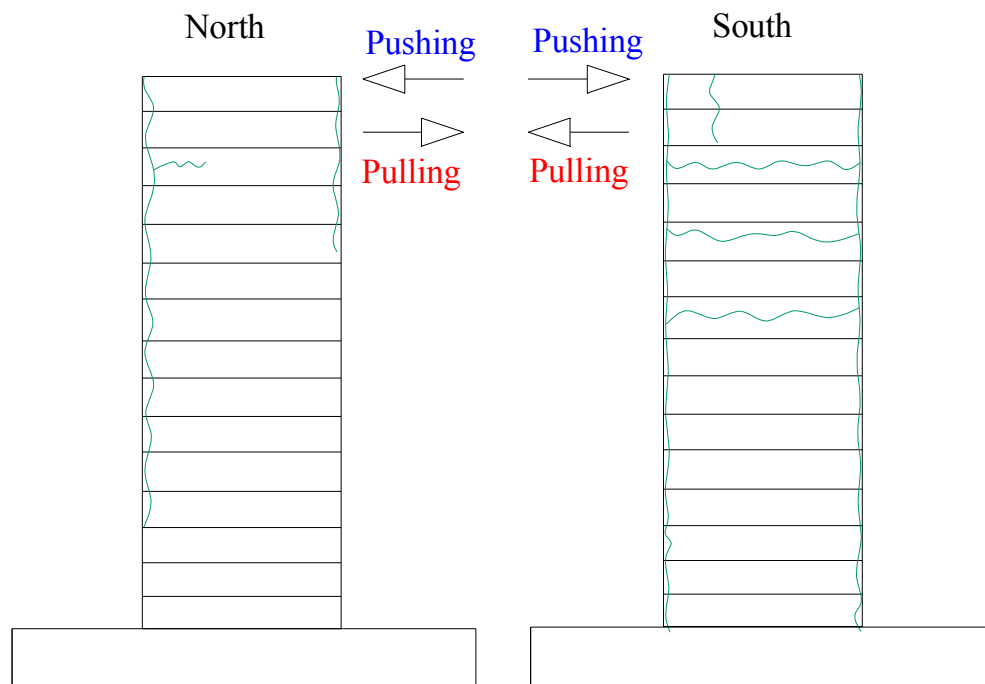


Figure E.278: Crack pattern of NS-X54 after -0.25% drift ratio.

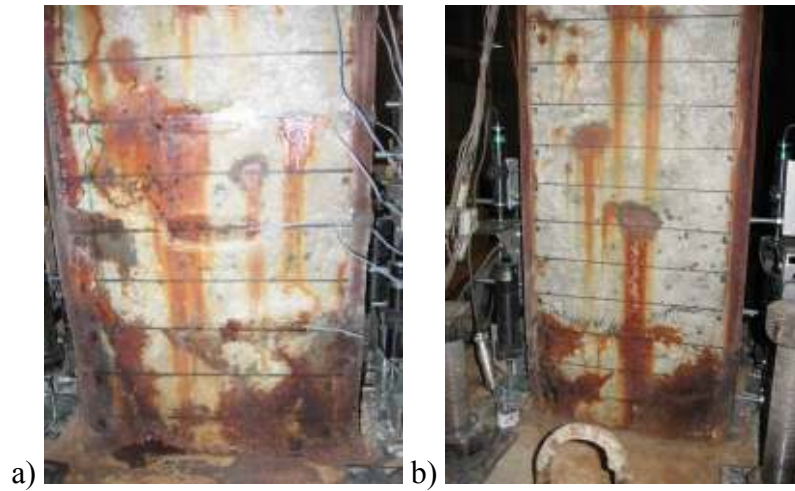


Figure E.279: a) North, and b) South view of NS-X54 after -0.5% drift ratio.

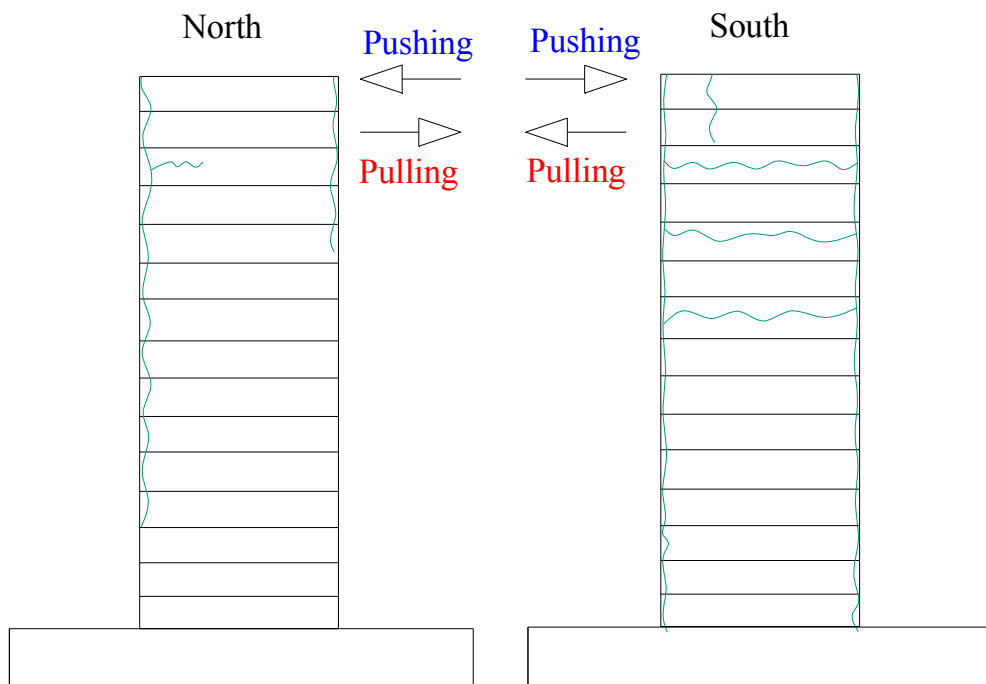


Figure E.280: Crack pattern of NS-X54 after -0.5% drift ratio.

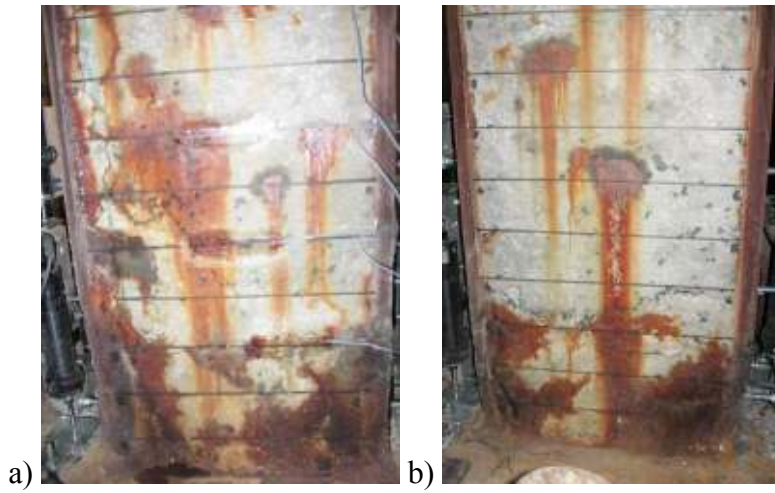


Figure E.281: a) North, and b) South view of NS-X54 after -0.75% drift ratio.

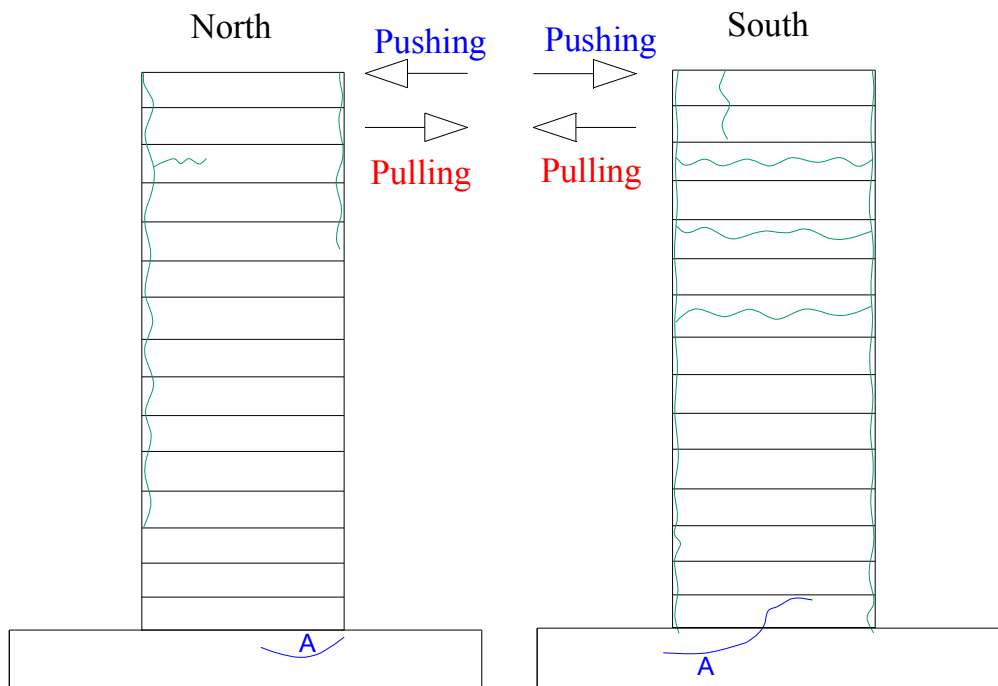


Figure E.282: Crack pattern of NS-X54 after -0.75% drift ratio.

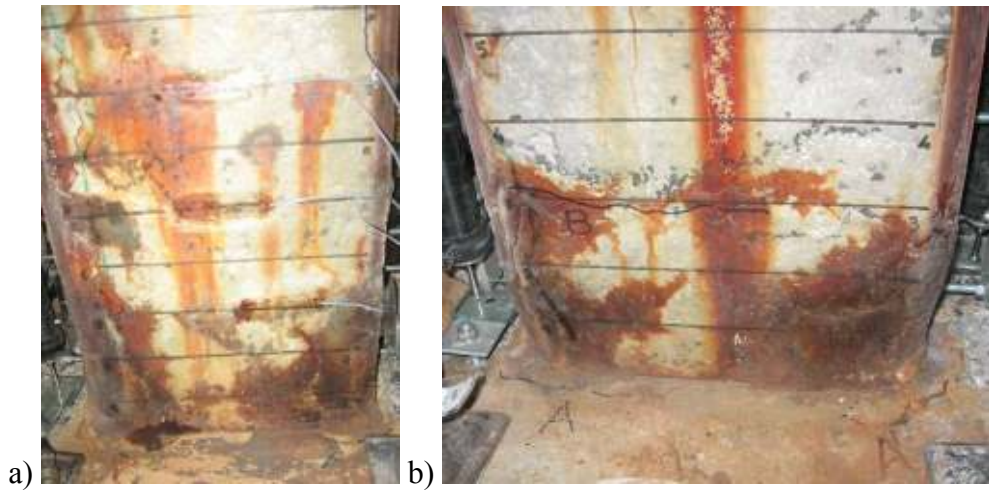


Figure E.283: a) North, and b) South view of NS-X54 after -1% drift ratio.

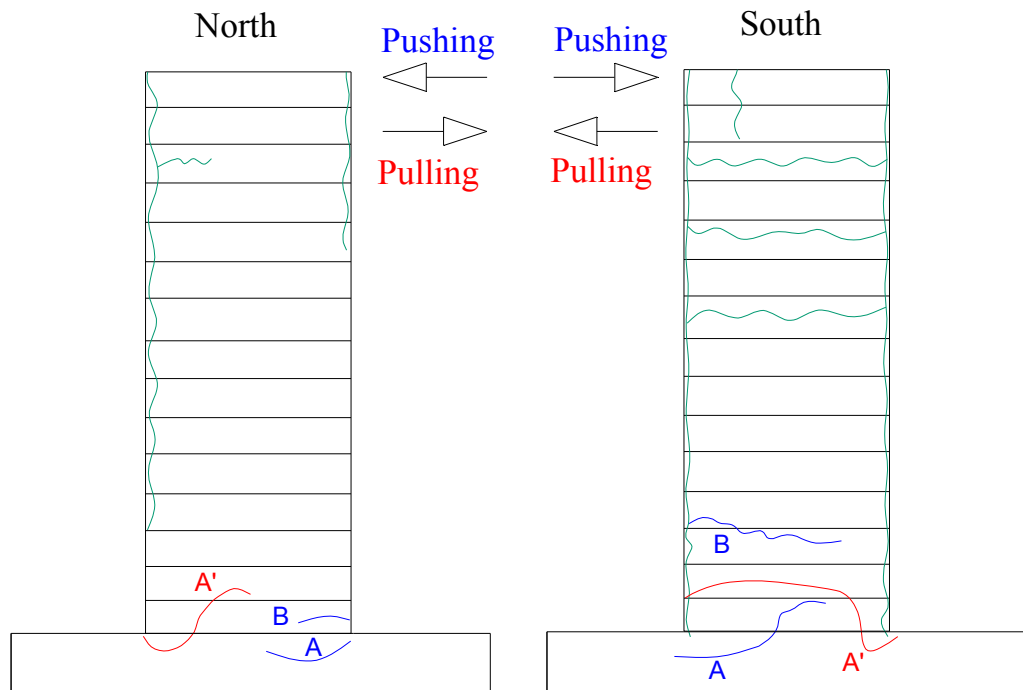


Figure E.284: Crack pattern of NS-X54 after -1% drift ratio.

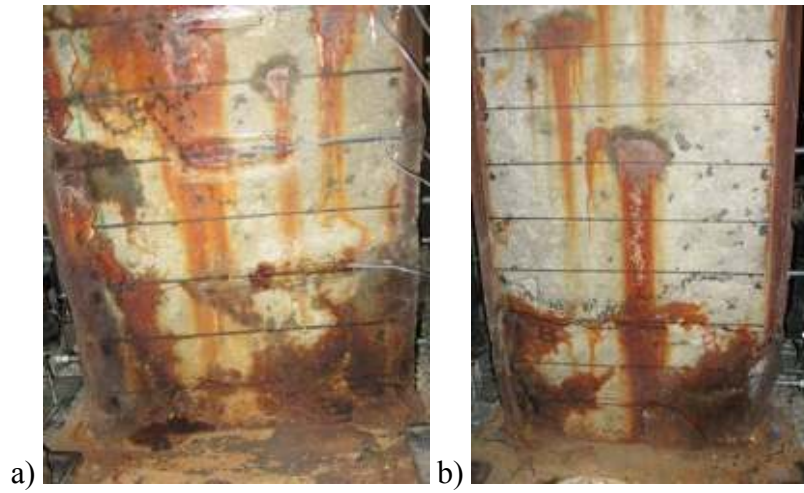


Figure E.285: a) North, and b) South view of NS-X54 after -1.5% drift ratio.

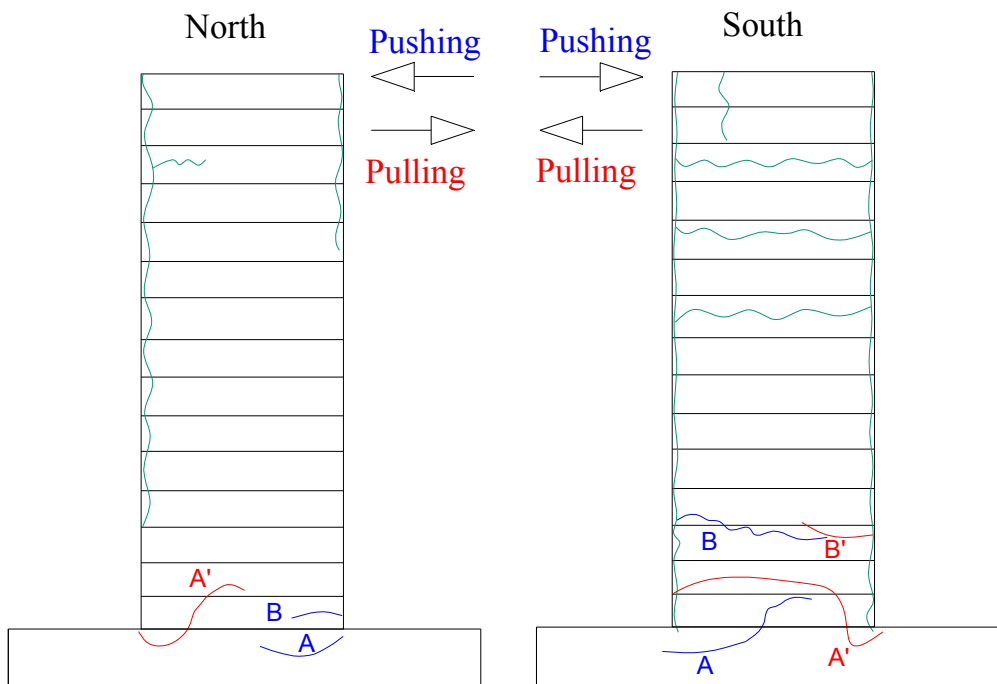


Figure E.286: Crack pattern of NS-X54 after -1.5% drift ratio.

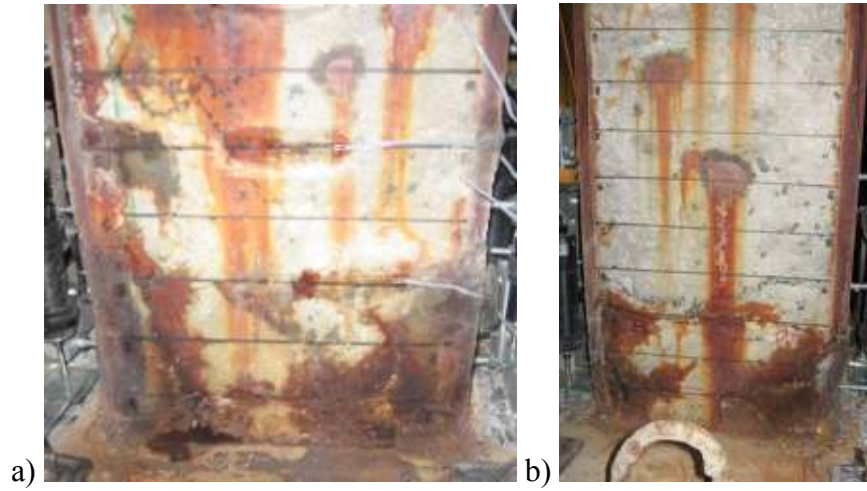


Figure E.287: a) North, and b) South view of NS-X54 after 2% drift ratio.

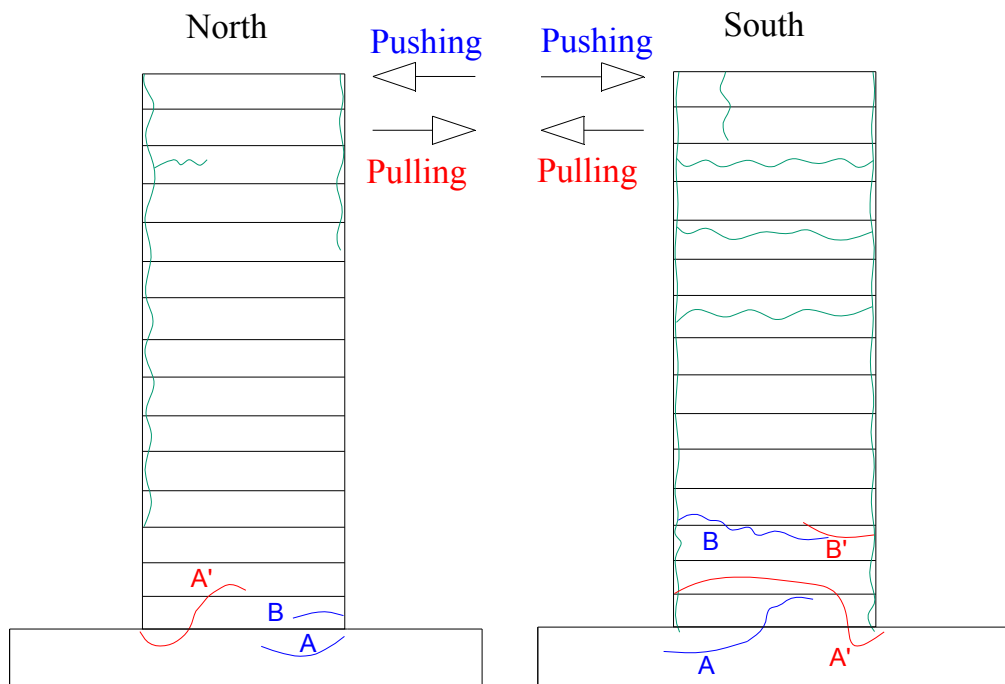


Figure E.288: Crack pattern of NS-X54 after -2% drift ratio.

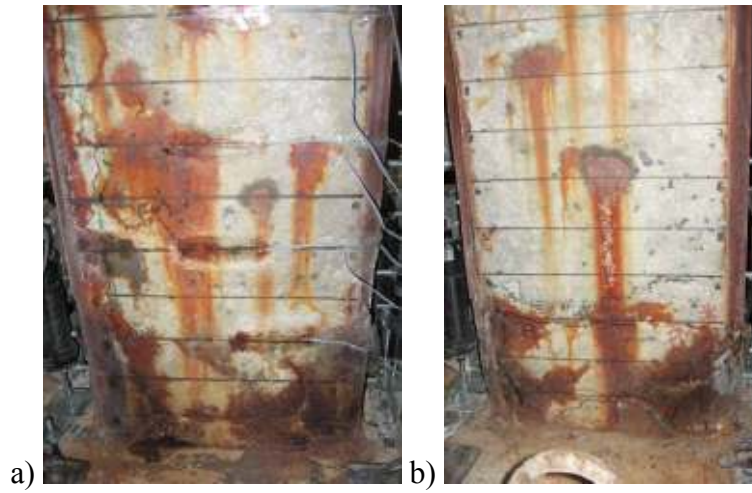


Figure E.289: a) North, and b) South view of NS-X54 after -2.5% drift ratio.

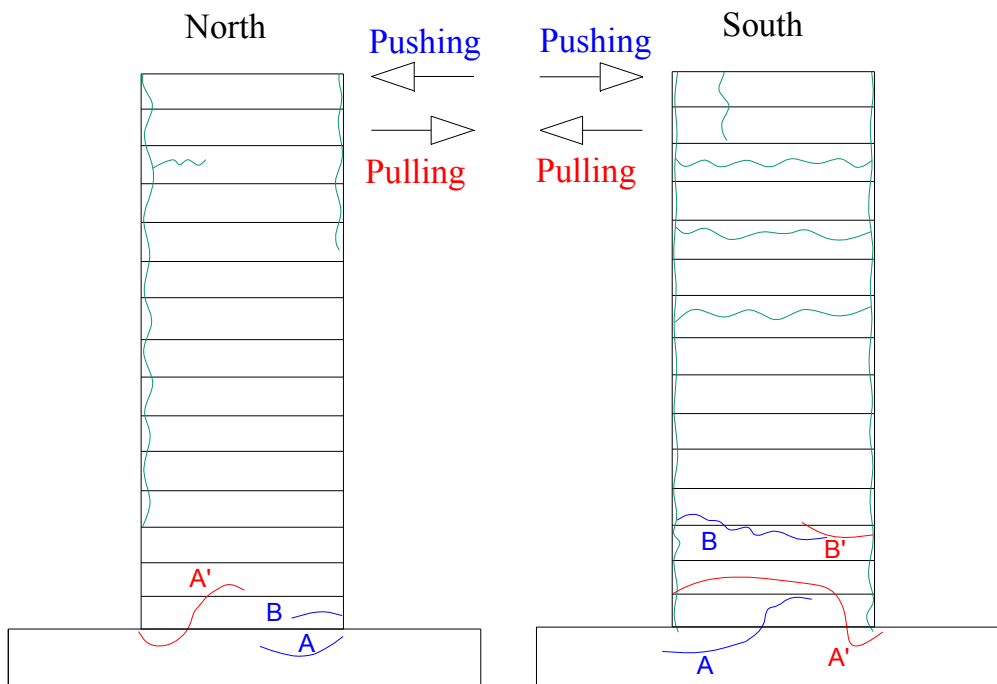


Figure E.290: Crack pattern of NS-X54 after -2.5% drift ratio.

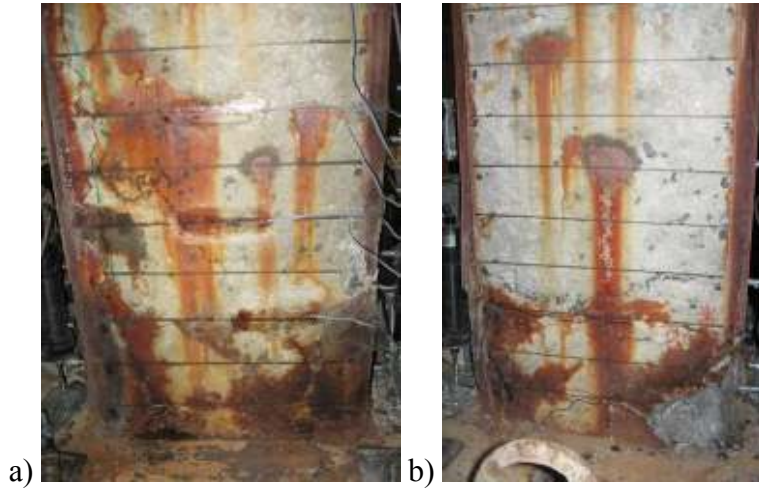


Figure E.291: a) North, and b) South view of NS-X54 after -3% drift ratio.

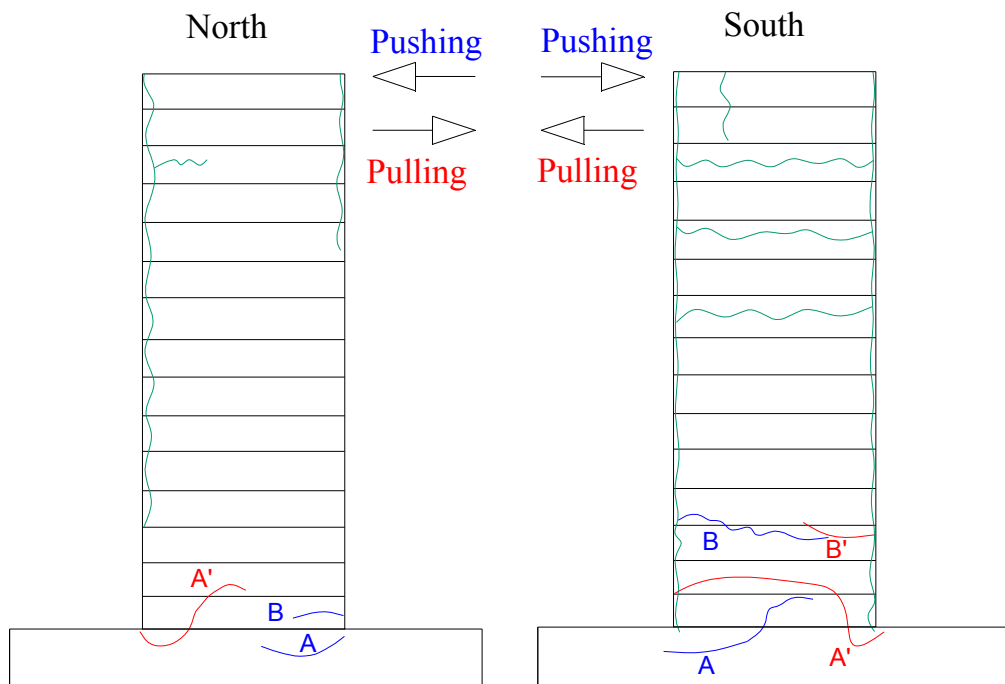


Figure E.292: Crack pattern of NS-X54 after -3% drift ratio.



Figure E.293: a) North, and b) South view of NS-X54 after -3.5% drift ratio.

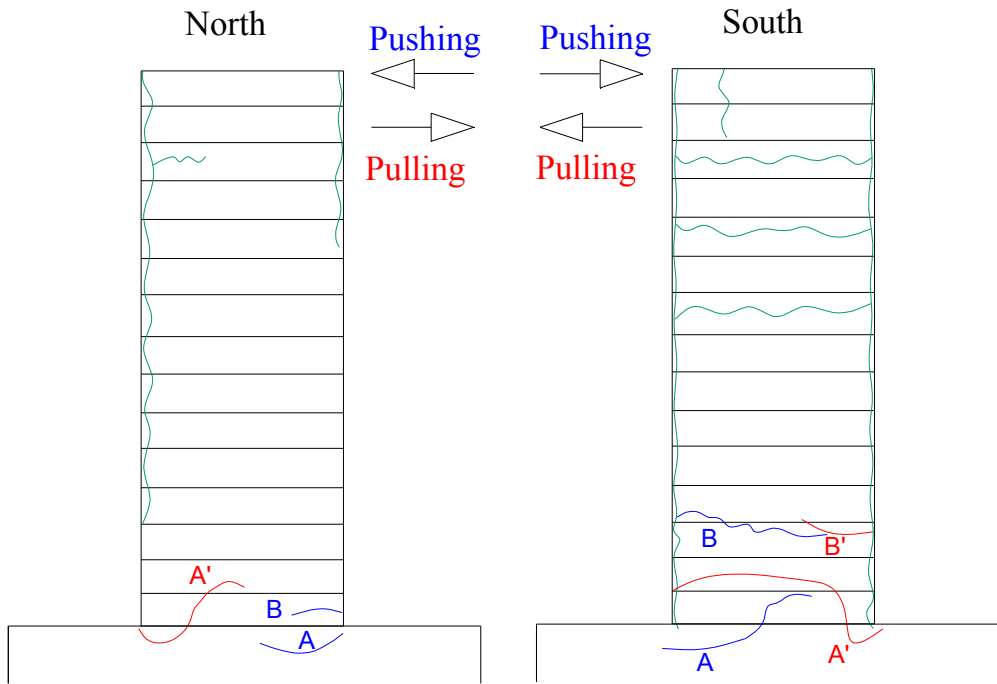


Figure E.294: Crack pattern of NS-X54 after -3.5% drift ratio.

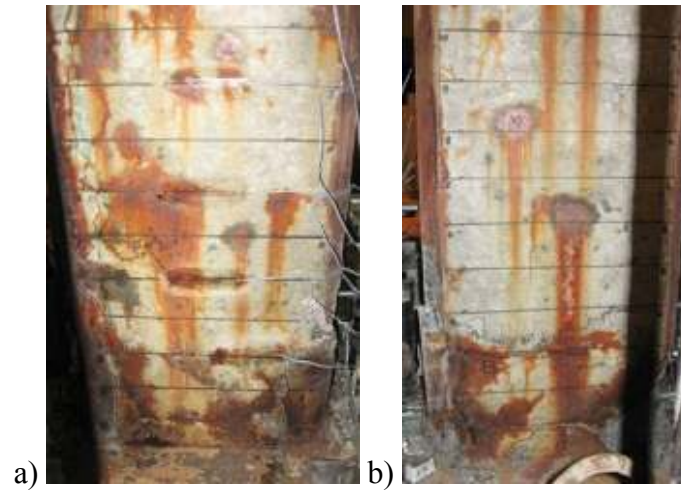


Figure E.295: a) North, and b) South view of NS-X54 after -4% drift ratio.

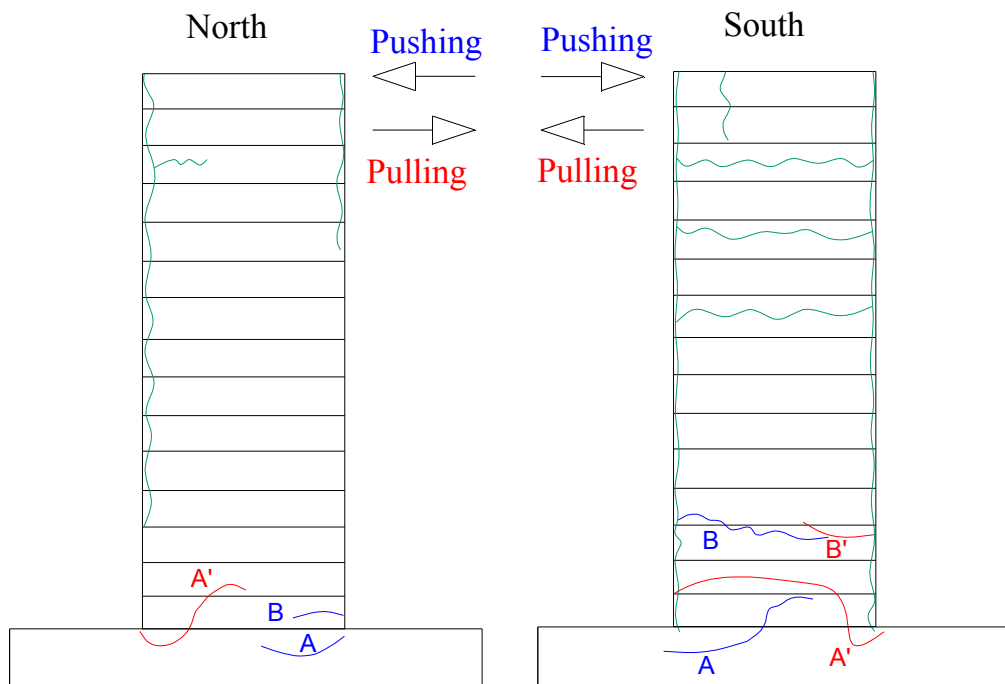


Figure E.296: Crack pattern of NS-X54 after -4% drift ratio.

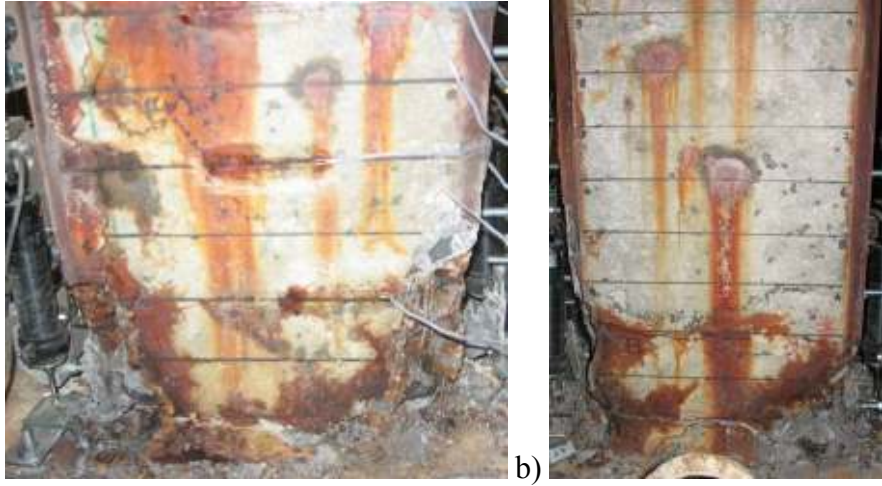


Figure E.297: a) North, and b) South view of NS-X54 after -4.5% drift ratio.

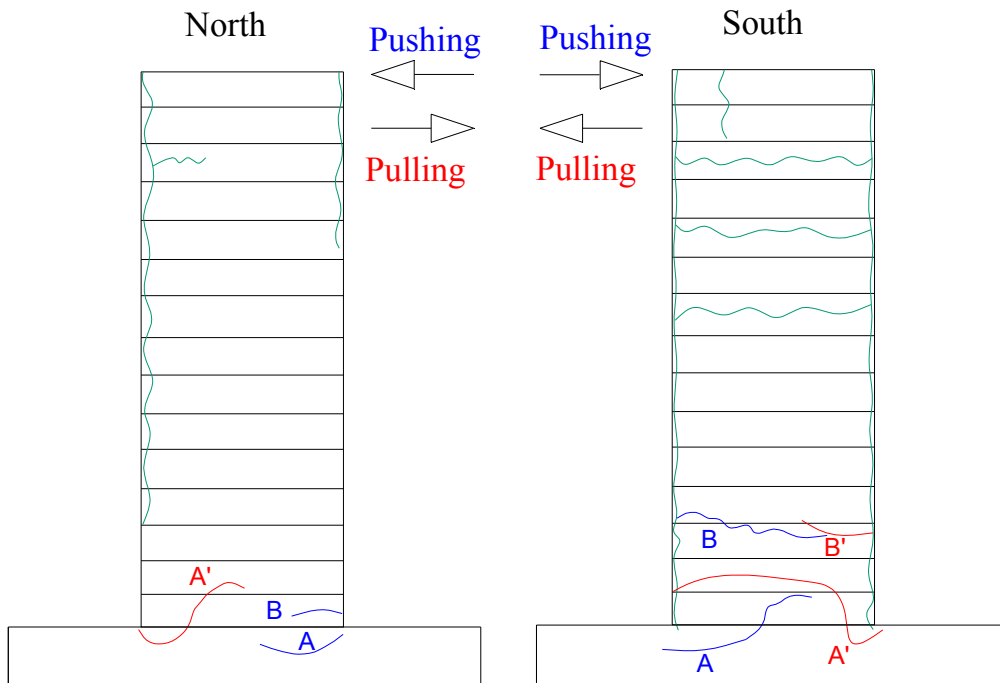


Figure E.298: Crack pattern of NS-X54 after -4.5% drift ratio.

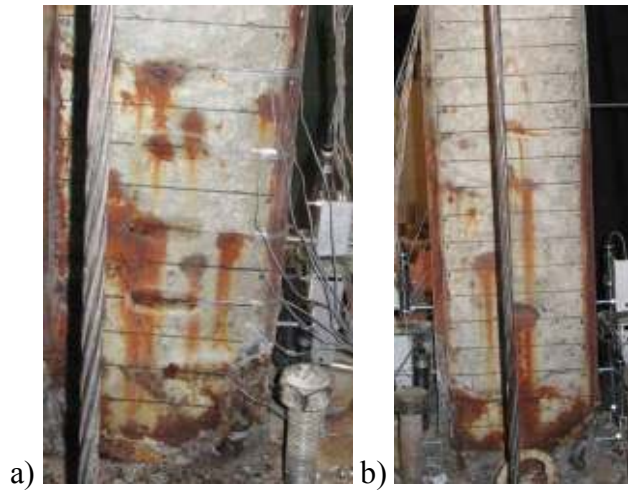


Figure E.299: a) North, and b) South view of NS-X54 after -5% drift ratio.

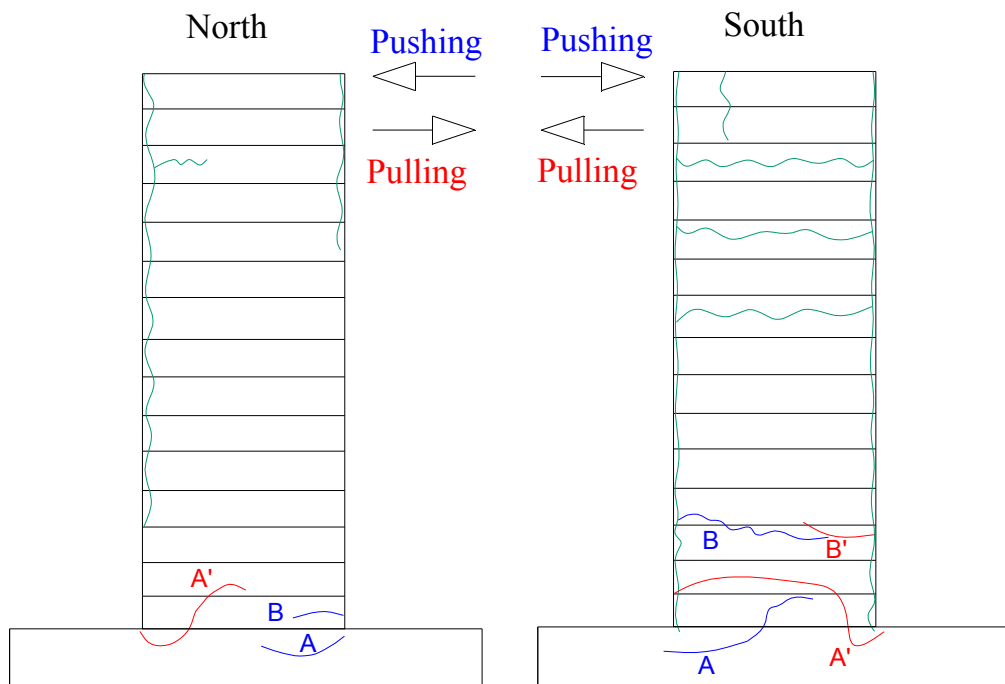


Figure E.300: Crack pattern of NS-X54 after -5% drift ratio.

APPENDIX F



a)



b)



c)

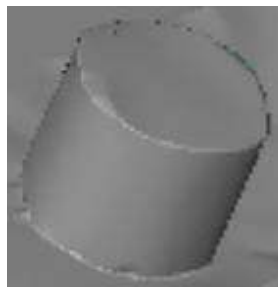
Figure F.1: a) Appearance of reinforcing bar taken out from the specimen LS-X0, b) Surface condition of the reinforcement bar observed through an optical stereo microscope, c) Scan view of the reinforcement bar with 3D optical scanner.



a)



b)

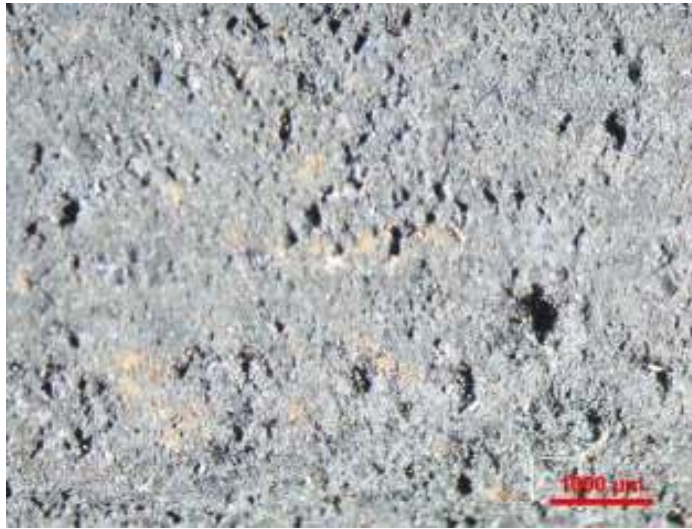


c)

Figure F.2: a) Appearance of reinforcing bar taken out from the specimen LS-X6, b) Surface condition of the reinforcement bar observed through an optical stereo microscope, c) Scan view of the reinforcement bar with 3D optical scanner.



a)



b)



c)

Figure F.3: a) Appearance of reinforcing bar taken out from the specimen LS-X8, b) Surface condition of the reinforcement bar observed through an optical stereo microscope, c) Scan view of the reinforcement bar with 3D optical scanner.



a)



b)



c)

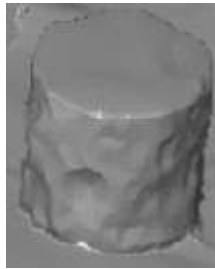
Figure F.4: a) Appearance of reinforcing bar taken out from the specimen LS-X12, b) Surface condition of the reinforcement bar observed through an optical stereo microscope, c) Scan view of the reinforcement bar with 3D optical scanner.



a)



b)

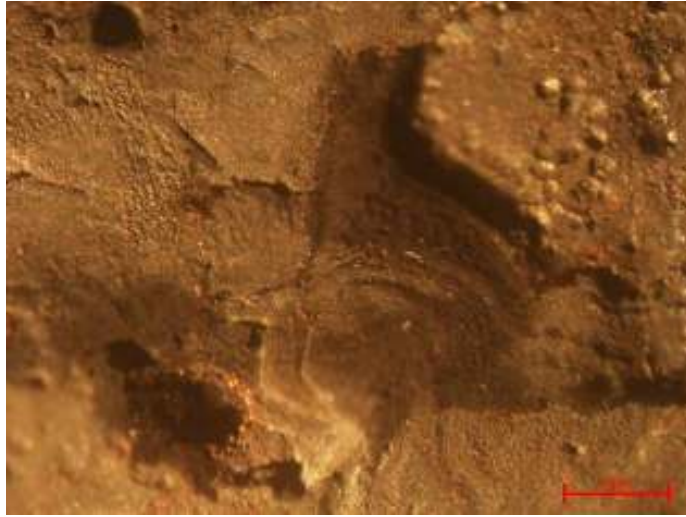


c)

Figure F.5: a) Appearance of reinforcing bar taken out from the specimen LS-X21, b) Surface condition of the reinforcement bar observed through an optical stereo microscope, c) Scan view of the reinforcement bar with 3D optical scanner.



a)



b)

Figure F.6: a) Appearance of reinforcing bar taken out from the specimen LS-X28, b) Surface condition of the reinforcement bar observed through an optical stereo microscope



a)



b)



c)

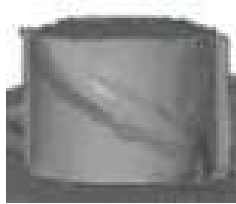
Figure F.7: a) Appearance of reinforcing bar taken out from the specimen NS-X0, b) Surface condition of the reinforcement bar observed through an optical stereo microscope, c) Scan view of the reinforcement bar with 3D optical scanner.



a)



b)



c)

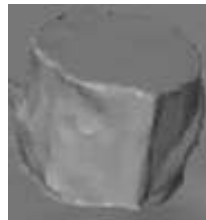
Figure F.8: a) Appearance of reinforcing bar taken out from the specimen NS-X13, b) Surface condition of the reinforcement bar observed through an optical stereo microscope, c) Scan view of the reinforcement bar with 3D optical scanner.



a)



b)



c)

Figure F.9: a) Appearance of reinforcing bar taken out from the specimen NS-X16, b) Surface condition of the reinforcement bar observed through an optical stereo microscope, c) Scan view of the reinforcement bar with 3D optical scanner.



a)



b)

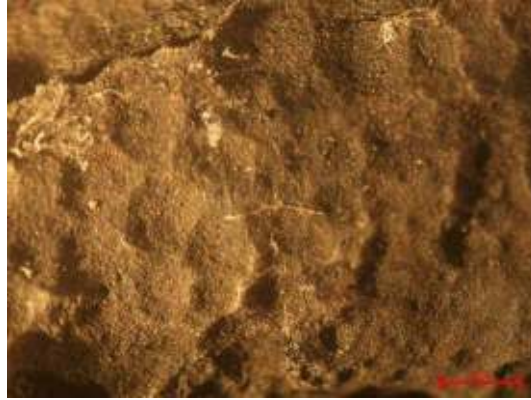


c)

Figure F.10: a) Appearance of reinforcing bar taken out from the specimen NS-X22, b) Surface condition of the reinforcement bar observed through an optical stereo microscope, c) Scan view of the reinforcement bar with 3D optical scanner.



a)

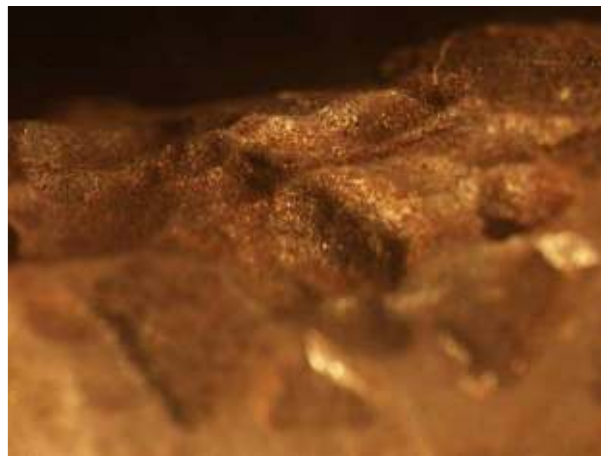


b)

Figure F.11: a) Appearance of reinforcing bar taken out from the specimen NS-X54, b) Surface condition of the reinforcement bar observed through an optical stereo microscope.



a)



b)

Figure F.12: a) Appearance of reinforcing bar taken out from the specimen LS-X19-H, b) Surface condition of the reinforcement bar observed through an optical stereo microscope

APPENDIX G

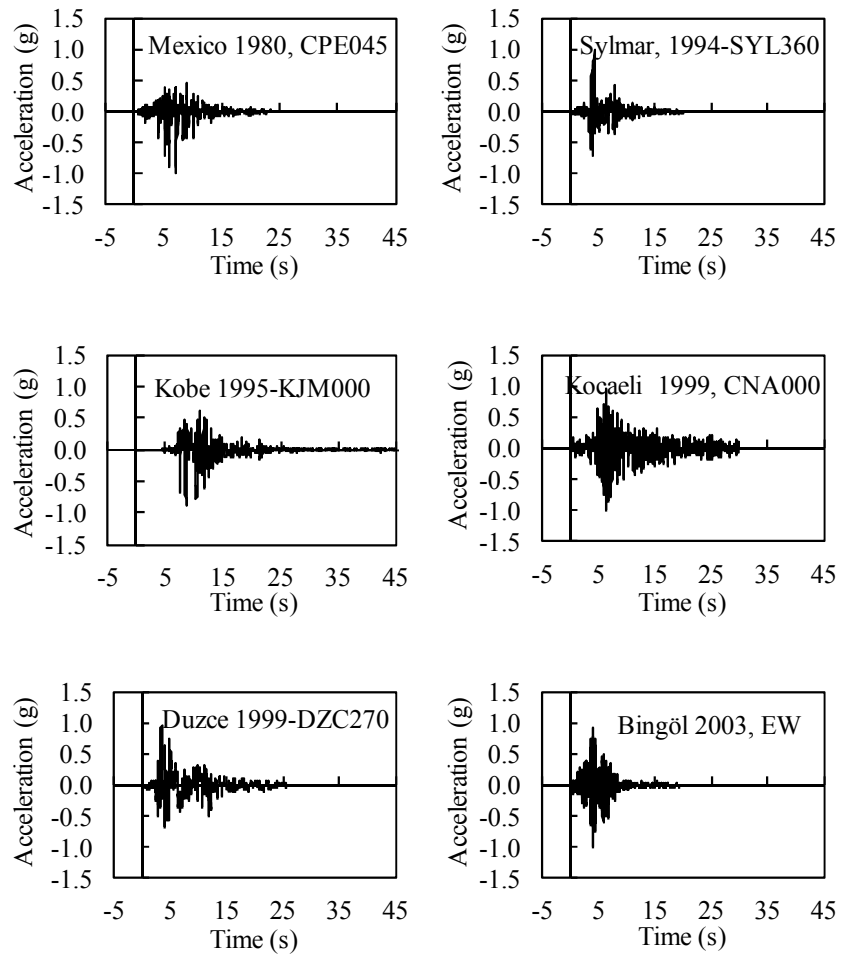


Figure G.1 : Earthquake records scaled to 0.95g.

APPENDIX H

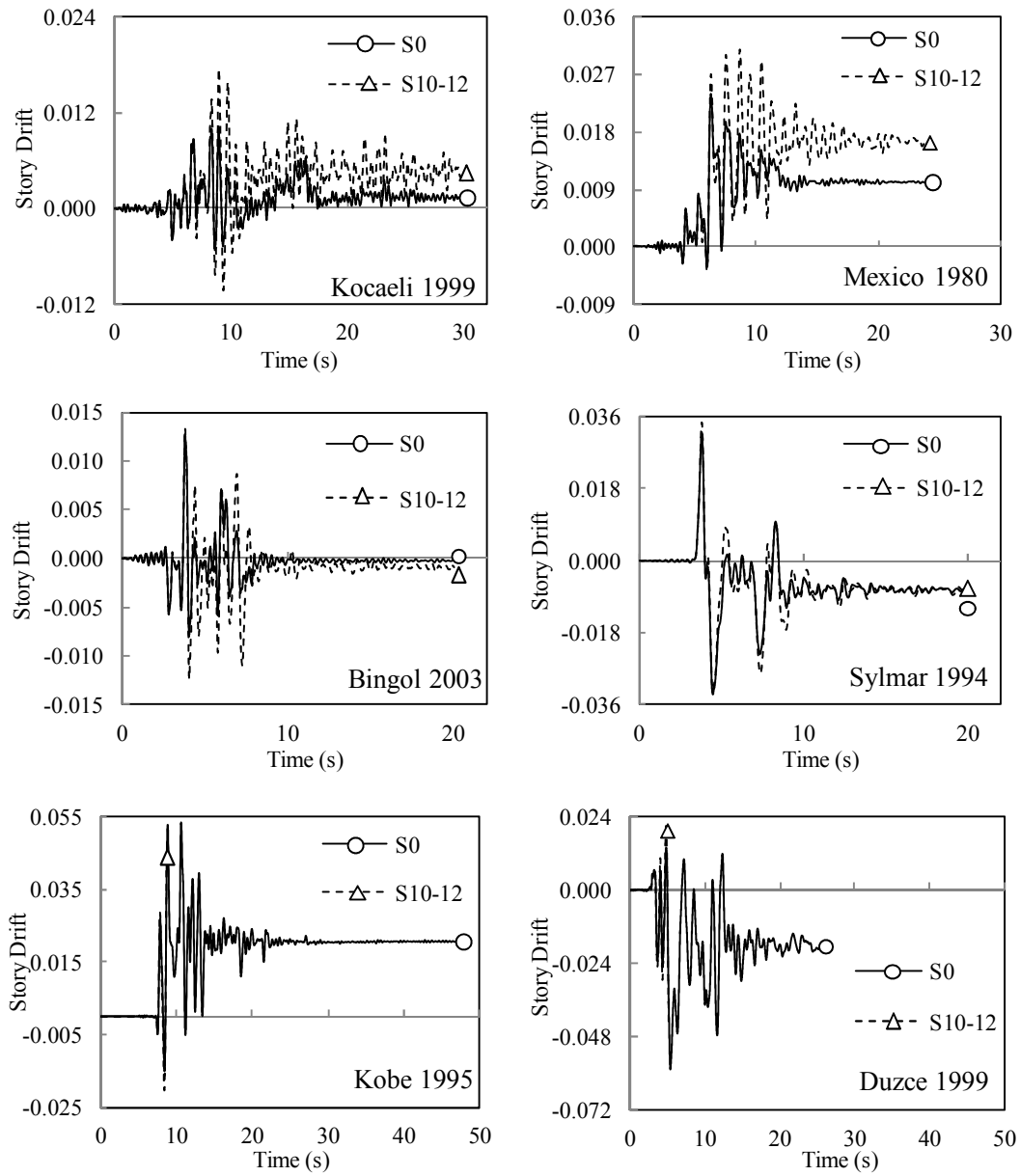


Figure H.1: Drift ratio-time relationships for first stories of S0, S10-12 buildings.

APPENDIX I

Table I.1 : Damage regions for base columns of S0 building for SYLMAR, 1994.

Column notation	Column type	Rotation (rad/m)	Plastic Hinge Length (Lp) (m)	Curvature (Kp) (1/m)	Unconfined concrete ϵ_c	Confined concrete ϵ_{cc}	Steel ϵ_{su}	MN		GV		GC		Damage region
								ϵ_c	ϵ_{su}	ϵ_{cc}	ϵ_{su}	ϵ_{cc}	ϵ_{su}	
K1	C0-30×80-5	0.0328	0.4	0.0820	0.0057	0.0034	0.0625	0.0035	0.01	0.00843	0.04	0.01091	0.06	Collapsing Region
K2	C0-30×80-10	0.0327	0.4	0.0818	0.0086	0.0066	0.0514	0.0035	0.01	0.00843	0.04	0.01091	0.06	Advanced Damage Region
K2	C0-30×80-10	0.0327	0.4	0.0818	0.0086	0.0066	0.0514	0.0035	0.01	0.00843	0.04	0.01091	0.06	Advanced Damage Region
K2	C0-30×80-10	0.0327	0.4	0.0818	0.0086	0.0066	0.0514	0.0035	0.01	0.00843	0.04	0.01091	0.06	Advanced Damage Region
K1	C0-30×80-5	0.0328	0.4	0.0820	0.0057	0.0034	0.0625	0.0035	0.01	0.00843	0.04	0.01091	0.06	Collapsing Region
K3	C0-65×65-5	0.0326	0.325	0.1003	0.0087	0.0059	0.0549	0.0035	0.01	0.00685	0.04	0.00869	0.06	Advanced Damage Region
K4	C0-65×65-10	0.0325	0.325	0.1000	0.0141	0.0111	0.0535	0.0035	0.01	0.00685	0.04	0.00869	0.06	Collapsing Region
K4	C0-65×65-10	0.0325	0.325	0.1000	0.0141	0.0111	0.0535	0.0035	0.01	0.00685	0.04	0.00869	0.06	Collapsing Region
K4	C0-65×65-10	0.0325	0.325	0.1000	0.0141	0.0111	0.0535	0.0035	0.01	0.00685	0.04	0.00869	0.06	Collapsing Region
K4	C0-65×65-10	0.0325	0.325	0.1000	0.0141	0.0111	0.0535	0.0035	0.01	0.00685	0.04	0.00869	0.06	Collapsing Region
K3	C0-65×65-5	0.0326	0.325	0.1003	0.0087	0.0059	0.0549	0.0035	0.01	0.00685	0.04	0.00869	0.06	Advanced Damage Region
K3	C0-65×65-5	0.0326	0.325	0.1003	0.0087	0.0059	0.0549	0.0035	0.01	0.00685	0.04	0.00869	0.06	Advanced Damage Region
K4	C0-65×65-10	0.0325	0.325	0.1000	0.0141	0.0111	0.0535	0.0035	0.01	0.00685	0.04	0.00869	0.06	Collapsing Region
K4	C0-65×65-10	0.0325	0.325	0.1000	0.0141	0.0111	0.0535	0.0035	0.01	0.00685	0.04	0.00869	0.06	Collapsing Region
K4	C0-65×65-10	0.0325	0.325	0.1000	0.0141	0.0111	0.0535	0.0035	0.01	0.00685	0.04	0.00869	0.06	Collapsing Region
K4	C0-65×65-10	0.0325	0.325	0.1000	0.0141	0.0111	0.0535	0.0035	0.01	0.00685	0.04	0.00869	0.06	Collapsing Region
K3	C0-65×65-5	0.0326	0.325	0.1003	0.0087	0.0059	0.0549	0.0035	0.01	0.00685	0.04	0.00869	0.06	Advanced Damage Region
K1	C0-30×80-5	0.0328	0.4	0.0820	0.0057	0.0034	0.0625	0.0035	0.01	0.00843	0.04	0.01091	0.06	Collapsing Region
K2	C0-30×80-10	0.0327	0.4	0.0818	0.0086	0.0066	0.0514	0.0035	0.01	0.00843	0.04	0.01091	0.06	Advanced Damage Region
K2	C0-30×80-10	0.0327	0.4	0.0818	0.0086	0.0066	0.0514	0.0035	0.01	0.00843	0.04	0.01091	0.06	Advanced Damage Region
K2	C0-30×80-10	0.0327	0.4	0.0818	0.0086	0.0066	0.0514	0.0035	0.01	0.00843	0.04	0.01091	0.06	Advanced Damage Region
K2	C0-30×80-10	0.0327	0.4	0.0818	0.0086	0.0066	0.0514	0.0035	0.01	0.00843	0.04	0.01091	0.06	Advanced Damage Region
K1	C0-30×80-5	0.0328	0.4	0.0820	0.0057	0.0034	0.0625	0.0035	0.01	0.00843	0.04	0.01091	0.06	Collapsing Region

Table I.2 : Damage regions for base columns of S10-12 building for SYLMAR, 1994.

Column notation	Column type	Rotation (rad/m)	Plastic Hinge Length (Lp) (m)	Curvature (Kp) (1/m)	Unconfined concrete ϵ_c	Confined concrete ϵ_{cc}	Steel ϵ_{su}	MN		GV		GC		Damage region
								ϵ_c	ϵ_{su}	ϵ_{cc}	ϵ_{su}	ϵ_{cc}	ϵ_{su}	
K1	C10-30×80-5-12	0.0341	0.192	0.1776	0.0112	0.0069	0.1214	0.0035	0.01	0.00843	0.04	0.01091	0.06	Collapsing Region
K2	C10-30×80-10-12	0.0340	0.192	0.1771	0.0241	0.0197	0.1110	0.0035	0.01	0.00843	0.04	0.01091	0.06	Collapsing Region
K2	C10-30×80-10-12	0.0340	0.192	0.1771	0.0241	0.0197	0.1110	0.0035	0.01	0.00843	0.04	0.01091	0.06	Collapsing Region
K2	C10-30×80-10-12	0.0340	0.192	0.1771	0.0241	0.0197	0.1110	0.0035	0.01	0.00843	0.04	0.01091	0.06	Collapsing Region
K2	C10-30×80-10-12	0.0340	0.192	0.1771	0.0241	0.0197	0.1110	0.0035	0.01	0.00843	0.04	0.01091	0.06	Collapsing Region
K1	C10-30×80-5-12	0.0341	0.192	0.1776	0.0112	0.0069	0.1214	0.0035	0.01	0.00843	0.04	0.01091	0.06	Collapsing Region
K3	C10-65×65-5-12	0.0339	0.192	0.1766	0.0141	0.0095	0.0893	0.0035	0.01	0.00685	0.04	0.00869	0.06	Collapsing Region
K4	C10-65×65-10-12	0.0338	0.192	0.1760	0.0270	0.0222	0.0805	0.0035	0.01	0.00685	0.04	0.00869	0.06	Collapsing Region
K4	C10-65×65-10-12	0.0338	0.192	0.1760	0.0270	0.0222	0.0805	0.0035	0.01	0.00685	0.04	0.00869	0.06	Collapsing Region
K4	C10-65×65-10-12	0.0338	0.192	0.1760	0.0270	0.0222	0.0805	0.0035	0.01	0.00685	0.04	0.00869	0.06	Collapsing Region
K4	C10-65×65-10-12	0.0338	0.192	0.1760	0.0270	0.0222	0.0805	0.0035	0.01	0.00685	0.04	0.00869	0.06	Collapsing Region
K3	C10-65×65-5-12	0.0339	0.192	0.1766	0.0141	0.0095	0.0893	0.0035	0.01	0.00685	0.04	0.00869	0.06	Collapsing Region
K3	C10-65×65-5-12	0.0339	0.192	0.1766	0.0141	0.0095	0.0893	0.0035	0.01	0.00685	0.04	0.00869	0.06	Collapsing Region
K4	C10-65×65-10-12	0.0338	0.192	0.1760	0.0270	0.0222	0.0805	0.0035	0.01	0.00685	0.04	0.00869	0.06	Collapsing Region
K4	C10-65×65-10-12	0.0338	0.192	0.1760	0.0270	0.0222	0.0805	0.0035	0.01	0.00685	0.04	0.00869	0.06	Collapsing Region
K4	C10-65×65-10-12	0.0338	0.192	0.1760	0.0270	0.0222	0.0805	0.0035	0.01	0.00685	0.04	0.00869	0.06	Collapsing Region
K4	C10-65×65-10-12	0.0338	0.192	0.1760	0.0270	0.0222	0.0805	0.0035	0.01	0.00685	0.04	0.00869	0.06	Collapsing Region
K3	C10-65×65-5-12	0.0339	0.192	0.1766	0.0141	0.0095	0.0893	0.0035	0.01	0.00685	0.04	0.00869	0.06	Collapsing Region
K1	C10-30×80-5-12	0.0341	0.192	0.1776	0.0112	0.0069	0.1214	0.0035	0.01	0.00843	0.04	0.01091	0.06	Collapsing Region
K2	C10-30×80-10-12	0.0340	0.192	0.1771	0.0241	0.0197	0.1110	0.0035	0.01	0.00843	0.04	0.01091	0.06	Collapsing Region
K2	C10-30×80-10-12	0.0340	0.192	0.1771	0.0241	0.0197	0.1110	0.0035	0.01	0.00843	0.04	0.01091	0.06	Collapsing Region
K2	C10-30×80-10-12	0.0340	0.192	0.1771	0.0241	0.0197	0.1110	0.0035	0.01	0.00843	0.04	0.01091	0.06	Collapsing Region
K2	C10-30×80-10-12	0.0340	0.192	0.1771	0.0241	0.0197	0.1110	0.0035	0.01	0.00843	0.04	0.01091	0.06	Collapsing Region
K1	C10-30×80-5-12	0.0341	0.192	0.1776	0.0112	0.0069	0.1214	0.0035	0.01	0.00843	0.04	0.01091	0.06	Collapsing Region

Table I.3 : Damage regions for base columns of S0 building for DUZCE, 1999.

Column notation	Column type	Rotation (rad/m)	Plastic Hinge Length (Lp) (m)	Curvature (Kp) (1/m)	Unconfined concrete ϵ_c	Confined concrete ϵ_{cc}	Steel ϵ_{su}	MN		GV		GC		Damage region
								ϵ_c	ϵ_{su}	ϵ_{cc}	ϵ_{su}	ϵ_{cc}	ϵ_{su}	
K1	C0-30×80-5	-6.31E-02	0.4	-0.1579	0.0104	0.0065	0.1100	0.0035	0.01	0.00843	0.04	0.01091	0.06	Collapsing Region
K2	C0-30×80-10	-6.31E-02	0.4	-0.1576	0.0188	0.0153	0.0884	0.0035	0.01	0.00843	0.04	0.01091	0.06	Collapsing Region
K2	C0-30×80-10	-6.31E-02	0.4	-0.1576	0.0188	0.0153	0.0884	0.0035	0.01	0.00843	0.04	0.01091	0.06	Collapsing Region
K2	C0-30×80-10	-6.31E-02	0.4	-0.1576	0.0188	0.0153	0.0884	0.0035	0.01	0.00843	0.04	0.01091	0.06	Collapsing Region
K2	C0-30×80-10	-6.31E-02	0.4	-0.1576	0.0188	0.0153	0.0884	0.0035	0.01	0.00843	0.04	0.01091	0.06	Collapsing Region
K1	C0-30×80-5	-6.31E-02	0.4	-0.1579	0.0104	0.0065	0.1100	0.0035	0.01	0.00843	0.04	0.01091	0.06	Collapsing Region
K3	C0-65×65-5	-6.29E-02	0.325	-0.1937	0.0222	0.0168	0.0995	0.0035	0.01	0.00685	0.04	0.00869	0.06	Collapsing Region
K4	C0-65×65-10	-6.29E-02	0.325	-0.1935	0.0321	0.0268	0.0868	0.0035	0.01	0.00685	0.04	0.00869	0.06	Collapsing Region
K4	C0-65×65-10	-6.29E-02	0.325	-0.1935	0.0321	0.0268	0.0868	0.0035	0.01	0.00685	0.04	0.00869	0.06	Collapsing Region
K4	C0-65×65-10	-6.29E-02	0.325	-0.1935	0.0321	0.0268	0.0868	0.0035	0.01	0.00685	0.04	0.00869	0.06	Collapsing Region
K4	C0-65×65-10	-6.29E-02	0.325	-0.1935	0.0321	0.0268	0.0868	0.0035	0.01	0.00685	0.04	0.00869	0.06	Collapsing Region
K3	C0-65×65-5	-6.29E-02	0.325	-0.1937	0.0222	0.0168	0.0995	0.0035	0.01	0.00685	0.04	0.00869	0.06	Collapsing Region
K3	C0-65×65-5	-6.29E-02	0.325	-0.1937	0.0222	0.0168	0.0995	0.0035	0.01	0.00685	0.04	0.00869	0.06	Collapsing Region
K4	C0-65×65-10	-6.29E-02	0.325	-0.1935	0.0321	0.0268	0.0868	0.0035	0.01	0.00685	0.04	0.00869	0.06	Collapsing Region
K4	C0-65×65-10	-6.29E-02	0.325	-0.1935	0.0321	0.0268	0.0868	0.0035	0.01	0.00685	0.04	0.00869	0.06	Collapsing Region
K4	C0-65×65-10	-6.29E-02	0.325	-0.1935	0.0321	0.0268	0.0868	0.0035	0.01	0.00685	0.04	0.00869	0.06	Collapsing Region
K4	C0-65×65-10	-6.29E-02	0.325	-0.1935	0.0321	0.0268	0.0868	0.0035	0.01	0.00685	0.04	0.00869	0.06	Collapsing Region
K3	C0-65×65-5	-6.29E-02	0.325	-0.1937	0.0222	0.0168	0.0995	0.0035	0.01	0.00685	0.04	0.00869	0.06	Collapsing Region
K1	C0-30×80-5	-6.31E-02	0.4	-0.1579	0.0104	0.0065	0.1100	0.0035	0.01	0.00843	0.04	0.01091	0.06	Collapsing Region
K2	C0-30×80-10	-6.31E-02	0.4	-0.1576	0.0188	0.0153	0.0884	0.0035	0.01	0.00843	0.04	0.01091	0.06	Collapsing Region
K2	C0-30×80-10	-6.31E-02	0.4	-0.1576	0.0188	0.0153	0.0884	0.0035	0.01	0.00843	0.04	0.01091	0.06	Collapsing Region
K2	C0-30×80-10	-6.31E-02	0.4	-0.1576	0.0188	0.0153	0.0884	0.0035	0.01	0.00843	0.04	0.01091	0.06	Collapsing Region
K2	C0-30×80-10	-6.31E-02	0.4	-0.1576	0.0188	0.0153	0.0884	0.0035	0.01	0.00843	0.04	0.01091	0.06	Collapsing Region
K1	C0-30×80-5	-6.31E-02	0.4	-0.1579	0.0104	0.0065	0.1100	0.0035	0.01	0.00843	0.04	0.01091	0.06	Collapsing Region

Table I.4 : Damage regions for base columns of S10-12 building for DUZCE, 1999.

Column notation	Column type	Rotation (rad/m)	Plastic Hinge Length (Lp) (m)	Curvature (Kp) (1/m)	Unconfined concrete ϵ_c	Confined concrete ϵ_{cc}	Steel ϵ_{su}	MN		GV		GC		Damage region
								ϵ_c	ϵ_{su}	ϵ_{cc}	ϵ_{su}	ϵ_{cc}	ϵ_{su}	
K1	C10-30×80-5-12	-4.45E-02	0.192	-0.2316	0.01475	0.00935	0.15	0.0035	0.01	0.00843	0.04	0.01091	0.06	Collapsing Region
K2	C10-30×80-10-12	-4.44E-02	0.192	-0.2311	0.03235	0.02668	0.14	0.0035	0.01	0.00843	0.04	0.01091	0.06	Collapsing Region
K2	C10-30×80-10-12	-4.44E-02	0.192	-0.2311	0.03235	0.02668	0.14	0.0035	0.01	0.00843	0.04	0.01091	0.06	Collapsing Region
K2	C10-30×80-10-12	-4.44E-02	0.192	-0.2311	0.03235	0.02668	0.14	0.0035	0.01	0.00843	0.04	0.01091	0.06	Collapsing Region
K2	C10-30×80-10-12	-4.44E-02	0.192	-0.2311	0.03235	0.02668	0.14	0.0035	0.01	0.00843	0.04	0.01091	0.06	Collapsing Region
K1	C10-30×80-5-12	-4.45E-02	0.192	-0.2316	0.01475	0.00935	0.15	0.0035	0.01	0.00843	0.04	0.01091	0.06	Collapsing Region
K3	C10-65×65-5-12	-4.43E-02	0.192	-0.2307	0.02504	0.01845	0.11	0.0035	0.01	0.00685	0.04	0.00869	0.06	Collapsing Region
K4	C10-65×65-10-12	-4.42E-02	0.192	-0.2303	0.03749	0.03124	0.10	0.0035	0.01	0.00685	0.04	0.00869	0.06	Collapsing Region
K4	C10-65×65-10-12	-4.42E-02	0.192	-0.2303	0.03749	0.03124	0.10	0.0035	0.01	0.00685	0.04	0.00869	0.06	Collapsing Region
K4	C10-65×65-10-12	-4.42E-02	0.192	-0.2303	0.03749	0.03124	0.10	0.0035	0.01	0.00685	0.04	0.00869	0.06	Collapsing Region
K4	C10-65×65-10-12	-4.42E-02	0.192	-0.2303	0.03749	0.03124	0.10	0.0035	0.01	0.00685	0.04	0.00869	0.06	Collapsing Region
K3	C10-65×65-5-12	-4.43E-02	0.192	-0.2307	0.02504	0.01845	0.11	0.0035	0.01	0.00685	0.04	0.00869	0.06	Collapsing Region
K3	C10-65×65-5-12	-4.43E-02	0.192	-0.2307	0.02504	0.01845	0.11	0.0035	0.01	0.00685	0.04	0.00869	0.06	Collapsing Region
K4	C10-65×65-10-12	-4.42E-02	0.192	-0.2303	0.03749	0.03124	0.10	0.0035	0.01	0.00685	0.04	0.00869	0.06	Collapsing Region
K4	C10-65×65-10-12	-4.42E-02	0.192	-0.2303	0.03749	0.03124	0.10	0.0035	0.01	0.00685	0.04	0.00869	0.06	Collapsing Region
K4	C10-65×65-10-12	-4.42E-02	0.192	-0.2303	0.03749	0.03124	0.10	0.0035	0.01	0.00685	0.04	0.00869	0.06	Collapsing Region
K4	C10-65×65-10-12	-4.42E-02	0.192	-0.2303	0.03749	0.03124	0.10	0.0035	0.01	0.00685	0.04	0.00869	0.06	Collapsing Region
K4	C10-65×65-10-12	-4.42E-02	0.192	-0.2303	0.03749	0.03124	0.10	0.0035	0.01	0.00685	0.04	0.00869	0.06	Collapsing Region
K3	C10-65×65-5-12	-4.43E-02	0.192	-0.2307	0.02504	0.01845	0.11	0.0035	0.01	0.00685	0.04	0.00869	0.06	Collapsing Region
K1	C10-30×80-5-12	-4.45E-02	0.192	-0.2316	0.01475	0.00935	0.15	0.0035	0.01	0.00843	0.04	0.01091	0.06	Collapsing Region
K2	C10-30×80-10-12	-4.44E-02	0.192	-0.2311	0.03235	0.02668	0.14	0.0035	0.01	0.00843	0.04	0.01091	0.06	Collapsing Region
K2	C10-30×80-10-12	-4.44E-02	0.192	-0.2311	0.03235	0.02668	0.14	0.0035	0.01	0.00843	0.04	0.01091	0.06	Collapsing Region
K2	C10-30×80-10-12	-4.44E-02	0.192	-0.2311	0.03235	0.02668	0.14	0.0035	0.01	0.00843	0.04	0.01091	0.06	Collapsing Region
K2	C10-30×80-10-12	-4.44E-02	0.192	-0.2311	0.03235	0.02668	0.14	0.0035	0.01	0.00843	0.04	0.01091	0.06	Collapsing Region
K1	C10-30×80-5-12	-4.45E-02	0.192	-0.2316	0.01475	0.00935	0.15	0.0035	0.01	0.00843	0.04	0.01091	0.06	Collapsing Region

Table I.5 : Damage regions for base columns of S0 building for BİNGÖL, 2003.

Column notation	Column type	Rotation (rad/m)	Plastic Hinge Length (Lp) (m)	Curvature (Kp) (1/m)	Unconfined concrete			Confined concrete			Steel			Damage region
					ϵ_c	ϵ_{cc}	ϵ_{su}	ϵ_c	ϵ_{cc}	ϵ_{su}	ϵ_c	ϵ_{su}	ϵ_{cc}	
K1	C0-30×80-5	0.0124	0.4	0.0310	0.00233	0.00143	0.02515	0.0035	0.01	0.00843	0.04	0.01091	0.06	Marked Damage Region
K2	C0-30×80-10	0.0123	0.4	0.0308	0.00315	0.00242	0.0191	0.0035	0.01	0.00843	0.04	0.01091	0.06	Marked Damage Region
K2	C0-30×80-10	0.0123	0.4	0.0308	0.00315	0.00242	0.0191	0.0035	0.01	0.00843	0.04	0.01091	0.06	Marked Damage Region
K2	C0-30×80-10	0.0123	0.4	0.0308	0.00315	0.00242	0.0191	0.0035	0.01	0.00843	0.04	0.01091	0.06	Marked Damage Region
K1	C0-30×80-5	0.0124	0.4	0.0310	0.00233	0.00143	0.02515	0.0035	0.01	0.00843	0.04	0.01091	0.06	Marked Damage Region
K3	C0-65×65-5	0.0122	0.325	0.0375	0.00332	0.00222	0.02161	0.0035	0.01	0.00685	0.04	0.00869	0.06	Marked Damage Region
K4	C0-65×65-10	0.0121	0.325	0.0372	0.00507	0.0039	0.02144	0.0035	0.01	0.00685	0.04	0.00869	0.06	Marked Damage Region
K4	C0-65×65-10	0.0121	0.325	0.0372	0.00507	0.0039	0.02144	0.0035	0.01	0.00685	0.04	0.00869	0.06	Marked Damage Region
K4	C0-65×65-10	0.0121	0.325	0.0372	0.00507	0.0039	0.02144	0.0035	0.01	0.00685	0.04	0.00869	0.06	Marked Damage Region
K4	C0-65×65-10	0.0121	0.325	0.0372	0.00507	0.0039	0.02144	0.0035	0.01	0.00685	0.04	0.00869	0.06	Marked Damage Region
K3	C0-65×65-5	0.0122	0.325	0.0375	0.00332	0.00222	0.02161	0.0035	0.01	0.00685	0.04	0.00869	0.06	Marked Damage Region
K3	C0-65×65-5	0.0122	0.325	0.0375	0.00332	0.00222	0.02161	0.0035	0.01	0.00685	0.04	0.00869	0.06	Marked Damage Region
K4	C0-65×65-10	0.0121	0.325	0.0372	0.00507	0.0039	0.02144	0.0035	0.01	0.00685	0.04	0.00869	0.06	Marked Damage Region
K4	C0-65×65-10	0.0121	0.325	0.0372	0.00507	0.0039	0.02144	0.0035	0.01	0.00685	0.04	0.00869	0.06	Marked Damage Region
K4	C0-65×65-10	0.0121	0.325	0.0372	0.00507	0.0039	0.02144	0.0035	0.01	0.00685	0.04	0.00869	0.06	Marked Damage Region
K4	C0-65×65-10	0.0121	0.325	0.0372	0.00507	0.0039	0.02144	0.0035	0.01	0.00685	0.04	0.00869	0.06	Marked Damage Region
K3	C0-65×65-5	0.0122	0.325	0.0375	0.00332	0.00222	0.02161	0.0035	0.01	0.00685	0.04	0.00869	0.06	Marked Damage Region
K1	C0-30×80-5	0.0124	0.4	0.0310	0.00233	0.00143	0.02515	0.0035	0.01	0.00843	0.04	0.01091	0.06	Marked Damage Region
K2	C0-30×80-10	0.0123	0.4	0.0308	0.00315	0.00242	0.0191	0.0035	0.01	0.00843	0.04	0.01091	0.06	Marked Damage Region
K2	C0-30×80-10	0.0123	0.4	0.0308	0.00315	0.00242	0.0191	0.0035	0.01	0.00843	0.04	0.01091	0.06	Marked Damage Region
K2	C0-30×80-10	0.0123	0.4	0.0308	0.00315	0.00242	0.0191	0.0035	0.01	0.00843	0.04	0.01091	0.06	Marked Damage Region
K2	C0-30×80-10	0.0123	0.4	0.0308	0.00315	0.00242	0.0191	0.0035	0.01	0.00843	0.04	0.01091	0.06	Marked Damage Region
K1	C0-30×80-5	0.0124	0.4	0.0310	0.00233	0.00143	0.02515	0.0035	0.01	0.00843	0.04	0.01091	0.06	Marked Damage Region

Table I.6 : Damage regions for base columns of S10-12 building for BİNGÖL, 2003.

Column notation	Column type	Rotation (rad/m)	Plastic Hinge Length (Lp) (m)	Curvature (Kp) (1/m)	MN			GV			GC			Damage region
					Unconfined concrete ϵ_c	Confined concrete ϵ_{cc}	Steel ϵ_{su}	ϵ_c	ϵ_{su}	ϵ_{cc}	ϵ_{su}	ϵ_{cc}	ϵ_{su}	
K1	C10-30×80-5-12	0.0129	0.192	0.0672	0.0041	0.0024	0.0475	0.0035	0.01	0.00843	0.04	0.01091	0.06	Advanced Damage Region
K2	C10-30×80-10-12	0.0128	0.192	0.0667	0.0070	0.0054	0.0434	0.0035	0.01	0.00843	0.04	0.01091	0.06	Advanced Damage Region
K2	C10-30×80-10-12	0.0128	0.192	0.0667	0.0070	0.0054	0.0434	0.0035	0.01	0.00843	0.04	0.01091	0.06	Advanced Damage Region
K2	C10-30×80-10-12	0.0128	0.192	0.0667	0.0070	0.0054	0.0434	0.0035	0.01	0.00843	0.04	0.01091	0.06	Advanced Damage Region
K2	C10-30×80-10-12	0.0128	0.192	0.0667	0.0070	0.0054	0.0434	0.0035	0.01	0.00843	0.04	0.01091	0.06	Advanced Damage Region
K1	C10-30×80-5-12	0.0129	0.192	0.0672	0.0041	0.0024	0.0475	0.0035	0.01	0.00843	0.04	0.01091	0.06	Advanced Damage Region
K3	C10-65×65-5-12	0.0127	0.192	0.0661	0.0050	0.0031	0.0362	0.0035	0.01	0.00685	0.04	0.00869	0.06	Marked Damage Region
K4	C10-65×65-10-12	0.0126	0.192	0.0656	0.0068	0.0051	0.0297	0.0035	0.01	0.00685	0.04	0.00869	0.06	Marked Damage Region
K4	C10-65×65-10-12	0.0126	0.192	0.0656	0.0068	0.0051	0.0297	0.0035	0.01	0.00685	0.04	0.00869	0.06	Marked Damage Region
K4	C10-65×65-10-12	0.0126	0.192	0.0656	0.0068	0.0051	0.0297	0.0035	0.01	0.00685	0.04	0.00869	0.06	Marked Damage Region
K4	C10-65×65-10-12	0.0126	0.192	0.0656	0.0068	0.0051	0.0297	0.0035	0.01	0.00685	0.04	0.00869	0.06	Marked Damage Region
K3	C10-65×65-5-12	0.0127	0.192	0.0661	0.0050	0.0031	0.0362	0.0035	0.01	0.00685	0.04	0.00869	0.06	Marked Damage Region
K3	C10-65×65-5-12	0.0127	0.192	0.0661	0.0050	0.0031	0.0362	0.0035	0.01	0.00685	0.04	0.00869	0.06	Marked Damage Region
K4	C10-65×65-10-12	0.0126	0.192	0.0656	0.0068	0.0051	0.0297	0.0035	0.01	0.00685	0.04	0.00869	0.06	Marked Damage Region
K4	C10-65×65-10-12	0.0126	0.192	0.0656	0.0068	0.0051	0.0297	0.0035	0.01	0.00685	0.04	0.00869	0.06	Marked Damage Region
K4	C10-65×65-10-12	0.0126	0.192	0.0656	0.0068	0.0051	0.0297	0.0035	0.01	0.00685	0.04	0.00869	0.06	Marked Damage Region
K4	C10-65×65-10-12	0.0126	0.192	0.0656	0.0068	0.0051	0.0297	0.0035	0.01	0.00685	0.04	0.00869	0.06	Marked Damage Region
K4	C10-65×65-10-12	0.0126	0.192	0.0656	0.0068	0.0051	0.0297	0.0035	0.01	0.00685	0.04	0.00869	0.06	Marked Damage Region
K3	C10-65×65-5-12	0.0127	0.192	0.0661	0.0050	0.0031	0.0362	0.0035	0.01	0.00685	0.04	0.00869	0.06	Marked Damage Region
K1	C10-30×80-5-12	0.0129	0.192	0.0672	0.0041	0.0024	0.0475	0.0035	0.01	0.00843	0.04	0.01091	0.06	Advanced Damage Region
K2	C10-30×80-10-12	0.0128	0.192	0.0667	0.0070	0.0054	0.0434	0.0035	0.01	0.00843	0.04	0.01091	0.06	Advanced Damage Region
K2	C10-30×80-10-12	0.0128	0.192	0.0667	0.0070	0.0054	0.0434	0.0035	0.01	0.00843	0.04	0.01091	0.06	Advanced Damage Region
K2	C10-30×80-10-12	0.0128	0.192	0.0667	0.0070	0.0054	0.0434	0.0035	0.01	0.00843	0.04	0.01091	0.06	Advanced Damage Region
K2	C10-30×80-10-12	0.0128	0.192	0.0667	0.0070	0.0054	0.0434	0.0035	0.01	0.00843	0.04	0.01091	0.06	Advanced Damage Region
K1	C10-30×80-5-12	0.0129	0.192	0.0672	0.0041	0.0024	0.0475	0.0035	0.01	0.00843	0.04	0.01091	0.06	Advanced Damage Region

Table I.7 : Damage regions for base columns of S0 building for MEXICO, 1980.

Column notation	Column type	Rotation (rad/m)	Plastic Hinge Length (Lp) (m)	Curvature (Kp) (1/m)	Unconfined concrete ϵ_c	Confined concrete ϵ_{cc}	Steel ϵ_{su}						Damage region	
							MN ϵ_c	ϵ_{su}	GV ϵ_{cc}	ϵ_{su}	GC ϵ_{cc}	ϵ_{su}		
K1	C0-30×80-5	0.0235	0.4	0.0588	0.0036	0.0022	0.0401	0.0035	0.01	0.00843	0.04	0.01091	0.06	Advanced Damage Region
K2	C0-30×80-10	0.0234	0.4	0.0585	0.0058	0.0045	0.0353	0.0035	0.01	0.00843	0.04	0.01091	0.06	Marked Damage Region
K2	C0-30×80-10	0.0234	0.4	0.0585	0.0058	0.0045	0.0353	0.0035	0.01	0.00843	0.04	0.01091	0.06	Marked Damage Region
K2	C0-30×80-10	0.0234	0.4	0.0585	0.0058	0.0045	0.0353	0.0035	0.01	0.00843	0.04	0.01091	0.06	Marked Damage Region
K2	C0-30×80-10	0.0234	0.4	0.0585	0.0058	0.0045	0.0353	0.0035	0.01	0.00843	0.04	0.01091	0.06	Marked Damage Region
K1	C0-30×80-5	0.0235	0.4	0.0588	0.0036	0.0022	0.0401	0.0035	0.01	0.00843	0.04	0.01091	0.06	Advanced Damage Region
K3	C0-65×65-5	0.0233	0.325	0.0717	0.0059	0.0040	0.0386	0.0035	0.01	0.00685	0.04	0.00869	0.06	Marked Damage Region
K4	C0-65×65-10	0.0232	0.325	0.0714	0.0095	0.0075	0.0375	0.0035	0.01	0.00685	0.04	0.00869	0.06	Advanced Damage Region
K4	C0-65×65-10	0.0232	0.325	0.0714	0.0095	0.0075	0.0375	0.0035	0.01	0.00685	0.04	0.00869	0.06	Advanced Damage Region
K4	C0-65×65-10	0.0232	0.325	0.0714	0.0095	0.0075	0.0375	0.0035	0.01	0.00685	0.04	0.00869	0.06	Advanced Damage Region
K4	C0-65×65-10	0.0232	0.325	0.0714	0.0095	0.0075	0.0375	0.0035	0.01	0.00685	0.04	0.00869	0.06	Advanced Damage Region
K3	C0-65×65-5	0.0233	0.325	0.0717	0.0059	0.0040	0.0386	0.0035	0.01	0.00685	0.04	0.00869	0.06	Marked Damage Region
K3	C0-65×65-5	0.0233	0.325	0.0717	0.0059	0.0040	0.0386	0.0035	0.01	0.00685	0.04	0.00869	0.06	Marked Damage Region
K4	C0-65×65-10	0.0232	0.325	0.0714	0.0095	0.0075	0.0375	0.0035	0.01	0.00685	0.04	0.00869	0.06	Advanced Damage Region
K4	C0-65×65-10	0.0232	0.325	0.0714	0.0095	0.0075	0.0375	0.0035	0.01	0.00685	0.04	0.00869	0.06	Advanced Damage Region
K4	C0-65×65-10	0.0232	0.325	0.0714	0.0095	0.0075	0.0375	0.0035	0.01	0.00685	0.04	0.00869	0.06	Advanced Damage Region
K4	C0-65×65-10	0.0232	0.325	0.0714	0.0095	0.0075	0.0375	0.0035	0.01	0.00685	0.04	0.00869	0.06	Advanced Damage Region
K3	C0-65×65-5	0.0233	0.325	0.0717	0.0059	0.0040	0.0386	0.0035	0.01	0.00685	0.04	0.00869	0.06	Marked Damage Region
K1	C0-30×80-5	0.0235	0.4	0.0588	0.0036	0.0022	0.0401	0.0035	0.01	0.00843	0.04	0.01091	0.06	Advanced Damage Region
K2	C0-30×80-10	0.0234	0.4	0.0585	0.0058	0.0045	0.0353	0.0035	0.01	0.00843	0.04	0.01091	0.06	Marked Damage Region
K2	C0-30×80-10	0.0234	0.4	0.0585	0.0058	0.0045	0.0353	0.0035	0.01	0.00843	0.04	0.01091	0.06	Marked Damage Region
K2	C0-30×80-10	0.0234	0.4	0.0585	0.0058	0.0045	0.0353	0.0035	0.01	0.00843	0.04	0.01091	0.06	Marked Damage Region
K2	C0-30×80-10	0.0234	0.4	0.0585	0.0058	0.0045	0.0353	0.0035	0.01	0.00843	0.04	0.01091	0.06	Marked Damage Region
K1	C0-30×80-5	0.0235	0.4	0.0588	0.0036	0.0022	0.0401	0.0035	0.01	0.00843	0.04	0.01091	0.06	Advanced Damage Region

Table I.8 : Damage regions for base columns of S10-12 building for MEXICO, 1980.

Column notation	Column type	Rotation (rad/m)	Plastic Hinge Length (Lp) (m)	Curvature (Kp) (1/m)	Unconfined concrete			Confined concrete			Steel			Damage region
					ϵ_c	ϵ_{cc}	ϵ_{su}	ϵ_c	ϵ_{su}	ϵ_{cc}	ϵ_{su}	ϵ_{cc}	ϵ_{su}	
K1	C10-30×80-5-12	0.0305	0.192	0.1589	0.0097	0.0058	0.1100	0.0035	0.01	0.00843	0.04	0.01091	0.06	Collapsing Region
K2	C10-30×80-10-12	0.0304	0.192	0.1583	0.0203	0.0165	0.0960	0.0035	0.01	0.00843	0.04	0.01091	0.06	Collapsing Region
K2	C10-30×80-10-12	0.0304	0.192	0.1583	0.0203	0.0165	0.0960	0.0035	0.01	0.00843	0.04	0.01091	0.06	Collapsing Region
K2	C10-30×80-10-12	0.0304	0.192	0.1583	0.0203	0.0165	0.0960	0.0035	0.01	0.00843	0.04	0.01091	0.06	Collapsing Region
K2	C10-30×80-10-12	0.0304	0.192	0.1583	0.0203	0.0165	0.0960	0.0035	0.01	0.00843	0.04	0.01091	0.06	Collapsing Region
K1	C10-30×80-5-12	0.0305	0.192	0.1589	0.0097	0.0058	0.1100	0.0035	0.01	0.00843	0.04	0.01091	0.06	Collapsing Region
K3	C10-65×65-5-12	0.0303	0.192	0.1578	0.0128	0.0087	0.0816	0.0035	0.01	0.00685	0.04	0.00869	0.06	Collapsing Region
K4	C10-65×65-10-12	0.0302	0.192	0.1573	0.0181	0.0142	0.0691	0.0035	0.01	0.00685	0.04	0.00869	0.06	Collapsing Region
K4	C10-65×65-10-12	0.0302	0.192	0.1573	0.0181	0.0142	0.0691	0.0035	0.01	0.00685	0.04	0.00869	0.06	Collapsing Region
K4	C10-65×65-10-12	0.0302	0.192	0.1573	0.0181	0.0142	0.0691	0.0035	0.01	0.00685	0.04	0.00869	0.06	Collapsing Region
K4	C10-65×65-10-12	0.0302	0.192	0.1573	0.0181	0.0142	0.0691	0.0035	0.01	0.00685	0.04	0.00869	0.06	Collapsing Region
K3	C10-65×65-5-12	0.0303	0.192	0.1578	0.0128	0.0087	0.0816	0.0035	0.01	0.00685	0.04	0.00869	0.06	Collapsing Region
K3	C10-65×65-5-12	0.0303	0.192	0.1578	0.0128	0.0087	0.0816	0.0035	0.01	0.00685	0.04	0.00869	0.06	Collapsing Region
K4	C10-65×65-10-12	0.0302	0.192	0.1573	0.0181	0.0142	0.0691	0.0035	0.01	0.00685	0.04	0.00869	0.06	Collapsing Region
K4	C10-65×65-10-12	0.0302	0.192	0.1573	0.0181	0.0142	0.0691	0.0035	0.01	0.00685	0.04	0.00869	0.06	Collapsing Region
K4	C10-65×65-10-12	0.0302	0.192	0.1573	0.0181	0.0142	0.0691	0.0035	0.01	0.00685	0.04	0.00869	0.06	Collapsing Region
K4	C10-65×65-10-12	0.0302	0.192	0.1573	0.0181	0.0142	0.0691	0.0035	0.01	0.00685	0.04	0.00869	0.06	Collapsing Region
K4	C10-65×65-10-12	0.0302	0.192	0.1573	0.0181	0.0142	0.0691	0.0035	0.01	0.00685	0.04	0.00869	0.06	Collapsing Region
K3	C10-65×65-5-12	0.0303	0.192	0.1578	0.0128	0.0087	0.0816	0.0035	0.01	0.00685	0.04	0.00869	0.06	Collapsing Region
K1	C10-30×80-5-12	0.0305	0.192	0.1589	0.0097	0.0058	0.1100	0.0035	0.01	0.00843	0.04	0.01091	0.06	Collapsing Region
K2	C10-30×80-10-12	0.0304	0.192	0.1583	0.0203	0.0165	0.0960	0.0035	0.01	0.00843	0.04	0.01091	0.06	Collapsing Region
K2	C10-30×80-10-12	0.0304	0.192	0.1583	0.0203	0.0165	0.0960	0.0035	0.01	0.00843	0.04	0.01091	0.06	Collapsing Region
K2	C10-30×80-10-12	0.0304	0.192	0.1583	0.0203	0.0165	0.0960	0.0035	0.01	0.00843	0.04	0.01091	0.06	Collapsing Region
K2	C10-30×80-10-12	0.0304	0.192	0.1583	0.0203	0.0165	0.0960	0.0035	0.01	0.00843	0.04	0.01091	0.06	Collapsing Region
K1	C10-30×80-5-12	0.0305	0.192	0.1589	0.0097	0.0058	0.1100	0.0035	0.01	0.00843	0.04	0.01091	0.06	Collapsing Region

Table I.9 : Damage regions for base columns of S0 building for KOBE, 1995.

Column notation	Column type	Rotation (rad/m)	Plastic Hinge Length (Lp) (m)	Curvature (Kp) (1/m)	MN			GV			GC			Damage region
					Unconfined concrete ϵ_c	Confined concrete ϵ_{cc}	Steel ϵ_{su}	ϵ_c	ϵ_{su}	ϵ_{cc}	ϵ_{su}	ϵ_{cc}	ϵ_{su}	
K1	C0-30×80-5	5.68E-02	0.4	0.1420	0.0095	0.0059	0.0993	0.0035	0.01	0.00843	0.04	0.01091	0.06	Collapsing Region
K2	C0-30×80-10	5.67E-02	0.4	0.1418	0.0188	0.0153	0.0884	0.0035	0.01	0.00843	0.04	0.01091	0.06	Collapsing Region
K2	C0-30×80-10	5.67E-02	0.4	0.1418	0.0188	0.0153	0.0884	0.0035	0.01	0.00843	0.04	0.01091	0.06	Collapsing Region
K2	C0-30×80-10	5.67E-02	0.4	0.1418	0.0188	0.0153	0.0884	0.0035	0.01	0.00843	0.04	0.01091	0.06	Collapsing Region
K2	C0-30×80-10	5.67E-02	0.4	0.1418	0.0188	0.0153	0.0884	0.0035	0.01	0.00843	0.04	0.01091	0.06	Collapsing Region
K1	C0-30×80-5	5.68E-02	0.4	0.1420	0.0095	0.0059	0.0993	0.0035	0.01	0.00843	0.04	0.01091	0.06	Collapsing Region
K3	C0-65×65-5	5.66E-02	0.325	0.1742	0.0185	0.0139	0.0838	0.0035	0.01	0.00685	0.04	0.00869	0.06	Collapsing Region
K4	C0-65×65-10	5.65E-02	0.325	0.1740	0.0292	0.0244	0.0795	0.0035	0.01	0.00685	0.04	0.00869	0.06	Collapsing Region
K4	C0-65×65-10	5.65E-02	0.325	0.1740	0.0292	0.0244	0.0795	0.0035	0.01	0.00685	0.04	0.00869	0.06	Collapsing Region
K4	C0-65×65-10	5.65E-02	0.325	0.1740	0.0292	0.0244	0.0795	0.0035	0.01	0.00685	0.04	0.00869	0.06	Collapsing Region
K4	C0-65×65-10	5.65E-02	0.325	0.1740	0.0292	0.0244	0.0795	0.0035	0.01	0.00685	0.04	0.00869	0.06	Collapsing Region
K3	C0-65×65-5	5.66E-02	0.325	0.1742	0.0185	0.0139	0.0838	0.0035	0.01	0.00685	0.04	0.00869	0.06	Collapsing Region
K3	C0-65×65-5	5.66E-02	0.325	0.1742	0.0185	0.0139	0.0838	0.0035	0.01	0.00685	0.04	0.00869	0.06	Collapsing Region
K4	C0-65×65-10	5.65E-02	0.325	0.1740	0.0292	0.0244	0.0795	0.0035	0.01	0.00685	0.04	0.00869	0.06	Collapsing Region
K4	C0-65×65-10	5.65E-02	0.325	0.1740	0.0292	0.0244	0.0795	0.0035	0.01	0.00685	0.04	0.00869	0.06	Collapsing Region
K4	C0-65×65-10	5.65E-02	0.325	0.1740	0.0292	0.0244	0.0795	0.0035	0.01	0.00685	0.04	0.00869	0.06	Collapsing Region
K4	C0-65×65-10	5.65E-02	0.325	0.1740	0.0292	0.0244	0.0795	0.0035	0.01	0.00685	0.04	0.00869	0.06	Collapsing Region
K3	C0-65×65-5	5.66E-02	0.325	0.1742	0.0185	0.0139	0.0838	0.0035	0.01	0.00685	0.04	0.00869	0.06	Collapsing Region
K1	C0-30×80-5	5.68E-02	0.4	0.1420	0.0095	0.0059	0.0993	0.0035	0.01	0.00843	0.04	0.01091	0.06	Collapsing Region
K2	C0-30×80-10	5.67E-02	0.4	0.1418	0.0188	0.0153	0.0884	0.0035	0.01	0.00843	0.04	0.01091	0.06	Collapsing Region
K2	C0-30×80-10	5.67E-02	0.4	0.1418	0.0188	0.0153	0.0884	0.0035	0.01	0.00843	0.04	0.01091	0.06	Collapsing Region
K2	C0-30×80-10	5.67E-02	0.4	0.1418	0.0188	0.0153	0.0884	0.0035	0.01	0.00843	0.04	0.01091	0.06	Collapsing Region
K2	C0-30×80-10	5.67E-02	0.4	0.1418	0.0188	0.0153	0.0884	0.0035	0.01	0.00843	0.04	0.01091	0.06	Collapsing Region
K1	C0-30×80-5	5.68E-02	0.4	0.1420	0.0095	0.0059	0.0993	0.0035	0.01	0.00843	0.04	0.01091	0.06	Collapsing Region

Table I.10: Damage regions for base columns of S10-12 building for KOBE, 1995.

Column notation	Column type	Rotation (rad/m)	Plastic Hinge Length (Lp) (m)	Curvature (Kp) (1/m)	Unconfined concrete ϵ_c	Confined concrete ϵ_{cc}	MN			GV		GC		Damage region
							Steel ϵ_{su}	ϵ_c	ϵ_{su}	ϵ_{cc}	ϵ_{su}	ϵ_{cc}	ϵ_{su}	
K1	C10-30×80-5-12	4.48E-02	0.192	0.2335	0.01475	0.00935	0.15	0.0035	0.01	0.00843	0.04	0.01091	0.06	Collapsing Region
K2	C10-30×80-10-12	4.47E-02	0.192	0.2330	0.03338	0.02742	0.14	0.0035	0.01	0.00843	0.04	0.01091	0.06	Collapsing Region
K2	C10-30×80-10-12	4.47E-02	0.192	0.2330	0.03338	0.02742	0.14	0.0035	0.01	0.00843	0.04	0.01091	0.06	Collapsing Region
K2	C10-30×80-10-12	4.47E-02	0.192	0.2330	0.03338	0.02742	0.14	0.0035	0.01	0.00843	0.04	0.01091	0.06	Collapsing Region
K1	C10-30×80-5-12	4.48E-02	0.192	0.2335	0.01475	0.00935	0.15	0.0035	0.01	0.00843	0.04	0.01091	0.06	Collapsing Region
K3	C10-65×65-5-12	4.46E-02	0.192	0.2326	0.02506	0.01891	0.11	0.0035	0.01	0.00685	0.04	0.00869	0.06	Collapsing Region
K4	C10-65×65-10-12	4.46E-02	0.192	0.2322	0.03749	0.03124	0.10	0.0035	0.01	0.00685	0.04	0.00869	0.06	Collapsing Region
K4	C10-65×65-10-12	4.46E-02	0.192	0.2322	0.03749	0.03124	0.10	0.0035	0.01	0.00685	0.04	0.00869	0.06	Collapsing Region
K4	C10-65×65-10-12	4.46E-02	0.192	0.2322	0.03749	0.03124	0.10	0.0035	0.01	0.00685	0.04	0.00869	0.06	Collapsing Region
K4	C10-65×65-10-12	4.46E-02	0.192	0.2322	0.03749	0.03124	0.10	0.0035	0.01	0.00685	0.04	0.00869	0.06	Collapsing Region
K3	C10-65×65-5-12	4.46E-02	0.192	0.2326	0.02506	0.01891	0.11	0.0035	0.01	0.00685	0.04	0.00869	0.06	Collapsing Region
K3	C10-65×65-5-12	4.46E-02	0.192	0.2326	0.02506	0.01891	0.11	0.0035	0.01	0.00685	0.04	0.00869	0.06	Collapsing Region
K4	C10-65×65-10-12	4.46E-02	0.192	0.2322	0.03749	0.03124	0.10	0.0035	0.01	0.00685	0.04	0.00869	0.06	Collapsing Region
K4	C10-65×65-10-12	4.46E-02	0.192	0.2322	0.03749	0.03124	0.10	0.0035	0.01	0.00685	0.04	0.00869	0.06	Collapsing Region
K4	C10-65×65-10-12	4.46E-02	0.192	0.2322	0.03749	0.03124	0.10	0.0035	0.01	0.00685	0.04	0.00869	0.06	Collapsing Region
K4	C10-65×65-10-12	4.46E-02	0.192	0.2322	0.03749	0.03124	0.10	0.0035	0.01	0.00685	0.04	0.00869	0.06	Collapsing Region
K3	C10-65×65-5-12	4.46E-02	0.192	0.2326	0.02506	0.01891	0.11	0.0035	0.01	0.00685	0.04	0.00869	0.06	Collapsing Region
K1	C10-30×80-5-12	4.48E-02	0.192	0.2335	0.01475	0.00935	0.15	0.0035	0.01	0.00843	0.04	0.01091	0.06	Collapsing Region
K2	C10-30×80-10-12	4.47E-02	0.192	0.2330	0.03338	0.02742	0.14	0.0035	0.01	0.00843	0.04	0.01091	0.06	Collapsing Region
K2	C10-30×80-10-12	4.47E-02	0.192	0.2330	0.03338	0.02742	0.14	0.0035	0.01	0.00843	0.04	0.01091	0.06	Collapsing Region
K2	C10-30×80-10-12	4.47E-02	0.192	0.2330	0.03338	0.02742	0.14	0.0035	0.01	0.00843	0.04	0.01091	0.06	Collapsing Region
K2	C10-30×80-10-12	4.47E-02	0.192	0.2330	0.03338	0.02742	0.14	0.0035	0.01	0.00843	0.04	0.01091	0.06	Collapsing Region
K1	C10-30×80-5-12	4.48E-02	0.192	0.2335	0.01475	0.00935	0.15	0.0035	0.01	0.00843	0.04	0.01091	0.06	Collapsing Region

Table İ.11 : Damage regions for base columns of S0 building for KOCAELİ, 1999

Column notation	Column type	Rotation (rad/m)	Plastic Hinge Length (Lp) (m)	Curvature (Kp) (1/m)	Unconfined concrete ϵ_c	Confined concrete ϵ_{cc}	Steel ϵ_{su}	MN		GV		GC		Damage region
								ϵ_c	ϵ_{su}	ϵ_{cc}	ϵ_{su}	ϵ_{cc}	ϵ_{su}	
K1	C0-30×80-5	0.0100	0.4	0.0250	0.0018	0.0012	0.0175	0.0035	0.01	0.00843	0.04	0.01091	0.06	Marked Damage Region
K2	C0-30×80-10	0.0099	0.4	0.0248	0.0026	0.0020	0.0150	0.0035	0.01	0.00843	0.04	0.01091	0.06	Marked Damage Region
K2	C0-30×80-10	0.0099	0.4	0.0248	0.0026	0.0020	0.0150	0.0035	0.01	0.00843	0.04	0.01091	0.06	Marked Damage Region
K2	C0-30×80-10	0.0099	0.4	0.0248	0.0026	0.0020	0.0150	0.0035	0.01	0.00843	0.04	0.01091	0.06	Marked Damage Region
K2	C0-30×80-10	0.0099	0.4	0.0248	0.0026	0.0020	0.0150	0.0035	0.01	0.00843	0.04	0.01091	0.06	Marked Damage Region
K1	C0-30×80-5	0.0100	0.4	0.0250	0.0018	0.0012	0.0175	0.0035	0.01	0.00843	0.04	0.01091	0.06	Marked Damage Region
K3	C0-65×65-5	0.0098	0.325	0.0302	0.0028	0.0021	0.0160	0.0035	0.01	0.00685	0.04	0.00869	0.06	Marked Damage Region
K4	C0-65×65-10	0.0097	0.325	0.0298	0.0031	0.0024	0.0132	0.0035	0.01	0.00685	0.04	0.00869	0.06	Marked Damage Region
K4	C0-65×65-10	0.0097	0.325	0.0298	0.0031	0.0024	0.0132	0.0035	0.01	0.00685	0.04	0.00869	0.06	Marked Damage Region
K4	C0-65×65-10	0.0097	0.325	0.0298	0.0031	0.0024	0.0132	0.0035	0.01	0.00685	0.04	0.00869	0.06	Marked Damage Region
K4	C0-65×65-10	0.0097	0.325	0.0298	0.0031	0.0024	0.0132	0.0035	0.01	0.00685	0.04	0.00869	0.06	Marked Damage Region
K3	C0-65×65-5	0.0098	0.325	0.0302	0.0028	0.0021	0.0160	0.0035	0.01	0.00685	0.04	0.00869	0.06	Marked Damage Region
K3	C0-65×65-5	0.0098	0.325	0.0302	0.0028	0.0021	0.0160	0.0035	0.01	0.00685	0.04	0.00869	0.06	Marked Damage Region
K4	C0-65×65-10	0.0097	0.325	0.0298	0.0031	0.0024	0.0132	0.0035	0.01	0.00685	0.04	0.00869	0.06	Marked Damage Region
K4	C0-65×65-10	0.0097	0.325	0.0298	0.0031	0.0024	0.0132	0.0035	0.01	0.00685	0.04	0.00869	0.06	Marked Damage Region
K4	C0-65×65-10	0.0097	0.325	0.0298	0.0031	0.0024	0.0132	0.0035	0.01	0.00685	0.04	0.00869	0.06	Marked Damage Region
K4	C0-65×65-10	0.0097	0.325	0.0298	0.0031	0.0024	0.0132	0.0035	0.01	0.00685	0.04	0.00869	0.06	Marked Damage Region
K3	C0-65×65-5	0.0098	0.325	0.0302	0.0028	0.0021	0.0160	0.0035	0.01	0.00685	0.04	0.00869	0.06	Marked Damage Region
K1	C0-30×80-5	0.0100	0.4	0.0250	0.0018	0.0012	0.0175	0.0035	0.01	0.00843	0.04	0.01091	0.06	Marked Damage Region
K2	C0-30×80-10	0.0099	0.4	0.0248	0.0026	0.0020	0.0150	0.0035	0.01	0.00843	0.04	0.01091	0.06	Marked Damage Region
K2	C0-30×80-10	0.0099	0.4	0.0248	0.0026	0.0020	0.0150	0.0035	0.01	0.00843	0.04	0.01091	0.06	Marked Damage Region
K2	C0-30×80-10	0.0099	0.4	0.0248	0.0026	0.0020	0.0150	0.0035	0.01	0.00843	0.04	0.01091	0.06	Marked Damage Region
K2	C0-30×80-10	0.0099	0.4	0.0248	0.0026	0.0020	0.0150	0.0035	0.01	0.00843	0.04	0.01091	0.06	Marked Damage Region
K1	C0-30×80-5	0.0100	0.4	0.0250	0.0018	0.0012	0.0175	0.0035	0.01	0.00843	0.04	0.01091	0.06	Marked Damage Region

Table I.12 : Damage regions for base columns of S10-12 building for KOCAELI, 1999.

Column notation	Column type	Rotation (rad/m)	Plastic Hinge Length (Lp) (m)	Curvature (Kp) (1/m)	Unconfined concrete ϵ_c	Confined concrete ϵ_{cc}	Steel ϵ_{su}	MN		GV		GC		Damage region
								ϵ_c	ϵ_{su}	ϵ_{cc}	ϵ_{su}	ϵ_{cc}	ϵ_{su}	
K1	C10-30×80-5-12	0.0172	0.192	0.0896	0.0048	0.0029	0.0549	0.0035	0.01	0.00843	0.04	0.01091	0.06	Advanced Damage Region
K2	C10-30×80-10-12	0.0171	0.192	0.0891	0.0085	0.0065	0.0514	0.0035	0.01	0.00843	0.04	0.01091	0.06	Advanced Damage Region
K2	C10-30×80-10-12	0.0171	0.192	0.0891	0.0085	0.0065	0.0514	0.0035	0.01	0.00843	0.04	0.01091	0.06	Advanced Damage Region
K2	C10-30×80-10-12	0.0171	0.192	0.0891	0.0085	0.0065	0.0514	0.0035	0.01	0.00843	0.04	0.01091	0.06	Advanced Damage Region
K2	C10-30×80-10-12	0.0171	0.192	0.0891	0.0085	0.0065	0.0514	0.0035	0.01	0.00843	0.04	0.01091	0.06	Advanced Damage Region
K1	C10-30×80-5-12	0.0172	0.192	0.0896	0.0048	0.0029	0.0549	0.0035	0.01	0.00843	0.04	0.01091	0.06	Advanced Damage Region
K3	C10-65×65-5-12	0.0170	0.192	0.0885	0.0061	0.0028	0.0439	0.0035	0.01	0.00685	0.04	0.00869	0.06	Advanced Damage Region
K4	C10-65×65-10-12	0.0169	0.192	0.0880	0.0089	0.0068	0.0377	0.0035	0.01	0.00685	0.04	0.00869	0.06	Marked Damage Region
K4	C10-65×65-10-12	0.0169	0.192	0.0880	0.0089	0.0068	0.0377	0.0035	0.01	0.00685	0.04	0.00869	0.06	Marked Damage Region
K4	C10-65×65-10-12	0.0169	0.192	0.0880	0.0089	0.0068	0.0377	0.0035	0.01	0.00685	0.04	0.00869	0.06	Marked Damage Region
K4	C10-65×65-10-12	0.0169	0.192	0.0880	0.0089	0.0068	0.0377	0.0035	0.01	0.00685	0.04	0.00869	0.06	Marked Damage Region
K3	C10-65×65-5-12	0.0170	0.192	0.0885	0.0061	0.0028	0.0439	0.0035	0.01	0.00685	0.04	0.00869	0.06	Advanced Damage Region
K3	C10-65×65-5-12	0.0170	0.192	0.0885	0.0061	0.0028	0.0439	0.0035	0.01	0.00685	0.04	0.00869	0.06	Advanced Damage Region
K4	C10-65×65-10-12	0.0169	0.192	0.0880	0.0089	0.0068	0.0377	0.0035	0.01	0.00685	0.04	0.00869	0.06	Marked Damage Region
K4	C10-65×65-10-12	0.0169	0.192	0.0880	0.0089	0.0068	0.0377	0.0035	0.01	0.00685	0.04	0.00869	0.06	Marked Damage Region
K4	C10-65×65-10-12	0.0169	0.192	0.0880	0.0089	0.0068	0.0377	0.0035	0.01	0.00685	0.04	0.00869	0.06	Marked Damage Region
K4	C10-65×65-10-12	0.0169	0.192	0.0880	0.0089	0.0068	0.0377	0.0035	0.01	0.00685	0.04	0.00869	0.06	Marked Damage Region
K4	C10-65×65-10-12	0.0169	0.192	0.0880	0.0089	0.0068	0.0377	0.0035	0.01	0.00685	0.04	0.00869	0.06	Marked Damage Region
K3	C10-65×65-5-12	0.0170	0.192	0.0885	0.0061	0.0028	0.0439	0.0035	0.01	0.00685	0.04	0.00869	0.06	Advanced Damage Region
K1	C10-30×80-5-12	0.0172	0.192	0.0896	0.0048	0.0029	0.0549	0.0035	0.01	0.00843	0.04	0.01091	0.06	Advanced Damage Region
K2	C10-30×80-10-12	0.0171	0.192	0.0891	0.0085	0.0065	0.0514	0.0035	0.01	0.00843	0.04	0.01091	0.06	Advanced Damage Region
K2	C10-30×80-10-12	0.0171	0.192	0.0891	0.0085	0.0065	0.0514	0.0035	0.01	0.00843	0.04	0.01091	0.06	Advanced Damage Region
K2	C10-30×80-10-12	0.0171	0.192	0.0891	0.0085	0.0065	0.0514	0.0035	0.01	0.00843	0.04	0.01091	0.06	Advanced Damage Region
K2	C10-30×80-10-12	0.0171	0.192	0.0891	0.0085	0.0065	0.0514	0.0035	0.01	0.00843	0.04	0.01091	0.06	Advanced Damage Region
K1	C10-30×80-5-12	0.0172	0.192	0.0896	0.0048	0.0029	0.0549	0.0035	0.01	0.00843	0.04	0.01091	0.06	Advanced Damage Region

APPENDIX J

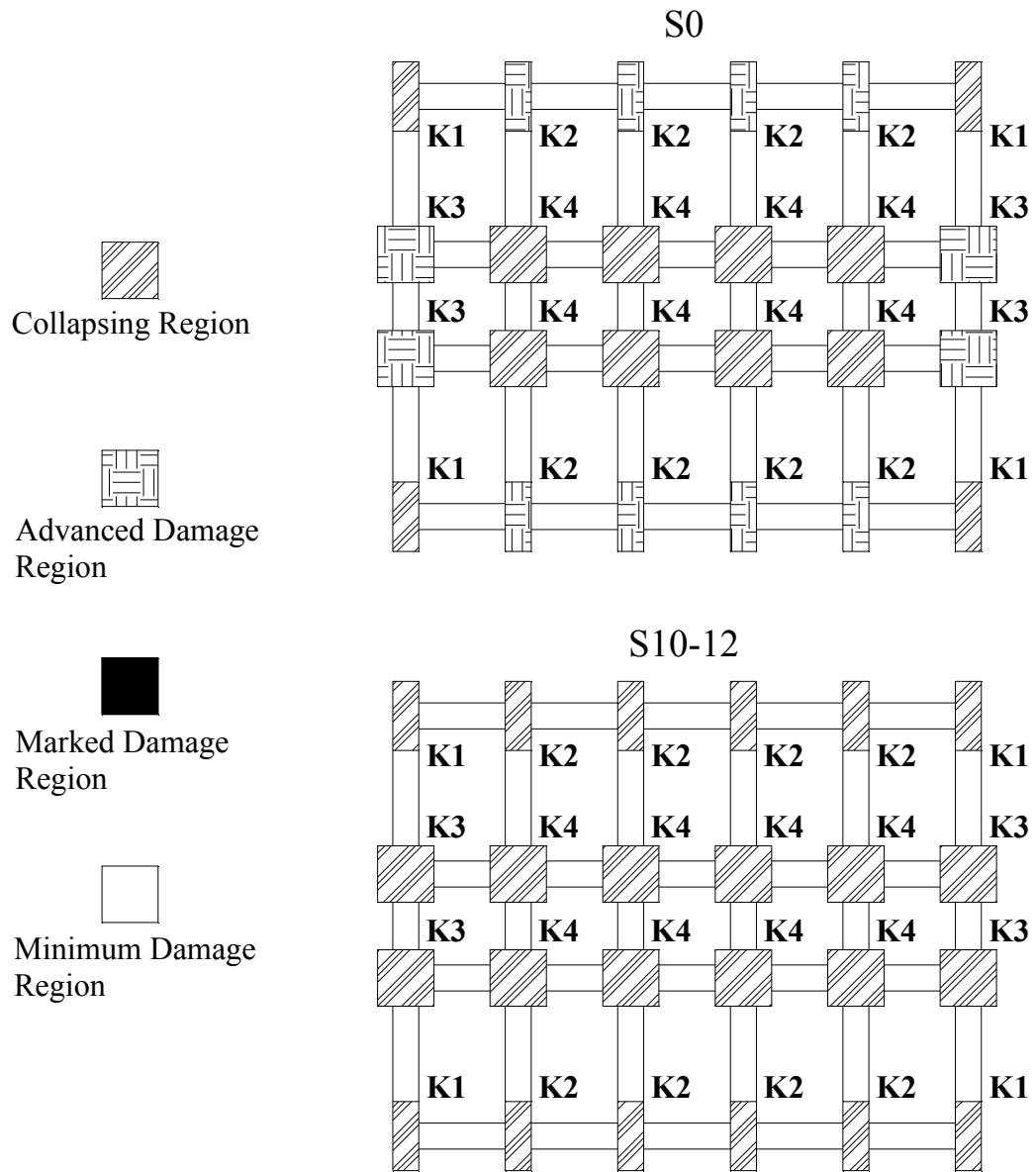


Figure J.1 : The view of damage levels of base columns of S0 ve S10-12 buildings on plan for SYLMAR, 1994.

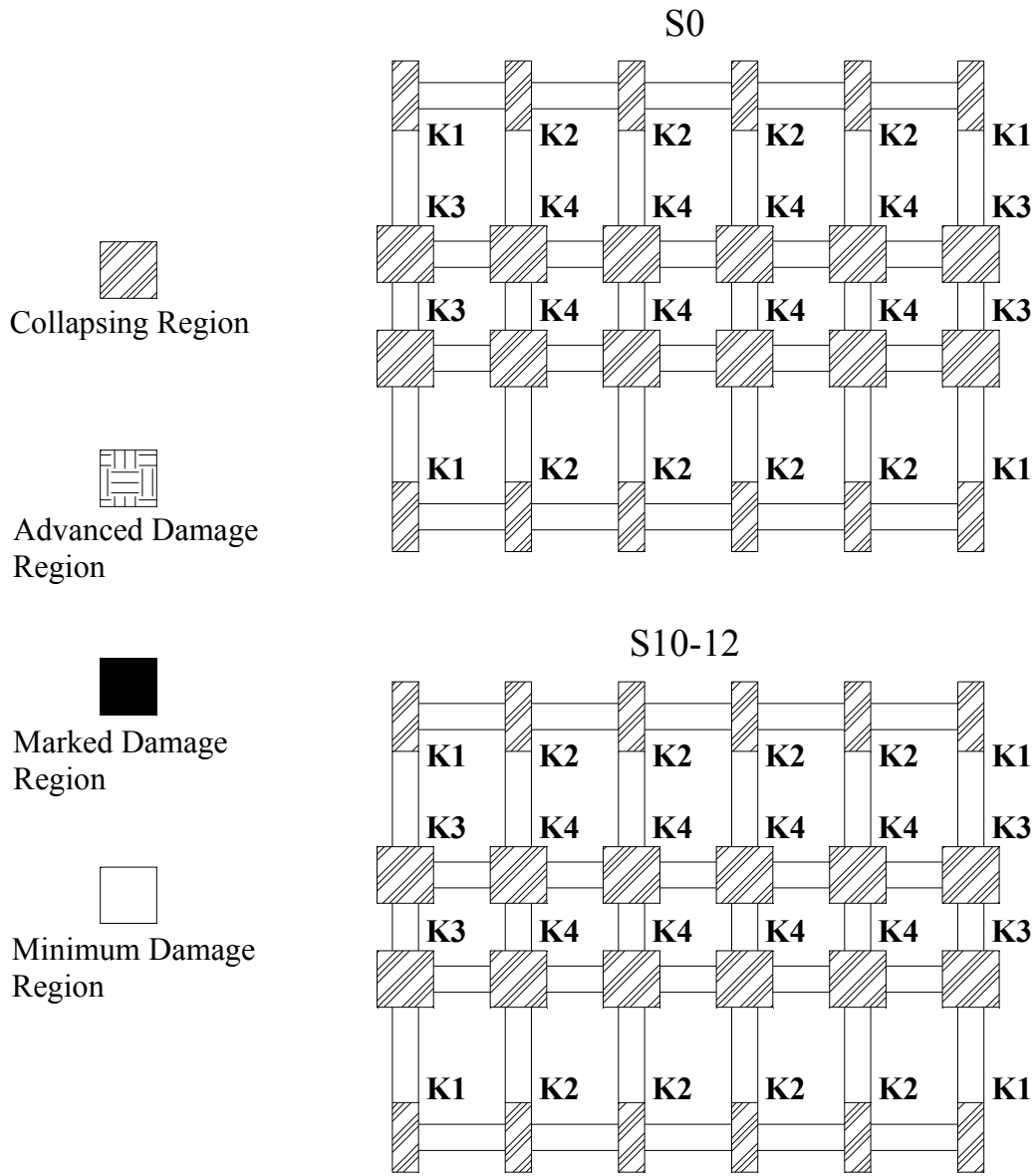


Figure J.2 : The view of damage levels of base columns of S0 ve S10-12 buildings on plan for KOBE, 1995.

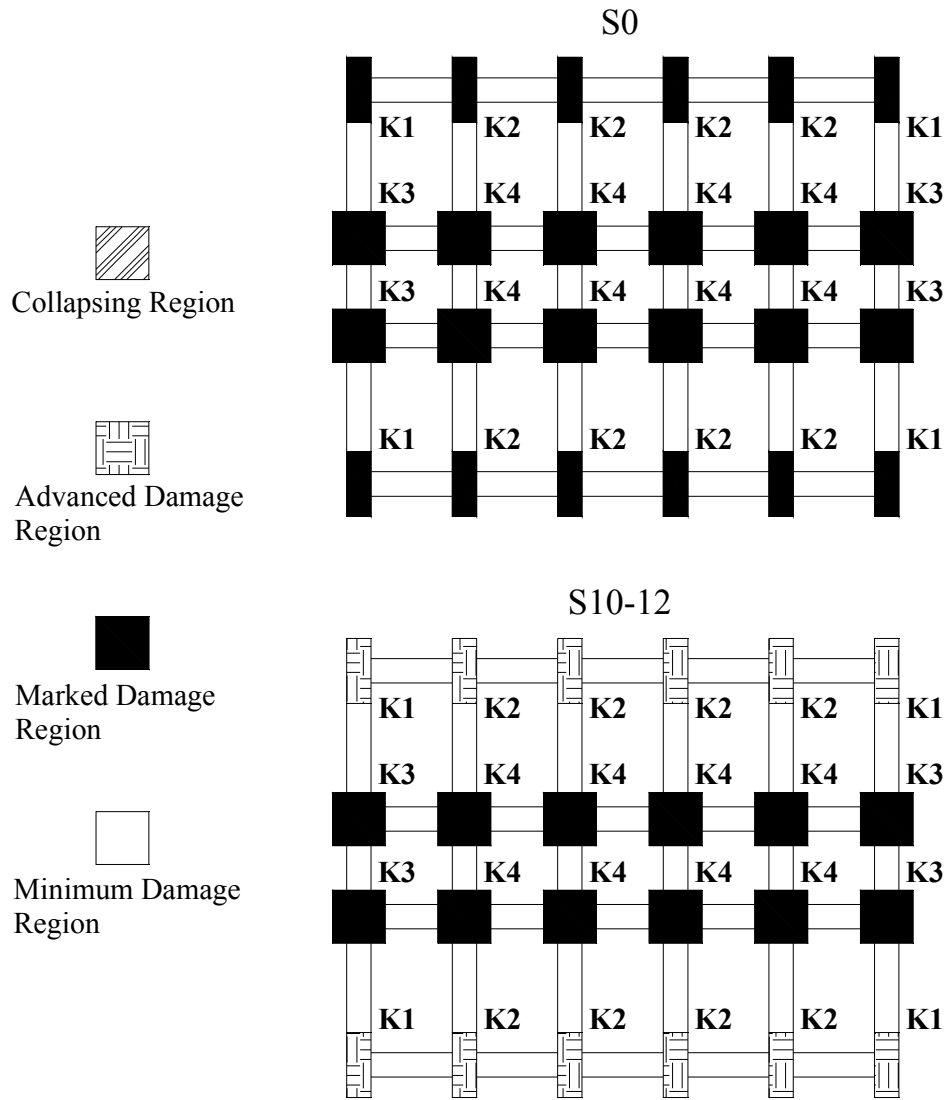


Figure J.3 : The view of damage levels of base columns of S0 ve S10-12 buildings on plan for BİNGÖL, 2003.

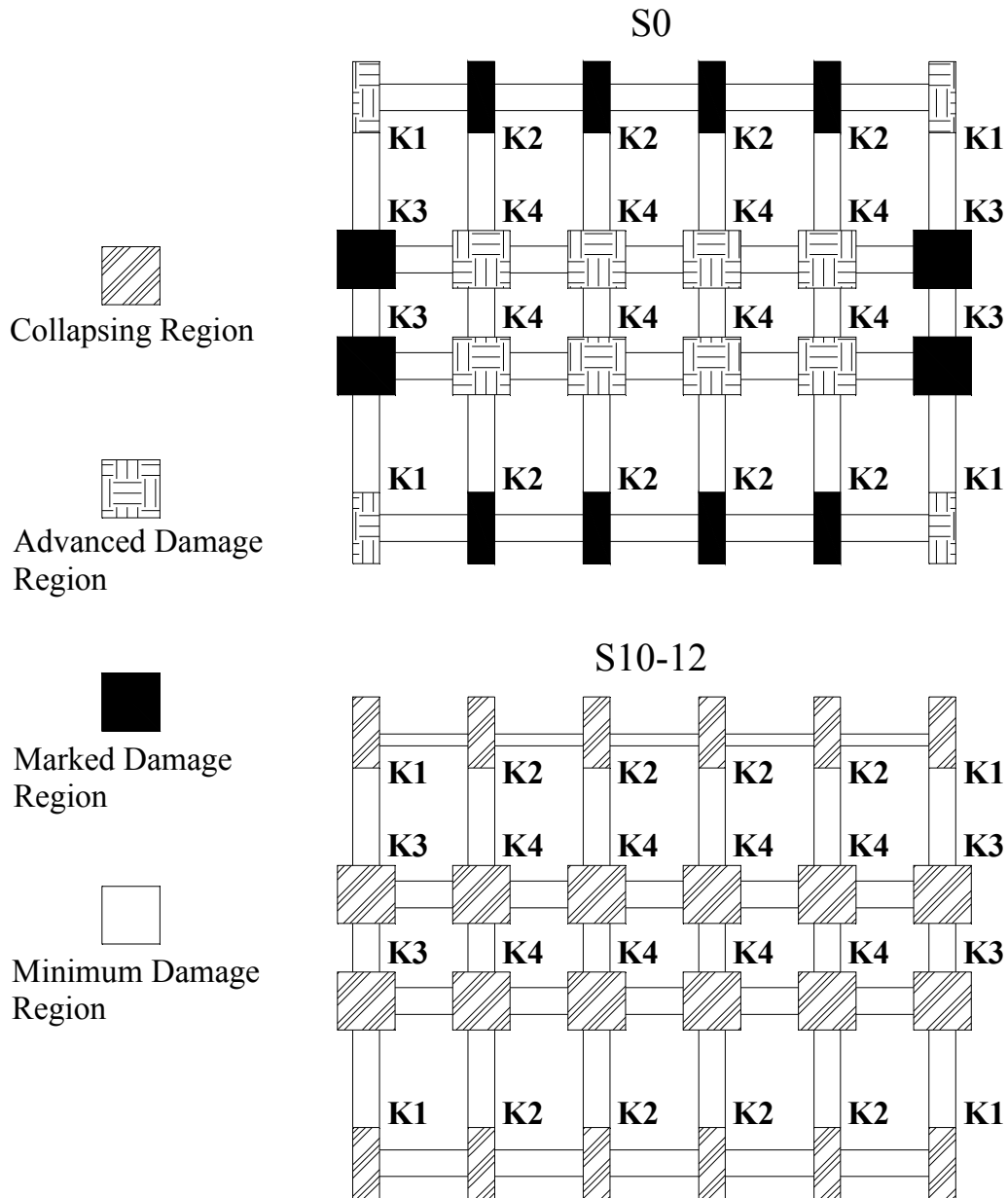


Figure J.4 : The view of damage levels of base columns of S0 ve S10-12 buildings on plan for MEXICO, 1980.

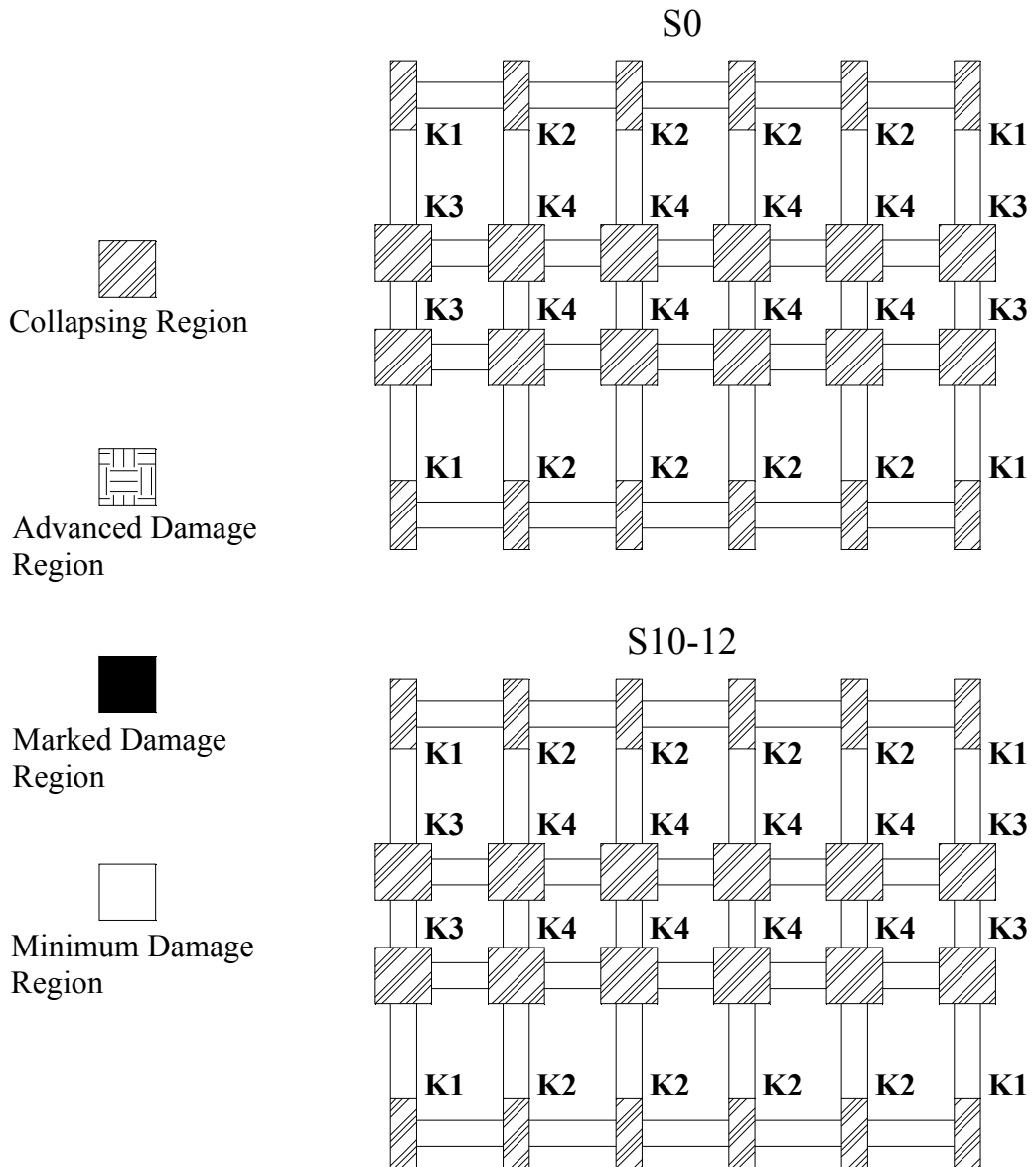


Figure J.5 : The damage levels of base columns of S0 ve S10-12 buildings on plan for DUZCE, 1999.

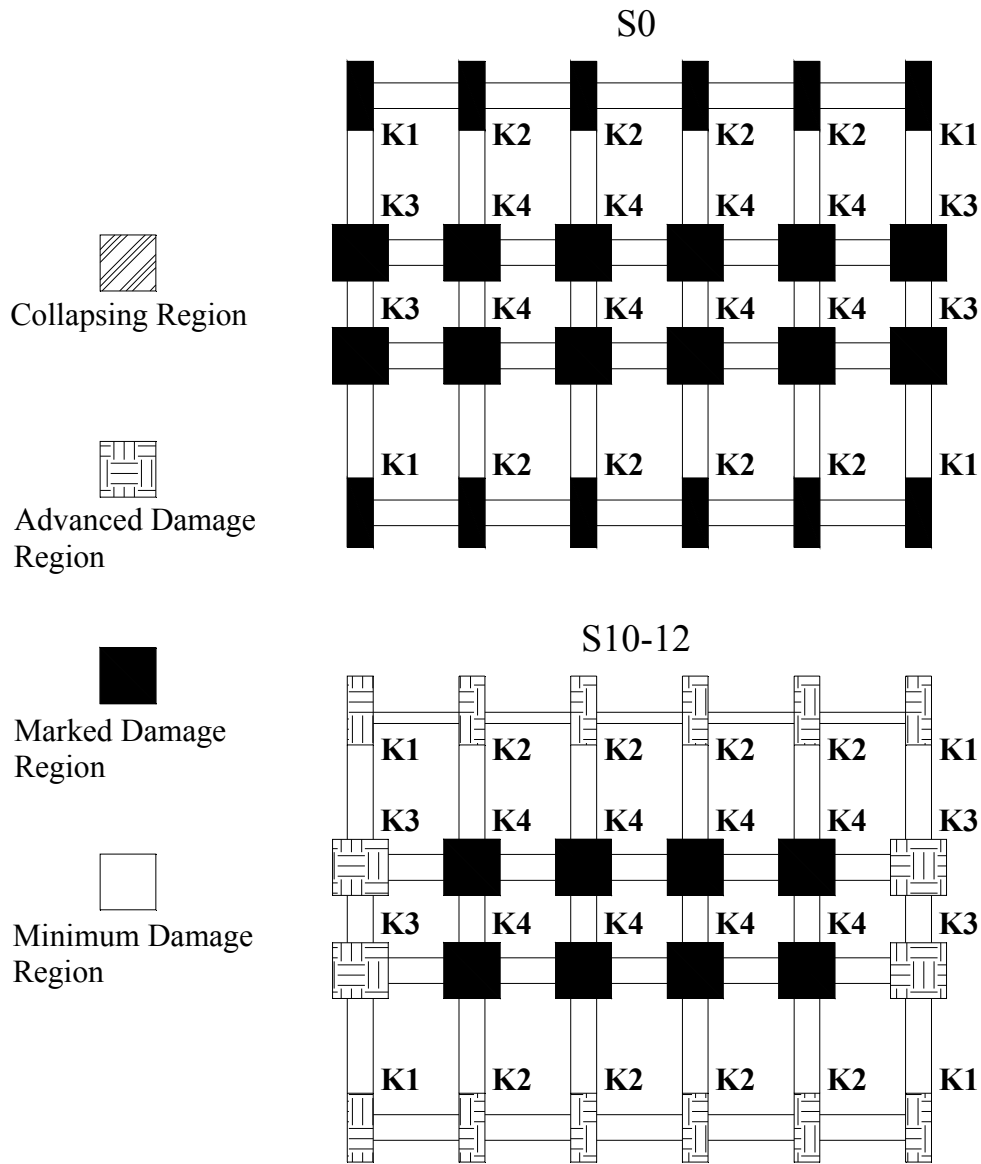


Figure J.6 : The damage levels of base columns of S0 ve S10-12 buildings on plan for KOCAELI, 1999.

CURRICULUM VITAE



Candidate's full name: Çağlar GÖKSU

Place and date of birth: Bolu-1977

Permanent Address: İstanbul Teknik Üniversitesi
İnşaat Fakültesi
Yapı ve Deprem Mühendisliği Laboratuvarı
Maslak-Sarıyer/ İSTANBUL

Universities and Colleges attended:

M.Sc., Structural Engineering, Trakya University Institute of Science and Technology, Çorlu, 2001-2004

B.Sc., Civil Engineering, Kocaeli University Engineering Faculty, Kocaeli, 1995-2000

Publications:

International Reviewed Journal Papers :

- **C.Goksu,** A. Polat, A. Ilki, 2011. An Attempt for Seismic Retrofit of Existing Sub-Standard RC Members under Reversed Cyclic Flexural Effects, *ASCE, Journal of Composites for Construction*, CCENG-517R1, doi. 10.1061/(ASCE)CC.1943-5614.0000256 (accepted to be published).
- P. Inci, **C. Goksu,** A. Ilki, 2012. Effects of Reinforcement Corrosion on the Performance of RC Frame Buildings Subjected to Seismic Actions (submitted to *ASCE, Journal of Performance of Constructed Facilities*).

International Conference Papers:

- M. Comert, **C. Goksu,** C. Cosgun, M. Ozubek and A. Ilki, 2010. Increasing Deformability of FRP Confined Low and Medium Strength Concrete through a Cement Based Mortar Layer, *Advances in Civil Engineering*, 27-30 September, Karadeniz Technical University, Trabzon, Turkey.
- **C. Goksu,** A. Ilki, N. Kumbasar, 2010. Failure Mechanisms of Old and New Type RC Columns after Reinforcement Corrosion, *Joint Symposium on Concrete Engineering*, 9 June, Istanbul, Turkey.

- M. Comert, **C. Goksu**, A. Ilki, 2010. Towards a Tailored Stress-Strain Behavior for FRP Confined Low Strength Concrete, 2010 PCI Annual Convention/Exhibition&Third International Fib Congress, 29 May-02 June, Washington, U.S.A..
- **C.Goksu**, E. Binbir, A. Ilki, N. Kumbasar, 2009. Seismic Behavior of RC Columns with Corroded Deformed Reinforcing Bars, Asian-Pacific Network of Centers for Earthquake Engineering Research Workshop, 13-14 August, Illinois, U.S.A., (CD-ROM).
- M. Comert, **C. Goksu**, A. Ilki, 2009. External Confinement of Concrete with Post-Tensioned GFRP Sheets-A Pilot Study, 9th International Symposium on Fiber Reinforced Polymer Reinforcement for Concrete Structures, 13–15 July, Sydney, Australia.
- **C. Goksu**, B. Demirtas, C. Demir, A. Ilki, N. Kumbasar, 2008. Seismic Behavior of Low Strength RC Columns with Corroded Plain Bar Reinforcement, The 14th World Conference on Earthquake Engineering, Paper ID: 12-01-0089, 12-17 October Beijing, China, (CD-ROM).
- A. Ilki, **C. Goksu**, C. Demir, N. Kumbasar, 2007. Seismic Analysis of a RC Frame Building with FRP Retrofitted Infill Walls, 6th Fracture Mechanics of Concrete and Concrete Structures, Vol.2, pp.1167-1176, 17-22 June, Catania, Italy.
- A. Ilki, C. Demir, **C. Goksu**, N. Kumbasar, 2006. Prefabricated SFRC Panels for Occupant Friendly Seismic Retrofit of Reinforced Concrete Columns, 8th National Conference on Earthquake Engineering, Paper No:1742, 18-22 April, San Francisco, USA, (CD-ROM).
- **C. Goksu**, C. Demir, K. Darilmaz, A. Ilki, N. Kumbasar, 2006. Static Nonlinear Analysis of a Retrofitted Typical Reinforced Concrete Building in Turkey, Paper No:690, 18-22 April, 8th National Conference on Earthquake Engineering, San Francisco, USA, (CD-ROM).

National Conference Papers

- P. Inci, **C. Goksu**, A. Ilki, 2011. Effect of Corrosion on RC Frames under Seismic Loading, 30 May-3 June, *Seventh National Conference on Earthquake Engineering*, Istanbul, Turkey.
- **C. Goksu**, H.Yıldız, A. Ilki, 2011. The Effects of Lap Spliced Low Strength RC Columns on Structural Performance under Different Axial Loads, 14-15 May, Meeting of Structural Mechanics Laboratories, Kocaeli, Turkey.